

Georgia State University

ScholarWorks @ Georgia State University

---

Biomedical Sciences Dissertations

Institute for Biomedical Sciences

---

12-16-2024

## Pharmacological Interventions of SARS-CoV-2, Effect of Prior Disease History on Measles-like Disease, and Molecular Characterization of the Nipah Virus Polymerase

Josef D. Wolf  
*Georgia State University*

Follow this and additional works at: [https://scholarworks.gsu.edu/biomedical\\_diss](https://scholarworks.gsu.edu/biomedical_diss)

---

### Recommended Citation

Wolf, Josef D., "Pharmacological Interventions of SARS-CoV-2, Effect of Prior Disease History on Measles-like Disease, and Molecular Characterization of the Nipah Virus Polymerase." Dissertation, Georgia State University, 2024.

[https://scholarworks.gsu.edu/biomedical\\_diss/20](https://scholarworks.gsu.edu/biomedical_diss/20)

This Dissertation is brought to you for free and open access by the Institute for Biomedical Sciences at ScholarWorks @ Georgia State University. It has been accepted for inclusion in Biomedical Sciences Dissertations by an authorized administrator of ScholarWorks @ Georgia State University. For more information, please contact [scholarworks@gsu.edu](mailto:scholarworks@gsu.edu).

Pharmacological Interventions of SARS-CoV-2, Effect of Prior Disease History on Measles-like  
Disease, and Molecular Characterization of the Nipah Virus Polymerase

by

Josef Dieter Wolf

Under the Direction of Richard K. Plemper, Ph.D.

A Dissertation Submitted in Partial Fulfillment of the Requirements for the Degree of

Doctor of Philosophy

in the Institute for Biomedical Sciences

Georgia State University

2024



## ABSTRACT

This dissertation focuses on enhancing our understanding of severe acute respiratory syndrome coronavirus 2 (SARS-CoV-2), respiratory syncytial virus (RSV), measles virus (MeV), and Nipah virus (NiV). These viruses represent significant public health challenges, with the potential to cause long-term health issues and substantial economic impacts. By developing effective treatments that interrupt viral transmission, exploring how past infections influence current susceptibility, pinpointing drug targets, advancing our structural knowledge of viral proteins, and gaining deeper mechanistic insights into pathogen replication, we can reduce disease-related complications and healthcare costs.

The therapeutic efficacy of several treatments was evaluated using the ferret and Roborovski dwarf hamster models of severe COVID-19-like lung disease. These treatments included molnupiravir, Paxlovid-like nirmatrelvir/ritonavir, GS-621763 (an oral prodrug of remdesivir), 4'-fluorouridine (4'-FIU), EDP-235, and BioBlock (a neutralizing antibody targeting the spike protein delivered via nasal spray). In the ferret model, molnupiravir, GS-621763, EDP-235, and BioBlock effectively prevented SARS-CoV-2 transmission between ferrets, while Paxlovid-like nirmatrelvir/ritonavir did not fully inhibit transmission. Additionally, 4'-FIU demonstrated strong antiviral activity against SARS-CoV-2 Wuhan lineage A and variants of concern (VOCs) alpha, delta, and gamma in ferrets, as well against RSV A in mice. In Roborovski dwarf hamsters, molnupiravir significantly reduced severe lung injury and viral lung titers for VOCs delta, gamma, and omicron. Similarly, Paxlovid-like nirmatrelvir/ritonavir reduced lung titers for VOCs delta and omicron in these hamsters.

This thesis also highlights the therapeutic potential of GHP-88309, a broad-spectrum paramyxovirus polymerase inhibitor, which can effectively counteract measles-like immune amnesia. It identifies an immune-priming mechanism that may explain the occurrence of bacterial superinfections following measles virus infection, offering insights that could reshape future treatment approaches for measles. Additionally, the thesis thoroughly evaluates the use of allosteric polymerase inhibitors as chemical probes to enhance the structural resolution of essential viral proteins. Furthermore, it expands our understanding of Nipah virus replication dynamics, revealing a promising target site for drug development.

INDEX WORDS: SARS-CoV-2, CDV, Nipah virus, phosphoprotein, polymerase inhibitor

Copyright by  
Josef Dieter Wolf  
2024

Pharmacological Interventions of SARS-CoV-2, Effect of Prior Disease History on Measles-like  
Disease, and Molecular Characterization of the Nipah Virus Polymerase

by

Josef Dieter Wolf

Committee Chair: Richard K. Plemper, Ph.D.

Committee: Margo A. Brinton, Ph.D.

Anice C. Lowen, Ph.D.

Electronic Version Approved:

Office of Academic Assistance – Graduate Programs

Institute for Biomedical Sciences

Georgia State University

November 2024

## DEDICATION

I dedicate this dissertation to my family. First and foremost, I extend my deepest gratitude to my wife, Sandra, and my son, Benicio, for their unwavering love and support (and to Sal as well). I am also profoundly thankful to my parents, Dieter and Denise, for their constant and immeasurable support throughout my entire journey.

## ACKNOWLEDGEMENTS

I would like to express my deepest gratitude to my mentor, Dr. Richard K. Plemper, for his invaluable support and guidance over the years. Your encouragement has instilled in me a genuine passion for science and has prepared me for my future career as a scientist.

I am also grateful to my committee members, Dr. Margo A. Brinton and Dr. Anice C. Lowen, for their support and the stimulating discussions that have significantly contributed to the development of my dissertation projects.

A special thank you goes to my friend and colleague, Dr. Robert M. Cox, for your countless support and advice throughout my PhD journey.

Additionally, I extend my thanks to all members of the Plemper and Cox labs, with a special mention to my closest friends, Dr. Carolin M. Lieber, Sujay F. Greenlund, Amir Karimi, Alexander I. Leach, and Michael R. Serrine (my support team). Michael, I especially appreciate our enlightening conversations about paramyxovirus protein-protein interactions. I would also like to thank a previous member of the Plemper lab, Venice DuPont, for providing a blueprint for my Nipah virus study.

Finally, I want to thank the Division of Animal Resources and the High Containment Core for their assistance and support throughout these years.

## TABLE OF CONTENTS

ACKNOWLEDGEMENTS .....	V
LIST OF TABLES .....	IX
LIST OF FIGURES.....	X
<b>1. INTRODUCTION.....</b>	<b>1</b>
<b>1.1 Therapeutics and Developmental Candidates of Focus.....</b>	<b>1</b>
<b>1.2 Featured Viruses of Concern .....</b>	<b>6</b>
<b>1.3 Severe Acute Respiratory Syndrome Coronavirus 2.....</b>	<b>8</b>
<b>1.4 Respiratory Syncytial Virus .....</b>	<b>10</b>
<b>1.5 Measles and Canine Distemper Virus .....</b>	<b>12</b>
<b>1.6 Nipah Virus .....</b>	<b>14</b>
<b>2. RESULTS AND DISCUSSIONS .....</b>	<b>17</b>
<b>2.1 Research topic: SARS-CoV-2 .....</b>	<b>17</b>
<b><i>2.1.1 Therapeutically Administered Ribonucleoside Analogue MK-4482/EIDD-2801</i></b>	
<b><i>Blocks SARS-CoV-2 Transmission in Ferrets .....</i></b>	<b>18</b>
<b><i>2.1.2 SARS-CoV-2 VOC Type and Biological Sex Affect Molnupiravir Efficacy in Severe</i></b>	
<b><i>COVID-19 Dwarf Hamster Model .....</i></b>	<b>26</b>
<b><i>2.1.3 Comparing Molnupiravir and Nirmatrelvir/Ritonavir Efficacy and the Effects on</i></b>	
<b><i>SARS-CoV-2 Transmission in Animal Models .....</i></b>	<b>39</b>

<b>2.1.4 Oral Prodrug of Remdesivir Parent GS-441524 is Efficacious Against SARS-CoV-2 in Ferrets .....</b>	<b>53</b>
<b>2.1.5 4'-Fluorouridine is an Oral Antiviral that Blocks Respiratory Syncytial Virus and SARS-CoV-2 Replication .....</b>	<b>63</b>
<b>2.1.6 EDP-235, a Novel Small Molecule Inhibitor of SARS-CoV-2 3CLpro for the Treatment of COVID-19.....</b>	<b>86</b>
<b>2.1.7 Anti-SARS-CoV-2 Antibodies in a Nasal Spray Efficiently Block Viral Transmission Between Ferrets .....</b>	<b>98</b>
<b>2.2 Research Topic: MeV and CDV .....</b>	<b>110</b>
<b>2.2.1 Therapeutic Mitigation of Measles-like Immune Amnesia and Exacerbated Disease after Prior Respiratory Virus Infections in Ferrets.....</b>	<b>110</b>
<b>2.2.2 Small-molecule Polymerase Inhibitor Protects Non-Human Primates from Measles and Reduces Shedding .....</b>	<b>126</b>
<b>2.2.3 Structural Basis of Paramyxo- and Pneumovirus Polymerase Inhibitors with Non-Nucleoside Small-Molecule Antivirals .....</b>	<b>133</b>
<b>2.3 Research Topic: NiV .....</b>	<b>155</b>
<b>2.3.1 Characterization of the Three-way Interplay Between Nipah Virus Phosphoprotein X-domain, the Polymerase, N-tail, and the N-core .....</b>	<b>155</b>
<b>3. CONCLUSIONS.....</b>	<b>171</b>
<b>3.1 Research Topic: SARS-CoV-2 .....</b>	<b>171</b>



<b>3.1.1 Summary of Key SARS-CoV-2 Findings .....</b>	<b>171</b>
<b>3.1.2 Evaluating Therapeutic Options for Treating SARS-CoV-2 .....</b>	<b>173</b>
<b>3.2 Research Topic: MeV and CDV .....</b>	<b>176</b>
<b>3.2.1 Summary of Key MeV and CDV Findings .....</b>	<b>176</b>
<b>3.2.2 Secondary Bacterial Superinfections and the Necessity for Enhanced Treatment         Strategies for Viral Infections.....</b>	<b>177</b>
<b>3.3 Research Topic: NiV .....</b>	<b>180</b>
<b>3.3.1 Summary of Key NiV Findings .....</b>	<b>180</b>
<b>3.3.2 Limitations of Using High-throughput Screening to Identify Novel Antivirals NiV         Targets .....</b>	<b>182</b>
<b>4. FUTURE DIRECTIONS .....</b>	<b>183</b>
<b>4.1 Essential Criteria of a Theoretical Chimeric Virus that Replicates using a NiV Polymerase         in a CedV Genetic Background.....</b>	<b>183</b>
<b>4.2 Strategies for Development of a Replication-competent Virus Utilizing a Native NiV         Polymerase, with Potential for Evaluation of Suitability for BSL3 Downgrading...</b>	<b>186</b>
<b>4.2.1 Generation of a Chimeric Virus - Approach One .....</b>	<b>186</b>
<b>4.2.2 Generation of a Chimeric Virus - Approach Two.....</b>	<b>187</b>
<b>4.2.3 Generation of a Chimeric Virus - Approach Three.....</b>	<b>188</b>
<b>REFERENCES.....</b>	<b>189</b>
<b>VITAE .....</b>	<b>208</b>

## LIST OF TABLES

1.1	Table 1 Therapeutics and Developments Candidates of Focus .....	3
2.1.2	Table 1 Analysis of Dwarf Hamster Survival after Infection with Different VOCs.....	31
2.1.2	Table 2 Analysis of Biological Sex as a Variable in Molnupiravir Efficacy in Dwarf Hamsters.....	33
2.1.3	Table 1 Single Dose Pharmacokinetics of Nirmatrelvir or Nirmatrelvir/Ritonavir in Roborovski Dwarf Hamster and Human Plasma.....	42
2.1.3	Table 2 Single Dose Pharmacokinetics of Nirmatrelvir/Ritonavir in Ferrets and Human Plasma .....	44
2.1.6	Table 1 Antiviral Activity of EDP-235 Against Infectious SARS-CoV-2.....	89
2.1.6	Table 2 Potency of EDP-235 Against Select Nirmatrelvir-associated Variants .....	89
2.1.6	Table 3 Broad-spectrum Activity of EDP-235 Against Human Coronaviruses .....	90
2.1.6	Table 4 EDP-235 Inhibits Zoonotic Coronaviruses .....	90
2.2.3	Table 1 Fully Characterized Compound Classes .....	139
2.2.3	Table 2 Compound Classes with Incomplete Biochemical Characterization .....	140
2.3.1	Table 1 Statistical Analysis of L-binding-deficient Mutant Transcomplementations with A688R <sup>a</sup> .....	163

## LIST OF FIGURES

1.2	Figure 1 Structure of SARS-CoV-2 .....	7
1.2	Figure 2 Genome Organization of Featured Paramyxoviruses .....	7
1.6	Figure 3 Transmission of Nipah Virus .....	16
1.6	Figure 4 Domain Organization of Nipah Virus Nucleocapsid Protein .....	16
2.1.1	Figure 1 SARS-CoV-2 Infects the Upper Respiratory Tract of Ferrets .....	20
2.1.1	Figure 2 Therapeutic MK-4482/EIDD-2801 is Orally Efficacious Against SARS-CoV-2 in Ferrets .....	21
2.1.1	Figure 3 Therapeutic Oral Treatment with MK-4482/EIDD-2801 Prevents Contact Transmission .....	22
2.1.2	Figure 1 Efficacy of NHC Against VOC in Cultured Cells and Primary HAEs .....	28
2.1.2	Figure 2 Therapeutic Molnupiravir is Efficacious Against a Panel of VOC in Ferrets .....	29
2.1.2	Figure 3 VOC Pathogenesis in Roborovski Dwarf Hamsters .....	30
2.1.2	Figure 4 Effects of Therapeutic Molnupiravir on SARS-CoV-2 Lung Virus Load .....	32
2.1.2	Figure 5 Single Oral Dose PK Properties of Molnupiravir in Roborovski Dwarf Hamsters	34
2.1.2	Figure 6 Molnupiravir Mitigates Lung Histopathology in VOC-infected Dwarf Hamsters .....	35
2.1.3	Figure 1 In Vitro Antiviral Activity of Nirmatrelvir .....	40
2.1.3	Figure 2 Efficacy of Paxlovid and Molnupiravir in Roborovski Dwarf Hamsters .....	41
2.1.3	Figure 3 VOC Omicron Lung Virus Load Following Antiviral Treatment .....	43
2.1.3	Figure 4 Efficacy of Paxlovid in Ferrets .....	44

2.1.3	Figure 5 Effect of Treatment with Paxlovid or Molnupiravir on SARS-CoV-2 Transmission	45
2.1.3	Figure 6 Prophylactic Treatment of Close Contacts with Paxlovid or Molnupiravir	46
2.1.4	Figure 1 Antiviral Potency of Remdesivir Analog GS-621763	55
2.1.4	Figure 2 Prophylactic Efficacy of GS-621763	56
2.1.4	Figure 3 Therapeutic Efficacy of GS-621763	57
2.1.4	Figure 4 GS-621763 Blocks Replication and Transmission of SARS-CoV2 VOC $\gamma$ $\alpha$ , Schematic of the Efficacy and Contract Transmission Study Design	58
2.1.5	Figure 1 4'-FIU is a Potent Broad-spectrum Antiviral	63
2.1.5	Figure 2 4'-FIU Induces a Delay Chain Stalling of RSV and SARS-CoV-2 RdRP	64
2.1.5	Figure 3 4'-FIU is Efficiently Anabolized in HAE cells and is Efficacious in Human Airway Epithelium Organoids	65
2.1.5	Figure 4 Therapeutic Oral Efficacy of 4'-FIU in the RSV Mouse Model	66
2.1.5	Figure 5 Efficacy of 4'-FIU Against SARS-CoV-2 Replication in HAE Organoids	67
2.1.5	Figure 6 Therapeutic Oral Efficacy of 4'-FIU Against Different SARS-CoV-2 Isolates in Ferrets	68
2.1.6	Figure 1 EDP-235 Inhibits SARS-CoV-2 3CLpro and Binds Reversibly to 3CLpro's Active Site	88
2.1.6	Figure 2 EDP-235 is Efficacious in a Prophylactic Syrian Hamster Model	91
2.1.6	Figure 3 EDP-235 Effectively Blocks Infection and Viral Transmission in Ferrets	92
2.1.7	Figure 1 Immunization Scheme Including Re-immunizations of Cows	100

2.1.7	Figure 2 The Ig Preparation Retrieved after Several Reimmunizations Shows High Potency in Blocking the In Vitro Interaction of ACE2 with the Tri S Proteins of Alpha, Delta, Omicron, and VOC Strains of SARS-CoV-2.....	101
2.1.7	Figure 3 Experimental Setup for Ferret Experiments .....	102
2.1.7	Figure 4 The Ig Preparation Effectively Inhibits Transmission of SARS-CoV-2 from Infected to Uninfected Ferrets .....	103
2.2.1	Figure 1 Therapeutic Treatment of Lethal CDV Infection in Ferrets.....	112
2.2.1	Figure 2 Ferret Model of CDV-induced Immune Amnesia.....	113
2.2.1	Figure 3 Therapeutic Efficacy of GHP-88309 Against recCDV-5804p NΔ425-479 .....	115
2.2.1	Figure 4 Fatal Lung Disease in Ferrets Infected with Respiratory Viruses prior to CDV Infection.....	116
2.2.1	Figure 5 Disease History Affects CDV-induced TFF Upregulation .....	118
2.2.1	Figure 6 Effect of Therapeutic Intervention on Severe Disease Outcomes .....	119
2.2.2	Figure 1 Single-dose Pharmacokinetics Study of ERDRP-0519 in Squirrel Monkeys .....	128
2.2.2	Figure 2 Effect of ERDRP-0519 on Manifestation of Clinical Signs in MeV-infected Squirrel Monkeys.....	129
2.2.2	Figure 3 Clinical Parameters of MeV Infection in Squirrel Monkeys .....	130
2.2.2	Figure 4 Histological Examination of Day 21 Post-infection .....	131
2.2.3	Figure 1 Architecture of the MeV L Protein.....	135
2.2.3	Figure 2 Channels and Loop Re-arrangements of the Mononegavirus Polymerase.....	137
2.2.3	Figure 3 Overview of Viral mRNA Capping and Methylation.....	138
2.2.3	Figure 4 GHP-88309, ERDRP-0519, JNJ-8003, and AVG-233 Compound Structures .....	140

2.2.3	Figure 5 Spatial Arrangement of Resistance Mutations .....	142
2.2.3	Figure 6 In Silico Docking of GHP-88309 in MeV L.....	144
2.2.3	Figure 7 Docking of ERDRP-0519 into MeV L.....	145
2.2.3	Figure 8 JNJ-8003 Bound to RSV L and AVG-233 Docked into RSV L .....	147
2.2.3	Figure 9 GHP-88309, ERDRP-0519, JNJ-8003, and AVG-233 Sequence Identity Analysis of Resistance Sites .....	148
2.2.3	Figure 10 GHP-88309, ERDRP-0519, JNJ-8003, and AVG-233 Sequence Identity Analysis of Predicted Interacting Residues.....	149
2.2.3	Figure 11 Distinct Binding Sites of GHP-88309, ERDRP-0519, AVG-233, and JNJ-8003 in the Mononegavirus Polymerase.....	150
2.3.1	Figure 1 Probing the N-More Binding Interface of NiV P-XD .....	157
2.3.1	Figure 2 Identification of an L Binding Microdomain in NiV P-XD .....	159
2.3.1	Figure 3 Evidence for an N-core Interacting Face in P-XD .....	161
2.3.1	Figure 4 Transcomplementation of L, N-MoRE, and N-core Binding-deficient Mutants	162
2.3.1	Figure 5 Double Mutant Tanscomplementations.....	164
2.3.1	Figure 6 Mechanistic Hypothesis of P-XD:N-MoRE Interaction with N-core .....	167
4.1	Figure 1 2D Schematic of Nipah Virus Phosphoprotein.....	184
4.1	Figure 2 Genome Organization of Proposed Recombinant Chimeric Virus Constructs..	186

## 1. INTRODUCTION

The primary objectives of this dissertation were to: i) identify broad-spectrum polymerase inhibitors targeting severe acute respiratory syndrome coronavirus 2 (SARS-CoV-2) and respiratory syncytial virus (RSV); ii) assess the efficacy of the direct-acting antiviral GHP-88309 for paramyxovirus infections, while also evaluating how prior respiratory virus infections influence measles severity; and iii) functionally and biochemically map the three binding interfaces of the Nipah virus (NiV) phosphoprotein's X-domain (XD). The findings presented here have advanced the pre-clinical development of antivirals for SARS-CoV-2 and RSV and highlighted a therapeutic window to prevent SARS-CoV-2 transmission. Additionally, this work enhances the understanding of how previous disease history can affect subsequent infections, provides mechanistic insights into NiV replication, and identifies a promising druggable target for combating NiV infection.

### 1.1 Therapeutics and Developmental Candidates of Focus

Many of the therapeutics discussed in this dissertation target the viral RNA-dependent RNA polymerase (RdRP). These antivirals are generally categorized into nucleoside and non-nucleoside inhibitors (Denel-Bobrowska & Olejniczak, 2022; Tian et al., 2021). Nucleoside inhibitors act as structural analogues of nucleosides, incorporating into the viral genome and interfering with replication through either chain-terminating or non-chain-terminating mechanisms. Chain-terminating nucleoside analogues prevent the extension of nascent RNA, while non-chain-terminating analogues allow RNA extension but induce lethal mutagenesis (Denel-Bobrowska & Olejniczak, 2022; Johnson & Dangerfield, 2021; Kabinger et al., 2021; C. M. Lieber & R. K. Plemper, 2022). Non-nucleoside, or allosteric, inhibitors disrupt viral replication

by altering the polymerase's conformation through alteration of the protein's intrinsic motions (Davis et al., 2015).

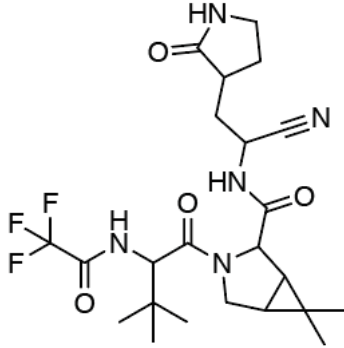
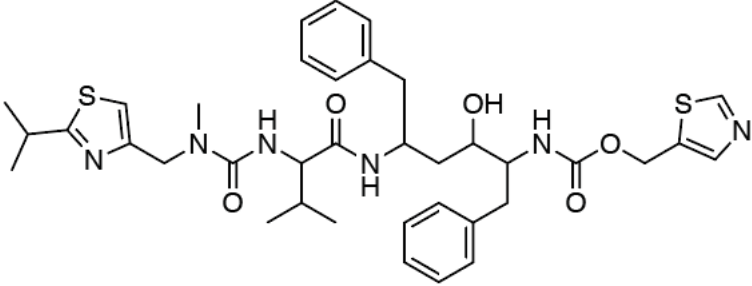
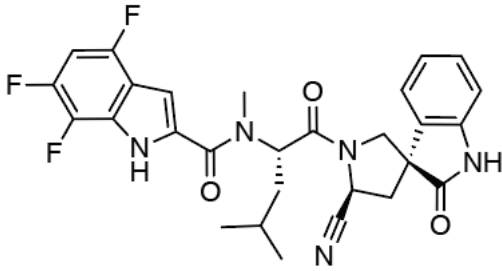
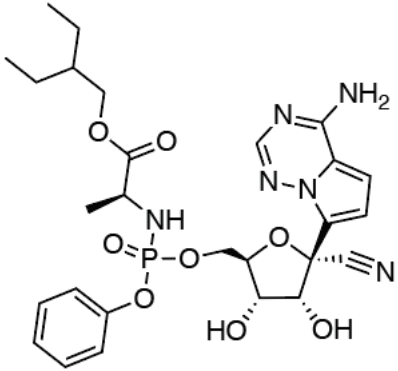
The viral RdRP is inherently a highly attractive therapeutic target for several reasons. Firstly, the viral polymerase is crucial for the enzymatic processes required for viral genome replication and transcription, and it is often highly conserved across different virus genera (Fearn & Plemper, 2017; Vicenti et al., 2021). This conservation can lead to a broad-spectrum antiviral activity profile. Additionally, escape mutations that arise due to the selective pressure of specific antivirals are usually poorly tolerated and can impose a fitness penalty on the virus (Kabinger et al., 2021), reducing the likelihood of resistance development. Moreover, because RdRP lacks homologs in host cells, there is a lower risk of host-directed off-target effects (Campagnola et al., 2011), minimizing the potential for undesirable side effects.

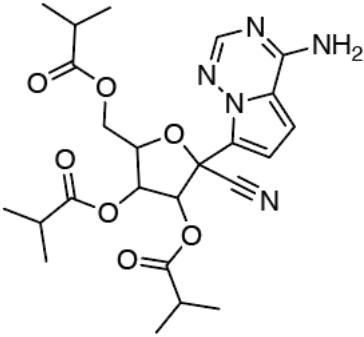
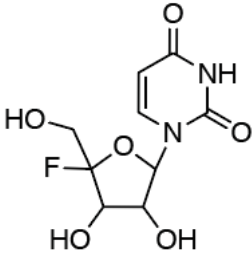
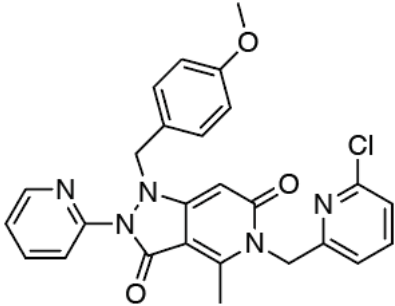
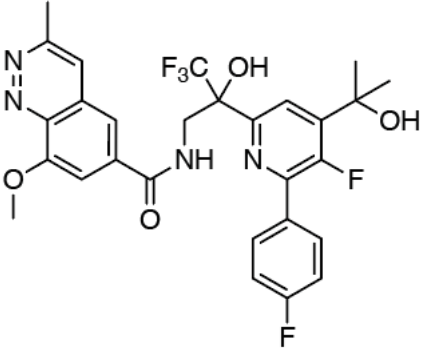
This dissertation explores therapeutics targeting three distinct viruses (Table 1): i) SARS-CoV-2: molnupiravir, ritonavir/nirmatrelvir, remdesivir, GS-621763, 4'-fluorouridine, EDP-235, and BioBlock; ii) RSV: 4'-fluorouridine, AVG-233, and JNJ-8003; and iii) measles virus: GHP-88309 and ERDRP-0519.

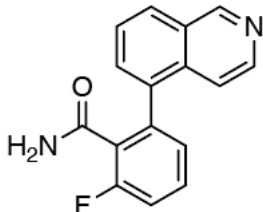
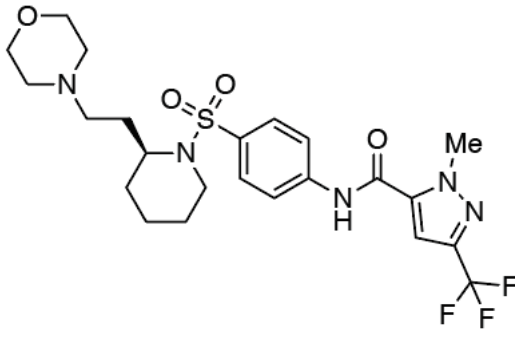
Molnupiravir is an orally administered prodrug of the non-chain terminating nucleoside analogue  $N^4$ -hydroxycytidine (NHC). It is converted to its active triphosphate form (NHC-TP), which integrates into the viral genome, leading to lethal mutagenesis (Kabinger et al., 2021). Paxlovid combines nirmatrelvir, a peptidomimetic targeting the SARS-CoV-2 3-chymotrypsin-like cysteine protease ( $3CL^{pro}$ ) active site, with ritonavir, which enhances nirmatrelvir's half-life by inhibiting cytochrome P450 enzymes CYP2D6 and CYP3A4 (Kumar et al., 1996; Carolin M.





Paxlovid: Nirmatrelvir	 <p>The chemical structure of Nirmatrelvir features a central bicyclic core (a bicyclo[2.2.1]heptane derivative) with a carbonyl group and a nitrogen atom. This core is substituted with a tert-butyl group, a trifluoromethyl group, and a side chain containing a nitrile group and a pyrrolidine ring.</p>	3CL <sup>pro</sup> inhibition
Paxlovid: Ritonavir	 <p>The chemical structure of Ritonavir is a complex molecule consisting of a central chiral center with multiple substituents. It includes a thiazole ring, a benzyl group, a hydroxyl group, and a thiazole ring connected via an amide linkage.</p>	CYP2D6 and CYP3A4 inhibition; improves nirmatrelvir half-life
EDP-235	 <p>The chemical structure of EDP-235 features a central bicyclic core with a nitrile group and a carbonyl group. It is substituted with a 2,4,6-trifluorophenyl group and a benzyl group.</p>	3CL <sup>pro</sup> inhibition
Remdesivir	 <p>The chemical structure of Remdesivir is a nucleoside analog. It features a ribose sugar ring with a cyano group at the 2' position and a phosphonate group at the 3' position. The phosphonate group is linked to a phenyl ring and a side chain containing a methyl group and a butyl group. The base is a pyrimidopyrimidinone derivative.</p>	Delayed chain termination

GS-621763		Delayed chain termination
4'-fluorouridine		Delayed chain termination
BioBlock	Not applicable	Neutralizing antibody; targets SARS-CoV-2 S protein
AVG-233		Blocks <i>de novo</i> polymerase initiation at the promoter
JNJ-8003		Blocks <i>de novo</i> polymerase initiation at the promoter

GHP-88309		Blocks <i>de novo</i> polymerase initiation at the promoter
ERDRP-0519		Prevents all phosphodiester bond formation

## 1.2 Featured Viruses of Concern

SARS-CoV-2, a positive-sense RNA virus from the family *Coronaviridae* (Figure 1) (Hu et al., 2021), and three negative-sense RNA viruses from the family *Paramyxoviridae*, RSV, measles virus (MeV), and Nipah virus (NiV) (Figure 2) (Aggarwal & Plemper, 2020), are major global public health concerns and are the primary focus of this dissertation. Since its emergence in 2020, SARS-CoV-2 has caused widespread devastation, with over 775 million reported cases and more than 7 million deaths globally (WHO, 2023b). Currently, three antivirals have been authorized for treatment of SARS-CoV-2 infections: molnupiravir, Paxlovid, and remdesivir (*Antivirals Agents, Including Antibody Products Summary Recommendations*, 2024).

In 2019, RSV was responsible for approximately 33 million infections and over 100,000 deaths among children under the age of five worldwide (Li et al., 2022). In the United States, RSV infections in people aged 65 and older lead to an estimated 60,000-160,000

hospitalizations and 6,000-10,000 deaths annually (CDC, 2023). Although ribavirin is the only FDA-approved antiviral for treating RSV in children, it is no longer recommended by the American Academy of Pediatrics due to having questionable efficacy data based on studies that relied on short-term outcome measures and lacked adequate controls (Ventre & Randolph, 2007), challenges with administration, significant side effects, a complex delivery system, and high treatment costs (Hoover et al., 2018).

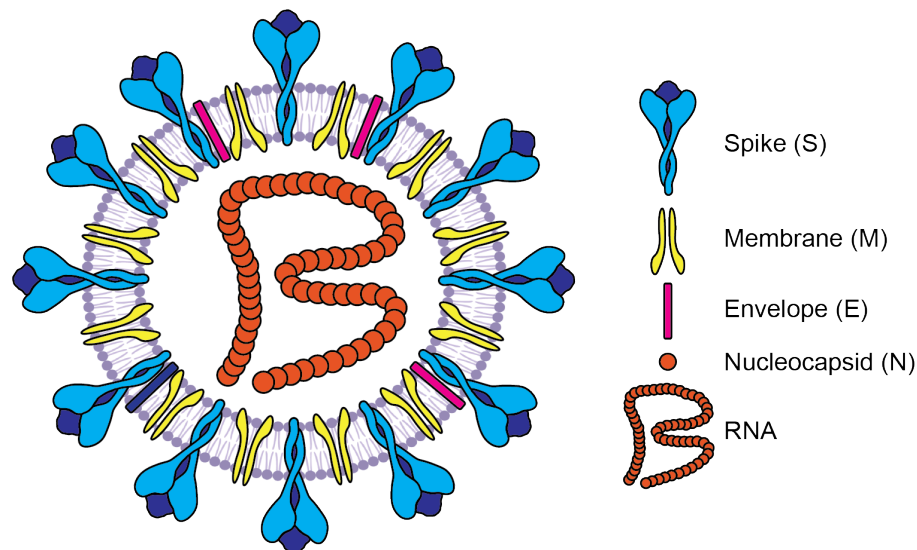


*Figure 1. Structure of SARS-CoV-2*

*Schematic of a SARS-CoV-2 virion containing a single-stranded, positive-sense RNA genome. Figure partially created with BioRender.com.*

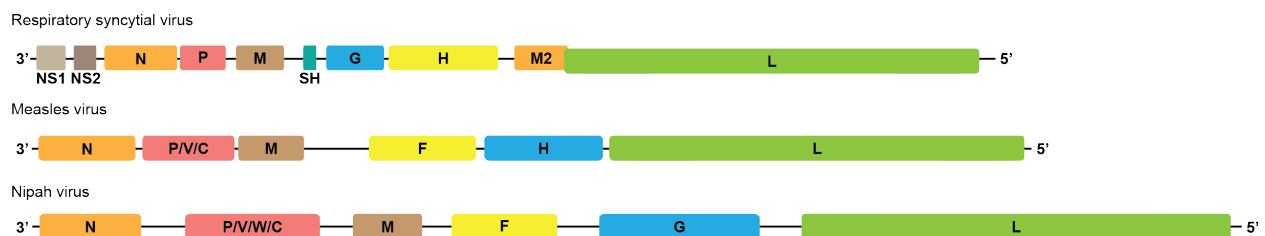


*Figure 2. Genome Organization of the Featured Paramyxoviruses*

*For each genome, the open reading frames and intergenic regions are shown on a relative scale. ORFs: non-structural protein 1 (NS1), non-structural protein 2 (NS2), nucleocapsid (N), phosphoprotein (P), matrix (M), short hydrophobic (SH), glycoprotein (G), hemagglutinin (H), fusion (F), M2, polymerase (L). The MeV and NiV P ORFs also encode the alternative genes, P, V, W, and/or C.*

In 2023, over 100,000 measles cases were reported globally (CDC, 2024c), and this number is expected to rise as vaccine hesitancy decreases coverage rates below the 95% needed for herd immunity (Pandey & Galvani, 2023). Since 2001, NiV has caused near-annual outbreaks in countries like India, Bangladesh, and Malaysia. In 2023, an outbreak in Kerala, India, resulted in 30 cases of NiV infection and approximately half the number of cases were the result of human-to-human transmission (Cui et al., 2024). Currently, there are no approved antiviral treatments for a measles (Peart Akindele et al., 2023) or NiV infection (Alam, 2022; Singh et al., 2024), underscoring the urgent need to develop effective drugs targeting these viruses.

### **1.3 Severe Acute Respiratory Syndrome Coronavirus 2**

In 2019, severe acute respiratory syndrome coronavirus 2 (SARS-CoV-2) emerged from an animal reservoir and swiftly became the notorious cause of the coronavirus disease 2019 (COVID-19) pandemic, which ravaged the world from 2020 to 2023, leading to substantial morbidity and mortality (Hu et al., 2021; Steiner et al., 2024). On December 12, 2019, a cluster of pneumonia-like cases was reported in Wuhan, China. By January 7, 2020, Chinese public health officials had identified the causative agent as a novel coronavirus. A week later, the WHO confirmed evidence of possible human-to-human transmission of SARS-CoV-2. SARS-CoV-2 infections quickly spread worldwide, and by March 11, 2020, the WHO declared COVID-19 a pandemic (CDC, March 15, 2023).

In October 2020, the U.S. Food and Drug Administration (FDA) approved remdesivir, the first intravenously administered antiviral for SARS-CoV-2 (FDA, 2020). Nearly nine months into the pandemic, the Pfizer-BioNTech mRNA vaccine received emergency use authorization (EUA)

from the FDA for individuals aged 16 and older. Around the same time, research presented in this dissertation was among the first to show that the orally available antiviral molnupiravir could interrupt SARS-CoV-2 transmission in a ferret model (Cox, Wolf, & Plemper, 2021). Following this, molnupiravir was granted EUA for COVID-19 treatment just three weeks later (NIH, 2024a). Most recently, in May 2023, the FDA approved a second oral antiviral, Paxlovid (FDA, 2023a). By July 2024, nearly 776 million COVID-19 cases had been reported globally, resulting in over 7 million deaths. The widespread administration of the initial vaccination series to more than 56% of the global population contributed to a reduction in the pandemic's impact (Narayanan et al., 2024; WHO, 2024). Although the World Health Organization (WHO) declared COVID-19 no longer a global health emergency in May 2023 (WHO, 2023a), SARS-CoV-2 infections continue at lower levels, with over 128,000 new cases and 1,800 deaths reported in June 2024 (WHO, 2024).

SARS-CoV-2, a virus in the genus *Betacoronavirus* and family *Coronaviridae*, is an enveloped, positive-sense, single-stranded RNA virus that infects both mammals and birds. It enters host cells through interaction between its spike (S) protein and the angiotensin-converting enzyme 2 (ACE2) receptor (Hoffmann et al., 2020; Hu et al., 2021; Steiner et al., 2024; Walls et al., 2020). Initially, the SARS-CoV-2 viral load is highest in the upper respiratory tract, but it can shift to be primarily in the lower respiratory tract as the infection progresses (Wölfel et al., 2020). The virus primarily spreads through respiratory aerosols due to its tissue tropism, and factors such as viral load, immune status, age, proximity, and exposure duration affect the likelihood of human-to-human transmission (Ma et al., 2021; Meyerowitz & Richterman, 2022; Meyerowitz et al., 2021). COVID-19 symptoms can range from asymptomatic

to severe. Mild cases may present with cough, sore throat, headache, general malaise, and fever, while more severe cases can lead to respiratory failure, multi-organ dysfunction, and death (NIH, 2024b).

To assess different aspects of human SARS-CoV-2 infections, this dissertation utilizes two animal models: the ferret transmission model and the Roborovski dwarf hamster model of severe COVID-19-like lung injury. In the studies referenced, ferrets were employed to model an asymptomatic SARS-CoV-2 infection and transmission, assessing the efficacy of antiviral therapeutics. Ferrets are particularly suitable for this purpose due to their respiratory system's similarity to that of humans, including their ability to sneeze and cough, which makes them a good model for studying viral transmission (Chu et al., 2022; Sun et al., 2010). However, a limitation of this model is that transmission rates are low for all variants of concern (VOCs), making the early pandemic Wuhan lineage A the preferred variant (Lieber et al., 2022). In contrast, Roborovski dwarf hamsters serve as a prominent model for severe COVID-19, as they develop a lower respiratory tract infection characterized by diffuse alveolar damage and thrombosis that closely mimics the pathogenicity of VOCs in humans and leads to severe and often fatal pneumonia (Lieber et al., 2022; Trimpert et al., 2020).

#### **1.4 Respiratory Syncytial Virus**

Respiratory syncytial virus (RSV), belonging to the genus *Orthopneumovirus* within the family *Paramyxoviridae* and the order *Mononegavirales*, is a major cause of lower respiratory tract infections that lead to hospitalization in infants and young children worldwide (Acosta et al., 2015; "Causes of severe pneumonia requiring hospital admission in children without HIV infection from Africa and Asia: the PERCH multi-country case-control study," 2019; Hall, 2010;



Nair et al., 2010; Wang et al., 2024). The only known natural hosts of RSV are humans and chimpanzees, but it can also infect animals such as cotton rats and mice, which are utilized as animal models for research (Domachowske et al., 2004; Graham et al., 2002).

RSV was first isolated from chimpanzees in 1955 (Blount et al., 1956), and a formalin-inactivated vaccine was tested in the United States in 1966. Unfortunately, the vaccine proved ineffective and, in some cases, actually worsened RSV disease in children (Acosta et al., 2015; Delgado et al., 2009; Mullard, 2008). In 1998, the monoclonal antibody Palivizumab was approved for prophylactic use in high-risk infants (Resch, 2017). Over 60 years after the formalin-inactivated vaccine's failure, the FDA approved two new RSV vaccines in May 2023: Arexvy (FDA, 2023b) and Abrysvo (Pfizer), both targeting the pre-fusion stabilized RSV fusion protein. In July 2023, the FDA also approved Nirsevimab-alip, a long-acting monoclonal antibody for use in babies and toddlers (FDA, 2023c). Most recently, in June 2024, the FDA approved a third RSV vaccine based on an mRNA platform, mRNA-1345 (mRESVIA) (Mullard, 2024). Despite these significant advancements in RSV prevention, no antivirals have yet received approval.

RSV, which has two antigenic subtypes (RSV-A and RSV-B) that are based on slightly different glycoprotein sequence identities, can cause a severe acute respiratory infection. By the age of two most, children have been infected by RSV (Felicetti et al., 2024; Rago et al., 2024). After an average incubation period of 4 to 6 days, RSV replicates in the nasal epithelium and the lower respiratory tract, respectively, causing symptoms such as rhinorrhea, sneezing, coughing, dyspnea, respiratory distress, and fever (CDC, 2024e; Jiang et al., 2023). In infants younger than two years of age, re-infection with RSV occurs in 30-75% of patients who had

experienced RSV before their first birthday. Repeat exposures to RSV throughout an individual's lifetime typically results in less severe symptoms and often limits the infection to the upper respiratory tract. However, viral migration into the lower respiratory tract still occurs in 25% of older children and adults (Felicetti et al., 2024; Jiang et al., 2023; Staadegaard et al., 2021; Wrotek et al., 2023).

### **1.5 Measles and Canine Distemper Virus**

Measles virus (MeV) and canine distemper virus (CDV), both members of the genus *Morbillivirus* within the family *Paramyxoviridae*, are extremely pathogenic and are among the most contagious viruses in this family (Quintero-Gil et al., 2019; Wilkes, 2022). While MeV is known to exclusively infect humans (with occasional cases in non-human primates), CDV affects a diverse range of animals, including those in the orders *Carnivora*, *Rodentia*, *Artiodactyla*, *Pilosa*, and *Primates* (Deem et al., 2000; Lunardi et al., 2018; Martinez-Gutierrez & Ruiz-Saenz, 2016; Rendon-Marin et al., 2019; Watson et al., 2020; Wilkes, 2022). Unlike MeV, which has a low fatality rate of about 1% in humans (CDC, 2024a, 2024b, 2024d; Crum, 1914), CDV can be fatal in certain animals, such as ferrets, with a 100% mortality rate (Krumm et al., 2014). Though no human cases of CDV have been documented, the virus could potentially evolve to infect humans with just a single point mutation in the hemagglutinin (H) protein (Bieringer et al., 2013; Ohno et al., 2003; Sakai et al., 2013). Fortunately, continued universal vaccination against MeV is expected to provide cross-protection to CDV from neutralizing antibodies, thus reducing the risk of such a cross-species transmission (de Vries et al., 2014).

Although measles was first clinically described in the 10th century CE by the Persian physician Abu Bakr Muhammad Ibn Zakariya Al Razi (commonly known as Rhazes) (Amr &

Tbakhi, 2007; Berche, 2022), selection-aware Bayesian molecular clock modeling suggests that MeV may have diverged from its close relative, the rinderpest virus, as early as the 6th century BCE (Düx et al., 2020). Before the introduction of the first vaccine in 1963, MeV was endemic worldwide, causing approximately 30 million cases and 2.6 million deaths annually (eClinicalMedicine, 2024). Since the year 2000, the widespread use of the highly effective MeV vaccine has reportedly prevented over 57 million deaths globally. Despite the disease being declared officially eliminated in the United States in 2000, travel-related cases continue to occur in at-risk populations each year, albeit at low levels (CDC, 2024a, 2024b, 2024c).

After exposure to MeV and an average incubation period of 10-15 days, the initial symptoms of measles typically include fever, cough, runny nose, conjunctivitis, and the appearance of tiny white spots inside the mouth known as Koplik's spots, which are a distinctive diagnostic sign of the infection (CDC, 2024d; Steichen & Dautheville, 2009). Within 2-4 days following these initial symptoms, a maculopapular rash develops and spreads from the head down to the rest of the body. This rash is a hallmark of measles, driven by a T-cell response to MeV-infected cells in the capillaries. The symptoms, including the rash, usually resolve within two weeks (CDC, 2024d; Yanagi et al., 2006).

Even after the resolution of symptoms, a significant concern is that, beyond infecting respiratory epithelial cells, the interaction between the viral H protein and the host cell surface receptor signaling lymphocyte activation molecule (CD150) enables lymphotropic morbilliviruses like MeV and CDV to also infect macrophages, dendritic cells, B- and T-cells, and hematopoietic stem cells (Laksono et al., 2016; Rendon-Marin et al., 2019; von Messling et al., 2006; von Messling et al., 2001; Yanagi et al., 2006). This ability allows these viruses to severely

deplete the population of CD150+ lymphocytes, including memory B- and T-cells, thereby erasing the host's pre-existing immune memory (Laksono et al., 2018; Mina et al., 2019; Morales & Muñoz, 2021; Petrova et al., 2019).

## 1.6 Nipah Virus

Nipah virus (NiV) is a highly pathogenic zoonotic paramyxovirus classified under the genus *Henipavirus* and the family *Paramyxoviridae* (Gaudino et al., 2020). The natural reservoir of this virus is fruit bats of the genus *Pteropus*, commonly known as flying foxes. NiV is typically transmitted to humans or other animals through contact with bat urine, feces, or saliva. In Malaysia, the primary reservoir hosts are *P. vampyrus* and *P. hypomelanus*, while in Bangladesh, it is *P. giganteus* (Kulkarni et al., 2013). The case fatality rate of NiV infection in humans varies significantly, ranging from 40% for the Malaysia strain to 90% for the Bangladesh strain (Gaudino et al., 2020).

The first cases of NiV were reported in 1998 during an outbreak on pig farms in the suburb of Ipoh, Perak, Malaysia. This outbreak caused respiratory illness and encephalitis in pigs, which then spread to pig farmers. The crisis led to the culling of over 1 million pigs, and by mid-1999, there had been 265 human cases and 105 deaths (Field et al., 2001; Looi & Chua, 2007; "Update: outbreak of Nipah virus--Malaysia and Singapore, 1999," 1999). NiV can enter the human population either through spillover from an intermediate animal host, as seen with pig-to-human transmission, or directly from bats to humans (Figure 3) (Clayton, 2017). Additionally, human-to-human transmission has been documented (Gaudino et al., 2020; Gurley, Montgomery, Hossain, Bell, et al., 2007; Gurley, Montgomery, Hossain, Islam, et al., 2007).

Nipah virus has broad cell tropism, interacting with host epithelial, endothelial, and neuronal cells via its surface glycoprotein (G) and the highly conserved mammalian cell receptors ephrin-B2 and ephrin-B3 (Laing et al., 2019; Negrete et al., 2005; Negrete et al., 2006; Xu et al., 2012). Viral entry is facilitated by the fusion (F) protein, which mediates the fusion of the viral membrane with the host cell membrane in a pH-independent manner (Lamp et al., 2013; Liu et al., 2013). Once inside the cytoplasm, viral RNA synthesis is carried out by the viral RNA-dependent RNA polymerase (RdRP), which includes the large (L) protein and the phospho (P) protein (Wolf et al., 2024). The RdRP complex interacts with the RNA template through a critical interaction between the P protein and the nucleocapsid (N) protein (Figure 4) (Bloyet et al., 2016; Communie et al., 2013; Du Pont et al., 2019; Ker et al., 2021; Ogino & Green, 2019).

With an average incubation period of 4 to 14 days (WHO, 2018), NiV initially replicates in the airways before advancing to a viremic phase. During this phase, the virus spreads systemically, infecting organ endothelial cells and the central nervous system, which can lead to a wide range of symptoms (Lamp et al., 2013). Symptoms vary in severity and may include acute respiratory distress, fever, headache, muscle pain, altered consciousness, brainstem dysfunction, and seizures (Alam, 2022; Hossain et al., 2008; WHO, 2018). The disease often progresses to viral encephalitis and can cause extensive damage to respiratory, vascular, and neurological tissues, which can result in multisystem organ failure and death. Survivors of NiV infection face a significant risk of developing long-term neurological deficits, with nearly 20% experiencing these lasting effects (Faus-Cotino et al., 2024; Sejvar et al., 2007).

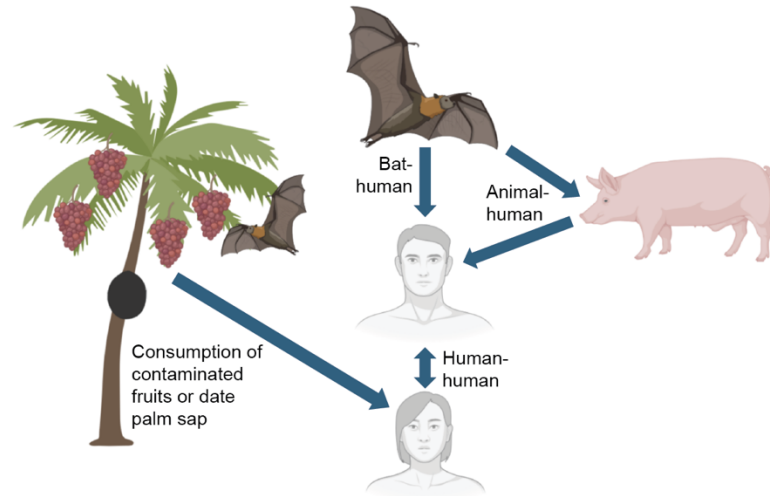


**Figure 3. Transmission of Nipah Virus**

*Nipah virus can be transmitted to humans directly by fruit bats, through an intermediate animal host such as a pig or horse, or by consumption of fruits or date palm sap that have been contaminated with NiV. Created with BioRender.com.*

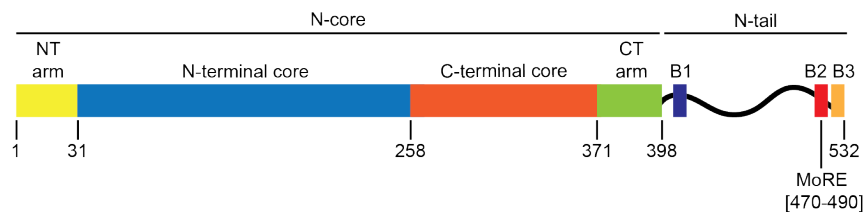


**Figure 4. Domain Organization of Nipah Virus Nucleocapsid Protein**

*Nucleocapsid protein is composed of a folded N-core and an intrinsically disordered C-terminal N-tail, which contains three microdomains, box 1 – box 3. The putative molecular recognition element (MoRE) that interacts with the X-domain (XD) of the P protein has been predicted based on the Hendra virus (HeV) N NMR predicted interaction with HeV P-XD.*

## 2. RESULTS AND DISCUSSIONS

The data in this dissertation are organized into three results sections, as follows:

i) Assessing the effectiveness of various SARS-CoV-2 antivirals in ferret and Roborovski dwarf hamster models to enhance their preclinical and clinical development.

ii) Exploring the therapeutic potential of the potent, broad-spectrum polymerase inhibitor GHP-88309 for treating measles-like CDV disease and preventing virus-induced immune amnesia in the ferret model. This section also thoroughly evaluates the use of GHP-88309 and other polymerase inhibitors as small-molecule chemical probes to enhance the structural resolution of the paramyxovirus polymerase.

iii) Mapping and characterizing three distinct NiV P-XD interfaces, which led to the identification of a transient interface between the N protein and P-XD crucial for polymerase activity.

The following sections include relevant publications that present the results of each study. For each publication, the title, author list, affiliations, references, and the full article with figures are all formatted according to the approved style of the journal. When applicable, web links to publicly available supplementary information—such as additional experimental results, detailed methods, statistical analyses, quantitative raw data, and extensive genomics/proteomics datasets—are also provided.

### 2.1 Research Topic: SARS-CoV-2

## 2.1.1 Therapeutically Administered Ribonucleoside Analogue MK-4482/EIDD-2801 Blocks

### SARS-CoV-2 Transmission in Ferrets

nature  
microbiology

LETTERS

<https://doi.org/10.1038/s41564-020-00835-2>



# Therapeutically administered ribonucleoside analogue MK-4482/EIDD-2801 blocks SARS-CoV-2 transmission in ferrets

Robert M. Cox<sup>1,2</sup>, Josef D. Wolf<sup>1,2</sup> and Richard K. Plemper<sup>1</sup>✉

**The coronavirus disease 2019 (COVID-19) pandemic is having a catastrophic impact on human health<sup>1</sup>. Widespread community transmission has triggered stringent distancing measures with severe socio-economic consequences. Gaining control of the pandemic will depend on the interruption of transmission chains until vaccine-induced or naturally acquired protective herd immunity arises. However, approved antiviral treatments such as remdesivir and reconvalescent serum cannot be delivered orally<sup>2,3</sup>, making them poorly suitable for transmission control. We previously reported the development of an orally efficacious ribonucleoside analogue inhibitor of influenza viruses, MK-4482/EIDD-2801 (refs. 4,5), that was repurposed for use against severe acute respiratory syndrome coronavirus 2 (SARS-CoV-2) and is currently in phase II/III clinical trials (NCT04405570 and NCT04405739). Here, we explored the efficacy of therapeutically administered MK-4482/EIDD-2801 to mitigate SARS-CoV-2 infection and block transmission in the ferret model, given that ferrets and related members of the weasel genus transmit the virus efficiently with minimal clinical signs<sup>6–9</sup>, which resembles the spread in the human young-adult population. We demonstrate high SARS-CoV-2 burden in nasal tissues and secretions, which coincided with efficient transmission through direct contact. Therapeutic treatment of infected animals with MK-4482/EIDD-2801 twice a day significantly reduced the SARS-CoV-2 load in the upper respiratory tract and completely suppressed spread to untreated contact animals. This study identified oral MK-4482/EIDD-2801 as a promising antiviral countermeasure to break SARS-CoV-2 community transmission chains.**

MK-4482/EIDD-2801 is the orally available pro-drug of the nucleoside analogue *N*<sup>3</sup>-hydroxycytidine (NHC), which has shown potent anti-influenza virus activity in mice, guinea pigs, ferrets and human airway epithelium organoids<sup>4,10,11</sup>. Acting through the induction of error catastrophe in virus replication<sup>4,12</sup>, NHC has broad-spectrum anti-RNA virus activity. In addition to ameliorating acute disease, we have demonstrated in a guinea pig transmission model that NHC effectively blocks the spread of influenza virus from infected animals to untreated contact animals<sup>11</sup>.

Several mouse models of severe acute respiratory syndrome coronavirus 2 (SARS-CoV-2) infection have been developed, some of which were also employed to confirm the in vivo efficacy of MK-4482/EIDD-2801 against betacoronaviruses<sup>13</sup>. However, human SARS-CoV-2 cannot productively infect mice without viral adaptation or introduction of human ACE2 into transgenic animals, and none of the mouse models support transmission to

uninfected mice<sup>14</sup>. Spill-back of SARS-CoV-2 to farmed minks, subsequent large-scale mink-to-mink transmission and, in some cases, zoonotic transmission back to humans revealed efficient viral spread among members of the weasel genus without previous adaptation<sup>6–9</sup>. Although mink farms reported elevated animal mortality and gastrointestinal and respiratory clinical signs<sup>15</sup>, outbreak follow-up revealed continued intra-colony spread for extended periods of time<sup>6</sup>, suggesting that the acute clinical signs in the majority of infected animals may be mild. These mink field reports corroborated results obtained with experimentally infected ferrets showing that mustelids of the weasel genus transmit SARS-CoV-2 efficiently without strong clinical disease manifestation<sup>16,17</sup>. As this presentation of SARS-CoV-2 infection resembles the experience of frequently asymptomatic or mildly symptomatic SARS-CoV-2 spread in the human young-adult population<sup>18</sup>, ferrets represent a relevant model species to assess therapeutic impact on SARS-CoV-2 transmission.

To first validate host invasion and tissue tropism of SARS-CoV-2 in ferrets, we inoculated animals intranasally with either  $1 \times 10^4$  or  $1 \times 10^5$  plaque-forming units (p.f.u.)—low- and high-inoculum group, respectively—of SARS-CoV-2 clinical isolate 2019-nCoV/USA-WA1/2020 per animal. The shed virus burden was monitored daily over a period of 10 d. The virus load in the upper and lower respiratory tract was determined for two animals from each inoculum group on days four and ten after infection, respectively.

Virus release from the upper respiratory tract peaked three days after infection and was undetectable by day seven in the animals of the high-inoculum group (Fig. 1a and Supplementary Table 1). Infection of animals in the low-inoculum group was less efficient. The shedding profiles correlated closely with the infectious particle load in nasal turbinates; a heavy virus tissue burden in the high-inoculum group was present on day four, which decreased substantially by approximately four orders of magnitude by day ten (Fig. 1b and Supplementary Table 2).

Infection with a low concentration of inoculum resulted in low virus loads in the turbinates on day 4 and undetectable burden thereafter. However, quantitation of viral RNA copy numbers in the turbinates using RT-qPCR revealed the continued presence of moderate (approximately  $10^4$  copies  $g^{-1}$  tissue) to high ( $\geq 10^7$  copies  $g^{-1}$  tissue) virus loads in the groups with low and high inoculums, respectively (Fig. 1c and Supplementary Table 3). Irrespective of the inoculum concentration, no infectious particles were detected in bronchoalveolar lavages or lung tissue samples (Extended Data Fig. 1). Several organ samples (lungs, heart, kidneys and liver) were also RT-qPCR-negative on both days 4 and 10 (Fig. 1d), confirming

<sup>1</sup>Institute for Biomedical Sciences, Georgia State University, Atlanta, GA, USA. <sup>2</sup>These authors contributed equally: Robert M. Cox, Josef D. Wolf.  
✉e-mail: [rplemper@gsu.edu](mailto:rplemper@gsu.edu)



## LETTERS

## NATURE MICROBIOLOGY

inefficient infection of the ferret lower respiratory tract and limited systemic host invasion. Only the small and large intestine samples were PCR-positive on day 4 after infection, and rectal swabs showed continued low-grade shedding of viral genetic material (Fig. 1e and Supplementary Table 4).

The animals in the high-inoculum group experienced a transient drop in body weight that reached a low plateau on days 5–6 after infection but recovered fully by the end of the study (Fig. 1f and Supplementary Table 5). One animal in the low-inoculum group showed a gradual slight reduction in body weight until the end of the study (day 10). No other clinical signs, such as fever or respiratory discharge, were noted. The complete blood counts (CBCs) taken every second day revealed no significant deterioration from the normal range in the overall white-blood-cell counts as well as lymphocyte, neutrophil and platelet populations of either inoculum group (Fig. 1g and Supplementary Table 6). The relative expression levels of type I and II interferon in the ferret peripheral blood mononuclear cells (PBMCs) sampled at 48-h intervals reached a plateau approximately 3 d after infection and stayed moderately elevated until the end of the study (Fig. 1h,i and Supplementary Table 7). IL-6 levels were moderately elevated in some animals but these changes did not reach statistical significance (Fig. 1j). However, we noted a prominent expression peak of select interferon-stimulated genes (ISGs) with antiviral effector function (MX1 and ISG15) 4 d after infection, followed by a return to baseline expression by the end of the study (Fig. 1k,l).

Before in vivo efficacy evaluation, we validated the potency of NHC against the SARS-CoV-2 clinical isolate 2019-nCoV/USA-WA1/2020 in cell culture (Fig. 2a). Four-parameter variable slope regression modelling of the dose-response data revealed 50 and 90% effective concentrations ( $EC_{50}$  and  $EC_{90}$ , respectively) of approximately 3.4  $\mu$ M and 5.4  $\mu$ M, respectively, which is within an approximately sixfold range of potency data reported for other human betacoronaviruses<sup>15</sup>. Based on these results, ferrets were infected with  $1 \times 10^5$  p.f.u. per animal in the subsequent MK-4482/EIDD-2801 efficacy tests and the levels of infectious virions in nasal lavages were determined twice daily (Fig. 2b). The viral burden in respiratory tissues was assessed 4 d after infection. In all treatment experiments, MK-4482/EIDD-2801 was administered twice a day (b.i.d.) through oral gavage. Dosing commenced 12 h after infection at 5 or 15 mg kg<sup>-1</sup> body weight, or 36 h after infection at 15 mg kg<sup>-1</sup>. The titres of shed virus in the nasal lavages were equivalent in all MK-4482/EIDD-2801 groups and vehicle-treated controls at the time of the first treatment (12 h after infection), indicating uniform inoculation of all animals in the study (Fig. 2c and Extended Data Fig. 2a). Initiation of therapy at the 12-h time point resulted in a significant reduction ( $P < 0.001$ ) of the shed virus load within 12 h, independently of the MK-4482/EIDD-2801 dose administered, and

infectious particles became undetectable within 24 h of the start of treatment. When first administered at the peak of virus shedding (36 h after infection), MK-4482/EIDD-2801 completely suppressed the release of infectious virions into nasal lavages within a slightly longer period of 36 h, whereas the vehicle control animals continued to shed infectious particles until the study end.

Only the vehicle-treated animals carried detectable virus burden in their nasal turbinates 3.5 d after infection (Fig. 2d and Extended Data Fig. 2b), indicating that MK-4482/EIDD-2801 had silenced all SARS-CoV-2 replication. SARS-CoV-2 RNA was still detectable in the nasal tissues extracted from animals in all groups, albeit significantly reduced ( $P = 0.0089$  and  $0.0081$  for the 5 and 15 mg kg<sup>-1</sup> MK-4482/EIDD-2801 groups, respectively) in the treated animals versus the vehicle controls (Fig. 2e and Extended Data Fig. 2c). The animals in the 12-h therapeutic groups showed a significant reduction ( $P \leq 0.044$ ) in effector ISG expression compared with the vehicle-treated animals, although no significant differences in relative interferon and IL-6 induction were observed (Extended Data Fig. 3a–f).

These results demonstrate the oral efficacy of therapeutic administration of MK-4482/EIDD-2801 against acute SARS-CoV-2 infection in the ferret model. Consistent with our previous pharmacokinetic and toxicology work-up of MK-4482/EIDD-2801 in ferrets, treatment did not cause any phenotypically overt adverse effects, and the white-blood-cell and platelet counts of the drug-experienced animals remained within the normal range (Extended Data Fig. 4).

SARS-CoV-2 shedding into the upper respiratory tract of ferrets establishes conditions for the productive spread from the infected source to uninfected contact animals<sup>16,17</sup>. To assess transmission efficiency, we co-housed intranasally infected source animals with two uninfected contact animals each for a period of 3 d, starting 30 h after the inoculation of the source animal (Fig. 3a). Nasal lavages and rectal swabs were obtained daily from all of the animals and blood was sampled at the start of the study and on days four and eight after the original infection. The viral burden and RNA copy numbers in the respiratory tissues were determined at the end of the co-housing phase (source animals) and at study termination (contact animals).

Infectious particles first emerged in the nasal lavages of some contact animals 24 h after the start of co-housing (Fig. 3b and Supplementary Table 8). By the end of the co-housing phase, all contact animals were infected and approached the peak virus-replication phase, demonstrating that transmission of SARS-CoV-2 among ferrets is rapid and highly efficient.

A second cohort of source animals inoculated in parallel with SARS-CoV-2 received oral MK-4482/EIDD-2801 at a dose of 5 mg kg<sup>-1</sup> body weight, administered b.i.d. starting 12 h after

**Fig. 1 | SARS-CoV-2 infects the upper respiratory tract of ferrets.** Ferrets ( $n = 4$  biologically independent animals) were intranasally inoculated with either  $1 \times 10^4$  or  $1 \times 10^5$  p.f.u. 2019-nCoV/USA-WA1/2020. **a**, Virus titre in nasal lavages collected daily. LOD, limit of detection. **b–f**, At 4 and 10 d post infection, two ferrets from each group were killed and the infection was characterized. **b**, Number of infectious virus particles in the nasal turbinates. **c**, Viral RNA was present in the nasal turbinates of all of the infected ferrets. **d**, Number of viral RNA copies, determined using quantitative PCR with reverse transcription (RT-qPCR), in select organs extracted from infected ferrets 4 or 10 d after infection. Two lung lobes (right (R.) and left (L.) cranial) per animal; SI, small intestine; LI, large intestine. **e**, Detection of 2019-nCoV/USA-WA1/2020 RNA in rectal swabs of ferrets inoculated with  $1 \times 10^5$  p.f.u. RNA was extracted from the rectal swabs and the absolute copy numbers were determined using RT-qPCR. **f**, Body weight of ferrets, measured daily and expressed as a percentage of their weight at day 0. **g**, CBC analysis, performed every second day. No noticeable differences were detected for any of the parameters tested, including total white blood cells (WBCs), lymphocytes, neutrophils and platelets. The shaded green areas represent the range of normal Vetscan HM5 laboratory values. **h–i**, Select interferon and cytokine responses in PBMCs harvested every two days after infection. Analysis by RT-qPCR relative to day 0 for animals infected with  $1 \times 10^5$  p.f.u. 2019-nCoV/USA-WA1/2020. **h,i**, The infected ferrets displayed elevated expression of *ifn- $\beta$*  (**h**) and *ifn- $\gamma$*  (**i**). **j**, Only some animals had moderately elevated levels of *il-6*. **k,l**, The interferon-stimulated genes *mx1* (**k**;  $P = 0.0192$  on day 4) and *isg15* (**l**;  $P = 0.009$  and  $P < 0.0001$  on days 2 and 4, respectively) showed a sharp peak on day 4 after infection. The number of independent biological repeats ( $n$ , individual animals) is shown for each subpanel. Statistical analysis was performed using a two-way analysis of variance (ANOVA) with Dunnett's post-hoc multiple comparison test. Symbols represent independent biological repeats (individual animals), lines connect the group mean  $\pm$  s.d. (**a,e–l**) and bar graphs show the mean (**b–d**).

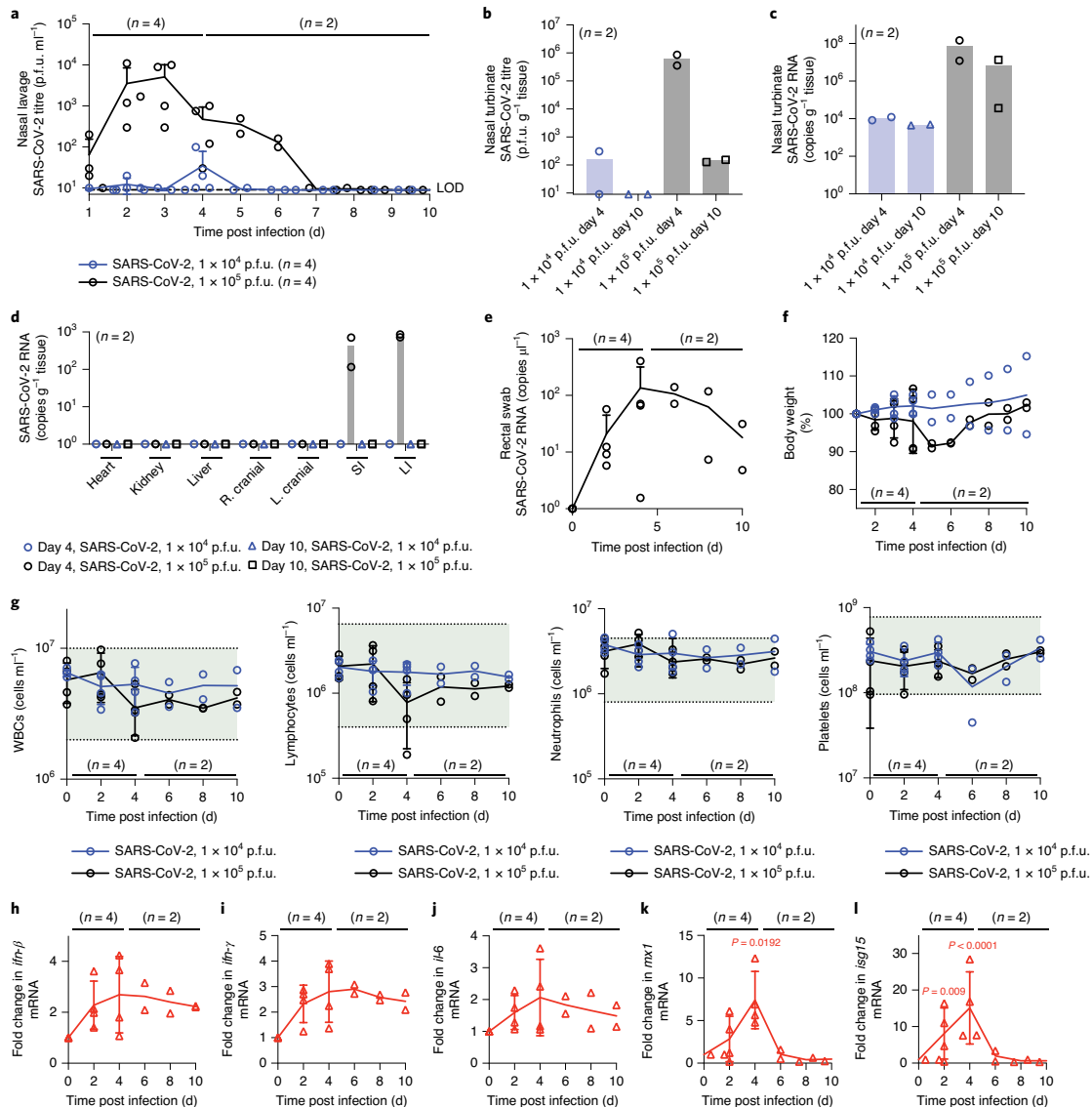
## NATURE MICROBIOLOGY

## LETTERS

infection. Productive infection of these animals was validated by the titres of SARS-CoV-2 in the nasal lavages 1 d after infection (Fig. 3b), which very closely matched those seen in the initial efficacy tests (Fig. 2c). Although we also co-housed the treated source animals with two untreated contacts each for nearly 3 d, no infectious SARS-CoV-2 particles were detected in any of the series of nasal lavages obtained from these contacts throughout the study or in any of the nasal turbinates sampled from the contact animal at end of the study (Fig. 3c and Supplementary Table 9).

The nasal turbinates extracted from the contacts of the vehicle-treated source animals contained high copy numbers of viral RNA, underscoring successful host invasion after transmission

(Fig. 3d and Supplementary Table 10). Consistent with our earlier observations, the turbinates of the treated source animals harboured moderate-to-high ( $\geq 10^5$  copies  $g^{-1}$  tissue) levels of viral RNA, although infectious particles could not be detected. In contrast, all respiratory tissues of the contacts co-housed with the source animals treated with MK-4482/EIDD-2801 remained SARS-CoV-2-genome free, indicating an absence of any low-grade virus replication that could have hypothetically progressed in these animals below the detection level of infectious particles (Fig. 3e,f and Supplementary Tables 11,12). Furthermore, SARS-CoV-2 RNA was present at low copy numbers in the intestinal tissue samples and rectal swabs of the vehicle source animals as well as their contacts but undetectable



## LETTERS

## NATURE MICROBIOLOGY

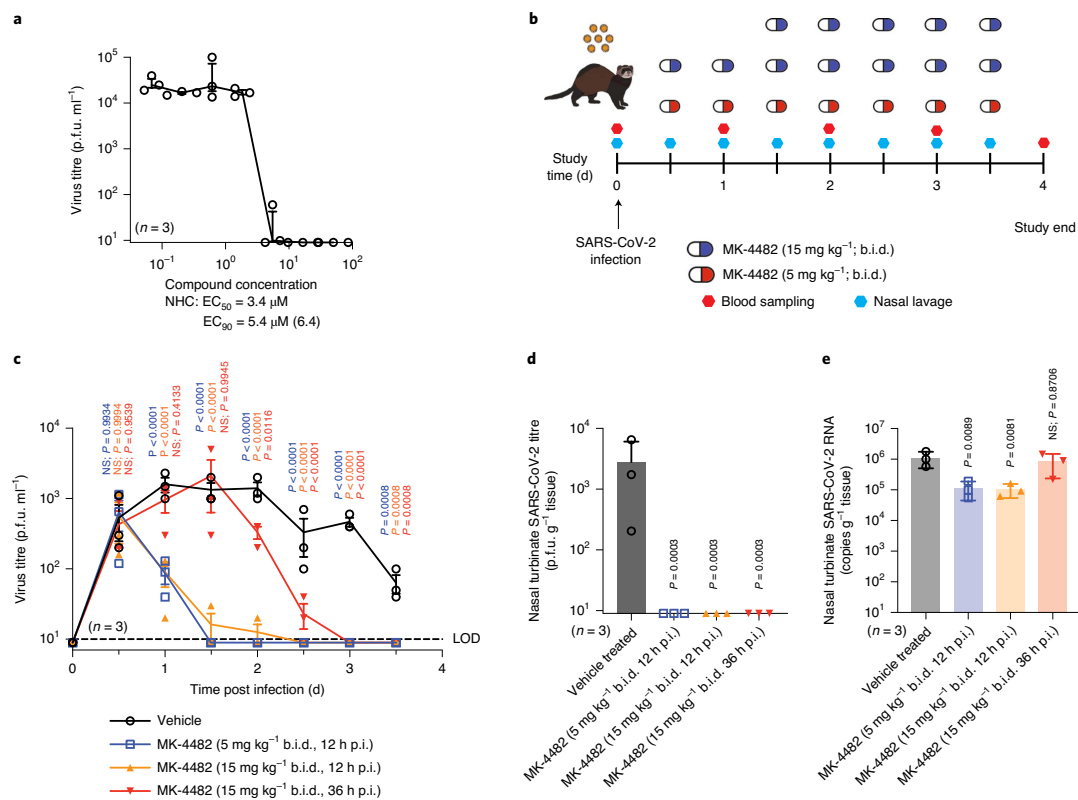


**Fig. 2 | Therapeutic MK-4482/EIDD-2801 is orally efficacious against SARS-CoV-2 in ferrets. a**, Dose-response inhibition test of NHC against SARS-CoV-2 in Vero E6 cells (multiplicity of infection of 0.1 p.f.u. per cell;  $n=3$  biologically independent experiments). The effective concentrations (EC<sub>50</sub> and EC<sub>90</sub>), shown with the upper 95% confidence interval limit in parenthesis) were derived from four-parameter variable slope regression modelling. **b**, Schematic of the therapeutic efficacy study. Ferrets ( $n=3$  biologically independent animals) were infected intranasally with  $1 \times 10^5$  p.f.u. 2019-nCoV/USA-WA1/2020 and either gavaged with vehicle or treated b.i.d. with MK-4482/EIDD-2801 commencing 12 ( $5 \text{ mg kg}^{-1}$  and  $15 \text{ mg kg}^{-1}$ ) or 36 h ( $15 \text{ mg kg}^{-1}$ ) after infection. Nasal lavages were collected twice a day and blood was collected every other day. Yellow circles represent SARS-CoV-2 and SARS-CoV-2-infected source animals. **c**, Viral titres of the nasal lavages of the infected ferrets from **b**. Treatment with MK-4482/EIDD-2801 significantly reduced the virus titres within 12 h of dosing onset in all treatment groups. Statistical analysis was performed using a two-way ANOVA with Dunnett's multiple comparison post-hoc test. **d,e**, Infectious particle (**d**) and viral RNA copy (**e**) numbers in the nasal turbinates of infected ferrets extracted 4 d after infection. Statistical analysis was performed using a one-way ANOVA with Dunnett's multiple comparison post-hoc test. **c–e**,  $P$  values are shown; NS, not significant; p.i., post infection. The number of independent biological repeats is shown for each panel. Symbols represent independent biological repeats (individual animals), lines connect the group mean  $\pm$  s.d. (**a,c**) and bar graphs show the mean  $\pm$  s.d. (**d,e**).

in the MK-4482/EIDD-2801-treated source group and co-housed contact animals.

Phylogenetic analysis of outbreaks in mink farms revealed prolonged intra-colony circulation and zoonotic mink-to-human transmission<sup>9</sup>, leading us to select ferrets—members of the weasel genus closely related to minks—as a SARS-CoV-2 transmission model. We noted that the experimental infection of ferrets was strongly dependent on the amount of viral inoculum used. Productive host invasion was only observed after intranasal delivery of  $1 \times 10^5$  p.f.u. SARS-CoV-2. The shed SARS-CoV-2 load in ferret nasal lavages, a core virological marker of a transmission model, showed good cross-study consistency. Our experiments returned peak shed virus titres of  $1 \times 10^3$ – $1 \times 10^4$  p.f.u. ml<sup>-1</sup>, closely resembling the ferret lavage titres found in two previous studies, which reported up to  $1 \times 10^4$  p.f.u. ml<sup>-1</sup> (ref. <sup>20</sup>) and

$1 \times 10^3$  median tissue culture infectious dose ml<sup>-1</sup> (ref. <sup>21</sup>) in nasal lavages, respectively.

Natural infection through direct contact was highly efficient, possibly reflecting the prolonged exposure of contact to source animals in a confined space. However, nearly all contacts started to shed virus within less than 24 h after the beginning of co-housing. This timeline indicates that transmission must have occurred shortly after the introduction of contact to the source animals, despite the fact that the shed viral titres of the source animals were only  $1 \times 10^3$  p.f.u. ml<sup>-1</sup> nasal lavage in this disease period. Transmission of SARS-CoV-2 between ferrets through the air has recently been demonstrated<sup>22</sup>. Our results underscore that natural infection with SARS-CoV-2 through large droplets, aerosols and/or fomites is highly productive.

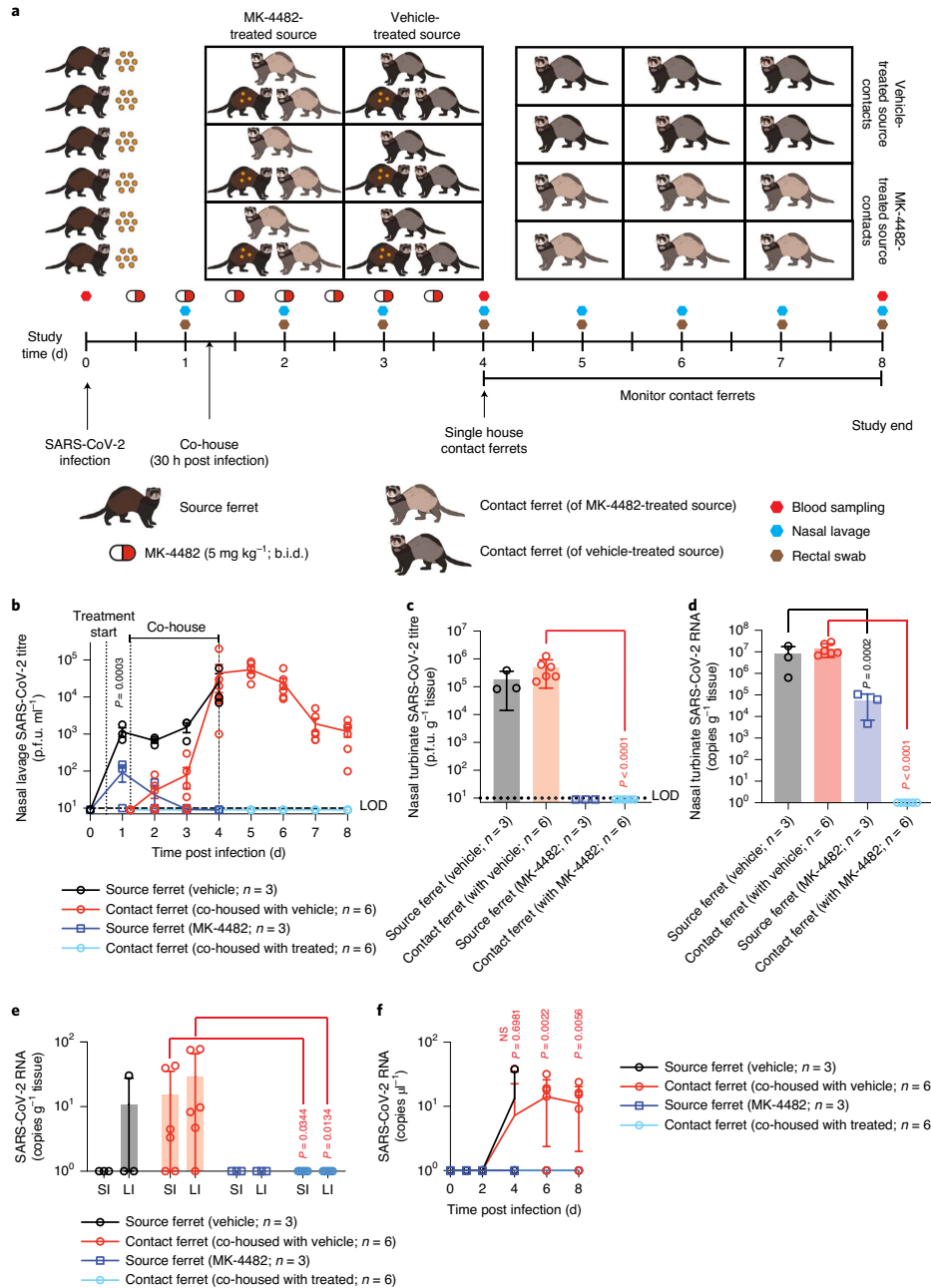
MK-4482/EIDD-2801 is currently being tested in advanced multi-centre clinical trials, which were launched after the successful

NATURE MICROBIOLOGY

LETTERS

completion of phase I safety trials (that is, [NCT04392219](#)). Although the dosages applied in these studies and human pharmacokinetic data have not yet been disclosed, Merck & Co. have revealed<sup>23</sup> that NHC reached levels in human blood that were safe and exceeded antiviral concentrations against SARS-CoV-2 in primary human

airway epithelia cultures (NHC EC<sub>50</sub> of approximately 0.5–1 μM; ref. <sup>15</sup>). Our pharmacokinetic profiles for MK-4482/EIDD-2801 revealed that NHC plasma concentrations ≥0.5 μM at trough (12 h after dosing based on a b.i.d. regimen) are reached after oral doses of approximately 130 and 10 mg kg<sup>-1</sup> were administered to cynomolgus



## LETTERS

## NATURE MICROBIOLOGY

**Fig. 3 | Therapeutic oral treatment with MK-4482/EIDD-2801 prevents contact transmission.** **a**, Schematic of the contact transmission study. Two groups of source ferrets ( $n=3$  biologically independent animals each) were infected with  $1 \times 10^5$  p.f.u. 2019-nCoV/USA-WA1/2020 and received MK-4482/EIDD-2801 treatment ( $5 \text{ mg kg}^{-1}$  b.i.d.) or vehicle starting 12 h after infection. At 30 h after infection, each source ferret was co-housed with two uninfected untreated contact ferrets. The source animals were euthanized after 3 d, and the contact ferrets were isolated and monitored for 4 d. Nasal lavages and rectal swabs were collected once a day and blood was sampled at 0, 4 and 8 d post infection. **b**, Source ferrets treated with MK-4482/EIDD-2801 had significantly lower virus titres than the vehicle animals 12 h after treatment commencement ( $P=0.0003$ ). The contacts of the vehicle-treated sources began to shed 2019-nCoV/USA-WA1/2020 within 20 h of co-housing. No virus could be detected in the untreated contacts of the source ferrets treated with MK-4482/EIDD-2801. Statistical analysis was performed using a two-way ANOVA with Sidak's multiple comparison post-hoc test;  $P$  values are shown. **c,d**, Infectious particle (**c**) and viral RNA copy (**d**) numbers in the nasal turbinates of the source and contact ferrets from **b** extracted 4 and 8 d after the start of the study, respectively. Statistical analysis was performed using a one-way ANOVA with Sidak's multiple comparison post-hoc test (**c**,  $P < 0.0001$  for intergroup comparison of contact animals; **d**,  $P = 0.0002$  and  $P < 0.0001$  for intergroup comparisons of the source and contact animals, respectively). **e,f**, Viral RNA copy number in the small (SI) and large (LI) intestine (**e**), and rectal swabs (**f**). The samples from the source ferrets treated with MK-4482/EIDD-2801 and their contacts were PCR-negative for viral RNA. Statistical analysis was performed using a one-way (**e**) or two-way (**f**) ANOVA with Sidak's multiple comparison post-hoc test. The samples being compared in the post-hoc tests (**c-f**) have been colour-coded black or red for the vehicle-treated source and contact ferrets, respectively. The number of independent biological repeats is shown for each panel.  $P$  values are shown. Symbols represent independent biological repeats (individual animals), lines connect the group mean  $\pm$  s.d. (**b,f**) and bar graphs show the mean  $\pm$  s.d. (**c-e**).

macaques and ferrets, respectively<sup>4</sup>. These calculations drove our decision to dose ferrets with the  $5 \text{ mg kg}^{-1}$  dose used in this study, which represents a conservative estimate of a safe human-dose equivalent based on all of the available information. Underscoring the high broad-spectrum antiviral potential of the drug,  $5 \text{ mg kg}^{-1}$  is also close to the lowest efficacious dose of MK-4482/EIDD-2801 against seasonal and pandemic influenza viruses in ferrets<sup>4,10</sup>.

Closely resembling our previous experience with influenza therapy<sup>4,10</sup>, MK-4482/EIDD-2801 was well tolerated and orally efficacious against SARS-CoV-2, reducing the upper respiratory virus load to below the detection level within 24 h of the first drug administration when therapy was initiated after the onset of virus shedding and by nearly two orders of magnitude when first administered at the peak of virus replication. Similarly, viral genetic material was undetectable in the gastrointestinal samples of the treated animals, which is consistent with previous observations of a sustained presence of the biologically active triphosphate form of NHC in all soft tissue, except liver, in different species<sup>4,12,24</sup>.

Importantly, treatment suppressed all transmission to the untreated direct contacts despite a prolonged direct proximity of the source and contact animals as well as detectable virus shedding from the source animals at the beginning of the co-housing phase. This complete block may indicate a bottom threshold of the shed SARS-CoV-2 load for successful spread. In addition, the genome integrity of some EIDD-2801-experienced virions shed from the treated animals may have been only partially compromised. Rather than being chain-terminating when incorporated by the viral polymerase, NHC undergoes spontaneous tautomeric interconversions, leading to base pairing either as cytosine or uracil<sup>25</sup>. The resulting randomly positioned transition mutations induce viral error catastrophe<sup>26</sup>, causing a collapse of the virus population. This mechanism of antiviral activity of NHC was demonstrated for alphaviruses<sup>12</sup>, pneumoviruses<sup>11</sup> and orthomyxoviruses<sup>4</sup>, and confirmed to equally apply to betacoronaviruses<sup>19</sup> and specifically SARS-CoVs<sup>13</sup>. In our study, a limited presence of the analogue in the viral genomes generated shortly after the start of treatment may have had a greater impact on natural invasion of an immune-competent host in vivo than on virus replication in type I interferon-deficient cultured cells such as the Vero E6 used for titration<sup>27</sup>. This view is consistent with the frequent observation (such as in ref. <sup>28</sup>) that many mutant viruses can be propagated in cell culture but are attenuated in vivo and incapable of productive host invasion.

Consistent with the conserved antiviral mechanism of action of NHC across diverse viral targets, several previous attempts to induce robust resistance to the compound in alphaviruses<sup>12</sup>, orthomyxoviruses<sup>4</sup> and betacoronaviruses<sup>19</sup> were unsuccessful, indicating a high genetic barrier against viral escape. For betacoronaviruses

specifically, a very moderate twofold increase in the  $EC_{50}$  concentration was reported after 30 passages in the presence of inhibitor<sup>19</sup>. Given that these mutations delayed viral replication and thus posed a fitness penalty, it is unlikely that clinical use of MK-4482/EIDD-2801 will result in the emergence of pre-existing resistance in circulating virus populations or trigger the appearance of viral variants with enhanced pathogenicity.

Our previous studies with influenza viruses in ferrets<sup>4</sup> and guinea pigs<sup>11</sup> furthermore demonstrate that the antiviral efficacy and transmission block by MK-4482/EIDD-2801 are not host-species restricted. A virological study of hospitalized patients with coronavirus disease 2019 (COVID-19) revealed that the average load of SARS-CoV-2 RNA copies detected in human sputum during the peak phase of infection is  $7.0 \times 10^6$  copies  $\text{ml}^{-1}$  (maximum of  $2.35 \times 10^9$  copies  $\text{ml}^{-1}$ )<sup>29</sup>. Attempts at virus isolation from human patients were generally unsuccessful when the samples contained  $< 1 \times 10^6$  RNA copies  $\text{ml}^{-1}$ . In ferrets, we found peak shedding titres of  $1 \times 10^5$ – $1 \times 10^4$  p.f.u.  $\text{ml}^{-1}$  in the nasal lavages and an earlier study reported that SARS-CoV-2 concentrations of up to  $1 \times 10^4$  p.f.u.  $\text{ml}^{-1}$  ferret nasal lavage correlates to up to  $1 \times 10^8$  viral RNA copies  $\text{ml}^{-1}$  (ref. <sup>20</sup>). These comparisons suggest that the peak viral RNA copy load in ferret nasal lavages recapitulates that seen in human sputum. At present, the tissue distribution and antiviral efficacy of MK-4482/EIDD-2801 in humans are still unknown. If ferret-based inhibition data of SARS-CoV-2 transmission are predictive of the effect in humans, however, patients with COVID-19 could become non-infectious within 24–36 h after the onset of oral treatment. Treatment with MK-4482/EIDD-2801, in particular when initiated early after infection, thus has the potential to provide threefold benefits: it may mitigate the risk of progression to severe disease and accelerate recovery, ease the emotional and socio-economic toll associated with mandatory prolonged isolation and aid in rapidly silencing local outbreaks.

### Methods

**Study design.** Ferrets (*Mustela putorius furo*) were used as an in vivo model to examine the efficacy of therapeutically administered oral MK-4482/EIDD-2801 against SARS-CoV-2 infection and virus transmission to uninfected contact animals. Viruses were administered to source animals through intranasal inoculation and the virus loads in nasal lavages and rectal swabs were monitored periodically as well as in respiratory tissues and a subset of organs 4 or 10 d after exposure. The virus titres were determined based on plaque assays and viral RNA copy numbers; blood samples were subjected to CBC analysis and RT-qPCR quantitation of the expression levels of select cytokine and innate antiviral effectors.

**Cells and viruses.** Vero E6 cells were obtained from the American Type Culture Collection (ATCC CRLK-1586) and cultured in DMEM medium supplemented with 7.5% heat-inactivated fetal bovine serum (FBS) at 37 °C with 5%  $\text{CO}_2$ . SARS-CoV-2 (2019-nCoV/USA-WA1/2020) was propagated using Vero E6 cells



## NATURE MICROBIOLOGY

## LETTERS

supplemented with 2% FBS. The virus stocks were stored at  $-80^{\circ}\text{C}$  and titres were determined by plaque assay. Vero E6 cells were authenticated by morphology and susceptibility to virus infection, and routinely checked for bacterial and mycoplasma contamination at intervals of 6 months.

**Virus yield reduction assay.** Vero E6 cells were seeded in 12-well plates ( $3 \times 10^6$  cells per well) 24 h before infection. The cells were infected using a multiplicity of infection of 0.1 p.f.u. per cell. SARS-CoV-2 was allowed to adsorb for 1 h at  $37^{\circ}\text{C}$ . Subsequently, the virus inoculum was removed and the cells were overlaid with medium containing threefold serial dilutions of NHC (50–0.68  $\mu\text{M}$ ) in DMEM supplemented with 2% FBS. The infected cells were incubated with compound for 48 h at  $37^{\circ}\text{C}$ , followed by virus titration by plaque assay. The  $\text{EC}_{50}$  and  $\text{EC}_{90}$  concentrations were calculated using four-parameter variable slope regression modelling.

**Plaque assay.** Samples were serially diluted (tenfold dilutions starting at a 1:10 initial dilution) in DMEM medium supplemented with 2% FBS containing Antibiotic-Antimycotic (Gibco). The serial dilutions were added to Vero E6 cells seeded in 12-well plates at  $3 \times 10^6$  cells per well 24 h previously. The virus was allowed to adsorb for 1 h at  $37^{\circ}\text{C}$ . Subsequently, the inoculum was removed and the cells were overlaid with 1.2% Avicel (FMC BioPolymer) in DMEM and incubated for 3 d at  $37^{\circ}\text{C}$  with 5%  $\text{CO}_2$ . The Avicel was removed and the cells were washed once with PBS, fixed with 10% neutral buffered formalin and plaques were visualized using 1% crystal violet.

**Establishing the infectious dose.** Female ferrets (6–10 months of age) were purchased from Triple F Farms. The ferrets were rested for 1 week following arrival, and then randomly assigned to groups and housed individually in ventilated negative-pressure cages in an ABSL-3 facility. To establish a suitable inoculum for the efficacy and transmission studies, the ferrets ( $n=4$ ) were inoculated intranasally with  $1 \times 10^4$  and  $1 \times 10^5$  p.f.u. 2019-nCoV/USA-WA1/2020 in 1 ml (0.5 ml per nare). The ferrets were anaesthetized with dexmedetomidine/ketamine before inoculation. Nasal lavages were performed on non-anaesthetized animals once a day using 1 ml PBS containing twofold concentrated Antibiotic-Antimycotic (Gibco). The nasal lavage fluids were stored at  $-80^{\circ}\text{C}$  until virus titration through plaque assays on Vero E6 cells. For blood sampling, the ferrets were anaesthetized with dexmedetomidine and approximately 0.5 ml blood was drawn from the anterior vena cava. A Vetscan HM5 (Abaxis) was used to perform CBCs in accordance with the manufacturer's protocol. Rectal swabs were performed every 2 d. Groups of two ferrets were killed 4 and 10 d post infection and their organs were harvested to determine the virus titres and presence of viral RNA in different tissues.

**Animals.** The group sizes were three ferrets per condition for all animal experiments. A power calculation ( $P < 0.05$ ; 80% power) predicted that this sample size was sufficient to detect a difference of  $1.19 \log_{10}$  p.f.u.  $\text{ml}^{-1}$  in virus titre in ferret nasal lavages. As no statistically informative reference datasets for the SARS-CoV-2 ferret model were available at the start of the study, we based this prospective calculation on our experience with a canine distemper virus ferret infection model that has shown a cumulative s.d. of 0.32 in our laboratory. In the transmission experiments, the ferrets were co-housed at a ratio of one source to two contact animals, three co-housing sets per condition. Incoming animals were randomly assigned to the different study groups; no blinding of investigators was performed.

**In vivo efficacy of MK-4482/EIDD-2801 in ferrets.** The groups of ferrets were inoculated with  $1 \times 10^5$  p.f.u. 2019-nCoV/USA-WA1/2020 in 1 ml (0.5 ml per nare). At 12 h after infection, three groups of ferrets were treated b.i.d. with vehicle (1% methylcellulose) or MK-4482/EIDD-2801 at a dosage of 5 or 15  $\text{mg kg}^{-1}$ , respectively. At 36 h after infection, a fourth group of ferrets began receiving b.i.d. treatment with MK-4482/EIDD-2801 at a dose of 15  $\text{mg kg}^{-1}$ . The compound was administered via oral gavage in 1% methylcellulose. After the start of treatment, b.i.d. dosing was continued until 4 d after infection. Nasal lavages were performed on all of the ferrets every 12 h. Blood samples were obtained every 2 d after infection and stored in  $\text{K}_2\text{-EDTA}$  tubes (Sarstedt CB 300). CBC analysis was performed on each blood sample in accordance with the manufacturer's protocols. After the CBC analysis, the red blood cells were lysed with ACK buffer (150 mM  $\text{NH}_4\text{Cl}$ , 10 mM  $\text{KHCO}_3$  and 0.01 mM EDTA pH 7.4) and the PBMCs were harvested and stored at  $-80^{\circ}\text{C}$  in RNAlater until further RT-qPCR analysis was performed. All of the ferrets were euthanized 4 d after infection and their organs were harvested to determine the virus titres and presence of viral RNA in different tissues.

**Contact transmission of SARS-CoV-2 in ferrets.** A group of six source ferrets, which were housed individually, were inoculated intranasally with  $1 \times 10^5$  p.f.u. 2019-nCoV/USA-WA1/2020. Twelve hours after infection, the source ferrets were split into two groups ( $n=3$  each) receiving vehicle or MK-4482/EIDD-2801 treatment at a dose of 5  $\text{mg kg}^{-1}$  b.i.d. by oral gavage. At 30 h post infection, each source ferret was co-housed with two uninfected and untreated contact ferrets. The ferrets were co-housed until 96 h after infection, when the source ferrets were

euthanized and the contact animals were housed individually. The contact animals were monitored for 4 d after separation from the source ferrets and then killed. Nasal lavages and rectal swabs were performed on all of the ferrets every 24 h. Blood samples were collected at 0, 4 and 8 d after the source ferret infection. For all ferrets, organs were harvested to determine the virus titres and the presence of viral RNA in different tissues.

**Titration of SARS-CoV-2 in tissue extracts.** For virus titration, the organs were weighed and homogenized in PBS. The homogenates were centrifuged at 2,000g for 5 min at  $4^{\circ}\text{C}$ . The clarified supernatants were harvested and used in subsequent plaque assays. For detection of viral RNA, the harvested organs were stored in RNAlater at  $-80^{\circ}\text{C}$ . The tissues were ground and the total RNA was extracted using an RNeasy mini kit (Qiagen). RNA was extracted from the rectal swabs using a ZR viral RNA kit (Zymo Research) in accordance with the manufacturer's protocols.

**SARS-CoV-2 RNA copy numbers.** Detection of SARS-CoV-2 RNA was performed using the nCoV\_IP2 primer-probe set (National Reference Center for Respiratory Viruses, Institut Pasteur) targeting the SARS-CoV-2 *RdRp* gene. An Applied Biosystems 7500 real-time PCR system using the StepOnePlus real-time PCR system was used to perform the RT-qPCR reactions. TaqMan fast virus 1-step master mix (Thermo Fisher Scientific) was used in combination with the nCoV\_IP2 primer-probe set to detect viral RNA. To quantitate the RNA copy numbers, a standard curve was created using a PCR fragment (nucleotides 12669–14146 of the SARS-CoV-2 genome) generated from viral complementary DNA using the nCoV\_IP2 forward primer and the nCoV\_IP4 reverse primer. The RNA values were normalized to the weights of the tissues used.

**Systemic interferon and cytokine profiling.** The relative expression of interferon, ISGs and cytokines was determined by real-time PCR analysis. RNA was extracted from PBMCs that were harvested at various time points after infection. Complementary DNA was reverse transcribed with SuperScript III (Invitrogen) using oligo-dT primers and analysed by real-time PCR using Fast SYBR Green master mix (Applied Biosystems). The signals were normalized to glyceraldehyde-3-phosphate dehydrogenase messenger RNA, analysed using the comparative threshold cycle ( $\Delta\Delta\text{C}_t$ ) method and expressed relative to day 0 of infection for each respective animal. The sequences of the primers used for the analyses are shown in Supplementary Table 13.

**Statistics and reproducibility.** The Microsoft Excel (versions 16.42 and 16.43) and GraphPad Prism (version 8.4.3) software packages were used for most of the data collection and analysis, respectively. Reverse transcription RT-qPCR data were collected and analysed using the StepOnePlus (version 2.1; Applied Biosystems) software package. The final figures were assembled using Adobe Illustrator (version CS6). One- or two-way ANOVAs with Dunnett's, Tukey's or Sidak's multiple comparisons post-hoc tests without further adjustments were used to evaluate statistical significance when more than two groups were compared or datasets contained two independent variables, respectively. The specific statistical test applied to individual studies is specified in the figure legends. The Source Data files summarize the statistical analyses (effect size, degrees of freedom and  $P$  values) of the respective datasets. Effect sizes between groups in the ANOVAs were calculated as  $\eta^2 = (\text{SS}_{\text{effect}}) / (\text{SS}_{\text{total}})$  for one-way ANOVA and  $\omega^2 = (\text{SS}_{\text{effect}} - (\text{df}_{\text{effect}})(\text{MS}_{\text{error}})) / (\text{MS}_{\text{error}} + \text{SS}_{\text{total}})$  for two-way ANOVA;  $\text{SS}_{\text{effect}}$ , sum of squares for the effect;  $\text{SS}_{\text{total}}$ , sum of squares for total;  $\text{df}_{\text{effect}}$ , degrees of freedom for the effect;  $\text{MS}_{\text{error}}$ , mean squared error. To determine the antiviral potency and cytotoxicity, the effective concentrations were calculated from dose-response datasets through four-parameter variable slope regression modelling; the values have been expressed with 95% confidence intervals when possible. A biological repeat refers to measurements taken from distinct samples, and the results obtained for each individual biological repeat are shown in the figures along with the exact size ( $n$ , number) of biologically independent samples, animals or independent experiments. The measure of the centre (connecting lines and columns) is the mean throughout. The error bars represent the s.d. throughout. For all experiments, the statistical significance level  $\alpha$  was set to  $< 0.05$ ; exact  $P$  values are shown in individual graphs or Supplementary Tables wherever possible.

**Ethics statement.** All animal work was performed in compliance with the Guide for the Care and Use of Laboratory Animals of the National Institutes of Health and the Animal Welfare Act Code of Federal Regulations. Experiments with SARS-CoV-2 involving ferrets were approved by the Georgia State Institutional Animal Care and Use Committee under protocol A20031. All experiments using infectious SARS-CoV-2 were approved by the Georgia State Institutional Biosafety Committee under protocol B20016 and performed in BSL-3/ABSL-3 facilities at the Georgia State University.

**Reporting Summary.** Further information on research design is available in the Nature Research Reporting Summary linked to this article.

## LETTERS

## NATURE MICROBIOLOGY

**Data availability**

All of the data generated or analysed during this study are included in this published article. Source data are provided with this paper.

**Code availability**

This study does not use custom codes. All of the commercial computer codes and algorithms used are specified in the Methods section.

Received: 3 November 2020; Accepted: 18 November 2020;

Published online: 3 December 2020

**References**

- Rodriguez Mega, E. COVID has killed more than one million people. How many more will die? *Nature* <https://doi.org/10.1038/d41586-020-02762-y> (2020).
- Martinot, M. et al. Remdesivir failure with SARS-CoV-2 RNA-dependent RNA-polymerase mutation in a B-cell immunodeficient patient with protracted Covid-19. *Clin. Infect. Dis.* <https://doi.org/10.1093/cid/ciaa1474> (2020).
- Humeniuk, R. et al. Safety, tolerability, and pharmacokinetics of remdesivir, an antiviral for treatment of COVID-19, in healthy subjects. *Clin. Transl. Sci.* **13**, 896–906 (2020).
- Toots, M. et al. Characterization of orally efficacious influenza drug with high resistance barrier in ferrets and human airway epithelia. *Sci. Transl. Med.* **11**, eaax5866 (2019).
- Toots, M. & Plemper, R. K. Next-generation direct-acting influenza therapeutics. *Transl. Res.* <https://doi.org/10.1016/j.trsl.2020.01.005> (2020).
- Salajegheh Tazerji, S. et al. Transmission of severe acute respiratory syndrome coronavirus 2 (SARS-CoV-2) to animals: an updated review. *J. Transl. Med.* **18**, 358 (2020).
- Oreshkova, N. et al. SARS-CoV-2 infection in farmed minks, the Netherlands, April and May 2020. *Euro Surveill.* <https://doi.org/10.2807/1560-7917.ES.2020.25.23.2001005> (2020).
- Enserink, M. Coronavirus rips through Dutch mink farms, triggering culls. *Science* **368**, 1169 (2020).
- Oude Munnink, B. B. et al. Transmission of SARS-CoV-2 on mink farms between humans and mink and back to humans. *Science* <https://doi.org/10.1126/science.abe5901> (2020).
- Toots, M. et al. Quantitative efficacy paradigms of the influenza clinical drug candidate EIDD-2801 in the ferret model. *Transl. Res.* **218**, 16–28 (2020).
- Yoon, J. J. et al. Orally efficacious broad-spectrum ribonucleoside analog inhibitor of influenza and respiratory syncytial viruses. *Antimicrob. Agents Chemother.* **62**, e00766-18 (2018).
- Uraikova, N. et al.  $\beta$ -D-N<sup>4</sup>-Hydroxycytidine is a potent anti- $\alpha$  virus compound that induces a high level of mutations in the viral genome. *J. Virol.* **92**, e01965-17 (2018).
- Sheahan, T. P. et al. An orally bioavailable broad-spectrum antiviral inhibits SARS-CoV-2 in human airway epithelial cell cultures and multiple coronaviruses in mice. *Sci. Transl. Med.* **12**, eabb5883 (2020).
- Han, K. et al. Lung expression of human ACE2 sensitizes the mouse to SARS-CoV-2 infection. *Am. J. Respir. Cell Mol. Biol.* <https://doi.org/10.1165/rcmb.2020-0354OC> (2020).
- Bruschke, C. *Nature and Food Quality Ministry of Agriculture* (Ministry of Agriculture, 2020).
- Schlottau, K. et al. SARS-CoV-2 in fruit bats, ferrets, pigs, and chickens: an experimental transmission study. *Lancet Microbe* **1**, e218–e225 (2020).
- Richard, M. et al. SARS-CoV-2 is transmitted via contact and via the air between ferrets. *Nat. Commun.* **11**, 3496 (2020).
- Davies, N. G. et al. Age-dependent effects in the transmission and control of COVID-19 epidemics. *Nat. Med.* **26**, 1205–1211 (2020).
- Agostini, M. L. et al. Small-molecule antiviral  $\beta$ -D-N<sup>4</sup>-hydroxycytidine inhibits a proofreading-intact coronavirus with a high genetic barrier to resistance. *J. Virol.* **93**, e01348-19 (2019).
- Shi, J. et al. Susceptibility of ferrets, cats, dogs, and other domesticated animals to SARS-coronavirus 2. *Science* **368**, 1016–1020 (2020).
- Park, S. J. et al. Antiviral efficacies of FDA-approved drugs against SARS-CoV-2 infection in ferrets. *mBio* **11**, e01114-20 (2020).
- Kutter, J. S. et al. SARS-CoV and SARS-CoV-2 are transmitted through the air between ferrets over more than one meter distance. Preprint at *bioRxiv* <https://doi.org/10.1101/2020.10.19.345363> (2020).
- Merck & Co. (Ridgeback Biotherapeutics) and Drug Innovations at Emory (DRIVE) – MK-4482 (formerly EIDD-2801). *Genetic Engineering and Biotechnology News* <https://www.genengnews.com/covid-19-candidates/ridgeback-biotherapeutics-and-drug-innovations-at-emory-drive/> (2020).
- Painter, G. R. et al. The prophylactic and therapeutic activity of a broadly active ribonucleoside analog in a murine model of intranasal Venezuelan equine encephalitis virus infection. *Antivir. Res.* **171**, 104597 (2019).
- Les, A., Adamowicz, L. & Rode, W. Structure and conformation of N<sup>4</sup>-hydroxycytosine and N<sup>4</sup>-hydroxy-5-fluorocytosine. A theoretical ab initio study. *Biochim. Biophys. Acta* **1173**, 39–48 (1993).
- Crotty, S., Cameron, C. E. & Andino, R. RNA virus error catastrophe: direct molecular test by using ribavirin. *Proc. Natl Acad. Sci. USA* **98**, 6895–6900 (2001).
- Desmyter, J., Melnick, J. L. & Rawls, W. E. Defectiveness of interferon production and of rubella virus interference in a line of African green monkey kidney cells (Vero). *J. Virol.* **2**, 955–961 (1968).
- Cox, R. M. et al. Orally efficacious broad-spectrum allosteric inhibitor of paramyxovirus polymerase. *Nat. Microbiol.* <https://doi.org/10.1038/s41564-020-0752-7> (2020).
- Wolfel, R. et al. Virological assessment of hospitalized patients with COVID-2019. *Nature* **581**, 465–469 (2020).

**Acknowledgements**

We thank M. Kumar for providing an aliquot of 2019-nCoV/USA-WA1/2020 stock, members of the GSU High Containment Core and the Department for Animal Research for support, and J. Sourimant and A. L. Hammond for critical reading of the manuscript. This work was supported, in part, by Public Health Service grant nos AI071002 (to R.K.P.) and AI141222 (to R.K.P.) from the NIH/NIAID. The funders had no role in the study design, data collection and interpretation or the decision to submit the work for publication.

**Author contributions**

R.M.C. and J.D.W. performed the virus-stock preparations; animal inoculations; sampling and necropsies; contributed to the experiment design, data analysis and presentation; and edited the manuscript. R.M.C. performed all of the RT-qPCR experiments and analyses. J.D.W. performed all of the CBC analyses. R.K.P. conceived, designed and coordinated the study; conceived and designed experiments; contributed to the animal inoculations and necropsies; contributed to data analysis and presentation; and wrote the manuscript.

**Competing interests**

The authors declare no competing interests.

**Additional information**

Extended data is available for this paper at <https://doi.org/10.1038/s41564-020-00835-2>.

Supplementary information is available for this paper at <https://doi.org/10.1038/s41564-020-00835-2>.

Correspondence and requests for materials should be addressed to R.K.P.

Reprints and permissions information is available at [www.nature.com/reprints](http://www.nature.com/reprints).

Publisher's note Springer Nature remains neutral with regard to jurisdictional claims in published maps and institutional affiliations.

Peer review statement *Nature Microbiology* thanks the anonymous reviewers for their contribution to the peer review of this work. Peer reviewer reports are available.

© The Author(s), under exclusive licence to Springer Nature Limited 2020

## 2.1.2 SARS-CoV-2 VOC Type and Biological Sex Affect Molnupiravir Efficacy in Severe COVID-19 Dwarf Hamster Model

nature communications



Article

<https://doi.org/10.1038/s41467-022-32045-1>

# SARS-CoV-2 VOC type and biological sex affect molnupiravir efficacy in severe COVID-19 dwarf hamster model

Received: 1 March 2022

Accepted: 14 July 2022

Published online: 29 July 2022

Check for updates

Carolin M. Lieber<sup>1,5</sup>, Robert M. Cox<sup>1,5</sup>, Julien Sourimant<sup>1</sup>, Josef D. Wolf<sup>1</sup>, Kate Juergens<sup>2</sup>, Quynh Phung<sup>2</sup>, Manohar T. Saindane<sup>3</sup>, Meghan K. Smith<sup>3</sup>, Zachary M. Sticher<sup>3</sup>, Alexander A. Kalykhalov<sup>3</sup>, Michael G. Natchus<sup>3</sup>, George R. Painter<sup>3</sup>, Kaori Sakamoto<sup>4</sup>, Alexander L. Greninger<sup>2</sup> & Richard K. Plemper<sup>1</sup> ✉

SARS-CoV-2 variants of concern (VOC) have triggered infection waves. Oral antivirals such as molnupiravir promise to improve disease management, but efficacy against VOC delta was questioned and potency against omicron is unknown. This study evaluates molnupiravir against VOC in human airway epithelium organoids, ferrets, and a lethal Roborovski dwarf hamster model of severe COVID-19-like lung injury. VOC were equally inhibited by molnupiravir in cells and organoids. Treatment reduced shedding in ferrets and prevented transmission. Pathogenicity in dwarf hamsters was VOC-dependent and highest for delta, gamma, and omicron. All molnupiravir-treated dwarf hamsters survived, showing reduction in lung virus load from one (delta) to four (gamma) orders of magnitude. Treatment effect size varied in individual dwarf hamsters infected with omicron and was significant in males, but not females. The dwarf hamster model recapitulates mixed efficacy of molnupiravir in human trials and alerts that benefit must be reassessed *in vivo* as VOC evolve.

By May 2022, SARS-CoV-2 has resulted in over 522 million cases and >6.2 million deaths worldwide<sup>1</sup>. Vaccines are widely available<sup>2,3</sup>, but recurring global infection waves have been fueled by limited longevity of vaccine-induced immunity, the hesitancy of population subgroups to vaccinate<sup>4,5</sup>, and increasingly contagious and/or vaccine-insensitive variants of concern (VOC) alpha (B.1.1.7 lineage), beta (B.1.351 lineage), gamma (P.1 lineage), delta (B.1.617.2 lineage), and omicron (B.1.1.529 lineage)<sup>6,7</sup>. VOC delta was the prevalent circulating variant during Summer and Fall 2021 due to replication to high titers, prolonged shedding from infected individuals, and propensity to induce breakthrough infections in vaccinees<sup>8–10</sup>. Since its first appearance in November 2021, VOC omicron has rapidly replaced delta as the dominant circulating strain in most geographical regions<sup>11</sup>, propelled

by sharply reduced sensitivity to neutralizing antibodies directed against earlier lineages and greatly increased infectivity<sup>12</sup>. Although clinical signs associated with VOC omicron are typically milder than those of its predecessors, record-high daily infection rates have driven high absolute hospitalization numbers, creating an urgent need for therapeutics to improve disease management.

Molnupiravir was the first orally available SARS-CoV-2 inhibitor approved for outpatient use against COVID-19<sup>13</sup>. Intermediate results of the early months of a large efficacy trial revealed an encouraging 50% reduction in hospitalizations in the treatment group, but later analysis of the full dataset showed only a 30% lower hospitalization rate overall<sup>14</sup>. Based on the geographical location of trial participants and VOC prevalence in the earlier versus later phase of the trial, an

<sup>1</sup>Center for Translational Antiviral Research, Institute for Biomedical Sciences, Georgia State University, Atlanta, GA 30303, USA. <sup>2</sup>Virology Division, Department of Laboratory Medicine, University of Washington, Seattle, WA 98185, USA. <sup>3</sup>Emory Institute for Drug Development, Emory University, Atlanta, GA 30329, USA. <sup>4</sup>Department of Pathology, College of Veterinary Medicine, University of Georgia, Athens, GA 30602, USA. <sup>5</sup>These authors contributed equally: Carolin M. Lieber, Robert M. Cox. ✉e-mail: [rplemper@gsu.edu](mailto:rplemper@gsu.edu)



## Article

<https://doi.org/10.1038/s41467-022-32045-1>

advisory board to the FDA considered the lower efficacy of molnupiravir against VOC delta as a possible explanation for the mixed results<sup>15</sup>. However, VOC delta was efficiently inhibited by the molnupiravir parent metabolite N<sup>4</sup>-hydroxycytidine (NHC) in ex vivo studies<sup>16</sup>, suggesting unchanged sensitivity to the drug.

Human airway epithelium organoids, ferrets, mice, and Syrian golden hamsters have emerged as preclinical models to assess the efficacy of anti-SARS-CoV-2 drug candidates. Ferrets recapitulate the predominant clinical presentation of SARS-CoV-2 in younger patients, characterized by a high viral load in the upper respiratory tract, strong viral shedding, and efficient airborne transmission<sup>17–19</sup>. By contrast, Syrian golden hamsters infected with SARS-CoV-2 develop transient pneumonia but do not recapitulate hallmark features of life-threatening severe COVID-19. Disease typically remains mild-to-asymptomatic in golden hamsters and animals fully recover within two weeks<sup>20</sup>. Lethal disease with severe histopathology affecting lung, liver, and kidney can be induced in transgenic K18-hACE2 mice expressing human ACE2, but organ distribution of the receptor is non-physiological, resulting in rapid neuro-invasion of the virus and the development of acute, lethal viral encephalitis<sup>21</sup>, which is not seen in human patients. Lacking is an efficacy model that recapitulates the acute lung injury of life-threatening COVID-19, thereby offering a relevant experimental platform to test the effect of molnupiravir on mitigating lung damage caused by different VOC and explore the impact of treatment on disease outcomes.

In this work, we test molnupiravir against a panel of VOC in cultured cells, human airway epithelium organoids, ferrets, and Roborovski dwarf hamsters, since these dwarf hamsters developed acute diffuse alveolar pneumonia and succumbed to infection<sup>22,23</sup> when infected with original SARS-CoV-2 isolates from 2020. We show that pathogenicity in dwarf hamsters is VOC-dependent with the highest lethality in the case of delta, gamma, and omicron. Independent of VOC tested, all molnupiravir-treated dwarf hamster survived infection, meeting a primary efficacy marker. However, the treatment effect size is VOC-specific and in animals infected with VOC omicron, virus load reduction was significant in males, but not females.

## Results

For quantitative comparison of molnupiravir activity against VOC alpha, beta, gamma, delta, and omicron in cultured cells, we determined half-maximal antiviral concentrations (EC<sub>50</sub>s) on VeroE6 cells stably expressing TMPRSS2 (Vero-TMPRSS2) (Fig. 1a). The molnupiravir parent compound NHC was used in all ex vivo experiments. Under these experimental conditions, inhibitory values were similar for the original SARS-CoV-2 WAI isolate and all VOC tested, ranging from 0.19 (gamma) to 0.62 (beta)  $\mu$ M.

### Consistent activity of molnupiravir against VOC in human airway organoids

To validate activity in disease-relevant primary human tissues, we added at the time of infection NHC at 10  $\mu$ M, equivalent to NHC plasma concentrations reached in human patients<sup>24</sup>, to the basolateral chamber of well-differentiated primary human airway epithelium (HAE) cultures grown at the air-liquid interface. After apical infection with the panel of five VOC, we titered apically shed progeny virions after 1, 2, and 3 days. The treatment instantly suppressed virus replication in the case of VOC alpha, beta, and delta, and within 2 days reduced the progeny load of all VOC to the level of detection (Fig. 1b). Parallel assessment of transepithelial electrical resistance (TEER) as an indicator of an intact tight junction network demonstrated that the drug preserved the integrity of the infected organoids (Supplementary Fig. 1). vehicle-treated controls showed significant reductions in TEER after infection, reflecting the breakdown of epithelium organization. Confocal microscopy confirmed that 10  $\mu$ M basolateral NHC suppressed viral replication, whereas abundant viral antigen (SARS-CoV-2

nucleocapsid and spike protein) was detected in vehicle-treated epithelia (Fig. 1c, Supplementary Figs. 2, 3).

### Efficacy of molnupiravir against VOC upper respiratory disease and transmission in ferrets

To assess in vivo efficacy of molnupiravir against VOC, we infected ferrets intranasally with  $1 \times 10^5$  pfu of VOC alpha, beta, gamma, delta, and omicron and monitored virus replication in the upper respiratory tract. All treated animals were dosed orally at 5 mg/kg b.i.d., starting 12 hours after infection (Fig. 2a) when shed SARS-CoV-2 becomes first detectable in ferret nasal lavages<sup>18,19</sup>. Lavage titers were determined in 12-hour intervals for the first 48 hours after infection, and once daily thereafter. Titters of shed VOC alpha, gamma, delta, and omicron peaked 1–2 days after infection at approximately  $10^3$  to  $10^4$  pfu per ml in vehicle-treated animals (Fig. 2b). Treatment with molnupiravir reduced shed progeny titers of all VOC to detection level within 12 hours. Consistent with previous experience with the ferret model<sup>18,19</sup>, infected animals developed no clinical signs. VOC beta did not establish a productive infection and was eliminated from further ferret experiments (Supplementary Fig. 3).

To explore the impact of treatment on transmission, we co-housed infected and treated source animals with uninfected and untreated sentinels for 48 hours, starting 42 hours after initiation of treatment (Fig. 2c). VOC delta was excluded from transmission studies, since we had not detected any infectious particles in nasal lavages of molnupiravir-treated animals at any time and nasal turbinates of treated animals extracted four days after infection did not contain any infectious particles (Supplementary Fig. 5). We tested VOC alpha in an independent transmission study, but included transmission arms in the efficacy studies with VOC gamma and omicron (Fig. 2b) to reduce overall animal numbers. After separation of source and contact animals on day 4 after infection, untreated sentinels were monitored for an additional four days for shed virions and viral RNA in nasal lavages, and then terminal titers in nasal turbinates were determined.

VOC alpha and gamma spread efficiently from vehicle-treated source animals to the sentinels (Fig. 2d, e), whereas VOC omicron did not transmit (Fig. 2f). RNA of VOC alpha and gamma became first detectable in nasal lavages of the contacts within 12 hours after initiation of co-housing, shed infectious particles emerged after 12 (VOC alpha) to 36 (VOC gamma) hours (Fig. 2e, f), and infectious alpha and gamma, but not omicron, particles were detectable in nasal turbinates extracted from sentinels of vehicle-treated source animals at study end (Supplementary Fig. 6). Treatment with molnupiravir fully suppressed transmission. No infectious particles or viral RNA were detectable in lavages of untreated sentinels, and nasal turbinates of these animals were virus and viral RNA-free at terminal assessment (Fig. 2e, f; Supplementary Fig. 6). These data demonstrate that oral molnupiravir is highly effective in controlling replication of all VOC in the ferret upper respiratory tract, significantly reducing shed virus titers and rapidly suppressing the spread of transmission-competent VOC to untreated naïve contacts.

### Different degrees of acute lung pathogenesis of VOC in Roborovski dwarf hamsters

To explore VOC pathogenicity in a candidate model of lethal COVID-19, we infected Roborovski dwarf hamsters intranasally with  $1 \times 10^5$  pfu each of the original SARS-CoV-2 WAI isolate or VOC alpha, beta, gamma, and omicron, or  $3 \times 10^4$  pfu of VOC delta (Fig. 3a) and monitored clinical signs and survival. Dwarf hamsters showed a rapid decline characterized by ruffled fur, lethargy, and dyspnea within two days of infection, which was accompanied by hypothermia and moderate to substantial loss of body weight (Fig. 3b, c). Severity and time to onset of clinical signs varied among—in order of increasing pathogenicity—VOC alpha, beta, omicron, gamma, and delta. Pathogenesis of VOC gamma was comparable to that of the original WAI isolate. The

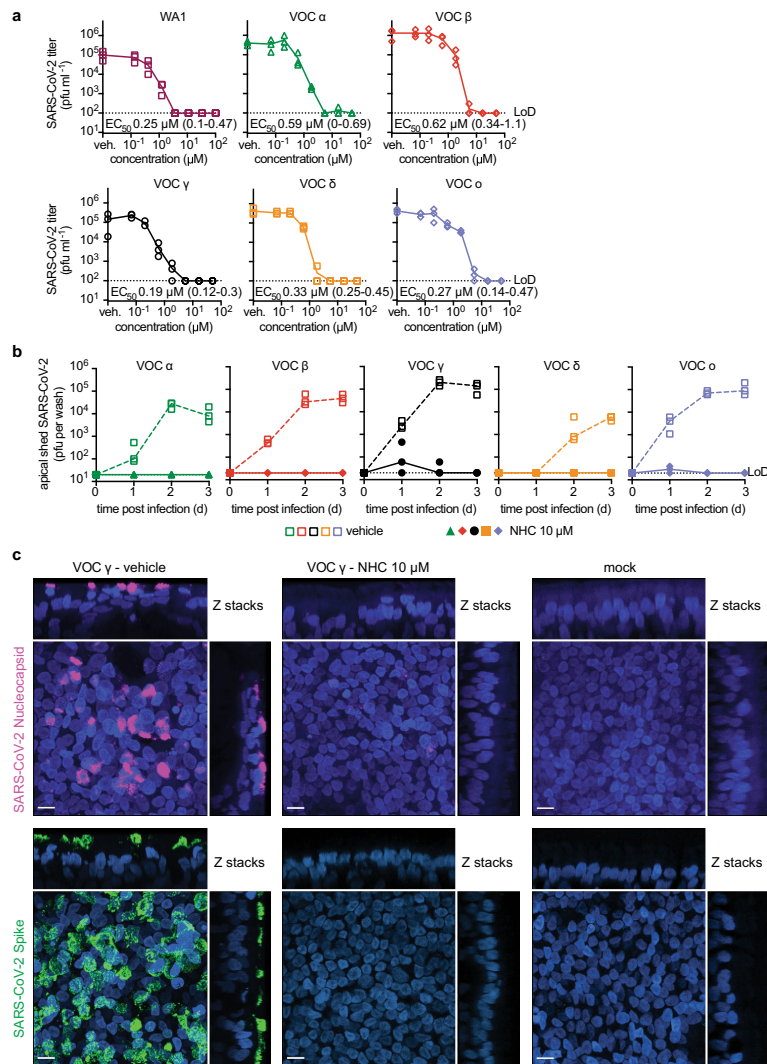


**Fig. 1 | Efficacy of NHC against VOC in cultured cells and primary HAEs.** **a** NHC dose-response assays against SARS-CoV-2 WA1 and VOC alpha, beta, gamma, delta, and omicron on VeroE6-TMPRSS2 cells. EC<sub>50</sub> values from non-linear regression modeling are shown with 95% confidence intervals in parenthesis. **b** Activity of 10  $\mu$ M basolateral NHC administered against VOC as in **a** on well-differentiated primary HAE organoids. Apically shed virus was harvested every 24 hours during a 3-day period after infection. **a**, **b** represent independent biological repeats, lines intersect group means. LoD limit of detection. **c** Confocal microscopy of primary

HAE organoids infected with SARS-CoV-2 VOC gamma. Basolateral NHC suppresses virus replication at 10  $\mu$ M. SARS-CoV-2 nucleocapsid (pink;  $\alpha$ -SARS-CoV-2 nucleocapsid), SARS-CoV-2 spike (green;  $\alpha$ -SARS-CoV-2 S) and nuclei (DAPI) were detected. Z stacks are shown, scale bars 10  $\mu$ m. Per condition and viral target, two independent transwells were processed, one stained for SARS-CoV-2 spike and one for SARS-CoV-2 nucleocapsid; representative fields of view are shown. Source data are provided as a Source Data file.

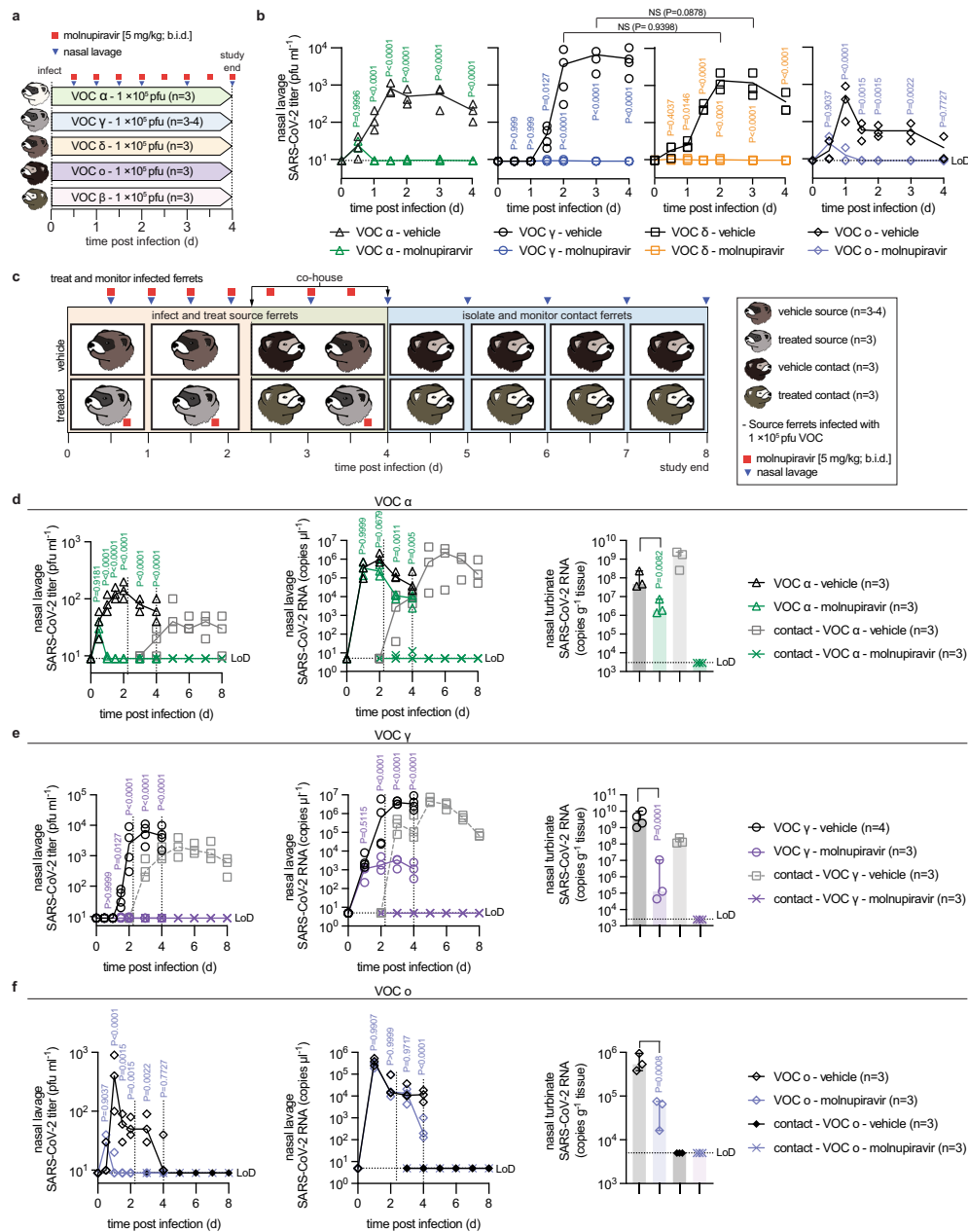
median survival of infected animals was shortened to 5.75 (WA1), 6 (omicron), 3.5 (beta, gamma), and 3 (delta) days after infection (Fig. 3d; Table 1). Approximately 80% of animals inoculated with VOC alpha survived the infection, making alpha the least lethal of the VOC tested.

We intended to determine viral tissue tropism and gross lung pathology three days after infection of subsets of dwarf hamsters with WA1 or the VOC associated with the overall highest mortality rate, gamma, delta, and omicron. However, animals infected with

delta succumbed to infection before the predefined endpoint, preventing analysis. Animals infected with WA1, gamma, or omicron consistently showed the highest viral RNA load in the lung, followed by the small and large intestine and spleen (Fig. 3e). Macroscopic analysis of extracted lungs showed substantial gross tissue damage involving large surface areas (Fig. 3f, Supplementary Fig. 7) and titration of lung homogenates confirmed fulminant viral pneumonia with median virus load of  $1 \times 10^5$  pfu/g lung tissue or greater (Fig. 3g).

Article

<https://doi.org/10.1038/s41467-022-32045-1>



A follow-up study with VOC delta at reduced inoculum amount ( $1 \times 10^4$  pfu intranasally) and shortened time to analysis (Fig. 3h) demonstrated the onset of lung tissue damage (Fig. 3i, Supplementary Fig. 8) and presence of high lung virus loads (Fig. 3j) only 12 hours after infection. Comparison analysis of VOC gamma 24 hours after infection confirmed that rapid viral invasion of the dwarf hamsters was not limited to VOC delta.

**Effect of VOC type and biological sex on prevention of lethal viral pneumonia**

VOC gamma, delta, and omicron were selected for an efficacy study assessing mitigation of viral pneumonia and acute lung injury with molnupiravir. Animals were inoculated with  $1 \times 10^4$  pfu intranasally to prevent premature death, followed by initiation of treatment (250 mg/kg orally b.i.d.) 12 hours after infection (Fig. 4a), when lung

## Article

<https://doi.org/10.1038/s41467-022-32045-1>**Fig. 2 | Therapeutic molnupiravir is efficacious against a panel of VOC in ferrets.**

**a** Treatment and monitoring schematic. Ferrets ( $n = 6$  total per VOC tested) were infected intranasally with  $1 \times 10^5$  pfu of VOC and treated orally with vehicle or molnupiravir (5 mg/kg b.i.d.), starting 12 hours after infection. **b** Infectious SARS-CoV-2 titers in nasal lavages of vehicle or molnupiravir-treated animals. **c** Schematic of transmission studies with VOC alpha, gamma, and omicron. For VOC alpha, fresh source ferrets ( $n = 6$ ) were used, for VOC gamma and omicron, transmission arms were added to **b**. Source animals were co-housed at a 1:1-ratio with uninfected and untreated contacts starting 42 hours after the beginning of treatment. Nasal lavages were obtained twice daily in the first 48 hours after infection, thereafter once daily. Nasal turbinates were extracted from source animals 4 days after infection and

untreated sentinels continued for an additional 4 days. **d-f** Transmission study with VOC alpha (**d**), gamma (**e**), and omicron (**f**). Shown are infectious titers in nasal lavages (left), viral RNA copies in the lavages (center), and nasal turbinate titers (right). Symbols in **b, d-f** represent independent biological repeats (virus load of individual animals), lines (**b, d-f**) intersect group medians, and columns (**c, e-g**) show group medians  $\pm 95\%$  confidence intervals. Statistical analysis with one-way (**d-f** turbinate titers) or two-way (**b, d-f** lavage titers) ANOVA with Tukey's (**d-f** turbinate titers) or Sidak's (**b, d-f** lavage titers) posthoc multiple comparison tests;  $P$  values are shown, NS not significant, LoD limit of detection. Source data are provided as a Source Data file.

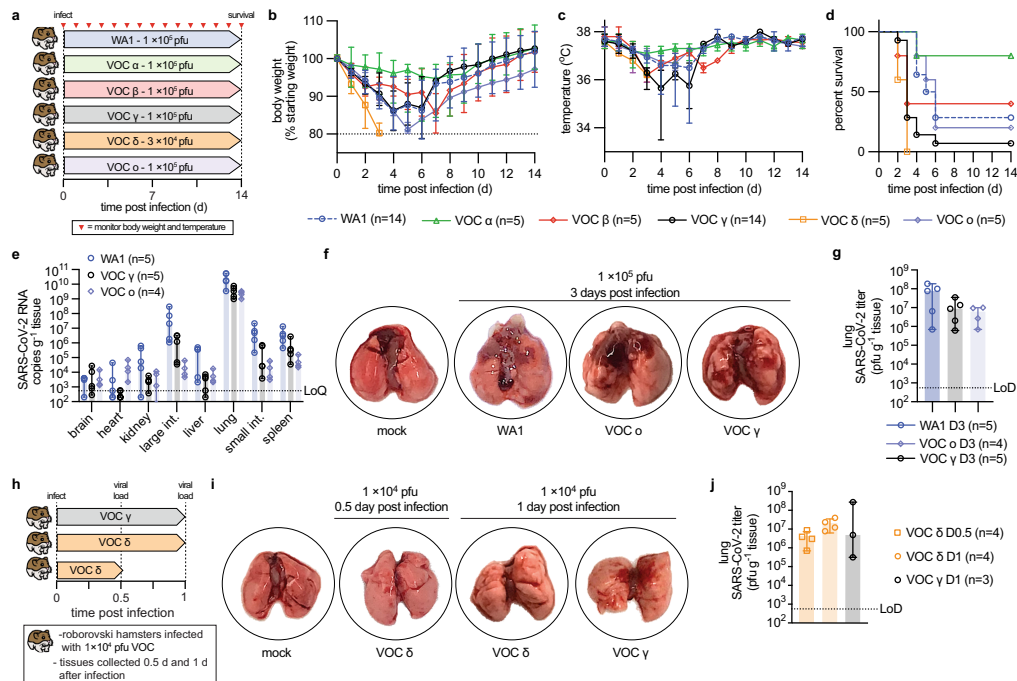


**Fig. 3 | VOC pathogenesis in Roborovski dwarf hamsters.** **a** Schematic of the dwarf hamster pathogenesis study. Animals were monitored for up to 14 days after intranasal infection with  $1 \times 10^5$  pfu each (VOC delta  $3 \times 10^4$  pfu per animal). Clinical signs were assessed once daily (red triangles). **b, c** Body weight (**b**) and temperature (**c**) of infected dwarf hamsters. **d** Survival curves of infected dwarf hamsters from **a**. **e** Viral RNA copies in select organs extracted from infected dwarf hamsters 3 days after infection. **f** Images of lungs from dwarf hamsters mock infected or inoculated with  $1 \times 10^5$  pfu of WA1, VOC omicron, or VOC gamma 3 days after infection. **g** Infectious titers from the lungs of dwarf hamsters shown in **f**. **h** Schematic of the

dwarf hamster pathogenesis study utilizing  $1 \times 10^4$  pfu of VOC delta and gamma. **i** Images of lungs extracted from dwarf hamsters mock infected or inoculated with  $1 \times 10^4$  pfu of VOC omicron or VOC gamma 0.5 (delta) and 1 day (delta and gamma) after infection. **j** Infectious titers from the lungs of dwarf hamsters shown in **i**. Symbols represent independent biological repeats (**e, g, j**), lines intersect group medians (**b, c**), columns show group medians  $\pm 95\%$  confidence intervals. LoD limit of detection, LoQ limit of quantitation. Source data are provided as a Source Data file.

virus load was high and first lung lesions became detectable (Fig. 3i, j). The higher molnupiravir dose compared to that administered to ferrets was used to compensate for the high metabolic activity of the dwarf hamsters<sup>25</sup> and is consistent with the dose level administered to other rodent species<sup>26,27</sup>. Oral molnupiravir alleviated clinical signs (Supplementary Fig. 9) and ensured complete survival of all treated animals independent of VOC type, whereas approximately 50% (gamma) and 90% (delta, omicron) of animals in the vehicle groups succumbed to the infection within 2 to 7 days (Fig. 4b). Lung virus load assessed three days after infection was consistently high (approximately  $10^7$ – $10^8$  pfu/g lung tissue) in all vehicle-treated groups (Fig. 4c). Treatment significantly lowered lung titers

independent of VOC type, but effect size varied greatly from approximately 1 (delta) to over 4 (gamma) orders of magnitude. Although likewise statistically significant compared to vehicle-treated animals, the impact of molnupiravir on omicron lung load showed major variation between individual animals, creating low, high, and super responder groups characterized by lung titer reductions of -1, 4, and >5 orders of magnitude, respectively (Fig. 4c). Infectious titers in the lung were closely mirrored by viral RNA copies present in lung and tracheas (Supplementary Fig. 10).

Having powered this study with approximately equal numbers of male and female animals in each group, we queried the dataset for a possible impact of biological sex on outcome (Fig. 4d). No significant

## Article

<https://doi.org/10.1038/s41467-022-32045-1>**Table 1 | Analysis of dwarf hamster survival after infection with different VOC**

ID	Median survival (d)	Survival (%)	Animal number (n)	Comparison	P value
WA1	5.75	28.571	14	–	n.a.
				VOC $\alpha$	0.0873
				VOC $\beta$	0.6119
				VOC $\gamma$	0.0031
				VOC $\delta$	<0.0001
VOC $\alpha$	n.d.	80	5	–	n.a.
				VOC $\beta$	0.1591
				VOC $\gamma$	0.0032
				VOC $\delta$	0.0031
				VOC $\omicron$	0.1177
VOC $\beta$	3	40	5	–	n.a.
				VOC $\gamma$	0.3278
				VOC $\delta$	0.1729
				VOC $\omicron$	0.8741
VOC $\gamma$	3	7.143	14	–	n.a.
				VOC $\delta$	0.0505
				VOC $\omicron$	0.0555
VOC $\delta$	3	0	5	–	n.a.
				VOC $\omicron$	0.0031
VOC $\omicron$	6	20	5	–	n.a.

Significance of differences in survival curves was determined with a two-sided Log-rank (Mantel-Cox) test. Source data are provided as a Source Data file.

differences in lung virus load between males and females were detected in any of the three vehicle groups, which was consistent with the absence of a correlation between biological sex and probability of survival of the vehicle-treated animals in our survival study (Supplementary Fig. 11). Comparison of lung virus burden of males and females in the molnupiravir-treated groups revealed no statistically significant differences in effect size in animals infected with VOC gamma or delta, but biological sex had a statistically significant influence on molnupiravir benefit of animals infected with omicron (Fig. 4d, Table 2). Whereas lung titer reductions in treated males were highly significant compared to vehicle-treated males, females, or all vehicle-treated animals combined, no significant change in lung virus load against any of these vehicle groups was detected in females treated with molnupiravir.

#### Pharmacokinetic (PK) properties of molnupiravir in dwarf hamsters

To explore whether in the dwarf hamster model PK properties of molnupiravir are unexpectedly affected by biological sex of the animals, we determined plasma profiles and tissue distribution after a single oral molnupiravir dose of 250 mg/kg body weight, administered to groups of males and females. As observed in other species<sup>28</sup>, the ester prodrug was rapidly hydrolyzed at intestinal absorption, leaving essentially only the molnupiravir parent NHC detectable in plasma samples (Fig. 5a). No major differences in PK parameters were observed between male and female dwarf hamsters (Fig. 5b, Supplementary Table 2). Tissue exposure of the corresponding bioactive anabolite NHC triphosphate (NHC-TP) was highest in spleen and lung, sustained in respiratory tissues at levels exceeding 10 nmol NHC-TP/g tissue over a  $\geq$ 8-hour period after dosing, and consistent between male and female animals (Fig. 5c).

#### VOC-specific adaptation of SARS-CoV-2 in dwarf hamsters

In earlier studies with SARS-CoV-2 in the ferret model<sup>18</sup>, we noted the rapid appearance of characteristic host adaptation mutations such as an L260F substitution in nsp6 and a Y453F mutation in spike<sup>29</sup> in virus populations extracted from ferret nasal turbinates. To probe for possible virus adaptations to the dwarf hamsters, we sequenced whole genomes of virus populations recovered from the different vehicle or molnupiravir treatment groups. No dwarf hamster-typical mutations were detected that were dominant across all VOC populations, but we detected several VOC type-specific substitutions with >20% allele frequency compared to the respective virus inoculum. Irrespective of treatment status, a spike D142G substitution was present in nearly all VOC delta populations, but no dominating mutations emerged in spike proteins of the different VOC gamma and omicron dwarf hamster reisolates (Supplementary Table 1). All recovered VOC gamma populations harbored an nsp6 V181F substitution and all VOC omicron populations contained the nsp6 L260F mutation that was originally considered to be characteristic for adaptation to weasels<sup>18</sup>. However, none of the recovered VOC delta populations contained substitutions in nsp6. We found isolated additional substitutions in some virus populations recovered from individual animals in the respective infection and treatment groups (Supplementary Table 1), but detected no correlation to relative viral fitness in vehicle-treated dwarf hamsters or link to molnupiravir treatment success.

#### Molnupiravir-mediated mitigation of lung histopathology

Macroscopic assessment of the lungs extracted three days after infection revealed severe tissue damage with large lesions covering ~30% (omicron) to 50% (gamma, delta) of the lung surface area of vehicle-treated animals (Fig. 6a, Supplementary Fig. 12). Molnupiravir treatment significantly reduced macroscopic tissue damage independent of VOC type (Fig. 6a, Supplementary Fig. 13). Histological examination of lungs extracted from animals infected with VOC gamma and delta revealed markers of severe viral infection in vehicle-treated animals, including perivascular cuffing, alveolitis, hyalinization of blood vessels, interstitial pneumonia, and leucocyte infiltration (Fig. 6b, Supplementary Fig. 14). One of the VOC gamma-infected animals developed pronounced peribronchiolar metaplasia. Due to the high lethality of VOC delta, only one animal of the vehicle group reached the predefined endpoint for tissue harvest in this study, whereas the others died prematurely and could not be examined. Molnupiravir alleviated histopathology associated with either VOC, decreasing immune cell infiltration and reducing signs of inflammation. Greater residual damage was detected in treated animals infected with VOC delta compared to gamma, which was consistent with the significantly greater molnupiravir-mediated reduction in gamma lung load detected in the efficacy study (Fig. 4c).

Immunohistochemistry analysis of the lung sections identified abundant viral antigen in animals of the vehicle-treated groups (Fig. 6c). Lung sections of molnupiravir-treated animals returned variable results depending on VOC, ranging from strong staining after infection with delta to complete absence of viral antigen after VOC gamma. This differential staining intensity recapitulated the differences observed in lung virus load and viral RNA copies after treatment of animals infected with VOC delta versus gamma (Fig. 4c, Supplementary Fig. 9). When we examined lung sections of molnupiravir-treated animals and surviving members of the vehicle groups two weeks after infection, no viral antigen was detectable and only minor signs of infection were visible (Supplementary Fig. 15), indicating that histopathological damage was transient in survivors.

These results demonstrate that acute lung injury occurs rapidly in the dwarf hamster model. Molnupiravir consistently improves clinical signs and overall disease outcomes independent of infecting VOC. However, the degree of lung virus load reduction is greatly affected by



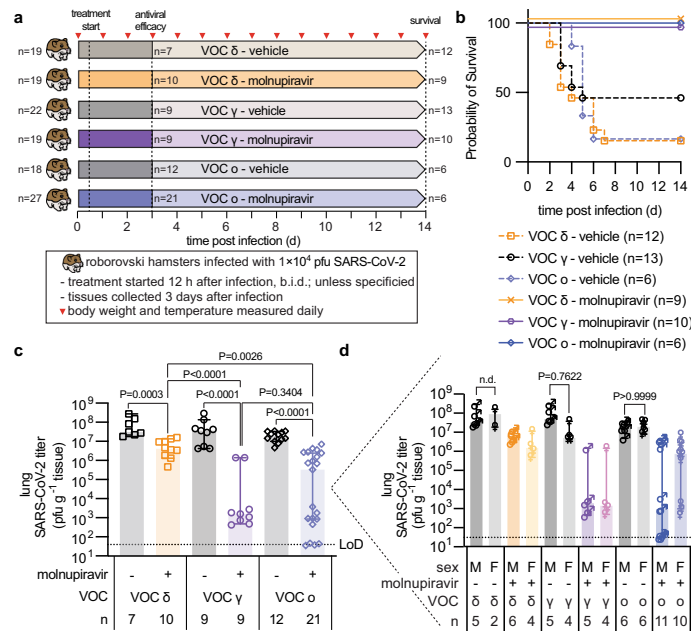


**Fig. 4 | Effects of therapeutic molnupiravir on SARS-CoV-2 lung virus load.**

**a** Schematic of the dwarf hamster efficacy study. Animals were monitored for up to 14 days after intranasal infection with  $1 \times 10^4$  pfu each. Clinical signs were assessed once daily (red triangles). Groups of dwarf hamsters were euthanized 3 days after infection to assess viral load and perform histological examinations. **b** Survival curves of infected dwarf hamsters from **a**. **c** Infectious titers from the lungs of dwarf

hamsters 3 days after infection as shown in **a**. **d** Role of biological sex on antiviral efficacy shown in **c**. Symbols represent independent biological repeats, columns show group medians (**c**, **d**), and error bars represent 95% confidence intervals. Significance was determined using unpaired two-tailed *t* tests (**c**) or two-way ANOVA with Sidak's posthoc multiple comparison tests without further adjustments (**d**); *P* values are shown. Source data are provided as a Source Data file.

VOC type and, in the case of infection with VOC omicron, influenced by the biological sex of the treated animal.

## Discussion

This study demonstrates efficacy of molnupiravir against relevant SARS-CoV-2 VOC alpha, gamma, delta, and omicron in human airway organoids, the ferret transmission model, and the Roborovski dwarf hamster model of life-threatening viral pneumonia. We show that the dwarf hamsters provide a robust experimental system to explore degrees of pathogenicity of different VOC<sup>30–33</sup>. The implications of these efficacy models for the anticipated pharmacological impact of molnupiravir are four-fold:

- Direct antiviral potency of the molnupiravir parent NHC against all VOC including delta and omicron was virtually identical in cultured cells and human organoids, and closely resembled that reported for the original WAI isolate<sup>18</sup>. We consider this outcome unsurprising since extensive past attempts to induce resistance to molnupiravir through adaptation of different viral targets had remained unsuccessful<sup>28,34,35</sup>. Based on a high genetic barrier preventing viral escape and the broad antiviral indication spectrum of molnupiravir<sup>38,34,36</sup>, there is no molecular rationale why genetically closely related SARS-CoV-2 VOC that has no history of prior molnupiravir exposure should be inherently less sensitive to the drug.
- Treatment with molnupiravir significantly reduced VOC shedding from the upper respiratory tract of ferrets, shortening the time in which a host is infectious. Accordingly, molnupiravir suppressed transmission to untreated sentinels. No VOC-specific differences in drug efficacy were apparent. However, all VOC, but gamma,

also grew to lower titers in the ferret upper respiratory tract than WAI<sup>18</sup> and omicron did not transmit at all. By contrast, original SARS-CoV-2 isolates spread readily between ferrets through contact and airborne transmission<sup>37</sup> and direct and reverse zoonotic transmission in the field have been reported for closely related minks<sup>38</sup>. Presumably reflecting increasing SARS-CoV-2 adaptation to the human host, this reduced ferret permissiveness for SARS-CoV-2 VOC interfered with a meaningful comparison analysis of treatment efficacy.

- It was speculated that the variable clinical performance of molnupiravir in the interim versus complete trial analysis could be attributable to lower effectiveness of the drug against VOC delta<sup>15</sup>. Delta indeed surged only when the trial was underway and a large subgroup of trial participants was enrolled from the South American region<sup>14</sup>, in which gamma happened to be dominant until Fall 2021. By revealing a strong correlation between effect size of molnupiravir efficacy and VOC type under controlled experimental conditions, the dwarf hamster model suggests VOC-dependent therapeutic benefit as a tangible explanation for the clinical conundrum. At present we cannot conclusively address, however, whether the difference in virus load reduction between VOC gamma and delta in dwarf hamsters recapitulates the variable clinical success of molnupiravir because of a common mechanism or due to a phenocopy effect. Although VOC delta and gamma replicated to similar lung titers in vehicle-treated animals, delta was associated with the shortest time-to-death. Individual VOC could indirectly modulate molnupiravir PK properties differentially by spreading to organs other than lung with distinct kinetics. However, our analysis of viral organ distribution in the

## Article

<https://doi.org/10.1038/s41467-022-32045-1>**Table 2 | Analysis of biological sex as a variable in molnupiravir efficacy in dwarf hamsters**

		VOC delta		
		molnupiravir		
		all	male	female
molnupiravir	all	n.a.	0.9992	0.987
	male	0.9992	n.a.	0.7337
	female	0.987	0.7337	n.a.
vehicle	all	0.0003	0.0126	0.0003
	male	0.0011	0.0272	0.0007
	female	n.d.	n.d.	n.d.
		VOC gamma		
		molnupiravir		
		all	male	female
molnupiravir	all	n.a.	0.9999	0.9999
	male	0.9999	n.a.	0.9999
	female	0.9999	0.9999	n.a.
vehicle	all	0.0001	0.0001	0.0001
	male	0.0001	0.0001	0.0001
	female	0.0006	0.0021	0.0056
		VOC omicron		
		molnupiravir		
		all	male	female
molnupiravir	all	n.a.	0.9889	0.9857
	male	0.9889	n.a.	0.5376
	female	0.9857	0.5376	n.a.
vehicle	all	0.0002	0.0001	0.0611
	male	0.0067	0.0012	0.2249
	female	0.0063	0.0012	0.2155

Significance was determined using two-way ANOVA with Sidak's multiple comparisons post-hoc test without further adjustments. Numbers specify P values; dark grey shading, P values >0.05; light grey shading, P values <0.05. Source data are provided as a Source Data file.

dwarf hamsters revealed very low viral RNA burden in liver, the primary site of drug metabolism<sup>39</sup>, and sustained antiviral NHC-TP exposure levels were reached in all tissues but brain. Alternatively, the rapid-onset lung histopathology seen with VOC delta may directly contribute to lower effect size of therapy.

- iv. Unexpectedly, molnupiravir efficacy against VOC omicron was variable between individual dwarf hamsters. Biological sex of the animals emerged as a correlate for therapeutic benefit of molnupiravir use against omicron, with treated males faring better overall than females. By contrast, biological sex had no effect on treatment benefit when dwarf hamsters were infected with VOC gamma or delta, which matched human trial data reported for

these VOC<sup>44</sup>. Dwarf hamsters are outbred and animals used in this study were not raised under controlled conditions, introducing individual differences in body weight, age, microbiome, drug metabolism, and/or prior disease history as additional variables, which certainly are all equally present also in human patients. However, dwarf hamsters were randomly assigned to the different study groups and these factors, if indeed of importance, should have resulted in equal individual variation in viral load in the vehicle group or in animals infected with VOC gamma or delta. Whole genome sequence analysis of VOC omicron populations recovered from the dwarf hamsters at the end of infection revealed furthermore no correlation between potential differential VOC omicron adaptation to the dwarf hamster host and effect size of molnupiravir therapy, pointing overall to high variability of omicron disease dynamics in treated dwarf hamsters.

In the absence of controlled clinical data assessing molnupiravir efficacy against omicron, it is currently unclear to what degree the dwarf hamster-derived results extend to human therapy. Our study demonstrates, however, that pharmacological mitigation of severe COVID-19 is complex and that attempts to predict drug efficacy based on unchanged ex vivo inhibitory concentrations alone<sup>16</sup> may be premature. The dwarf hamster-based results illuminates that VOC-specific differences in treatment effect size may be present in vivo, alerting to the need to continuously reassess therapeutic benefit of approved antivirals for individual patient subgroups as SARS-CoV-2 evolves and potential future VOC may emerge.

## Methods

### Ethics statement

All experiments involving infectious SARS-CoV-2 were approved by the Georgia State Institutional Biosafety Committee under protocol B20016 and performed in BSL-3/ABSL-3 facilities at the Georgia State University.

All animal studies were performed in compliance with the Guide for the Care and Use of Laboratory Animals of the National Institutes of Health and the Animal Welfare Act Code of Federal Regulations. Experiments with SARS-CoV-2 involving ferrets and dwarf hamsters were approved by the Georgia State Institutional Animal Care and Use Committee under protocols A20031 and A21019, respectively.

### Study design

This study used female ferrets (*Mustela putorius furo*) family mustelids, genus mustela, 6–10 months of age, and male and female Roborovski dwarf hamsters (*Phodopus roborovskii*), family cricetidae, genus phodopus, 3–10 months of age as in vivo models to assess the therapeutic efficacy of orally administered molnupiravir against infections with different SARS-CoV-2 VOC. Ferrets were used to examine the effect of molnupiravir on upper respiratory infection and transmission. Roborovski dwarf hamsters were used to study the effects of molnupiravir treatment on severe disease associated with lower respiratory tract infection and acute lung injury. VOC were administered to animals through intranasal inoculation. For ferrets, upper respiratory tract viral titers were assessed routinely through nasal lavages and upper respiratory tract tissues. For dwarf hamsters, animals were monitored twice daily for clinical signs, and viral loads were determined in respiratory tract tissues at endpoint. Virus loads were determined by plaque assays and RT-qPCR quantitation.

### Cells

African green monkey kidney cells VeroE6 (ATCC CRL-1586™), Calu-3 (ATCC HB-55™), and VeroE6-TMPRSS2 (BPS Bioscience #78081) were cultivated at 37 °C with 5% CO<sub>2</sub> in Dulbecco's Modified Eagle's Medium (DMEM) supplemented with 7.5% heat-inactivated fetal bovine serum (FBS). Normal human bronchial/tracheal epithelial cells (NHBE) (Lonza

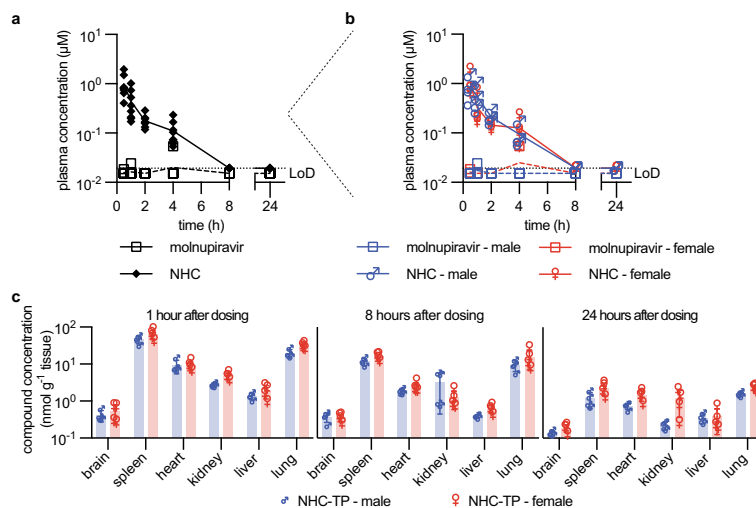


**Fig. 5 | Single oral dose PK properties of molnupiravir in Roborovski dwarf hamsters.** Male and female dwarf hamsters were gavaged with molnupiravir at (250 mg/kg body weight). **a** Plasma concentrations of molnupiravir and NHC, determined over a 24-hour period after dosing. **b** Plasma concentrations from **a**, showing male and female subgroups; LoD level of detection (0.0193 µM for

NHC (shown); 0.0152 µM for molnupiravir). **c** Tissue distribution of NHC-TP-1, 8-, and 24-hours after dosing in male and female dwarf hamsters. Symbols show results for individual animals (**a–c**), columns represent group means (**c**);  $n = 4$  each per biological sex and time point (**a–c**). Source data are provided as a Source Data file.

Bioscience, cat# CC-2540S, lot# 0000646466, passage 3, donor M4) from a 38-year-old male were expanded in PneumaCult-Ex Plus (Stemcell Technologies cat# 05040) and differentiated in PneumaCult-ALI (Stemcell Technologies cat# 05001) for 8 weeks following the manufacturer's instructions. To protect the privacy of donors and tissue suppliers, Lonza Bioscience does not provide copies of donor records or tissue source agreements to customers. Lonza holds donor consent and legal authorizations that give permission for all research use. These consent and authorization documents do not identify specific types of research testing. If used for research purposes only, the donor consent applies. All cells were authenticated and checked for mycoplasma prior to use.

#### Antibodies

SARS-CoV-2 N and goblet cells were co-stained using rabbit anti-SARS-CoV-2 Nucleocapsid monoclonal antibody (HL453) (Invitrogen, cat# MA5-36272; validation datasheet at <https://www.thermofisher.com/antibody/product/SARS-CoV-2-Nucleocapsid-Antibody-clone-HL453-Monoclonal/MA5-36272>) (1:100 dilution) and mouse anti-MUC5AC (45MI) (ThermoFisher, cat# MA5-12175; validation datasheet at <https://www.thermofisher.com/antibody/product/MUC5AC-Antibody-clone-45MI-Monoclonal/MA5-12175>) (1:200 dilution) as primary antibodies, respectively. Donkey anti-goat (Alexa Fluor® 568 (ThermoFisher Scientific, cat# A-11057; validation datasheet at <https://www.thermofisher.com/antibody/product/Donkey-anti-Goat-IgG-H-L-Cross-Adsorbed-Secondary-Antibody-Polyclonal/A-11057>) and rabbit anti-mouse IgG (H + L) cross-adsorbed secondary antibody (Alexa Fluor® 488) (ThermoFisher Scientific, cat# A-11059; validation datasheet at <https://www.thermofisher.com/antibody/product/Rabbit-anti-Mouse-IgG-H-L-Cross-Adsorbed-Secondary-Antibody-Polyclonal/A-11059>) (1:500 dilution) were used as secondary antibodies. For staining of SARS-CoV-2 S, mouse anti-SARS-CoV-1 and 2 Spike protein monoclonal antibody (IA9) (Abcam, cat# ab273433; validation datasheet at <https://www.abcam.com/sars-spike-glycoprotein-antibody-1a9-ab273433.html>) (1:200 dilution) and goat anti-mouse IgG (H + L) highly cross-adsorbed secondary antibody (Alexa Fluor® 488)

(Invitrogen, cat# A-11029; validation datasheet at <https://www.thermofisher.com/antibody/product/Goat-anti-Mouse-IgG-H-L-Highly-Cross-Adsorbed-Secondary-Antibody-Polyclonal/A-11029>) (1:500 dilution), were used as primary and secondary antibodies, respectively. For staining of ciliated cells, rabbit anti-beta IV tubulin recombinant antibody conjugated with Alexa Fluor® 647 (EPRI6775) (Abcam, cat# ab204034; validation datasheet at <https://www.abcam.com/alexa-fluor-647-beta-iv-tubulin-antibody-epri6775-ab204034.html>) (1:100 dilution) was used.

#### Viruses

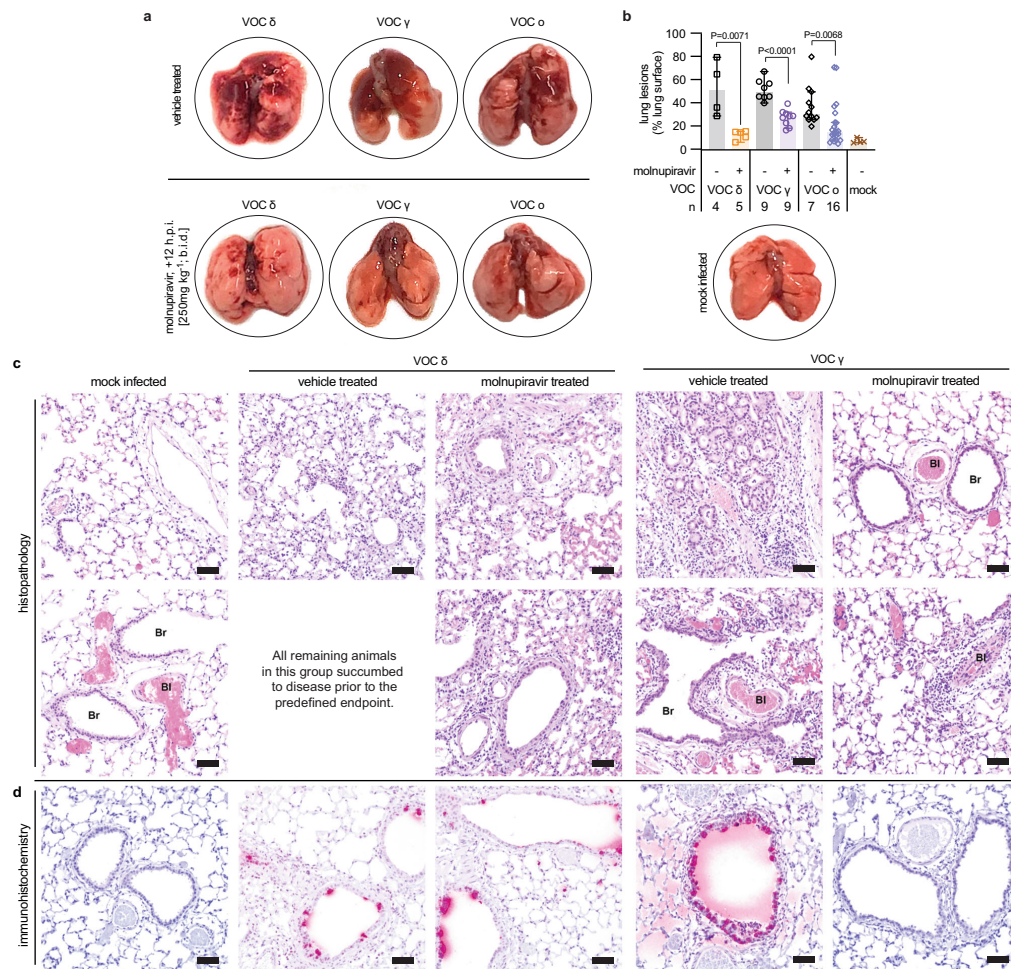
The following SARS-CoV-2 isolates were obtained from BEI resources, amplified on Calu-3 cells. SARS-CoV-2 (WAI; lineage A, isolate USA-WAI/2020, BEI cat# NR-52281), VOC alpha (lineage B.1.1.7, isolate USA/CA\_CDC\_5574/2020, BEI cat# NR-54011), VOC beta (lineage B.1.351, isolate hCoV-19/South Africa/KRISP-K005325/2020, BEI cat# NR-54009), and VOC gamma (lineage P.1, isolate hCoV-19/Japan/TY7-503/2021 (Brazil P.1), BEI cat# NR-54982). VOC delta (lineage B.1.617.2, clinical isolate #2333067) and VOC omicron (lineage B.1.1.529, WA-UW-21120120771) were obtained from the Northwestern Reference laboratory and amplified on Calu-3 cells. All viruses were authenticated by whole genome next-generation sequencing prior to use.

#### Virus yield reduction

12-well plates were seeded with  $2 \times 10^5$  cells per well the day before infection. Each isolate was diluted in DMEM to achieve a multiplicity of infection of 0.1 pfu/cell, adsorbed on cells for 1 hour at 37 °C followings which the inoculum was removed and replaced with DMEM with 2% heat-inactivated FBS. The media contained additionally 0.1% DMSO (vehicle) and the indicated concentration of NHC (EIDD-1931). After 48 hours at 37 °C, the cell supernatant was harvested aliquoted, and frozen at -80 °C before titration by standard plaque assay. Log viral titers were normalized using the average top plateau of viral titers to define 100% and were analyzed through 4-parameter variable slope non-linear regression modeling slope to determine EC<sub>50</sub> and 95% confidence intervals (Prism; GraphPad).



## Article

<https://doi.org/10.1038/s41467-022-32045-1>

**Fig. 6 | Molnupiravir mitigates lung histopathology in VOC-infected dwarf hamsters.** **a** Images of lungs from dwarf hamsters mock infected or inoculated with  $1 \times 10^4$  pfu of VOC delta, gamma, or omicron, treated with vehicle or molnupiravir, and harvested 3 days after infection. **b** Quantitation of macroscopic lesions as a percent of total visible lung surface area for infected dwarf hamsters treated with vehicle or molnupiravir; *n* values are shown. Mock infected lungs (*n* = 4) were included as a reference. Symbols represent independent biological repeats,

columns show group medians. Significance was determined using unpaired two-tailed *t* tests; *P* values are shown. **c, d** Histopathology (**c**) and immunohistochemistry (**d**) of dwarf hamster lung slices from groups harvested 3 days after infection. Staining with hematoxylin and eosin (**c**) or  $\alpha$ -SARS-CoV-2 S (**d**). Br bronchioles, Bl blood vessel, scale bar 50  $\mu$ m. Each image represents tissue from an individual animal, all individual animals analyzed are shown in Supplementary Fig. 14. Source data are provided as a Source Data file.

### Confocal microscopy

Eight-week differentiated HAE cells were infected (or mock-infected) with  $3 \times 10^4$  pfu of SARS-CoV-2 VOC and fixed on day 3 after infection. For co-staining of SARS-CoV-2 N and goblet cells, cells were permeabilized for 30 minutes with a 200  $\mu$ l apical overlay of PBS with 0.1% Triton X-100 and 3% bovine serum albumin (BSA), then the overlay was removed and cells were apically incubated with 100  $\mu$ l of primary antibodies in wash buffer (PBS with 0.05% Tween20 and 0.3% BSA) for 1 hour at RT. After three 5-minute 200  $\mu$ l-washes with wash buffer, cells were incubated with secondary antibodies in wash buffer for 1 hour at RT. Cells were subsequently incubated with Hoechst 34580 (1:1000 dilution in wash buffer) for 5 minutes and washed three times. Membranes were then excised

and mounted using Prolong Diamond antifade mountant overnight at RT (ThermoFisher Scientific). For co-staining of SARS-CoV-2 S and ciliated cells, the same method was used with a saturation step with PBS with 0.05% Tween20 and 3% BSA in lieu of a permeabilization step. Image captures were performed with a Zeiss Axio Observer Z.1 and an LSM 800 confocal microscope with AiryScan, controlled with the Zeiss Zen 3.1 Blue software package (Windows 10). Representative pictures were taken with a  $\times 63$  Plan-Apochromat (NA: 1.40, oil) objective. Digital pictures are pseudocolored for optimal presentation. For clarity of presentation, the intensity of staining was digitally balanced in between different virus isolates with Zeiss Zen 3.1 Blue, while keeping the same processing for the conditions that are directly compared (vehicle vs treatment).

## Article

<https://doi.org/10.1038/s41467-022-32045-1>**Plaque assay**

Samples were serially diluted (tenfold dilutions starting at a 1:10 initial dilution) in DMEM medium supplemented with 2% FBS containing Antibiotic-Antimycotic (Gibco). The serial dilutions were added to Vero E6 cells seeded in 12-well plates at  $3 \times 10^5$  cells per well 24 hours before. The virus was allowed to adsorb for 1 hour at 37 °C. Subsequently, the inoculum was removed, and the cells were overlaid with 1.2% Avicel (FMC BioPolymer) in DMEM and incubated for 3 days at 37 °C with 5% CO<sub>2</sub>. After three days, the Avicel was removed, cells were washed once with PBS, fixed with 10% neutral buffered formalin, and plaques were visualized using 1% crystal violet. For dwarf hamsters infected with VOC gamma, delta, and omicron, plaque assays were performed with VeroE6-TMPRSS2 cells.

**In vivo efficacy of molnupiravir in ferrets against VOC**

Ferrets were purchased from Triple F Farms, PA. Groups of ferrets were inoculated with  $1 \times 10^5$  pfu of VOC alpha or delta (1 ml; 0.5 ml per nare). Twelve hours after infection, groups of ferrets were treated twice daily (b.i.d.) with vehicle (1% methylcellulose) or molnupiravir at a dose of 5 mg/kg in 1% methylcellulose. Treatments were administered by oral gavage and continued every 12 hours until 4 days after infection. All ferrets were euthanized 4 days after infection and tissues were harvested to determine SARS-CoV-2 titers and the presence of viral RNA.

**Efficacy and contact transmission of VOC in ferrets**

Two groups of six source ferrets were inoculated intranasally with  $1 \times 10^5$  pfu of VOC alpha, gamma, or omicron. After 12 hours, groups of source ferrets were further divided into two groups, receiving vehicle ( $n = 3$  for VOC alpha;  $n = 4$  for VOC gamma) or molnupiravir treatment (5 mg/kg b.i.d.) administered by oral gavage. At 54 hours after infection, each source ferret was co-housed with uninfected and untreated contacts. Ferrets were co-housed until 96 hours after infection, when source ferrets were euthanized and contact ferrets were housed individually. All contact ferrets were monitored for 4 days after separation from source ferrets and then euthanized. Nasal lavages were performed on source ferrets twice daily until cohousing started. After cohousing started, nasal lavages were performed on all ferrets every 24 hours. Nasal turbinates were harvested for all ferrets after euthanization to determine infectious titers and the presence of viral RNA.

**In vivo pathogenicity of VOC in dwarf hamsters**

Female and male dwarf hamsters (2–4 months of age) were purchased from Dierengroothandel Ron Van Der Vliet, Netherlands. The dwarf hamsters were humanely quarantined under ABSL-2 conditions until study start. After a minimum resting period of 2 weeks after arrival, animals were randomly assigned to groups for individual studies, transferred into an ABSL-3 facility immediately prior to study start, and housed singly in ventilated negative-pressure cages during the studies. To establish a pathogenicity profile, dwarf hamsters were inoculated intranasally with  $1 \times 10^5$  pfu in 50 µl (25 µl per nare), unless otherwise stated (VOC delta  $3 \times 10^4$ ). The dwarf hamsters were anaesthetized with dexmedetomidine/ketamine before inoculation. Groups of dwarf hamsters were euthanized 14 days after infection and their organs were harvested to determine the presence of viral RNA in different tissues (WAI and VOC gamma only).

**In vivo efficacy of molnupiravir in dwarf hamsters**

Groups of dwarf hamsters were inoculated with  $1 \times 10^4$  pfu in 50 µl (25 µl per nare). At 12 hours after infection, the dwarf hamsters were treated b.i.d. with vehicle (1% methylcellulose) or molnupiravir at a dosage of 250 mg/kg body weight, respectively. The compound was administered via oral gavage in 1% methylcellulose. After the start of treatment, b.i.d. dosing was continued until 12 days after infection. Subgroups of dwarf hamsters were euthanized 3 days after infection. All studies were terminated 14 days after infection. Organs were

harvested to determine virus titers and the presence of viral RNA in different tissues. For PK studies, dwarf hamsters received a single oral dose of 250 mg/kg body weight molnupiravir. Blood was sampled at 0.5, 1, 2, 4, 8, and 24 hours after dosing from four animals per biological sex and plasma extracts prepared. Individual dwarf hamsters were sampled not more than twice. Organ samples were extracted 1, 8, and 24 hours after dosing. Molnupiravir, and NHC and its anabolites were analyzed using a qualified LC/MS/MS method<sup>28</sup>, calculations with WinNonlin 8.3.3.33.

**Titration of SARS-CoV-2 in tissue extracts**

For virus titration, the organs were weighed and homogenized in PBS. The homogenates were centrifuged at  $2000 \times g$  for 5 minutes at 4 °C. The clarified supernatants were harvested, frozen, and used in subsequent plaque assays. For detection of viral RNA, the harvested organs were stored in RNAlater at  $-80$  °C. The tissues were homogenized, and the total RNA was extracted using a RNeasy mini kit (Qiagen).

**Quantitation of SARS-CoV-2 RNA copy numbers**

SARS-CoV-2 RNA was detected using the nCoV\_IP2 primer-probe set (National Reference Center for Respiratory Viruses, Institute Pasteur) which targets the SARS-CoV-2 RdRP gene. RT-qPCR reactions were performed using an Applied Biosystems 7500 real-time PCR system using the StepOnePlus 2.1 real-time PCR package. The nCoV\_IP2 primer-probe set (nCoV\_IP2-12669Fw ATGAGCTTAGTCCTGTTG; nCoV\_IP2-12759Rv CTCCTTTGTTGTGTTGT; nCoV\_IP2-12696bProbe(+) 5'FAM-AGATGCTTGTGCTGCCGTA-3'BHQ-1) was used in combination with TaqMan fast virus 1-step master mix (ThermoFisher Scientific) to detect viral RNA. A standard curve was created using a PCR fragment (nt 12669-14146 of the SARS-CoV-2 genome) generated from viral complementary DNA using the nCoV\_IP2 forward primer and the nCoV\_IP4 reverse primer to quantitate the RNA copy numbers. RNA copy numbers were normalized to the weight of tissues used.

**SARS-CoV-2 genome sequencing**

SARS-CoV-2 positive specimens were sequenced using metagenomic next-generation sequencing<sup>40</sup>, Swift Biosciences SNAP panel<sup>41</sup>, and/or Illumina COVIDSeq following the manufacturer's protocol. Sequencing reads were analyzed and visualized using cutadapt 1.9, bwa version 0.7.17, Picard 2.18.15, VarScan 2.3, Annovar 2018Apr16 version for the Longitudinal Analysis of Viral Alleles (LAVA; available at <https://github.com/michellejlin/lava>) pipeline with references MZ433225.1 for VOC gamma, NC\_045512.2 for VOC delta, and OL965129.1 for VOC omicron<sup>42</sup>. Sequencing reads are available in NCBI BioProject PRJNA803552 (<https://www.ncbi.nlm.nih.gov/bioproject/?term=PRJNA803552>).

**Statistics and reproducibility**

The Microsoft Excel (versions 16.52) and Numbers (version 10.1) software packages were used for most data collection. The GraphPad Prism (version 9.1.0) software package was used for data analysis. Reverse transcription RT-qPCR data were collected and analyzed using the StepOnePlus (version 2.1; Applied Biosystems) software package. Figures were assembled using Adobe Illustrator (version CS6). Power analyses were carried out using GPower 3.1. T-tests were used to evaluate statistical significance between experiments with two sets of data. One- and two-way ANOVAs with Dunnett's, Tukey's, or Sidak's comparisons post-hoc tests without further modifications were used to evaluate statistical significance when more than two groups were compared or datasets contained two independent variables, respectively. Specific statistical tests are specified in the figure legends for individual studies. The Supplementary Dataset 1 summarize all statistical analyses (effect sized, *P* values, and degrees of freedom), respectively. Effect sizes between groups were calculated as  $\eta^2 = \frac{SS_{\text{effect}}}{SS_{\text{total}}}$ .

## Article

<https://doi.org/10.1038/s41467-022-32045-1>

for one-way ANOVA and  $\omega^2 = \frac{SS_{\text{effect}} - (df_{\text{effect}}) \times (MS_{\text{error}})}{MS_{\text{error}} + SS_{\text{total}}}$  for two-way ANOVA;  $df_{\text{effect}}$ , degrees of freedom for the effect;  $SS_{\text{total}}$ , sum of squares for total;  $SS_{\text{effect}}$ , sum of squares for the effect;  $MS_{\text{error}}$ , mean square error. Effective concentrations for antiviral potency were calculated from dose-response datasets through four-parameter variable slope regression modelling. A biological repeat refers to measurements taken from distinct samples, and the results obtained for each individual biological repeat are shown in the figures along with the exact size ( $n$ , number) of biologically independent samples, animals, or independent experiments. The measure of the center (connecting lines and columns) is the mean throughout unless otherwise specified. The statistical significance level ( $\alpha$ ) was set to <0.05 for all experiments. Exact P values are shown in Supplementary Dataset 1 and in individual graphs when possible.

## Reporting summary

Further information on research design is available in the Nature Research Reporting Summary linked to this article.

## Data availability

The metagenomic sequencing reads generated in this study have been deposited in the NCBI BioProject database under accession code [PRJNA803552](https://www.ncbi.nlm.nih.gov/bioproject/PRJNA803552). All other data generated in this study are provided in this published article and the Supplementary Information/Source Data file. Source data are provided in this paper.

## Code availability

Metagenomic sequencing reads were analyzed and visualized using the LAVA pipeline<sup>42</sup> (available at <https://github.com/michellejin/lava>). All commercial computer codes and algorithms used are specified in the Methods section.

## References

1. WHO. WHO Coronavirus (COVID-19) Dashboard, <<https://covid19.who.int>> (2021).
2. Polack, F. P. et al. Safety and efficacy of the BNT162b2 mRNA Covid-19 vaccine. *N. Engl. J. Med.* **383**, 2603–2615 (2020).
3. Jackson, L. A. et al. An mRNA vaccine against SARS-CoV-2 - preliminary report. *N. Engl. J. Med.* **383**, 1920–1931 (2020).
4. Dror, A. A. et al. Vaccine hesitancy: the next challenge in the fight against COVID-19. *Eur. J. Epidemiol.* **35**, 775–779 (2020).
5. Fisher, K. A. et al. Attitudes toward a potential SARS-CoV-2 vaccine: a survey of U.S. adults. *Ann. Intern. Med.* **173**, 964–973 (2020).
6. Garcia-Beltran, W. F. et al. Multiple SARS-CoV-2 variants escape neutralization by vaccine-induced humoral immunity. *Cell* **184**, 2372–2383.e2379 (2021).
7. Zhou, D. et al. Evidence of escape of SARS-CoV-2 variant B.1.351 from natural and vaccine-induced sera. *Cell* **184**, 2348–2361.e2346 (2021).
8. Mlcochova, P. et al. SARS-CoV-2 B.1.617.2 Delta variant replication and immune evasion. *Nature* **599**, 114–119 (2021).
9. Reardon, S. How the Delta variant achieves its ultrafast spread. *Nature*, <https://doi.org/10.1038/d41586-021-01986-w> (2021).
10. Planas, D. et al. Reduced sensitivity of SARS-CoV-2 variant Delta to antibody neutralization. *Nature* **596**, 276–280 (2021).
11. Kupferschmidt, K. & Vogel, G. Omicron threat remains fuzzy as cases explode. *Science* **375**, 9–10 (2022).
12. Perez-Then, E. et al. Neutralizing antibodies against the SARS-CoV-2 Delta and Omicron variants following heterologous CoronaVac plus BNT162b2 booster vaccination. *Nat. Med.*, <https://doi.org/10.1038/s41591-022-01705-6> (2022).
13. GOV.UK First oral antiviral for COVID-19, Lagevrio (molnupiravir), approved by MHRA <https://www.gov.uk/government/news/first-oral-antiviral-for-covid-19-lagevrio-molnupiravir-approved-by-mhra>. (2021).
14. Molnupiravir - US Food and Drug Administration (<https://www.fda.gov/media/154472/download>). (2021).
15. Kozlov, M. Merck's COVID pill loses its lustre: what that means for the pandemic. *Nature* (2021).
16. Prince, T. et al. Antiviral activity of molnupiravir precursor NHC against SARS-CoV-2 Variants of Concern (VOCs) and its therapeutic window in a human lung cell model. *bioRxiv* <https://doi.org/10.1101/2021.11.23.469695> (2021).
17. Sourimant, J. et al. 4'-Fluorouridine is an oral antiviral that blocks respiratory syncytial virus and SARS-CoV-2 replication. *Science*, eabj5508 (2021).
18. Cox, R. M., Wolf, J. D. & Plemper, R. K. Therapeutically administered ribonucleoside analogue MK-4482/EIDD-2801 blocks SARS-CoV-2 transmission in ferrets. *Nat. Microbiol.* **6**, 11–18 (2021).
19. Cox, R. M. et al. Oral prodrug of remdesivir parent GS-441524 is efficacious against SARS-CoV-2 in ferrets. *Nat. Commun.* **12**, 6415 (2021).
20. Gruber, A. D., Firsching, T. C., Trimpert, J. & Diertel, K. Hamster models of COVID-19 pneumonia reviewed: how human can they be? *Vet. Pathol.*, 3009858211057197, <https://doi.org/10.1177/03009858211057197> (2021).
21. Lee, C. Y. & Lowen, A. C. Animal models for SARS-CoV-2. *Curr. Opin. Virol.* **48**, 73–81 (2021).
22. Trimpert, J. et al. The Roborovski Dwarf hamster is a highly susceptible model for a rapid and fatal course of SARS-CoV-2 Infection. *Cell Rep.* **33**, 108488 (2020).
23. Zhai, C. et al. Roborovski hamster (*Phodopus roborovskii*) strain SH101 as a systemic infection model of SARS-CoV-2. *Virulence* **12**, 2430–2442 (2021).
24. Painter, W. P. et al. Human safety, tolerability, and pharmacokinetics of molnupiravir, a novel broad-spectrum oral antiviral agent with activity against SARS-CoV-2. *Antimicrob. Agents Chemother.* <https://doi.org/10.1128/AAC.02428-20> (2021).
25. Bauer, B. A. & Besch-Williford, C. in *The Laboratory Rabbit, Guinea Pig, Hamster, and Other Rodents* (eds. M. A. Suckow, K. A. Stevens, & R. P. Wilson) Ch. 37, 935–946 (Academic Press, 2012).
26. Rosenke, K. et al. Orally delivered MK-4482 inhibits SARS-CoV-2 replication in the Syrian hamster model. *Nat. Commun.* **12**, 2295 (2021).
27. Wahl, A. et al. SARS-CoV-2 infection is effectively treated and prevented by EIDD-2801. *Nature* **591**, 451–457 (2021).
28. Toots, M. et al. Characterization of orally efficacious influenza drug with high resistance barrier in ferrets and human airway epithelia. *Sci. Transl. Med.* **11**, <https://doi.org/10.1126/scitranslmed.aax5866> (2019).
29. Oude Munnink, B. B. et al. Transmission of SARS-CoV-2 on mink farms between humans and mink and back to humans. *Science* **371**, 172–177 (2021).
30. Fisman, D. N. & Tuite, A. R. Evaluation of the relative virulence of novel SARS-CoV-2 variants: a retrospective cohort study in Ontario, Canada. *CMAJ* **193**, E1619–E1625 (2021).
31. Ong, S. W. X. et al. Clinical and virological features of SARS-CoV-2 variants of concern: a retrospective cohort study comparing B.1.1.7 (Alpha), B.1.315 (Beta), and B.1.617.2 (Delta). *Clin. Infect. Dis.*, <https://doi.org/10.1093/cid/ciab721> (2021).
32. Sheikh, A. et al. SARS-CoV-2 Delta VOC in Scotland: demographics, risk of hospital admission, and vaccine effectiveness. *Lancet* **397**, 2461–2462 (2021).
33. Nealon, J. & Cowling, B. J. Omicron severity: milder but not mild. *Lancet*, [https://doi.org/10.1016/S0140-6736\(22\)00056-3](https://doi.org/10.1016/S0140-6736(22)00056-3) (2022).
34. Urakova, N. et al. beta-d-N (4)-hydroxycytidine is a potent anti-alphavirus compound that induces a high level of mutations in the viral genome. *J. Virol.* **92**, <https://doi.org/10.1128/JVI.01965-17> (2018).

## Article

<https://doi.org/10.1038/s41467-022-32045-1>

35. Agostini, M. L. et al. Small-molecule antiviral beta-d-N (4)-hydroxycytidine inhibits a proofreading-intact coronavirus with a high genetic barrier to resistance. *J. Virol.* **93**, <https://doi.org/10.1128/JVI.01348-19> (2019).
36. Yoon, J. J. et al. Orally efficacious broad-spectrum ribonucleoside analog inhibitor of influenza and respiratory syncytial viruses. *Antimicrob. Agents Chemother.* **62**, <https://doi.org/10.1128/AAC.00766-18> (2018).
37. Richard, M. et al. SARS-CoV-2 is transmitted via contact and via the air between ferrets. *Nat. Commun.* **11**, 3496 (2020).
38. Enserink, M. Coronavirus rips through Dutch mink farms, triggering culls. *Science* **368**, 1169 (2020).
39. Remmer, H. The role of the liver in drug metabolism. *Am. J. Med.* **49**, 617–629 (1970).
40. Greninger, A. L. et al. Rapid metagenomic next-generation sequencing during an investigation of hospital-acquired human parainfluenza virus 3 infections. *J. Clin. Microbiol.* **55**, 177–182 (2017).
41. Addetia, A. et al. Sensitive recovery of complete SARS-CoV-2 genomes from clinical samples by use of swift biosciences' SARS-CoV-2 multiplex amplicon sequencing panel. *J. Clin. Microbiol.* **59**, <https://doi.org/10.1128/JCM.02226-20> (2020).
42. Lin, M. J., Shean, R. C., Makhous, N. & Greninger, A. L. LAVA: a streamlined visualization tool for longitudinal analysis of viral alleles. *bioRxiv*, <https://doi.org/10.1101/2019.12.17.879320> (2019).

**Acknowledgements**

We thank members of the GSU High Containment Core and the Department for Animal Resources for support, and A.L. Hammond for critical reading of the manuscript. This work was supported, in part, by Public Health Service grants AIO71002 (to R.K.P.) and AI141222 (to R.K.P.), from the NIH/NIAID. The funders had no role in study design, data collection, interpretation, or the decision to submit the work for publication.

**Author contributions**

C.M.L., R.M.C., and R.K.P. conceived and designed the experiments. C.M.L., R.M.C., J.S., J.D.W., and R.K.P. conducted most of the experiments. K.J., Q.P., and A.L.G. performed next-generation sequencing. M.T.S. performed chemical synthesis. M.S., Z.S., and A.A.K. performed mass spectrometry analysis. M.G.N. and G.R.P. provided critical materials. K.S. performed histopathology of organ samples. C.M.L., R.M.C.,

J.S., A.L.G., and R.K.P. analyzed the data. R.M.C. and R.K.P. wrote the manuscript.

**Competing interests**

M.G.N. and G.R.P. are coinventors on patent 20190022116, N<sup>4</sup>-Hydroxycytidine and derivatives and anti-viral uses related thereto, covering composition of matter and method of use of EIDD-2801 for antiviral therapy. This study could affect their personal financial status. All other authors declare no competing interests.

**Additional information**

**Supplementary information** The online version contains supplementary material available at <https://doi.org/10.1038/s41467-022-32045-1>.

**Correspondence** and requests for materials should be addressed to Richard K. Plemper.

**Peer review information** *Nature Communications* thanks Megan Shaw and the other anonymous reviewer(s) for their contribution to the peer review of this work. Peer review reports are available.

**Reprints and permission information** is available at <http://www.nature.com/reprints>

**Publisher's note** Springer Nature remains neutral with regard to jurisdictional claims in published maps and institutional affiliations.

**Open Access** This article is licensed under a Creative Commons Attribution 4.0 International License, which permits use, sharing, adaptation, distribution and reproduction in any medium or format, as long as you give appropriate credit to the original author(s) and the source, provide a link to the Creative Commons license, and indicate if changes were made. The images or other third party material in this article are included in the article's Creative Commons license, unless indicated otherwise in a credit line to the material. If material is not included in the article's Creative Commons license and your intended use is not permitted by statutory regulation or exceeds the permitted use, you will need to obtain permission directly from the copyright holder. To view a copy of this license, visit <http://creativecommons.org/licenses/by/4.0/>.

© The Author(s) 2022



### 2.1.3 Comparing Molnupiravir and Nirmatrelvir/Ritonavir Efficacy and the Effects on SARS-CoV-2 Transmission in Animal Models

nature communications



Article

<https://doi.org/10.1038/s41467-023-40556-8>

## Comparing molnupiravir and nirmatrelvir/ritonavir efficacy and the effects on SARS-CoV-2 transmission in animal models

Received: 28 November 2022

Accepted: 1 August 2023

Published online: 07 August 2023

Check for updates

Robert M. Cox<sup>1,5</sup>, Carolin M. Lieber<sup>1,5</sup>, Josef D. Wolf<sup>1</sup>, Amirhossein Karimi<sup>1</sup>, Nicole A. P. Lieberman<sup>2</sup>, Zachary M. Sticher<sup>3</sup>, Pavitra Roychoudhury<sup>2</sup>, Meghan K. Andrews<sup>3</sup>, Rebecca E. Krueger<sup>3</sup>, Michael G. Natchus<sup>3</sup>, George R. Painter<sup>3,4</sup>, Alexander A. Kolykhalov<sup>3</sup>, Alexander L. Greninger<sup>2</sup> & Richard K. Plemper<sup>1</sup>✉

Therapeutic options against SARS-CoV-2 are underutilized. Two oral drugs, molnupiravir and paxlovid (nirmatrelvir/ritonavir), have received emergency use authorization. Initial trials suggested greater efficacy of paxlovid, but recent studies indicated comparable potency in older adults. Here, we compare both drugs in two animal models; the Roborovski dwarf hamster model for severe COVID-19-like lung infection and the ferret SARS-CoV-2 transmission model. Dwarf hamsters treated with either drug survive VOC omicron infection with equivalent lung titer reduction. Viral RNA copies in the upper respiratory tract of female ferrets receiving 1.25 mg/kg molnupiravir twice-daily are not significantly reduced, but infectious titers are lowered by >2 log orders and direct-contact transmission is stopped. Female ferrets dosed with 20 or 100 mg/kg nirmatrelvir/ritonavir twice-daily show 1–2 log order reduction of viral RNA copies and infectious titers, which correlates with low nirmatrelvir exposure in nasal turbinates. Virus replication resurges towards nirmatrelvir/ritonavir treatment end and virus transmits efficiently (20 mg/kg group) or partially (100 mg/kg group). Prophylactic treatment with 20 mg/kg nirmatrelvir/ritonavir does not prevent spread from infected ferrets, but prophylactic 5 mg/kg molnupiravir or 100 mg/kg nirmatrelvir/ritonavir block productive transmission. These data confirm reports of similar efficacy in older adults and inform on possible epidemiologic benefit of antiviral treatment.

Vaccines and antivirals have helped to limit disease severity in the coronavirus disease 2019 (COVID-19) pandemic. However, extensive viral spread continues, affecting even those with vaccine or naturally-acquired immunity<sup>1–3</sup>. The rise of new SARS-CoV-2 variants of concern

(VOC) capable of escaping preexisting immunity has undermined the hope of rapidly ending the pandemic through large-scale vaccination campaigns<sup>1,4,5</sup>, and indirect immune imprinting may never allow vaccine boosters to be successful against future viral evolution. In 2021,

<sup>1</sup>Center for Translational Antiviral Research, Georgia State University Institute for Biomedical Sciences, Atlanta, GA 30303, USA. <sup>2</sup>Virology Division, Department of Laboratory Medicine and Pathology, University of Washington, Seattle, WA 98185, USA. <sup>3</sup>Emory Institute for Drug Development, Emory University, Atlanta, GA, USA. <sup>4</sup>Department of Pharmacology, Emory University, Atlanta, GA 30322, USA. <sup>5</sup>These authors contributed equally: Robert M. Cox, Carolin M. Lieber. ✉e-mail: [rplemper@gsu.edu](mailto:rplemper@gsu.edu)

## Article

<https://doi.org/10.1038/s41467-023-40556-8>

the FDA granted emergency use authorizations for two orally available antivirals, molnupiravir and paxlovid<sup>27</sup>. Molnupiravir, a prodrug of the broad-spectrum nucleoside analog N<sup>4</sup>-hydroxycytidine<sup>8</sup>, targets the viral RNA polymerase, triggering lethal viral mutagenesis<sup>9,10</sup>. Paxlovid consists of two components, the peptidomimetic viral main protease (M<sup>pro</sup>) inhibitor nirmatrelvir and the cytochrome P450 enzyme inhibitor ritonavir<sup>11</sup>, which is required to improve pharmacokinetic properties of nirmatrelvir. Having formed covalent dead-end complexes with nirmatrelvir, M<sup>pro</sup> is unable to process the viral polyprotein, interrupting the viral replication cycle. Initial phase II/III clinical trials suggested superior efficacy of paxlovid compared to molnupiravir, reporting 89% versus 30% reduction in patient hospitalization and death<sup>12,13</sup>.

These initial data and extensive public discussion of possible carcinogenic potential of molnupiravir triggered elevation of paxlovid to standard-of-care (SOC)-like status for treatment of vulnerable patient populations in the United States<sup>14</sup>. However, a carcinogenicity study in the Tg.rasH2 mouse model to assess carcinogenic potential of molnupiravir demonstrated that continuous dosing for 6 months was not carcinogenic<sup>15</sup>, addressing speculations about drug safety. Recent large-scale clinical trials and retrospective assessments of therapeutic benefit have revealed that efficacy of paxlovid is substantially lower than initially seen against VOC delta<sup>12,16,17</sup>, whereas therapeutic benefit of molnupiravir in older adults was underestimated<sup>15,17</sup> and molnupiravir treatment reduced the time to first recovery of high-risk vaccinated adults by ~4 days<sup>18</sup>. In these studies, neither drug provided significant therapeutic benefit to younger adults below 65 years of age<sup>12,19</sup>.

Assessing the effect of post-exposure prophylactic treatment of household contacts of a confirmed SARS-CoV-2 case with paxlovid, the Evaluation of Protease Inhibition for COVID-19 in Post-Exposure Prophylaxis (EPIC-PEP) trial showed a slight reduction of preventing transmission, but benefit was not statistically significant<sup>20,21</sup>. Preliminary results of the comparable prevention of household transmission MOVE-AHEAD trial with molnupiravir revealed a similarly reduced likelihood of contacts to turn SARS-CoV-2 PCR test positive post-baseline, which was also not statistically significant<sup>22</sup>. Both prophylactic trials monitored viral RNA copy numbers as a primary endpoint. Clinical reports demonstrated rebounding virus replication in patients who have received paxlovid<sup>2,23,24</sup> or molnupiravir<sup>25</sup> and anecdotal cases of SARS-CoV-2 transmission at rebound have further questioned whether treatment may provide epidemiologic benefit through reducing the risk of SARS-CoV-2 spread. Mustelids such as mink and ferret are highly permissive for SARS-CoV-2, experiencing high virus loads predominantly in the upper respiratory tract and supporting efficient virus spread<sup>26–28</sup>. Using the ferret SARS-CoV-2 transmission model, we have established in previous work that oral molnupiravir blocks productive, direct-contact transmission of

infectious particles to untreated sentinel ferrets within 18 h of treatment start<sup>27,29</sup>, but paxlovid has not been tested in the transmission model.

In this work, we compare efficacy of molnupiravir and nirmatrelvir/ritonavir in the Roborovski dwarf hamster model of severe COVID-19-like viral pneumonia and the ferret transmission model. Results demonstrate that both drugs provide significant therapeutic benefit against SARS-CoV-2 pneumonia when administered early after infection. Both the rodent and non-rodent animal model reveal a non-linear correlation of viral RNA copy number and infectious viral titer reduction after treatment with molnupiravir, whereas reductions by nirmatrelvir/ritonavir are directly proportional. Infectious virus load in the upper respiratory tract emerges as a correlate for SARS-CoV-2 transmission success in ferrets, and molnupiravir treatment completely suppresses transmission at all dose levels tested, including those not associated with a significant reduction of viral RNA copy numbers in the upper respiratory tract.

## Results

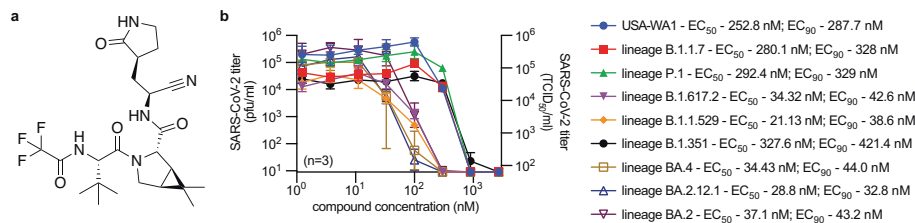
To validate sourced nirmatrelvir stocks (Fig. 1a), we determined antiviral potency on cultured VeroE6-TMPRSS2 cells against SARS-CoV-2 isolates representing lineage A (USA-WA1/2020), lineage B.1.1.7 (VOC alpha; hCoV-19/USA/CA/UCSD.5574/2020), lineage B.1.351 (VOC beta; hCoV-19/South Africa/KRISP-K005325/2020), lineage P.1 (VOC gamma; hCoV-19/Japan/TY7-503/2021), lineage B.1.617.2 (VOC delta; clinical isolate #233067), lineage B.1.1.529 (VOC omicron; hCoV-19/USA/WA-UW-21120120771/2021) lineage BA.2 (clinical isolate 22012361822A), lineage BA.2.12.1 (hCoV-19/USA/WA-CDC-UW22050170242/2022), and lineage BA.4 (hCoV-19/USA/WA-CDC-UW22051283052/2022) (Fig. 1b).

## In vitro efficacy of nirmatrelvir against current VOC

Infected cells were incubated with serial dilutions of nirmatrelvir in media containing 2  $\mu$ M CP-100356, a P-glycoprotein inhibitor added to limit rapid compound efflux<sup>30</sup>. Nirmatrelvir exhibited nanomolar potency against all VOCs tested, returning half-maximal (EC<sub>50</sub>) and 90% maximal (EC<sub>90</sub>) concentrations ranging from 21.1 to 327.6 nM and 32.8 to 421.4 nM, respectively, which recapitulated results of previous in vitro dose-response studies<sup>31,32</sup>.

## Prevention of severe SARS-CoV-2 disease in Roborovski dwarf hamsters

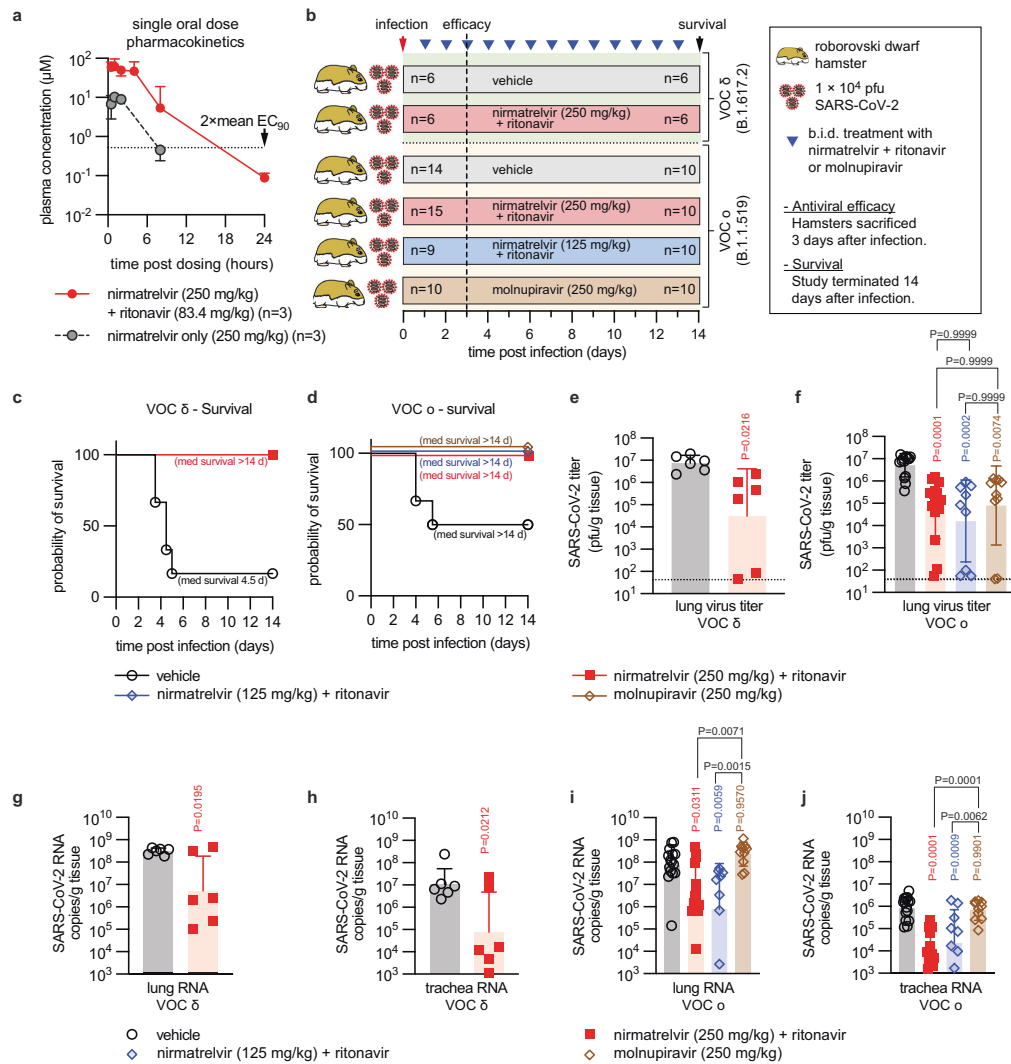
Infected single-oral dose pharmacokinetics (PK) properties of nirmatrelvir delivered alone or in combination with ritonavir. Hamsters were administered 250 mg/kg nirmatrelvir with or without 83.3 mg/kg ritonavir. In the absence of ritonavir, 250 mg/kg nirmatrelvir delivered a plasma exposure level of 22,400 h  $\times$  ng/ml (Fig. 2a, Table 1). When combined with ritonavir, nirmatrelvir plasma exposure



**Fig. 1 | In vitro antiviral activity of nirmatrelvir.** **a** Structure of nirmatrelvir. **b** Nirmatrelvir dose-response assays against SARS-CoV-2 WA1, and lineages B.1.1.7 (VOC  $\alpha$ ), B.1.351 (VOC  $\beta$ ), P.1 (VOC  $\gamma$ ), B.1.617.2 (VOC  $\delta$ ), B.1.1.529, BA.2, B.1.2.12.1, and BA.4 on VeroE6-TMPRSS2 cells. The number of independent repeats ( $n$ ) used in each experiment is shown ( $n$  = numbers of biologically independent samples).

Symbols represent, and lines intersect, group geometric means  $\pm$  SD; numbers denote 50 and 90% inhibitory concentrations (EC<sub>50</sub> and EC<sub>90</sub>, respectively), determined through non-linear 4-parameter variable slope regression modeling. Source data are provided as a Source data file.

## Article

<https://doi.org/10.1038/s41467-023-40556-8>

**Fig. 2 | Efficacy of paxlovid and molnupiravir in Roborovski dwarf hamsters.**

**a** Plasma concentration of nirmatrelvir over 24-h after dosing. Single oral dose of nirmatrelvir (250 mg/kg), with (red circles) or without (black circles) ritonavir (83.4 mg/kg). Symbols show group geometric means  $\pm$  SD and lines intersect means. Dotted line indicates 2  $\times$  mean  $\text{EC}_{50}$  against different VOC, determined in cell culture in Fig. 1b. **b** Antiviral efficacy study schematic. Animals were infected intranasally with  $1 \times 10^4$  pfu of VOC delta or omicron and monitored for 14 days after infection. Clinical signs were assessed once daily (blue triangles). Viral load was determined in a duplicate set of animals 3 days after infection. The numbers of animals ( $n$  = number of independent animals) used in the efficacy (left) and survival

(right) studies are shown. **c, d** Survival curves of VOC delta (**c**) or omicron (**d**) infected dwarf hamsters from **(b)** Log-rank (Mantel-Cox) test, median survival (med survival) is shown. **e, f** Lung virus titers 3 days after infection with VOC delta (**e**) or omicron (**f**) as shown in **(b)**; dotted lines denote limit of detection. **g–j** Lung (**g, i**) and trachea (**h, j**) viral RNA copies after infection with VOC delta (**e, g, i**) or omicron (**f, h, j**) as shown in **(b)**. Symbols represent independent biological repeats; columns show group geometric means  $\pm$  SD. Significance was determined using unpaired 2-sided  $t$  tests (**e, g, h**) or one-way ANOVA Tukey's post hoc test (**i, j**) or Kruskal–Wallis test and Dunn's post hoc test (**f**);  $P$  values are shown. Source data are provided as a Source data file.

was 215,000  $\text{h} \times \text{ng/ml}$ , confirming that ritonavir, equivalent to its effect in human patients, efficiently slows nirmatrelvir metabolism in the dwarf hamsters. Previously, we have demonstrated that 250 mg/kg molnupiravir yields plasma exposure of  $\text{N}^4$ -hydroxycytidine, the systemic metabolite of molnupiravir<sup>33</sup>, of 376  $\text{h} \times \text{ng/ml}$  in dwarf hamsters<sup>29</sup>. Human patients taking paxlovid or molnupiravir show

nirmatrelvir exposure of 28,220  $\text{h} \times \text{ng/ml}$ <sup>34,35</sup> and  $\text{N}^4$ -hydroxycytidine exposure of 8200  $\text{h} \times \text{ng/ml}$ <sup>36</sup>, respectively.

Matching the design of our previous molnupiravir dwarf hamster efficacy studies<sup>29</sup>, we initiated oral treatment with paxlovid 12 h after intranasal infection of the dwarf hamsters with  $1 \times 10^4$  pfu of VOC delta or omicron (lineage B.1.1.529), and continued treatment in a twice-daily

## Article

<https://doi.org/10.1038/s41467-023-40556-8>**Table 1 | Single dose pharmacokinetics of nirmatrelvir or nirmatrelvir/ritonavir in Roborovski dwarf hamster and human plasma**

Drug	Species	Dose (mg/kg)	T <sub>max</sub> (h)	C <sub>max</sub> (ng/ml)	AUC <sub>inf</sub> (hours × ng/ml)	t <sub>1/2</sub> (h)	Reference
Nirmatrelvir/ritonavir	Roborovski dwarf hamster	250/83	1	34,200	215,000	2.21	This study
Nirmatrelvir	Roborovski dwarf hamster	250	1	5320	22,400	1.36	This study
Nirmatrelvir/ritonavir	Human	250/100 <sup>a</sup>	2.75	2882	28,220	6.94	34
Molnupiravir	Human	800 <sup>a</sup>	1.75	2770	8200	1.18	36
Molnupiravir	Roborovski dwarf hamster	250	0.5	251	376	1.62	29

<sup>a</sup>Human doses are expressed as absolute amount, not mg/kg.

(b.i.d.) regimen (Fig. 2b). In the VOC omicron infection group, we included molnupiravir, dosed at 250 mg/kg b.i.d., and low-dose paxlovid (125 mg/kg nirmatrelvir and 83.3 mg/kg ritonavir) arms for comparison of effect size and/or dose-dependency of potency. The 12-h time-to-treatment-onset was chosen due to rapid disease progression in the dwarf hamster model<sup>29</sup>, which mimics human patients at transition stage to complicated COVID-19. As we have reported for molnupiravir treatment after VOC delta infection<sup>29</sup>, all treated dwarf hamsters met the primary efficacy endpoint and survived infection independent of VOC used, meeting the primary efficacy endpoint (Fig. 2c, d). By contrast, 83% and 50% of vehicle-treated animals had succumbed to the disease 6 days after infection with VOC delta and omicron, respectively. Drug-treated animals displayed minimal, if any, clinical signs, whereas dwarf hamsters in vehicle groups experienced hyperthermia and body weight loss (Supplementary Fig. 1).

Virus burden in lungs of duplicate sets of equally infected and treated dwarf hamsters was determined 3 days after infection to determine effect size of treatment. Both VOC delta and omicron replicated efficiently in the dwarf hamsters, each reaching peak lung virus loads of  $-10^7$  pfu/g lung tissue (Fig. 2e, f). Treatment of VOC delta-infected dwarf hamsters with paxlovid significantly lowered virus burden, resembling the reduction in VOC delta lung titer that we had previously observed after treatment with molnupiravir<sup>29</sup>. However, effect size of treatment varied by several orders of magnitude between individual animals. We had noticed variation in effect size in molnupiravir-treated dwarf hamsters infected with VOC omicron before, but not VOC delta<sup>29</sup>. Head-to-head comparison of paxlovid and molnupiravir under identical experimental conditions in dwarf hamsters infected with VOC omicron demonstrated statistically significant reduction in lung virus load by either drug compared to vehicle-treated hamsters, but no statistically significant differences in effect size between both drugs or between the paxlovid dose groups (Fig. 2f).

Assessment of viral RNA copies in the lung and, in addition, trachea samples after infection with VOC delta (Fig. 2g, h) and omicron (Fig. 2i–k) revealed proportional reduction of viral RNA and infectious particles in lung samples of paxlovid-treated animals. However, no statistically significant reduction in lung viral RNA copies was detected in animals of the molnupiravir group, despite the highly significant reduction in infectious virus titer in these samples. Viral RNA copies in trachea samples of the respective paxlovid and molnupiravir groups mirrored the lung data. These results reveal similar efficacy of paxlovid and molnupiravir in reducing infectious virus titers in lung and preventing lethal disease in the dwarf hamster model. The non-linear correlation between reduction of infectious viral titers and viral RNA copy numbers in molnupiravir recipients suggested that a large proportion of viral RNA synthesized in molnupiravir-experienced animals may be bio-inactive.

To assess possible virus rebound after treatment, we discontinued treatment with either paxlovid (250 mg/kg nirmatrelvir/ritonavir, b.i.d.) or molnupiravir (250 mg/kg b.i.d.) five days after infection with VOC omicron and determined lung virus load on days 5 and 9 (Fig. 3a). All treated animals survived without developing clinical signs, whereas vehicle-treated animals experienced severe weight loss and hyperthermia, and ~50% succumbed to infection by day 5 (Fig. 3b, c).

Infectious VOC omicron titers in lungs were reduced equally by paxlovid and molnupiravir compared to peak titers (day 3) in vehicle-treated animals (Fig. 3d). On day 5, no statistically significant differences between either treatment group and vehicle-treated animals were detectable. Lung virus load in all groups approached the limit of detection by day 9 without signs of virus rebound in the treatment groups.

**Paxlovid treatment of SARS-CoV-2 infection in ferrets**

To assess the impact of nirmatrelvir treatment on upper respiratory disease, we employed the SARS-CoV-2 ferret infection model<sup>27,28,37,38</sup>. To ensure cross-species consistency of nirmatrelvir PK, we again administered the compound first in a single oral dose at two levels, 20 mg/kg and 100 mg/kg, each in combination with 6 mg/kg ritonavir. Overall nirmatrelvir plasma exposure in ferrets was  $32,700 \text{ h} \times \text{ng/ml}$  and  $49,500 \text{ h} \times \text{ng/ml}$  for the 20 and 100 mg/kg groups, respectively (Fig. 4a; Table 2), indicating a dose-dependent, but not dose-proportional, PK profile of paxlovid.

Both dose levels were advanced to efficacy testing after intranasal infection of ferrets with  $1 \times 10^5$  pfu of SARS-CoV-2 isolate USA-WAI/2020 (lineage A), which most efficiently replicates and spreads in ferrets<sup>27,29,37,39,40</sup> and other members of the Mustela genus<sup>41,42</sup>. Treatment was initiated 12 h after infection and continued b.i.d., and nasal lavages collected twice daily to determine shed virus load (Fig. 4b). Characteristic for this model<sup>27,28,37,38</sup>, SARS-CoV-2-infected ferrets displayed no overt clinical signs (Supplementary Fig. 2). Virus replicated efficiently in vehicle-treated animals, reaching plateau titers of  $-10^5$  pfu/ml shed virus and  $10^5$  RNA copies/μl nasal lavage 48 h after infection, which were maintained until study day 4 (Fig. 4c, d). By study end, both infectious viral titers and viral RNA copies in lavages of the 20 mg/kg nirmatrelvir/ritonavir group were reduced by ~1.4 log orders.

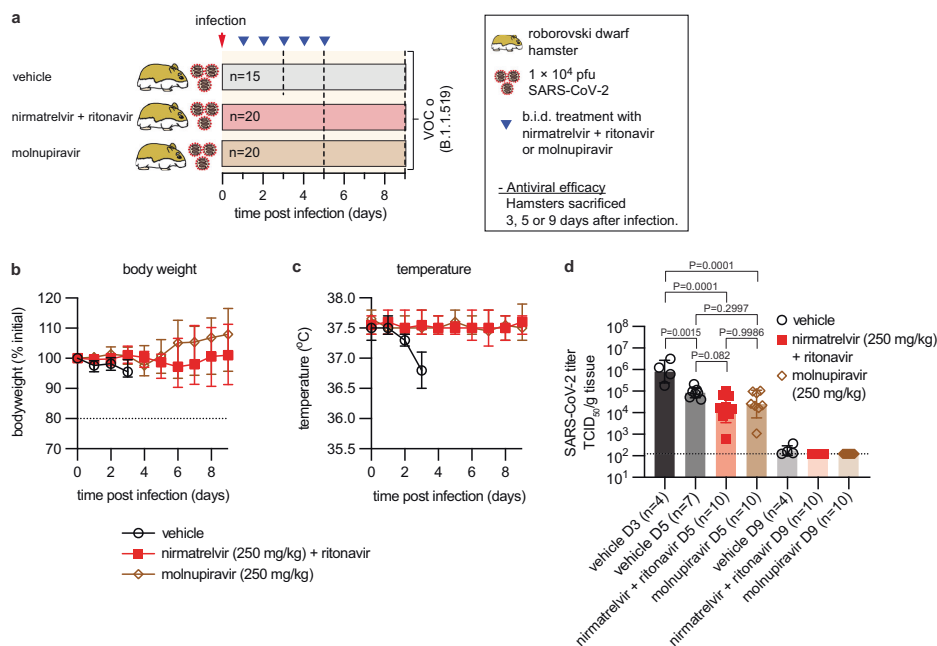
Ferrets receiving 100 mg/kg nirmatrelvir/ritonavir experienced a significant titer reduction in nasal lavages, but did not fully clear the infection. Rather, we noted a slight increase of virus replication in both nirmatrelvir/ritonavir dose groups 3.5 days after treatment start. Whole genome sequencing of virus populations in nasal lavage and turbinate samples taken from these animals revealed that most had acquired an N501T or Y453F substitution in the spike protein, which are characteristic for SARS-CoV-2 adaptation to replication in mustelids<sup>27</sup> (Supplementary Fig. 3), but no signature resistance mutation to nirmatrelvir in nsp5<sup>43–45</sup> emerged as allele-dominant (uploaded as NCBI BioProject PRJNA894555). At study end, infectious titers and viral RNA copies in nasal turbinate tissues were statistically significantly reduced in nirmatrelvir/ritonavir-treated animals compared to the vehicle group (Fig. 4e, f).

**Effect of paxlovid treatment on transmission from SARS-CoV-2-infected ferrets**

To examine the effect of nirmatrelvir/ritonavir treatment on SARS-CoV-2 spread, we subjected treated ferrets to a direct-contact transmission study, first co-housing infected and treated source ferrets with untreated contact animals 42 h after treatment initiation (Fig. 5a). Source animals were infected intranasally with SARS-CoV-2 WAI as before, followed by nirmatrelvir/ritonavir treatment in a b.i.d. regimen



## Article

<https://doi.org/10.1038/s41467-023-40556-8>

**Fig. 3 | VOC omicron lung virus load following antiviral treatment.** **a** Schematic of the study design. Treatment with nirmatrelvir/ritonavir or molnupiravir was initiated 12 h after infection, continued b.i.d., and terminated 5 days after infection. **b, c** Roborovski dwarf hamster body weight (**b**) and temperature (**c**) in animals infected with VOC omicron and treated with drug or vehicle. Symbols show, and lines intersect, group means  $\pm$  SD. Dotted line in (**b**) denotes predefined endpoint. **d** Infectious virus titers in lung tissue extracted on days 3 (D3; vehicle only), 5 (D5)

and 9 (D9) after infection. The number of animals ( $n$  = independent animals) used in each experiment is specified. Symbols represent independent biological repeats (individual animals); columns denote geometric means  $\pm$  SD. Two-way ANOVA with main effects only, Tukey's multiple comparison post hoc test;  $P$  values are shown. Dotted line denotes limit of detection. Source data are provided as a Source data file.

at 20 or 100 mg/kg. For comparison with the only drug in clinical use that reportedly suppresses viral transmission in this model<sup>27,29</sup>, we added molnupiravir treatment groups, dosed orally b.i.d. at 1.25 mg/kg, 2.5 mg/kg, or 5 mg/kg. All treatments were initiated 12 h after infection. Equivalent amounts of shed infectious viral particles were detected in all source animal groups at the time of treatment start, confirming productive infection of all animals (Fig. 5b, c, Supplementary Fig. 4). None of the animals developed clinical signs (Supplementary Fig. 5). Shed virus and RNA copy numbers of vehicle and nirmatrelvir/ritonavir-treated sources resembled that of the initial efficacy study (Supplementary Fig. 6), whereas shed infectious titers in two of the three molnupiravir arms rapidly declined, reaching detection level  $\sim$ 3 days after treatment start (Fig. 5b–d). Recapitulating the dwarf hamster results, viral RNA copy numbers and infectious viral titers in lavages of molnupiravir-treated ferrets followed a non-linear correlation, amounting only to an  $\sim$ 0.5 log order difference to vehicle-treated animals in the 1.25 mg/kg molnupiravir group by study end (Fig. 5e), but a statistically highly significant reduction in infectious titers of approximately two orders of magnitude (Fig. 5c).

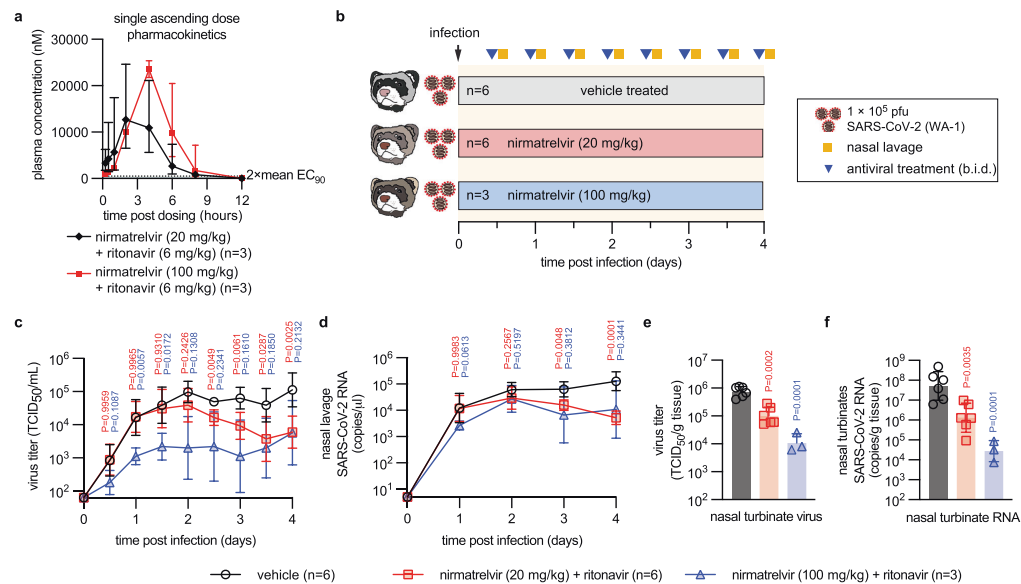
SARS-CoV-2 spread rapidly to sentinels of vehicle-treated source animals. As noted before<sup>27,29</sup>, molnupiravir treatment of source animals rapidly reduced infectious viral titers, suppressing all transmission to untreated naïve contacts in all molnupiravir dose groups including the 1.25 mg/kg group (Fig. 5c, e). By contrast, viral spread to sentinels of ferrets receiving 20 mg/kg b.i.d. nirmatrelvir/ritonavir was delayed, but ultimately all contacts were infected and viral titers in nasal lavages were virtually identical to those of sentinels of vehicle-treated animals,

indicating uninterrupted transmission. Treating source ferrets with 100 mg/kg nirmatrelvir/ritonavir reduced transmission rates, but productive viral transfer still occurred in one of the three contact pairs examined (Fig. 5b, d). Again, virus populations in lavage and turbinate samples of these animals had acquired mustelid-characteristic species adaptation mutations in the spike protein in most cases (Supplementary Fig. 7), but whole genome sequencing did not reveal any allele-dominant resistance mutation to nirmatrelvir in nsp5 (uploaded as NCBI BioProject PRJNA894555).

Viral titers and RNA copies in nasal turbinates determined 4 days after infection in source animals and 4 days after the end of co-housing in contact animals (study day 8) revealed turbinate titers and viral RNA copies in sentinels of sources that had received 20 mg/kg nirmatrelvir/ritonavir indistinguishable from those of animals that had been co-housed with vehicle-treated sources (Fig. 5d, e). One of three contacts of the 100 mg/kg nirmatrelvir/ritonavir recipients showed vehicle-equivalent viral burden in upper respiratory tissues at study end. No infectious particles or viral RNA was detectable in nasal turbinates extracted from contacts of all molnupiravir treatment groups (Fig. 5h, i), confirmed a sterilizing effect of molnupiravir on transmission in all dose groups. Comparison of infectious titers (Fig. 5h) versus viral RNA copies (Fig. 5i) in turbinates of the different molnupiravir dose level source animals underscored the notion that a large proportion of viral RNA synthesized in the presence of molnupiravir was bio-inactive.

We hypothesized that the discrepancy between comparable performance of nirmatrelvir/ritonavir and molnupiravir in dwarf hamster lung tissue and differential effect on viral spread may be due to poor

## Article

<https://doi.org/10.1038/s41467-023-40556-8>

**Fig. 4 | Efficacy of paxlovid in ferrets.** **a** Plasma concentration of nirmatrelvir determined over a 12-h period after a single oral dose. Nirmatrelvir was dosed at 20 mg/kg (black diamonds) or 100 mg/kg (red squares), each in combination with 6 mg/kg ritonavir. Symbols represent group means  $\pm$  SD and lines intersect means. Dotted line indicates  $2 \times$  mean  $EC_{50}$  against different VOC, determined in cell culture in Fig. 1b. **b** Antiviral efficacy study schematic. Ferrets ( $n = 15$  total) were infected intranasally with  $1 \times 10^5$  pfu of SARS-CoV-2 USA/WA-1. After 12 h, groups of ferrets were treated orally with vehicle or 20 mg/kg or 100 mg/kg nirmatrelvir/ritonavir. The number of animals ( $n =$  independent animals) used in each experiment is specified. **c, d** Infectious SARS-CoV-2 titers (**c**) and SARS-CoV-2 RNA copies (**d**) in nasal lavages of animals shown in (**b**). **e, f** Infectious titers (**e**) and SARS-CoV-2 RNA copies (**f**) in nasal turbinates extracted four days after infection. Symbols in (**c-f**) represent independent biological repeats (virus load of individual animals); lines (**c, d**) intersect, and columns (**e, f**) show, group geometric means  $\pm$  SD. Statistical analysis with one-way (**e, f**) or two-way (**c, d**) ANOVA with Dunnett's (**c-f**) post hoc tests;  $P$  values are shown. Source data are provided as a Source data file.

**Table 2 | Single dose pharmacokinetics of nirmatrelvir/ritonavir in ferret and human plasma**

Drug	Species	Dose (mg/kg)	$T_{max}$ (h)	$C_{max}$ (ng/ml)	$AUC_{inf}$ (hours $\times$ ng/ml)	$t_{1/2}$ (h)	Reference
Nirmatrelvir/ritonavir	Ferret	20/6	2.33	8990	32,700	1.05	This study
Nirmatrelvir/ritonavir	Ferret	100/6	4	11,800	49,500	0.74	This study
Nirmatrelvir/ritonavir	Human	250/100 <sup>a</sup>	2.75	2882	28,220	6.94	34
Molnupiravir	Human	800 <sup>a</sup>	1.75	2770	8200	1.18	36
Molnupiravir	Ferret	4	1.7	907	3421	8.2	33
Molnupiravir	Ferret	7	1.5	2851	7569	9.2	33
Molnupiravir	Ferret	20	1.8	3992	18,793	4.7	33
Molnupiravir	Macaque	130	1.62	2644	25,299	1.77	33

<sup>a</sup>Human doses are expressed as absolute amount, not mg/kg.

nirmatrelvir exposure in upper respiratory tract tissues. Assessing drug levels at anticipated peak (3 h after dosing, -30 min after plasma  $C_{max}$ ) and trough (12 h after dosing) revealed statistically significantly lower nirmatrelvir levels in nasal turbinates compared to all other soft tissues but brain (Fig. 5j).

#### Prophylactic treatment of uninfected direct contact ferrets

In the EPIC-PEP and MOVE-AHEAD trials, prophylactic administration of paxlovid or molnupiravir, respectively, to adults exposed to household members did not significantly reduce the risk of infection<sup>20–22</sup>. We prophylactically treated uninfected ferrets with 20 mg/kg or 100 mg/kg nirmatrelvir/ritonavir or 5 mg/kg molnupiravir, all in b.i.d. regimen, followed by co-housing with infected, but untreated, source animals 12 h later (Fig. 6a). Treatment of the

sentinels was continued b.i.d. for 5.5 days, shed virus in nasal lavages of source and sentinels monitored daily, and virus load in the upper respiratory tract determined 6 days after infection.

We detected shed virus in lavages of all contacts receiving vehicle within 24 h of co-housing, indicating productive transmission (Fig. 6b). Again, none of the animals developed clinical signs (Supplementary Fig. 8). Prophylactic 20 mg/kg nirmatrelvir/ritonavir delayed transmission by -48 h, but ultimately all sentinels were productively infected and shed virus titers reached by study end were indistinguishable from those of the vehicle group. In contrast, no infectious SARS-CoV-2 particles emerged in lavages of sentinels prophylactically treated with 100 mg/kg nirmatrelvir/ritonavir or 5 mg/kg molnupiravir. Quantitation of viral RNA in lavage samples groups largely mirrored the virus titer profiles (Fig. 6c). However, low amounts ( $<10^3$  RNA copies/ $\mu$ l) of

Article

<https://doi.org/10.1038/s41467-023-40556-8>

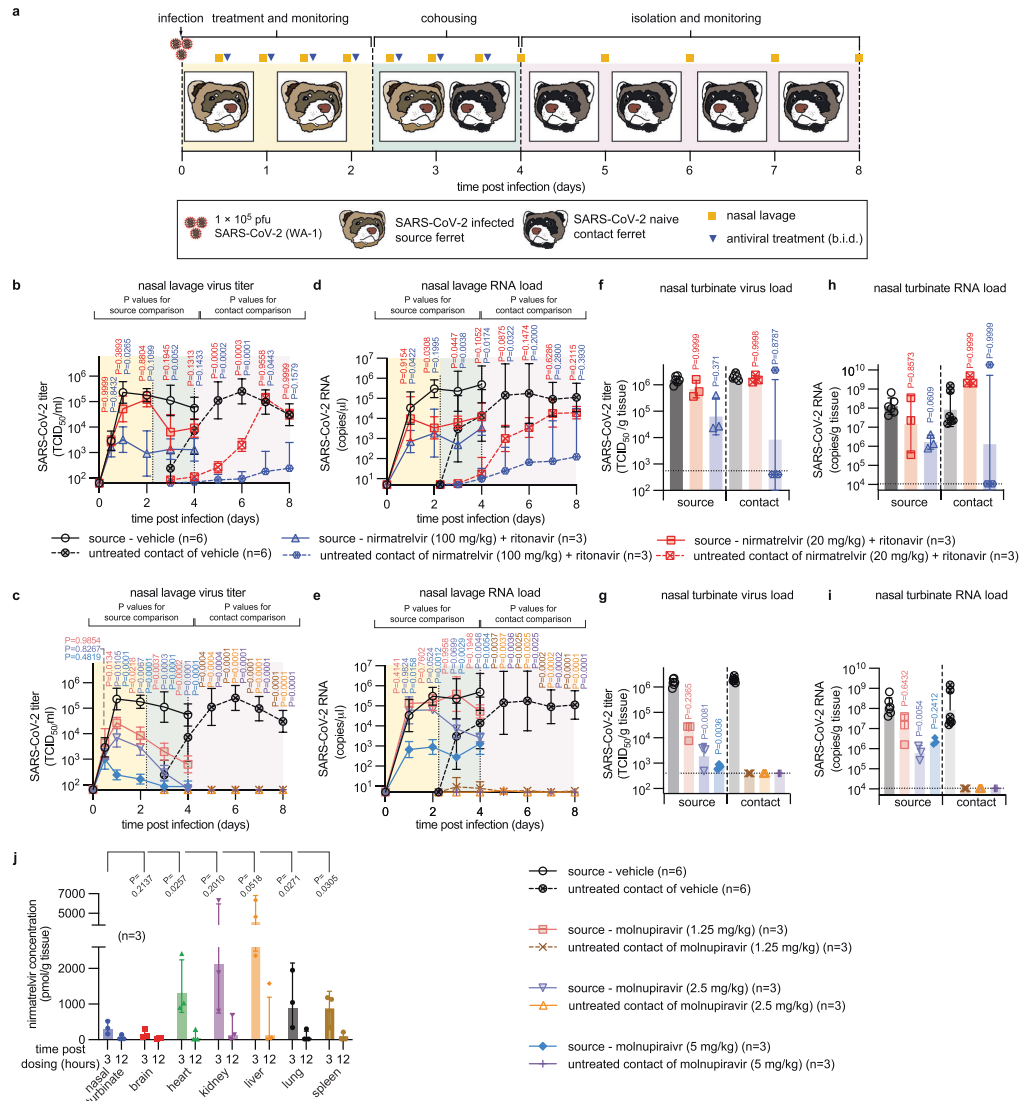


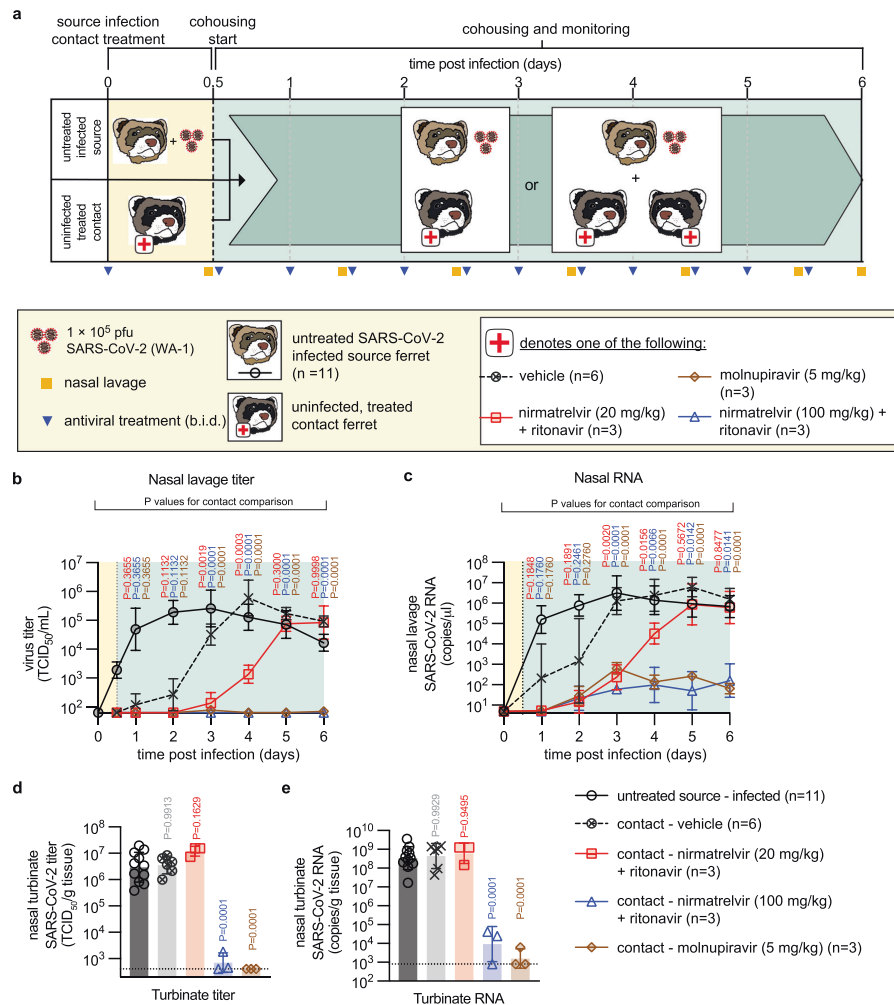
**Fig. 5 | Effect of treatment with paxlovid or molnupiravir on SARS-CoV-2 transmission. a** Transmission study schematic. **b–e** Direct-contact transmission study. Results are disaggregated into nirmatrelvir/ritonavir (**b–e**) and molnupiravir (**f–i**) treatment groups; vehicle-treated animals are shown in both sets. Infectious titers (**b, c**) and RNA copies (**d, e**) of SARS-CoV-2 present in nasal lavages of source and contact ferrets. Nasal turbinate titers (**f, g**) and RNA copies (**h, i**) in nasal turbinates extracted from source and contact animals on study days 4 and 8, respectively. Symbols (**b–e**) represent, and lines intersect, geometric means ± SD; x-axes denote level of detection. Symbols (**f–i**) represent independent biological

repeats (results from individual animals); columns denote geometric means ± SD; dotted lines specify level of detection. **j** nirmatrelvir exposure in selected ferret organs at anticipated peak and trough after single-dose administration of nirmatrelvir + ritonavir. The number of animals (*n* = independent animals) used in each experiment is specified. Symbols represent independent biological repeats (results from individual animals); columns denote means ± SD. Statistical analysis with one-way (**f–i**) or two-way (**b–e**) ANOVA with Dunnett’s post hoc tests (**b–e**), Kruskal–Wallis test with Dunn’s post hoc tests (**f–i**), or ratio paired two-sided *t* test (**j**); *P* values are shown. Source data are provided as a Source data file.

SARS-CoV-2 RNA were present also in lavages of the 5 mg/kg molnupiravir and 100 mg/kg nirmatrelvir/ritonavir groups, demonstrating that co-housing with untreated source animals efficiently exposed sentinels of all four study arms to SARS-CoV-2. Infectious virus load in nasal turbinates of animals treated with 20 mg/kg nirmatrelvir/

ritonavir was statistically indistinguishable from that found in the vehicle group (Fig. 6d). Turbinates of one of the contacts treated with 100 mg/kg nirmatrelvir/ritonavir harbored some infectious particles, whereas turbinates of all sentinels receiving 5 mg/kg molnupiravir did not contain infectious SARS-CoV-2 at study end. We detected high RNA

## Article

<https://doi.org/10.1038/s41467-023-40556-8>

**Fig. 6 | Prophylactic treatment of close contacts with paxlovid or molnupiravir. a** Prophylaxis study schematic. **b, c** Infectious titers (**b**) and RNA copies (**c**) of SARS-CoV-2 present in nasal lavages of source and contact ferrets. The number of animals ( $n$  = independent animals) in each experiment is specified. **d, e** Nasal turbinate titers (**d**) and RNA copies (**e**) in nasal turbinates extracted from source and contact animals on study day 6. Symbols (**b, c**) represent, and lines intersect,

geometric means  $\pm$  SD; x-axes denote level of detection. Symbols (**d, e**) represent independent biological repeats (results from individual animals); columns denote geometric means  $\pm$  SD; dotted lines specify level of detection. Statistical analysis with one-way (**d, e**) or two-way (**b, c**) ANOVA with Dunnett's *post hoc* tests; *P* values are shown. Source data are provided as a Source data file.

copy numbers in all 20 mg/kg nirmatrelvir/ritonavir recipients, which were statistically equivalent to those derived from vehicle-treated animals (Fig. 6e). Low levels of viral RNA were furthermore observed in the turbinates of two animals of the 100 mg/kg nirmatrelvir/ritonavir group and one animal in the 5 mg/kg molnupiravir group. One 100 mg/kg nirmatrelvir/ritonavir animal and the other two 5 mg/kg molnupiravir recipients remained viral RNA free.

## Discussion

The retrospective analyses of members of Clalit Health Services<sup>16,19</sup> and a retrospective cohort study from the Hong Kong VOC omicron wave<sup>17</sup> demonstrated that both paxlovid<sup>16</sup> and molnupiravir<sup>19</sup> significantly lowered the risk of progression to severe disease and deaths in older

adults. However, a direct comparison of drug efficacy was not possible due to imbalances in baseline characteristics of the study groups such as patient comorbidities, age, and vaccine status<sup>16</sup>. To assess efficacy of both drugs against COVID-19 of different severity under equivalent experimental conditions, we employed the Rborovski dwarf hamster and ferret models of SARS-CoV-2 infection.

Establishing a correlation between animal and human dose levels is complex. Interspecies allometric scaling to convert dose-based systemic exposure from animals to humans can confound predictive power of animal models<sup>47</sup>. Although no scaling was required for our study since plasma exposure levels of both nirmatrelvir<sup>34</sup> and N<sup>4</sup>-hydroxycytidine<sup>36</sup>, the systemic metabolite of molnupiravir<sup>33</sup> were known (included in Tables 1, 2), comparison dose selections can still be

## Article

<https://doi.org/10.1038/s41467-023-40556-8>

undermined by, for instance, host species-specific differences in drug plasma binding, tissue penetration, viral replication kinetics, and drug half-life.

To place ferret dose levels in context to clinical data, we therefore evaluated for each drug individually treatment effect size in the animal model and human patients. Since accurate and reproducible quantitation of infectious viral titers in human nasopharyngeal swabs is difficult<sup>48</sup>, viral RNA copies have become the clinical standard and RNA copy number reduction in the upper respiratory tract represents the sole quantitative biomarker that is available across multiple species including humans. Clinical trials reported an  $-0.5$  log order reduction of viral RNA copies by molnupiravir<sup>49</sup>, and  $0.89$ – $0.93$  log orders by paxlovid<sup>12,21</sup>. An equivalent effect size was achieved in the ferret upper respiratory tract by  $1.25$  mg/kg molnupiravir ( $-0.5$  log order reduction) and  $20$  mg/kg nirmatrelvir/ritonavir ( $1.4$  log order reduction), each administered in b.i.d. regimen.

In the case of paxlovid, the correlation between viral RNA copy and infectious titer reductions was approximately linear in the models. A viral mutagen such as molnupiravir, however, once incorporated into viral RNA, can destroy bioactivity of this RNA without proportionally reducing the number of physical RNA copies, which may result in underappreciation of its antiviral effect based on RNA copy numbers alone. Both the dwarf hamster and ferret model illustrate that this difference between reduction of infectious virus titer and viral RNA molecules becomes most pronounced at low molnupiravir exposure, veering in some cases from statistically insignificant (RNA copies) to several orders of magnitude (infectious titer) in the same sample.

It is undocumented at present whether a similar discrepancy between viral RNA copy number and infectious viral titer reduction applies to clinical samples. Since the effect is consistent across rodent and non-rodent host models and appears to be directly linked to the mechanism of action of molnupiravir, quantitating viral RNA copies without assessing RNA bioactivity may be at risk of being misleading in the case of viral mutagens such as molnupiravir and may, therefore, not represent an informative primary endpoint for clinical trials. Support for this notion comes from qualitative infectious viral load data determined in the phase 2a clinical trial of molnupiravir<sup>49</sup>. After a 5-day treatment course, infectious virus particles could be isolated from patients in the placebo group, but not from patients receiving molnupiravir, although these patients experienced only an  $-0.5$  log order decrease in viral RNA copies in the upper respiratory tract.

An antiviral effect size-based approach could not be applied to the dwarf hamster model of acute SARS-CoV-2 pneumonia, since viral RNA copy number reductions in the human lower respiratory tract are unknown. Based on our PK information, N<sup>4</sup>-hydroxycytidine<sup>29</sup> plasma exposure in dwarf hamsters was over 20-fold lower than that in humans, whereas nirmatrelvir exposure exceeded that achieved in humans by over 7.5-fold, suggesting that the dwarf hamster model may overestimate efficacy of nirmatrelvir/ritonavir against acute lung disease.

Acknowledging this caveat, the dwarf hamster model supported three major conclusions: (i) both drugs met the primary efficacy endpoint, ensuring complete survival of treated animals; (ii) both drugs statistically significantly reduced lung virus burden compared to vehicle-treated animals; and (iii) treatment benefit provided by either drug showed variations between individual animals when dwarf hamsters were infected with VOC omicron. We have recently reported that in the case of molnupiravir, biological sex of the treated dwarf hamsters contributes to effect<sup>29</sup>. Although not powered for a full statistical analysis, nirmatrelvir/ritonavir performance in dwarf hamsters did not suggest an equivalent role of biological sex on effect size against VOC omicron. We hypothesize that differences in the kinetics of viral host invasion between individual dwarf hamsters may contribute to this variation of effect size. In toto, the dwarf hamster model recapitulated the main conclusions of retrospective clinical studies in older adults<sup>7</sup>;

both drugs mitigated advance to severe disease, preventing acute lung injury and death.

Prolonged self-isolation periods after a positive SARS-CoV-2 test impose considerable social hardship on the individual patient and economic burden on societies<sup>50–52</sup>, which has resulted in eroding public compliance with self-quarantine during the course of the pandemic<sup>53</sup>. In addition to direct therapeutic benefit, pharmacologically shortening the duration of the infectious period will improve patient quality of life and may provide epidemiologic benefit through interruption of viral transmission chains<sup>54,55</sup>. We have established efficient suppression of SARS-CoV-2 transmission in the ferret model by molnupiravir dosed at  $5$  mg/kg b.i.d.<sup>27,29</sup> and experimental nucleoside analog antivirals<sup>37</sup> in previous work, and demonstrated in this study that therapeutic administration of  $1.25$  mg/kg molnupiravir or  $100$  mg/kg nirmatrelvir/ritonavir to ferrets fully or partially, respectively, suppressed transmission to untreated direct contacts. At these dose levels, either drug reduced shed infectious viral titers to  $-10^3$  TCID<sub>50</sub> units/ml nasal lavage fluid, which appears to represent a threshold for productive direct-contact SARS-CoV-2 transmission in the ferret model. SARS-CoV-2 transmitted in all pairs of the  $20$  mg/kg nirmatrelvir/ritonavir group, which reduced viral titers to  $-10^4$  TCID<sub>50</sub> units/ml nasal lavage fluid, indicating that infectious viral titer in the ferret upper respiratory tract is a correlate for transmission success.

Whole genome sequencing of virus populations isolated from paxlovid-experienced ferrets provided no evidence that replication resurgence and transmission both from and to paxlovid-treated animals in our study were supported by emerging resistance to nirmatrelvir<sup>43–45</sup>. Rather, poor control of SARS-CoV-2 spread in ferrets coincided with significantly lower nirmatrelvir levels in the upper respiratory tract than lung and other soft tissues but brain, identifying nasal turbinates as a privileged organ of low nirmatrelvir exposure. This effect could be ferret-specific, since tissue drug exposure levels cannot be readily determined in humans. However, rebounding virus replication in paxlovid recipients<sup>2,23,24</sup> and the lack of efficacy in patients <65 years of age, in which SARS-CoV-2 infection resides primarily in the upper respiratory tract, are consistent with low nirmatrelvir exposure also in human upper respiratory tissues.

Prophylactic dosing of contact ferrets with  $20$  mg/kg paxlovid did not prevent transmission from infected animals, recapitulating the outcome of the failed EPIC-PEP trial<sup>20,21</sup>. Interestingly,  $20$  mg/kg nirmatrelvir/ritonavir was also the ferret dose that mediated a similar viral RNA copy number reduction to that seen in humans receiving paxlovid. Since also prophylactic molnupiravir did not prevent infection in the MOVE-AHEAD trial<sup>22</sup>, an equally negative outcome of prophylactic  $1.25$  mg/kg molnupiravir was likely, prompting us not to commit additional animals for an experimental confirmation. However,  $5$  mg/kg prophylactic molnupiravir fully, and  $100$  mg/kg prophylactic nirmatrelvir/ritonavir partially, suppressed infection, indicating that higher dose levels, as long as compatible with safety margins, provide prophylactic efficacy in ferrets.

Trials with appropriately selected endpoints will be required to determine whether molnupiravir over-proportionally reduces infectious SARS-CoV-2 titers, compared to viral RNA copy numbers, also in the human upper respiratory tract. Due to differences in the dynamics of viral host invasion and replication in humans versus animals, extrapolation of therapeutic time windows from animal models to human patients is challenging. Despite the potential of host species-specific effects, this study affirms retrospective clinical analyses that early treatment of older adult patients at elevated risk of progression to severe COVID-19 with either paxlovid or molnupiravir will provide significant therapeutic benefit. We demonstrate in two animal model species, one rodent and one non-rodent, that infectious particle titers, but not viral RNA copy numbers, should be assessed to determine efficacy of a viral mutagen such as molnupiravir. Infectious viral load in the upper respiratory tract emerged as a correlate for SARS-CoV-2



## Article

<https://doi.org/10.1038/s41467-023-40556-8>

transmission success in ferrets. Therapeutic molnupiravir, administered at a dose not associated with a significant reduction of viral RNA copy numbers, completely suppressed transmission in ferrets.

## Methods

### Ethics and inclusion statement

All in vivo studies were performed in compliance with the Guide for the Care and Use of Laboratory Animals, National Institutes of Health guidelines, and the Animal Welfare Act Code of Federal Regulations. Experiments with SARS-CoV-2 involving ferrets were approved by the Georgia State Institutional Animal Care and Use Committee under protocol A20031. Experiments with SARS-CoV-2 involving Roborovski dwarf hamsters were approved by the Georgia State Institutional Animal Care and Use Committee under protocol A21019. All experiments using infectious SARS-CoV-2 strains were approved by the Georgia State Institutional Biosafety Committee under protocol B20016 and performed in BSL-3/ABSL-3 facilities at the Georgia State University.

### Study design

Male and female Roborovski dwarf hamsters (*Phodopus roborovskii*, 3–4 months old) and female ferrets (*Mustela putorius furo*, 6–10 months old) were used as in vivo models to assess the therapeutic efficacy of orally administered nirmatrelvir against infection with SARS-CoV-2. Prior to studies, hamsters and ferrets were rested for at least five days. Roborovski dwarf hamsters were used to study the effects of nirmatrelvir treatment on severe disease associated with lower respiratory tract infection, acute lung injury, and death. Ferrets were used to examine the effect of nirmatrelvir on upper respiratory infection and transmission. SARS-CoV-2 infections were established in animals through intranasal inoculation. For hamsters, animals were monitored regularly for clinical signs and viral loads were determined in respiratory tract tissues at endpoint. For ferrets, upper respiratory tract viral titers were assessed at least once daily through nasal lavages. In addition, upper respiratory tract tissues were harvested at endpoint to assess upper respiratory tract viral loads. Virus loads were determined by plaque assays or TCID<sub>50</sub> and RT-qPCR quantitation.

### Cells

VeroE6-TMPRSS2 (BPS Bioscience #78081) and Calu-3 (ATCC HB-55™) cells were cultivated at 37 °C with 5% CO<sub>2</sub> in Dulbecco's modified Eagle's medium (DMEM) supplemented with 7.5% heat-inactivated fetal bovine serum (FBS). All cells were authenticated phenotypically and tested routinely in 3-months intervals for absence of mycoplasma contamination prior to use.

### Viruses

SARS-CoV-2 USA-WA1 (lineage A, isolate USA-WA1/2020, BEI cat# NR-52281) was obtained from BEI resources and amplified on Calu-3 cells. SARS-CoV-2 isolates for lineage B.1.1.7 (VOC α; hCoV-19/USA/CA/UCSD\_5574/2020), lineage B.1.351 (VOC β; hCoV-19/South Africa/KRISP-K005325/2020), lineage P.1 (VOC γ; hCoV-19/Japan/TY7-503/2021), lineage B.1.617.2 (VOC δ; clinical isolate #233067), lineage B.1.1.529 (VOC o; hCoV-19/USA/WA-UW-21120120771/2021) lineage BA.2 (clinical isolate 22012361822A), lineage BA.2.12.1 (hCoV-19/USA/WA-CDC-UW22050170242/2022), and lineage BA.4 (hCoV-19/USA/WA-CDC-UW22051283052/2022) were obtained from UW Virology and amplified on Calu-3 cells. All viruses were titered on VeroE6-TMPRSS2 cells and virus stocks were authenticated by whole genome next-generation sequencing prior to use.

### Virus yield reduction

Nirmatrelvir was dissolved in water-free DMSO at 10 mM stock concentration and stored in single-use aliquots at –80 °C. Cells were seeded 14 h prior to experimentation in 24-well plates at  $2 \times 10^5$  cells per well in 400 μl per well DMEM + 7.5% FBS supplemented with 2 μM

CP-100356. Serial dilutions were generated in culture media containing 2 μM CP-100356 spanning a final concentration range from 2700 to 1.4 nM (3-fold serial dilution; 8 steps; dilution series were prepared 2-fold overconcentrated (54000 to 2.8 nM)). Every concentration of each test article was assessed in 3 biological (independent) repeats. Vehicle-treated control cultures DMSO volume equivalents corresponding to the highest test compound concentration. Serial dilutions were transferred to target wells (500 μl per well), immediately followed by infection with SARS-CoV-2 (multiplicity of infection 0.1 pfu per cell) in 100 μl per well (viral dilution media contained 2 μM CP-100356). Infected plates were incubated in a humidified incubator at 37 °C and 5% CO<sub>2</sub> for 48 h. Progeny virus titers in culture supernatants were determined through plaque-forming or TCID<sub>50</sub> assay on VeroE6-TMPRSS2 cells. Inhibitory concentrations were calculated based on 4-parameter variable slope regression models.

### SARS-CoV-2 titration by plaque assay

All samples were serially diluted in DMEM media supplemented with 2% FBS and antibiotic-antimycotic solution (Gibco). Dilutions were added to VeroE6-TMPRSS2 cells seeded 24 h earlier in 12-well plates at  $3 \times 10^5$  cells per well. Dilutions were allowed to adsorb for 2 h at 37 °C. Following adsorption, inoculum was removed, and cells were overlaid with 1.2% Avicel (FMC BioPolymer) in DMEM supplemented with antibiotic-antimycotic solution and incubated at 37 °C with 5% CO<sub>2</sub>. After incubating for 3 days, Avicel was removed, cells were washed with PBS and fixed with 10% neutral buffered formalin. Plaques were visualized using 1% crystal violet.

### Single-dose pharmacokinetics in hamsters

Groups of hamsters were administered a single oral dose of nirmatrelvir (250 mg/kg; 0.5% MC with 2% Tween80) with or without ritonavir (83.4 mg/kg; 20% ethanol). Blood was harvested retro-orbitally using plain micro-hematocrit capillary tubes (Duran Wheaton Kimble) and collected in K<sub>2</sub>EDTA capillary tubes (Sarstedt Microvette CB300) 0.5, 1, 2, 4, 8, and 24 h after dosing. Plasma was clarified by centrifugation (4 °C, 450 × g, 5 min). To determine tissue concentrations of nirmatrelvir, groups of hamsters were sacrificed 1, 8, and 24 h after dosing and selected tissues were harvested, flash-frozen in liquid nitrogen, and stored at –80 °C. Nirmatrelvir concentrations were analyzed using a qualified LC/MS/MS method, and PK parameters were calculated using non-compartmental analysis with WinNonlin 8.3.3.33. MS analysis defined the analyte area response, internal area response, and transitions (Q1 to Q3). Raw MS data are shown in Supplementary Data 2.

### Hamster efficacy studies

Groups of male and female Roborovski dwarf hamsters were anesthetized using ketamine/dexmedetomidine and infected with 10<sup>4</sup> pfu per animal (50 μl total volume, 25 μl per nare). Anesthesia was reversed with atipamezole. Hamsters were monitored daily (body weight, temperature, and clinical score). Treatment started 12 h after infection with nirmatrelvir (200 μl, 0.5% MC with 2% Tween80; 250 mg/kg or 125 mg/kg b.i.d.) and ritonavir (50 μl, 20% EtOH; 83.3 mg/kg, b.i.d.). Treatment continued twice daily for 5 and 7 days after infection for VOC δ and VOC o, respectively. Treatment was discontinued for VOC δ after 5 days due to treated hamsters developing pronounced diarrhea. Groups of hamsters were euthanized three days after infection to assess lower respiratory tract viral load. Lungs were harvested, washed with sterile phosphate buffered saline, and homogenized in PBS supplemented with antibiotic-antimycotic using a bead blaster (3 bursts of 30 s at 4 °C each, 30 s pause between bursts; Bead Blaster 24R, Benchmark). Lung homogenates were clarified by centrifugation (20,000 × g, 10 min, 4 °C), aliquoted, and stored at –80 °C until processed. For RNA quantification, lungs and tracheas were harvested and homogenized in RNeasy RNA lysis buffer (Qiagen) in accordance with the manufacturers protocol.

## Article

<https://doi.org/10.1038/s41467-023-40556-8>**Assessing viral rebound in hamsters**

Male and female dwarf hamsters (6 months old) were randomly assigned in different groups. Upon arrival, all animals were rested for 72 h prior to being transferred into single-ventilated cages to an ABSL-3 facility. For infections, animals were anesthetized using ketamine/dexdomitor and infected intranasally with  $10^4$  pfu (50  $\mu$ l) SARS-CoV-2 VOC o (B.1.1.519). Treatment was initiated 12 h post infection using nirmatrelvir (200  $\mu$ l, 0.5% MC with 2% Tween80; 250 mg/kg) and ritonavir (50  $\mu$ l, 20% EtOH; 83.3 mg/kg, b.i.d.), molnupiravir (200  $\mu$ l, 1% MC; 250 mg/kg; b.i.d.) or vehicle (200  $\mu$ l, 0.5% MC with 2% Tween80). Twice-daily treatment continued until five days post infection. Vehicle animals were euthanized on days 3, 5, and 9, nirmatrelvir and molnupiravir-treated hamsters were euthanized on days 5 and 9. Lungs were harvested, washed with sterile phosphate buffered saline, and homogenized in PBS supplemented with antibiotic-antimycotic using a bead blaster (3 bursts of 30 s at 4 °C each, 30 s pause between bursts; Bead Blaster 24R, Benchmark). Lung homogenates were clarified by centrifugation (20,000  $\times g$ , 10 min, 4 °C), aliquoted and stored at -80 °C until processed. Virus titers were determined by TCID<sub>50</sub> assays.

**Single ascending dose pharmacokinetics in ferrets**

Groups of ferrets were administered a single oral dose of nirmatrelvir at a dosage of 20 mg/kg ( $n = 3$ ) or 100 mg/kg ( $n = 3$ ); (2 ml; 0.5% MC with 2% Tween80) with ritonavir (1 ml; 6 mg/kg; 20% EtOH). A dosage of 6 mg/kg ritonavir was selected based on previous studies in ferrets (53). Drug was administered by oral gavage using a 12 french catheter (Cure Medical). After each gavage, the catheter line was flushed using high calorie liquid diet (3.5 ml; DYNE, PetAg). Blood was harvested in K<sub>2</sub>EDTA capillary tubes (Sarstedt Microvette CB300) at 0.25, 0.5, 1, 2, 4, 6, 8, and 12 h after dosing. Plasma was clarified by centrifugation (4 °C, 450  $\times g$ , 5 min), aliquoted and stored at -80 °C. To determine tissue concentrations of nirmatrelvir, groups of ferrets were sacrificed 3 and 12 h after dosing and selected tissues were harvested, flash-frozen in liquid nitrogen, and stored at -80 °C. Nirmatrelvir concentrations were analyzed using a qualified LC/MS/MS method, and PK parameters were calculated using non-compartmental analysis with WinNonlin 8.3.3.33. Raw MS data are shown in Supplementary Data 2.

**In vivo efficacy testing in ferrets against VOCs**

Groups of ferrets were anesthetized with ketamine/dexmedetomidine and inoculated with  $1 \times 10^5$  pfu of SARS-CoV-2 USA-WA1 (lineage A, isolate USA-WA1/2020, BEI cat# NR-52281; 1 ml, 0.5 ml per nare). Following infection, anesthesia was reversed using atipamezole. Treatment was initiated 12 h after infection and continued twice daily until study end (4 days after infection). Ferrets were treated with vehicle ( $n = 6$ ; 0.5% MC with 2% Tween80), nirmatrelvir/ritonavir (20 ( $n = 6$ ) or 100 ( $n = 3$ ) mg/kg nirmatrelvir; 6 mg/kg ritonavir). Treatments were administered by oral gavage using a 12 french catheter (Cure Medical), starting 12 h after infection in consecutive 2 ml (20 or 100 mg/kg nirmatrelvir; 2 ml 0.5% MC with 2% Tween80) and 1 ml (6 mg/kg ritonavir; 1 ml 20% ethanol) dose volumes. Molnupiravir was formulated in 1% methylcellulose and administered in 3 ml dose volume. After each gavage, the catheter line was flushed using high calorie liquid diet (3.5 ml; DYNE, PetAg). Nasal lavages were collected every 12 h after study start in sterile PBS containing antibiotics and antimycotics (Anti-Anti; Gibco). All ferrets were euthanized 4 days after infection and tissues were harvested to determine SARS-CoV-2 titers and the presence of viral RNA.

**Effect of treatment on SARS-CoV-2 contact transmission in ferrets**

A group of source ferrets were inoculated intranasally with  $1 \times 10^5$  pfu of SARS-CoV-2 USA-WA1 (lineage A, isolate USA-WA1/2020, BEI cat# NR-52281; 1 ml, 0.5 ml per nare). Twelve hours after infections, source ferrets were further divided into groups ( $n = 3$ ), receiving vehicle,

molnupiravir (1.25 mg/kg, b.i.d.; 2.5 mg/kg, b.i.d.; or 5 mg/kg, b.i.d.); or nirmatrelvir (20 or 100 mg/kg, b.i.d. in 2 ml 0.5% MC with 2% Tween80 + ritonavir (6 mg/kg in 1 ml 20% ethanol)), in all cases administered via oral gavage. At 54 h after infection, each source ferret was co-housed with one uninfected and untreated contact ferret. Co-housing continued until 96 h after infection, when sourced ferrets were euthanized and contact ferrets were separated and housed individually. All contact ferrets were monitored for 4 days after separation from source ferrets and then euthanized. Nasal lavages were performed on source ferrets twice daily until co-housing ended. After co-housing started, nasal lavages were performed on all contact ferrets every 24 h. Upon euthanizing ferrets, nasal turbinates were harvested to determine infectious titers and the presence of viral RNA.

**Effect of prophylactic treatment on direct contact transmission**

At study onset, one group of source ferrets were inoculated intranasally with  $1 \times 10^5$  pfu of SARS-CoV-2 USA-WA1 (lineage A, isolate USA-WA1/2020, BEI cat# NR-52281; 1 ml, 0.5 ml per nare) and isolated from uninfected ferrets. At the same time, twice-daily treatment regimens were initiated on groups of uninfected ferrets using nirmatrelvir (20 mg/kg) + ritonavir ( $n = 3$ ) or nirmatrelvir (100 mg/kg) + ritonavir ( $n = 3$ ), molnupiravir (5 mg/kg;  $n = 3$ ), or vehicle. Nirmatrelvir was administered in 2 ml (20 or 100 mg/kg in 0.5% MC with 2% Tween80) followed by administration of ritonavir in 1 ml (6 mg/kg in 1 ml 20% ethanol). Molnupiravir was administered in 3 ml (1% methylcellulose). The catheter line was then flushed using high calorie liquid diet (3.5 ml; DYNE, PetAg). Treatment was continued for 6 days until study end. Twelve hours after infection, untreated and infected source ferrets were co-housed with treated contact ferrets. Per approved IACUC protocols, maximal density in the ventilated large animal caging system is 3 ferrets/cage. Therefore, an asymmetrical co-housing matrix had to be applied, consisting of a randomly assigned source to contact animal ratio of either 1:1 or 1:2. After co-housing commenced, nasal lavages were collected every 24 h, and ferrets were monitored until study end. Six days after infecting source ferrets, all animals were euthanized, and nasal turbinates were harvested to determine infectious titers and the presence of viral RNA.

**Titration of SARS-CoV-2 in tissue extracts**

For virus titration, the organs were weighed and homogenized in PBS supplemented with antibiotic-antimycotic solution (Gibco). Tissues were homogenized using a bead blaster (3 bursts of 30 s at 4 °C each, 30 s pause between bursts; Bead Blaster 24R, Benchmark). Tissue homogenates were clarified by centrifugation (20,000  $\times g$  for 5 min at 4 °C). The clarified supernatants were harvested, frozen and used in subsequent TCID<sub>50</sub> or plaque assays. For detection of viral RNA, the harvested organs were homogenized in lysis buffer (Qiagen), and the total RNA was extracted using a RNeasy mini kit (Qiagen). For nasal lavages, RNA was extracted using a Quick-RNA Viral Kit (Zymo) in accordance with the manufacturer's protocols.

**Quantitation of SARS-CoV-2 RNA**

SARS-CoV-2 RNA was detected using the nCoV\_IP2 primer-probe set (nCoV\_IP2-12669Fw ATGAGCTTAGTCCTGTTG; nCoV\_IP2-12759Rv CTCCTTTGTTGTGTTGT; nCoV\_IP2-12696bProbe+) 5'FAM-AGATGTC TTGTGCTGCCGGTA-3'BHQ-1) (National Reference Center for Respiratory Viruses, Institut Pasteur). RT-qPCR reactions were performed using an QuantStudio 3 real-time PCR system using the QuantStudio Design and Analysis package. The nCoV\_IP2 primer-probe set was used with Taqman Fast Virus 1-step master mix (Thermo Fisher Scientific) to detect viral RNA. A PCR fragment (nt 12669-14146 of the SARS-CoV-2 genome) generated from viral complementary DNA using the nCoV\_IP2 forward primer and the nCoV\_IP4 reverse primer (nCoV\_IP4-14146Rv CTGGTCAAGGTTAATATAGG) was used to create a standard curve to

## Article

<https://doi.org/10.1038/s41467-023-40556-8>

quantitate the RNA copy numbers. RNA copy numbers were normalized to the weight of tissues used.

**SARS-CoV-2 genome sequencing**

SARS-CoV-2 positive specimens were sequenced using IDT xGen SARS-CoV-2 Amplicon Panel (previously Swift Biosciences SNAP panel), following the manufacturer's protocol. Sequencing reads were processed and analyzed using TAYLOR default settings available at [https://github.com/greninger-lab/covid\\_swift\\_pipeline](https://github.com/greninger-lab/covid_swift_pipeline) (<https://doi.org/10.5281/zenodo.6142073>). Sequencing reads are available in NCBI BioProject under access code [PRJNA894555](https://www.ncbi.nlm.nih.gov/bioproject/PRJNA894555).

**Statistics and reproducibility**

The Microsoft Excel (versions 16.52) and Numbers (version 10.1) software packages were used for data collection. The GraphPad Prism (version 9.4.1) software package was used for data analysis. Reverse transcription RT-qPCR data were collected and analyzed using the QuantStudio Design and Analysis (version 1.5.2; Applied Biosystems) software package. Figures were assembled and generated with Adobe Illustrator (version 27.5). T-tests were used to evaluate statistical significance between experiments with two sets of data. To evaluate statistical significance when more than two groups were compared or datasets contained two independent variables, one- and two-way ANOVAs, respectively, were used with Tukey's, Dunnett's, or Sidak's multiple comparisons post hoc tests as specified in figure legends. Specific statistical tests are specified in the figure legends for individual studies. Supplementary Data 1 summarizes statistical analyses (effect sized, *P* values, and degrees of freedom) of the respective datasets. Effect sizes between groups were calculated as  $\eta^2 = (SS_{\text{effect}})/(SS_{\text{total}})$  for one-way ANOVA and  $\omega^2 = (SS_{\text{effect}} - (df_{\text{effect}})(MS_{\text{error}}))/MS_{\text{error}} + SS_{\text{total}}$  for two-way ANOVA;  $SS_{\text{effect}}$ , sum of squares for the effect;  $SS_{\text{total}}$ , sum of squares for total;  $df_{\text{effect}}$ , degrees of freedom for the effect;  $MS_{\text{error}}$ , mean square error. Effective concentrations for antiviral potency were calculated from dose-response virus yield reduction assay datasets through four-parameter variable slope regression modeling. A biological repeat refers to measurements taken from distinct samples, and the results obtained for each individual biological repeat are either shown in the figures along with the exact size (*n*, number) of biologically independent samples, animals, and independent experiments or results are presented as geometric means  $\pm$  SD along with the exact size (*n*, number) of biologically independent samples represented. The measure of the center (connecting lines and columns) is specified in the figure legends. The statistical significance level ( $\alpha$ ) was set to  $<0.05$  for all experiments. Exact *P* values are shown in Supplementary Data 1 and in individual graphs when possible. Quantitative source data for each biologically independent sample are provided in the Source data file.

**Reporting summary**

Further information on research design is available in the Nature Portfolio Reporting Summary linked to this article.

**Data availability**

The amplicon tiling sequencing reads generated in this study have been deposited in the NCBI BioProject database under accession code [PRJNA894555](https://www.ncbi.nlm.nih.gov/bioproject/PRJNA894555). All other data generated in this study are provided in this article, the supplementary information, supplementary data files, and the Source data file. Source data are provided with this paper.

**Code availability**

Sequencing reads were analyzed using the TAYLOR pipeline (available at [https://github.com/greninger-lab/covid\\_swift\\_pipeline](https://github.com/greninger-lab/covid_swift_pipeline)). All commercial computer codes and algorithms used are specified in "Methods".

**References**

- Garcia-Beltran, W. F. et al. Multiple SARS-CoV-2 variants escape neutralization by vaccine-induced humoral immunity. *Cell* **184**, 2372–2383.e2379 (2021).
- Wang, Z. et al. mRNA vaccine-elicited antibodies to SARS-CoV-2 and circulating variants. *Nature* **592**, 616–622 (2021).
- Zhou, D. et al. Evidence of escape of SARS-CoV-2 variant B.1.351 from natural and vaccine-induced sera. *Cell* **184**, 2348–2361.e2346 (2021).
- Cao, Y. et al. Humoral immune response to circulating SARS-CoV-2 variants elicited by inactivated and RBD-subunit vaccines. *Cell Res.* **31**, 732–741 (2021).
- Tuekprakhon, A. et al. Antibody escape of SARS-CoV-2 Omicron BA.4 and BA.5 from vaccine and BA.1 serum. *Cell* **185**, 2422–2433.e2413 (2022).
- Cavazzoni, P. *Emergency Use Authorization* 108 (2022).
- Cavazzoni, P. *Emergency Use Authorization* 105 (2022).
- Yoon, J. J. et al. Orally efficacious broad-spectrum ribonucleoside analog inhibitor of influenza and respiratory syncytial viruses. *Antimicrob. Agents Chemother.* **62**, 10–1128 (2018).
- Crotty, S., Cameron, C. E. & Andino, R. RNA virus error catastrophe: direct molecular test by using ribavirin. *Proc. Natl Acad. Sci. USA* **98**, 6895–6900 (2001).
- Urakova, N. et al. beta-d-N (4)-hydroxycytidine is a potent anti-alphavirus compound that induces a high level of mutations in the viral genome. *J. Virol.* **92**, 10-1128 (2018).
- Zeldin, R. K. & Petruschke, R. A. Pharmacological and therapeutic properties of ritonavir-boosted protease inhibitor therapy in HIV-infected patients. *J. Antimicrob. Chemother.* **53**, 4–9 (2004).
- Hammond, J. et al. Oral nirmatrelvir for high-risk, nonhospitalized adults with Covid-19. *N. Engl. J. Med.* **386**, 1397–1408 (2022).
- Jayk Bernal, A. et al. Molnupiravir for oral treatment of Covid-19 in nonhospitalized patients. *N. Engl. J. Med.* **386**, 509–520 (2022).
- Zhou, S. et al. beta-d-N4-hydroxycytidine inhibits SARS-CoV-2 through lethal mutagenesis but is also mutagenic to mammalian cells. *J. Infect. Dis.* **224**, 415–419 (2021).
- Merck and Ridgeback Biotherapeutics Provide Update on New Clinical and Non-Clinical Studies of LAGEVRIO™ (molnupiravir). <https://www.merck.com/news/merck-and-ridgeback-biotherapeutics-provide-update-on-new-clinical-and-non-clinical-studies-of-lagevrio-molnupiravir/> (2022).
- Arbel, R. et al. Nirmatrelvir use and severe Covid-19 outcomes during the Omicron surge. *N. Engl. J. Med.* **387**, 790–798 (2022).
- Wong, C. K. H. et al. Real-world effectiveness of early molnupiravir or nirmatrelvir-ritonavir in hospitalised patients with COVID-19 without supplemental oxygen requirement on admission during Hong Kong's omicron BA.2 wave: a retrospective cohort study. *Lancet Infect. Dis.* **22**, 1681–1693 (2022).
- Butler, C. C. et al. Molnupiravir plus usual care versus usual care alone as early treatment for adults with COVID-19 at increased risk of adverse outcomes (PANORAMIC): an open-label, platform-adaptive randomised controlled trial. *Lancet* **401**, 281–293 (2023).
- Arbel, A. et al. Molnupiravir use and severe Covid-19 outcomes during the Omicron surge. *Res. Sq. Preprint* (Version 1) available at Research Square <https://doi.org/10.21203/rs.3.rs-2115769/v1> (2022).
- NCT05047601. A Study of a Potential Oral Treatment to Prevent COVID-19 in Adults Who Are Exposed to Household Member(s) With a Confirmed Symptomatic COVID-19 Infection. <https://clinicaltrials.gov/ct2/show/NCT05047601?term=NCT05047601&draw=2&rank=1> (2022).
- Pfizer. Pfizer Shares Top-Line Results from Phase 2/3 EPIC-PEP Study of PAXLOVID™ for Post-Exposure Prophylactic Use. <https://www.pfizer.com/news/press-release/press-release-detail/pfizer-shares-top-line-results-phase-23-epic-pep-study> (2022).



## Article

<https://doi.org/10.1038/s41467-023-40556-8>

22. Merck Provides Update on Phase 3 MOVE-AHEAD Trial Evaluating LAGEVRIO™ (molnupiravir) for Post-exposure Prophylaxis for Prevention of COVID-19. <https://www.merck.com/news/merck-provides-update-on-phase-3-move-ahead-trial-evaluating-lagevrio-molnupiravir-for-post-exposure-prophylaxis-for-prevention-of-covid-19/> (2023).
23. Anderson, A. S., Caubel, P. & Rusnak, J. M. Nirmatrelvir–ritonavir and viral load rebound in Covid-19. *N. Engl. J. Med.* **387**, 1047–1049 (2022).
24. Charness, M. E. et al. Rebound of SARS-CoV-2 infection after nirmatrelvir-ritonavir treatment. *N. Engl. J. Med.* **387**, 1045–1047 (2022).
25. Wang, L. et al. COVID-19 rebound after Paxlovid and Molnupiravir during January–June 2022. Preprint at *medRxiv* <https://doi.org/10.1101/2022.06.21.22276724> (2022).
26. Oude Munnink, B. B. et al. Transmission of SARS-CoV-2 on mink farms between humans and mink and back to humans. *Science* **371**, 172–177 (2021).
27. Cox, R. M., Wolf, J. D. & Plemper, R. K. Therapeutically administered ribonucleoside analogue MK-4482/EIDD-2801 blocks SARS-CoV-2 transmission in ferrets. *Nat. Microbiol.* **6**, 11–18 (2021).
28. Kim, Y. I. et al. Infection and rapid transmission of SARS-CoV-2 in ferrets. *Cell Host Microbe* **27**, 704–709.e702 (2020).
29. Lieber, C. M. et al. SARS-CoV-2 VOC type and biological sex affect molnupiravir efficacy in severe COVID-19 dwarf hamster model. *Nat. Commun.* **13**, 4416 (2022).
30. Hoffman, R. L. et al. Discovery of ketone-based covalent inhibitors of coronavirus 3CL proteases for the potential therapeutic treatment of COVID-19. *J. Med. Chem.* **63**, 12725–12747 (2020).
31. Owen, D. R. et al. An oral SARS-CoV-2 M(pro) inhibitor clinical candidate for the treatment of COVID-19. *Science* **374**, 1586–1593 (2021).
32. Vangeel, L. et al. Remdesivir, Molnupiravir and Nirmatrelvir remain active against SARS-CoV-2 Omicron and other variants of concern. *Antivir. Res.* **198**, 105252 (2022).
33. Toots, M. et al. Characterization of orally efficacious influenza drug with high resistance barrier in ferrets and human airway epithelia. *Sci. Transl. Med.* **11**, eaax5866 (2019).
34. Singh, R. S. P. et al. Innovative randomized phase I study and dosing regimen selection to accelerate and inform pivotal COVID-19 trial of nirmatrelvir. *Clin. Pharm. Ther.* **112**, 101–111 (2022).
35. Toussi, S. S. et al. Pharmacokinetics of oral nirmatrelvir/ritonavir, a protease inhibitor for treatment of COVID-19, in subjects with renal impairment. *Clin. Pharm. Ther.* **112**, 892–900 (2022).
36. Painter, W. P. et al. Human safety, tolerability, and pharmacokinetics of molnupiravir, a novel broad-spectrum oral antiviral agent with activity against SARS-CoV-2. *Antimicrob. Agents Chemother.* **65**, e02428-20 (2021).
37. Cox, R. M. et al. Oral prodrug of remdesivir parent GS-441524 is efficacious against SARS-CoV-2 in ferrets. *Nat. Commun.* **12**, 6415 (2021).
38. Shi, J. et al. Susceptibility of ferrets, cats, dogs, and other domesticated animals to SARS-coronavirus 2. *Science* **368**, 1016–1020 (2020).
39. Patel, D. R. et al. Transmission and protection against reinfection in the ferret model with the SARS-CoV-2 USA-WA1/2020 reference isolate. *J. Virol.* **95**, e0223220 (2021).
40. Sourimant, J. et al. 4'-Fluorouridine is an oral antiviral that blocks respiratory syncytial virus and SARS-CoV-2 replication. *Science* **375**, 161–167 (2022).
41. Sikkema, R. S. et al. Risks of SARS-CoV-2 transmission between free-ranging animals and captive mink in the Netherlands. *Transbound Emerg. Dis.* **69**, 3339–32349 (2022).
42. Virtanen, J. et al. Experimental infection of mink with SARS-COV-2 Omicron variant and subsequent clinical disease. *Emerg. Infect. Dis.* **28**, 1286–1288 (2022).
43. Heilmann, E. et al. SARS-CoV-2 3CL(pro) mutations selected in a VSV-based system confer resistance to nirmatrelvir, ensitrelvir, and GC376. *Sci. Transl. Med.* **15**, eabq7360 (2022).
44. Hu, Y. et al. Naturally occurring mutations of SARS-CoV-2 main protease confer drug resistance to nirmatrelvir. *ACS Cent. Sci.* <https://doi.org/10.1021/acscentsci.3c00538> (2023).
45. Iketani, S. et al. Multiple pathways for SARS-CoV-2 resistance to nirmatrelvir. *Nature* **613**, 558–564 (2023).
46. Zarebska-Michaluk, D. & Flisiak, R. Early oral antiviral use in patients hospitalised with COVID-19. *Lancet Infect. Dis.* **22**, 1650–1651 (2022).
47. Nair, A. B. & Jacob, S. A simple practice guide for dose conversion between animals and human. *J. Basic Clin. Pharm.* **7**, 27–31 (2016).
48. Wolfel, R. et al. Virological assessment of hospitalized patients with COVID-2019. *Nature* **581**, 465–469 (2020).
49. Fischer, W. A. 2nd et al. A phase 2a clinical trial of molnupiravir in patients with COVID-19 shows accelerated SARS-CoV-2 RNA clearance and elimination of infectious virus. *Sci. Transl. Med.* **14**, eabl7430 (2022).
50. De Giacomo, A. et al. Psychological impact of the SARS-CoV-2 pandemic in children with neurodevelopmental disorders and their families: evaluation before and during covid-19 outbreak among an Italian sample. *Riv. Psichiatr.* **56**, 205–210 (2021).
51. Tang, S., Xiang, M., Cheung, T. & Xiang, Y. T. Mental health and its correlates among children and adolescents during COVID-19 school closure: The importance of parent-child discussion. *J. Affect Disord.* **279**, 353–360 (2021).
52. Wu, C. et al. Analysis of psychological status and effect of psychological intervention in quarantined population during the epidemic of SARS-CoV-2. *Medicine* **100**, e25951 (2021).
53. Panda, P. K. et al. Psychological and behavioral impact of lockdown and quarantine measures for COVID-19 pandemic on children, adolescents and caregivers: a systematic review and meta-analysis. *J. Trop. Pediatr.* **67**, fmaa122 (2021).
54. Chung, P. C. & Chan, T. C. Impact of physical distancing policy on reducing transmission of SARS-CoV-2 globally: perspective from government's response and residents' compliance. *PLoS ONE* **16**, e0255873 (2021).
55. Wilder-Smith, A. What is the vaccine effect on reducing transmission in the context of the SARS-CoV-2 delta variant? *Lancet Infect. Dis.* **22**, 152–153 (2022).

**Acknowledgements**

We thank the Georgia State University Department of Animal Resources and High Containment Core for Assistance and J-J Yoon for technical support. This study was supported, in part, by public health service grants AI141222 (to R.K.P.) and AI171403 project 1 (to R.K.P.) and Scientific Core D (to A.L.G.) from the NIH/NIAID.

**Author contributions**

R.M.C., C.M.L., and R.K.P. conceived and designed the experiments. R.M.C., C.M.L., J.D.W., A.K., and R.K.P. conducted most of the experiments. R.M.C. created all figure schematics. A.L.G., N.A.P.L., and P.R. performed next-generation sequencing. M.K.A., R.E.K., Z.M.S., and A.A.K. performed mass spectrometry analysis. M.G.N. and G.R.P. provided critical materials. R.M.C., C.M.L., N.A.P.L., A.L.G., and R.K.P. analyzed the data. R.M.C. and R.K.P. wrote the manuscript.

**Competing interests**

G.R.P., M.G.N., and A.A.K. receive licensing fees and royalties based on Emory's sublicense of the molnupiravir technology to Ridgeback Biotherapeutics, and a family member of GRP serves as the Chief Medical

**Article**<https://doi.org/10.1038/s41467-023-40556-8>

Officer of Ridgeback. This technology is the subject of the research described in this paper. The terms of this arrangement have been reviewed and approved by Emory University in accordance with its conflict-of-interest policies. R.K.P. reports contract testing from Enanta Pharmaceuticals and Atea Pharmaceuticals, and research support from Gilead Sciences, outside of the described work. R.M.C. reports consulting for Merck & Co, outside of the described work. A.L.G. reports contract testing from Abbott, Cepheid, Novavax, Pfizer, Janssen, and Hologic and research support from Gilead Sciences and Merck, outside of the described work. All other authors declare that they have no competing interests to report.

**Additional information**

**Supplementary information** The online version contains supplementary material available at <https://doi.org/10.1038/s41467-023-40556-8>.

**Correspondence** and requests for materials should be addressed to Richard K. Plemper.

**Peer review information** *Nature Communications* thanks the anonymous reviewer(s) for their contribution to the peer review of this work. A peer review file is available.

**Reprints and permissions information** is available at <http://www.nature.com/reprints>

**Publisher's note** Springer Nature remains neutral with regard to jurisdictional claims in published maps and institutional affiliations.

**Open Access** This article is licensed under a Creative Commons Attribution 4.0 International License, which permits use, sharing, adaptation, distribution and reproduction in any medium or format, as long as you give appropriate credit to the original author(s) and the source, provide a link to the Creative Commons license, and indicate if changes were made. The images or other third party material in this article are included in the article's Creative Commons license, unless indicated otherwise in a credit line to the material. If material is not included in the article's Creative Commons license and your intended use is not permitted by statutory regulation or exceeds the permitted use, you will need to obtain permission directly from the copyright holder. To view a copy of this license, visit <http://creativecommons.org/licenses/by/4.0/>.

© The Author(s) 2023

## 2.1.4 Oral Prodrug of Remdesivir Parent GS-441524 is Efficacious Against SARS-CoV-2 in

### Ferrets



#### ARTICLE



<https://doi.org/10.1038/s41467-021-26760-4>

OPEN

# Oral prodrug of remdesivir parent GS-441524 is efficacious against SARS-CoV-2 in ferrets

Robert M. Cox<sup>1</sup>, Josef D. Wolf<sup>1</sup>, Carolin M. Lieber<sup>1</sup>, Julien Sourimant<sup>1</sup>, Michelle J. Lin<sup>2</sup>, Darius Babusis<sup>3</sup>, Venice DuPont<sup>3</sup>, Julie Chan<sup>3</sup>, Kim T. Barrett<sup>3</sup>, Diane Lye<sup>3</sup>, Rao Kalla<sup>3</sup>, Kwon Chun<sup>3</sup>, Richard L. Mackman<sup>3</sup>, Chengjin Ye<sup>4</sup>, Tomas Cihlar<sup>3</sup>, Luis Martinez-Sobrido<sup>4</sup>, Alexander L. Greninger<sup>2</sup>, John P. Billelo<sup>3</sup> & Richard K. Plemper<sup>1</sup>✉

Remdesivir is an antiviral approved for COVID-19 treatment, but its wider use is limited by intravenous delivery. An orally bioavailable remdesivir analog may boost therapeutic benefit by facilitating early administration to non-hospitalized patients. This study characterizes the anti-SARS-CoV-2 efficacy of GS-621763, an oral prodrug of remdesivir parent nucleoside GS-441524. Both GS-621763 and GS-441524 inhibit SARS-CoV-2, including variants of concern (VOC) in cell culture and human airway epithelium organoids. Oral GS-621763 is efficiently converted to plasma metabolite GS-441524, and in lungs to the triphosphate metabolite identical to that generated by remdesivir, demonstrating a consistent mechanism of activity. Twice-daily oral administration of 10 mg/kg GS-621763 reduces SARS-CoV-2 burden to near-undetectable levels in ferrets. When dosed therapeutically against VOC P.1 gamma  $\gamma$ , oral GS-621763 blocks virus replication and prevents transmission to untreated contact animals. These results demonstrate therapeutic efficacy of a much-needed orally bioavailable analog of remdesivir in a relevant animal model of SARS-CoV-2 infection.

<sup>1</sup>Center for Translational Antiviral Research, Institute for Biomedical Sciences, Georgia State University, Atlanta, GA, USA. <sup>2</sup>Virology Division, Department of Laboratory Medicine and Pathology, University of Washington, Seattle, WA, USA. <sup>3</sup>Gilead Sciences Inc, Foster City, CA, USA. <sup>4</sup>Texas Biomedical Research Institute, San Antonio, TX, USA. ✉email: [rplemper@gsu.edu](mailto:rplemper@gsu.edu)

## ARTICLE

NATURE COMMUNICATIONS | <https://doi.org/10.1038/s41467-021-26760-4>

The global COVID-19 pandemic has resulted in far more than 150 million cases and an estimated 3.5 million deaths.

The socioeconomic and geopolitical impact of the pandemic is unprecedented and will most likely become fully evident only in postpandemic years. To date, remdesivir is the only small molecule antiviral therapeutic approved by the FDA for the treatment of COVID-19<sup>1</sup>. Originally discovered for respiratory syncytial virus<sup>2</sup>, remdesivir is a mono-phosphoramidate prodrug of a ribonucleoside analog that must be administered intravenously<sup>3</sup>. The obligatory parenteral delivery limits access of COVID-19 outpatients to remdesivir treatment, thereby narrowing the therapeutic window in which a direct-acting antiviral targeting an acute viral infection is expected to have its greatest effect<sup>4</sup>.

Orally active COVID-19 therapeutics have the potential to maximize patient benefit and ideally prevent progression to severe disease. Several oral therapeutic candidates such as EIDD-2801/molnupiravir<sup>5–7</sup> and AT-527<sup>8</sup> are in advanced stages of clinical trials, but currently, only remdesivir has shown confirmed efficacy for COVID-19 treatment in humans<sup>9</sup>. Following intravenous administration and despite its short plasma half-life, remdesivir is sufficiently stable in non-rodent species to distribute to tissues, such as the lung, where it is rapidly converted to its monophosphate metabolite and then efficiently anabolized to the bioactive triphosphate GS-443902 (Fig. 1a)<sup>2,10,11</sup>. An alternative strategy to generate GS-443902 could be to directly administer the remdesivir parent nucleoside GS-441524, but due to less efficient metabolism of GS-441524 to its monophosphate, higher daily systemic exposures of GS-441524 than those obtained from intravenous remdesivir are required to generate equivalent concentrations of GS-443902 in lung tissue. In addition, GS-441524 has displayed poor oral bioavailability in several species<sup>2,12,13</sup>. In order to obtain high exposures after oral delivery, a prodrug strategy to improve oral absorption was employed leading to the identification of GS-621763, which demonstrated high oral bioavailability in two relevant animal species including non-human primates<sup>2</sup>.

SARS-CoV-2 efficiently infects mustelids such as ferrets and mink, and both the direct and reverse zoonotic transmission between mink and humans have been reported<sup>14,15</sup>. Infected ferrets show only mild clinical signs, but the virus readily replicates in the upper respiratory tract and shed virus load in nasal lavages is high, supporting efficient animal-to-animal transmission<sup>6</sup>. Consequently, ferrets recapitulate the presentation of SARS-CoV-2 in the majority of human cases, especially in children and younger adults<sup>16,17</sup>.

In this study, we used the ferret model to test the oral anti-SARS-CoV-2 efficacy of GS-621763. The GS-621763 prodrug is presystemically hydrolyzed to afford high systemic exposures of GS-441524 (Fig. 1a). Having determined the plasma pharmacokinetic (PK) profile following oral administration of GS-621763 in ferrets, we examined the effect of oral GS-621763 administered therapeutically against the original SARS-CoV-2 USA-WA1/2020 (WA1/2020) strain and the recently emerged, highly prevalent VOC P.1 (γ) lineage<sup>18,19</sup>.

## Results

Prior to in vivo testing, we assessed antiviral potency of both GS-621763 and its metabolite GS-441524 against lineage A isolate WA1/2020 and three recently emerged VOC, hCoV-19/USA/CA\_UCSD\_5574/2020 ((α), lineage B.1.1.7; CA/2020), hCoV-19-South Africa/KRISP-K005325/2020 ((β), lineage B.1.351; SA/2020), and hCoV-19/Japan/TY7-503/2021 ((γ), lineage P.1; BZ/2021) in cultured cells.

**Antiviral activity against VoCs.** Half-maximal effective concentrations (EC<sub>50</sub>) in SARS-CoV-2-infected Vero E6 cells were

highly consistent, ranging from 0.11 to 0.73 μM for GS-621763 (Fig. 1b, Supplementary Table 1) and from 0.11 to 0.68 μM for GS-441524 (Fig. 1c, Supplementary Table 1). Analogous potency ranges were obtained when luciferase-expressing WA1/2020 reporter viruses were examined in dose-response assays in A549 cells stably expressing human ACE2 (A549-hACE2) (Supplementary Table 1)<sup>20</sup>. Toxicity-testing of GS-621763, remdesivir, and GS-441524 in different cell lines and primary human cells derived from different donors revealed half-maximal cytotoxic concentrations (CC<sub>50</sub>) of 40 to >100 μM (Fig. 1d, Supplementary Table 1), 36 to >100 μM (Supplementary Fig. 1, Supplementary Table 1) and >100 μM (Fig. 1e, Supplementary Table 1), respectively, corresponding to selectivity indices (SI = CC<sub>50</sub>/EC<sub>50</sub>) of GS-621763 > 137 in VeroE6 and >51 in A549-ACE2 cells. The efficacy of GS-441524 and GS-621763 was in parallel assessed on well-differentiated primary human airway epithelium cultures grown at the air-liquid interface and apically infected with VOC γ (Fig. 1f–g). Basolaterally added GS-441524 or GS-621763 displayed similar potency in this disease-relevant human tissue model, returning EC<sub>50</sub> values of 2.83 and 3.01 μM, respectively. Parallel measurement of transepithelial electrical resistance demonstrated that epithelium integrity was fully preserved at basolateral drug concentrations ≥3 μM.

**Pharmacokinetics following oral administration.** Assessment of GS-621763 plasma PK parameters in the ferret revealed excellent oral bioavailability (Fig. 2a), extensive cleavage presystemically to generate high exposures of GS-441524 in the blood (Supplementary Table 2), efficient distribution to soft tissues of the respiratory system (lung), and confirmed anabolism to bioactive GS-443902 (Supplementary Table 3). Following a single 30 mg/kg oral dose of GS-621763 in ferrets, the daily systemic exposure (AUC<sub>0–24h</sub>) of GS-441524 was 81 μM.h, 4.5 fold higher than the exposure following IV remdesivir at 10 mg/kg and approximately 10-fold greater than that observed following a 200/100 mg IV remdesivir dose in human<sup>21</sup>. Lower levels of bioactive GS-443902 were formed from oral 30 mg/kg GS-621763 dosing compared to 10 mg/kg IV remdesivir (Supplementary Table 3), illustrating the difference in intracellular activation efficiency of the phosphoramidate prodrug remdesivir compared to systemic parent nucleoside GS-441524.

**Prophylactic efficacy in ferrets.** To test antiviral efficacy, we infected ferrets intranasally with 1 × 10<sup>5</sup> plaque-forming units (pfu) of WA1/2020, followed by twice daily (b.i.d.) oral treatment with GS-621763 at 20 mg/kg body weight for four days (Fig. 2b). Treatment was initiated at the time of infection, nasal lavages collected in 12-h intervals, and respiratory tissues harvested 4 days after infection. Shed SARS-CoV-2 load in nasal lavages of vehicle-treated animals reached plateau 1.5 days after infection at approximately 1 × 10<sup>4</sup> pfu/mL, whereas virus was transiently detectable in lavages of only one ferret of the GS-621763-treatment group at 12 h after infection (Fig. 2c). Clinical signs overall are minor in the ferret model<sup>6</sup>. However, only animals of the vehicle group showed elevated body temperature (Fig. 2d) and reduced weight gain (Fig. 2e). The virus was undetectable in the nasal turbinates extracted from treated animals 4 days after infection, compared to a robust load of approximately 5 × 10<sup>4</sup> pfu/g nasal turbinate of animals of the vehicle group (Fig. 2f). Viral RNA copy numbers found in lavages (Fig. 2g) and turbinates (Fig. 2h) mirrored the infectious titer results, revealing a consistent, statistically significant difference between the vehicle and treatment groups of two and three orders of magnitude, respectively. Consistent with prior studies<sup>6</sup>, no infectious virions or viral RNA were detectable in the lower respiratory tract (Fig. 2i, j).

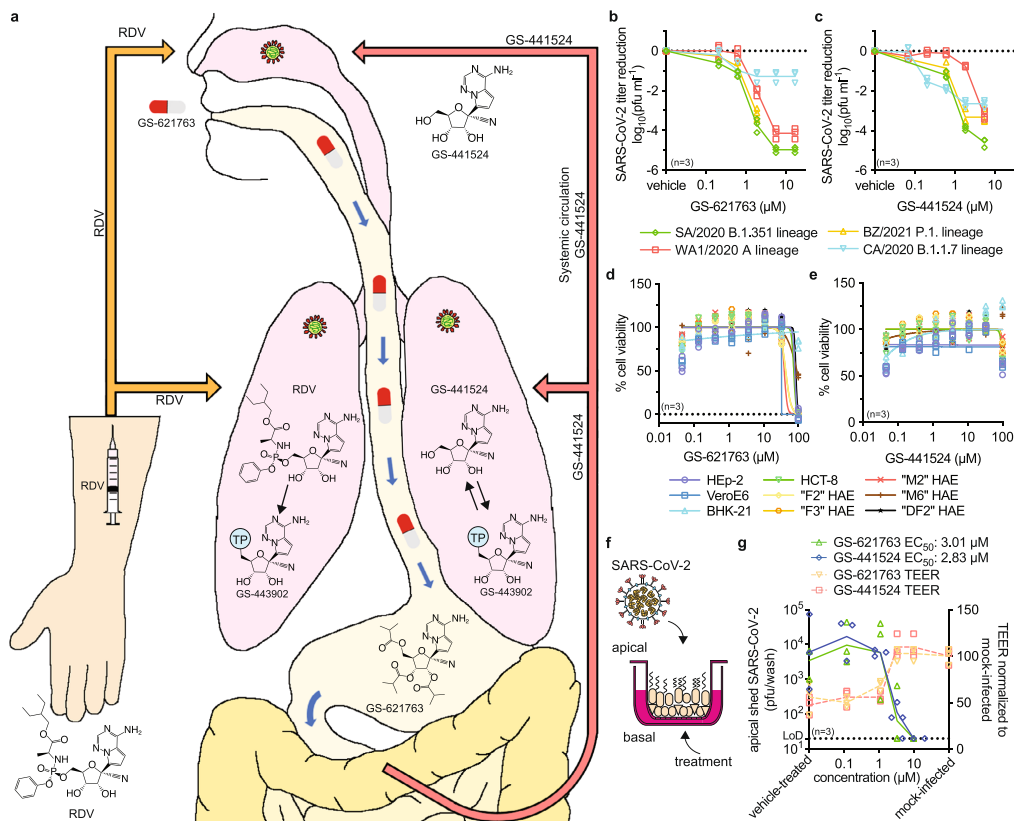


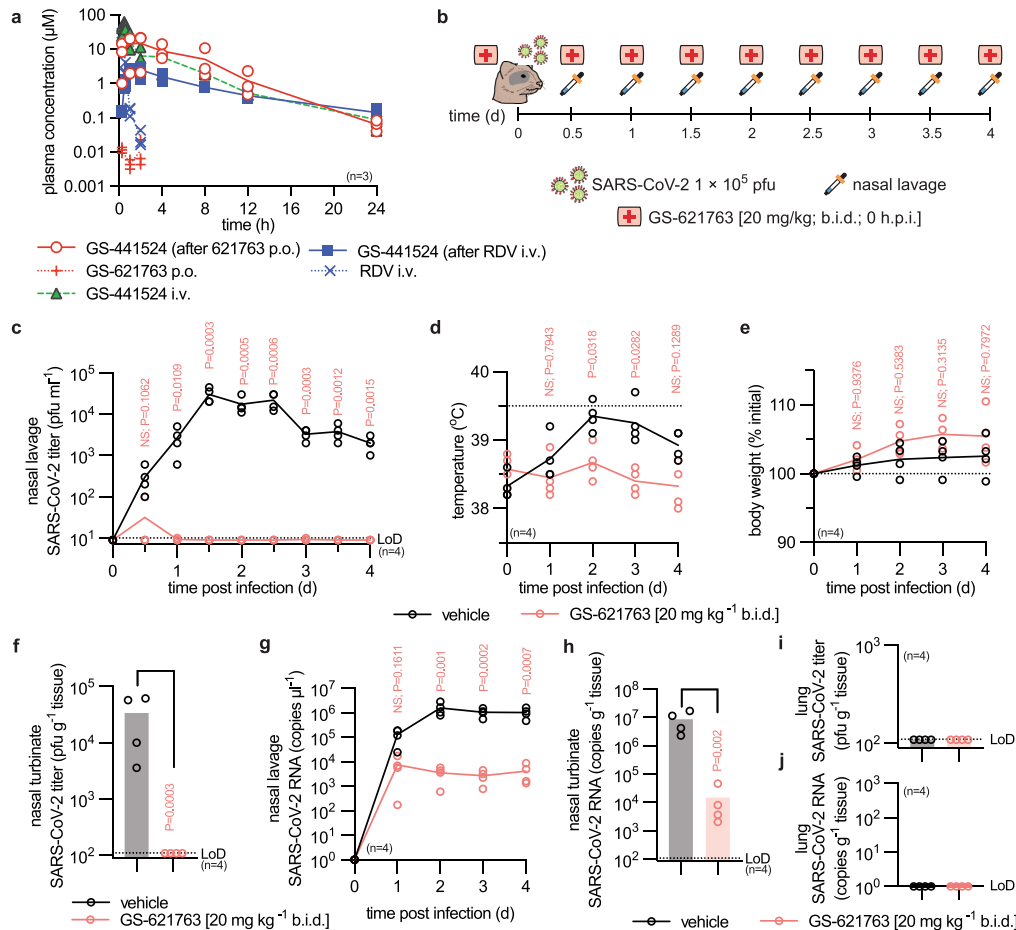
**Fig. 1** Antiviral potency of remdesivir analog GS-621763. **a** Schematic depicting metabolism of remdesivir (RDV; orange arrows) and GS-621763 (red/white pills; red arrows) after injection or oral uptake, respectively. Remdesivir distributes into tissues (e.g., lung) and is efficiently metabolized intracellularly to GS-443902 (TP = triphosphate). Conversely, GS-441524 is the dominant plasma metabolite after intestinal absorption of orally administered GS-621763 and is subsequently analogized to GS-443902 in the tissues. **b–c** Virus yield reduction of SARS-CoV-2 clinical isolates WA1/2020 (red squares), CA/2020 (blue triangles), SA/2020 (green diamonds), and BZ/2021 (yellow triangles) representing the A, B.1.1.7 (α), B.1.351 (β) and P.1 (γ) lineages, respectively, by GS-621763 (**b**) and GS-441524 (**c**) on VeroE6 cells. EC<sub>50</sub> concentrations are specified in Supplementary Table 1. **d–e** In vitro cytotoxicity profiles of GS-621763 (**d**) and GS-441524 (**e**) on VeroE6 (blue squares), HEp-2 (purple circles), BHK-21 (light blue triangles), HCT-8 (green triangles) and a panel of primary HAE cells from independent donors ("F2" (yellow diamonds), "F3" (orange circles), "M2" (red "+" symbols), "M6" (brown "+" symbols), "DF2" (black stars)). **f** schematic of well-differentiated air-liquid interface HAE cultures. **g** HAEs were infected from the apical side with SARS-CoV-2 VOC γ and treated from the basolateral side with GS-621763 or GS-441524. Apically shed virus titers (green triangles and blue diamonds for GS-621763 or GS-441524, respectively) on day after infection and the impact of treatment on preserving tissue integrity (transepithelial electrical resistance (TEER) (orange triangles and red squares for GS-621763 or GS-441524, respectively)) are shown. LoD, the limit of detection. In (**b–e**, **g**), symbols represent individual biological repeats ( $n = 3$ ), lines (**b–c**, **g**) intersect the mean, lines in (**d–e**) depict nonlinear regression models.

**Therapeutic efficacy and lowest efficacious dose.** To determine the lowest efficacious dose in a clinically more relevant therapeutic setting, we initiated oral treatment 12 h after infection, when the shed virus is first detectable in nasal lavages, at the 10 mg/kg and 3 mg/kg body weight levels, administered b.i.d. (Fig. 3a). EIDD-2801/molnupiravir at 5 mg/kg b.i.d. was given as reference following an identical therapeutic b.i.d. regimen<sup>6</sup>. EIDD-2801 was included as a reference compound, since at the time of study EIDD-2801 was the only nucleoside analog with demonstrated oral efficacy against SARS-CoV-2 in the ferret model. Shed virus load was significantly lower in all treated animals than in the vehicle group within 12 h of treatment onset (Fig. 3b). Virus load in nasal lavages of ferrets receiving GS-

621763 at 3 mg/kg plateaued approximately one order of magnitude lower than in those from vehicle animals, while treatment with GS-621763 at 10 mg/kg or EIDD-2801/molnupiravir reduced shedding to near-detection level by day 3 after infection. Consistent with this inhibitory effect, treatment with 3 mg/kg GS-621763 reduced burden in the turbinates by one order of magnitude (Fig. 3c), while virus burden approached the limit of detection in animals of the 10 mg/kg GS-621763 and EIDD-2801/molnupiravir treatment groups. No significant differences in clinical signs were noted between vehicle animals and any of the treatment groups (Fig. 3d, e).

Viral RNA was detectable in nasal lavages and turbinates of all animals, underscoring efficient infection. However, RNA copies

## ARTICLE

NATURE COMMUNICATIONS | <https://doi.org/10.1038/s41467-021-26760-4>

**Fig. 2 Prophylactic efficacy of GS-621763.** **a** Single-dose PK study in ferrets showing plasma concentrations of GS-441524, GS-621763, and remdesivir (RDV) as specified after dosing with GS-621763 (30 mg/kg; p.o.; red “+” symbols), remdesivir (10 mg/kg; i.v.; blue “x” symbols), and GS-441524 (20 mg/kg; i.v.; green triangles). Symbols represent individual biological repeats ( $n = 3$ ), lines depict sample means. **b** Schematic of the prophylactic efficacy study design. Ferrets were infected intranasally with  $1 \times 10^5$  pfu WA1/2020 (virus symbol). Groups ( $n = 4$ ) were gavaged b.i.d. (first aid symbol) with vehicle or GS-621763 (20 mg/kg) starting at the time of infection. Nasal lavages (pipet symbol) were harvested twice daily. All animals were terminated 4 days after infection. **c** Virus titers from nasal lavages; LoD, limit of detection. **d** Temperature measurements collected once daily. **e** Body weight measured once daily. **f** Infectious titers of SARS-CoV-2 in nasal turbinates harvested four days after infection. **g** SARS-CoV-2 RNA copies present in nasal lavages. **h** SARS-CoV-2 RNA copies detected in nasal turbinates. **i–j** SARS-CoV-2 infectious particles (i) and SARS-CoV-2 RNA copies (j) in lungs four days after infection. Symbols for vehicle-treated and GS-621763 treated ferrets are shown as black and red circles, respectively (**c–j**). The number of independent biological repeats (individual animals) is shown in each subpanel, symbols represent independent biological repeats, lines (**c–e, g**) and bar graphs (**f, h–j**) connect or show samples mean, respectively, and *P* values are stated. 2-way ANOVA with Sidak’s post hoc multiple comparison tests (**c–e, g**) or two-tailed *t* test (**f, h**).

showed a statistically significant mean reduction in the 10 mg/kg GS-621763 and EIDD-2801/molnupiravir groups compared to vehicle (Fig. 3f, g). These results confirm the oral efficacy of therapeutic GS-621763 against WA1/2020 in a relevant animal model of upper respiratory infection.

**Inhibition of replication and transmission of VOC  $\gamma$ .** To probe the anti-SARS-CoV-2 indication spectrum of GS-621763, we applied the efficacious regimen, 10 mg/kg GS-621763 b.i.d. started 12 h after infection, to recently emerged VOC  $\gamma^{22}$  in a combined

efficacy and transmission study (Fig. 4a). After an initial replication delay, the shed virus became detectable in vehicle-treated animals 1.5 days after infection, then rapidly reached a robust plateau of nearly  $10^4$  pfu/mL nasal lavage on day 2 after infection (Fig. 4b). Quantitation of viral RNA copies mimicked the profile of the infectious titers, although a low viral RNA load was present in lavages already on the first day after infection (Fig. 4c). Viral titers and RNA copies in nasal turbinates determined 4 days after infection were likewise high, ranging from  $10^4$  to  $10^5$  pfu/g tissue (Fig. 4d) and  $10^8$  to  $10^{10}$  RNA copies/g tissue (Fig. 4e), respectively. However, no infectious VOC  $\gamma$  virions or viral RNA were



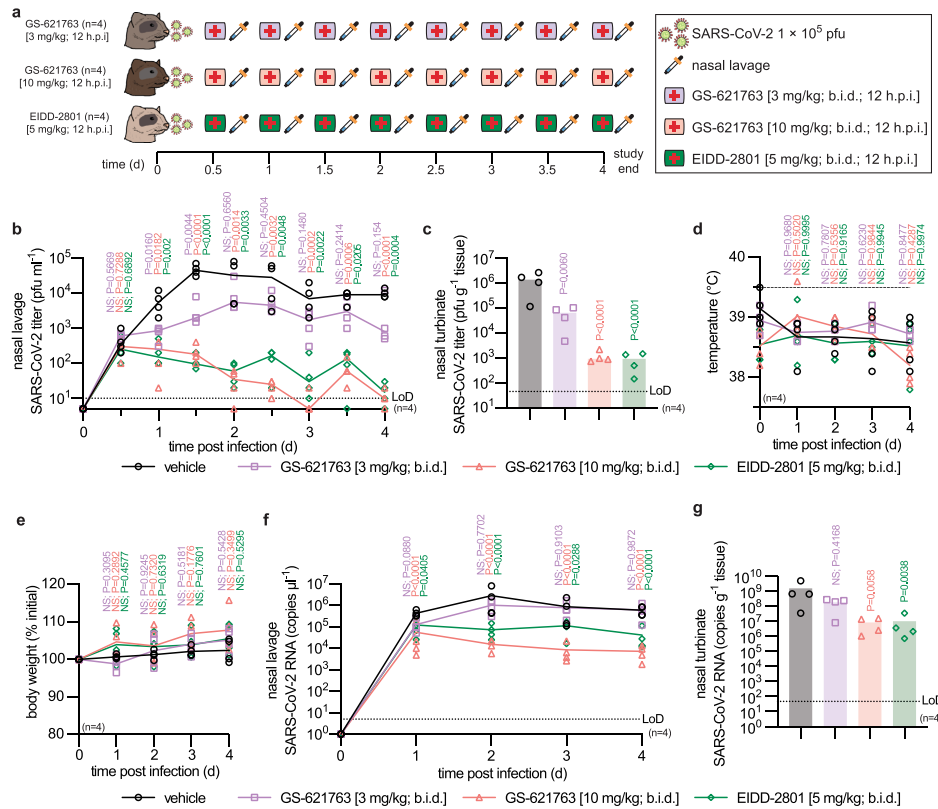


**Fig. 3 Therapeutic efficacy of GS-621763.** **a** Schematic of the therapeutic efficacy study design. Ferrets were infected intranasally with  $1 \times 10^5$  pfu WA1/2020. Symbols as described for Fig. 2a. Starting 12 h after infection, groups of ferrets ( $n = 4$ ) were gavaged b.i.d. with vehicle (black circles in b–g), GS-621763 (3 mg/kg (purple first aid symbol; purple circles in b–g)) or 10 mg/kg (pink first aid symbol; red circles in b–g)), or treated with EIDD-2801 (5 mg/kg (green first aid symbol; green diamonds in b–g)). Nasal lavages were harvested twice daily. Animals were terminated 4 days after infection. **b** Virus titers from nasal lavages. **c** Infectious titers of SARS-CoV-2 in nasal turbinates harvested four days after infection. **d** Temperature measurements collected once daily. **e** Body weight measured once daily. **f** SARS-CoV-2 RNA copies present in nasal lavages. **g** SARS-CoV-2 RNA copies detected in nasal turbinates. The number of independent biological repeats (individual animals) is shown in each subpanel. Symbols represent independent biological repeats, lines (**b**, **d**, **e**, **f**) and bar graphs (**c**, **g**) connect or show samples mean, respectively, and *P* values are stated. 1-way (**c**, **g**) or 2-way (**b**, **d**, **e**, **f**) ANOVA with Dunnett’s post hoc multiple comparison tests. LoD limit of detection.

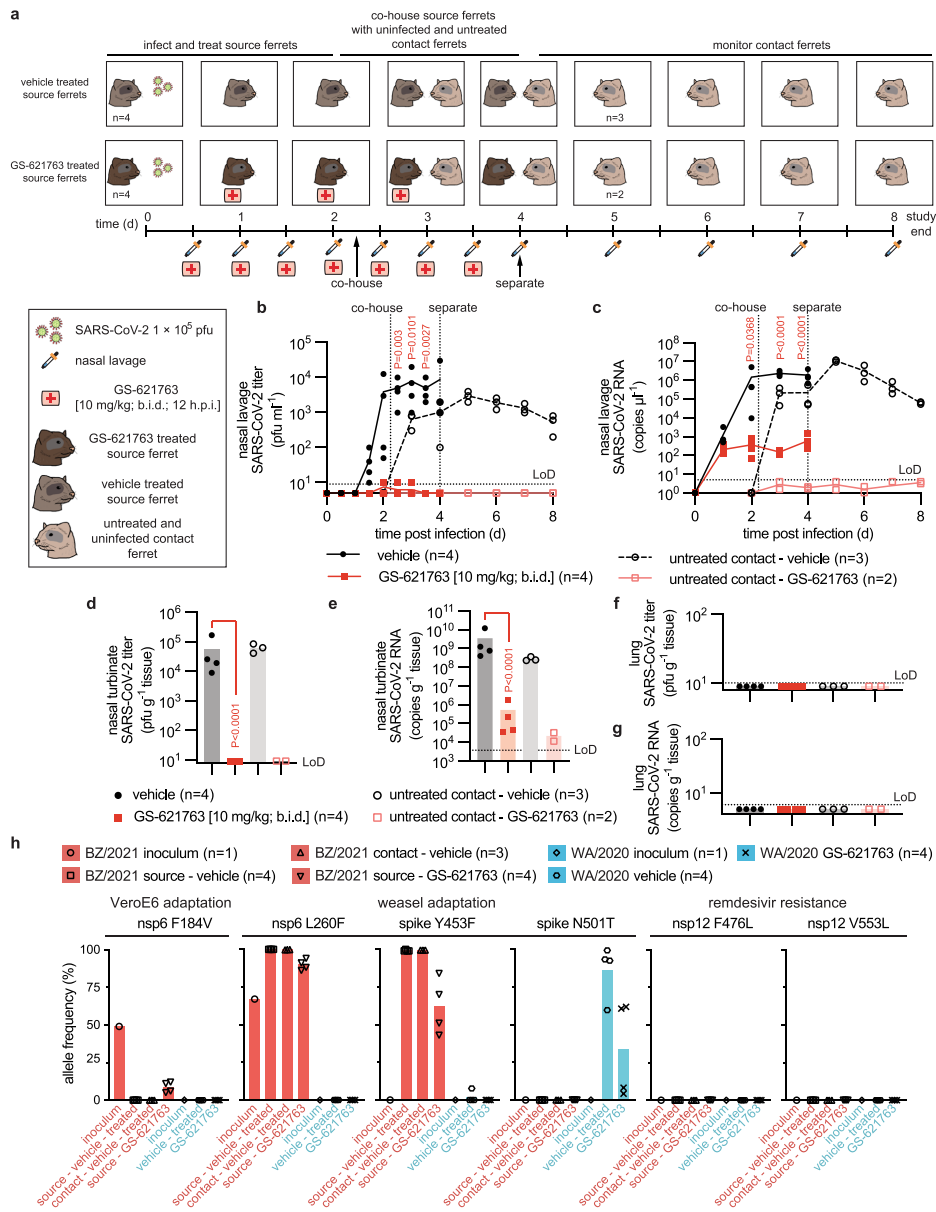
detected in the lungs of any of these animals (Fig. 4f, g), and no clinical signs such as changes in body weight or fever emerged (Supplementary Fig. 2a, b). This presentation mimicked our previous experience with WA1/2020<sup>6</sup>, indicating that VOC  $\gamma$  does not invade the ferret host more aggressively than WA1/2020. Treatment of VOC  $\gamma$  infection with oral GS-621763 was highly efficacious, reducing both shed virus burden and tissue titers to undetectable levels (Fig. 4b, d) and lowering viral RNA copies in nasal lavages and turbinates by over three orders of magnitude (Fig. 4c, e).

Whole genome sequencing of the virus inoculum and virus populations extracted from nasal turbinates confirmed the presence of mutations characteristic for the P.1 VOC<sup>23</sup> (Fig. 4h, Supplementary Dataset 1). In addition, we noted an L260F substitution in nsp6 associated with SARS-CoV-2 adaptation to weasels<sup>14</sup> that had a 60%-allele frequency in the VOC  $\gamma$  inoculum. Four days after infection of ferrets, this mutation had become fully dominant and a second characteristic weasel

mutation, Y453F in the spike protein that was first noted in several clusters of SARS-CoV-2 outbreaks in mink farms<sup>14</sup>, had emerged in addition (Fig. 4h, Supplementary Dataset 1). We furthermore noted the presence of an F184V exchange in nsp6 of the VOC  $\gamma$  inoculum, which arose during amplification in VeroE6 cells<sup>23</sup> and was rapidly counterselected against in the ferret host. In contrast, the WA1/2020 inoculum used for our ferret studies did not contain any unreported additional changes (Fig. 4h, Supplementary Dataset 2). WA1/2020 also acquired a weasel-characteristic mutation when passed through ferrets, N501T in the receptor binding domain of the spike protein<sup>14</sup>, but no changes in nsp6 were detected and only one animal harbored a virus population with Y453F substitution in low (8%) allele frequency. Neither the GS-621763-experienced VOC  $\gamma$  nor WA1/2020 populations contained remdesivir resistance mutations previously selected in SARS-CoV-2 (i.e., E802D in nsp12<sup>24</sup>) or the related mouse hepatitis virus<sup>25</sup> (i.e., F476L and V553L in nsp12) nor did any new variants arise in nsp12 at >5% allele

ARTICLE

NATURE COMMUNICATIONS | <https://doi.org/10.1038/s41467-021-26760-4>



frequency, when viruses were extracted from treated animals at the time of termination (Fig. 4h, Supplementary Datasets 1, 2).

All vehicle-treated animals efficiently transmitted VOC  $\gamma$  to untreated direct-contact ferrets (Fig. 4b–e). Co-housing was started 54 h after infection and continued until termination of the source animals. Shed VOC  $\gamma$  replicated in the contacts without delay, becoming first detectable in nasal lavages within 12 h after initiation of co-housing. This altered replication profile corroborated VOC  $\gamma$  adaptation to the ferret host in the source animals,

and virus populations recovered from contacts of vehicle-treated source animals indeed contained both the L260F exchange in nsp6 and the Y453F mutation in spike (Fig. 4h, Supplementary Dataset 1). Consistent with efficient inhibition of VOC  $\gamma$  replication in the treated source animals by oral GS-621763, treatment completely blocked virus transmission to untreated direct-contact animals. None of the contacts of treated source ferrets shed infectious particles or viral RNA at any time (Fig. 4b, c), infectious viral particles were absent from nasal turbinates 5.5 days after initiation



**Fig. 4 GS-621763 blocks replication and transmission of SARS-CoV-2 VOC  $\gamma$**  **a**, Schematic of the efficacy and contact transmission study design. All ferrets were infected intranasally with  $1 \times 10^5$  pfu BZ/2021 (virus symbol). Symbols as described for Fig. 2a. Groups of ferrets ( $n = 4$ ) were gavaged b.i.d. with vehicle (black circles in **b-g**) or GS-621763 (10 mg/kg; red squares in **b-g**) starting at 12 h after infection. Nasal lavages were harvested twice daily. On the second day after infection, vehicle and GS-621763 ferrets were cohoused with untreated contact ferrets (black open circles and red open squares for vehicle and GS-621763 contact ferrets, respectively). Source ferrets were terminated 4 days after infection and all contact animals were terminated on study day 8. **b** Virus titers from nasal lavages. **c**, SARS-CoV-2 RNA copies present in nasal lavages. **d** Infectious titers of SARS-CoV-2 in nasal turbinates harvested four days after infection. **e** SARS-CoV-2 RNA copies detected in nasal turbinates. **f** Infectious titers of SARS-CoV-2 in lung tissue. **g** SARS-CoV-2 RNA copies present in lung tissue. In (**b-g**), the number of independent biological repeats (individual animals) is shown in each subpanel. Symbols represent independent biological repeats, lines (**b, c**) and bar graphs (**d-g**) connect or show sample means, respectively, and *P* values are stated. 1-way (**d, e**) or 2-way (**b, c**) ANOVA with Tukey's (**d, e**) or Sidak's (**b, c**) post hoc multiple comparison tests. **h**, Metagenome sequence analysis of inoculum WA1/2020 (blue bar; black diamonds;  $n = 1$ ) and BZ/2021 (red bar; black circles;  $n = 1$ ) viruses, BZ/2021 RNA extracted from ferret nasal turbinates four days after infection (red bars; black squares and downward pointing triangles for vehicle ( $n = 4$ ) and GS-621763 treated ( $n = 4$ ) ferrets, respectively), WA1/202 RNA extracted from ferret nasal turbinates four days after infection (blue bars; black hexagons and "x" symbols for vehicle ( $n = 4$ ) and GS-621763 treated ( $n = 4$ ) ferrets, respectively) and BZ/2021 populations extracted from nasal lavages of contacts of vehicle-treated source animals (red bars; black upward pointing triangles;  $n = 3$ ). Relative allele frequencies of signature residues are shown. Symbols represent independent biological repeats (virus population of individual animals), columns show group means. LoD limit of detection.

of co-housing (Fig. 4d), and only a low level of viral RNA ( $<10^5$  copies/g nasal turbinate) was detected in nasal turbinates of the contact animals (Fig. 4e).

### Discussion

This study demonstrates oral efficacy of the remdesivir analog GS-621763 against the early clinical SARS-CoV-2 isolate WA1/2020 and one of the recently emerged VOC in the ferret model. After oral administration of GS-621763, only low systemic levels of intact prodrug were transiently observed. The parent nucleoside GS-441524 was the major metabolite detected in blood, more than three orders of magnitude higher than intact prodrug, indicating efficient conversion upon intestinal absorption. GS-441524 metabolism inside cells to the same intracellular bioactive triphosphate GS-443902 in tissues links GS-621763 to the well-understood mechanism of action of remdesivir, which blocks SARS-CoV-2 replication by triggering delayed chain termination of the nascent viral RNA chain<sup>26</sup> and/or template-dependent inhibition after incorporation into viral antigenomic RNA<sup>27</sup>. Systemic GS-441524 is less efficient at forming the bioactive GS-443902 in the lungs of ferrets compared to systemic remdesivir, but the exposure of GS-441524 achieved following oral dosing of GS-621763 is sufficient to overcome this difference and generate substantial levels of bioactive GS-443902. The more persistent but lower plasma levels of GS-441524 following intravenous remdesivir are a result of efficient formation of triphosphate in tissues from remdesivir, followed by slow dephosphorylation to GS-441524, which then appears in plasma, as evidenced by its similar half-life with that of the triphosphate GS-443902 in PBMC<sup>21</sup>.

Although GS-443902 levels in ferret respiratory tissues after a single 30 mg/kg oral dose of GS-621763 trailed those of intravenous 10 mg/kg remdesivir by approximately fourfold at 24 h, a minimal daily oral dose of 20 mg/kg GS-621763 (10 mg/kg b.i.d.) provided full therapeutic benefit, rapidly reducing shed virus titers to near-undetectable. However, as the GS-443902 active metabolite is quantitated from gross tissue samples, we cannot compare GS-443902 levels resulting from either GS-621763 or remdesivir dosing in distinct respiratory cell types. If human oral bioavailability of GS-621763 is consistent with that observed in ferrets, and the model is predictive of antiviral potential, the dose levels identified in the ferret study as fully efficacious in upper respiratory tract correspond to a feasible human daily dose of approximately 250 mg oral GS-621763.

An observed difference of approximately two to three orders of magnitude between the infectious titers and viral RNA copy numbers in the ferrets closely resembled that described in earlier reports<sup>6,28,29</sup>, demonstrating high reproducibility of the model.

At present, the correlation between upper respiratory tract SARS-CoV-2 load at early stages after human infection and the likelihood of progression to viral pneumonia and severe COVID-19 has not been fully understood. However, clinical studies have linked higher upper respiratory virus burden to a heightened patient risk of developing severe COVID-19, requiring intubation or intensive care, and having an unfavorable outcome<sup>30</sup>. Based on these clinical data and the rapid reduction of upper respiratory virus burden seen in the ferret model, we expect that early initiation of oral treatment, ideally immediately following a positive diagnostic test and before the onset of clinical signs<sup>31,32</sup>, holds high promise to block viral invasion of the lower respiratory tract and viral pneumonia that necessitates hospitalization.

Recently emerged SARS-CoV-2 variants such as VOC  $\gamma$  are a major concern because of their high prevalence and increased frequency of transmission<sup>18,33</sup>. Ferrets infected with VOC  $\gamma$  did not develop more severe clinical signs than after infection with WA1/2020 and the virus did not advance to the lower respiratory tract, indicating that pathogenicity of this VOC is not fundamentally different from that of WA1/2020 in this model. Peak viral burden and shed virus loads of VOC  $\gamma$ -infected ferrets were equivalent to those of WA1/2020. Reflecting that analysis of circulating SARS-CoV-2 VOC worldwide has yielded no evidence of widespread transmission of remdesivir-resistant strains<sup>24,25,34</sup>, GS-621763 and its metabolite GS-441524 were comparably potent against VOC  $\alpha$ ,  $\beta$ , and  $\gamma$  as against WA1/2020 in cell culture. Importantly, oral GS-621763 was highly efficacious against VOC  $\gamma$  in vivo, reducing infectious titers to near-undetectable levels rapidly after treatment initiation. Whole genome sequencing of GS-621763-experienced viruses recovered from treated ferrets likewise revealed no allele variations in candidate remdesivir resistance sites, indicating that SARS-CoV-2 does not rapidly escape from inhibition by GS-621763 in vivo.

Based on the high transmissibility of VOC  $\gamma$  in the field and very efficient direct-contact transmission of SARS-CoV-2 between ferrets<sup>35</sup>, we assessed the impact of oral GS-621763 on VOC  $\gamma$  spread among ferrets. To recapitulate what we consider a realistic scenario for exploring pharmacological interference in community transmission, we therapeutically treated the infected source animals but left their contacts untreated. In this relevant experimental setting, treatment with the same GS-621763 dose of 10 mg/kg b.i.d. completely blocked transmission of VOC  $\gamma$ , resembling the performance of oral EIDD-2801/molnupiravir in the model<sup>6</sup>.

These results build confidence that a new generation of orally available broad-spectrum antivirals is emerging that should allow initiation of treatment early after infection and promise to

## ARTICLE

NATURE COMMUNICATIONS | <https://doi.org/10.1038/s41467-021-26760-4>

efficiently interrupt community transmission chains. In addition to immediately contributing to ending the COVID-19 pandemic and containing the continued evolution of increasingly contagious SARS-CoV-2 VOC<sup>36–38</sup>, an oral analog of the broad-spectrum antiviral drug remdesivir with confirmed *in vivo* efficacy may become a cornerstone in the first-line defense against future pandemic threats.

**Methods**

**Study design.** Ferrets (*Mustela putorius furo*) were used as an *in vivo* model to determine efficacy of the orally available remdesivir analog GS-621763 against SARS-CoV-2 infection and transmission to untreated and uninfected contact animals. Oral bioavailability and pharmacokinetic properties of GS-621763 in ferrets were assessed prior to infecting any animals with SARS-CoV-2. For efficacy and transmission studies, anesthetized ferrets were inoculated intranasally with SARS-CoV-2. Nasal lavages were performed periodically at predefined time points to measure virus load. Temperature and body weight were measured once daily for all animals. At four days after infection (study day 8 for contact ferrets), animals were euthanized and nasal turbinates extracted to measure virus load in the upper respiratory tract. SARS-CoV-2 titers were determined by plaque assay and viral RNA copies quantified by RT-qPCR.

**Cells and viruses.** African green monkey kidney VeroE6 (ATCC<sup>®</sup>, cat# CRL-1586<sup>™</sup>), human lung adenocarcinoma epithelial Calu-3 (ATCC<sup>®</sup> HTB-55<sup>™</sup>), human epithelial/HeLa contaminant HEp-2 (ATCC<sup>®</sup>, cat# CCL-23<sup>™</sup>), and baby hamster kidney BHK-21 (ATCC<sup>®</sup>, cat# CCL-10<sup>™</sup>) cells were cultivated in a humidified chamber at 37 °C and 5% CO<sub>2</sub> in Dulbecco's Modified Eagle's medium (DMEM) (Corning, cat# 10-013-CV, lot# 05721000) supplemented with 7.5% (10% for Calu-3) heat-inactivated fetal bovine serum (FBS) (Corning, cat# 35-010-CV, lot# 14020001). Human epithelial colon adenocarcinoma HCT-8 cells (ATCC<sup>®</sup> cat# CCL-244<sup>™</sup> lot# 70036111) were cultivated at 37 °C and 5% CO<sub>2</sub> in Roswell Park Memorial Institute (RPMI-1640) medium (Quality biological, cat# 112-024-101, lot# 723411) supplemented with 2 mM L-glutamine (Gibco, cat# 23030-081) and 10% heat-inactivated FBS.

A549-hACE2 cells that stably express human angiotensin-converting enzyme 2 (hACE2) were grown in the culture medium supplemented with 10 µg/mL Blastidin S. Primary human airway epithelial (HAE) cells from multiple donors were cultivated at 37 °C and 5% CO<sub>2</sub> in Bronchial Epithelial Cell Growth Medium (BEGM) BulletKit following the provider's instructions (Lonza, cat# CC-3171 lot# 0000889952 with supplement cat# CC-4175 lot# 0000848033). Human Bronchial Tracheal Epithelial cells (HBTEC) were derived from the following donors: "F2" from a 29-year old Caucasian female (Lifeline, cat# FC-0035, lot# 5101); "F3" from a 42-year old Caucasian female (Lonza, cat# CC-2540S, lot# 0000519670); "M2" from a 40-year old Caucasian male (Lonza, cat# CC-2540S, lot# 0000667744); and "M6" from a 48-year old Caucasian male (Lonza, cat# CC-2540S, lot# 0000544414). Diseased (Asthma) Human Bronchial Epithelial (DHBE) cells "DF2" were from a 55-year old Caucasian female (Lonza, cat# 00194911 S, lot# 0000534647). Primary HAE was used for cytotoxicity assays at passage ≤3. Cell lines were routinely checked for mycoplasma and bacterial contamination.

SARS-CoV-2 strains were obtained from BEI and propagated using Calu-3 cells supplemented with 2% FBS in accordance with approved biosafety level 3 protocols. Virus stocks were stored at –80 °C. Stock virus titers were determined by plaque assay and stocks authenticated through metagenomic sequencing.

**Plaque assays.** Vero E6 cells were seeded in 12-well plates at 3 × 10<sup>5</sup> cells per well. The following day, samples were serially diluted in DMEM containing Antibiotic-Antimycotic (Gibco) supplemented with 2% FBS. Dilutions were then added to cells and incubated for 1 h at 37 °C. Cells were subsequently overlaid with 1.2% Avicel 581-NF (FMC BioPolymer) in DMEM containing Antibiotic-Antimycotic (Gibco) and allowed to incubate for 3 days at 37 °C with 5% CO<sub>2</sub>. After 3 days, the overlay was removed, cells were washed once with phosphate buffered saline (PBS) and fixed with neutral buffered formalin (10%) for 15 min. Plaques were then visualized using 1% crystal violet followed by washing with water.

**Compound sources and chemical synthesis.** Remdesivir was either purchased from MedChemExpress (cat# HY-104077, batch# 46182) or synthesized at Gilead Sciences, Inc. GS-441524 was either purchased from MedChemExpress (cat# HY-103586, batch# 62110) or synthesized at Gilead Sciences Inc. GS-621763 was synthesized at Gilead Sciences Inc.<sup>2</sup> <sup>1</sup>H NMR (300 MHz, CHCl<sub>3</sub>-d<sub>3</sub>) δ 11.15 (bs, 1H), 8.27 (bs, 1H), 7.95 (s, 1H), 7.32 (m, 1H), 7.07 (m, 1H), 6.05 (d, J = 6.0 Hz, 1H), 5.44 (t, J = 5.1 Hz, 1H), 4.66 (t, J = 3.6 Hz, 1H), 4.32 (m, 2H), 2.73–2.52 (m, 3H), 1.27–1.14 (m, 18H). LC-MS (B) *m/z* = 502.2 [M + H], 500.1 [M – H]. All EIDD-2801/molnupiravir used in this study was provided by Gilead Sciences Inc., sourced from MedChemExpress.

**Cytotoxicity assays.** In each well of 96-well plates, 7500 cells were seeded (Corning, cat# 3598). Cells were incubated with threefold serial dilutions of

compound from a 100 µM maximum concentration. Each plate included 4 wells of positive (100 µM cycloheximide (Millipore Sigma, cat# C7698-5G)) and negative (vehicle (0.2% dimethyl sulfoxide (DMSO))) controls for normalization. Plates were incubated in a humidified chamber at 37 °C and 5% CO<sub>2</sub> for 72 h. PrestoBlue<sup>™</sup> Cell Viability Reagent (ThermoFisher Scientific, cat# A13262) was added in each well (10 µl/well) and fluorescence recorded on a Synergy H1 multimode microplate reader (BioTek) after 1-h incubation (excitation 560 nm, emission 590 nm). Raw data was normalized with the formula: % cell viability = 100 × (signal sample – signal positive control)/(signal negative control – signal positive control). Fifty percentage cytotoxic concentrations (CC<sub>50</sub>) and 95% confidence intervals after nonlinear regression were determined using the inhibitor vs normalized response equation in Prism 9.1.0 for MacOS (GraphPad). For cytotoxicity assays in A549-hACE2 cells, compounds (200 nM) were spotted onto 384-well plates prior to seeding 5000 A549-hACE2 cells/well in a volume of 40 µl culture medium. The plates were incubated at 37 °C for 48 h with 5% CO<sub>2</sub>. On day 2, 40 µl of CellTiter-Glo (Promega) was added and mixed 5 times. Plates were read for luminescence on an Envision (PerkinElmer) and CC<sub>50</sub> values calculated using a nonlinear four parameter regression model.

**Virus yield reduction.** In 12-well plates 16 h before infection, 2 × 10<sup>5</sup> VeroE6 cells were seeded per well. Confluent monolayers were then infected with the indicated virus at a multiplicity of infection (MOI) of 0.1 pfu/cell for 1 h at 37 °C with frequent rocking. Inoculum was removed and replaced with 1 mL of DMEM with 2% FBS and the indicated concentration of compound. Cells were incubated at 37 °C and 5% CO<sub>2</sub> for 48 h. Supernatant were harvested, aliquoted and stored at –80 °C before being analyzed by plaque assay.

**Reporter virus assays.** A549-hACE2 cells (12,000 cells per well in medium containing 2% FBS) were plated into a white clear-bottomed 96-well plate (Corning) at a volume of 50 µl. On the next day, compounds were added directly to cultures as 3-fold serial dilutions with a Tecan D300e digital liquid dispenser, with DMSO volumes normalized to that of the highest compound concentration (final DMSO concentration < 0.1%). The diluted compound solutions were mixed with 50 µl of SARS-CoV-2-Nluc (MOI 0.025 pfu/cell), expressing a nano luciferase reporter protein (kind gift of Xuping Xie and Pei-Yong Shi (University of Texas Medical Branch; Galveston, TX)). At 48 h postinfection, 75 µl Nano luciferase substrate solution (Promega) was added to each well. Luciferase signals were measured using an Envision microplate reader (Perkin Elmer). The relative luciferase signals were calculated by normalizing the luciferase signals of the compound-treated groups to that of the DMSO-treated groups (set as 100%). EC<sub>50</sub> values were calculated using a nonlinear four parameter variable slope regression model.

**Air-liquid interface (ALI) human airway epithelial cells (HAE) shed viral titer reduction.** Approximately 150,000 viable "F3" cells per cm<sup>2</sup> at passage three were seeded on Transwell 6.5 mm polyester membrane insert with 0.4 µm pore size (Corning, cat# 3470). Upon reaching confluence (day 4 postseeding), basal media was removed and replaced with PneumaCult-Ex Plus (Stemcell Technologies cat# 05040), while apical media was removed to create an air-liquid interface. Beating cilia, mucus production and transepithelial electrical resistance (TEER) > 300 Ohm<sup>2</sup>cm<sup>2</sup> were noticeable ~3 weeks post ALI, confirming successful differentiation. Cells were maintained in a differentiated state with weekly apical washes of mucus with PBS for 5 months before infection. One hour prior to infection, TEER was measured with 150 µl PBS and basal media was replaced with fresh media containing indicated serial dilutions (threefold down from 10 µM) of GS-621763 or GS-441524 or vehicle (dimethylsulfoxide 0.1%). The apical side was infected with ~25,000 PFU of SARS-CoV-2 gamma isolate grown on Calu-3 cells (lineage P.1., isolate hCoV-19/Japan/TY7-503/2021 (BZ/2021; Brazil P.1), BEI cat# NR-54982) in 100 µl DMEM for 1 h at 37 °C, then the inoculum was removed and washed with PBS twice. Cells were incubated for 3 days at 37 °C before final TEER measure and fixation with 10 % neutral buffered formalin for 1 h. Shed apical viruses were harvested with 200 µl PBS for 30 min at 37 °C 48 and 72 h postinfection and viral titers were estimated by plaque assay. To determine EC<sub>50</sub>s, log viral titers were normalized using the average top plateau of viral titers to define 100% and were analyzed with a nonlinear regression with the variable slope with Prism 9.0.1 for MacOS (GraphPad). TEER were measured with the EVOM or EVOM3 system (World Precision Instruments).

**Pharmacokinetics.** Female ferrets were either intravenously administered 10 mg/kg remdesivir as a 30-min infusion or orally administered 30 mg/kg GS-621763, after which plasma was isolated at 7–9 timepoints postadministration. Plasma samples underwent methanol protein precipitation followed by centrifugation. The resulting supernatants were isolated, evaporated to dryness under nitrogen and reconstituted with 5% acetonitrile for injection onto an LC-MS/MS system (Sciex API-4500). Concentrations of remdesivir, GS-621763, and GS-441524 were determined using 9-point calibration curves spanning at least 3 orders of magnitude, with quality control samples to ensure accuracy and precision, prepared in normal ferret plasma. Analytes were separated by a 50 × 3.0 mm, 2.55 µm Synergi Polar-RP 30 A column (Phenomenex, Inc.) using a mobile phase A consisting of 10 mM ammonium formate with 0.1% formic acid and a mobile phase B consisting

of 0.1% formic acid in acetonitrile. A multi-stage linear gradient from 5% to 95% mobile phase B at a flow rate of 1 mL/min was employed for analyte separation (Shimadzu). Pharmacokinetic parameters were calculated using Phoenix Win-Nonlin (version 8.2, Certara) and concentration-time profiles generated using Prism (version 8, GraphPad). Ferret lungs were collected at 24 h following initiation of drug administration. Whole tissues were quickly isolated and immediately placed into liquid nitrogen and stored at  $-80^{\circ}\text{C}$  until processing and LC-MS/MS analysis<sup>2</sup>. Reported values for lung total nucleosides are the sum of (GS-441524 and mono-, di-, and triphosphate (GS-443902) metabolites).

**Ferret efficacy studies.** Female ferrets (6–10 months old, *Mustela putorius furo*) were purchased from Triple F Farms. Ferrets were rested for 7 days after arrival. Ferrets were then housed individually or in groups of 2 in ventilated negative-pressure cages in an ABSL-3 facility. Based on the previous experiments<sup>5</sup>, ferrets were randomly assigned to groups ( $n = 4$ ) and used as an in vivo model to examine the efficacy of orally administered compounds against SARS-CoV-2 infection. No blinding of investigators was performed. Ferrets were anesthetized using dexmedetomidine/ketamine and infected intranasally with  $1 \times 10^5$  pfu 2019-nCoV/USA-WA1/2020 in 1 mL (0.5 mL per ear). Body weight and rectal temperature were measured once daily. Nasal lavages were performed twice daily using 1 mL sterile PBS (containing Antibiotic-Antimycotic (Gibco)). Nasal lavage samples were stored at  $-80^{\circ}\text{C}$  until virus titration could be performed by plaque assay. Treatment (once daily (q.d.) or twice daily (b.i.d.)) was initiated at either 0 or 12 h after infection and continued until 4 days postinfection with either vehicle (2.5% dimethyl sulfoxide; 10% Kolliphor HS-15; 10% Labrasol; 2.5% propylene glycol; 75% water) or compound. Four days after infection, ferrets were euthanized, and tissues and organs were harvested and stored at  $-80^{\circ}\text{C}$  until processed.

**Contact transmission in ferrets.** Eight ferrets were anesthetized and inoculated intranasally with  $1 \times 10^5$  pfu of hCoV-19/Japan/TY7-503/2021. Twelve hours after infection, ferrets were split into two groups ( $n = 4$ ; 2 ferrets per cage) and treated with vehicle or GS-621763 ( $10 \text{ mg kg}^{-1}$ ) twice daily (b.i.d.) via oral gavage. At 54 h after infection, uninfected and untreated contact ferrets (two contacts for GS-621763; three contacts for vehicle) were co-housed with source ferrets. Co-housing was continued until 96 h after infection and source ferrets were euthanized. Contact ferrets were housed individually and monitored for an additional 4 days after separation from source ferrets and subsequently euthanized. Nasal lavages were performed on all source ferrets every 12 h and all contact ferrets every 24 h. For all ferrets, nasal turbinates and lung tissues were harvested to determine viral titers and the detection of viral RNA.

**SARS-CoV-2 titration in tissue extracts.** Selected tissues were weighed and mechanically homogenized in sterile PBS. Homogenates were clarified by centrifugation ( $2000 \times g$ ) for 5 min at  $4^{\circ}\text{C}$ . Clarified homogenates were then serially diluted and used in plaque assays to determine virus titer as described above.

**Quantitation of SARS-CoV-2 RNA copy numbers.** To probe viral RNA in selected tissues, samples were harvested and stored in RNAlater at  $-80^{\circ}\text{C}$ . Total RNA from tissues was isolated using a RNeasy mini kit (Qiagen), in accordance with the manufacturer's protocol. For nasal lavage samples, total RNA was extracted using a ZR viral RNA kit (Zymo Research) in accordance with the manufacturer's protocol. SARS-CoV-2 RNA was detected using the nCoV\_IP2 primer-probe set (National Reference Center for Respiratory Viruses, Pasteur Institute) (Supplementary Table 4). An Applied Biosystems 7500 using the StepOnePlus real-time PCR system was used to perform RT-qPCR reactions. The nCoV\_IP2 primer-probe set was used in combination with TaqMan fast virus 1-step master mix (Thermo Fisher Scientific) to detect viral RNA. SARS-CoV-2 RNA copy numbers were calculated using a standard curve created from serial dilutions of a PCR fragment (12669–14146 nt of the SARS-CoV-2 genome). For RNA copies in tissue samples, RNA copies were normalized to the weights of the tissues used.

**Next-generation sequencing.** To authenticate virus stocks, metagenomic sequencing was performed as described<sup>39,40</sup>, while to sequence lower viral load in vivo samples the COVID-Seq (Illumina) amplicon tiling protocol was used. For metagenomic sequencing, viral RNA was treated with Turbo DNase I (Thermo Fisher), converted to cDNA using random hexamers and SuperScript IV reverse transcriptase, and double-stranded cDNA created using Sequenase v2.0. Sequencing libraries for both sets of libraries were generated using Nextera Flex (Illumina) and cleaned using  $0.8 \times$  Ampure XP beads and pooled equimolarly before sequencing on an Illumina  $1 \times 100$  bp NextSeq2000 run. Raw fastq reads were adapter- and quality-trimmed with Trimmomatic v0.39<sup>41</sup>. To interrogate potential resistance alleles, reference-based mapping to NC\_045512.2 was carried out using our modified Longitudinal Analysis of Viral Alleles (LAVA—<https://github.com/michellejlin/lava>)<sup>42</sup> pipeline. LAVA constructs a candidate reference genome from early passage virus using bwa<sup>43</sup>, removes PCR duplicates with Picard, calls variants with VarScan<sup>44,45</sup>, and converts these changes into amino acid changes with Annovar<sup>46</sup>. Consensus sequences were called with TAYLOR<sup>39</sup> and deposited in

NCBI GenBank. Accession numbers (Supplementary Table 5) are as follows: input strain WA1/2020, MZ433205; WA1/2020 recovered from ferrets, MZ433206 - MZ433213; input strain BZ/2021, MZ433225; BZ/2021 recovered from source ferrets, MZ433214 - MZ433221; BZ/2021 recovered from contacts of vehicle-treated source ferrets, MZ433222–MZ433224. Raw reads for these sequences are publicly available on SRA (BioProject PRJNA740065).

**Ethics statement.** All in vivo efficacy studies were conducted at Georgia State University in compliance with the Animal Welfare Act Code of Federal Regulations and the Guide for the Care and Use of Laboratory Animals of the National Institutes of Health. All studies involving SARS-CoV-2-infected ferrets were approved by the Georgia State Institutional Animal Care and Use Committee under protocol A20031. Experiments at Georgia State University using infectious SARS-CoV-2 were performed in BSL-3/ABSL-3 facilities at Georgia State University and approved by the Georgia State Institutional Biosafety Committee under protocol B20016. Experiments at Gilead Sciences, Inc. using infectious SARS-CoV-2 were performed in a BSL-3 facility and approved by an institutional biosafety committee.

**Statistics and reproducibility.** The Microsoft Excel (versions 16.42, 16.43, and 16.48), GraphPad Prism (versions, 8.0, 9.0.1, and 9.1.0), and Numbers (version 10.1) software packages were used for data collection and analysis. One-way or two-way ANOVA with Dunnett's or Tukey's multiple comparisons post hoc test were used to evaluate statistical significance when comparing more than two groups or two independent variables. When comparing two variables, a two-tailed unpaired t-test was performed to determine statistical significance. The specific statistical test used to individual studies is specified in the figure legends. RT-qPCR data were collected and analyzed using the StepOnePlus (version 2.1; Applied Biosystems) software package. Final figures were assembled in Adobe Illustrator (version CS6). All numerical raw data and summaries of individual statistical analyses are provided in supplementary datasets 3 and 4. Effect sizes between groups in the ANOVAs were calculated as  $\eta^2 = (SS_{\text{effect}})/(SS_{\text{total}})$  for one-way ANOVA and  $\omega^2 = (SS_{\text{effect}} - (df_{\text{effect}})(MS_{\text{error}}))/MS_{\text{error}} + SS_{\text{total}}$  for two-way ANOVA ( $SS_{\text{effect}}$ , sum of squares for the effect;  $SS_{\text{total}}$ , the sum of squares for total;  $df_{\text{effect}}$ , degrees of freedom for the effect;  $MS_{\text{error}}$ , mean squared error). The statistical significance level  $\alpha$  was set to  $<0.05$  for all experiments. Exact P values are shown in the individual graphs. Appropriate sample sizes were determined using power analyses (GPower 3.1; University of Duesseldorf).

**Reporting Summary.** Further information on research design is available in the Nature Research Reporting Summary linked to this article.

## Data availability

All next-generation sequencing data is publicly available on SRA (BioProject PRJNA740065). All accession codes for sequence data are available in Supplementary Table 5. Sequencing data is summarized in Supplementary Data 1–2. All data generated and analyzed during this study are included in this published article (and its supplementary information files). Source data and statistical analyses for Figs. 1–4, Supplementary Tables 13 and Supplementary Figs. 1–2 are provided with the paper in Supplementary Data 3–4.

## Code availability

This study does not use proprietary codes. All computer codes and algorithms used are specified in the Methods section.

Received: 30 July 2021; Accepted: 22 October 2021;

Published online: 05 November 2021

## References

1. U.S. Food & Drug Administration. FDA Approves First Treatment for COVID-19. <https://www.fda.gov/news-events/press-announcements/fda-approves-first-treatment-covid-19> (last accessed 06/06/2021), 2020).
2. Mackman, R. L. et al. Prodrugs of a 1'-CN-4-Aza-7,9-dideazaadenosine C-Nucleoside Leading to the Discovery of Remdesivir (GS-5734) as a Potent Inhibitor of Respiratory Syncytial Virus with Efficacy in the African Green Monkey Model of RSV. *J. Med. Chem.* **64**, 5001–5017 (2021).
3. Siegel, D. Discovery and Synthesis of a Phosphoramidate Prodrug of a Pyrrolo[2,1-f][triazin-4-amino] Adenine C-Nucleoside (GS-5734) for the Treatment of Ebola and Emerging Viruses. *J. Med. Chem.* **60**, 1648–1661 (2017).
4. Meganck, R. M. & Baric, R. S. Developing therapeutic approaches for twenty-first-century emerging infectious viral diseases. *Nat. Med.* **27**, 401–410 (2021).
5. Toots, M. et al. Characterization of orally efficacious influenza drug with high resistance barrier in ferrets and human airway epithelia. *Sci. Transl. Med.* **11**, eaax5866 (2019).

## ARTICLE

NATURE COMMUNICATIONS | <https://doi.org/10.1038/s41467-021-26760-4>

6. Cox, R. M., Wolf, J. D. & Plemper, R. K. Therapeutically administered ribonucleoside analogue MK-4482/EIDD-2801 blocks SARS-CoV-2 transmission in ferrets. *Nat. Microbiol.* **6**, 11–18 (2021).
7. Painter W. P. et al. Human Safety, Tolerability, and Pharmacokinetics of a Novel Broad-Spectrum Oral Antiviral Compound, Molnupiravir, with Activity Against SARS-CoV-2. *medRxiv*, <https://doi.org/10.1101/2020.12.10.20235747> (2020).
8. Good, S. S. et al. AT-527, a Double Prodrug of a Guanosine Nucleotide Analog, Is a Potent Inhibitor of SARS-CoV-2 In Vitro and a Promising Oral Antiviral for Treatment of COVID-19. *Antimicrob. Agents Chemother.* **65**, e02479–20 (2021).
9. Beigel, J. H. et al. Remdesivir for the Treatment of Covid-19 - Final Report. *N. Engl. J. Med.* **383**, 1813–1826 (2020).
10. Pruijssers, A. J. et al. Remdesivir Inhibits SARS-CoV-2 in Human Lung Cells and Chimeric SARS-CoV Expressing the SARS-CoV-2 RNA Polymerase in Mice. *Cell Rep.* **32**, 107940 (2020).
11. Humeniuk, R. et al. Safety, Tolerability, and Pharmacokinetics of Remdesivir, An Antiviral for Treatment of COVID-19, in Healthy Subjects. *Clin. Transl. Sci.* **13**, 896–906 (2020).
12. Wei, D. et al. Potency and pharmacokinetics of GS-441524 derivatives against SARS-CoV-2. *Bioorg. Med. Chem.* **46**, 116364 (2021).
13. Li, Y. et al. Remdesivir Metabolite GS-441524 Effectively Inhibits SARS-CoV-2 Infection in Mouse Models. *J. Med. Chem.*, <https://doi.org/10.1021/acs.jmedchem.0c01929> (2021).
14. Oude Munnink, B. B. et al. Transmission of SARS-CoV-2 on mink farms between humans and mink and back to humans. *Science* **371**, 172–177 (2021).
15. Richard, M. et al. SARS-CoV-2 is transmitted via contact and via the air between ferrets. *Nat. Commun.* **11**, 3496 (2020).
16. Felsenstein, S. & Hedrich, C. M. SARS-CoV-2 infections in children and young people. *Clin. Immunol.* **220**, 108588 (2020).
17. Zhu, N. et al. A Novel Coronavirus from Patients with Pneumonia in China, 2019. *N. Engl. J. Med.* **382**, 727–733 (2020).
18. Tracking SARS-CoV-2 variants\*. [www.who.int](http://www.who.int). Retrieved 1 June 2021., 2021).
19. Faria, N. R. et al. Genomics and epidemiology of the P.1 SARS-CoV-2 lineage in Manaus, Brazil. *Science* **372**, 815–821 (2021).
20. Mossel, E. C. et al. Exogenous ACE2 expression allows refractory cell lines to support severe acute respiratory syndrome coronavirus replication. *J. Virol.* **79**, 3846–3850 (2005).
21. Humeniuk, R. et al. Pharmacokinetic, Pharmacodynamic, and Drug-Interaction Profile of Remdesivir, a SARS-CoV-2 Replication Inhibitor. *Clin. Pharmacokinet.* **60**, 569–583 (2021).
22. Fiege, J. K. et al. Single cell resolution of SARS-CoV-2 tropism, antiviral responses, and susceptibility to therapies in primary human airway epithelium. *PLoS Pathog.* **17**, e1009292 (2021).
23. bei RESOURCES <https://www.beiresources.org/Catalog/animalviruses/NR-54982.aspx> retrieved on 06/09/2021. (2021).
24. Szemiel, A. M. et al. In vitro evolution of Remdesivir resistance reveals genome plasticity of SARS-CoV-2. *bioRxiv*, 2021.2002.2001.429199, <https://doi.org/10.1101/2021.02.01.429199> (2021).
25. Agostini, M. L. et al. Coronavirus Susceptibility to the Antiviral Remdesivir (GS-5734) Is Mediated by the Viral Polymerase and the Proofreading Exoribonuclease. *mBio* **9**, e00221–18 (2018).
26. Gordon, C. J. et al. Remdesivir is a direct-acting antiviral that inhibits RNA-dependent RNA polymerase from severe acute respiratory syndrome coronavirus 2 with high potency. *J. Biol. Chem.* **295**, 6785–6797 (2020).
27. Tchesnokov, E. P. et al. Template-dependent inhibition of coronavirus RNA-dependent RNA polymerase by remdesivir reveals a second mechanism of action. *J. Biol. Chem.* **295**, 16156–16165 (2020).
28. Park, S. J. et al. Antiviral Efficacies of FDA-Approved Drugs against SARS-CoV-2 Infection in Ferrets. *mBio* **11**, <https://doi.org/10.1128/mBio.01114-20> (2020).
29. Shi, J. et al. Susceptibility of ferrets, cats, dogs, and other domesticated animals to SARS-coronavirus 2. *Science* **368**, 1016–1020 (2020).
30. Maltzou, H. C. et al. Association Between Upper Respiratory Tract Viral Load, Comorbidities, Disease Severity, and Outcome of Patients With SARS-CoV-2 Infection. *J. Infect. Dis.* **223**, 1132–1138 (2021).
31. de Wit, E. et al. Prophylactic and therapeutic remdesivir (GS-5734) treatment in the rhesus macaque model of MERS-CoV infection. *Proc. Natl Acad. Sci. U. S. A.* **117**, 6771–6776 (2020).
32. Williamson, B. N. et al. Clinical benefit of remdesivir in rhesus macaques infected with SARS-CoV-2. *Nature* **585**, 273–276 (2020).
33. Faria, N. R. et al. Genomics and epidemiology of a novel SARS-CoV-2 lineage in Manaus, Brazil. *medRxiv*, <https://doi.org/10.1101/2021.02.26.21252554> (2021).
34. Lo, M. K. et al. Remdesivir targets a structurally analogous region of the Ebola virus and SARS-CoV-2 polymerases. *Proc. Natl Acad. Sci.* **117**, 26946–26954 (2020).
35. Kutter, J. S. et al. SARS-CoV and SARS-CoV-2 are transmitted through the air between ferrets over more than one meter distance. *Nat. Commun.* **12**, 1653 (2021).
36. Abdoal Karim, S. S. & de Oliveira, T. New SARS-CoV-2 Variants - Clinical, Public Health, and Vaccine Implications. *N. Engl. J. Med.* **384**, 1866–1868 (2021).
37. Pearson, C. A. B. et al. Estimates of severity and transmissibility of novel SARS-CoV-2 variant 501Y.V2 in South Africa. <https://cmmid.github.io/topics/covid19/sa-novel-variant.htm> (London: CMMID Repository, 2021).
38. Davies, N. G. et al. Estimated transmissibility and impact of SARS-CoV-2 lineage B.1.1.7 in England. *Science* **372**, eabg3055 (2021).
39. Addetia, A. et al. Sensitive Recovery of Complete SARS-CoV-2 Genomes from Clinical Samples by Use of Swift Biosciences' SARS-CoV-2 Multiplex Amplicon Sequencing Panel. *J. Clin. Microbiol.* **59**, e02226–20 (2020).
40. Greninger, A. L. et al. Rapid Metagenomic Next-Generation Sequencing during an Investigation of Hospital-Acquired Human Parainfluenza Virus 3 Infections. *J. Clin. Microbiol.* **55**, 177–182 (2017).
41. Bolger, A. M., Lohse, M. & Usadel, B. Trimmomatic: a flexible trimmer for Illumina sequence data. *Bioinformatics* **30**, 2114–2120 (2014).
42. Lin, M. J., Shean, R. C., Makhosou, N. & Greninger, A. L. LAVA: a streamlined visualization tool for longitudinal analysis of viral alleles. *bioRxiv*, 2019.2012.2017.879320, <https://doi.org/10.1101/2019.12.17.879320> (2019).
43. Li, H. & Durbin, R. Fast and accurate short read alignment with Burrows-Wheeler transform. *Bioinformatics* **25**, 1754–1760 (2009).
44. Koboldt, D. C. et al. VarScan: variant detection in massively parallel sequencing of individual and pooled samples. *Bioinformatics* **25**, 2283–2285 (2009).
45. Koboldt, D. C., Larson, D. E., Chen, K., Ding, L. & Wilson, R. K. Massively parallel sequencing approaches for characterization of structural variation. *Methods Mol. Biol.* **838**, 369–384 (2012).
46. Wang, K., Li, M. & Hakonarson, H. ANNOVAR: functional annotation of genetic variants from high-throughput sequencing data. *Nucleic Acids Res.* **38**, e164 (2010).

**Acknowledgements**

We thank BEI Resources for SARS-CoV-2 isolates, X. Xie and P.-Y. Shi for providing SARS-CoV-2-Nluc, A. Shornikov of the Gilead Sample Bank group for compound distribution, the High Containment Core and the Department for Animal Research of Georgia State University for support, and A. L. Hammond and D. Porter for critical reading of the manuscript.

**Author contributions**

J.P.B. and R.K.P. coordinated the study. R.M.C. and J.S. performed virus-stock preparations and virus titrations. R.M.C., J.D.W., C.M.L. and R.K.P. performed animal inoculations, nasal lavage sampling, animal necropsies, and/or titration of virus from ferrets. R.M.C. extracted RNA from all animal samples and performed all RT-qPCR experiments and analyses. J.S. performed virus reduction assays and cytotoxicity assessments. D.B. coordinated pharmacokinetics studies in ferrets. K.T.B. and D.L. prepared compound formulations. V.D.P., J.P.B. and J.C. performed reporter virus and cytotoxicity assays in ACE2-A549 cells. R.K., K.C. and R.L.M. synthesized and sourced compounds. M.J.L. and A.L.G. performed all next-generation sequencing and analyses. R.M.C. created all figure schematics. R.M.C., J.S., J.P.B. and R.K.P. were responsible for experimental design, data analysis, and data presentation. R.M.C., J.D.W., C.M.L., J.S., D.B., L.S.M., A.L.G., R.L.M., C.Y., J.P.B. and T.C. edited the manuscript. J.P.B. and R.K.P. conceived and designed the study. R.K.P. wrote the manuscript. This work was supported by Gilead Sciences Inc. and, in part, by Public Health Service grants AI153400 (to RKP) and AI141222 (to RKP) from the NIH/NIAID. NIH/NIAID had no role in study design, data collection, and interpretation, or the decision to submit the work for publication.

**Competing interests**

All authors affiliated with Gilead Sciences may hold stock or stock options in Gilead Sciences Inc. R.K.P. was the principal investigator of a Gilead-sponsored research agreement with Georgia State University. He has received funding from Gilead Sciences Inc. to support parts of this work. All other authors declare no competing interests.

**Additional information**

**Supplementary information** The online version contains supplementary material available at <https://doi.org/10.1038/s41467-021-26760-4>.

**Correspondence** and requests for materials should be addressed to Richard K. Plemper.

**Peer review information** *Nature Communications* thanks Ralph Tripp and the other, anonymous, reviewer(s) for their contribution to the peer review of this work. Peer reviewer reports are available.

**Reprints and permission information** is available at <http://www.nature.com/reprints>

**Publisher's note** Springer Nature remains neutral with regard to jurisdictional claims in published maps and institutional affiliations.



## 2.1.5 4'-Fluorouridine is an Oral Antiviral that Blocks Respiratory Syncytial Virus and SARS-CoV-2 Replication

## RESEARCH

## RESEARCH ARTICLE

## CORONAVIRUS

### 4'-Fluorouridine is an oral antiviral that blocks respiratory syncytial virus and SARS-CoV-2 replication

Julien Sourimant<sup>1</sup>, Carolin M. Lieber<sup>1</sup>, Megha Aggarwal<sup>1</sup>, Robert M. Cox<sup>1</sup>, Josef D. Wolf<sup>1</sup>, Jeong-Joong Yoon<sup>1</sup>, Mart Toots<sup>1</sup>, Chengin Ye<sup>2</sup>, Zachary Sticher<sup>3</sup>, Alexander A. Kolykhalov<sup>3,4</sup>, Luis Martinez-Sobrido<sup>2</sup>, Gregory R. Bluemel<sup>3,4</sup>, Michael G. Natchus<sup>3</sup>, George R. Painter<sup>3,4,5</sup>, Richard K. Plumper<sup>1,6,\*</sup>

The COVID-19 pandemic has underscored the critical need for broad-spectrum therapeutics against respiratory viruses. Respiratory syncytial virus (RSV) is a major threat to pediatric patients and older adults. We describe 4'-fluorouridine (4'-FlU, EIDD-2749), a ribonucleoside analog that inhibits RSV, related RNA viruses, and severe acute respiratory syndrome coronavirus 2 (SARS-CoV-2), with high selectivity index in cells and human airway epithelia organoids. Polymerase inhibition within *in vitro* RNA-dependent RNA polymerase assays established for RSV and SARS-CoV-2 revealed transcriptional stalling after incorporation. Once-daily oral treatment was highly efficacious at 5 milligrams per kilogram (mg/kg) in RSV-infected mice or 20 mg/kg in ferrets infected with different SARS-CoV-2 variants of concern, initiated 24 or 12 hours after infection, respectively. These properties define 4'-FlU as a broad-spectrum candidate for the treatment of RSV, SARS-CoV-2, and related RNA virus infections.

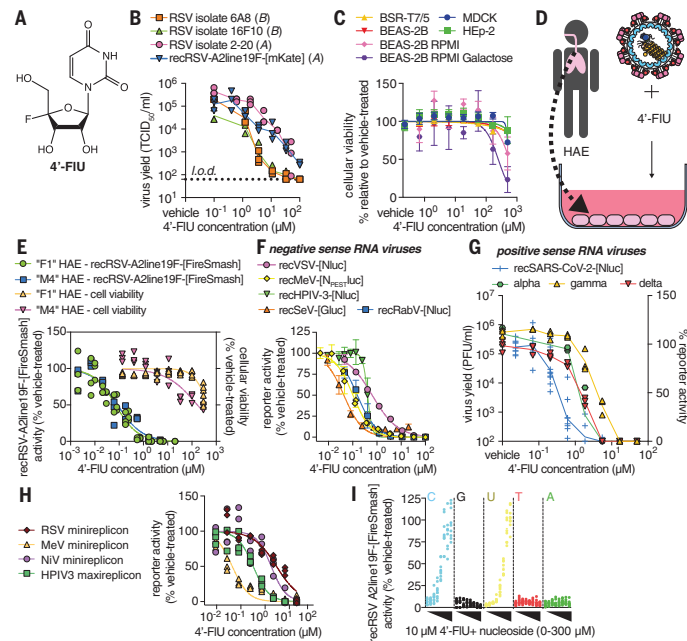
The COVID-19 experience has highlighted the need for orally bioavailable broad-spectrum antivirals that may be quickly deployed against newly emerging viral pathogens. Remdesivir—a direct-acting broad-spectrum antiviral—is still the only small-molecule therapeutic approved for use

against severe acute respiratory syndrome coronavirus 2 (SARS-CoV-2) infection in the United States, but it requires intravenous administration. The ensuing restriction to hospitalized patients compromises its clinical effect as treatment is initiated too late in the infection cycle (1). We have demonstrated the

efficacy of orally available EIDD-2801 (molnupiravir) against influenza viruses in human organoid models and ferrets (2), and subsequent animal and human data showed that the antiviral efficacy of molnupiravir extends to SARS-CoV-2 *in vivo* (3, 4). Molnupiravir acts by inducing lethal viral mutagenesis after incorporation into viral genomic RNA of influenza viruses (2) and betacoronaviruses (5). The drug was recently approved in the United Kingdom and is currently considered for emergency use authorization against COVID-19 in the United States. However, even with this accelerated development timeline, molnupiravir only became available to patients nearly 2 years into the pandemic. To have a substantial effect on a mounting pandemic, an antiviral must be approved for human use before a new pathogen emerges, making the case for the development of broad-spectrum antivirals.

We have identified respiratory syncytial virus (RSV) disease as a viable primary indication for a candidate broad-spectrum antiviral, on the basis of the unaddressed major health threat imposed by RSV and well-established protocols for clinical trials of anti-RSV therapeutics. RSV infections are responsible for over 58,000 hospitalizations of children <5 years of age in the United States annually, and ~177,000 hospitalizations of adults > the age of 65 (6–9). Despite this major health and economic burden, no therapeutics have been licensed specifically

**Fig. 1. 4'-FlU is a potent broad-spectrum antiviral.** (A) Chemical structure of 4'-FlU. (B) Virus yield reduction of RSV clinical isolates 6A8, 16F10, 2-20, and recombinant recRSV-A2line19F-[mKate] [(A) or (B) antigenic subgroup]. (C) HEP-2, MDCK, BHK-T7, and BEAS-2B cell lines were assayed for reduction in cell metabolism by 4'-FlU. (D and E) recRSV-A2line19F-[FireSMASH] dose response inhibition and cytotoxicity assay with human airway epithelial (HAE) cells (D) from two donors in the presence of indicated 4'-FlU concentrations (E). (F) Dose-response inhibition of a panel of recombinant mononegaviruses by 4'-FlU. (G) Dose-response inhibition of recSARS-CoV-2-[Nluc] and virus yield reduction of alpha, gamma, and delta VoC isolates by 4'-FlU. (H) Dose-response inhibition of transiently expressed polymerase complexes from mononegaviruses MeV, RSV, NiV, or HPIV-3 by 4'-FlU. (I) recRSV-A2line19F-[FireSMASH]-infected cells were treated with 10  $\mu$ M 4'-FlU and serial dilutions of exogenous nucleotides in extracellular media. Viral activity was determined by reporter activity. Symbols represent independent repeats [(B), (E), (G), (H), and (I)] or mean with standard deviation [(C) and (F)], and lines represent means.  $n \geq 3$ , EC<sub>50</sub>s, and CC<sub>50</sub>s are reported in tables S1 and S2, and all source data are provided in data S2.



## RESEARCH | RESEARCH ARTICLE

for treatment of RSV disease (10). Anti-RSV drug discovery efforts have increasingly focused on inhibiting the viral RNA-dependent RNA polymerase (RdRP) complex (11). The core polymerase machinery comprises the large (L) polymerase protein, its obligatory cofactor [the phosphoprotein (P)], and the encapsidated negative-sense RNA genome (11). Allosteric inhibitors of RSV L have potent activity as seen, for instance, with the experimental drug candidates AVG-233 (12) and inhaled PC786 (13).

In search of a drug that is active against RSV and SARS-CoV-2, is orally available, and acts through a distinct mechanism of activity (MOA) from molnupiravir, we explored 4'-fluorine substitutions in a series of analogs of the molnupiravir parent molecule.  $N^4$ -hydroxycytidine (NHC) (14). The focus on 4'-fluorine ribose substitutions was motivated by the small atomic radius and strong stereoelectronic effect of fluorine that can influence backbone conformation flexibility, which may lead to improved selectivity indices (SIs), increased lipophilicity, and greater metabolic stability (15). A synthetic intermediate in the approach to 4'-fluoro- $N^4$ -hydroxycytidine (compound 5 in fig. S1) was deprotected to provide 4'-FIU (Fig. 1A), which emerged as a broadly active antiviral when biotested.

#### 4'-FIU is a broad-spectrum mononegavirus inhibitor with high SI

Following the approach of using RSV disease as a primary indication to advance a new candidate broad-spectrum antiviral, we first assessed activity of 4'-FIU against a recombinant RSV A2-line19F (recRSV A2-L19F) (16) and clinical RSV isolates on immortalized HEp-2 cells. The compound showed potent dose-dependent activity against all RSV strains tested, returning half-maximal effective concentrations ( $EC_{50}$  values) ranging from 0.61 to 1.2  $\mu$ M (Fig. 1B and table S1). This cell culture potency was on par with the previously reported anti-RSV activity of NHC (fig. S2). Global metabolic activity of established human and animal cell lines (HEp-2, MDCK, BHK-T7, and BEAS-2B) remained unaltered after they were exposed to 4'-FIU (up to 500  $\mu$ M), indicating that the antiviral effect is a result of cytotoxicity (Fig. 1C and table S2). When glucose was replaced with galactose as a carbohydrate source to link cell metabolic activity strictly to mitochondrial oxidation (17), we determined a half-maximal

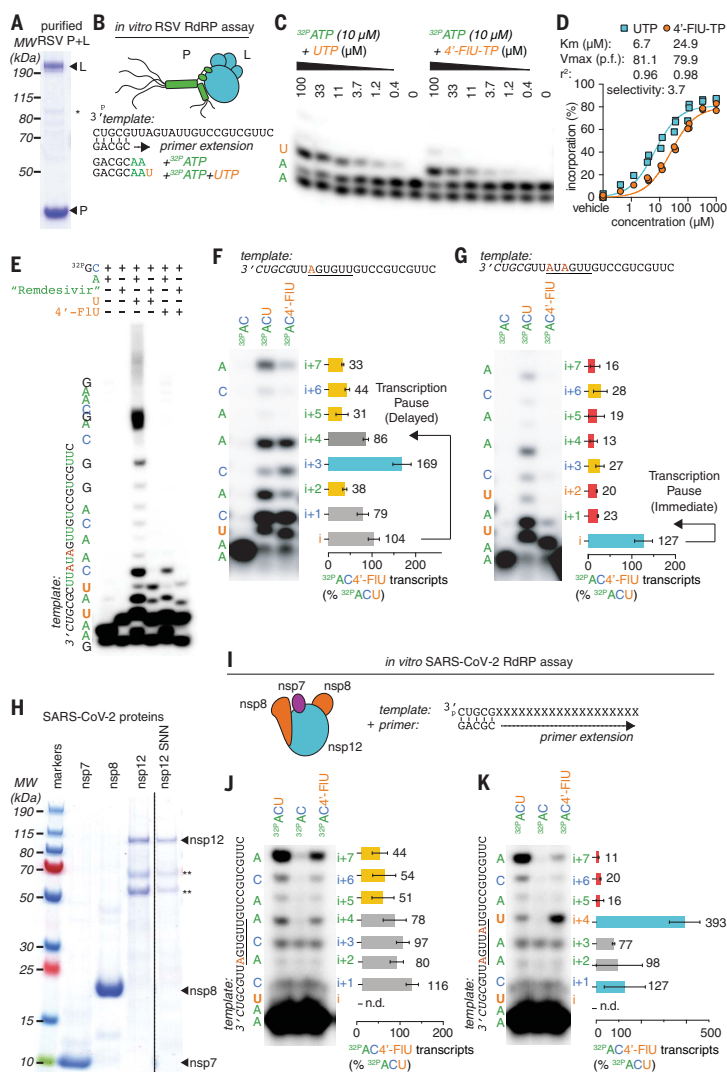


**Fig. 2. 4'-FIU induces a delayed stalling of RSV and SARS-CoV-2 RdRP.** (A) SDS-PAGE with Coomassie blue staining of recombinant RSV RdRP complexes (L and P proteins). (B) Schematics of the primer extension assay. (C) Urea-polyacrylamide gel electrophoresis (PAGE) fractionation of RNA transcripts produced through primer extension by the RSV RdRP in the presence of the indicated nucleotides ( $n = 3$ ). (D) Kinetic analysis of autoradiographs from (C). Nonlinear regression with the Michaelis-Menten model.  $K_m$  and  $V_{max}$  with 95% confidence intervals (CIs) and goodness of fit ( $r^2$ ) are indicated. (E to G) Urea-PAGE fractionation of RNA transcripts produced by RSV RdRP in the presence of the indicated templates and nucleotides. "Remdesivir" denotes the addition of the remdesivir active metabolite GS-443902, a well-characterized "delayed chain terminator". 4'-FIU-TP bands in (F) to (G) were normalized to the corresponding band after UTP incorporation. Bars represent mean and error bars represent standard deviation ( $n = 3$ ). (H) Purified recombinant SARS-CoV-2 RdRP complexes (nsp7, 8, and 12 proteins) "nsp12 SNN" denotes a catalytically inactive mutant. (I to K) Urea-PAGE fractionation of RNA transcripts produced by SARS-CoV-2 RdRP in the presence of the indicated templates and nucleotides. Stars denote cellular contaminants. Uncropped autoradiograph replicates are provided in data S1.

<sup>1</sup>Center for Translational Antiviral Research, Georgia State University, Atlanta, GA 30303, USA. <sup>2</sup>Texas Biomedical Research Institute, San Antonio, TX 78227, USA. <sup>3</sup>Emory Institute for Drug Development, Emory University, Atlanta, GA 30322, USA. <sup>4</sup>Drug Innovation Ventures at Emory (DRIVE), Atlanta, GA 30322, USA. <sup>5</sup>Department of Pharmacology, Emory University School of Medicine, Atlanta, GA 30322, USA. <sup>6</sup>Department of Pediatrics, Emory University School of Medicine, Atlanta, GA 30322, USA. \*Corresponding author. Email: rplemper@gsu.edu

## RESEARCH | RESEARCH ARTICLE

cytotoxic concentration ( $CC_{50}$ ) of 4'-FIU of 250  $\mu$ M (Fig. 1C and table S2).

When tested on disease-relevant primary human airway epithelial cells (HAEs) derived from two different donors (Fig. 1D), 4'-FIU showed a  $\geq 17$ -fold increase in anti-RSV potency relative to that on HEp-2 cells; however, the low cytotoxicity levels remained unchanged ( $CC_{50}$  169  $\mu$ M) (Fig. 1E), resulting in a high SI ( $SI = EC_{50}/CC_{50}$ ) of  $\geq 1877$ . Consistent with these findings, quantitative immunocytochemistry on HAE cells confirmed that 4'-FIU reduced steady-state levels of nuclear- (SDH-A;  $IC_{50}$  272.8  $\mu$ M) and mitochondrial- (COX-I;  $IC_{50}$  146.8  $\mu$ M) encoded proteins only at high concentrations (fig. S3).

We next explored the 4'-FIU indication spectrum. We assessed a panel of negative-sense RNA viruses of the paramyxovirus and rhabdovirus families, including measles virus (MeV), human parainfluenza virus type 3 (HPIV3), Sendai virus (SeV), vesicular stomatitis virus (VSV), and rabies virus (RabV). Like RSV, these viruses belong to the mononegavirus order, and we found that 4'-FIU demonstrated submicromolar active concentrations (Fig. 1F and table S1). Testing a representative of phylogenetically distant positive-sense RNA viruses, the betacoronavirus SARS-CoV-2 was also sensitive to 4'-FIU, with  $EC_{50}$  values ranging from 0.2 to 0.6  $\mu$ M against isolates of different lineages (Fig. 1G and table S1).

At initial mechanistic characterization, 4'-FIU inhibited RSV and paramyxovirus RdRP complex activity in cell-based minireplicon systems (Fig. 1H and table S1). The RdRP activity of Nipah virus (NiV)—a highly pathogenic zoonotic paramyxovirus with pandemic potential (18)—was also efficiently inhibited by 4'-FIU in a NiV minireplicon reporter assay. The antiviral effect of 4'-FIU was dose-dependently reversed by addition of an excess of exogenous pyrimidines (cytidine and uridine)—but not purines—to the cultured cells, which is consistent with competitive inhibition of RdRP activity (2, 19) (Fig. 1I).

#### Incorporation of 4'-FIU by RSV and SARS-CoV-2 RdRP causes sequence-modulated transcriptional stalling

To characterize the molecular MOA of 4'-FIU, we purified recombinant RSV L and P proteins expressed in insect cells (Fig. 2A) and determined performance of the bioactive 5'-triphosphate form of 4'-FIU (4'-FIU-TP) within *in vitro* primer extension assays (20) (Fig. 2B). In the presence of radio-labeled adenosine triphosphate (ATP) and an increasing amount of uridine triphosphate (UTP), RSV RdRP complexes elongated the primer until reaching a G in third position on the template strand, and continued further upon addition of CTP (Fig. 2C) (fig. S4 and data S1). Replacing UTP with 4'-FIU-TP resulted in efficient primer extension

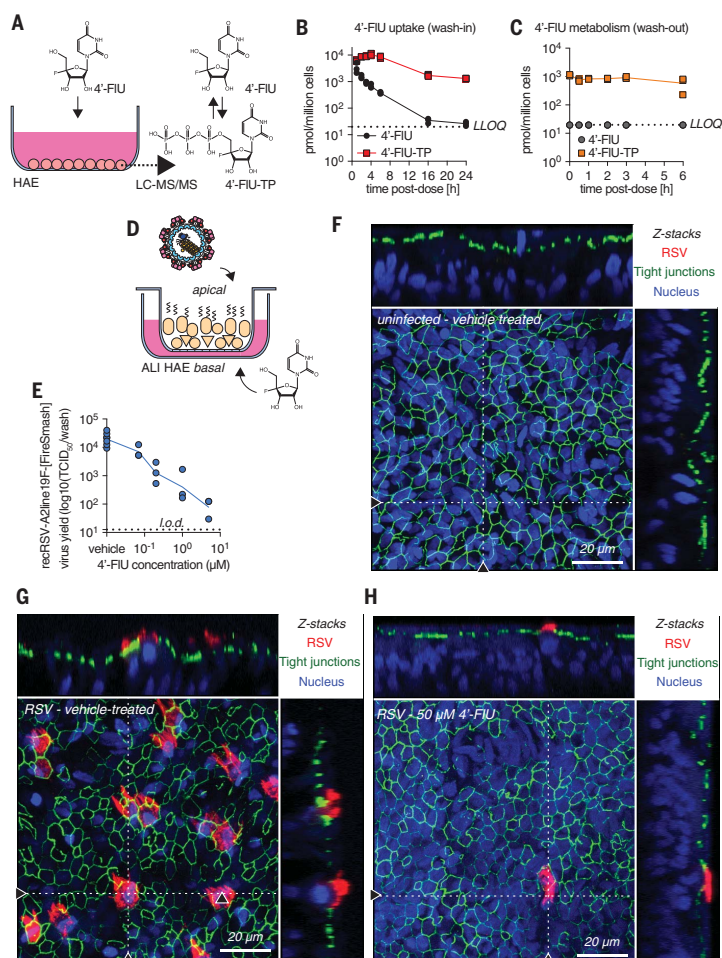


**Fig. 3. 4'-FIU is efficiently anabolized in HAE cells and is efficacious in human airway epithelium organoids.** (A to C) 4'-FIU cellular uptake and metabolism in "F1" HAE cells quantified by mass spectrometry (A). Intracellular concentration of 4'-FIU(-TP) after exposure to 20  $\mu$ M 4'-FIU for 0, 1, 2, 3, 4, 6, 16, and 24 hours (B), or 24-hour incubation followed by removal of the compound for 0, 0.5, 1, 2, 3, and 6 hours before quantification (C) ( $n = 3$ ). The low limit of quantitation (LLOQ) for 4'-FIU (19.83 pmol/ $10^6$  cells) is indicated by the dashed line. (D) HAE cells were matured at the air-liquid interface (ALI). (E) Virus yield reduction of recRSV-A2line19F-[FireSMASH] was shed from the apical side in ALI HAE after incubation with serial dilutions of 4'-FIU on the basal side ( $n = 3$ ). (F to H) Confocal microscopy of ALI HAE cells infected with recRSV-A2line19F-[FireSMASH], at 5 days after infection. RSV-infected cells, tight junctions, and nuclei were stained with anti-RSV, anti-ZO-1, and Hoechst 34580. z-stacks of 30 1- $\mu$ m slices with 63 $\times$  oil objective. Dotted lines, x-z and y-z stacks; scale bar, 20  $\mu$ m. In all panels, symbols represent independent biological repeats and lines represent means.

up to the third nucleotide, confirming that RSV RdRP recognizes and incorporates 4'-FIU in place of UTP (Fig. 2C). Incorporation kinetics (21) showed only a moderate reduction in substrate affinity for 4'-FIU-TP compared with UTP (Fig. 2D). Further addition

of CTP to the reaction mix resulted in limited elongation rather than the expected full-length product, which suggested delayed polymerase stalling by incorporated 4'-FIU (fig. S4 and data S1). Direct side-by-side comparison with GS-443902—the active metabolite of remdesivir



## RESEARCH | RESEARCH ARTICLE

and a “delayed polymerase stalling” inhibitor well characterized for SARS-CoV-2—along with RSV and other RNA viruses (21, 22), corroborated this antiviral effect of 4'-FIU-TP (Fig. 2E and data S1).

When a modified template coded for incorporation of only a single UTP (Fig. 2F and data S1), primers elongated preferentially to position  $i + 3$  after 4'-FIU-TP, whereas the efficiency of full elongation was strongly reduced compared with extension in the presence of UTP. However, repositioning the incorporation site further downstream in the template triggered immediate polymerase stalling at position  $i$  (fig. S5), indicating template sequence dependence of the inhibitory effect. Transcription stalling at  $i$  or  $i + 3$  was also observed after multiple 4'-FIU incorporations: An AxXxx template (Fig. 2G) and direct tandem incorporations through an AAXxX template (fig. S5) caused stalling at position  $i$ ,

whereas increasing spacer length between the incorporated uridines shifted preferential stalling to  $i+3$  (fig. S5). This variable delayed polymerase-stalling event within one to four nucleotides of the incorporation site was equally prominent when we examined de novo initiation of RNA synthesis at the promoter with a synthetic native RSV promoter sequence rather than extension of primer-template pairs (fig. S6).

Purification of a core SARS-CoV-2 polymerase complex [nonstructural proteins (nsp) 7, 8, and 12] from bacterial cell lysates (23, 24) (Fig. 2H) and assessment of RdRP bioactivity in equivalent primer-extension in vitro polymerase assays (Fig. 2I) again demonstrated incorporation of 4'-FIU-TP in place of UTP by the coronavirus RdRP (Fig. 2J), but there was no sign of immediate polymerase stalling. However, SARS-CoV-2 polymerase stalling was triggered by multiple incorporations of 4'-FIU-TP, and was particularly prominent when a sec-

ond incorporation of 4'-FIU-TP occurred at the  $i+4$  position (Fig. 2K and fig. S7). Primer extension was blocked when the nsp12 subunit was omitted or an nsp12 variant carrying mutations in the catalytic site was used, confirming specificity of the reaction (fig. S7 and data S1).

#### 4'-FIU is rapidly anabolized, metabolically stable, and potently antiviral in disease-relevant well-differentiated HAE cultures

Quantitation of 4'-FIU and its anabolites in primary HAE cells (Fig. 3A) demonstrated rapid intracellular accumulation of 4'-FIU, reaching a level of 3.42 nmol/million cells in the first hour of exposure (Fig. 3B). Anabolism to bioactive 4'-FIU-TP was efficient, resulting in concentrations of 10.38 nmol per million cells at peak (4 hours after start of exposure) and 1.31 nmol per million cells at plateau (24 hours). The anabolite was metabolically stable, remaining present in sustained concentrations of

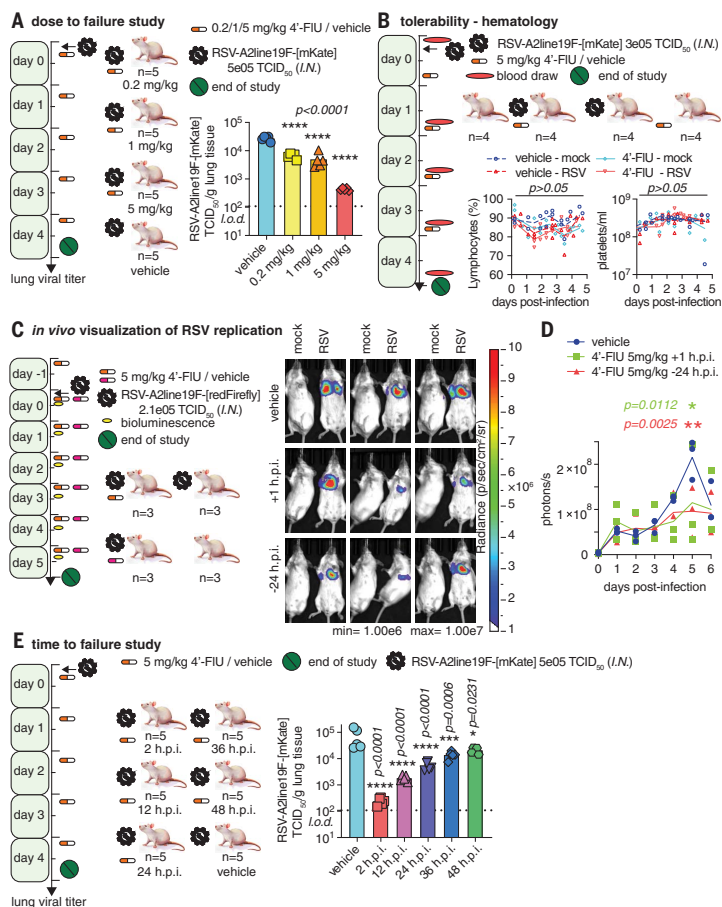


**Fig. 4. Therapeutic oral efficacy of 4'-FIU in the RSV mouse model.** (A) Balb/cJ mice were inoculated with recRSV-A2line19F-[mKate] and treated as indicated. At 4.5 days after infection, viral lung titers were determined with TCID<sub>50</sub> titration ( $n = 5$ ). (B) Balb/cJ mice were inoculated with recRSV-A2line19F-[mKate] or mock-infected, and treated as indicated. Blood samples were collected before infection and at 1.5, 2.5, 3.5, and 4.5 days after infection; lymphocyte proportions with platelets/ml are represented over time ( $n = 4$ ). (C) Balb/cJ mice were inoculated with recRSV-A2line19F-[redFirefly] and treated as indicated. In vivo luciferase activity was measured daily. (D) Total photon flux from mice lungs from (C) over time ( $n = 3$ ). (E) Balb/cJ mice were inoculated with recRSV-A2line19F-[mKate] and treated as indicated. At 4.5 days after infection, viral lung titers were determined with TCID<sub>50</sub> titration ( $n = 5$ ). In all panels, symbols represent individual values, and bars or lines represent means. One-way ordinary analysis of variance (ANOVA) with Tukey's post hoc multiple comparisons (B) and (I) or two-way ANOVA with Dunnett's post hoc multiple comparison (C) and (G). h.p.i., hours post-infection.

Downloaded from https://www.science.org at Georgia State University on April 29, 2024



## RESEARCH | RESEARCH ARTICLE

~1 nmol/million cells over a 6-hour monitoring period, corresponding to an extrapolated half-life of 9.7 hours (Fig. 3C).

To explore efficacy in a disease-relevant human tissue model, we cultured the HAEs at the air-liquid interface, inducing the formation of a well-differentiated three-dimensional (3D) airway epithelium that included ciliated and mucus-producing cells (25) (Fig. 3D). Adding 4'-FIU to the basolateral chamber of the transwells after apical infection of the epithelium with RSV potently reduced apical virus shedding with an EC<sub>50</sub> of 55 nM (Fig. 3E). Overall titer reduction spanned nearly four orders of magnitude, ranging from  $3.86 \times 10^4$  median tissue culture infectious dose (TCID<sub>50</sub>) in control cells to 78.18 TCID<sub>50</sub> at 5  $\mu$ M basolateral 4'-FIU, approaching the level of detection.

Confocal microscopy validated formation of a pseudostratified organization of the epithelium with tight junctions in the airway epithelium tissue model (Fig. 3F), visualized efficient RSV replication in vehicle-treated tissue models (Fig. 3G), and confirmed near-sterilizing antiviral efficacy in the presence of 50  $\mu$ M basolateral 4'-FIU (Fig. 3H and figs. S8 and S9). Under the latter conditions, positive staining for RSV antigens was rarely detected.

#### 4'-FIU is orally efficacious in a therapeutic dosing regimen in a small-animal model of RSV infection

To test 4'-FIU efficacy in vivo, we used the mouse model of RSV infection (supplementary text), challenging animals with reRSV-A2-L19F, which efficiently replicates in mice (16). In a dose-to-failure study, we infected BALB/cJ mice intranasally and initiated once-daily oral treatment 2 hours after infection at 0.2, 1, or 5 mg 4'-FIU per kilogram of body weight. Treatment at all dose levels resulted in a statistically significant reduction in lung virus load compared with vehicle-treated animals (Fig. 4A). The antiviral effect was dose dependent and approached nearly two orders of magnitude at the 5 mg/kg dose. Consistent with high metabolic stability in HAEs, a twice-daily dosing regimen did not significantly enhance efficacy (fig. S10). Because animal appearance, body weight, temperature (fig. S11), and relative lymphocyte and platelet counts (Fig. 4B and fig. S12) were unchanged in the 5 mg/kg group compared with vehicle-treated animals, we selected this dose for further studies.

For a longitudinal assessment of therapeutic benefit, we used an in vivo imaging system (IVIS) with a red-shifted luciferase (26) expressing an RSV reporter virus generated for this study. This assay allows for a noninvasive spatial appreciation of intrahost viral dissemination. Daily imaging (Fig. 4C and fig. S13) revealed considerable reduction of biolumi-

nescence intensity in lungs of 4'-FIU-treated animals at 5 days after infection, corresponding to peak viral replication, independent of whether treatment was initiated 24 hours before or 1 hour after infection (Fig. 4D). This IVIS profile is consistent with reduced viral replication and ameliorated viral pneumonia in treated animals.

To probe the therapeutic window of 4'-FIU, we initiated treatment at 2, 12, 24, 36, and 48 hours after infection. All treatment groups showed a statistically significant reduction of lung virus burden compared with vehicle-treated animals, but effect size was dependent on the time of treatment initiation (Fig. 4E and fig. S14). On the basis of our experience with

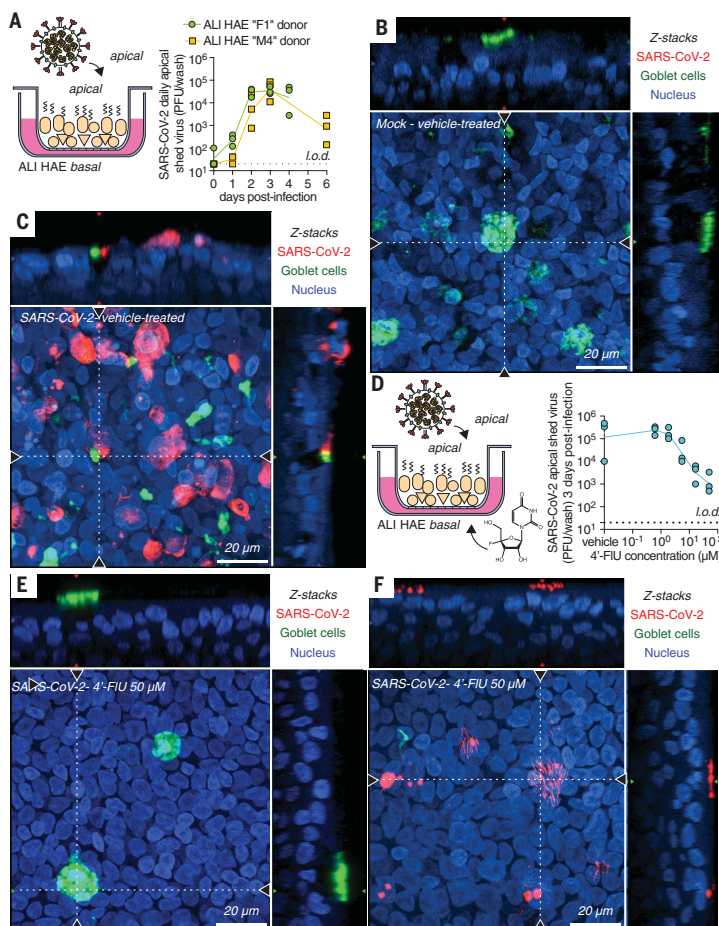


**Fig. 5. Efficacy of 4'-FIU against SARS-CoV-2 replication in HAE organoids.** (A) Multicycle growth curve of SARS-CoV-2 WA1 isolate on ALI HAE from two donors. Shed virus was harvested daily and titered by plaque assay ( $n = 3$ ). (B and C) Confocal microscopy of ALI HAE cells from "F1" donor mock-infected (B) or infected (C) with SARS-CoV-2 WA1 isolate, 3 days after infection. SARS-CoV-2 infected cells, goblet cells, and nuclei were stained with anti-SARS-CoV-2 N immunostaining, anti-MUC5AC immunostaining, and Hoechst 34580, pseudocolored in red, green, and blue, respectively. z-stacks of 35- $\mu$ m slices (1  $\mu$ m thick) with 63 $\times$  objective with oil immersion. Dotted lines represent the location of x-z and y-z stacks; scale bar, 20  $\mu$ m. In all panels, symbols represent independent biological repeats and lines represent means. (D) Virus yield reduction of SARS-CoV-2 WA1 clinical isolate shed from the apical side in ALI HAE after incubation with serial dilutions of 4'-FIU on the basal side ( $n = 3$ ). (E and F) Confocal microscopy of ALI HAE cells infected with SARS-CoV-2 WA1 isolate and treated with 50  $\mu$ M 4'-FIU 3 days after infection. Rare ciliated cells positive for N are represented in (F).

## RESEARCH | RESEARCH ARTICLE

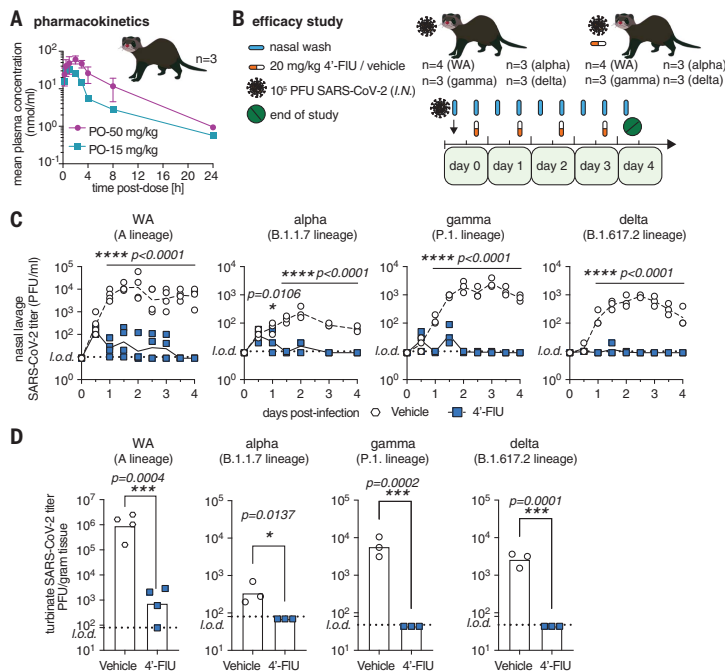


**Fig. 6. Therapeutic oral efficacy of 4'-FIU against different SARS-CoV-2 isolates in ferrets.** (A) Single oral dose (15 or 50 mg/kg bodyweight) pharmacokinetic properties of 4'-FIU in ferret plasma ( $n = 3$ ). (B) Ferrets were inoculated with SARS-CoV-2 WA1 or VoC alpha, gamma, or delta, and treated as indicated. (C) Nasal lavages were performed twice daily and viral titers were determined by plaque assay [ $n = 4$  (WA1) or  $n = 3$  (alpha, gamma, delta)]. (D) Viral titers in nasal turbinates 4 days after infection. In all panels, symbols represent individual independent biological repeats and lines show mean values. Two-way ANOVA with Sidak's post hoc multiple comparison (C) and unpaired  $t$  test (D).

therapeutic intervention in related respiratory RNA viruses that cause lethal disease (25), we required a reduction in lung virus load of at least one order of magnitude. With this constraint, the therapeutic window of 4'-FIU was extended to 24 hours after infection in mice.

#### 4'-FIU is effective against SARS-CoV-2 in HAE and the ferret model

To test activity against SARS-CoV-2 in the human airway organoids, we first confirmed that the WA1 isolate replicated efficiently in the HAEs of all donors tested (Fig. 5, A to C, and fig. S15). Treatment of infected organoids with basolateral 4'-FIU dose-dependently reduced apical virus shedding, albeit with a limited maximal effect size of ~ two orders of magnitude at 50  $\mu$ M (Fig. 5D). Confocal microscopy revealed that the epithelium was largely devoid of SARS-CoV-2 nucleocapsid proteins under these conditions (Fig. 5E), with only sporadic staining detectable in a small subset of ciliated cells (Fig. 5F and fig. S15).

To probe for a corresponding antiviral effect in vivo, we determined the efficacy of oral 4'-FIU against an early pandemic isolate (WA1) and VoC alpha, gamma, and delta in the ferret model (27), which recapitulates hallmarks of uncomplicated human infection (3). For dose level selection in ferrets, we determined single oral dose ferret pharmacokinetic (PK) profiles of 4'-FIU. When administered at 15 or 50 mg/kg, peak plasma concentrations ( $C_{max}$ ) of 4'-FIU reached 34.8 and 63.3  $\mu$ M, respectively, and overall exposure was  $154 \pm 27.6$  and  $413.1 \pm 78.1$  hours $\times$ nmol/ml, respectively, revealing good oral dose-proportionality (Fig. 6A and table S3). On the basis of this PK performance, we selected once-daily dosing at 20 mg/kg body weight for efficacy tests (Fig. 6B).

Intranasal infection of ferrets with  $1 \times 10^5$  PFU of each isolate resulted in rapid viral shedding into the upper respiratory tract, which plateaued in vehicle-treated animals 48 to 60 hours after infection (Fig. 6C). Therapeutic treatment with 4'-FIU initiated 12 hours

after infection reduced virus burden in nasal lavages by approximately three orders of magnitude (WA1) to <50 PFU/ml within 12 hours of treatment onset. All three VoC were highly sensitive to 4'-FIU, remaining below the level of detection 36 to 48 hours after onset of oral treatment. Viral titers in nasal turbinate tissue extracted 4 days after infection (Fig. 6D) and associated viral RNA copy numbers (fig. S16) correlated with this reduction in shed virus load. Shedding of infectious particles ceased completely in all animals after 2.5 days of treatment (3 days post-infection).

#### Conclusions

This study identifies and characterizes the ribonucleoside analog 4'-FIU, which potently inhibits pathogens of different clinically relevant negative and positive-sense RNA virus families. The compound causes delayed stalling of RSV and SARS-CoV-2 polymerases within in vitro RdRP assays, reminiscent of the antiviral effect of remdesivir (28, 29). However, 4'-FIU can also trigger immediate RdRP stalling depending on sequence context, suggesting steric hindrance of polymerase advance or of accommodating the next incoming nucleotide as the underlying MOA. We cannot exclude that additional effects further enhance the antiviral effect in cellula as proposed for other nucleoside analogs (30). Slightly lower sensitivity of SARS-CoV-2 to 4'-FIU compared with RSV could be a result of the exonuclease activity of the coronavirus polymerase, which can eliminate ribonucleoside analogs (31, 32). Alternatively, coronavirus RdRP may have a greater capacity to tolerate the compound, because SARS-CoV-2 RdRP showed a higher tendency than RSV polymerase to advance after 4'-FIU-TP incorporation in the RdRP assays, which do not contain exonuclease functionality.

Once-daily oral administration to mice and ferrets significantly reduced the burden of RSV and SARS-CoV-2, respectively, when treatment was initiated up to 24 (RSV) or 12 (SARS-CoV-2) hours after infection. Because RSV (33) and SARS-CoV-2 (34) host invasion is slower in humans, these data outline a viable therapeutic window for human treatment. Equally potent activity against SARS-CoV-2 VoC alpha, gamma, and delta demonstrated broad anticoronavirus efficacy of 4'-FIU, building confidence that the compound will remain active against future VoC that may be increasingly less responsive to spike-targeting vaccines or antibody therapeutics. Formal tolerability studies are pending, but 4'-FIU was well tolerated by the human organoid models and efficacious in murids and mustelids. Blood analysis of treated mice uncovered no anti-proliferative effect of 4'-FIU on the hematopoietic system. These results establish 4'-FIU as a broad-spectrum orally efficacious inhibitor

## RESEARCH | RESEARCH ARTICLE

of major RNA viruses, making it a promising therapeutic option for RSV disease and COVID-19, and a much-needed contributor to improvement of pandemic preparedness.

## REFERENCES AND NOTES

- J. H. Beigel *et al.*, *N. Engl. J. Med.* **383**, 1813–1826 (2020).
- M. Toots *et al.*, *Sci. Transl. Med.* **11**, eaab5866 (2019).
- R. M. Cox, J. D. Wolf, R. K. Plumper, *Nat. Microbiol.* **6**, 11–18 (2021).
- G. R. Painter *et al.*, *Antiviral Res.* **171**, 104597 (2019).
- T. P. Sheahan *et al.*, *Sci. Transl. Med.* **12**, eaab5883 (2020).
- A. R. Falsey, P. A. Hennessey, M. A. Formica, C. Cox, E. E. Walsh, *N. Engl. J. Med.* **352**, 1749–1759 (2005).
- B. Rha *et al.*, *Pediatrics* **146**, e20193611 (2020).
- T. Shi *et al.*, *J. Infect. Dis.* **222** (suppl. 7), S577–S583 (2020).
- T. Shi *et al.*, *Lancet* **390**, 946–958 (2017).
- G. S. Cockerill, J. A. D. Good, N. Matthews, *J. Med. Chem.* **62**, 3206–3227 (2019).
- R. Fearn, R. K. Plumper, *Virus Res.* **234**, 87–102 (2017).
- R. M. Cox *et al.*, *J. Biol. Chem.* **293**, 16761–16777 (2018).
- J. DeVincenzo *et al.*, *J. Infect. Dis.* **212**, 1676 (2016).
- J. J. Yoon *et al.*, *Antimicrob. Agents Chemother.* **62**, e00766-18 (2018).
- P. Richardson, *Expert Opin. Drug Discov.* **16**, 1261–1286 (2021).
- M. L. Moore *et al.*, *J. Virol.* **83**, 4185–4194 (2009).
- L. D. Marroquin, J. Hynes, J. A. Dykens, J. D. Jamieson, Y. Will, *Toxicol. Sci.* **97**, 539–547 (2007).
- S. P. Luby, *Antiviral Res.* **100**, 38–43 (2013).
- Based on the current knowledge of the pyrimidine salvage pathway, it must be assumed that the large excess of extracellular cytidine leads to conversion of CTP to UTP via cytidine deaminase (CDA), competing with 4'-FILL.
- B. Ludeke, R. Fearn, *Virology* **540**, 66–74 (2020).
- E. P. Tchesnokov, J. Y. Feng, D. P. Porter, M. Götte, *Viruses* **11**, 326 (2019).
- C. J. Gordon *et al.*, *J. Biol. Chem.* **295**, 6785–6797 (2020).
- T. L. Dangerfield, N. Z. Huang, K. A. Johnson, Expression and purification of tag-free SARS-CoV-2 RNA-dependent RNA polymerase in *Escherichia coli*. *STAR Protoc.* **2**, 100357 (2021).
- Our nsp12 preparations contain a mixture of 'GroEL' and 'tf' and nsp12 as described before, the latter representing 19% and 18% of the protein content of the preparations containing catalytically active and inactive nsp12, respectively.
- M. Toots *et al.*, *Transl. Res.* **218**, 16–28 (2020).
- S. M. Coleman, A. McGregor, *Future Virol.* **10**, 169–183 (2015).
- Male ferrets were not included in this study for practical reasons as they are territorial and available ABSL3 space cannot accommodate the number of cages that this study would require to achieve meaningful statistical power.
- G. Kocic *et al.*, *Nat. Commun.* **12**, 279 (2021).
- E. P. Tchesnokov *et al.*, *J. Biol. Chem.* **295**, 16156–16165 (2020).
- J. J. Feld, J. H. Hoofnagle, *Nature* **436**, 967–972 (2005).
- E. C. Smith, H. Blanc, M. C. Surdel, M. Vignuzzi, M. R. Denison, *PLoS Pathog.* **9**, e1003565 (2013).
- E. Minskaia *et al.*, *Proc. Natl. Acad. Sci. U.S.A.* **103**, 5108–5113 (2006).
- C. M. El Saleeby, A. J. Bush, L. M. Harrison, J. A. Aitken, J. P. Devincenzo, *J. Infect. Dis.* **204**, 996–1002 (2011).
- B. Oberfeld *et al.*, *Cell* **181**, 954–954.e1 (2020).

## ACKNOWLEDGMENTS

We thank C. F. Basler for providing the Calu-3 cells, D. Waugh for plasmid pRK792-encoding TEV protease (Addgene plasmid #8830), the Georgia State University High Containment Core and the Department for Animal Research for support, and A. L. Hammond for critical reading of the manuscript. **Funding:** This work was supported in part by Public Health Service grants AI153400, AI071002, and AI141222 (to R.K.P.) from the NIH/NIAID. The funders had no role in the study design, data collection and interpretation, or the decision to submit the work for publication. **Author contributions:** Conceptualization: M.G.N., G.R.P., and R.K.P. Investigation: J.S., R.M.C., M.T., J.Y., C.M.L., M.A., J.D.W., Z.S., and R.K.P. Resources: G.R.B., A.A.K., L.M.S., and R.K.P. Visualization: G.R.B. and J.S. Validation: J.S. and R.K.P.

**Funding acquisition:** R.K.P. **Project administration:** M.G.N. and R.K.P. **Supervision:** G.R.P. and R.K.P. **Writing – original draft:** J.S. and R.K.P. **Writing – review and editing:** J.S. and R.K.P. **Competing interests:** G.R.B. and G.R.P. are inventors on patent WO 2019/1736002 covering composition of matter and use of EIDD-2749 and its analogs as an antiviral treatment. This study could affect their personal financial status. All other authors declare that they have no competing interests. **Data and materials availability:** All data are available in the main text or the supplementary materials. Materials and methods are available as supplementary materials at the Science website. Transfer of EIDD-2749 material to other institutions for research purposes is covered by MTAs from Emory University. This work is licensed under a Creative Commons Attribution 4.0 International (CC BY 4.0) license, which permits unrestricted use, distribution, and reproduction in any medium, provided the original work is properly cited. To view a copy of this license, visit <https://creativecommons.org/licenses/by/4.0/>. This license does not apply to figures/photos/artwork or other content included in the article that is credited to a third party; obtain authorization from the rights holder before using such material.

## SUPPLEMENTARY MATERIALS

[science.org/doi/10.1126/science.abj5508](https://doi.org/10.1126/science.abj5508)

Materials and Methods  
Supplementary Text  
Figs. S1 to S18  
Tables S1 to S3  
References (35, 36)  
MDAR Reproducibility Checklist  
Data S1 and S2

[View/request a protocol for this paper from Bio-protocol.](#)

19 May 2021; resubmitted 4 October 2021  
Accepted 29 November 2021  
Published online 2 December 2021  
[10.1126/science.abj5508](https://doi.org/10.1126/science.abj5508)



Supplementary Materials for

**4'-Fluorouridine is an oral antiviral that blocks respiratory syncytial virus and SARS-CoV-2 replication**

Julien Sourimant *et al.*

Corresponding author: Richard K. Plemper, rplemper@gsu.edu

*Science* 375, 161 (2022)  
DOI: 10.1126/science.abj5508

**The PDF file includes:**

Materials and Methods  
Supplementary Text  
Figs. S1 to S18  
Tables S1 to S3  
References

**Other Supplementary Material for this manuscript includes the following:**

MDAR Reproducibility Checklist  
Data S1 and S2

## Materials and Methods

### Study design

The objectives of this study were to explore the mechanism of action and preclinical efficacy of the ribonucleoside analog 4'-FIU against RSV and SARS-CoV-2, using disease-relevant human airway epithelium models and appropriate animal models to assess bioavailability and antiviral efficacy, the mouse model for RSV and the ferret model for SARS-CoV-2. Treatment was considered efficacious when statistically significant reduction in virus titers in nasal lavages (ferrets) and respiratory tissues (mice and ferrets) was observed. Efficacy and cytotoxicity of the drug candidate in multiple cell lines including human airway epithelium were assessed by four-parameter variable-slope regression modeling of 50% inhibitory and cytotoxic concentrations. Timeline endpoints were predefined before initiation of experiments. The number of animals per group (3 to 5, as specified in each figure legend) in *in vivo* efficacy experiments was selected to provide sufficient statistical power to detect a significant biological effect such as a reduction in viral titers of at least one order of magnitude, based on our previous experience with these models. Before initiation of each individual study, animals were randomly assigned to treatment and control groups. No blinding was used. Primary numerical data are shown in Data S2.

### Experimental design of mice experiments

6-8-week old female Balb/cJ mice (Jackson laboratory, cat# 000651) were housed in an ABSL-2 facility and rested for 4-5 days. For efficacy studies, mice were randomly divided into groups (n=5) and infected intranasally with  $5 \times 10^5$  TCID<sub>50</sub> (25  $\mu$ l per nares) of recRSV-A2line19F-[mKate] in PBS while under anesthesia with ketamine/xylazine. Treatment (4'-FIU or vehicle) was administered at the indicated time post-infection via oral gavage in a 200  $\mu$ l suspension of 0.5% Tween80 in 10 mM sodium citrate in water. Temperature and food consumption were monitored daily, body weight was determined twice daily. All animals were euthanized at 4.5 days after infection and lungs were harvested. To determine lung viral titers, lungs were weighed and homogenized with a bead beater in 300  $\mu$ l PBS in 3 bursts of 20 seconds by 5-minute rest on ice after each cycle. Samples were clarified for 5 minutes at 4°C and 20,000 $\times$ g, supernatant aliquoted and stored at -80°C before being titrated by median tissue culture infectious dose (TCID<sub>50</sub>) normalized per gram of lung tissue and per ml of lysate. For *in vivo* live imaging, mice were infected with recRSV-A2line19F-[redFirefly] in PBS and treatment was initiated at the indicated time. Bioluminescence was monitored once daily at the indicated time after isoflurane anesthesia and retro-orbital injection with 100  $\mu$ l of 100 mg/ml D-luciferin (Goldbio). Acquisition was initiated 30s after substrate injection in an IVIS Spectrum (Caliper LifeSciences). Acquisition parameters were a sequence of 9 $\times$ 30-second exposures with medium binning (binning=8), small aperture (f=1) and large field of view (D - 22) using Living Image 4.5.4 Software for Windows 10. For tolerability studies, mice were infected with 300,000 TCID<sub>50</sub> recRSV-A2line19F-[mKate] or mock and treated with 5mg/kg mice body weight 4'-FIU at 12 hours post-infection once daily for 4 days. Blood samples were collected prior to infection and at 1.5, 2.5, 3.5, and 4.5 days post-infection. Complete blood counts were performed with a VETSCAN HM5 (Abaxis) following the manufacturer's protocol.

### Experimental design of ferret experiments

6-10-month old female ferrets (*Mustela putorius furo*; Triple F Farms) were used as an *in vivo* model to examine the therapeutic efficacy of orally administered 4'-FIU against SARS-CoV-2

infection. Group sizes of 3-4 ferrets were used for efficacy studies. Animals were randomly assigned to the different study groups. No blinding was performed. Viruses were administered to animals through intranasal inoculation. Ferrets were inoculated with SARS-CoV-2 ( $1 \times 10^5$  pfu of 2019-nCoV/USA-WA1/2020 or hCoV-19/USA/CA\_CDC\_5574/2020) in 1 ml (0.5 ml per nare). At 12 hours after infection, a group of ferrets was treated once daily (*q.d.*) with vehicle (10 mM sodium citrate with 0.5% (v/v) Tween 80) or 4'-FIU at a dosage of 20 mg kg<sup>-1</sup>, respectively. Nasal lavages were collected every 12 hours for all ferrets. Once daily dosing was continued for 4 days post infection. All animals were euthanized 4 days after the infection was started. Organs and tissues were harvested and stored at -80°C until processed.

For virus titration, samples were weighed and homogenized in sterile PBS. Tissue homogenates were clarified by centrifugation (2,000×g for 5 minutes at 4°C). The clarified supernatants were then harvested and used in plaque assays. For detection of viral RNA, total RNA was extracted from organs using a RNeasy mini kit (Qiagen), in accordance with the manufacturer's protocol. Total RNA was extracted from nasal lavages using a ZR viral RNA kit (Zymo Research) in accordance with the manufacturer's protocols. Virus titers were determined by plaque assays and viral RNA copy numbers were determined by RT-qPCR quantitation.

#### **SARS-CoV-2 RNA copy numbers**

Detection of SARS-CoV-2 RNA was performed using the nCoV\_IP2 primer-probe set (National Reference Center for Respiratory Viruses, Pasteur Institute). RT-qPCR reactions were performed on an Applied Biosystems 7500 real-time PCR system using the StepOnePlus real-time PCR system. Viral RNA was detected using the nCoV\_IP2 primer-probe set in combination with TaqMan fast virus 1-step master mix (Thermo Fisher Scientific). Viral RNA copy numbers were determined based on a standard curve created using a PCR fragment (nucleotides 12669–14146 of the SARS-CoV-2 genome) as previously described. The RNA values were normalized to the weights of the tissues used.

#### **Institutional Animal Care and Use Committee (IACUC) approval statement.**

All animal work was performed at Georgia State University in compliance with the Guide for the Care and Use of Laboratory Animals of the National Institutes of Health. Mouse work was approved by the GSU Institutional Animal Use and Care Committee (IACUC) under protocols A17019 and A20012, ferret work was approved under protocol A20031.

#### **Cells**

African green monkey kidney cells VeroE6 (ATCC® CRL-1586™), Vero/hSLAM (expressing human signaling lymphocytic activation molecule), Madin-Darby canine kidney cells (MDCK, ATCC® CCL-34™), human lung adenocarcinoma epithelial cells Calu-3 (ATCC® HTB-55™), human epithelial/HeLa contaminant HEp-2 cells (ATCC® CCL-23™), human bronchial epithelial BEAS-2B (ATCC® CRL-9609™) and baby hamster kidney cells (BHK-21; ATCC® CCL-10™) stably expressing either T7 polymerase (BSR-T7/5) or G protein of rabies virus strain SAD-B19 (BSR-RVG) were cultivated at 37°C and 5% CO<sub>2</sub> in Dulbecco's Modified Eagle's medium (DMEM) supplemented with 7.5% fetal bovine serum (FBS). Insect cells from *Spodoptera Frugiperda* (SF9, ATCC® CRL-1711™) were propagated in suspension using Sf-900 II serum-free media (SFM) (Thermo Scientific) at 28°C. All cell lines used in this study are routinely checked for mycoplasma and microbial contamination. Mammalian cell transfections were performed using GeneJuice transfection reagent (Invitrogen) while insect cell transfections

were performed using Cellfectin II transfection reagent (Gibco). Normal primary human bronchial/tracheal epithelial cells (HBTEC) from a 30-year old female (LifeLine Cell Technology, cat# LM-0050, lot# 3123, passage 2, “donor F1”) were grown in BronchiaLife cell culture medium (LifeLine Cell Technology). Normal human bronchial/tracheal epithelial cells (NHBE) (Lonza Bioscience, cat# CC-2540S, lot# 0000646466, passage 2, donor “M4”) from a 38 year-old male were cultured in PneumaCult-Ex Plus (Stemcell Technologies cat# 05040) following the manufacturer’s instructions.

### Plasmids

Plasmids to rescue recombinant RSV A2 with line19 F harboring a mKate reporter (labelled here as recRSV-A2line19F-[mKate]) or RSV A2 with line19 F with hyperfusogenic F\_D489E substitution and FireSMASH reporter (labelled here as recRSV-A2line19F-[FireSmash]) were previously described. To rescue a recombinant RSV harboring a red-shifted firefly luciferase (labelled as recRSV-A2line19F-[redFirefly]), we swapped the mKate reporter of the pSynkRSV-line19F vector with the redFirefly sequence in a succession of steps: 1) We fused immediately downstream of the redFirefly sequence from pCMV-Red Firefly (ThermoFisher Scientific cat. 16156) a sequence containing the RSV L noncoding region, L gene end, NS1/NS2 intergenic junction with a BlnI restriction site, mimicking the sequence downstream of mKate on the pSynkRSV-line19F vector. The assembly was used with NEBuilder (New England Biolabs) and the primer sets 5’- GCGGCCGCAAATCAGCC and 5’-TCATCACATCTTGCCACGG for pCMV-Red Firefly and with 5’- ccgtggccaagatgtgatgaGTATTCAATTATAGTTATTAATAAACTTAACAG) and 5’- gagctgatttgcggccgcGCTAAGCAAGGGAGTTAAATTTAAG for the downstream sequence with BlnI. 2) The sequence of redFirely and its downstream sequence up to the BlnI site were amplified by PCR to insert a second BlnI site immediately upstream of the redFirefly sequence using primers 5’-catcatGCTTAGCatggaaaatggaaaacg and 5’- gagctgatttgcggccgcGCTAAGCAAGGGAGTTAAATTTAAG, mimicking the sequence upstream of mKate on the pSynkRSV-line19F vector. The amplified product was digested with BlnI (New England Biolabs) and purified. 3) Since BlnI is not a unique site on the pSynkRSV-line19F vector, we generated an intermediate shuttle vector by inserting a fragment from pSynkRSV-line19F vector encompassing the leader promoter sequence to the nucleoprotein gene and containing mKate, by digesting it with AvrII (New England Biolabs) and PmeI (New England Biolabs). In parallel we digested and purified the backbone of a pCDNA 3.1 (ThermoFisher Scientific cat. V79020) with AvrII (New England Biolabs) and PmeI (New England Biolabs), and the two fragments were ligated with the t4 ligase ((New England Biolabs). 4) The shuttle vector was opened with BlnI to release the mKate segment and the backbone purified, and ligated to the purified amplicon of step (2) containing redFirefly. 5) The shuttle vector with redFirefly was opened with AvrI and PmeI and the insert ligated back to the backbone of the pSynkRSV-line19F vector. The final construct was confirmed with Sanger sequencing. For expression of SARS-CoV-2 nsp12, nsp8 and nsp7, SARS-CoV-2 RNA was isolated from stocks of isolate USA-WA1/2020 (BEI# NR-52281) and reverse transcribed using superscript III (Invitrogen). The resulting cDNA was used as a template for the amplification of nsp7, nsp8 and nsp12 encoding genes the primer 5’- CTGGACATATGGCAGCAGCCATCATCATCATCACAGCAGCGCGAAAACCTG TATTTTCAGGGCTCTAAAATGTCAGATGTAAAG and 5’- CTAGAGCGGCCCTATTGTAAGGTTGCCCTGTTG (nsp7), 5’-



CTGGATCTAGAAATAATTTTGTTTAACTTTAAGAAGGAGATATAATGGGCAGCAGCC ATCATCATCATCAT and 5'-CTAGAGCGGCCCGCCTACTGTAATTTGACAGCAGAATTG (nsp8), and 5'-CTGGACATATGTCAGCTGATGCACAATCG and 5'-CTAGACTCGAGGCCCTGAAAATACAGGTTTTTCGCCGCTGCTCTGTAAGACTGTATGC GGTG (nsp12). PCR amplified products were individually cloned into pET30a(+) expression vector (Novagen) with tobacco etch virus protease-cleavable 6×His tag at the N-terminus of nsp7 and nsp8, and at the C-terminus of nsp12 using appropriate restriction sites and cloning strategies, bringing the cloned genes under T7 promoter control. A catalytically inactive variant of nsp12 was generated by site-directed mutagenesis, modifying residues 762-SDD in the conserved catalytic motif C to 762-SNN with appropriately designed primers.

### Viruses

Recombinant RSVs were rescued as described previously; briefly, BSR-T7/5 cells were co-transfected with the cDNA genome along with helper plasmids encoding the RSV L, N, P and M2-1 protein, further amplified on HEp-2 cells after a freeze-thaw cycle and supernatant clarification (1800×g, 5 minutes, 4°C). Stocks were prepared as described previously by infecting 50% confluent HEp-2 cells in 15cm dishes at a multiplicity of infection (MOI) of 0.01 TCID<sub>50</sub>/cell, incubated at 37°C overnight then transferred to 32°C for five days. Infected cells were scraped, virions released with a freeze/thaw cycle and supernatant clarified (1800×g, 5 minutes, 4°C). Screening-grade stocks of recRSV-A2line19F-[FireSmash]) were grown in the presence of 3 μM asunaprevir to reduce accumulation of Firefly luciferase and further purified at the interface of a 20%/60% sucrose gradient in TNE buffer (50 mM Tris/Cl pH 7.2, 10 mM EDTA) with centrifugation at 30,000rpm on a SW41 rotor (Beckman Coulter) for 2 hours at 4°C. Clinical RSV B isolates 16F10 (GenBank: KY674983.1) and 6A8 (GenBank: MF001044.1) were a kind gift from A. Greninger. Samples were collected from patient nasal wash specimens in 2017, cultured on primary rhesus monkey kidney (RhMK) cells, and amplified once on HEp-2 cells prior to use in this study. RSV viral titers were determined using standard 50% tissue infective dose (TCID<sub>50</sub>) assay in HEp-2 cells and 96 well plates, with a Spearman and Karber based method using either fluorescence or immunostaining for detection. Recombinant measles virus strain Edmonston with nano luciferase reporter including a destabilizing PEST sequence (labelled here as recMeV-[N<sub>PEST</sub>luc]) was rescued and amplified on Vero/hSLAM cells. Recombinant respiroviruses human parainfluenza 3 virus with Nano luciferase reporter (HPIV3-JS NanoLuc, labelled here recHPIV-3-[Nluc]), Sendai virus with Gaussia luciferase reporter labelled here recSeV-[Gluc] were rescued and amplified on VeroE6 cells. Recombinant rhabdoviruses, vesicular stomatitis virus (Indiana strain) with Nano luciferase reporter (labelled here as recVSV-[Nluc]) and rabies virus strain SAD-B19 with G deletion and Nano luciferase reporter (labelled here as recRabV-[Nluc]) were rescued and authenticated through RT-PCR and Sanger-sequencing. SARS-CoV-2 early isolate USA-WA1/2020 (BEI# NR-52281) A lineage, and variants of concerns (VoC) alpha (isolate USA/CA\_CDC\_5574/2020 (BEI# NR-54011) B.1.1.7 lineage), gamma (isolate hCoV-19/Japan/TY7-503/2021 (BEI#: NR-54982) P.1. lineage) and delta (isolates hCoV-19/USA/PHC658/2021 (BEI#: NR-55611) (VeroE6 virus yield reduction) and GISAID 2333067 (efficacy in ferrets) lineage B.1.617.2), were sequence-validated and amplified on Calu-3 cells, in DMEM supplemented with 2% FBS following approved procedures in biosafety level 3 containment. Recombinant SARS-CoV-2 with USA-WA1/2020 genetic background expressing Nanoluciferase reporter, denoted recSARS-CoV-2-



[Nluc] in this manuscript, has been previously described (35).

#### **Minireplicon assays**

For RSV-derived minireplicon assays, a plasmid expressing the RSV minigenome containing the firefly luciferase reporter, under control of RNA pol I promoter, and a set of helper plasmids expressing codon-optimized RSV P, L, N and M2-1 proteins, under the control of CMV promoter, were co-transfected with GeneJuice reagent (Millipore Sigma) following manufacturer's instructions in 50% confluent HEK-293T cells. For dose-response experiments, cells were transfected in 96-well plate format. 3-fold serial dilutions of compounds 4'-FIU or NHC were prepared in triplicate using a Nimbus liquid handler (Hamilton) and transferred on transfected cells 4 hours post-transfection. At 48 hours post-transfection, luciferase activities were determined using ONE-Glo luciferase substrate (Promega) and a H1 synergy plate reader (BioTek). Each plate contained 4 wells of each positive and negative control (minireplicon with media containing dimethyl sulfoxide (DMSO) or minireplicon with L-expressing plasmid replaced by pCDNA3.1). Normalized luciferase activities were analyzed with the formula: % inhibition =  $(\text{Signal}_{\text{Sample}} - \text{Signal}_{\text{Min}}) / (\text{Signal}_{\text{Max}} - \text{Signal}_{\text{Min}}) \times 100$ , and dose response curves were further analyzed by normalized non-linear regression with variable slope to determine 50% effective concentration (EC<sub>50</sub>) and 95% CIs Prism 9.0.1 for MacOS (GraphPad). Similarly, luciferase activities from MeV strain Edmonston-based minireplicon (firefly luciferase), NiV minireplicon (Nano luciferase) and the recHPiV3-JS-NanoLuc (Nano luciferase, labelled in this context as HPiV3 maxireplicon), were transfected in BSR-T7/5 as previously described.

#### **Dose response antiviral assays**

For reporter-based dose-response assays, 3-fold serial dilutions of 4'-FIU or NHC were prepared in triplicate using a Nimbus liquid handler (Hamilton) and transferred to 96-well plates seeded the day before at 50% confluence in 96-well plate format. Immediately after addition of compound, cells were infected with either recRSV-A2line19F-[FireSmash], recMeV-[NPESTluc] recHPiV-3-[Nluc], recSeV-[Gluc], recVSV-[Nluc], or recRabV-[Nluc] at MOI 0.2 TCID<sub>50</sub>/cell. At 48 hours post-transfection, luciferase activities of reporter-expressing viruses were determined using either ONE-Glo luciferase substrate, Nano-Glo Dual-Luciferase substrate (Promega) and a H1 synergy plate reader (Biotek). Each plate contained 4 wells each of positive and negative control (infected cells with media containing DMSO or 100 μM cycloheximide, respectively). Normalized luciferase activities were analyzed with the formula: % inhibition =  $(\text{Signal}_{\text{Sample}} - \text{Signal}_{\text{Min}}) / (\text{Signal}_{\text{Max}} - \text{Signal}_{\text{Min}}) \times 100$ , and dose response curves were further analyzed by normalized non-linear regression with variable slope to determine 50% effective concentration (EC<sub>50</sub>) and 95% CIs with Prism 9.0.1 for MacOS (GraphPad). For RSV virus yield reduction, HEP-2 cells were infected with recRSV-A2line19F-[mKate] or clinical isolates in 12-well plate format at MOI 0.1 TCID<sub>50</sub>/cell for 2 hours at 37°C. Inoculum was removed and replaced with DMEM with 2% FBS and indicated concentrations of compound and cells were incubated for 3 days. Viral titers were determined by standard TCID<sub>50</sub> with fluorescence or immunostaining for detection. For SARS-CoV-2 virus yield reduction on VeroE6 cells, cells were seeded in 12-well plates (300,000 cells per well) the day before infection, infected at a MOI of 0.1 PFU/cell with a 1 hour absorption step and inoculum was removed and replaced with fresh DMEM with 2% FBS and indicated concentrations of 4'-FIU (vehicle: 0.1% DMSO). Infected cells were incubated with compound for 48 hours at 37 °C, followed by virus titration by standard plaque assay. Log viral titers were normalized using the average top plateau of viral

titers to define 100% and were analyzed with a non-linear regression with variable slope to determine EC<sub>50</sub> and 95% CIs with Prism 9.0.1 for MacOS (Graphpad).

#### **Cytotoxicity assays**

To determine the effect of compound on cell metabolism, HEp-2, MDCK, Beas-2B, or BHK-T7 cells were seeded at 50% confluence in 96-well plates and were incubated with 3-fold serial dilution of 4'-FIU from 500  $\mu$ M as described for dose-response assays, including positive and negative controls for normalization. After 48-hour incubation at 37°C, cells were incubated with PrestoBlue (ThermoFisher Scientific) for 1 hour at 37°C and fluorescence measured with a H1 synergy plate reader (Biotek). 50% cytotoxic concentrations (CC<sub>50</sub>) and 95% CIs after normalized non-linear regression and variable slope were determined using Prism 9.0.1 for MacOS (GraphPad). To uncover potential mitochondrial toxicity masked by the Crabtree effect, BEAS-2B cells were also incubated in the presence of glucose-free RPMI media supplemented with galactose as carbohydrate source. To further assess the potential inhibitory effect on mitochondrial and nuclear polymerases, HBTEC cells were seeded at 50% confluence in 96 well plates and incubated with 3-fold dilutions of compound, and intracellular concentration of two mitochondrial proteins, the mitochondrial DNA-encoded COX-I and the nuclear DNA-encoded SDH-A was determined with the in-cell ELISA Mitobiogenesis kit following the manufacturer's instructions (Abcam cat# ab110217).

#### **Ribonucleotide competition of RSV inhibition**

HEp-2 cells were infected with RSV-A2line19F-[FireSMASH] at a MOI of 0.1 TCID<sub>50</sub>/cell, maintenance media was supplemented with 4'-FIU at 10  $\mu$ M alone or in combination with 0.1 to 300  $\mu$ M exogenous ribonucleosides (Sigma-Aldrich). Firefly luciferase reporter activity was quantified at 48 hours post-infection. Values are expressed relative to the values for the vehicle-treated samples.

#### **Recombinant RSV L and P protein production and purification**

For purification of RSV L and P proteins (A2 strain), a pFastBac Dual plasmid (Invitrogen) containing the codon-optimized open reading frames of L and P proteins under the control of polyhedrin and p10 promoters, respectively, was used to recover recombinant baculoviruses using the Bac-to-Bac Baculovirus Expression System and SF9 cells. The P protein sequence contains a C-terminal 6-histidines tag separated by a tobacco etch virus (TEV) cleavage site, allowing co-purification of L-P complexes by immobilized metal affinity chromatography (IMAC). SF9 cells were infected in suspension with MOI 1 PFU/cell for 72-80 hours, pelleted and gently lysed on ice for 45 minutes with a buffer containing 50 mM NaH<sub>2</sub>PO<sub>4</sub> [pH 8.0], 150 mM NaCl, 20 mM imidazole, 0.5% NP-40 with Pierce Protease Inhibitor and Pierce universal nuclease (ThermoFisher Scientific). Clarified lysates (30 minutes, 15,000 $\times$ g, 4°C) were incubated for 2 hours with shaking with pre-equilibrated HisPur Ni-NTA Resin (ThermoFisher Scientific). After 5 washes with 10 bed volumes of lysis buffer with 60 mM imidazole, proteins were eluted with 3 bed volumes of lysis buffer with 250 mM imidazole. Eluates were dialyzed overnight in storage buffer: 20 mM Tris-HCl [pH 7.4], 150 mM NaCl, 10% glycerol, 1 mM dithiothreitol, aliquoted and stored at -80°C. Uncropped SDS-PAGE scans are available in Data S1.

#### **Recombinant SARS-CoV-2 nsp7, nsp8, and nsp12 protein production and purification**

The sequence confirmed constructs of nsp7 and nsp8 were transformed into BL21(DE3)pLysS cells. For the expression of nsp12 in *E. coli*, first chaperon plasmid pG-Tf2 (Takara Biosciences) was transformed into BL21 cells to enhance correct folding and solubility of recombinant proteins, followed by transformation with pET30a-nsp12 plasmid. The transformed cells were grown in Luria-Bertani (LB) broth for nsp7 and nsp8 at 37°C until the OD<sub>600</sub> reached 0.6. nsp7 and nsp8 cultures were induced with 0.5 mM isopropyl β-d-1-thiogalactopyranoside (IPTG) (Teknova) and the temperature was reduced to 18°C. The expression culture was grown for ~16 hours. nsp12 expression was performed by growing the cells in Terrific broth (TB) at 37°C until the OD<sub>600</sub> reached 0.6. Tetracycline was added to a final concentration of 10 ng/ml and the temperature was reduced to 18°C. After half an hour incubation, 0.5 mM IPTG was added to the culture and incubated at 18°C for ~16 hours. Cells were harvested by centrifugation and the cell pellet was stored at -20°C until further use. The cell pellet was resuspended in lysis buffer (Tris 50 mM pH 8.0, NaCl 200 mM, glycerol 10%, 20 mM imidazole, protease inhibitor cocktail (Pierce), Pierce universal nuclease (ThermoFisher Scientific)) with 0.3mg/ml lysozyme and incubated on ice for ~20 minutes. The samples were sonicated for ~6-8 minutes. Cell debris were separated by centrifugation at 14,000×g for 30 minutes, clarified supernatant collected, and loaded on to HisPur Ni-NTA resin (ThermoFisher Scientific) pre-equilibrated with lysis buffer and incubated for ~45 minutes at 4°C. Beads were washed extensively with wash buffer (Tris 50 mM pH 8.0, NaCl 200 mM, 10% glycerol containing 20-100 mM imidazole), and proteins eluted with Tris 50 mM pH 8.0, NaCl 200 mM, glycerol 10% containing 250 mM imidazole. The purified fractions were pooled, and the histidine tag was cleaved by adding TEV protease to the purified protein which was also simultaneously dialyzed overnight against the 1 L dialysis buffer (Tris 30 mM pH 7.4, NaCl 150 mM, glycerol 10%). Dialyzed 6×His tag cleaved proteins were re-incubated with HisPur Ni-NTA resin pre-equilibrated with Tris 50 mM pH 7.4, NaCl 200 mM, glycerol 10%, 20mM imidazole for 15 minutes. Flow through containing the tag cleaved proteins was collected and the resin was further washed with buffer containing imidazole. The desired His tag cleaved fractions were pooled and dialyzed against storage buffer (Tris 25 mM pH 7.4, NaCl 150 mM, glycerol 10%, DTT 1 mM) at 4°C overnight. The proteins were concentrated to final concentrations of 60, 30 and 6 μM for nsp7, nsp8 and nsp12 respectively, flash frozen and stored at -80°C for further use. Two additional polypeptides that co-purified with nsp12 likely represent host Gro-EL (60 kDa) and trigger factor (Tf) (56 kDa) proteins. Uncropped SDS-PAGE scans are available in Data S1.

#### ***In vitro* RNA synthesis assays**

3' primer-extension assays were performed based on an established assay with modifications. Briefly, purified polymerase complexes (100-200 ng of L protein) were incubated in 5 μl final volume with a transcription buffer containing 20 mM Tris-HCl pH 7.4 [RT], 30 mM NaCl, 10% glycerol, 1 mM dithiothreitol, 8 mM MgCl<sub>2</sub>, 4 μM RNA template, 20 μM RNA primer, indicated concentrations of nucleotides and 1 μCi of (alpha)32P-labelled ATP (Perkin-Elmer). HPLC-purified 5' phosphorylated RNA templates and non-phosphorylated RNA primers (Sigma-Aldrich) were used to reduce non-specific extension of the template. Reactions were performed for 1 hour at 30°C and the reaction was stopped with 1 volume of deionized formamide with 25 mM ethylenediaminetetraacetic acid (EDTA). Following 5 minutes denaturation at 95 °C, samples were separated by 7M urea Tris-Borate-EDTA 20% polyacrylamide gel electrophoresis and visualized by autoradiography with X-ray films (CL-Xposure, ThermoFisher Scientific) or with a storage phosphor screen BAS IP MS 2040 E (GE Healthcare Life Sciences) and imaged

with Typhoon FLA 7000 (GE Healthcare Life Sciences). Densitometry analysis was performed using FIJI 2.1.0. For quantifications of nucleotide incorporation kinetics, the intensity of each band corresponding to a primer-extension product was individually measured for each lane, and either the band corresponding to the UTP incorporation or the pooled primer-extension products following initial UTP incorporation were normalized to the pooled intensities of all the primer-extension products in that lane. As an optional assistance to data visualization, we implemented the following color-coding: 0-25% red, 25-75% orange, 75-125% grey, >125%: blue. Enzyme kinetics ( $V_{max}$  and  $K_m$ ) were determined using the Michaelis-Menten equation with Prism 9.0.0 for macOS (GraphPad). Nucleoside selectivity was determined using the nucleotide analog/nucleotide ratio of each  $V_{max}/K_m$  ratio. For side-by-side comparison of elongation products, reactions were performed as previously noted with saturating concentration of 300  $\mu$ M of UTP or 4'-FIU-TP. Each band corresponding to a primer-extended product containing 4'-FIU-TP was directly normalized to the equivalent UTP-containing band. For *de novo* RNA synthesis, an RNA template corresponding to the 25 nt of the RSV trailer complement sequence was incubated at 2  $\mu$ M with RSV RdRP (100-200 ng of L), 8 mM  $MgCl_2$ , 1 mM dithiothreitol, indicated concentrations of each nucleotides and 10  $\mu$ Ci of (alpha) $^{32}P$ -labelled GTP (Perkin-Elmer), 20 mM Tris-HCl [pH 7.4], 15 mM NaCl, 10 % glycerol. Reactions were equilibrated 5 minutes at 30°C before addition of RSV RdRP, then incubated at 30°C for 3 hours. RNAs were precipitated overnight at -20°C with 2.5 volumes of ethanol, 0.1 volume of 3M sodium acetate plus 625 ng of glycogen (ThermoFisher Scientific). Pellets were washed with 75% ethanol, dried and resuspended in 10  $\mu$ l of 50% deionized formamide. After 5 minutes denaturation at 95°C, RNAs were separated as described previously and visualized by autoradiography using CL-XPosure™ Film (ThermoFisher Scientific). SARS-CoV-2 polymerase *in vitro* assays were set up analogous to the protocol described above. All three separately purified proteins nsp7 (6  $\mu$ M), nsp8 (3  $\mu$ M) and nsp12 (300 nM) were incubated in 20 mM Tris-HCl pH 7.4, 10% glycerol, 1 mM dithiothreitol, 5 mM  $MgCl_2$ , 1  $\mu$ M RNA template, 20  $\mu$ M RNA primer, 20 nM ATP, 20 nM CTP and 1  $\mu$ Ci of (alpha) $^{32}P$ -labelled ATP (Perkin-Elmer). Primer-template sets were used as described above. For the comparison of primer extension reaction 200 nM of UTP or 4'-FIU-TP was used. Uncropped autoradiograms including biological repeats are available in Data S1. GS-443902 (remdesivir triphosphate) was provided by MedChemExpress cat# HY-126303C.

#### Cellular uptake and anabolism

$10^5$  HBTECs were seeded per well in 24-well plates. The next day the media was supplemented with 20  $\mu$ M 4'-FIU or vehicle (DMSO). For wash-in studies, cell culture media was removed at the indicated time-point and cells were washed twice with Dulbecco's modified phosphate buffered saline without calcium and magnesium (DPBS) and harvested using 500  $\mu$ l of ice-cold 70% methanol. Cellular extracts were clarified by centrifugation at 16,000 $\times$ g for 10 minutes at 4°C and stored at -20°C until further analysis. For wash-out studies, cells were incubated in the presence of 20  $\mu$ M 4'-FIU or vehicle (DMSO) for 24 hours, then washed twice with DPBS and incubated with maintenance media for the indicated time point before harvesting. 4'-FIU and 4'-FIU-TP anabolite were quantitated by qualified internal standard-based LC-MS/MS method using an Agilent 1200 system (Agilent Technologies) equipped with a SeQuant ZIC-pHILIC column (The Nest Group). MS analysis was performed on a QTrap 5500 mass spectrometer (AB Sciex) using negative-mode electrospray ionization (ESI) in the multiple-reaction-monitoring (MRM) mode. Data analysis was done with Analyst software (AB Sciex). The lower limit of

quantitation (LLOQ) for 4'-FIU was 1.04 ng/ml of the cell extraction solution, which corresponded to 19.83 pmol/10<sup>6</sup> cells in these experiments.

#### **Air-liquid interfaces of primary human airway epithelial (HAE) cells**

30,000 HBTEC or NHBE cells at passage 2 were seeded on 6 mm 0.4 µm pore size polyester inserts (Corning Costar Transwell) and differentiated at an air-liquid interface using Air-Liquid Interface Differentiation Medium (Lifeline cell technology, cat# LL-0023) for the former or Pneumacult-ALI (Stemcell Technologies cat# 05001) according to the manufacturer's instruction. Transepithelial electrical resistance was monitored using the EVOM instrument and STX2 electrode (World Precision Instrument).

#### **Apical shed viral titer determination**

Differentiated primary cells were washed on the apical side with phosphate-buffered saline (PBS) without calcium and magnesium. Cells were infected apically either with recRSV-A2line19F-[mKate] (500,000 TCID<sub>50</sub>) or SARS-CoV-2 for (40,000 PFU) for 2 hours at 37°C. Compound was added in the basal media at the indicated concentrations and 0.1% final DMSO. To harvest shed virus, ALI-HAE cells were incubated apically with 200 µl Dulbecco's phosphate-buffered saline without calcium and magnesium at 37°C for 30 minutes, aliquoted and stored at -80°C before titration. For RSV, shed viruses were harvested at peak at day 3 post-infection, and titered by standard TCID<sub>50</sub>. For SARS-CoV-2, samples were harvested at 24, 48, 72 and 96 hours post-infection ("donor F1") or 24, 48, 72 and 144 hours post-infection ("donor M4"). For SARS-CoV-2 titration, VeroE6 cells were seeded in 12-well plates at 200,000 cells per well. The next day, samples were thawed and serially diluted three times with 10-fold dilutions in DMEM. VeroE6 cell-culture media was removed and cells were incubated with 100 µl of diluted inoculum with rocking every 10 minutes for 1 hour at 37°C. The overlay medium (DMEM+2% FBS+1.2% microcrystalline cellulose Avicel 581-NF (FMC)) was added on the cells and the plates were incubated for three days at 37°C. The plaques were revealed after two washes with PBS, 1-hour fixation with 10% neutral buffered formalin, and 15 minutes coloration with a 1% crystal violet solution in 20% ethanol.

#### **Antibodies**

For immunostaining of infected cells in virus titer determination, fixed and permeabilized cells were successively stained with goat anti-RSV 1:1000 (Millipore Sigma, cat. AB1128) followed by donkey anti-goat HRP-coupled 1:1000 (Jackson ImmunoResearch cat. 705-035-147) and infected cells were visualized with Trueblue peroxidase substrate according to the manufacturer's instructions (KPL). For RSV confocal microscopy experiments, fixed and permeabilized cells were stained with mouse anti-(human) ZO-1 1:50 (BD Biosciences, cat. 610966), goat anti-RSV 1:1000 (Millipore Sigma, cat. AB1128), rabbit anti-beta IV Tubulin recombinant antibody Alexa Fluor® 647-conjugated [EPR16775] 1:100 (Abcam, cat. ab204034) followed by donkey anti-goat Alexa Fluor 568 1:500 (ThermoFisher Scientific, cat. A-11057) and rabbit anti-mouse IgG (H+L) cross-adsorbed secondary antibody, Alexa Fluor 488 1:500 (ThermoFisher Scientific, cat. A1059). For SARS-CoV-2 confocal microscopy, cells were stained with rabbit anti-SARS-CoV-2 Nucleocapsid monoclonal antibody (HL453) (Invitrogen, MA5-36272) 1:100 and mouse anti-MUC5AC 1:200 (ThermoFisher MA5-12175), followed by donkey anti-goat Alexa Fluor 568 1:500 (ThermoFisher Scientific, cat. A-11057) and rabbit anti-

mouse IgG (H+L) Cross-Adsorbed Secondary Antibody, Alexa Fluor 488 1:500 (ThermoFisher Scientific, cat. A-11059).

#### **Confocal microscopy**

Differentiated human airway epithelial cells were either infected (or mock-infected) with recRSV-A2line19F-[FireSmash] (500,000 TCID<sub>50</sub>), washed with PBS daily and fixed at 5 days post-infection with 200  $\mu$ l of 4% paraformaldehyde in PBS for 1 hour at RT, or were infected (or mock-infected) with 40,000 plaque-forming units of SARS-CoV-2 isolate USA-WA1/2020 (BEI# NR-52281) and fixed at day 3 post-infection. Cells were permeabilized for 20 minutes with PBS with 0.1% Triton X-100 and 3% bovine serum albumin (BSA). After three 5-minute washes with wash buffer (PBS with 0.3% BSA), cells were incubated with 100  $\mu$ l of primary antibody in wash buffer for 1 hour at RT. After 3 $\times$ 5 minutes 200  $\mu$ l washes with wash buffer, cells were incubated with secondary antibody in wash buffer for 1 hour at RT. Cells were washed and incubated with Hoechst 34580 at 1/1000 in wash buffer for 5 minutes. After three 5-minute washes with wash buffer, membranes were cut and mounted between glass slides and coverslips using Prolong Diamond antifade mountant (ThermoFisher Scientific) and edges were sealed with nail polish. Image capture were performed with a Zeiss LSM 800 confocal microscope coupled with an Airyscan module and the Zeiss Zen Blue software.

#### **Statistical analysis**

Source data for all numerical assays conducted in this study are provided in Data S2. Excel and GraphPad Prism software packages were used for data analysis. One-way and two-way ANOVA or mixed-effects model analysis as appropriate with Tukey's, Sidak's or Dunnett's multiple comparisons post-hoc tests without further adjustments - as specified in figure legends - were used to evaluate statistical significance when more than two groups or two parameters were compared. The specific statistical test applied to individual studies is specified in figure legends. When calculating antiviral potency and cytotoxicity, effective concentrations were calculated from dose-response data sets through 4-parameter variable slope regression modeling, and values are expressed with 95% CIs when they could be determined. Biological repeat refers to measurements taken from distinct samples, and results obtained for each biological repeat are shown in the figures along with the exact sample size (n). For all experiments, the statistical significance level alpha was set to <0.05, exact P values are shown in individual graphs.

#### **Synthetic chemistry**

5'-Deoxy-5'-iodouridine (Fig. S16). A 1 L three-necked round-bottomed flask flushed with argon and fitted with a thermometer and addition funnel was charged with uridine (35 g, 143 mmol), triphenylphosphine (56.4 g, 215 mmol), imidazole (14.64 g, 215 mmol), and anhydrous THF (400 ml). The suspension was stirred vigorously for 30 minutes while cooling to 0°C and then treated with a THF (100 ml) solution of iodine (40 g, 157.7 mmol) dropwise over a 2-hour period. The mixture was warmed to room temperature. After 16 hours, tlc (10% methanol in methylene chloride) indicated complete consumption of starting uridine. The mixture was concentrated under vacuum followed by a solvent exchange with isopropanol (400 ml). Upon cooling with an ice-bath the product precipitated out of solution as a white solid which was collected by vacuum filtration and washed with ice-cold isopropanol (150 ml) followed by hexanes (100 ml) to give 5'-deoxy-5'-uridine (35 g, 69% yield).

$^1\text{H}$  NMR (400 MHz,  $\text{DMSO-}d_6$ )  $\delta$  11.40 (s, 1H), 7.68 (d,  $J = 8.1$  Hz, 1H), 5.80 (d,  $J = 5.9$  Hz, 1H), 5.68 (dd,  $J = 8.0, 2.2$  Hz, 1H), 5.50 (d,  $J = 5.8$  Hz, 1H), 5.38 (d,  $J = 5.0$  Hz, 1H), 4.19 (q,  $J = 5.7$  Hz, 1H), 3.86 (dq,  $J = 14.0, 4.5$  Hz, 2H), 3.55 (dd,  $J = 10.5, 5.4$  Hz, 1H), 3.40 (dd,  $J = 10.5, 6.5$  Hz, 1H).

4',5'-Didehydro-5'-deoxyuridine (Fig. S16). In a 1 L round-bottomed flask, a suspension of 5'-deoxy-5'-iodouridine (34.55 g, 226 mmol) in methanol (350 ml) was treated with sodium methoxide (67.3 ml, 293 mmol). Upon heating to 60°C the mixture became homogeneous. After 3.5 hours, the mixture was cooled to room temperature and acidified to pH 7 by treating with dry ice. The mixture was filtered, concentrated under vacuum and then purified by column chromatography over silica gel using a mobile phase of 10% methanol in methylene chloride to give 4',5'-Didehydro-5'-deoxyuridine (11.2 g, 51% yield) as a white solid.

$^1\text{H}$  NMR (400 MHz,  $\text{DMSO-}d_6$ )  $\delta$  11.44 (s, 1H), 7.59 (d,  $J = 8.1$  Hz, 1H), 5.96 (d,  $J = 5.4$  Hz, 1H), 5.64 (d,  $J = 8.1$  Hz, 1H), 5.60 (d,  $J = 5.8$  Hz, 1H), 5.46 (d,  $J = 5.7$  Hz, 1H), 4.38 (t,  $J = 5.5$  Hz, 1H), 4.33 (s, 1H), 4.24 (q,  $J = 5.5$  Hz, 1H), 4.17 (d,  $J = 1.8$  Hz, 1H).

5'-Deoxy-4'-fluoro-5'-iodouridine (Fig. S16). An oven-dried 500 ml round-bottomed flask was charged with 4',5'-didehydro-5'-deoxyuridine (6.55 g, 29 mmol) and anhydrous acetonitrile (60 ml). The suspension was stirred vigorously for 30 minutes, cooled to 0°C under argon and then treated with triethylamine-trihydrofluoride (2.36 ml, 14.5 mmol) followed by the addition of *N*-iodosuccinimide (8.47 g, 37.7 mmol). After 1 hour at 0°C, the mixture was warmed to room temperature for 16 hours and then filtered. The collected solid was washed with methylene chloride (75 ml) followed by ether (75 ml) and then dried under high vacuum to give 5'-deoxy-4'-fluoro-5'-iodouridine (4.2 g, 40%) as an off-white solid.

$^1\text{H}$  NMR (400 MHz,  $\text{Methanol-}d_4$ )  $\delta$  7.77 (d,  $J = 8.1$  Hz, 1H), 6.05 (s, 1H), 5.69 (d,  $J = 8.1$  Hz, 1H), 4.43 (dd,  $J = 18.2, 6.5$  Hz, 1H), 4.25 (d,  $J = 6.6$  Hz, 1H), 3.85 – 3.63 (m, 2H).

$^{19}\text{F}$  NMR (376 MHz,  $\text{Methanol-}d_4$ )  $\delta$  -112.49 (ddd,  $J = 20.9, 18.1, 6.1$  Hz).

2',3'-Di-*O*-acetyl-5'-deoxy-4'-fluoro-5'-iodouridine (Fig. S16). A 500 ml round-bottomed flask was charged with 5'-deoxy-5'-iodo-4'-fluorouridine (15 g, 40.3 mmol), 4-dimethylaminopyridine (250 mg, 2.02 mmol), triethylamine (16.8 ml, 120.9 mmol) and methylene chloride (200 ml). The mixture was treated dropwise with acetic anhydride (11.4 ml, 120.9 mmol) while maintaining a reaction temperature below 30°C. After 3 hours at room temperature, the reaction mixture was quenched with saturated sodium bicarbonate solution. The organic layer was separated, washed with water followed by 1N HCl, dried and concentrated under vacuum to give 2',3'-di-*O*-acetyl-5'-deoxy-4'-fluoro-5'-iodouridine (16 g, 87%) as an off-white solid.

$^1\text{H}$  NMR (400 MHz,  $\text{DMSO-}d_6$ )  $\delta$  11.60 (d,  $J = 2.1$  Hz, 1H), 7.77 (d,  $J = 8.0$  Hz, 1H), 6.03 (d,  $J = 2.4$  Hz, 1H), 5.83 – 5.67 (m, 2H), 5.57 (dd,  $J = 7.4, 2.4$  Hz, 1H), 3.63 (dd,  $J = 11.8, 8.2$  Hz, 1H), 3.51 (dd,  $J = 22.9, 11.8$  Hz, 1H), 2.09 (s, 6H).

$^{19}\text{F}$  NMR (376 MHz,  $\text{DMSO-}d_6$ )  $\delta$  -105.54 (m).

5'-(3-Chlorobenzoyloxy)-2',3'-di-*O*-acetyl-4'-fluorouridine (Fig. S16). A 100 ml round-bottomed flask was charged with tetrabutylammonium hydrogen sulfate (3.64 g, 10.7 mmol) 1-[(4*R*,6*R*)-4'-Fluoro-4-(iodomethyl)-2,2-dimethyl-6,6a-dihydro-3*H*-furo[3,4-*d*][1,3]dioxol-6-yl]pyrimidine-2,4-dione (11.7g, 28.39mmol), 3-chlorobenzoic acid (1.76 g, 11.2 mmol), potassium phosphate dibasic (1.68 g, 9.65 mmol) and water (11 ml). After stirring for 20 minutes, the mixture was treated with a methylene chloride (30 ml) solution of 2',3'-di-*O*-acetyl-5'-deoxy-4'-fluoro-5'-iodouridine (2.00 g, 4.38 mmol) followed by the addition of 3-chloroperoxybenzoic acid (4.93 g, 22.0 mmol) in 4 portions over a 30-minute period. The

mixture continued to stir at RT for 16 hours. The mixture was periodically treated with additional potassium phosphate dibasic to maintain pH 3.5. The reaction mixture was quenched by addition of sodium sulfite (5 g) in small portions while maintaining a reaction temperature below 30°C. After stirring for an additional 15 minutes, the mixture was filtered through a pad of Celite. The aqueous layer of the filtrate was extracted with methylene chloride (2 × 15 ml), and then combined organic layers were concentrated under vacuum. The resulting residue was redissolved in ethyl acetate (100 ml) and washed with 1N HCl (2 × 50 ml) followed by saturated sodium carbonate solution (2 × 50 ml). The organic layer was concentrated and the resulting solid purified by column chromatography over silica gel (21 mm x 160 mm) using an ethyl acetate/hexane gradient to give 5'-(3-chlorobenzoyloxy)-2',3'-di-*O*-acetyl-4'-fluorouridine (1.1 g, 52% yield) as a white solid.

<sup>1</sup>H NMR (400 MHz, DMSO-*d*<sub>6</sub>) δ 11.59 (s, 1H), 7.94 (d, *J* = 7.7 Hz, 1H), 7.89 (s, 1H), 7.78 (d, *J* = 8.1 Hz, 2H), 7.60 (t, *J* = 7.9 Hz, 1H), 6.10 (s, 1H), 5.94 (dd, *J* = 20.2, 7.4 Hz, 1H), 5.64 (dd, *J* = 30.4, 7.6 Hz, 2H), 4.73 – 4.48 (m, 2H), 2.09 (s, 3H), 2.01 (s, 3H).

<sup>19</sup>F NMR (376 MHz, DMSO-*d*<sub>6</sub>) δ -115.94 (dt, *J* = 20.7, 10.6 Hz).

4'-Fluorouridine (6) (Fig. S16). A thick wall round-bottomed pressure vessel was charged with 5'-(3-chlorobenzoyloxy)-2',3'-di-*O*-acetyl-4'-fluorouridine (1.55 g, 3.2 mmol) and 4N ammonia in methanol (4.15 ml, 191.8 mmol). The mixture was stirred at RT for 1.5 hours after which time tlc (10% methanol in methylene chloride) indicated complete consumption of starting material. The mixture was concentrated under vacuum at 19°C, and the resulting residue triturated with methyl *tert*-butyl ether. The solid was co-evaporated with methanol and then recrystallized from ethanol (15 ml) to give 4'-fluorouridine (300 mg, 36% yield) as a white solid.

<sup>1</sup>H NMR (400 MHz, DMSO-*d*<sub>6</sub>) δ 11.41 (s, 1H), 7.67 (d, *J* = 8.1 Hz, 1H), 5.97 (d, *J* = 2.8 Hz, 1H), 5.66 (d, *J* = 5.4 Hz, 1H), 5.64 (d, *J* = 8.1 Hz, 1H), 5.47 (t, *J* = 5.9 Hz, 1H), 5.16 (d, *J* = 8.8 Hz, 1H), 4.24 (ddd, *J* = 17.7, 8.8, 6.5 Hz, 1H), 4.12 (td, *J* = 6.0, 2.8 Hz, 1H), 3.54 (t, *J* = 5.6 Hz, 2H).

<sup>19</sup>F NMR (376 MHz, DMSO-*d*<sub>6</sub>) δ -120.94 (dt, *J* = 17.7, 5.4 Hz).

LCMS Calculated for C<sub>9</sub>H<sub>12</sub>FN<sub>2</sub>O<sub>6</sub> [M+H<sup>+</sup>]: 263.0; found: 263.0

2',3'-Di-*O*-benzyloxycarbonyl-5'-deoxy-4'-fluoro-5'-iodouridine (Fig. S17). A 150 ml round-bottomed flask was charged with 5'-deoxy-5'-iodo-4'-fluorouridine (2.6 g, 6.99 mmol) and methylene chloride (35 ml). After stirring for 20 minutes at RT, the suspension was cooled to 0°C and treated with benzyl chloroformate (4.49 ml, 31.44 mmol) followed by dropwise addition of 1-methylimidazole (3.34 ml, 41.93 mmol) over a 10-minute period. The mixture was stirred an additional 10 minutes at 0°C and then allowed to slowly warm to room temperature. After 18 hours, the turbid mixture was diluted with methylene chloride (120 ml) and washed with 0.5 M HCl solution (75 ml), water (50 ml), and brine (50 ml). The organic layer was separated, dried over sodium sulfate and concentrated under vacuum. The resulting residue was purified by column chromatography over silica gel (80 g) eluting with a methylene chloride/methanol gradient. Pure product containing fractions were combined and concentrated under vacuum to give 2',3'-di-*O*-benzyloxycarbonyl-5'-deoxy-4'-fluoro-5'-iodouridine (4.2 g, 94% yield) as a white solid.

<sup>1</sup>H NMR (400 MHz, CDCl<sub>3</sub>) δ 9.02 (s, 1H), 7.44 – 7.28 (m, 10H), 7.14 (d, *J* = 8.0 Hz, 1H), 5.86 – 5.72 (m, 2H), 5.69 – 5.57 (m, 2H), 5.19 (d, *J* = 4.3 Hz, 2H), 5.09 (d, *J* = 3.1 Hz, 2H), 3.71 – 3.35 (m, 2H).

<sup>19</sup>F NMR (376 MHz, CDCl<sub>3</sub>) δ -107.06 (td, *J* = 18.6, 7.3 Hz).



2',3'-Di-*O*-benzyloxycarbonyl-4'-fluorouridine (Fig. S17). In a 100 ml round-bottomed flask a 55% tetrabutylammonium hydroxide solution in water (8.04 ml, 9.37mmol) was adjusted to pH 3.5 by dropwise addition of trifluoroacetic acid (0.72 ml, 9.37 mmol) while maintaining a temperature below 25°C. The mixture was then treated with a methylene chloride (15 ml) solution of 2',3'-di-*O*-benzyloxycarbonyl-5'-deoxy-4'-fluoro-5'-iodouridine (2 g, 3.12mmol) followed by addition of 3-chloroperbenzoic acid (3.6 g, 15.62 mmol) in portions over a 30 minutes period. After 1 hour the pH drifted to pH 1.4. The mixture was adjusted back to pH 3.5 with 1N sodium hydroxide and allowed to stir for 16 hours after which time tlc (10% methanol in methylene chloride) and LCMS indicated complete conversion. The reaction mixture was quenched by addition of sodium thiosulfate (3.21 g, 20.31 mmol) slowly in portions while maintaining a temperature below 25°C. After stirring for 30 minutes, the methylene chloride layer was separated, and the aqueous layer extracted with additional methylene chloride (2 × 30 ml). Combined organic layers were dried over sodium sulfate, concentrated, and purified by column chromatography over silica gel (80 g) eluting with 60% ethyl acetate in hexanes followed by a second column of silica gel (80 g) eluting with a methylene chloride/methanol gradient to give 2',3'-di-*O*-benzyloxycarbonyl-4'-fluorouridine (1.05 g, 63% yield) as a white solid.

<sup>1</sup>H NMR (400 MHz, CDCl<sub>3</sub>) δ 9.30 (s, 1H), 7.39 – 7.29 (m, 10H), 7.21 (d, *J* = 8.1 Hz, 1H), 5.83 (dd, *J* = 17.8, 7.0 Hz, 1H), 5.77 – 5.71 (m, 2H), 5.61 (dd, *J* = 7.0, 2.4 Hz, 1H), 5.17 (d, *J* = 4.8 Hz, 2H), 5.09 (s, 2H), 3.86 (q, *J* = 5.8, 4.9 Hz, 2H), 3.06 (s, 1H).

<sup>19</sup>F NMR (376 MHz, CDCl<sub>3</sub>) δ -121.03 (dt, *J* = 17.7, 4.6 Hz).

4'-Fluorouridine 5'-*O*-triphosphate (Fig. S17). A 10 ml round-bottomed flask charged with 2',3'-di-*O*-benzyloxycarbonyl-4'-fluorouridine (348 mg, 0.66 mmol) and anhydrous trimethyl phosphate (3.5 ml). After stirring for 20 minutes at room temperature, the solution was cooled to 0°C and treated with 1-methyl-imidazole (115 μL, 1.44 mmol) followed by dropwise addition of phosphorus oxychloride (122 μL, 1.31 mmol) over a 40-minute period. The mixture continued to stir at 0°C for 3.5 hours after which time tlc (10% methanol in DCM and then 7:2:1

*i*PrOH:NH<sub>4</sub>OH:water) indicated complete phosphorylation. The mixture was treated with tributylamine (0.94 ml, 3.94 mmol), tris(tetrabutylammonium)pyrophosphate (887 mg, 0.98 mmol), and anhydrous DMF (1.5 ml). After 1 hour at RT, the reaction mixture was quenched with 100 mM TEAB (20 ml), stirred for 1 hour, degassed by pump-fill with argon (3x) and treated with 10% palladium on carbon (100 mg). After cooling with an ice-bath, the mixture was pump-filled with hydrogen (2x) followed by vigorous stirring under atm pressure of hydrogen for 30 minutes. After vacuum evacuation of the reaction vessel, the mixture was filtered through a pad of Celite and the collected palladium washed with water (2 × 20 ml). Combined filtrates were washed with ether (4 × 60 ml) and then concentrated under vacuum at 25°C. After co-evaporation with water (2 × 25 ml), the crude triphosphate was purified by column chromatography over DEAE-Sephadex GE A-25 (10 mm × 130 mm) eluting with a buffer gradient from 100 mM (450 ml) to 500 mM TEAB (450 ml). Pure product containing fractions as determined by tlc (8:1:1 NH<sub>4</sub>OH:*i*PrOH:water) were combined and concentrated under vacuum with the bath temperature set at 25°C. The solid was dissolved in methanol (1 ml) and treated with saturated solution of sodium perchlorate in acetone (10 ml). The resulting white precipitate was collected by centrifuge, washed with acetone (5 × 5 ml), dissolved in water (1 ml), and concentrated by lyophilization to yield 4'-fluoro-uridine 5'-*O*-triphosphate (3.14 mg, 0.81% yield) as the tetrasodium salt.

$^1\text{H}$  NMR (400 MHz,  $\text{D}_2\text{O}$ )  $\delta$  7.77 (d,  $J = 8.0$  Hz, 1H), 6.15 (d,  $J = 1.9$  Hz, 1H), 5.91 (d,  $J = 8.1$  Hz, 1H), 4.72 – 4.57 (m, 1H), 4.41 (d,  $J = 6.3$  Hz, 1H), 4.30 (ddd,  $J = 10.2, 6.3, 3.0$  Hz, 1H), 4.17 (dt,  $J = 10.8, 5.0$  Hz, 1H).  $^{31}\text{P}$  NMR (162 MHz,  $\text{D}_2\text{O}$ )  $\delta$  -7.81(d), -11.84 (d,  $J = 19.2$  Hz), -22.23 (t).  $^{19}\text{F}$  NMR (376 MHz,  $\text{D}_2\text{O}$ )  $\delta$  -121.09 (unresolved dt,  $J = 19.2$  Hz). LCMS Calculated for  $\text{C}_9\text{H}_{13}\text{FN}_2\text{O}_{15}\text{P}_3$   $[\text{M}-\text{H}^+]$ : 500.9; found: 500.8

**Supplementary text**

**Limitations of the mouse model for RSV.** The mouse model for RSV infection does not fully recapitulate human infection. Specifically, mice do not exhibit major clinical signs and the first site of virus replication is the lower respiratory tract, resulting in viral pneumonia, whereas in the human host RSV initially replicates in upper respiratory tissues and progression to the small airways marks transition to severe disease. The most robust and widely accepted measure for antiviral efficacy is therefore the measure of viral lung titers at the peak of replication (day 4-5 after infection). In addition to determining lung virus load, we followed viral replication longitudinally, using a recombinant virus that expresses a luciferase reporter and live bioluminescence imaging of whole animals (Figure 4C). This model provides a spatial localization of replication and allows for the visualization of RSV replication over time with a reduced number of animals. It comes with additional limitations, however, since it measures expression of a luciferase reporter encoded by the viral genome rather than actual titers of infectious progeny virions in the lung. As previously reported (36), a high baseline luciferase signal is derived from the incoming virus inoculum and thus independent of productive virus replication. Due to high stability of the luciferase protein, subsequent replication can only result in a comparably moderate increase in signal strength over time, inherently limiting the dynamic range of the RSV IVIS assay.

## 2.1.6 EDP-235, a Novel Small Molecule Inhibitor of SARS-CoV-2 3CLpro for the Treatment of COVID-19

nature communications



Article

<https://doi.org/10.1038/s41467-024-50931-8>

# The small molecule inhibitor of SARS-CoV-2 3CLpro EDP-235 prevents viral replication and transmission in vivo

Received: 21 December 2023

Accepted: 23 July 2024

Published online: 01 August 2024

Check for updates

Michael H. J. Rhodin<sup>1</sup>✉, Archie C. Reyes<sup>1</sup>, Anand Balakrishnan<sup>1</sup>, Nalini Bisht<sup>1</sup>, Nicole M. Kelly<sup>1</sup>, Joyce Sweeney Gibbons<sup>1</sup>, Jonathan Lloyd<sup>1</sup>, Michael Vaine<sup>1</sup>, Tessa Cressey<sup>1</sup>, Miranda Crepeau<sup>1</sup>, Ruichao Shen<sup>1</sup>, Nathan Manalo<sup>1</sup>, Jonathan Castillo<sup>1</sup>, Rachel E. Levene<sup>1</sup>, Daniel Leonard<sup>1</sup>, Tianzhu Zang<sup>1</sup>, Lijuan Jiang<sup>1</sup>, Kellye Daniels<sup>1</sup>, Robert M. Cox<sup>2</sup>, Carolin M. Lieber<sup>2</sup>, Josef D. Wolf<sup>2</sup>, Richard K. Plemper<sup>2</sup>, Sarah R. Leist<sup>3</sup>, Trevor Scobey<sup>3</sup>, Ralph S. Baric<sup>3</sup>, Guoqiang Wang<sup>1</sup>, Bryan Goodwin<sup>1</sup> & Yat Sun Or<sup>1</sup>

The COVID-19 pandemic has led to the deaths of millions of people and severe global economic impacts. Small molecule therapeutics have played an important role in the fight against SARS-CoV-2, the virus responsible for COVID-19, but their efficacy has been limited in scope and availability, with many people unable to access their benefits, and better options are needed. EDP-235 is specifically designed to inhibit the SARS-CoV-2 3CLpro, with potent nanomolar activity against all SARS-CoV-2 variants to date, as well as clinically relevant human and zoonotic coronaviruses. EDP-235 maintains potency against variants bearing mutations associated with nirmatrelvir resistance. Additionally, EDP-235 demonstrates a  $\geq 500$ -fold selectivity index against multiple host proteases. In a male Syrian hamster model of COVID-19, EDP-235 suppresses SARS-CoV-2 replication and viral-induced hamster lung pathology. In a female ferret model, EDP-235 inhibits production of SARS-CoV-2 infectious virus and RNA at multiple anatomical sites. Furthermore, SARS-CoV-2 contact transmission does not occur when naïve ferrets are co-housed with infected, EDP-235-treated ferrets. Collectively, these results demonstrate that EDP-235 is a broad-spectrum coronavirus inhibitor with efficacy in animal models of primary infection and transmission.

The global emergence of severe acute respiratory syndrome coronavirus 2 (SARS-CoV-2) and its associated respiratory disease, coronavirus disease 2019 (COVID-19), has resulted in >770 million reported cases and approximately 7 million deaths recorded to date worldwide<sup>1</sup>. The COVID-19 health crisis has led to the development of a diverse arsenal of therapeutics<sup>2</sup> that have been critical in mitigating severe clinical outcomes<sup>3-7</sup>. Approved small molecule therapeutics directly targeting SARS-CoV-2 include the nucleoside inhibitors

remdesivir and molnupiravir, and the protease inhibitors nirmatrelvir and ensitrelvir (the latter is only approved for use in Japan as of this writing). While these therapies have been crucial life-saving tools, there remains a strong need for new therapies with improved dosing regimens, efficacies, and patient eligibility.

Upon viral entry into a host cell, the positive-sense RNA genome of SARS-CoV-2 is translated by cellular ribosomes to produce two polyproteins, ppla and pplab. Subsequently, two viral proteinases,

<sup>1</sup>Enanta Pharmaceuticals, Inc., Watertown, MA, USA. <sup>2</sup>Institute for Biomedical Sciences, Georgia State University, Atlanta, GA, USA. <sup>3</sup>Department of Epidemiology, Gillings School of Global Public Health, University of North Carolina at Chapel Hill, Chapel Hill, NC, USA. ✉e-mail: [mrhodin@enanta.com](mailto:mrhodin@enanta.com)

## Article

<https://doi.org/10.1038/s41467-024-50931-8>

papain-like cysteine protease and 3C-like protease (3CLpro), cleave pp1a and pp1ab into 16 non-structural proteins whereby the enzymatic activity of the 3CLpro is driven by a catalytic dyad (C145-H41)<sup>8</sup>. The conservation of structure and mechanism of action across coronaviruses as well as the indispensable nature of the 3CLpro for the virus's life cycle make it an excellent therapeutic target<sup>9,10</sup>. Small molecule inhibitors targeting viral proteases have historically proven successful for the treatment of human immunodeficiency virus and hepatitis C virus<sup>11,12</sup>. Prior to the emergence of SARS-CoV-2, there was ongoing development of inhibitors against the 3CLpro of severe acute respiratory syndrome coronavirus (SARS-CoV)<sup>8,9</sup>. The sequence, structural identity, and mechanism of hydrolysis of the 3CLpro is highly conserved in SARS-CoV-2 as compared to SARS-CoV<sup>8,13–15</sup>, thereby providing a strong rationale for the development of SARS-CoV-2 3CLpro inhibitors.

To date, the FDA has approved the use of one anti-SARS-CoV-2 agent that inhibits the 3CLpro of SARS-CoV-2, ritonavir-boosted nirmatrelvir (Paxlovid)<sup>16,17</sup>. Ritonavir, an inhibitor of cytochrome P450 3A4, is co-administered with nirmatrelvir to increase nirmatrelvir's pharmacokinetic half-life<sup>17–19</sup>. The EPIC-HR trial demonstrated that Paxlovid is typically well-tolerated in SARS-CoV-2 infected individuals<sup>20</sup>. However, there are adverse reactions and contraindications that may arise with the use of ritonavir, which has limited the approved populations for which this therapeutic is recommended<sup>19,21</sup>.

The development of antiviral resistance is a concern, particularly for RNA viruses<sup>22</sup>. Unfortunately, the continued emergence of SARS-CoV-2 variants increases the possibility of rendering current treatment measures less efficacious<sup>23–28</sup>. To reduce the medical impact of viral evolution and escape from immune and antiviral countermeasures, it is critical to continue developing novel therapeutics to combat SARS-CoV-2. To date, widespread transmission of nirmatrelvir-resistant variants has not been reported. However, it is possible that drug selective pressure could drive the development of clinically meaningful resistance. Indeed, several *in vitro* studies have determined that nirmatrelvir can select for variants bearing mutations in 3CLpro which may impact its efficacy<sup>27,29–32</sup>. A recent case report determined that two of these *in vitro*-generated mutations, E166V and L50F, were isolated from an immunocompromised individual infected with SARS-CoV-2 and treated with Paxlovid<sup>28</sup>.

Climate change and continued human encroachment on wildlife natural habitats will continue to drive zoonotic spillover events<sup>33,34</sup>, and the possibility of a future viral zoonotic event stemming from the coronavirus subfamily *Orthocoronavirinae* within the *Coronaviridae* family should not be ignored. To date, nine coronaviruses have been identified that can infect and cause illness in humans: human coronavirus (HCoV) 229E, HCoV-NL63, canine coronavirus (*Alphacoronaviruses*), porcine deltacoronavirus (*Deltacoronavirus*), HCoV-OC43, HCoV-HKU1, Middle East respiratory syndrome coronavirus (MERS-CoV), SARS-CoV, and SARS-CoV-2 (*Betacoronaviruses*)<sup>35–37</sup>. Within the past two decades, three of these zoonotic spillover events have caused global epidemics or pandemics with the emergence of SARS-CoV in 2002 and MERS-CoV in 2012. It is likely that the 2019 coronavirus zoonotic spillover of SARS-CoV-2 into humans will not be the last.

EDP-235 is a 3CLpro inhibitor that is under development for the treatment of COVID-19 as a once-a-day oral medication without the need for ritonavir boosting<sup>38</sup>. Herein, we report the pre-clinical characterization of EDP-235, highlighting its pan-coronavirus activity, including efficacy against other zoonotic coronaviruses that could potentially cause future spillover events. We demonstrate EDP-235's ability to inhibit SARS-CoV-2 3CLpro variants bearing mutations associated with nirmatrelvir resistance with equal or improved potency relative to nirmatrelvir. Furthermore, we establish that EDP-235 is highly efficacious in both Syrian hamsters and ferrets. Finally, therapeutically dosed EDP-235 is shown to prevent viral transmission

among cohoused, untreated ferrets, underscoring the potential of EDP-235 to possibly prevent household transmission of SARS-CoV-2.

## Results

**EDP-235 reversibly binds and inhibits the 3CLpro of SARS-CoV-2**

A fluorescence resonance energy transfer (FRET) assay using the recombinant ancestral SARS-CoV-2 (USA-WA1/2020) 3CLpro and a synthetic substrate that mimics the natural substrate of the 3CLpro was used to screen and identify di- and tri-peptidomimetic inhibitors of the SARS-CoV-2 3CLpro<sup>39,40</sup>. This led to the discovery of the nitrile-based peptidomimetic inhibitor EDP-235 (Fig. 1a inset). Kinetic studies were performed to evaluate the mechanism of inhibition of SARS-CoV-2 3CLpro. EDP-235 is a time-dependent, tight-binding, reversible covalent, substrate competitive inhibitor with a  $K_i^{app}$  of 3.0 nM and inhibits SARS-CoV-2 3CLpro with a half-maximal inhibitory concentration ( $IC_{50}$ ) of 4.0 nM (Fig. 1a and Supplementary Figs. 1–5, and Supplementary Table 1). To further confirm the mode of inhibition, a crystal structure of EDP-235 in complex with SARS-CoV-2 3CLpro was generated, from data collected to 2 Å (Fig. 1b, c and Supplementary Table 2). Under these conditions, EDP-235 is bound to the proteolytic active site of 3CLpro (Fig. 1b, c), where the sulfhydryl group of the catalytic residue C145 reacts with the nitrile group of EDP-235 to form a covalent thioimide linkage. The spirolactam moiety of EDP-235 forms hydrogen bonds with several amino acids in the active site, including a potential interaction with the backbone amide of F140, the side chain of H163, and the side chain of E166. An H- $\pi$  interaction is observed between leucine P2 of EDP-235 and H41. Additionally, the sidechain of Q189 may stabilize EDP-235 through weak hydrogen bonding with the trifluoroindole moiety of EDP-235. Other interactions include a pair of hydrogen bonds between the trifluoroindole moiety of EDP-235 and E166 and a possible F-amide n- $\pi^*$  interaction with P168. These observations are consistent with the kinetic studies and provide a structural rationale for the competitive mode of inhibition.

**EDP-235 has potent antiviral activity against SARS-CoV-2**

We assessed the ability of EDP-235 to inhibit the replication of SARS-CoV-2 utilizing different cell systems and readouts described in Table 1. In a SARS-CoV-2 replicon system<sup>41,42</sup>, EDP-235 displayed a 4.5 nM half-maximal effective concentration ( $EC_{50}$ ). These results were recapitulated in infectious virus assays using cytopathic effect (CPE) and viral yield reduction (VYR) endpoints using various derivatives of Vero cells. Unlike human airway epithelial cells, monkey kidney-derived Vero E6 cells express high levels of the efflux transporter P-glycoprotein 1 (PGP)<sup>43</sup>. Given the possibility of 3CLpro inhibitors to serve as PGP substrates, antiviral assays utilizing Vero E6 cells were performed in the presence and absence of the PGP inhibitor (PGPi) CP-100356<sup>44</sup>. In Vero E6 cells infected with ancestral (A: SARS-CoV-2 USA-WA1/2020), B (Germany/BavPat1/2020), Delta (B.1.617.2), or Omicron (B.1.1.529) strains, EDP-235 inhibited CPE and virion production with  $EC_{50}$ s ranging from 11–22 nM and 3–7.4 nM, in the absence and presence of PGPi, respectively. Using a VYR assay endpoint in the more permissive Vero E6-TMPRSS2 cells, EDP-235 inhibited multiple SARS-CoV-2 Omicron variants of interest with  $EC_{50}$ s ranging from 10 to 73 nM (Table 1). Viral inhibition curves for these data are included in Supplementary Fig. 6. Comparable results were obtained for FRET biochemical assays with  $IC_{50}$ s ranging from 1.9 to 5.7 nM for all 3CLpro variants assessed (Supplementary Table 3 and Supplementary Fig. 7).

Since SARS-CoV-2 predominately replicates in lung epithelial cells, we evaluated the potency of EDP-235 in a more relevant cellular architecture. We utilized primary human airway epithelial cells maintained at an air-liquid interface (pHAEC-ALI). EDP-235 inhibited viral replication, as quantified by 50% tissue culture infectious dose ( $TCID_{50}$ ), of SARS-CoV-2 lineage B with  $EC_{50/90}$  values of 29/33 nM, respectively. Near-identical potency values were derived when reverse-

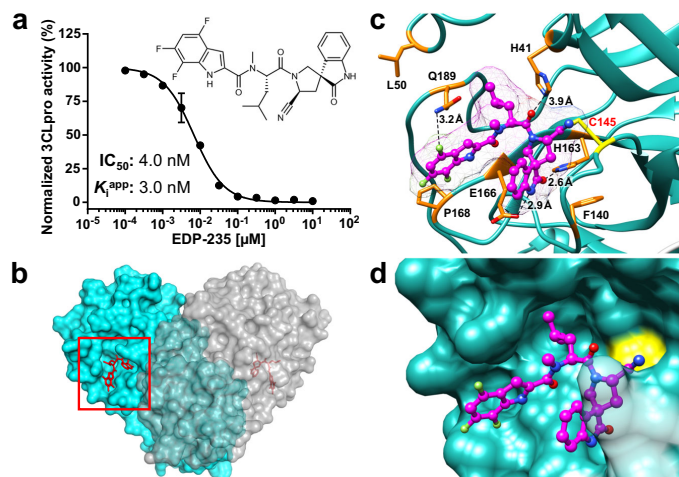


**Fig. 1 | EDP-235 inhibits SARS-CoV-2 3CLpro and binds reversibly to 3CLpro's active site.** **a** Structure of EDP-235 and its FRET 3CLpro inhibition activity. Representative data are mean  $\pm$  standard deviation of technical replicates from one experiment with non-linear regression fit ( $n = 6$  independent experiments used to derive  $IC_{50}$  and  $K_i^{app}$  values). **b** Semi-transparent surface representation of the X-ray crystal structure of SARS-CoV-2 3CLpro dimer (shown in cyan and gray) in complex with EDP-235 solved to 2 Å. EDP-235 is represented by red stick structure. **c** Detailed cartoon representation of the binding interactions between EDP-235 and residues located in SARS-CoV-2 3CLpro catalytic active site. Hydrogen bonds are depicted between the NH side chain of H136 with the spyrrolactam C = O of EDP-235, the C = O

side chain of E166 with the spyrrolactam NH of EDP-235, the NH side chain of H41 with amide C = O of EDP-235, and the NH side chain of Q189 with the trifluoromethyl F of EDP-235. The catalytic residue C145 is represented as a yellow stick configuration and monomer coloration is matched to (**b**, **d**). The surface map of 3CLpro and electron density of EDP-235 was rendered using UCSF Chimera. **d** A close-up semi-transparent surface representation of EDP-235 in the binding pocket. 3CLpro = 3C-like protease; FRET = fluorescence resonance energy transfer;  $IC_{50}$  = half-maximal inhibitory concentration;  $K_i^{app}$  = apparent inhibition constant; SARS-CoV-2 = severe acute respiratory syndrome coronavirus 2; UCSF = University of California San Francisco.

transcriptase-quantitative polymerase chain reaction (RT-qPCR) was used to monitor viral replication (Table 1).

Across all strains and readouts, EDP-235's in vitro potencies were equivalent to or improved upon those observed for nirmatrelvir. No cytotoxicity was detected in Vero E6, HuH-7, Madin-Darby canine kidney, A549-ACE2, MRC5, or HeLa cells exposed to EDP-235 for 72 hours (h) at concentrations up to 50,000 nM (Supplementary Fig. 8). EDP-235 has weak inhibition ( $IC_{50} \geq 2 \mu M$ ) of mammalian cysteine proteases and an excellent selectivity index (SI)  $\geq 500$ -fold compared to its inhibition of SARS-CoV-2 3CLpro (Supplementary Table 4). EDP-235 did not inhibit any other host protease families at tested concentrations ( $IC_{50} > 100 \mu M$ ).

#### EDP-235 maintains activity against known SARS-CoV-2 nirmatrelvir-resistant variants

Since the development of SARS-CoV-2 antiviral resistance is a possibility, the activity of EDP-235 was assessed against 24 single-residue and 17 multi-residue 3CLpro variants associated with nirmatrelvir resistance. The most well-known and clinically documented of these were the 3CLpro L50F and E166V point mutations<sup>27–30</sup>. The potency of EDP-235 against these 3CLpro variants ranged from an  $IC_{50}$  of 3–184 nM, with nirmatrelvir subject to greater loss of potency ( $IC_{50}$  4–>10,000 nM) (Table 2, Supplementary Fig. 7, and Supplementary Table 5 for expanded variant testing). EDP-235 showed a >5-fold decrease in potency for 21 variants, with nirmatrelvir suffering even greater potency reductions against these variants. However, each of these variants had 7–125-fold reductions in enzymatic efficiency relative to ancestral 3CLpro, indicating a detrimental impact on enzymatic activity, and consequentially a possible decrease in both viral fitness and potential to replicate to levels associated with infection and transmission.

Circulating SARS-CoV-2 variants bearing mutations in 3CLpro within the EDP-235 binding site could potentially lead to emergence of clinical drug resistance. Analysis of the SARS-CoV-2 3CLpro co-crystal with EDP-235 revealed 22 residues within 5 Å of EDP-235. To identify circulating SARS-CoV-2 variants with mutations at these 22 sites, we conducted a search of the GISAID database for variants that had a prevalence  $\geq 1\%$  of sequencing reads. We identified 15 variants as of January 2022. When these mutations were engineered into SARS-CoV-2 3CLpro, we did not observe any EDP-235 resistance in the biochemical FRET assay.  $IC_{50}$ s for these variants ranged from 2.2 to 13 nM with 4 variants having no detectable enzymatic activity (Supplementary Table 6 and Supplementary Fig. 7). Some inactivating mutations such as C145F (active site mutation) could have arisen due to sequencing errors for very low frequency variants or other inaccuracies in the GISAID database.

#### EDP-235 is a pan-coronavirus inhibitor

Beyond the current threat of SARS-CoV-2, several other coronaviruses are known to infect humans. We therefore evaluated the prospect of EDP-235 to serve as a pan-coronavirus inhibitor. EDP-235 maintained nanomolar to sub-nanomolar potency against all coronaviruses tested in antiviral and biochemical assays (Table 3). The 3CLpro amino acid sequences from the Toronto-2 and HKU-39849 strains of SARS-CoV are 100% conserved, and EDP-235 inhibited the biochemical activity of this protease with an  $IC_{50}$  of 1.9 nM. As expected, EDP-235 limited replication of both SARS-CoV clinical isolates with  $EC_{50}$  values ranging from <0.5 to 24 nM. In addition, EDP-235 potently inhibited the replication of HCoV-229E (<10 nM  $EC_{50}$ s in multiple assay formats), HCoV-OC43 (57 nM  $EC_{50}$ ), HCoV-HKU1 (3.8 nM  $IC_{50}$ ), and HCoV-NL63 (6.1 nM  $EC_{50}$ ). These data are summarized in Table 3 and Supplementary Fig. 9.

## Article

<https://doi.org/10.1038/s41467-024-50931-8>**Table 1 | Antiviral activity of EDP-235 against infectious SARS-CoV-2**

SARS-CoV-2	Assay	+/-	EDP-235 [nM]			Nirmatrelvir [nM]			
			PGPI	EC <sub>50</sub>	EC <sub>90</sub>	N	EC <sub>50</sub>	EC <sub>90</sub>	N
A	HuH-7, Replicon, Luciferase <sup>1</sup>	-	4.5	24	16	15	118	48	
	Vero E6, CPE <sup>2</sup>	-	22	32	2	-	-	-	
B	Vero E6, VYR <sup>3</sup>	+	5.1	11	2	42	50	2	
		-	11	32	6	904	3247	4	
	3D pHAEC-ALI, VYR <sup>3</sup>	-	29	33	1	-	-	-	
	3D pHAEC-ALI, RT-qPCR <sup>3</sup>	-	27	33	1	-	-	-	
Alpha	B.1.1.7	Vero E6, VYR <sup>3</sup>	-	46	175	4	-	-	
Beta	B.1.351	Vero E6, VYR <sup>3</sup>	-	44	134	4	-	-	
Delta	B.1.617.2	Vero E6, CPE <sup>2</sup>	-	15	17	6	1743	2463	2
		+	4.3	6.2	5	17	42	3	
Omicron	B.1.1.529	Vero E6, CPE <sup>2</sup>	-	15	16	2	2541	4056	1
		+	7.4	14	7	37	56	1	
	Vero E6-TMPRSS2, VYR <sup>4</sup>	+	10	25	3	34	42	1	
		-	18	25	3	-	-	-	
	BA.2	Vero E6-TMPRSS2, VYR <sup>4</sup>	+	18	25	3	-	-	
	BA.2.12.1	Vero E6-TMPRSS2, VYR <sup>4</sup>	+	22	34	3	-	-	
	BA.4	Vero E6-TMPRSS2, VYR <sup>4</sup>	+	19	25	3	-	-	
	BA.5.1	Vero E6-TMPRSS2, VYR <sup>4</sup>	+	39	67	3	-	-	
	BQ.1.1	Vero E6-TMPRSS2, VYR <sup>4</sup>	+	30	43	3	-	-	
	XBB.1.5	Vero E6-TMPRSS2, VYR <sup>4</sup>	+	19	42	3	57	68	6
	EG.5.1	Vero E6-TMPRSS2, VYR <sup>4</sup>	+	72	86	3	69	78	3
	EG.5.1.1	Vero E6-TMPRSS2, VYR <sup>4</sup>	+	73	92	3	142	134	3
	EG.5.2	Vero E6-TMPRSS2, VYR <sup>4</sup>	+	54	68	3	43	79	3
	BA.2.86	Vero E6-TMPRSS2, VYR <sup>4</sup>	+	55	75	3	92	104	3
JN.1.1	Vero E6-TMPRSS2, VYR <sup>4</sup>	+	37	58	3	151	170	3	

SARS-CoV-2 antiviral activity was assessed at multiple facilities. For studies in the Vero cell lineage, CP-100356 (0.5 μM or 2 μM, +PGPI) was included. Experiments performed at: Enanta Pharmaceuticals<sup>1</sup>; Southern Research (SR)<sup>2</sup>; Viroclinics Biosciences (VCB)<sup>3</sup>; Georgia State University (GSU).

**Table 2 | Potency of EDP-235 against select nirmatrelvir-associated variants**

3CLpro	3CLpro [nM]	k <sub>cat</sub> /K <sub>m</sub> [(M <sup>-1</sup> s <sup>-1</sup> ) <sup>-1</sup> ]	IC <sub>50</sub> [nM]	
			EDP-235	Nirmatrelvir
Ancestral	10	4.5 × 10 <sup>4</sup>	4	4
L50F	100	3.7 × 10 <sup>4</sup>	3	4.4
E166H	100	9.0 × 10 <sup>2</sup>	92	>10,000
E166V	100	3.6 × 10 <sup>2</sup>	113	>10,000
T211/E166V	100	7.0 × 10 <sup>2</sup>	100	>10,000
L50F/E166V	10	6.3 × 10 <sup>2</sup>	72	>10,000
L50F/E166A/L167F	40	7.6 × 10 <sup>2</sup>	184	1200

FRET assay; data are mean from three individual experiments.

EDP-235 was also tested against a broad panel of other human RNA viruses that encode proteases using infectious cell culture assays, however no activity was observed beyond the coronaviruses.

**Zoonotic CoVs are inhibited by EDP-235**

As a zoonotic spillover event remains a constant threat, we sought to determine if EDP-235 could inhibit zoonotic CoVs. Viral species were selected based on percent sequence identity of the receptor binding domain (RBD) compared to that of SARS-CoV-2<sup>45</sup>, on the assumption that a high RBD sequence identity is an important factor which may portend an increased likelihood of a spillover event. Three bat and two pangolin CoV species, as well as the porcine epidemic diarrhea virus (PEDV) (included as an outlier species based on lack of RBD sequence

conservation) were tested in a FRET assay. EDP-235 exhibited an IC<sub>50</sub> < 3 nM against all tested zoonotic 3CLpro (Table 4, and Supplementary Fig. 10). We also explored EDP-235's ability to block viral replication of infectious zoonotic CoVs recombinantly engineered to express NanoLuc luciferase<sup>46-48</sup>. These viruses were previously isolated from pangolin and bat species and have a high degree of similarity to SARS-CoV, MERS, and SARS-CoV-2. In line with the biochemical assays, EDP-235 maintained activity against each of the infectious zoonotic viruses (EC<sub>50</sub> 6.9–21 nM) (Table 4).

**EDP-235 is efficacious in a SARS-CoV-2 hamster model**

Syrian hamsters can recapitulate many features of COVID-19<sup>49,50</sup>. Therefore, we evaluated the in vivo efficacy of EDP-235 using a Syrian hamster model (Fig. 2). Hamsters were grouped into four cohorts of either naïve dosed with vehicle (0.5% methylcellulose) or infected dosed with vehicle, EDP-235 at 200 mg/kg twice daily (BID), or EDP-235 at 500 mg/kg BID. Hamsters were intranasally infected with 6 × 10<sup>3</sup> TCID<sub>50</sub> of SARS-CoV-2 (USA/WA1/2020) and compound dosing was oral. Prophylactic oral dosing commenced 1 h pre-challenge and lasted for 3.5 days, with sacrifice 4 days post-infection (dpi). While infected vehicle-treated animals exhibited rapid weight loss, EDP-235 prevented SARS-CoV-2-induced weight loss (Fig. 2b). Further evaluation with immunohistochemistry (IHC) staining of the lungs for viral nucleoprotein (N) revealed a remarkably reduced amount of staining in EDP-235-treated animals as compared to infected, vehicle-treated animals (Fig. 2c, d). Hematoxylin and eosin (H&E) lung staining revealed the majority of the lung tissue from infected vehicle-treated animals was affected by SARS-CoV-2 (abundant dark consolidations, Fig. 2e arrows), while EDP-235-treated animals did not have such findings



## Article

<https://doi.org/10.1038/s41467-024-50931-8>**Table 3 | Broad-spectrum activity of EDP-235 against human coronaviruses**

Virus (Clinical Isolate)	Assay Details	+/- PGPI	IC <sub>50</sub> or EC <sub>50</sub> [nM]	N
SARS-CoV	Biochemical <sup>1</sup>	-	5.4	3
	Toronto-2 isolate, Vero E6 / CPE <sup>2</sup>	+	24	2
	HKU-39849 isolate, Vero E6 / VYR <sup>3</sup>	+	< 0.5	3
MERS-CoV	Biochemical <sup>1</sup>	-	70	3
	EMC/2012 isolate, Vero E6 / VYR <sup>3</sup>	+	7	4
HCoV-229E	Biochemical <sup>1</sup>	-	1.9	3
	MRC-5 / CPE <sup>1</sup>	-	3.6	16
	MRC-5 / RT-qPCR <sup>1</sup>	-	1.4	2
	3D pHAEC-ALI / RT-qPCR <sup>1</sup>	-	0.66	3
HCoV-OC43	Biochemical <sup>1</sup>	-	3.4	3
	HCT-8 / RT-qPCR <sup>1</sup>	-	47	2
HCoV-HKU1	Biochemical <sup>1</sup>	-	3.8	3
HCoV-NL63	Biochemical <sup>1</sup>	-	1.8	3
	LLC-MK2 / RT-qPCR <sup>1</sup>	-	6.1	6

The antiviral activity of EDP-235 against six HCoVs. For infectious viral studies in the Vero cell lineage, 2 μM CP-100356 (+PGPI) was included. Experiments performed at <sup>1</sup> Enanta Pharmaceuticals; <sup>2</sup> SR; <sup>3</sup> VCB.

(Fig. 2e). Cumulative histopathology scoring of alveolar hemorrhage, alveolar inflammation, interstitial inflammation, vascular inflammation, bronchial-alveolar hyperplasia, perivascular edema, and immunoreactivity showed significant decreases in EDP-235-treated animals relative to infected vehicle-treated animals (Fig. 2f). Lung viral loads displayed significant differences between EDP-235-treated and untreated animals at study endpoint, with the former demonstrating multi log<sub>10</sub> reductions in live virus, genomic viral RNA (gRNA), and sub-genomic viral RNA (sgRNA) (Fig. 2g-i).

#### EDP-235 therapeutically blocks SARS-CoV-2 replication and transmission in ferrets

While Syrian hamsters recapitulate the pathology produced in human SARS-CoV-2 infection, they are not as well suited to evaluate viral transmission as ferrets. Ferrets replicate SARS-CoV-2 to high titers in their upper airways and have previously been employed in the study of SARS-CoV-2 transmission<sup>51,52</sup>. The ferret model was used to evaluate EDP-235's ability to therapeutically halt viral replication and to prevent transmission from infected to naïve animals (Fig. 3). Prior to in vivo work, a 24 h oral single dose pharmacokinetic study was performed in ferrets, administering either 200 or 500 mg/kg. While no pharmacokinetic dose response was observed between the 200 and 500 mg/kg dosing groups (Supplementary Fig. 11), it was noted that plasma exposure levels were comparable to those seen in human phase 1 clinical studies. This was especially true when compared to the human 400 mg fed state, with the exception that EDP-235's half-life in ferrets dosed at 200 mg/kg was ~2-3-fold reduced compared to that observed in humans (6.7 h versus 13-22 h geometric mean in humans)<sup>53</sup>. For these pharmacokinetic parameter reasons, 200 mg/kg ferret dosing was selected for the efficacy study, given either once per day (QD) or BID. Ferrets were inoculated intranasally with 1 × 10<sup>5</sup> plaque-forming units (PFU) of SARS-CoV-2 USA/WA1/2020. At 12 h post-infection (hpi), animals were dosed orally with either vehicle or EDP-235 for three days. At 60 hpi, uninfected and untreated naïve ferrets were co-housed 1:1 with infected ferrets and monitored for 5.5 days for viral transmission (Fig. 3a).

All ferrets were clinically scored daily as none/normal for lethargy, orbital tightening, diarrhea, respiratory distress, activity, nasal

**Table 4 | EDP-235 inhibits zoonotic coronaviruses**

Assay	Host	3CLpro Species	% Amino Acid Identity of RBD	IC <sub>50</sub> or EC <sub>50</sub> [nM]	
Biochemical 3CLpro FRET <sup>1</sup>	Human	SARS-CoV-2	100	4.0	
		RaTG13/2013	82	1.7	
		RmYN02/2019	43	1.9	
	Bat	RshSTT200/2010	74	1.9	
		Pangolin	P5L/2017	81	2.6
			MP789/2019	98	2.5
Pig	PEDV	12	1.5		
NanoLuc infectious virus in cells <sup>2</sup>	Pangolin	pgCoV	97	13	
		WIV1	75	8.4	
	Bat	WIV16	75	16	
		SHC014	76	21	
		BtCoV/II/GD/2014-422 (MERS-422)	22	6.9	

Performed at <sup>1</sup>Enanta Pharmaceuticals (data are mean values from two individual experiments) and <sup>2</sup>University of North Carolina at Chapel Hill (data are mean values from four individual experiments). Percent amino acid sequence identity for biochemical assays was calculated based on alignment to the RBD of SARS-CoV-2 Wuhan-Hu-1 (NC\_045512.2)<sup>45</sup>. Alignments were performed using Geneious.

discharge, and neurological symptoms. Primary-infected animals maintained consistent weight and temperature (Fig. 3b, c). On each study day, rectal swab and nasal wash samples were obtained. Nasal turbinates were collected upon sacrifice, and viral replication was evaluated. Viral loads increased rapidly in primary infected vehicle-treated animals, peaking at 2-3 dpi (Fig. 3d-f). Across all readouts and dosing cohorts, EDP-235 rapidly reduced viral loads in initially infected ferrets (Fig. 3d-h), with significant virion reductions observed in the first samples obtained 12 h post-dosing (Fig. 3e). After 48 h of dosing, virion levels were below the LoD, representing a > 3 log<sub>10</sub> drop relative to vehicle-treated animals.

Viral transmission occurred rapidly (within 12 h of co-housing), from vehicle-treated source animals to untreated contact animals, with peak viral loads observed 2.5 days post-co-housing. Both EDP-235 dosing regimens completely suppressed viral transmission, as ferrets co-housed with EDP-235-treated infected ferrets had undetectable viral loads (Fig. 3d-h). In contrast to primary-infected ferrets, contact ferrets co-housed with the infected vehicle-treated ferrets showed significant weight loss and increases in body temperature (Fig. 3b, c). This change was likely driven by a ferret-adaptive spike mutation in the RBD, NS01T, which can emerge rapidly<sup>54</sup>, and was observed in sequenced virus collected from primary infected vehicle-treated ferrets on day 4. Shotgun metagenomic next-generation sequencing of day 4 viruses from EDP-235-treated animals was used to detect any potential resistance mutations but read-depths were insufficient to call any variants, likely due to the high efficacy of EDP-235.

#### Discussion

In this study, we present the in vitro and in vivo characterization of EDP-235, an oral antiviral, specifically designed to target the 3CLpro of SARS-CoV-2. While the real-world efficacy of targeting the 3CLpro has been established with nirmatrelvir, the need for additional therapeutics with a simpler dosing regimen, expanded patient eligibility through fewer drug-drug interactions, improved tolerability, enhanced potency, and reduced resistance liability would benefit those suffering from COVID-19<sup>3,55</sup>. The in vitro data reported here demonstrate improvements by EDP-235 relative to nirmatrelvir regarding potency, resistance, and in preventing transmission in ferret studies. EDP-235 is currently in development with once-daily dosing without the use of any boosting agent such as ritonavir.

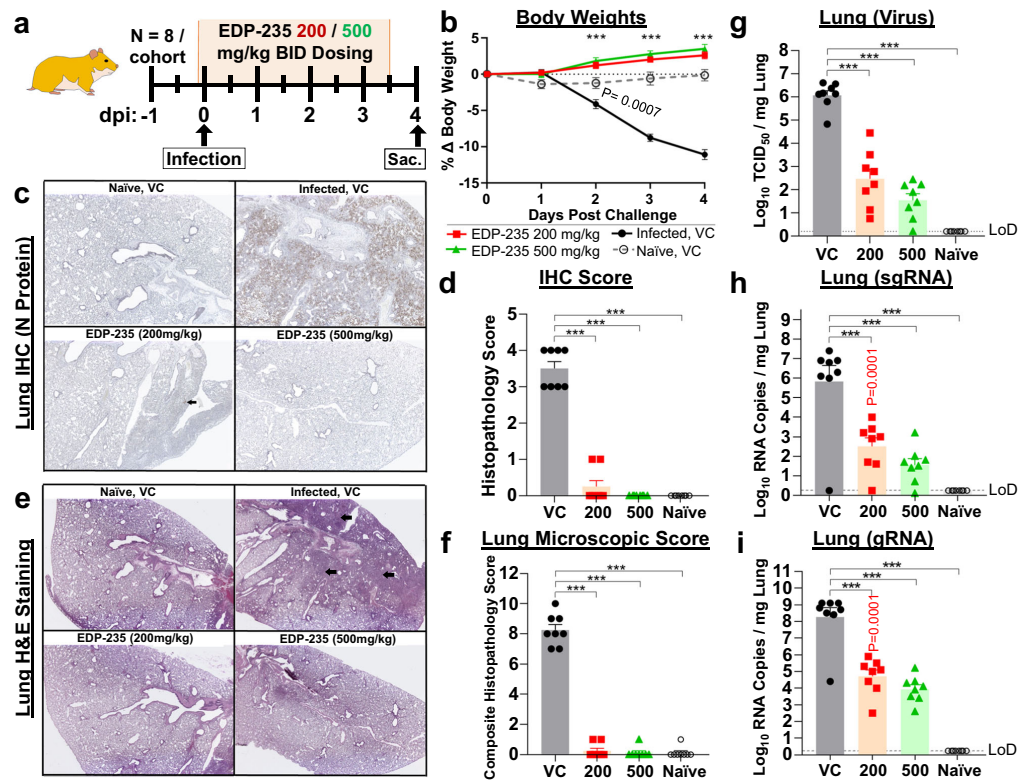


**Fig. 2 | EDP-235 is efficacious in a prophylactic Syrian hamster model.** **a** Study design. Hamsters were orally dosed with EDP-235 or vehicle 1 h prior to intranasal inoculation with  $6 \times 10^3$  TCID<sub>50</sub>/animal SARS-CoV-2 USA/WA1/2020 or PBS for naive. **b** Percent body weight change from 0-day baseline (n = 8 per cohort). **c** IHC staining of terminal lung samples for SARS-CoV-2 N protein (brown) (2X magnification). Minimal focal immunoreactivity seen in 200 mg/kg animal (arrow). Representative images shown (n = 8 per cohort). **d** Sections of panel C were scored from 1 (minimal/minor) to 5 (severe/overwhelming) (n = 8 per cohort). **e** H&E stain of terminal lung samples (1.25X magnification). SARS-CoV-2 effects characterized by dark consolidated lung regions (arrows). Representative images shown (n = 8 per cohort). **f** Left lung composite histopathology score. Microscopic finding categories were alveolar hemorrhage, alveolar/interstitial inflammation, vascular inflammation, bronchial-alveolar hyperplasia, perivascular edema, and

immunoreactivity. Each variable scored from 1-5 as in (d) (n = 8 per cohort). **g** Infectious virus titer in terminal lung samples (n = 8 per cohort). **h** sgRNA (N protein) in terminal lung samples (n = 8 per cohort). **i** gRNA (N protein) in terminal lung samples (n = 8 per cohort). All graphs are mean  $\pm$  SEM; statistical significance determined versus infected VC by 2-way ANOVA with Tukey's (b) or 1-way ANOVA with Dunnett's (d, f, g, h, i) post hoc test. All P values were < 0.0001 unless indicated otherwise in the figure. ANOVA = analysis of variance; g/sgRNA = genomic/sub-genomic RNA; h = hour; H&E = hematoxylin and eosin; IHC = immunohistochemistry; LoD = Limit of Detection; N protein = nucleocapsid protein; PBS = phosphate buffered saline; sac. = sacrifice; SARS-CoV-2 = severe acute respiratory syndrome coronavirus 2; SEM = standard error of the mean; TCID<sub>50</sub> = median tissue culture infectious dose; VC = vehicle control.

Across a range of orthogonal assays, EDP-235 demonstrated potent nanomolar efficacy against multiple SARS-CoV-2 lineages and variants. EDP-235 has a SI  $\geq$  500fold for the 3CLpro versus 30 human proteases and 50% cellular cytotoxicity concentration values of  $> 10 \mu\text{M}$ . These results indicate minimal off-target effects resulting in low toxicity. In the phase 2 SPRINT trial<sup>56</sup>, EDP-235 was generally safe and well tolerated with a low frequency of adverse events (1.3%, 6.4%, and 2.6% for 200 mg, 400 mg, and placebo arms respectively), with no serious adverse events or discontinuations observed, providing further evidence of the safety of EDP-235 in people.

The potent antiviral efficacy of EDP-235 extends beyond SARS-CoV-2 to other clinically relevant HCoVs. These endemic HCoVs are estimated to be responsible for 10–30% of all common cold infections<sup>57</sup>. Notably, EDP-235 also demonstrates activity against bat, pangolin, and pig zoonotic CoVs, effectively inhibiting the 3CLpros of

these species as well as their ability to replicate in cell culture. While SARS-CoV-2 currently poses the greatest health threat to people, there remains a risk of zoonotic spillover events, especially given humanity's widespread encroachment on natural animal habitats. EDP-235's broad-spectrum pan-coronavirus activity, and thus utility against future emerging CoVs, highlights its significance in the context of pandemic preparedness. Additionally, the rare documented cases of SARS-CoV-2 cross-transmission occurring between humans and other mammals<sup>58,59</sup> speaks to the ability of the virus to evolve undetected prior to re-infection in humans. These observations underscore the necessity of a broad-spectrum coronavirus inhibitor.

As SARS-CoV-2 mutates to better infect human cells and evade our adaptive immune system, real-world examples of emerging resistance present therapeutic challenges. Previously approved monoclonal antibody treatments have lost their effectiveness due to rapid and

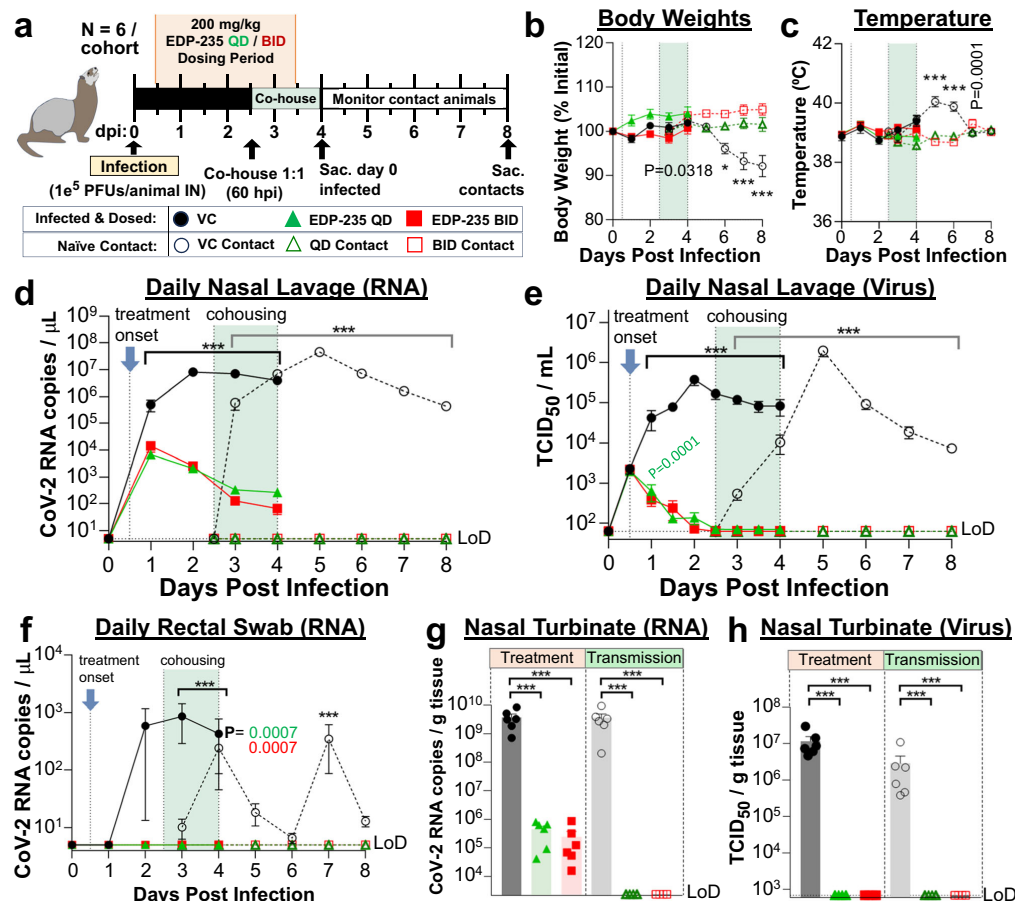


**Fig. 3 | EDP-235 effectively blocks infection and viral transmission in ferrets.** a Study design. Ferrets were infected with  $1 \times 10^5$  PFU of SARS-CoV-2 USA/WA1/2020 intranasally. 12 hpi, animals were orally dosed with vehicle or EDP-235 QD or BID. 60 hpi uninfected and untreated ferrets were co-housed 1:1 with infected dosed animals. Originally infected animals were sacrificed 4 dpi while the contact ferrets were monitored for an additional 4 days. b Percent body weight change from baseline (0 days) (n = 6 per cohort). c Animal temperature (n = 6 per cohort). d Nasal lavage viral load determined by RT-qPCR (*nsp9* gene) (n = 6 per cohort). e Nasal lavage infectious virus quantified by TCID<sub>50</sub> (n = 6 per cohort). f Rectal swab viral load determined by RT-qPCR (*nsp9* gene) (n = 6 per cohort). g Endpoint (day 4 or day 8) nasal turbinate viral load determined by RNA levels of *nsp9* (n = 6 per cohort). h Infectious virus in endpoint nasal turbinates determined by TCID<sub>50</sub> (n = 6

per cohort). All graphs are mean  $\pm$  SEM. All P-values were < 0.0001 unless indicated otherwise in the figure. Statistics are for both QD and BID differences versus vehicle and were run using 2-way ANOVA with Tukey's (b–f) or 1-way ANOVA with Dunnett's (g, h) post hoc test. In (b–f), both QD and BID treatment resulted in the same statistical significance versus vehicle-treated animals in both primary challenged and contact animals except where noted in (e). ANOVA = analysis of variance; BID = twice daily; dpi = days post-infection; hpi = hours post-infection; LoD = limit of detection; *nsp9* = non-structural protein 9; PFU = plaque-forming units; QD = once a day; RT-qPCR = reverse transcription quantitative polymerase chain reaction; sac = sacrifice; SARS-CoV-2 = severe acute respiratory syndrome coronavirus 2; SEM = standard error of the mean; TCID<sub>50</sub> = median tissue culture infectious dose; VC = vehicle control.

continual spike mutations<sup>24</sup>. Encouragingly, there has been limited development of resistance to the nucleoside analogs remdesivir and molnupiravir, as well as the 3CLpro inhibitor nirmatrelvir<sup>28,60,61</sup>. However, multiple in vitro studies have selected for 3CLpro mutations conferring resistance to nirmatrelvir<sup>27,29–32</sup>, so the possibility of clinical resistance remains.

In cross-resistance testing, EDP-235 matched or improved upon the antiviral potency of nirmatrelvir across all assessed variants. Variant EDP-235 resistance was inversely proportional to 3CLpro activity, with EDP-235 potency shifts > 5-fold suffering 7–125-fold reductions in enzymatic activity. These deficiencies may contribute to the lack of

emergence of the most drug-resistant variants in patient populations, as they are likely fitness-impaired. Indeed, the 3CLpro's lack of sequence-plasticity<sup>45</sup> likely contributes to EDP-235's broad activity across both human and zoonotic coronaviruses.

The translatability of the Syrian golden hamster model to human clinical benefit has been established with the 3CLpro inhibitors nirmatrelvir and ensitrelvir<sup>62,63</sup>. Pathophysiology in hamsters resembles the early pathology of SARS-CoV-2 in people, with histological changes, high viral loads achieved in the lungs, and associated clinical signs<sup>49,64</sup>. EDP-235 was protective against virus-induced weight loss, and significantly reduced viral burden and lung histopathology. Given

## Article

<https://doi.org/10.1038/s41467-024-50931-8>

the translatability of the hamster model, these results suggest that EDP-235 has the potential to not only reduce viral load but also improve clinical symptoms.

The ferret model's utility as a predictor of clinical relevance for people has also been established with remdesivir, molnupiravir, and nirmatrelvir<sup>52,54,65</sup>. In ferrets, SARS-CoV-2 replicates to high titers primarily in the upper airways. While ferrets do not generally present with clinical signs, they do function well as a transmission model of disease<sup>51</sup>. Our ferret study was designed to evaluate the antiviral effect of EDP-235 when dosed therapeutically, as well as its ability to prevent SARS-CoV-2 contact transmission to treatment-naïve animals co-housed 48 h post-treatment of the infected animals. Indeed, not only did EDP-235 show potent antiviral effects in primary-infected ferrets, it also completely prevented transmission to treatment-naïve animals. The ability to prevent or reduce transmission has broad implications with regards to isolation of infected individuals and quarantine of household contacts.

Social isolation following infection with SARS-CoV-2 is disruptive to the lives of both the infected and their families<sup>66,67</sup>. This also carries broader economic and social burdens, from lost productivity with isolation to continued viral transmission enabled by a premature return to social settings. Both Pfizer's phase 2/3 EPIC-PEP trial of Paxlovid and Merck's MOVE-AHEAD phase 3 trial of Lagevrio explored post-exposure prophylactic treatment to prevent this transmission, but while positive trends were observed for both studies, neither was able to reach statistical significance over placebo<sup>68,69</sup>. Similar results were seen in a ferret model; nirmatrelvir administered with ritonavir was dosed to match human exposure levels. However, this failed to block transmission to untreated contact animals in a similar design to our own study, or when dosed prophylactically post-exposure<sup>52</sup>. Conversely, parallel testing of molnupiravir prevented such transmission in ferrets. While the methodologies of this molnupiravir ferret work differed from the Merck clinical trial design (infected-dosed ferrets prevented transmission to naïve versus patient prophylactic administration post-exposure did not), these results somewhat obscure the translatability of ferret transmission studies to human clinical benefit<sup>52,65</sup>. Despite this ambiguity, the ability of EDP-235 to prevent viral transmission between ferrets, while nirmatrelvir did not, suggests EDP-235 may offer a distinct advantage over Paxlovid in blocking transmission to close contacts. Having an antiviral agent which could enable not only a faster but also a safer return of infected individuals to social environments would be of great benefit.

In summary, EDP-235 is a potent oral inhibitor of SARS-CoV-2, with consistent potencies against all commonly circulating variants tested to date as well as against other human and non-human coronaviruses. EDP-235 is highly selective for the coronavirus 3CLpro active site and has no measurable cytotoxicity up to 10  $\mu$ M. EDP-235 demonstrated an improved profile over nirmatrelvir in cross-resistance testing against known SARS-CoV-2 3CLpro variants found both naturally and through in vitro selection<sup>27,28</sup>. In animal testing, EDP-235 protected Syrian golden hamsters from viral-induced distress and histopathology, with multi-log<sub>10</sub> reductions in viral titers and RNA levels. In the ferret model, therapeutic EDP-235 treatment rapidly decreased both viral titers and RNA below the LoD and prevented transmission to untreated co-housed ferrets. EDP-235's potential as a treatment for COVID-19 should continue to be evaluated in human clinical trials.

## Methods

### Cell culture, viruses, and compounds

HuH-7 (JCRB0403), LLC-MK2 (CCL-7), HCT-8 (CCL-244), and MRC5 (CCL-171) cells were obtained from JCRB (HuH-7) or ATCC and cultured in Dulbecco's Modified Eagle Medium (Corning), OPTI-MEM reduced serum media (Gibco), Roswell Park Memorial Institute 1640 medium

(Gibco), or Eagle's Minimum Essential Medium (Corning) respectively. All cell lines were supplemented with either 2% (LLC-MK2 cells) or 10% fetal bovine serum (Gibco) and 1X Anti/Anti or 1X penicillin and streptomycin (Gibco). HuH-7 cells were supplemented with 1X GlutaMAX (Gibco). All cell lines tested negative for mycoplasma contamination (MycAlert™ Mycoplasma Detection Kit, Lonza). HCT-8 and MRC-5 cell lines were authenticated using STR profiling. HuH-7 cell line was authenticated using isozyme analysis. LLC-MK2 cell line was not authenticated by vendor.

HCoV-229E (University of Texas Medical Branch, and ATCC), was propagated in MRC-5 cells. HCoV-NL63 (BEI Resources) was amplified in LLC-MK2 cells. HCoV-OC43 (University of Texas Medical Branch) was grown in HCT-8 cells. HCoV-229E, HCoV-NL63 and HCoV-OC43 were propagated at an MOI of 0.1. When infected monolayers had 60–70% CPE, viruses were collected, pre-clarified, supplemented with cryoprotectant agents, and titered by TCID<sub>50</sub> or plaque assays. Southern Research (SR) obtained and titered SARS-CoV-2 USA-WA1/2020, B.1.617.2, B.1.1.529 strains, and SARS-CoV Toronto 2. Viroclinics Biosciences (VCB) obtained and titered SARS-CoV-2 Germany/BavPat1/2020, B.1.351, B.1.1.7, SARS-CoV HKU-39849, and MERS-CoV EMC/2012 strains. Georgia State University (GSU) obtained and titered SARS-CoV-2 B.1.1.529, BA.2, BA.2.12.1, BA.4, BA.5.1, BQ.1.1, XBB.1.5, EG.5.1, EG.5.1.1, EG.5.2, and BA.2.86 strains. SR and VCB obtained Vero E6 cells from ATCC. GSU obtained Vero E6-TMPRSS2 cells from BBS Bioscience.

Unless otherwise specified, all cells, virus infections and cell-based assays were incubated at 37 °C in a humidified and 5% CO<sub>2</sub> atmosphere.

All compounds were synthesized by Enanta Pharmaceuticals, Inc. EDP-235 and Nirmatrelvir had purity of 98.6% and 98.2%, respectively. Compounds were resuspended in dimethyl sulfoxide (DMSO) and added manually or with an automated liquid handler (ECHO 650 Beckman Coulter). CP-100356 was purchased from Axon Medchem with a purity of 98.7%. All compounds utilized in this study meet community criteria for chemical probes.

### Biochemical assays

IC<sub>50</sub>s were determined using a previously established FRET assay<sup>40</sup>. Briefly, ancestral (USA-WA1/2020), variants described, or zoonotic SARS-CoV-2 3CLpro proteins were expressed and purified from *E. coli* (Shanghai ChemPartner Co.). Recombinant proteins were incubated at room temperature for 30 min with increasing concentrations of compound (EDP-235 or nirmatrelvir) in 50 mM HEPES pH 7.5, 5 mM NaCl, 1 mM EDTA, 0.1 mg/mL BSA, 1 mM DTT, and 0.01% volume per volume TritonX-100. The FRET substrate, Tamra-SIT-SAVLQSGFRKMK-Dabcyl-OH, (BACHEM Holding) was added 30 minutes post-incubation, and fluorescence was measured over 1 h at room temperature (Envision, PerkinElmer). Progress curves were used to determine the initial velocities with IC<sub>50</sub>s and hill coefficient values calculated as previously described in ref. 70. The final concentration of 3CLpro protein was 2.5–100 nM, and FRET substrate was 20–40  $\mu$ M. Variations in concentrations were due to inherent differences in 3CLpro activity and FRET substrate affinity. For time-dependent inhibition experiments, progress curves obtained at various concentrations of EDP-235 against ancestral 3CLpro without preincubation were corrected for baseline by subtraction of the no enzyme progress curves. Individual baseline corrected progress curves were fitted to the time-dependent inhibition model using non-linear regression fitting in GraphPad Prism<sup>70</sup>. The reversibility of inhibition was evaluated through incubation with varying 3CLpro concentrations (0–50  $\mu$ M) with 50  $\mu$ M of EDP-235 for 2 h at RT, followed by jump-dilution with 20  $\mu$ M FRET substrate as given above. The progress curves for activity recovery were then fitted to the time-dependent inhibition model. To determine the  $K_i^{app}$  of 3 nM, kinetic mechanism experiments were performed with FRET substrate concentrations ranging from 0 to 100  $\mu$ M and the FRET substrate being



## Article

<https://doi.org/10.1038/s41467-024-50931-8>

added at time 0.  $K_i^{app}$  values were generated by fitting to substrate competitive inhibition with respect to the FRET peptide<sup>30</sup>.

**X-ray crystallography and structure determination**

X-ray crystallography work was performed at Evotec. Crystals were grown over two days in a 200 mM sodium thiocyanate, 20 percent weight per volume polyethylene glycol 3350 (MDL JCSG+ condition B2) with a drop ratio of 30:63:6 (protein:reservoir:seed suspension). Mass spectrometry was used to confirm the covalent attachment of EDP-235 and the 3CLpro. To collect diffraction data, the crystal was transferred to a drop of neat reservoir solution, to this was added 10% weight per volume polyethylene glycol 400 in reservoir solution. The resulting drop was stirred until homogenous with a final composition of 5% weight per volume of polyethylene glycol 400 in reservoir condition. The crystal was promptly cryo-cooled by dunking into liquid nitrogen. An X-ray diffraction dataset to 2.0 Å was recorded with the Advanced Photon Source (Argonne National Laboratory), using IMCA-CAT's beamline at full transmission and an oscillation range of 0.2° and exposure time of 0.02 seconds per frame for 900 frames. The wavelength of the X-ray beam was 1.000 Å. Integration, scaling and merging of the diffraction data was performed with autoPROC STARANISO software (1.1.7 (20211020), 2.3.87 beta for linux64-ifort made on Jun 08 2022 at 02:21:31, Global Phasing Ltd.). Molecular replacement was performed using Phaser as implemented in the CCP4i suite (CCP4 Interface version 7.1.018). The ligand model and its crystallographic restraints were created using Grade2 software (version 1.2.0, Global Phasing Ltd.). Refinement of the structure, including generation of restraints for the covalent link between the ligand and C145, was performed using the crystallography software Buster (2.11.8 (22-FEB-2023), Global Phasing Ltd.) with manual rebuilding and water placement in COOT (0.9.7, Emsley, University of Cambridge). Additional crystallography details can be found in the Supplementary methods, Supplementary Table 2, and Supplementary Fig. 12.

**SARS-CoV-2 replicon screening**

A bacterial artificial chromosome encoding a SARS-CoV-2 (USA-WA1/2020) replicon was purchased (Telesis Bio) and a modified screening protocol for SARS-CoV-2 replicon system was developed in-house<sup>31,42</sup>. The replicon fragment and a codon-optimized SARS-CoV-2 N (GeneART, Invitrogen) were PCR amplified (Platinum SuperFi II PCR Master Mix, Invitrogen), in vitro transcribed with mMESAGE mMACHINE T7 Ultra (Invitrogen) and purified using the Monarch kit (New England Biolabs) per manufacturers' recommendations. 650 ng of replicon and N were electroporated using the Neon Transfection System (Invitrogen) at 1700V-20ms-1 pulse into HuH-7 cells (110<sup>7</sup> cells/mL) following the manufacturers' protocol. Cells were diluted to 800 cells/μL by adding complete HuH-7 media excluding penicillin and streptomycin, and compounds were added. Electroporated HuH-7 cells containing no RNA and treated with DMSO were used as a low control. High control contained SARS-CoV-2 replicon, N RNA, and was treated with DMSO. Plates were incubated for 20 h and luminescence was measured using the Renilla-Glo<sup>®</sup> Luciferase Assay Reagent (Promega). The percent residual activity of the replicon was determined after normalizing to DMSO-treated low and high controls.

**Coronavirus infectious virus assays**

BSL3-experiments were performed at multiple facilities: Georgia State University (GSU), Southern Research (SR) and Viroclinics Biosciences (VCB). Vero E6-TMPRSS2 cells were seeded 14 h pre-infection (GSU), or Vero E6 cells were seeded in suspension at the time of infection (SR and VCB). Monolayers were infected with an MOI of 0.1 (SARS-CoV-2 Omicron strains), 0.002 (SARS-CoV-2 lineage A USA-WA1/2020 and Delta strains, SARS-CoV Toronto-2 isolate), or 0.001 (SARS-CoV-2 lineage B Germany/BavPat1/2020 isolate, Alpha and Beta strains, SARS-CoV HKU-39849 isolate and MERS-CoV EMC/2012 isolate). EDP-235 in

the presence or absence of 0.5–2 μM PGPI was added at the time of infection. Results were determined as follows: at 48 hpi, the supernatant was collected and titered by either TCID<sub>50</sub> or plaque assay (GSU). At 72 hpi, cell health was determined using Cell-Titer-Glo (Promega) per manufacturer's instructions and luminescence was measured (CLARIOstar, BMG LabTech Inc.) (SR). After 18–24 hpi, cells were immunostained for SARS-CoV-2 N protein and foci were counted (Immunospot Image Analyzer) (VCB). All experiments performed at GSU using infectious SARS-CoV-2 strains were approved by the Georgia State Institutional Biosafety Committee under protocol B20016 and performed in BSL-3/ABSL-3 facilities.

SARS-CoV-2 3D pHAEC experiments were performed at VCB, with Mucilair pHAEC tissues sourced from Epithelix. Tissues were pre-treated basolaterally with EDP-235 for 2 h prior to apical infection at MOI of 1 (SARS-CoV-2 lineage B Germany/BavPat1/2020 isolate) for 1 h. The inoculum was removed, tissues were washed and incubated for 48 h. At 24 and 48 hpi, 200 μL apical samples were harvested for analysis by TCID<sub>50</sub> and RT-qPCR.

HCoV-229E, OC43 and NL63 antiviral assays were performed at Enanta Pharmaceuticals, Inc., and were assessed in MRC-5, HCT-8, and LLC-MK2 cells, respectively. MRC-5 cells were infected in suspension at an MOI of 0.05 and incubated at 34 °C for 6 days. HCT-8 and LLC-MK2 cells were seeded 24 h prior to infections and monolayers were infected at 100 TCID<sub>50</sub> (OC43) or an MOI of 0.01 (NL63). OC43 and NL63 infections were incubated at 34 and 32 °C, respectively, for 7 days. For CPE-based assays, cell health was assessed using ATP-lite (Perkin Elmer), and luminescence was measured (Envision). For RT-qPCR-based endpoints, viral RNA was extracted from cells and supernatant (Quick-RNA Viral 96 Kit, Zymo Research) and quantified by RT-qPCR using TaqMan RNA-to-Ct-1Step (Applied Biosystems) on the POD Quant Studio 7 Flex Machine (Thermo Fisher).

For HCoV-229E infections in 3D pHAEC EpiAirway sourced from a 23-year-old Caucasian male (MatTek, AIR-100), apical surfaces were washed once with transepithelial electrical resistance buffer, and DMSO or compound was added to the basal media. Adsorptions were performed apically for 1.5 h with 2 × 10<sup>5</sup> PFU per tissue. After 1.5 h the adsorption inoculum was removed, the apical surface was washed once with transepithelial electrical resistance buffer, and plates incubated for 5 days. The basal media was changed once after 2-3 days, maintaining DMSO or compound concentration. Total RNA was extracted using RNAqueous Total RNA Isolation Kit (ThermoFisher), and viral RNA was quantified using RT-qPCR as described above.

Infectious zoonotic CoV antiviral assays were performed at University of North Carolina, Chapel Hill. Reporter *sarbecoviruses* or *merbecoviruses* expressing recombinant nanoluciferase were used to perform cell-based antiviral assays in either A549-hACE2 or Huh7.5 cells, respectively. Reporter viruses were generated from infectious clones as previously described in refs. 47,48,71. Briefly, 2 × 10<sup>4</sup> A549-hACE2 or 2.5 × 10<sup>4</sup> Huh7.5 cells were seeded 24 h before infection with DMSO normalized across the plate. Cells were infected at a MOI of 0.1 for 1 h after which the inoculum was removed, and monolayers washed one time. A dilution series of compound was added to the monolayer and replication was measured at 24 hpi by addition of NanoGlo Luciferase Assay System (Promega).

**Cytotoxicity assays**

Cytotoxicity assays were performed identically to their respective viral efficacy studies, but without addition of virus and using a cell viability readout.

**Protease selectivity**

Selectivity of EDP-235 was determined as described in the biochemical assays section of these Methods. Additional materials and conditions are listed in Supplementary Table 7. All work was performed at Reaction Biology.

## Article

<https://doi.org/10.1038/s41467-024-50931-8>**In vivo studies**

Studies with male golden Syrian hamsters 1–2 months of age were run at BIOQUAL, Inc. with eight animals per cohort. Hamster in vivo studies involving SARS-CoV-2 were performed in accordance with BIOQUAL standard procedures, the Association for Assessment and Accreditation of Laboratory Animal Care, the Animal Welfare Act, the Public Health Service Policy on Human Care and Use of Laboratory Animals, and Centers for Disease Control. Experiments with SARS-CoV-2 involving hamsters were performed under Institutional Animal Care and Use Committee-approved protocol #22-101P and were sourced from Envigo. Intramuscular anesthesia was used for all procedures. Vehicle and EDP-235 doses (20 and 50 mg/mL) were prepared in 0.5% methylcellulose in deionized water and mixed for 30 min prior to and during oral dosing. Viral intranasal inoculation of SARS-CoV-2 USA/WA1/2020 (generated by BIOQUAL) was delivered as  $3 \times 10^4$  PFU per nostril in 50  $\mu$ L PBS, with the head tilted back for 20 s. Animal body weight symptoms were recorded throughout the study. At 4 dpi, animals were euthanized. The whole lung was collected during necropsy, with weight and physical observations recorded before sectioning and snap-freezing or storage in 10% neutral buffered formalin. Nares and tracheas were collected and snap frozen. TCID<sub>50</sub> analysis was run on lung, nares, and trachea samples. RT-qPCR (*N* gene) analysis was run on lung and nares samples. Histopathology services were performed by Experimental Pathology Laboratories, Inc. Fixed lung was processed for IHC detection of SARS-CoV-2 nucleocapsid protein, using a SARS-CoV-2 (COVID-19) nucleocapsid antibody on formalin-fixed paraffin-embedded tissue. Anti-SARS-CoV-2, 0.02  $\mu$ g/mL, primary antibody (ProSci, 9099; SARS-CoV-2 (COVID-19) Nucleocapsid Antibody) was applied to tissues overnight at 4 °C ( $\pm 2^\circ$ C) followed by ImmPRESS Polymer Anti-Rabbit IgG Reagent (made in goat, RTU, Vector Labs, MP-7451) for 30 min, DAB solution (3 min), and counterstained with hematoxylin.

Studies with female ferrets 6–10 months of age sourced from Triple F farms were run at GSU with six animals per cohort. All in vivo studies involving ferrets were performed in compliance with the Guide for the Care and Use of Laboratory Animals, National Institutes of Health guidelines, and the Animal Welfare Act Code of Federal Regulations. Experiments with SARS-CoV-2 involving ferrets were approved by the Georgia State Institutional Animal Care and Use Committee under protocol A20031. Vehicle and EDP-235 doses (200 mg/kg BID or QD) were prepared in 0.5% methylcellulose in deionized water before each dosing. Ferrets received intranasal viral inoculation of  $1 \times 10^5$  PFU of SARS-CoV-2 USA/WA1/2020, and oral dosing of vehicle or EDP-235 began at 12 hpi and continued for three days. At 60 hpi (48 h post-treatment initiation), each ferret was co-housed with an uninfected, untreated contact ferret until day 4. Source ferrets were euthanized on day 4, and contact ferrets were further monitored before being euthanized on day 8. Homogenized nasal turbinates were collected from all ferrets subsequent to euthanizing. On days 0–4, nasal lavages from source and contact ferrets were collected twice a day. On days 5–8, nasal lavages were collected from contact ferrets once a day. Weight and temperature were recorded from all ferrets once a day, and a rectal swab was taken. Lavage and turbinate samples were subject to TCID<sub>50</sub> analysis to determine infectious viral load. RT-qPCR (*nsp9* gene) was used to quantify RNA copies in lavage, turbinates, and rectal swab samples.

**Pharmacokinetic studies**

Ferret plasma exposure levels and pharmacokinetic calculations were determined as follows; performed at Enanta Pharmaceuticals, Inc. Following a single oral dose of EDP-235 in 3 female ferrets per arm, plasma samples were collected at 1, 2, 3, 4, 6, 8, 12, and 24 h. Subsequently, plasma samples were deproteinized with acetonitrile (Fisher)

and an internal standard acetonitrile solution. Post centrifugation, quantitation of EDP-235 within the supernatant was determined by liquid chromatography-tandem mass spectrometric method. Calibrators were prepared with blank plasma and standards following the same procedure as sample preparation.

**Materials and data analysis**

Primer/probe sequences utilized in Methods are listed in Supplementary Table 8. Data analysis for all experiments was performed in GraphPad Prism (version 10.1.2 (324)) or XLfit (version 2405, Microsoft Excel). Binding constants and best-fit equations were determined using GraphPad Prism Software. Efficacy, and cytotoxicity concentrations were calculated with a variable slope four-parameter logistic model.

**Reporting summary**

Further information on research design is available in the Nature Portfolio Reporting Summary linked to this article.

**Data availability**

All source data used in this study are provided in the Supplementary Information/Source Data files. The EDP-235 bound 3CLpro X-ray crystal structure can be found at the protein data bank (<https://www.rcsb.org/>). PDB accession #: 8VDJ. Source data are provided with this paper.

**References**

- World Health Organization. *Coronavirus disease (COVID-19)*. (2023).
- Li, G., Hilgenfeld, R., Whitley, R. & De Clercq, E. Therapeutic strategies for COVID-19: progress and lessons learned. *Nat. Rev. Drug Discov.* **22**, 449–475 (2023).
- Hammond, J. et al. Oral Nirmatrelvir for High-Risk, Nonhospitalized Adults with Covid-19. *N. Engl. J. Med.* **386**, 1397–1408 (2022).
- Jayk Bernal, A. et al. Molnupiravir for Oral Treatment of Covid-19 in Nonhospitalized Patients. *N. Engl. J. Med.* **386**, 509–520 (2022).
- Matrajt, L., Brown, E. R., Cohen, M. S., Dimitrov, D. & Janes, H. Could widespread use of antiviral treatment curb the COVID-19 pandemic? A modeling study. *BMC Infect. Dis.* **22**, 683 (2022).
- Khunte, M., Kumar, S., Salomon, J. A. & Bilinski, A. Projected COVID-19 Mortality Reduction From Paxlovid Rollout. *JAMA Health Forum* **4**, e230046 (2023).
- Mukae, H. et al. Efficacy and Safety of Ensitrelvir in Patients With Mild-to-Moderate Coronavirus Disease 2019: The Phase 2b Part of a Randomized, Placebo-Controlled, Phase 2/3 Study. *Clin. Infect. Dis.* **76**, 1403–1411 (2023).
- Pillaiyar, T., Manickam, M., Namasivayam, V., Hayashi, Y. & Jung, S.-H. An Overview of Severe Acute Respiratory Syndrome-Coronavirus (SARS-CoV) 3CL Protease Inhibitors: Peptidomimetics and Small Molecule Chemotherapy. *J. Med. Chem.* **59**, 6595–6628 (2016).
- Yang, H. et al. The crystal structures of severe acute respiratory syndrome virus main protease and its complex with an inhibitor. *Proc. Natl. Acad. Sci. USA* **100**, 13190–13195 (2003).
- Ziebuhr, J., Snijder, E. J. & Gorbalenya, A. E. Virus-encoded proteinases and proteolytic processing in the Nidovirales. *J. Gen. Virol.* **81**, 853–879 (2000).
- Lv, Z., Chu, Y. & Wang, Y. HIV protease inhibitors: a review of molecular selectivity and toxicity. *HIV AIDS (Auckl.)* **7**, 95–104 (2015).
- de Leuw, P. & Stephan, C. Protease inhibitors for the treatment of hepatitis C virus infection. *GMS Infect. Dis.* **5**, Doc08 (2017).
- Jin, Z. et al. Structure of Mpro from SARS-CoV-2 and discovery of its inhibitors. *Nature* **582**, 289–293 (2020).
- Kandwal, S. & Fayne, D. Genetic conservation across SARS-CoV-2 non-structural proteins - Insights into possible targets for treatment of future viral outbreaks. *Virology* **581**, 97–115 (2023).

## Article

<https://doi.org/10.1038/s41467-024-50931-8>

15. Anand, K., Ziebuhr, J., Wadhvani, P., Mesters, J. R. & Hilgenfeld, R. Coronavirus Main Proteinase (3CLpro) Structure: Basis for Design of Anti-SARS Drugs. *Science* **300**, 1763–1767 (2003).
16. Antiviral and Antibody Products Summary Recommendations. COVID-19 Treatment Guidelines <https://www.covid19treatmentguidelines.nih.gov/therapies/antivirals-including-antibody-products/summary-recommendations/>.
17. Owen, D. R. et al. An oral SARS-CoV-2 M(pro) inhibitor clinical candidate for the treatment of COVID-19. *Science* **374**, 1586–1593 (2021).
18. Loos, N. H. C., Beijnen, J. H. & Schinkel, A. H. The Mechanism-Based Inactivation of CYP3A4 by Ritonavir: What Mechanism? *Int. J. Mol. Sci.* **23**, 9866 (2022).
19. Eng, H. et al. Disposition of Nirmatrelvir, an Orally Bioavailable Inhibitor of SARS-CoV-2 3C-Like Protease, across Animals and Humans. *Drug Metab. Dispos.* **50**, 576–590 (2022).
20. Pfizer Announces Additional Phase 2/3 Study Results Confirming Robust Efficacy of Novel COVID-19 Oral Antiviral Treatment Candidate in Reducing Risk of Hospitalization or Death | Pfizer. <https://www.pfizer.com/news/press-release/press-release-detail/pfizer-announces-additional-phase-23-study-results>.
21. Lam, C. & Patel, P. Nirmatrelvir-Ritonavir. in *StatPearls* (StatPearls Publishing, Treasure Island (FL), 2023).
22. Duffy, S. Why are RNA virus mutation rates so damn high? *PLoS Biol.* **16**, e3000003 (2018).
23. Cox, M. et al. SARS-CoV-2 variant evasion of monoclonal antibodies based on in vitro studies. *Nat. Rev. Microbiol.* **21**, 112–124 (2023).
24. Hoffmann, M. et al. The Omicron variant is highly resistant against antibody-mediated neutralization: Implications for control of the COVID-19 pandemic. *Cell* **185**, 447–456.e11 (2022).
25. Zabidi, N. Z. et al. Evolution of SARS-CoV-2 Variants: Implications on Immune Escape, Vaccination, Therapeutic and Diagnostic Strategies. *Viruses* **15**, 944 (2023).
26. Fernandes, Q. et al. Emerging COVID-19 variants and their impact on SARS-CoV-2 diagnosis, therapeutics and vaccines. *Ann. Med.* **54**, 524–540 (2022).
27. Iketani, S. et al. Multiple pathways for SARS-CoV-2 resistance to nirmatrelvir. *Nature* **613**, 558–564 (2023).
28. Zuckerman, N. S., Bucris, E., Keidar-Friedman, D., Amsalem, M. & Brosh-Nissimov, T. Nirmatrelvir resistance - de novo E166V/L50V mutations in an immunocompromised patient treated with prolonged nirmatrelvir/ritonavir monotherapy leading to clinical and virological treatment failure - a case report. *Clin. Infect. Dis.* <https://doi.org/10.1093/cid/ciad494>. (2023).
29. Flynn, J. M. et al. Systematic Analyses of the Resistance Potential of Drugs Targeting SARS-CoV-2 Main Protease. *ACS Infect. Dis.* **9**, 1372–1386 (2023).
30. Jochmans, D. et al. The Substitutions L50F, E166A, and L167F in SARS-CoV-2 3CLpro Are Selected by a Protease Inhibitor In Vitro and Confer Resistance To Nirmatrelvir. *mBio* **14**, e0281522 (2023).
31. Zhou, Y. et al. Nirmatrelvir-resistant SARS-CoV-2 variants with high fitness in an infectious cell culture system. *Sci. Adv.* **8**, eadd7197 (2022).
32. Heilmann, E. et al. SARS-CoV-2 3CL<sup>pro</sup> mutations selected in a VSV-based system confer resistance to nirmatrelvir, ensitrelvir, and GC376. *Sci. Transl. Med.* **15**, eabq7360 (2023).
33. Carlson, C. J. et al. Climate change increases cross-species viral transmission risk. *Nature* **607**, 555–562 (2022).
34. Gebara, M. F., May, P. H. & Platals, G. Pandemics, conservation, and human-nature relations. *Clim. Change Ecol.* **2**, 100029 (2021).
35. Human Coronavirus Types | CDC. <https://www.cdc.gov/coronavirus/types.html> (2021).
36. Vlasova, A. N. et al. Novel Canine Coronavirus Isolated from a Hospitalized Patient With Pneumonia in East Malaysia. *Clin. Infect. Dis.* **74**, 446–454 (2022).
37. Lednicky, J. A. et al. Independent infections of porcine deltacoronavirus among Haitian children. *Nature* **600**, 133–137 (2021).
38. Enanta Pharmaceuticals, Inc. *NCT05616728. A Study to Evaluate EDP-235 in Non-hospitalized Adults With COVID-19 (SPRINT)*. (2022).
39. Chia, C. S. B. & See, Y. Y. Novel Coronavirus Main Protease Di- and Tripeptide Inhibitors for Treating COVID-19. *ACS Med. Chem. Lett.* **13**, 1388–1389 (2022).
40. Hoffman, R. L. et al. Discovery of Ketone-Based Covalent Inhibitors of Coronavirus 3CL Proteases for the Potential Therapeutic Treatment of COVID-19. *J. Med. Chem.* **63**, 12725–12747 (2020).
41. He, X. et al. Generation of SARS-CoV-2 reporter replicon for high-throughput antiviral screening and testing. *Proc. Natl. Acad. Sci. USA* **118**, e2025866118 (2021).
42. Khan, J. Q. et al. Generation of a SARS-CoV-2 Reverse Genetics System and Novel Human Lung Cell Lines That Exhibit High Virus-Induced Cytopathology. *Viruses* **15**, 1281 (2023).
43. De Rosa, M. F., Silience, D., Ackerley, C. & Lingwood, C. Role of multiple drug resistance protein 1 in neutral but not acidic glycosphingolipid biosynthesis. *J. Biol. Chem.* **279**, 7867–7876 (2004).
44. Kalgutkar, A. S. et al. N-(3,4-dimethoxyphenethyl)-4-(6,7-dimethoxy-3,4-dihydroisoquinolin-2[1H]-yl)-6,7-dimethoxyquinazolin-2-amine (CP-100,356) as a ‘chemical knock-out equivalent’ to assess the impact of efflux transporters on oral drug absorption in the rat. *J. Pharm. Sci.* **98**, 4914–4927 (2009).
45. Zhou, H. et al. Identification of novel bat coronaviruses shed light on the evolutionary origins of SARS-CoV-2 and related viruses. *Cell* **184**, 4380–4391.e14 (2021).
46. Martinez, D. R. et al. Chimeric spike mRNA vaccines protect against Sarbecovirus challenge in mice. *Science* **373**, 991–998 (2021).
47. Hou, Y. J. et al. Host range, transmissibility and antigenicity of a pangolin coronavirus. *Nat. Microbiol.* **8**, 1820–1833 (2023).
48. Tse, L. V. et al. A MERS-CoV antibody neutralizes a pre-emerging group 2c bat coronavirus. *Sci. Transl. Med.* **15**, eadg5567 (2023).
49. Sia, S. F. et al. Pathogenesis and transmission of SARS-CoV-2 in golden hamsters. *Nature* **583**, 834–838 (2020).
50. Chan, J. F. et al. Simulation of the Clinical and Pathological Manifestations of Coronavirus Disease 2019 (COVID-19) in a Golden Syrian Hamster Model: Implications for Disease Pathogenesis and Transmissibility. *Clin. Infect. Dis.* **71**, 2428–2446 (2020).
51. Richard, M. et al. SARS-CoV-2 is transmitted via contact and via the air between ferrets. *Nat. Commun.* **11**, 3496 (2020).
52. Cox, R. M. et al. Comparing molnupiravir and nirmatrelvir/ritonavir efficacy and the effects on SARS-CoV-2 transmission in animal models. *Nat. Commun.* **14**, 4731 (2023).
53. Del La Rosa, G. *EDP-235, an Oral, Once Daily, Ritonavir-Free, 3CL Protease Inhibitor for the Treatment of COVID-19: Results from Phase 1 Study in Healthy Subjects*. (2023).
54. Cox, R. M. et al. Oral prodrug of remdesivir parent GS-441524 is efficacious against SARS-CoV-2 in ferrets. *Nat. Commun.* **12**, 6415 (2021).
55. Toussi, S. S., Hammond, J. L., Gerstenberger, B. S. & Anderson, A. S. Therapeutics for COVID-19. *Nat. Microbiol.* **8**, 771–786 (2023).
56. Enanta Pharmaceuticals, Inc. *SPRINT Data Presentation*. (2023).
57. Paules, C. I., Marston, H. D. & Fauci, A. S. Coronavirus Infections—More Than Just the Common Cold. *JAMA* **323**, 707–708 (2020).
58. Feng, A. et al. Transmission of SARS-CoV-2 in free-ranging white-tailed deer in the United States. *Nat. Commun.* **14**, 4078 (2023).
59. CDC. COVID-19 and Your Health. *Centers for Disease Control and Prevention* <https://www.cdc.gov/coronavirus/2019-ncov/daily-life-coping/animals.html> (2020).
60. Hirotsu, Y. et al. Multidrug-resistant mutations to antiviral and antibody therapy in an immunocompromised patient infected with SARS-CoV-2. *Med* **4**, 813–824.e4 (2023).



## Article

<https://doi.org/10.1038/s41467-024-50931-8>

61. Sanderson, T. et al. A molnupiravir-associated mutational signature in global SARS-CoV-2 genomes. *Nature* 1–3. <https://doi.org/10.1038/s41586-023-06649-6>. (2023)
62. Abdelnabi, R. et al. The oral protease inhibitor (PF-07321332) protects Syrian hamsters against infection with SARS-CoV-2 variants of concern. *Nat. Commun.* **13**, 719 (2022).
63. Sasaki, M. et al. S-217622, a SARS-CoV-2 main protease inhibitor, decreases viral load and ameliorates COVID-19 severity in hamsters. *Sci. Transl. Med.* **15**, eabq4064 (2023).
64. Braxton, A. M. et al. Hamsters as a Model of Severe Acute Respiratory Syndrome Coronavirus-2. *Comp. Med.* **71**, 398–410 (2021).
65. Cox, R. M., Wolf, J. D. & Plemper, R. K. Therapeutically administered ribonucleoside analogue MK-4482/EIDD-2801 blocks SARS-CoV-2 transmission in ferrets. *Nat. Microbiol.* **6**, 11–18 (2021).
66. Clair, R., Gordon, M., Kroon, M. & Reilly, C. The effects of social isolation on well-being and life satisfaction during pandemic. *Humanit Soc. Sci. Commun.* **8**, 28 (2021).
67. Jeffers, A. et al. Impact of Social Isolation during the COVID-19 Pandemic on Mental Health, Substance Use, and Homelessness: Qualitative Interviews with Behavioral Health Providers. *IJERPH* **19**, 12120 (2022).
68. Mullard, A. Pfizer's small-molecule antiviral misses on COVID prevention. *Nat. Rev. Drug Discov.* **21**, 406–406 (2022).
69. Alpizar, S. A. et al. Molnupiravir for intra-household prevention of COVID-19: The MOVE-AHEAD randomized, placebo-controlled trial. *J. Infect.* **87**, 392–402 (2023).
70. Tonge, P. J. Quantifying the Interactions between Biomolecules: Guidelines for Assay Design and Data Analysis. *ACS Infect. Dis.* **5**, 796–808 (2019).
71. Rappazzo, C. G. et al. Broad and potent activity against SARS-like viruses by an engineered human monoclonal antibody. *Science* **371**, 823–829 (2021).

**Acknowledgements**

We thank Jiajun Zhang, the Enanta Medicinal Chemistry, and CMC teams for assistance with compound needs and manuscript review. We also thank Ian Cade and the Evotec team for manuscript assistance and their work generating the EDP-235-bound crystal structure of the 3CLpro as well as the PDB upload. The development of live reporter sarbecovirus NanoLuc luciferase drug assays was supported by an NIH AID grant to R.S.B. (AI171292).

**Author contributions**

Assay development, execution, data generation, and analysis performed by M.H.J.R., A.C.R., A.B., N.B., N.M.K., J.S.G., J.L., M.V., T.C., M.C., N.M., J.C., R.E.L., D.L., T.Z., R.M.C., C.M.L., J.D.W., and T.S. Experimental design, project guidance and oversight performed by M.H.J.R., A.C.R., A.B., N.M.K., J.S.G., M.V., T.C., J.C., L.J., K.D., R.K.P., S.R.L., R.S.B., G.W., B.G., and Y.S.O.. EDP-235 compound design and generation performed

by R.S., G.W., and Y.S.O.. Manuscript writing performed in chief by M.H.J.R., N.M.K., and J.S.G.. All authors contributed to manuscript review and editing.

**Competing interests**

M.H.J.R., A.C.R., A.B., N.B., N.M.K., J.S.G., J.L., M.V., T.C., M.C., R.S., N.M., J.C., R.E.L., D.L., T.Z., L.J., K.D., G.W., B.G., and Y.S.O. are either current or former employees of Enanta Pharmaceuticals and received salary and stock compensation during this study. R.M.C., C.M.L., J.D.W., R.K.P., S.R.L., T.S., and R.S.B. received funding from Enanta Pharmaceuticals. R.K.P. reports contract testing from Atea Pharmaceuticals and research support from Gilead Sciences, outside of the described work.

**Additional information**

**Supplementary information** The online version contains supplementary material available at <https://doi.org/10.1038/s41467-024-50931-8>.

**Correspondence** and requests for materials should be addressed to Michael H. J. Rhodin.

**Peer review information** *Nature Communications* thanks Kris White, and the other, anonymous, reviewers for their contribution to the peer review of this work. A peer review file is available.

**Reprints and permissions information** is available at <http://www.nature.com/reprints>

**Publisher's note** Springer Nature remains neutral with regard to jurisdictional claims in published maps and institutional affiliations.

**Open Access** This article is licensed under a Creative Commons Attribution-NonCommercial-NoDerivatives 4.0 International License, which permits any non-commercial use, sharing, distribution and reproduction in any medium or format, as long as you give appropriate credit to the original author(s) and the source, provide a link to the Creative Commons licence, and indicate if you modified the licensed material. You do not have permission under this licence to share adapted material derived from this article or parts of it. The images or other third party material in this article are included in the article's Creative Commons licence, unless indicated otherwise in a credit line to the material. If material is not included in the article's Creative Commons licence and your intended use is not permitted by statutory regulation or exceeds the permitted use, you will need to obtain permission directly from the copyright holder. To view a copy of this licence, visit <http://creativecommons.org/licenses/by-nc-nd/4.0/>.

© The Author(s) 2024

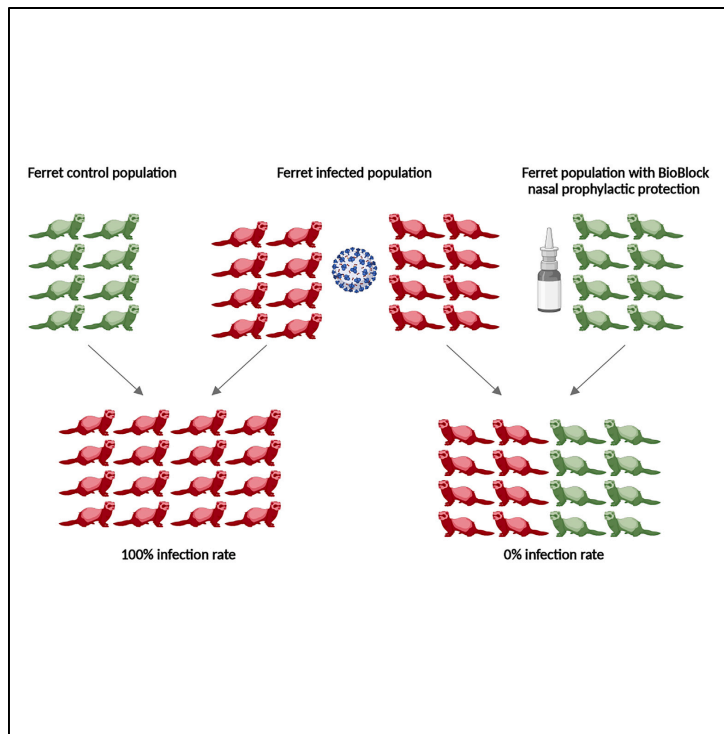
## 2.1.7 Anti-SARS-CoV-2 Antibodies in a Nasal Spray Efficiently Block Viral Transmission Between Ferrets

iScience

CellPress  
OPEN ACCESS

Article

### Anti-SARS-CoV-2 antibodies in a nasal spray efficiently block viral transmission between ferrets



Kiira Gildemann,  
Mari-Liis Tsernant,  
Laura Liivand, ...,  
Mart Ustav, Jr.,  
Mart Ustav,  
Joachim Matthias  
Gerhold

joachim.gerhold@icosagen.com

#### Highlights

Bovine colostrum-derived antibodies can neutralize SARS-CoV-2

These neutralizing antibodies work on different variants of concern

The antibodies were formulated into a nasal spray

The spray solution administered to ferrets blocked virus transmission 100%

Gildemann et al., iScience 27, 110326  
July 19, 2024 © 2024 The Authors. Published by Elsevier Inc.  
<https://doi.org/10.1016/j.isci.2024.110326>



## Article

## Anti-SARS-CoV-2 antibodies in a nasal spray efficiently block viral transmission between ferrets

Kiira Gildemann,<sup>1</sup> Mari-Liis Tsernant,<sup>1</sup> Laura Liivand,<sup>1</sup> Retti Ennomäe,<sup>1</sup> Väino Poikalainen,<sup>2</sup> Lembit Lepasalu,<sup>2</sup> Siimu Rom,<sup>3</sup> Ants Kavak,<sup>4</sup> Robert Marsden Cox,<sup>5</sup> Josef Dieter Wolf,<sup>5</sup> Carolin Maria Lieber,<sup>5</sup> Richard Karl Plemper,<sup>5</sup> Andres Männik,<sup>1</sup> Mart Ustav, Jr.,<sup>1</sup> Mart Ustav,<sup>1</sup> and Joachim Matthias Gerhold<sup>1,6,\*</sup>

## SUMMARY

**Severe acute respiratory syndrome coronavirus 2 (SARS-CoV-2) continues to spread in the population. We recently reported the production of bovine colostrum-derived antibodies that can neutralize the virus. These have been formulated into a nasal spray. The immunoglobulin preparation is capable of blocking interaction of the trimeric spike protein (Tri S) of SARS-CoV-2 with the cellular receptor angiotensin-converting enzyme 2 (ACE2), entry of a pseudovirus carrying the Tri S into ACE2 over-expressing human embryonic kidney (HEK) cells, and entry of the virus into live Vero E6 cells. Using an ELISA assay, we demonstrate here that this holds true for different SARS-CoV-2 variants of concern. Using the ferret transmission model, we show that the nasal spray formulation of anti-SARS-CoV-2 immunoglobulins efficiently blocks transmission of SARS-CoV-2 from infected to uninfected ferrets. The results indicate that the use of the nasal spray in humans can add an effective additional layer of protection against the virus, and might be applicable for other viruses of the upper respiratory tract.**

## INTRODUCTION

Vaccination, naturally acquired immunity, and social distancing have contributed to ending the severe acute respiratory syndrome coronavirus 2 (SARS-CoV-2) pandemic. Yet endemic transmission of the virus continues, making the quest for additional countermeasures, such as antiviral therapeutics, an urgent priority.<sup>1</sup> SARS-CoV-2 presents a trimeric spike protein (Tri S) on its surface. Binding of this protein, specifically of the receptor binding domain (RBD) of the spike protein 1 (S1) subunit, to the cellular receptor protein angiotensin-converting enzyme 2 (ACE2) triggers the viral entry cascade, ultimately resulting in infection.<sup>2</sup> Neutralizing antibodies (nAb) have the potential to halt this process by binding to the SARS-CoV-2 Tri S protein, sterically preventing its interaction with ACE2 and, consequently, blocking entry of SARS-CoV-2 into cells.<sup>3</sup>

We recently reported the use of bovine colostrum-derived nAb as a prophylactic agent against SARS-CoV-2<sup>4</sup> and a resulting nasal spray formulation called BioBlock, which has been in use in the Estonian population since spring 2021. The preparation and quality control of the colostrum-derived antibody formulation was described in detail in our previous report.<sup>4</sup> In brief, defatted and casein-depleted colostrum was incubated at a low pH of 3.3 to inactivate potential viral contaminants. The immunoglobulin (Ig)-enriched fraction was then prepared by precipitation with 2 M ammonium sulfate, and the precipitated proteins (mainly Igs) were dissolved in 1 × DPBS (Dulbecco's Phosphate Buffered Saline). The preparation was further dialyzed against 1 × DPBS, sterile filtered, pasteurized, and evaluated for protein integrity. Concentration was determined using SDS-PAGE and measurement of UV absorbance at 280 nm. After final formulation, the product was evaluated for pH, viscosity, polydispersity index, and sterility.<sup>4</sup> The nAbs contained in the nasal spray formulation were derived from the colostrum of cows immunized with the spike proteins of SARS-CoV-2. *In vitro*, they showed very high efficacy in blocking the interaction of Tri S and ACE2 and inhibited viral entry in three different experimental setups. We hypothesized that the presence of the designed formulation in the nasal mucosa would prevent virus docking to ACE2 of mucosal cells and thereby block viral entry through the nasal cavity. If correct, prophylactic administration of the nAb should also inhibit transmission of SARS-CoV-2. In a mouse model, intra-nasal administration of a human-derived monoclonal antibody indeed inhibited infection with SARS-CoV-2.<sup>5</sup>

<sup>1</sup>Icosagen Cell Factory OÜ, Össu, Kambja vald, 61713 Tartumaa, Estonia

<sup>2</sup>Teadus ja Tegu OÜ, Märja, 61406 Tartu, Tartumaa, Estonia

<sup>3</sup>Chemi-Pharm AS, Tännassilma, 76404 Harjumaa, Estonia

<sup>4</sup>Department of Clinical Veterinary Medicine, Institute of Veterinary Medicine and Animal Sciences, Estonian University of Life Sciences, 51014 Tartu, Estonia

<sup>5</sup>Center for Translational Antiviral Research, Georgia State University Institute for Biomedical Sciences, Atlanta, GA 30303, USA

<sup>6</sup>Lead contact

\*Correspondence: joachim.gerhold@icosagen.com

<https://doi.org/10.1016/j.isci.2024.110326>



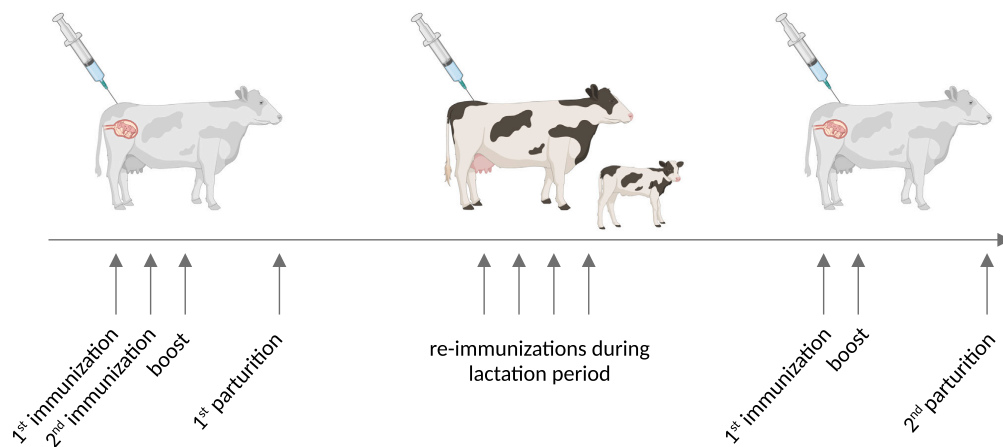


**Figure 1. Immunization scheme including re-immunizations of cows**

Animals were initially immunized during the third trimester of pregnancy about 60, 21, and 14 days before parturition. Cows were then further immunized about every 5–8 weeks during the lactation/gestation period. In the third trimester of the next pregnancy, about 42 and 14 days before parturition, the next immunizations were conducted.

Ferrets have evolved as a leading animal model for the evaluation of vaccines and therapeutics against respiratory virus infections including influenza viruses,<sup>6</sup> pneumo- and paramyxoviruses,<sup>7</sup> and SARS-CoV-2.<sup>8,9</sup> Contributing to high predictive power of the model are similar relative proportions of the ferret and human upper and lower respiratory tract and comparable density of submucosal glands in the bronchial wall and generations of terminal bronchioles.<sup>7</sup> Infection of ferrets with SARS-CoV-2 results predominantly in upper respiratory disease with high virus shedding and efficient transmission, resembling disease presentation in the majority of human adults.<sup>10</sup>

In this study, we investigated whether BioBlock is capable of blocking the transmission of SARS-CoV-2 from infected to uninfected ferrets.

We demonstrate that the previously characterized nasal spray formulation of BioBlock, containing colostrum-derived anti-SARS-CoV-2 neutralizing antibodies, is highly effective in suppressing transmission of the virus in a population containing both infected and uninfected subjects. We show that such polyclonal preparations are highly efficacious against newly emerged virus variants. The re-vaccination scheme used for cows results in neutralizing antibodies against SARS-CoV-2 that are effective against highly mutated novel SARS-CoV-2 strains, which were not previously known and therefore not included as antigens during the original immunizations.

## RESULTS

Cows in the third trimester of pregnancy were immunized with a total of three injections of either the SARS-CoV-2 RBD or Tri S. The initial immunization took place at approximately 60 days before the calculated date of parturition, a first booster was administered 21 days later, and a final booster was given approximately 2 weeks before birth of the calf.<sup>4</sup> We thereafter continued immunizations with a mixture of SARS-CoV-2 variants of concern (VOC) Alpha, Beta, and Gamma-derived RBD proteins throughout the lactation period (commonly 9–10 months), at intervals of 5–8 weeks, delivering a total amount of 0.1 mg of protein mixture (Figure 1). The cows were re-impregnated 2 months after birth of the calf. When VOC Delta emerged and became predominant, the immunization strategy was changed to using 0.1 mg of VOC Delta-derived S1 protein for re-immunizations. Six weeks before the 2<sup>nd</sup> parturition, immunization was conducted with 0.1 mg of the VOC Delta RBD and about 3 weeks prior to expected calving with 0.3 mg of VOC Delta S1 protein (Figure 1).

### A colostrum-derived Ig preparation from re-immunized cows is highly efficient in blocking ACE2 and SARS-CoV-2 trimeric spike interaction

We prepared Igs from colostrum according to our previously described procedure<sup>4</sup> and validated efficacy *in vitro*, using an inverted enzyme-linked immunosorbent assay (ELISA) protocol. We found that neutralization capacity coincided well with pseudovirus and cytopathic effect-based neutralization assays.<sup>4</sup> The ELISA test makes use of the interaction of the Tri S with ACE2. In the absence of neutralizing antibodies, signals (expressed as optical density [OD] at a wavelength of 450 nm; OD450) were strong, since labeled ACE2 bound to the Tri S protein. As neutralizing antibodies emerged in the sample preparation, signals gradually decreased, resulting in very low intensities (OD450) as high concentrations of neutralizing antibodies were present. We coated ELISA plates with Tri S proteins of Alpha, Delta, or Omicron strains and subjected the Ig preparation of the re-immunized cows and a non-immunized cow to analyses (Figure 2). We observed that half-maximal

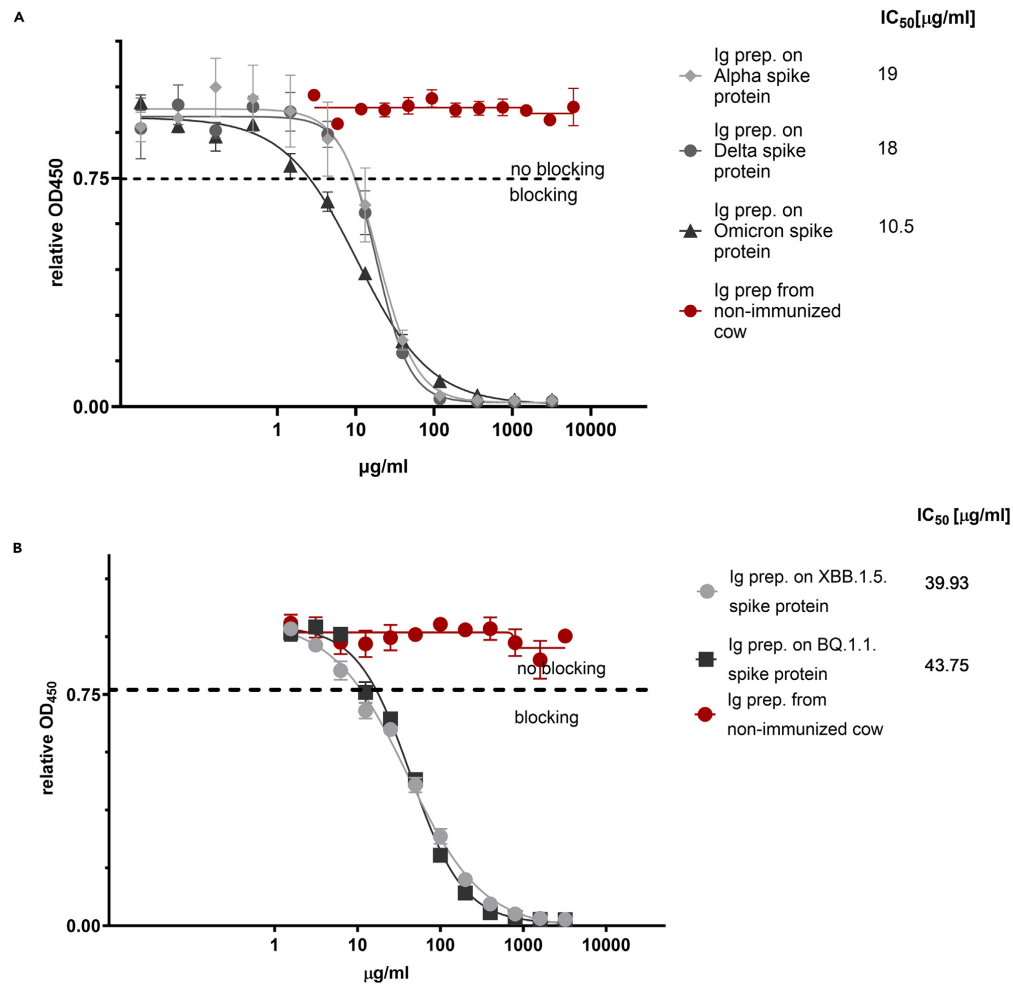


**Figure 2. The Ig preparation retrieved after several reimmunizations shows high potency in blocking the *in vitro* interaction of ACE2 with the Tri S proteins of Alpha, Delta, Omicron, and VOC strains of SARS-CoV-2**

(A) Activity of the Ig preparation against the Tri S proteins of the Alpha, Delta, and Omicron strains of SARS-CoV-2 *in vitro*. In contrast, the preparation derived from colostrum of a non-immunized cow did not show any inhibition of the interaction between ACE2 and Tri S *in vitro*.

(B) Activity of the Ig preparation against VOC BQ.1.1 and XBB.1.5. Employing our inverted ELISA analyses, we observed good efficacy of the nAbs in blocking Tri S–ACE2 interaction. Half-maximal inhibition (IC<sub>50</sub>) was determined through a non-linear regression analysis with a variable slope (four parameters). XY-plots for the Ig preparation analyses are presented with non-linear fit and standard deviations (SD); n = 3 replicates.

inhibition (IC<sub>50</sub>) was 10–20 µg/mL depending on the analyzed VOC. This was in a much lower range than we had observed with the initial Ig preparation from previous immunizations employing the same assay,<sup>4</sup> indicating maturation of immune responses due to repetitive boosting doses (Figure 2A). Most importantly, the quality of the immune response improved. All immunizations were done with antigens from VOC Alpha, Beta, Gamma, and Delta, but the subsequently emerged VOC Omicron was also potently neutralized. VOC Omicron has more than 50 mutations compared to the original SARS-CoV-2 strain, 32 of which are located in the spike protein and 26 are unique to Omicron compared to the VOCs that served as antigens.<sup>11</sup>



CellPress  
OPEN ACCESS

iScience  
Article

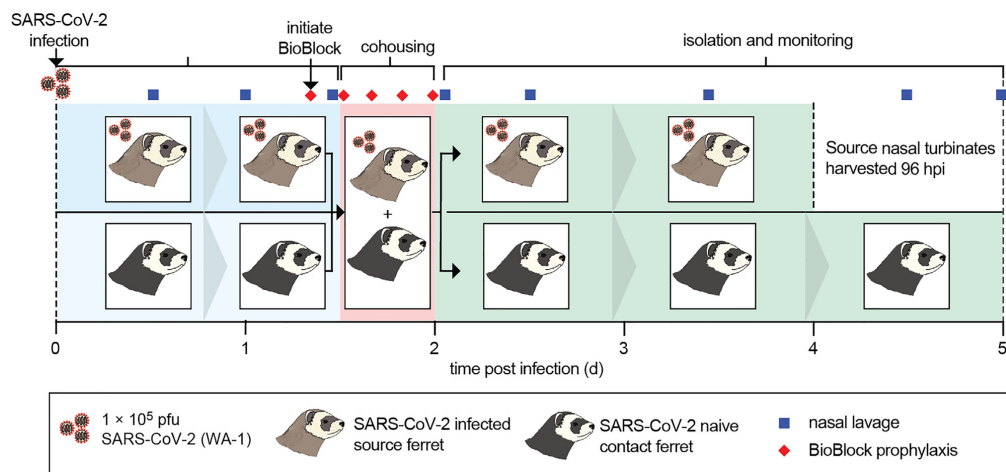


**Figure 3. Experimental setup for ferret experiments**

Depicted are uninfected (dark gray; contact) and infected (light gray; source) ferrets. Blue background indicates the time uninfected and infected ferrets were housed separately. Source ferrets for SARS-CoV-2 were infected 1.5 days prior to cohousing. Nasal lavages of infected source animals and naive contact ferrets were taken every 12 h (blue squares). Four hours prior to cohousing of source and contact animals, a first dose of BioBlock and buffer alone (red rhombs), respectively, were administered. During cohousing (pink background) contact ferrets were treated with BioBlock or buffer alone every 4 h (red rhombs). After 12 h animals were separated and monitored further (green background). After termination of the experiment, nasal turbinates were harvested. The duration of the experiment in days is indicated below the colored boxes.

We further tested the Ig preparation from the colostrum of re-immunized cows for *in vitro* efficacy against the Tri S proteins of the VOC Omicron 2 isolates BQ.1.1 and XBB.1.5 (Figure 2B), which evolved after the initial appearance of Omicron and carried even more differences in the spike protein than the initial Omicron isolate.<sup>12,13</sup> Albeit at somewhat lower efficiency compared to neutralization of VOC Alpha, Delta, and Omicron 1, the preparation was still very potent in inhibiting VOC Omicron 2-derived Tri S-ACE2 interactions, showing IC<sub>50</sub> values of 44 and 40  $\mu\text{g/mL}$  for the BQ.1.1 and XBB.1.5 isolates, respectively.

#### A nasal spray containing colostrum-derived nAbs against SARS-CoV-2 blocks transmission of the virus with high efficacy

Since we had previously formulated the Ig preparation of immunized cows into a nasal spray (BioBlock) and had shown the component antibodies to persist on the human nasal mucosa for at least 4 h,<sup>1</sup> we next employed the ferret model (Figure 3) to test whether a prophylactic nasal spray administration of BioBlock would prevent SARS-CoV-2 transmission to healthy subjects, recapitulating a community transmission scenario in which people are in close contact with infected individuals for a defined period of time. We conducted the study in two replicates and treated a total of 8 ferrets with the nasal spray formulation at 0.236 mg/kg. Eight control animals received the nasal spray vehicle without the Ig preparation. After an initial nasal lavage with either the colostrum-derived nasal spray formulation or vehicle alone 4 h prior to co-housing, each treated animal was housed with a SARS-CoV-2 (WA-1 strain)-infected source animal (source to sentinel ratio 1:1) in a direct-contact setting. Treatment of the contacts with the spray-formulation BioBlock was continued in 4-h intervals for the duration of co-housing (12 h total). Subsequently, both donor and recipient animals were monitored for another 96 h, followed by extraction of respiratory tissues and determination of infectious viral titers and viral RNA copies. The study timeline is shown in Figure 3.

We observed that nasal lavages of source animals (vehicle source and treated source) showed high titers of SARS-CoV-2 (50% tissue culture infectious dose [TCID<sub>50</sub>] of  $10^5$  two days post infection) (Figure 4A). The buffer-treated sentinels started to show measurable titers (TCID<sub>50</sub> of  $10^5$  to  $10^6$ ) 2 days post infection (dpi) and high titers (TCID<sub>50</sub> of  $10^5$  to  $10^6$ ) 6 dpi. These findings were corroborated by viral RNA copies present in nasal lavages (Figure 4B), which reached  $10^5$ – $10^6$  copies 1–4 dpi. Vehicle-treated contacts turned PCR-positive ( $10^2$  RNA copies) 1 dpi and developed high viral load ( $10^6$  copies) 6 dpi (Figure 4B).

Contrary to efficient viral spread to vehicle-treated contacts, all sentinels that had received BioBlock were not productively infected—neither developing measurable viral titers nor showing a rise in viral RNA copies (Figures 4A and 4B)—confirming efficient protection by BioBlock against viral transmission from infected to uninfected subjects *in vivo*.

At study end, viral titers and viral RNA copy numbers were determined in nasal turbinates extracted from all animals (Figures 4C and 4D). We observed high virus burden in all source- and vehicle-treated contact animals, whereas turbinates of sentinels that had received BioBlock

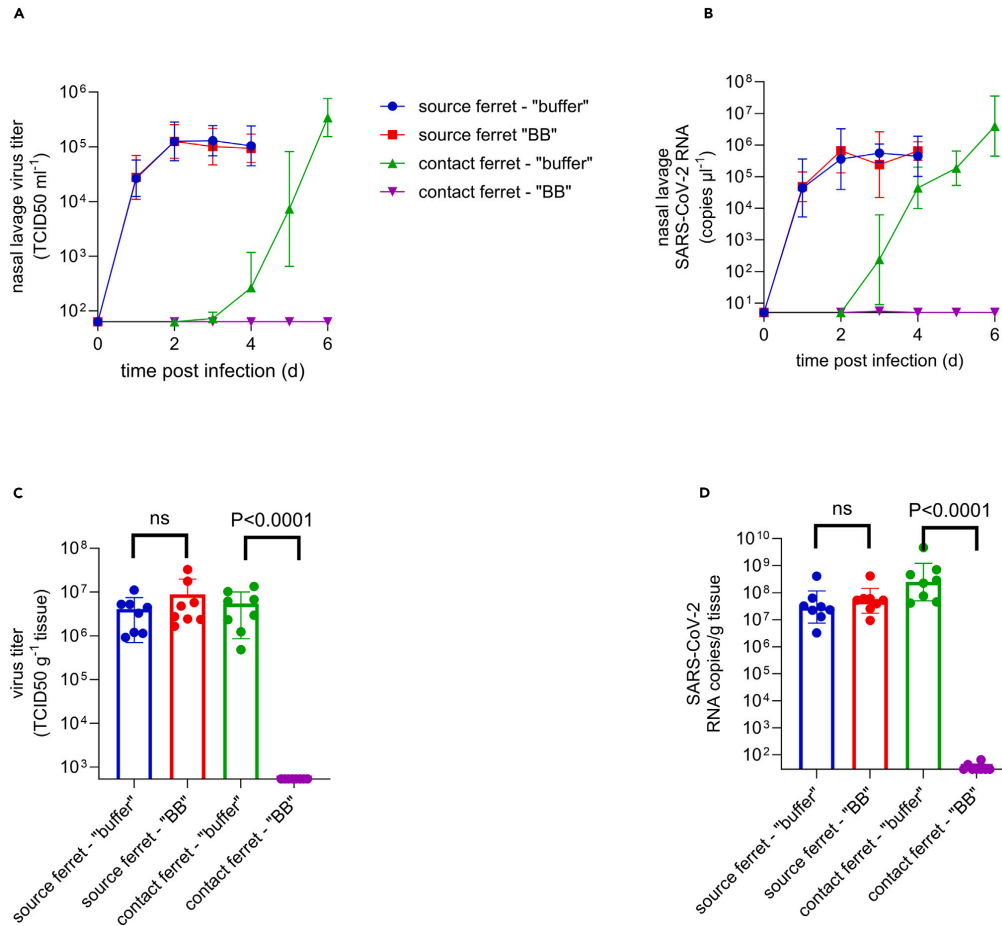


**Figure 4. The Ig preparation effectively inhibits transmission of SARS-CoV-2 from infected to uninfected ferrets**

(A) Virus titers in nasal lavages from animals carrying SARS-CoV-2 (source ferret) and those exposed to the virus (contact ferret) are depicted. One day after infection, source animals showed high titers of the virus with a further elevation on day 2. Titers stayed high until the animals were terminated. BioBlock-treated animals were monitored from day 2 until day 6 (termination of the experiment). Green triangles and line depict the buffer-alone treated animals and show a clear rise in viral titer on day 4 which rapidly climbs until day 6. During the same period, animals treated with BioBlock-containing solution (purple triangles and line) did not reveal a significant rise in viral titer.

(B) RNA copy numbers of the nasal lavages confirmed viral titration results. After termination of the experiment, nasal turbinates were collected.

(C and D) Source ferrets (blue bars) and buffer-treated contact animals (green bars) showed high SARS-CoV-2 titers (C) and RNA copy numbers (D). Source animals (red bars) of ferrets to be co-housed with BioBlock-treated animals were likewise efficiently infected, but prophylactic BioBlock suppressed transmission to contacts (magenta bars). XY-plots in Figures 4A and 4B are presented with geometric SD. Data presented in Figures 4C and 4D were not normally distributed and thus log transformed. Ordinary one-way ANOVA was then used with Brown-Forsythe test for equal variances. Correction for multiple comparisons was conducted using Šidák's test. For statistical analyses  $p$  values < 0.05 were considered to be statistically significant. Data in boxplots are presented as mean with SD.  $n = 8$  animals for each treatment (total 32).





prophylaxis were virus-free. This finding fully supported the conclusion that intranasal treatment of ferrets with prophylactic BioBlock fully protected against SARS-CoV-2 transmission.

## DISCUSSION

We demonstrate in this study that anti-SARS-CoV-2 nAb derived from bovine colostrum are highly effective against a range of SARS-CoV-2 VOC and potentially block viral spread from infected source animals to prophylactically treated contact animals in the ferret transmission model. Previously, we established the high potential of the bovine Ig preparation *in vitro*.<sup>4</sup> However, this achievement was restricted to the original Wuhan strain and closely related VOC Alpha, Beta, Gamma, and Delta. This first generation of VOC was replaced in less than a year by the newly emerged VOC Omicron lineage, which is considerably different from the original SARS-CoV-2 isolate and VOC Alpha, Beta, Gamma, and Delta.<sup>11</sup>

Although the efficacy of the initial Ig preparation against different VOC was encouraging, we still chose to re-immunize cows that had given birth to calves after initial immunization. We did so throughout the entire lactation period. As new variants emerged sequentially, we reacted and conducted immunizations with the respective VOC as they emerged (Alpha, Beta, Gamma, and Delta). The cows had been re-impregnated, which enabled us to re-apply the initial immunization scheme prior to birth of the calf, in which we immunized and boosted during the third trimester of pregnancy. This immunization was done using the Delta spike protein. Coincidentally, this was the time that Omicron emerged. Here we showed that the formulation prepared without known Omicron antigens was also very effective against different Omicron lineages, whose spike protein has numerous mutations compared to the antigens used to immunize cows.<sup>11</sup> This is quite different from what has been seen with anti-SARS-CoV-2 therapeutic monoclonal antibodies, as the antibodies created against pre-Omicron variants mostly lost their potency when Omicron and its sub-lineages emerged.<sup>12,13</sup> Although not demonstrated experimentally yet, this observation further supports the theory that the polyclonal nature of the Ig preparation may be the main contributing factor in the broad neutralizing capacity in comparison to monoclonal antibodies. It seems less likely that the existence of one “super-broad” neutralizing antibody species in the colostrum ensures its extraordinary capability. Perhaps more importantly, cows immunized with antigens from “old” virus strains also developed a protective response against “new” virus strains that were not yet known when this immunization took place. More generally, this would provide an exceptional opportunity to develop effective protective formulations against mutated pathogens even before changes occur and spread in the infected population. Such an approach, if implemented widely and in a timely manner, could offer a significant epidemiological benefit by controlling (restricting) community transmission. Thus, our results provide proof-of-concept that colostrum-derived polyclonal antibody preparations may have superior practical value in situations that call for efficient control of a rapidly changing respiratory pathogen.

Through measures like social distancing, mask-wearing, and hand hygiene, the spread of a virus can be reduced.<sup>14</sup> This prevents new infections and lowers the overall burden of the disease in the community. Controlling community transmission helps to break the chain of infection, lowering the reproduction number (R0) of the virus.<sup>15</sup> This, in turn, leads to a decrease in the number of cases and the potential for outbreaks. Furthermore, controlled transmission helps to avoid overwhelming healthcare systems.<sup>16</sup> Lower case numbers mean that hospitals and healthcare facilities can better manage and provide adequate care for those infected without being stretched beyond capacity. Controlling transmission is also crucial for protecting vulnerable populations such as the elderly, immunocompromised individuals, and those with underlying health conditions.<sup>17</sup> These groups are more susceptible to severe outcomes from viral infections. Some viral infections can lead to long-term health complications even in individuals with mild or asymptomatic cases.<sup>18</sup> Controlling transmission reduces the overall burden of disease and helps minimize these secondary health effects. In addition, controlling community transmission supports vaccination efforts.<sup>19</sup> Vaccines are more effective in preventing severe outcomes and reducing transmission when implemented in a population with lower baseline infection rates. As such, the prophylactic function of BioBlock may significantly impact the epidemiology of SARS-CoV-2 as use of the spray is intended to prevent spreading of the virus.

## Limitations of the study

In order to assess the occurrence of nAbs, a surrogate ELISA was employed. Although evaluated and previously successfully used in our studies, care should be taken in interpreting the results. The ELISA used in this study was corroborated in our earlier study by a pseudovirus assay and a cytopathic cell-based assay. Both showed similar results for the immunoglobulin preparation as did the ELISA method. However, the accepted gold standard in the field is the plaque reduction neutralization test (PRNT).<sup>20</sup> Still, several limitations are discussed for the PRNT, among them scalability (low throughput), long turnaround times, and the requirement of BSL3 (biosafety level 3) facilities and qualified personnel.<sup>20</sup> Since we showed consistent results for the ELISA method employed in this study,<sup>4</sup> we are confident that our surrogate assay delivers credible results. As discussed elsewhere, heparin in blood sample preparations can affect the results of SARS-CoV-2 nAbs detection.<sup>20</sup> Since neither the Ig preparations nor BioBlock contain heparin or have been in contact with it, it is not expected that the results produced by our surrogate assays are compromised in any way.

We acknowledge that the number of test animals (a total of 32) might be considered small. In fact, for each transmission study, we employed a total of 8 treated ferrets (4 treated animals, 4 animals administered with the spray buffer only, and 2 replicates). Ferrets have been established as a large animal model of SARS-CoV-2 upper respiratory tract infection and transmission. They are a non-rodent USDA (United States Department of Agriculture)-controlled species. Group sizes used in this study are consistent with previously published work using this model (see, for e.g., study by Cox et al.<sup>21</sup>). Raw data in this study were subjected to full statistical analysis and were found to be statistically significant. Yet, the design of studies involving large research animals is complex and requires careful evaluation of the potential additional knowledge-gain versus animal welfare concerns and bioethics considerations. Our selected study design represents a scientifically justified compromise between these divergent interests that was approved by all stakeholders including the research scientists and the responsible IACUC (Institutional Animal Care and Use Committee).



The results presented here show that the nasal spray treatment protected uninfected animals under conditions that mimic the situation in the real population of interest. The method of infection was not artificial administration of large amounts of viral particles, but natural transmission from infected animals. However, we also clearly understand the limitations of the model used, and that the evidence presented here derives from *in vitro* assays and animal experiments. The only way to confirm the actual protective effect in humans is through a clinical trial with a control group in conditions where the viral infection rate is high enough to reliably demonstrate the effect of the preparation. Nonetheless, the clinical potential of the approach is supported by the ferret model, which revealed complete protection against infection by intranasally delivered prophylactic BioBlock.

### STAR★METHODS

Detailed methods are provided in the online version of this paper and include the following:

- [KEY RESOURCES TABLE](#)
- [RESOURCE AVAILABILITY](#)
  - Lead contact
  - Materials availability
  - Data and code availability
- [EXPERIMENTAL MODEL AND STUDY PARTICIPANT DETAILS](#)
  - Animal subjects
  - Ethics statement
- [METHOD DETAILS](#)
  - Ferret studies
  - SARS-CoV-2 neutralizing antibody ELISA
- [QUANTIFICATION AND STATISTICAL ANALYSIS](#)

### ACKNOWLEDGMENTS

We thank the Georgia State University Department of Animal Resources and High Containment Core for Assistance. This study was supported by funding from Enterprise Estonia, grant number 2014-2020.4.02.21-0317.

### AUTHOR CONTRIBUTIONS

Conceptualization: J.M.G., M.U., M.U.J., A.M., K.G., and R.K.P. Methodology: R.K.P., M.U.J., J.M.G., and A.M. Formal analysis: R.K.P., R.M.C., A.M., J.M.G., and K.G. Investigation: R.K.P., R.M.C., J.D.W., C.M.L., and R.E. Resources: K.G., M.L.-T., L. Liivand, V.P., L. Lepasalu, S.R., and A.K. Writing – original draft: J.M.G., K.G., and A.M. writing – review and editing: R.K.P., M.U., M.U.J., A.K., J.M.G., K.G., and A.M. Visualization: R.M.C., A.M., J.M.G., and K.G. Supervision: J.M.G., A.M., M.U.J., and R.K.P. Project administration: J.M.G. Funding acquisition: M.U. and M.U.J.

### DECLARATION OF INTERESTS

The drug product used in this study is marketed and sold in Estonia since 2021.

This study was supported by the funding from Enterprise Estonia grant number 2014-2020.4.02.21-0317.

The use of bovine colostrum as a prophylactic agent against SARS-CoV-2 has been patented (US patent application no 63/160,833).

Work at Georgia State University for this study was carried out under a contract agreement from Icosagen. R.K.P. reports research contract testing from Enanta Pharmaceuticals and Atea Pharmaceuticals, and research support from Gilead Sciences, outside of the described work. R.M.C. reports consulting for Merck & Co, outside of the described work.

Received: January 19, 2024

Revised: April 17, 2024

Accepted: June 18, 2024

Published: June 20, 2024

### REFERENCES

1. Li, G., Hilgenfeld, R., Whitley, R., and De Clercq, E. (2023). Therapeutic strategies for COVID-19: progress and lessons learned. *Nat. Rev. Drug Discov.* 22, 449–475. <https://doi.org/10.1038/s41573-023-00672-y>.
2. Donoghue, M., Hsieh, F., Baronas, E., Godbout, K., Gosselin, M., Stagliano, N., Donovan, M., Woolf, B., Robison, K., Jeyaseelan, R., et al. (2000). A Novel Angiotensin-Converting Enzyme-Related Carboxypeptidase (ACE2) Converts Angiotensin I to Angiotensin 1–9. *Circ. Res.* 87, e1–e9. <https://doi.org/10.1161/01.RES.87.5.e1>.
3. Chen, Y., Zhao, X., Zhou, H., Zhu, H., Jiang, S., and Wang, P. (2023). Broadly neutralizing antibodies to SARS-CoV-2 and other human coronaviruses. *Nat. Rev. Immunol.* 23, 23.



- 189–199. <https://doi.org/10.1038/s41577-022-00784-3>.
4. Kangro, K., Kurašin, M., Gildemann, K., Sankovski, E., Žušinaite, E., Lello, L.S., Pert, R., Kavak, A., Poikalainen, V., Lepasalu, L., et al. (2022). Bovine colostrum-derived antibodies against SARS-CoV-2 show great potential to serve as prophylactic agents. *PLoS One* 17, e0268806. <https://doi.org/10.1371/journal.pone.0268806>.
  5. Halve, S., Kupke, A., Vanshylla, K., Liberta, F., Gruell, H., Zehner, M., Rohde, C., Krähling, V., Gellhorn Serra, M., Kreer, C., et al. (2021). Intranasal Administration of a Monoclonal Neutralizing Antibody Protects Mice against SARS-CoV-2 Infection. *Viruses* 13, 1498. <https://doi.org/10.3390/v13081498>.
  6. Belsler, J.A., Eckert, A.M., Huynh, T., Gary, J.M., Ritter, J.M., Tumpey, T.M., and Maines, T.R. (2020). A Guide for the Use of the Ferret Model for Influenza Virus Infection. *Am. J. Pathol.* 190, 11–24. <https://doi.org/10.1016/j.ajpath.2019.09.017>.
  7. Enkirch, T., and von Messling, V. (2015). Ferret models of viral pathogenesis. *Virology* 479–480, 259–270. <https://doi.org/10.1016/j.virol.2015.03.017>.
  8. Cox, R.M., Wolf, J.D., and Plemper, R.K. (2021). Therapeutically administered ribonucleoside analogue MK-4482/EIDD-2801 blocks SARS-CoV-2 transmission in ferrets. *Nat. Microbiol.* 6, 11–18. <https://doi.org/10.1038/s41564-020-00835-2>.
  9. Cox, R.M., Wolf, J.D., Lieber, C.M., Sourimant, J., Lin, M.J., Babusis, D., DuPont, V., Chan, J., Barrett, K.T., Lye, D., et al. (2021). Oral prodrug of remdesivir parent GS-441524 is efficacious against SARS-CoV-2 in ferrets. *Nat. Commun.* 12, 6415. <https://doi.org/10.1038/s41467-021-26760-4>.
  10. de Vries, R.D., Rockx, B., Haagmans, B.L., Herfst, S., Koopmans, M.P., and de Swart, R.L. (2021). Animal models of SARS-CoV-2 transmission. *Curr. Opin. Virol.* 50, 8–16. <https://doi.org/10.1016/j.coviro.2021.06.007>.
  11. Chatterjee, S., Bhattacharya, M., Nag, S., Dhama, K., and Chakraborty, C. (2023). A Detailed Overview of SARS-CoV-2 Omicron: Its Sub-Variants, Mutations and Pathophysiology, Clinical Characteristics, Immunological Landscape, Immune Escape, and Therapies. *Viruses* 15, 167. <https://doi.org/10.3390/v15010167>.
  12. Tao, K., Tzou, P.L., Kosakovsky Pond, S.L., Ioannidis, J.P.A., and Shafer, R.W. (2022). Susceptibility of SARS-CoV-2 Omicron Variants to Therapeutic Monoclonal Antibodies: Systematic Review and Meta-analysis. *Microbiol. Spectr.* 10, e0092622. <https://doi.org/10.1128/spectrum.00926-22>.
  13. Planas, D., Saunders, N., Maes, P., Guivel-Benhassine, F., Planchais, C., Buchrieser, J., Bolland, W.H., Porrot, F., Staropoli, I., Lemoine, F., et al. (2022). Considerable escape of SARS-CoV-2 Omicron to antibody neutralization. *Nature* 602, 671–675. <https://doi.org/10.1038/s41586-021-04389-z>.
  14. Chiu, N.C., Chi, H., Tai, Y.L., Peng, C.C., Tseng, C.Y., Chen, C.C., Tan, B.F., and Lin, C.Y. (2020). Impact of Wearing Masks, Hand Hygiene, and Social Distancing on Influenza, Enterovirus, and AII-Cause Pneumonia During the Coronavirus Pandemic: Retrospective National Epidemiological Surveillance Study. *J. Med. Internet Res.* 22, e21257. <https://doi.org/10.2196/21257>.
  15. Linka, K., Peirlinck, M., and Kuhl, E. (2020). The reproduction number of COVID-19 and its correlation with public health interventions. *Comput. Mech.* 66, 1035–1050. <https://doi.org/10.1007/s00466-020-01880-8>.
  16. Haldane, V., De Foo, C., Abdalla, S.M., Jung, A.S., Tan, M., Wu, S., Chua, A., Verma, M., Shrestha, P., Singh, S., et al. (2021). Health systems resilience in managing the COVID-19 pandemic: lessons from 28 countries. *Nat. Med.* 27, 964–980. <https://doi.org/10.1038/s41591-021-01381-y>.
  17. Wünsch, K., Anastasiou, O.E., Alt, M., Brochhagen, L., Cherneha, M., Thümmel, L., van Baal, L., Madel, R.J., Lindemann, M., Taube, C., et al. (2022). COVID-19 in Elderly, Immunocompromised or Diabetic Patients—From Immune Monitoring to Clinical Management in the Hospital. *Viruses* 14, 746. <https://doi.org/10.3390/v14040746>.
  18. Davis, H.E., Mccorkell, L., Vogel, J.M., and Topol, E.J. (2023). Long COVID: major findings, mechanisms and recommendations. *Nat. Rev. Microbiol.* 21, 133–146. <https://doi.org/10.1038/s41579-022-00846-2>.
  19. Devi, M.B., Devi, A., Gupta, P.K., and Tripathi, D. (2022). Response of vaccination on community transmission of COVID-19: a dynamical approach. *Eur. Phys. J. Spec. Top.* 231, 3749–3765. <https://doi.org/10.1140/epjs/s11734-022-00652-0>.
  20. Bewley, K.R., Coombes, N.S., Gagnon, L., McInroy, L., Baker, N., Shaik, I., St-Jean, J.R., St-Amant, N., Buttigieg, K.R., Humphries, H.E., et al. (2021). Quantification of SARS-CoV-2 neutralizing antibody by wild-type plaque reduction neutralization, microneutralization and pseudotyped virus neutralization assays. *Nat. Protoc.* 16, 3114–3140. <https://doi.org/10.1038/s41596-021-00536-y>.
  21. Cox, R.M., Lieber, C.M., Wolf, J.D., Karimi, A., Lieberman, N.A.F., Sticher, Z.M., Roychoudhury, P., Andrews, M.K., Krueger, R.E., Natchus, M.G., et al. (2023). Comparing molnupiravir and nirmatrelvir/ritonavir efficacy and the effects on SARS-CoV-2 transmission in animal models. *Nat. Commun.* 14, 4731. <https://doi.org/10.1038/s41467-023-40556-8>.



## STAR★METHODS

## KEY RESOURCES TABLE

REAGENT or RESOURCE	SOURCE	IDENTIFIER
<b>Bacterial and virus strains</b>		
SARS-CoV-2 WA-1 isolate	BEI Resources	NR-52281
<b>Biological samples</b>		
Immunoglobulin preparation from bovine colostrum, batch 003	This study	BOSS Ig 003
BioBlock nasal spray	Medihex	<a href="https://www.medihex.com/en/products/bioblock/">https://www.medihex.com/en/products/bioblock/</a>
Nasal spray buffer w/o antibody solution	This study	N/A
<b>Chemicals, peptides, and recombinant proteins</b>		
SARS-CoV-2 trimeric spike proteins	This study	N/A
ACE2-hFc protein	Icosagen AS	P-308-100
<b>Critical commercial assays</b>		
EZ-Link™ NHS-PEG4 Biotinylation Kit	ThermoFisher Scientific	21455
Pierce™ High Sensitivity Streptavidin-HRP	ThermoFisher Scientific	21132
ELISA plates; Maxisorp F8 Nunclmmunomodule	ThermoFisher Scientific	468667
ELISA reader (spectrophotometer) MultiSkan FC	ThermoFisher Scientific	51119000
<b>Experimental models: Organisms/strains</b>		
Ferret ( <i>Mustela putorius furo</i> )	Triple F Farms	NA
<b>Software and algorithms</b>		
GraphPad Prism v10.0	GraphPad Software Inc	<a href="https://www.graphpad.com/">https://www.graphpad.com/</a>

## RESOURCE AVAILABILITY

## Lead contact

Further information and requests for resources and reagents should be directed to and will be fulfilled by the lead contact, Joachim M. Gerhold ([joachim.gerhold@icosagen.com](mailto:joachim.gerhold@icosagen.com)).

## Materials availability

SARS-CoV-2 trimeric S proteins, ACE2-hFc protein used in this study are available either commercially from Icosagen Cell Factory OÜ and Icosagen AS or the [lead contact](#) with a completed Materials Transfer Agreement. The viral strain used in this study is commercially available. Biological samples will be made available on request, but we may require payment and/or a completed Materials Transfer Agreement if there is potential for commercial application.

## Data and code availability

- All data reported in this paper will be shared by the [lead contact](#) upon request.
- This paper does not report original code.
- Any additional information required to reanalyze the reported data in this paper is available from the [lead contact](#) upon request.

## EXPERIMENTAL MODEL AND STUDY PARTICIPANT DETAILS

## Animal subjects

This study used female ferrets (*Mustela putorius furo*), family mustelids, genus mustela, 6-10 months of age. Upon receipt, all ferrets were housed under standard ABSL-1 conditions for an acclimatization period of 72 hours. After 72 hours, ferrets were transferred to ABSL-3 facilities at Georgia State University. All animals were provided standard ferret enrichment and monitored at least once daily throughout the course of



the study. Biological sex of research animals was determined based on examination of external genitalia. Ferret studies were carried out with female animals only. No sex-based analyses were performed because co-housing studies may not be carried out with male ferrets (IACUC protocol A20031), since males are territorial and highly combative when co-housed, resulting in severe injury from fight wounds that would require termination of the study. The study design does not allow for the use of singly housed male ferrets. Sourced animals were randomly assigned to cages by animal support staff blinded for the study. Cages were randomly assigned to study groups, animals weighed, and infected as specified. The investigators were not blinded to group allocation for data collection and analysis for any experiment performed in this study due to size of the research group with clearance for experimentation under high biocontainment conditions required for work with live SARS-CoV-2. Ferrets are large animals that cannot be handled by a single investigator for the experiments reported under ABSL3 conditions and resources available did not allow involvement of additional personnel that would have been required for blinding. All *in vivo* studies with SARS-CoV-2 involving ferrets were approved by the Georgia State Institutional Animal Care and Use Committee under protocol A20031, in compliance with the Guide for the Care and Use of Laboratory Animals, National Institutes of Health guidelines, and the Animal Welfare Act Code of Federal Regulations. All experiments using infectious SARS-CoV-2 strains were approved by the Georgia State Institutional Biosafety Committee under protocol B20016 and performed in BSL-3/ABSL-3 facilities at the Georgia State University.

#### Ethics statement

All *in vivo* studies were performed in compliance with the Guide for the Care and Use of Laboratory Animals, National Institutes of Health guidelines, and the Animal Welfare Act Code of Federal Regulations. Experiments with SARS-CoV-2 involving ferrets were approved by the Georgia State Institutional Animal Care and Use Committee under protocol A20031. All experiments using infectious SARS-CoV-2 strains were approved by the Georgia State Institutional Biosafety Committee under protocol B20016 and performed in BSL-3/ABSL-3 facilities at Georgia State University.

#### METHOD DETAILS

##### Ferret studies

Female ferrets (n=4/group; 6-10 months old; Triple F Farms) were infected intranasally with 1x10<sup>5</sup> PFU of SARS-CoV-2 WA1. Source ferrets were co-housed with BioBlock or vehicle-treated sentinels at a 1:1 ratio starting 36 hours after infection. Sentinels were intranasally administered BioBlock (0.236 mg/kg) or vehicle (1 ml total dose volume; 500  $\mu$ L per nare) in 4-hour intervals starting 4 hours prior to the onset of co-housing. Treatment was continued through the 12-hour co-housing period, for a total of five BioBlock administrations. Source and sentinel animals were separated at the end of the 12-hour co-housing period, and clinical signs, bodyweight, and temperature monitored once daily. Nasal lavages were collected from all animals once daily. Source animals were terminated 96 hours after infection and nasal turbinates extracted. Sentinel animals were terminated 84 hours after cohousing start and nasal turbinates extracted. Infectious SARS-CoV-2 titers and viral RNA copy numbers were determined in nasal lavage samples and homogenized nasal turbinates by virus titration on Vero-TMPRSS2 cells and RT-qPCR, respectively.

##### SARS-CoV-2 neutralizing antibody ELISA

The efficacy of the Ig preparation in blocking the angiotensin-converting enzyme 2 (ACE2) receptor interaction with the SARS-CoV-2 trimeric spike protein receptor-binding domain (RBD) was determined using an inverted ELISA method.

96-well ELISA microtiter plates (Maxisorp F8 Nunc-ImmunoModule, Cat.-no 468667, Thermo Scientific) were coated with SARS-CoV-2 trimeric spike proteins of VOC alpha, delta, or omicron (B.1.1.529, XBB.1.5, BQ.1.1) at 2.5  $\mu$ g/ml (100  $\mu$ l per well) in coating buffer (1x PBS, pH 7.4) for 16 to 24 hours at 4°C. The coating solution was then aspirated, and wells washed 4 times with 300  $\mu$ l wash-buffer (1 x PBS, 0.05% Tween 20, pH 7.4) using an automated ELISA plate washer. After removal of any residual wash-buffer by tapping plates upside down on dry, clean paper towels, plates were blocked adding 300  $\mu$ l per well of a blocking buffer (PBS, 1% BPLA, 2% sucrose, pH 7.4). Plates were covered and kept at room temperature for at least one or up to two hours. The blocking buffer was aspirated, and plates were dried at 35°C in a thermostat for 15-16 hours. In case plates were not used immediately, they were vacuum sealed and kept at 4°C until further use. All necessary reagents were equilibrated to room temperature prior to conducting experiments.

Ig preparation samples were two-fold diluted in 12 steps starting from 3200  $\mu$ g/ml into analysis buffer (1x PBS, 0.5% BPLA, 2% sucrose, 0.1% Proclin 300). 50  $\mu$ l per well of samples were added to the plates in triplicates. Covered plates were incubated for 20 minutes on an orbital microtiter plate shaker at 450 rpm. Next, 50  $\mu$ l of enzyme conjugate (1x PBS, 0.5% BPLA, 0.5  $\mu$ g/ml of biotinylated ACE2-fc, 0.02  $\mu$ g/ml Streptavidin-HRP (Pierce™ High Sensitivity Streptavidin-HRP, ThermoFisher Scientific, cat.-no. 21132), 0.1% Proclin 300, pH 7.4) was added without touching the samples in the wells. Prior to use, ACE2-fc (Icosagen AS cat.-no P-308-100) was biotinylated using an EZ-Link™ NHS-PEG4 Biotinylation Kit (ThermoFisher Scientific, cat.-no. 21455). Plates were covered and incubated on an orbital microtiter plate shaker at 450 rpm for 30 minutes, then aspirated and washed 4 times with 300  $\mu$ l wash buffer (as above). 100  $\mu$ l TMB VII (Biopanda) was added to each well. The plates were covered and incubated for 10 minutes on an orbital microtiter plate shaker at 450 rpm. The coloring reaction was stopped by addition of 50  $\mu$ l stop solution (0.5 M H<sub>2</sub>SO<sub>4</sub>). Plates were briefly shaken, incubated for 1-2 minutes and the optical density (OD) at a wavelength of 450 nm was measured with an ELISA plate reader (spectrophotometer).

OD<sub>450</sub> values of measured samples were divided by the mean value of the eight repeated samples of a negative control (analysis buffer, composition as above) to obtain relative OD<sub>450</sub> values. Samples with a relative OD<sub>450</sub> value of <0.75 were considered sufficient in blocking



ACE2 binding. The threshold of 0.75 was previously determined as the limit of detection (LoD) by comparison of negative sera and sera from COVID19-patients (measurements of level of blank (LoB) and level of detection (LoD) according to the CLSI standard EP17-A2). Data were analyzed, plotted, and graphically summarized using GraphPad Prism 10 (GraphPad Software Inc.).

#### QUANTIFICATION AND STATISTICAL ANALYSIS

GraphPad Prism version 10 was used to conduct statistical analyses and generation of XY- and boxplots.

Half-maximal inhibition ( $IC_{50}$ ) was determined through a non-linear regression analysis with a variable slope (four parameters). XY-plots for the immunoglobulin preparation analyses are presented with non-linear fit and standard deviations (SD); n=3 replicates.

XY-plots in Figures 4A and 4B are presented with geometric SD.

Data presented in Figures 4C and 4D were not normally distributed and thus log transformed. The normality test showed Gaussian distribution after transformation. Ordinary one-way ANOVA was then used with Brown-Forsythe test for equal variances. Correction for multiple comparisons was conducted using Šidák's test. For statistical analyses p values <0.05 were considered to be statistically significant. Data in boxplots are presented as mean with SD. n=8 for each treatment (total 32).

Statistical tests used and sample size can be found in the figure legends.

## 2.2 Research Topic: MeV and CDV

### 2.2.1 Therapeutic Mitigation of Measles-like Immune Amnesia and Exacerbated Disease after Prior Respiratory Virus Infections in Ferrets

nature communications



Article

<https://doi.org/10.1038/s41467-024-45418-5>

# Therapeutic mitigation of measles-like immune amnesia and exacerbated disease after prior respiratory virus infections in ferrets

Received: 3 November 2023

Accepted: 23 January 2024

Published online: 08 February 2024

Check for updates

Robert M. Cox<sup>1</sup>, Josef D. Wolf<sup>1</sup>, Nicole A. Lieberman<sup>2</sup>, Carolin M. Lieber<sup>1</sup>, Hae-Ji Kang<sup>1</sup>, Zachary M. Sticher<sup>3</sup>, Jeong-Joong Yoon<sup>1</sup>, Meghan K. Andrews<sup>3</sup>, Mugunthan Govindarajan<sup>3</sup>, Rebecca E. Krueger<sup>3</sup>, Elizabeth B. Sobolik<sup>2</sup>, Michael G. Natchus<sup>3</sup>, Andrew T. Gewirtz<sup>1</sup>, Rik L. deSwart<sup>4</sup>, Alexander A. Kolykhalov<sup>3</sup>, Khan Hekmatyar<sup>5</sup>, Kaori Sakamoto<sup>6</sup>, Alexander L. Greninger<sup>2</sup> & Richard K. Plemper<sup>1</sup>✉

Measles cases have surged pre-COVID-19 and the pandemic has aggravated the problem. Most measles-associated morbidity and mortality arises from destruction of pre-existing immune memory by measles virus (MeV), a paramyxovirus of the morbillivirus genus. Therapeutic measles vaccination lacks efficacy, but little is known about preserving immune memory through antivirals and the effect of respiratory disease history on measles severity. We use a canine distemper virus (CDV)-ferret model as surrogate for measles and employ an orally efficacious paramyxovirus polymerase inhibitor to address these questions. A receptor tropism-intact recombinant CDV with low lethality reveals an 8-day advantage of antiviral treatment versus therapeutic vaccination in maintaining immune memory. Infection of female ferrets with influenza A virus (IAV) A/CA/07/2009 (H1N1) or respiratory syncytial virus (RSV) four weeks pre-CDV causes fatal hemorrhagic pneumonia with lung onslaught by commensal bacteria. RNAseq identifies CDV-induced overexpression of trefoil factor (TFF) peptides in the respiratory tract, which is absent in animals pre-infected with IAV. Severe outcomes of consecutive IAV/CDV infections are mitigated by oral antivirals even when initiated late. These findings validate the morbillivirus immune amnesia hypothesis, define measles treatment paradigms, and identify priming of the TFF axis through prior respiratory infections as risk factor for exacerbated morbillivirus disease.

After years of the COVID-19 pandemic, over 40 million children worldwide are at risk of measles due to delayed vaccination<sup>1</sup> and temporary SARS-CoV-2 viral dominance<sup>2</sup>. Acute measles has a case-fatality rate of ~1%, but lasting immunosuppression constitutes a major

health threat after recovery from the primary infection<sup>3,4</sup>. Morbilliviruses such as MeV and CDV invade their hosts through infection of alveolar macrophages (AMs) and dendritic cells (DCs), using signaling lymphocyte activation molecule (CD150) as receptor<sup>5</sup>. Subsequently,

A full list of affiliations appears at the end of the paper. ✉ e-mail: [rplemper@gsu.edu](mailto:rplemper@gsu.edu)



## Article

<https://doi.org/10.1038/s41467-024-45418-5>

peripheral blood mononuclear cell (PBMC)-supported cell-associated viremia ensues, until viral re-entry into the respiratory tract and infection of epithelial cells through the basolaterally-expressed Nectin-4 receptor<sup>6</sup>. Viral replication during the viremic phase in CD150<sup>+</sup> lymphocytes in peripheral blood and primary, secondary, and tertiary lymphoid tissues depletes CD150-positive lymphocytes, including memory T and B cells, reducing host antibody repertoire and erasing immune memory<sup>3,4</sup>. Such MeV-induced immune amnesia is hypothesized to increase vulnerability to opportunistic infections, leading to significantly increased morbidity and mortality rates from unrelated infectious diseases in the years following primary measles<sup>7</sup>. Treatment options of acute measles are limited to supportive care, IgG therapy in some high-income countries<sup>8</sup>, and quarantine of the patient. The exceptionally high infectivity of MeV<sup>9</sup> and vaccine hesitancy resulted in a measles resurgence in many European countries in 2019 even prior to the COVID-19 pandemic<sup>10</sup>. Yet temporary pausing of vaccination campaigns in low and middle-income countries during the pandemic has exacerbated the MeV resurgence and major measles outbreaks are anticipated globally<sup>10</sup>. Despite the severity of this health threat, experimental insight is lacking into the time window for prevention of MeV-induced immune-suppression through direct-acting antivirals (DAAs) and the consequences of a large measles wave coinciding with high activity of unrelated respiratory viruses such as influenza virus and RSV.

We previously developed an orally efficacious morbillivirus polymerase inhibitor, ERDRP-0519, which fully protects ferrets against a lethal CDV infection in a post-exposure prophylactic dosing regimen<sup>11</sup>. We recently identified a structurally and mechanistically distinct broadened-spectrum paramyxovirus polymerase inhibitor, GHP-88309, which is orally efficacious against parainfluenzaviruses and blocks morbilliviruses with sub-micromolar potency in cell culture<sup>12</sup>. Using these compounds, we established in this work measles treatment paradigms and explored the effect of prior disease history on severity of morbillivirus infection.

## Results

To verify efficient oral delivery of GHP-88309 to ferrets, we determined single-dose pharmacokinetic (PK) profiles after oral administration at 50 and 150 mg/kg bodyweight. GHP-88309 demonstrated dose-dependent plasma exposure of 177.8 h × nmol/ml and 754.1 h × nmol/ml, respectively, and sustained tissue distribution exceeding 1 nmol/g tissue 12 h after administration (Supplementary Fig. S1a, b; Supplementary Table S1). Twice daily (b.i.d.) oral dosing at 15 and 50 mg/kg in a 14-day non-formal tolerability study revealed no signs of drug-induced toxicity or abnormalities in serum chemistry (Supplementary Fig. S2a–d) and an abbreviated repeated-dose PK study confirmed consistent exposure on day 7 (Supplementary Fig. S3; Supplementary Table S2). Average trough GHP-88309 plasma concentration in the 50 mg/kg b.i.d. group was 2.4 μM, which was equivalent to >2 × EC<sub>50</sub> against CDV<sup>12</sup>. This dose of GHP-88309 was used for all subsequent experiments.

### Oral GHP-88309 expands to 8-days the time window of full protection compared to near-exposure vaccination

Efficacy of GHP-88309, ERDRP-0519, and therapeutic vaccination was compared in CDV-naïve ferrets infected with reporter-free, highly pathogenic recombinant recCDV-5804p (recCDV)<sup>13</sup>, followed by oral treatment with GHP-88309 (50 mg/kg, b.i.d.) initiated 3, 5, or 7 days post infection (dpi) or oral ERDRP-0519 (50 mg/kg, b.i.d.) started 3 dpi (Fig. 1a). Animals in vaccination groups received Purevax CDV vaccine 28, 3, or 1 day prior to, or 1 day after, infection in a prime-boost (28-day group: -28-day prime, -14-day boost) or prime only (all other groups) regimen. A reference group received Distemink CDV vaccine at 2 months of age. There was no statistically significant differences CDV nAb titers between the Purevax prime-boost and Distemink

vaccination groups (Supplementary Fig. S4a). All animals were furthermore fully vaccinated against rabies virus (RABV) by their supplier and confirmed to have α-RABV antibodies prior to use (Supplementary Fig. S4b). Ferrets were monitored daily for clinical signs of morbillivirus disease (fever, rash, loss of bodyweight) and in regular intervals for PBMC-associated viremia, complete blood counts (CBC), and titer of α-RABV neutralizing antibodies (nAbs) (Fig. 1a). All vehicle-treated animals succumbed within 12 days of infection (Fig. 1b) and developed severe clinical signs (Supplementary Fig. S5a–e), whereas GHP-88309 mediated complete survival and statistically significantly reduced virus load (Fig. 1c) when treatment was initiated 3 or 5 dpi, at the onset of viremia and rash, respectively. Treatment started 7 dpi did not significantly improve outcome, and ERDRP-0519 treatment started 3 dpi only partially protected against infection with this wild type recCDV, which is more virulent than the fluorescent recCDV reporter strain used previously<sup>11</sup>. Fully prime-boost vaccinated animals were protected, but neither post-exposure nor 1-day pre-exposure vaccination was efficacious and, moreover, 2 of 3 animals vaccinated prophylactically 3 days prior to infection also succumbed. Clinical signs in animals of all GHP-88309 treatment groups, except the 7-dpi arm, were unremarkable 12 dpi (Fig. 1d; Supplementary Fig. S5), whereas ERDRP-0519-treated animals showed moderate, and vehicle-treated animals severe, clinical signs.

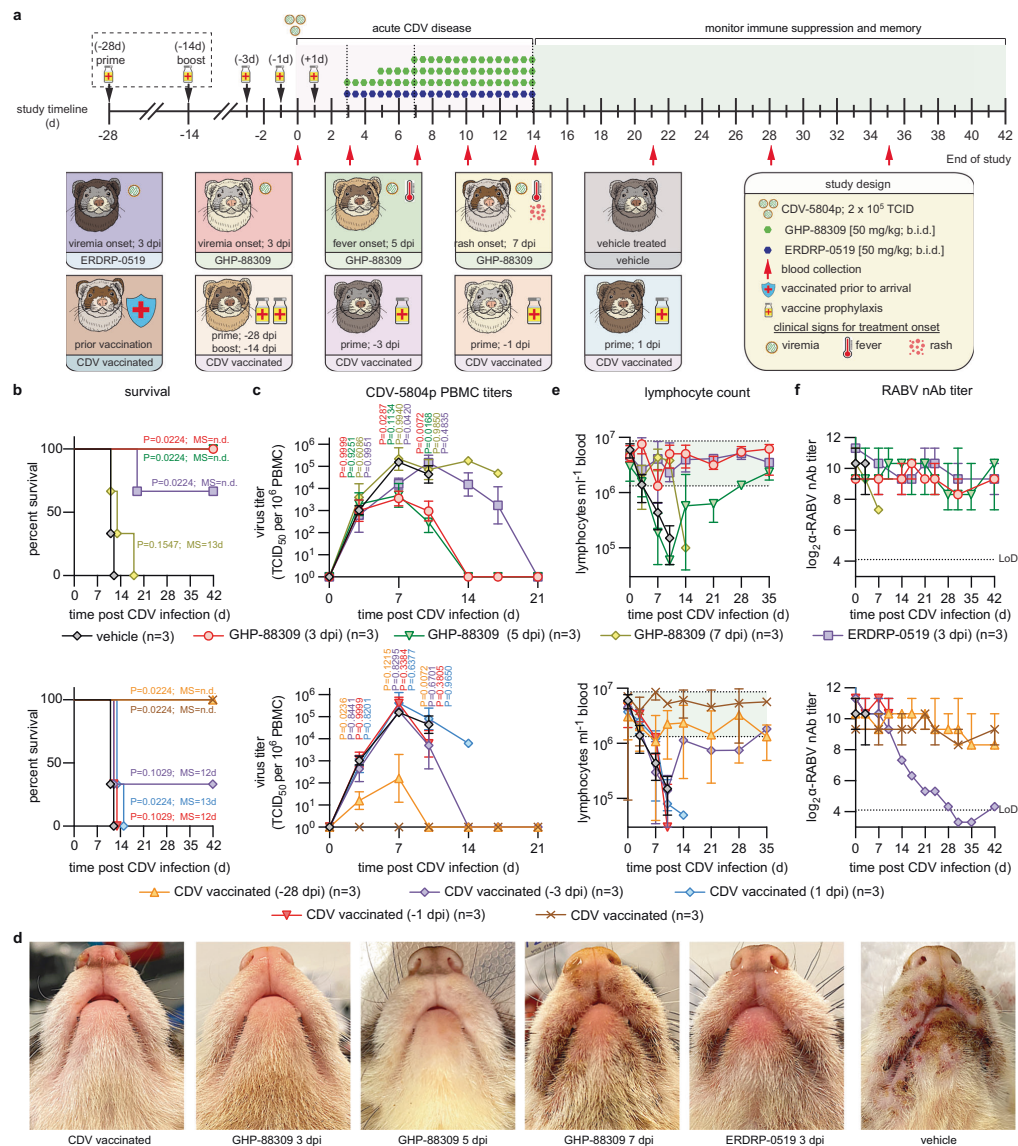
Lymphocyte counts in the vehicle group dropped rapidly by approximately two orders of magnitude by 12 dpi (Fig. 1e). Both GHP-88309 and ERDRP-0519 treatment initiated up to 3 dpi prevented lymphocytopenia. GHP-88309 started 5 dpi did not alleviate initial PBMC collapse, but resulted in populations rapidly recovering such that lymphocytopenia resolved within 4 weeks. Fully vaccinated animals did not develop lymphocytopenia. However, the single surviving animal of the -3 dpi prophylactic vaccination group also experienced temporary collapse of the PBMC population. Pre-existing unrelated humoral immunity, assessed using α-RABV nAbs as a biomarker, was fully preserved in animals of the 5 dpi and earlier treatment groups, but was permanently destroyed in the surviving animal of the -3 dpi vaccination group (Fig. 1f). Thus, GHP-88309 prevents acute lethal morbillivirus infection and mitigates lymphopenia up to 5 days post-infection thereby providing extending the intervention opportunity by at least 8 days compared to near-exposure vaccination. Based on superior oral efficacy of GHP-88309 compared to ERDRP-0519, we selected GHP-88309 for all subsequent experiments.

### Confirmation of immune amnesia hypothesis via recCDV with tunable polymerase processivity

The 100% lethality of recCDV in untreated ferrets within 2 weeks of exposure precluded use of this model in exploring questions relevant to human morbillivirus-induced disease in which lethality is slower and less uniform. To surmount this hurdle, we engineered an attenuated recCDV with intact viral receptor tropism. Previously, we demonstrated that variable length deletions of 39–55 amino acids in the structurally disordered CDV nucleocapsid (N) protein tail domain affect polymerase processivity to different degrees, resulting in genetically stable tunable recCDV attenuation<sup>14</sup>. Employing a 55-amino acid deletion recCDV NΔ425-479 strain, we compared virulence and severity of immune suppression with that of unmodified recCDV and a previously described tropism-altered recCDV Nectin-4-blind mutant strain<sup>7</sup> that cannot engage the Nectin-4 epithelial cell receptor (Fig. 2a).

Clinical signs caused by the different recombinant strains, which were all in an otherwise identical recCDV-5804p genetic background, varied from severe for recCDV NΔ425-479, similar to the parental recCDV, to unremarkable for recCDV Nectin-4-blind (Fig. 2b, c; Supplementary Fig. S6a–d). All recCDV Nectin-4-blind and a majority of recCDV NΔ425-479-infected animals survived, whereas ferrets inoculated with unmodified recCDV died within 12 days of infection (Fig. 2d). Surviving animals mounted a robust α-CDV nAb response within three

## Article

<https://doi.org/10.1038/s41467-024-45418-5>

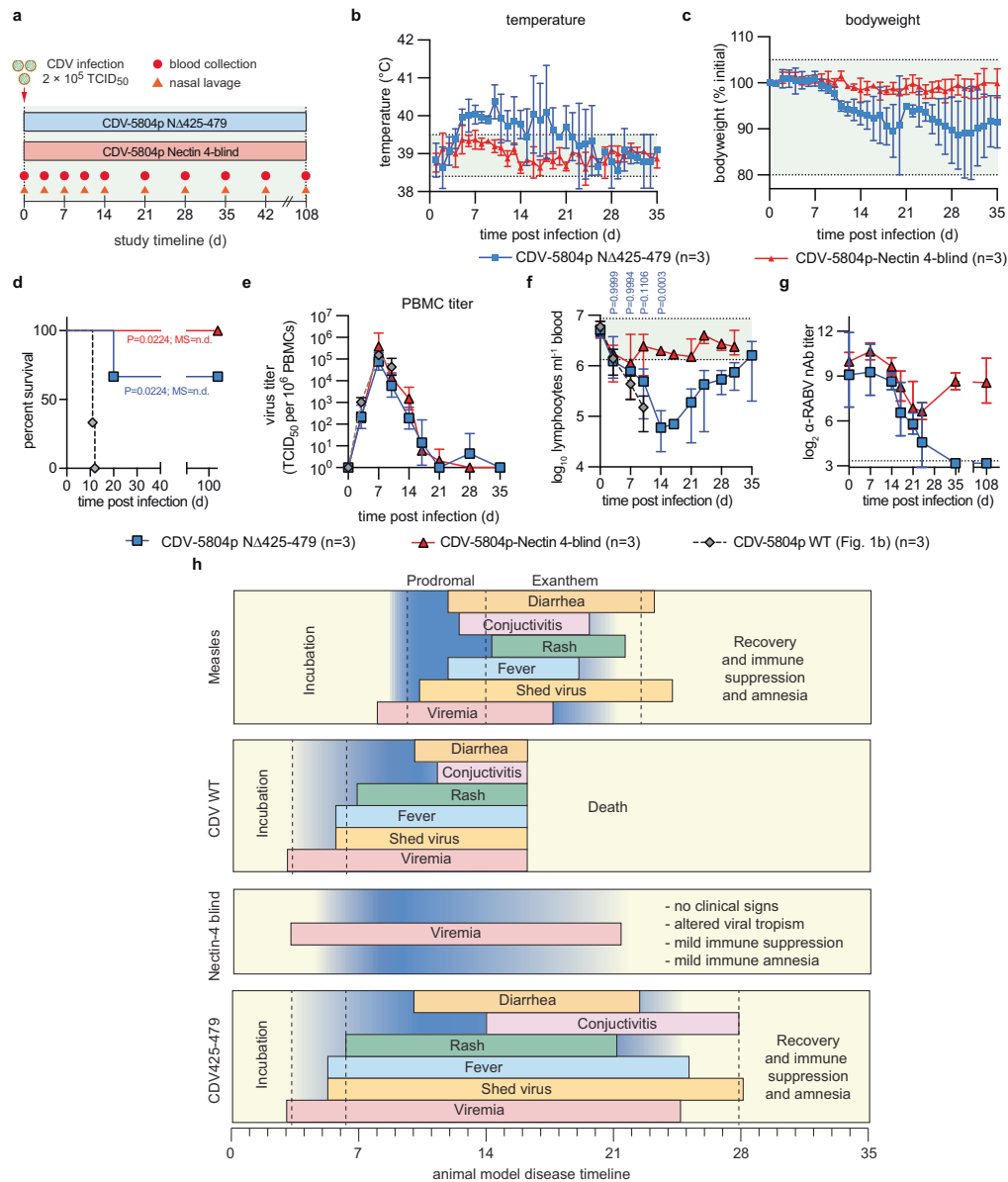
**Fig. 1 | Therapeutic treatment of lethal CDV infection in ferrets.** Ferrets were infected with a lethal challenge of CDV and treated with GHP-88309, ERDRP-0519, or therapeutic vaccination. **a** Schematic of the study design. Ferrets were infected with wild-type recCDV-5804p and monitored for 6 weeks. Symbols in the different boxes show clinical presentation of animals when treatment of the respective group was initiated. **b** Survival curves of ferrets infected in (a). log-rank (Mantel-Cox) test, median survival is stated. **c** PBMC associated viremia titers of CDV infected ferrets shown in (a). 2-way ANOVA with Dunnett's post-hoc test. **d** Images

of ferrets taken 12 days after infection with recCDV-5804p. **e** Lymphocyte counts from infected ferrets measured during the duration of the study detailed in (a). Green shading denotes normal range. **f** RABV neutralizing antibody titers from CDV infected ferrets. Symbols (c, e, f) represent geometric means ± geometric SD, lines intersect means. In (b–e), top row shows results for inhibitor-treated groups, bottom row for vaccinated animals; LoD, limit of detection; n = 3. Source data are provided as a Source Data file.

weeks of infection (Supplementary Fig. S6e). PBMC-associated primary viremia titers of all three strains were statistically identical in the first 2 weeks after infection until animals inoculated with parental recCDV had succumbed (Fig. 2e). Subsequently, viremia in recCDV Nectin-4-

blind animals fully resolved, whereas ferrets infected with recCDV NΔ425-479 entered a 3-week low-level secondary viremia phase. Only animals inoculated with recCDV NΔ425-479 experienced lymphocytopenia with initial kinetics similar to that of the recCDV-infected

## Article

<https://doi.org/10.1038/s41467-024-45418-5>

**Fig. 2 | Ferret model of CDV-induced immune amnesia.** **a** Study schematic. Ferrets were infected intranasally with recCDV-5804p NΔ425-479 or recCDV-5804p-Nectin 4-blind and monitored for 108 days. Nasal lavages were taken from recCDV-5804p NΔ425-479 infected ferrets only. Blood was sampled regularly from all animals. **b–g** Body temperature (**b**), bodyweight (**c**), survival curves (**d**), PBMC-associated viremia titers (**e**), lymphocyte counts (**f**), and RABV neutralizing antibody titers (**g**) of ferrets infected with the different recCDV-5804p. Symbols

represent arithmetic (**b, c**) or geometric (**e–g**) means  $\pm$  arithmetic or geometric SD, lines intersect means; log-rank (Mantel-Cox) test, median survival is stated (**d**); 2-way ANOVA with Sidak's post-hoc test (**f**); n numbers as specified. **h**, 2D schematic comparing disease dynamics and clinical signs of measles virus infections in humans, with wild-type recCDV-5804p, recCDV-5804p-Nectin 4-blind, and recCDV-5804p NΔ425-479 infections in ferrets. Source data are provided as a Source Data file.

## Article

<https://doi.org/10.1038/s41467-024-45418-5>

group (Fig. 2f; Supplementary Fig. S7a–d), whereas no statistically significant changes in lymphocyte counts were detected in ferrets infected with recCDV Nectin-4-blind, confirming over-attenuation of this recombinant. In the recCDV NΔ425-479-infected animals, lymphocytopenia fully resolved 4 weeks after infection. Pre-existing humoral α-RABV immunity collapsed within 3 weeks of recCDV NΔ425-479 infection and was not restored over a 3-month post-recovery period (Fig. 2g), whereas recCDV Nectin-4-blind caused only a temporary moderate decline in α-RABV nAbs titers that spontaneously resolved within 4 weeks of infection.

A comparison of clinical signs after infection of ferrets with the three recCDV strains with the presentation of human measles revealed that recCDV NΔ425-479 disease recapitulates hallmarks of human morbillivirus disease, albeit with accelerated onset of clinical signs (Fig. 2h). Thus, we have developed a relevant surrogate animal model of human measles that strongly supports the morbillivirus immune amnesia hypothesis.

#### Treatment at the onset of clinical signs alleviates morbillivirus immune amnesia

To explore the degree to which primary clinical signs of morbillivirus disease and immune amnesia can be mitigated pharmacologically, we initiated oral treatment with GHP-88309 at four discrete disease stages after infection with recCDV NΔ425-479: first onset of fever (5 dpi), rash (7 dpi), severe disease with diarrhea and conjunctivitis (10 dpi), and the first fatality in the vehicle group (24 dpi) (Fig. 3a). Treatment was continued b.i.d. until α-CDV nAbs became detectable in serum samples. In addition to following α-RABV immunity, we administered quadrivalent influenza vaccine to all animals 28 days prior to infection with CDV (-28-day prime, -14-day boost). Animals were monitored for 5 months post-CDV and the response to broad innate immune stimulation through intramuscular (i.m.) flagellin, infection with influenza virus A/CA/07/2009 (H1N1) (pdmCA09) and A/WI/67/2005 (H3N2), and homotypic rechallenge with pathogenic recCDV-5804p determined 8, 9.5, 12.5, and 18.5 weeks, respectively, after the original CDV infection.

All GHP-88309-treated animals and all ferrets of a CDV-vaccinated reference group survived until study end, whereas approximately 50% of ferrets in the vehicle group succumbed to recCDV NΔ425-479 within 26 days of infection (Fig. 3b; Supplementary Fig. S8a, b). Oral GHP-88309 started 5 dpi significantly reduced CDV viremia titers (Fig. 3c), but later initiation of treatment did not affect severity or duration of primary viremia. However, first administration of GHP-88309 up to 10 dpi statistically significantly shortened virus shedding into nasal lavages (Fig. 3d). Treatment started at the end of acute disease (24 dpi) did not modulate height or duration of viremia or virus shedding. Lymphocytopenia was suppressed in ferrets of the 5 dpi GHP-88309 group, resembling CDV-vaccine-mediated protection, and alleviated in the 7 dpi GHP-88309 group (Fig. 3e). In animals first treated later than 7 dpi, lymphocytopenia was severe, closely resembling that in the vehicle group, and lymphocyte counts regained pre-infection levels only ~10 weeks after CDV infection. Studies in nonhuman primates infected with MeV have revealed that viral RNA remains detectable in PBMCs up to 90 days after infection<sup>15</sup>. Recapitulating this phenotype, we detected CDV RNA for over 64 days in PBMCs extracted from ferrets of all groups, except for CDV-vaccinated animals and ferrets first treated with GHP-88309 5 or 7 dpi (Fig. 3f). Early treatment onset thus accelerated viral clearance and prevented persistence of viral RNA, which correlated with statistically significantly earlier appearance of α-CDV nAbs (Fig. 3g). Whole genome sequencing of viruses recovered from GHP-88309-experienced animals 8–37 dpi with CDV did not reveal emergence of GHP-88309-characteristic<sup>12</sup> resistance mutations (Supplementary Dataset S1).

Upon stimulation of animals with 50 μg flagellin i.m. post-recovery from acute CDV, we monitored expression of a panel of pro-

inflammatory markers by PBMCs harvested before, or 1, 2, and 24 h after, stimulation (Supplementary Fig. S9). Body temperature was increased in all animals after flagellin injection without significant differences in marker expression between groups (Fig. 3h), indicating that innate response to an immunogen was not compromised after recovery from acute CDV disease.

Animals of all groups had robust α-RABV (Fig. Fig. 3i) and α-IAV (Fig. 3j) humoral immunity prior to CDV infection. Treatment with GHP-88309 5 dpi fully preserved nAbs titers, identical to the protective effect of CDV vaccination. Animals in all later treatment groups experienced a rapid decline in α-RABV and α-IAV nAbs titers over a 30–40 day period post-CDV infection, which was indistinguishable from that seen in the vehicle group and, in the case of α-RABV immunity, irreversible. However, low levels of α-IAV nAbs were present in the GHP-88309 7- and 10-dpi treatment groups at the time of challenge with pdmCA09 9.5 weeks after CDV infection. Accordingly, animals in both the 5- and 7-dpi GHP-88309 groups showed significantly reduced peak shed influenza virus load (Fig. 3k) and alleviated clinical signs of pdmCA09 infection (Supplementary Fig. S10a, b). All animals infected with pdmCA09 mounted a robust neutralizing response 2 weeks after challenge (Supplementary Fig. S10c), indicating that CDV infection erased pre-existing immunity, but had no lasting suppressive effect on humoral immune competence to a new challenge post-recovery.

Since α-pdmCA09 nAbs are not cross-protective against subtype H3N2 IAVs, they can only provide protection by heterosubtypic immunity<sup>16</sup>. We therefore inoculated animals with an A/WI/67/2005 (H3N2) 3 weeks after the pdmCA09 challenge (87 dpi with CDV) to assess cell-mediated immune competence. As expected, ferrets of the CDV vaccine and 5-dpi GHP-88309 treatment groups had retained high α-H3N2 nAbs titers induced by the quadrivalent influenza vaccine (Supplementary Fig. S10d). Humoral α-H3N2 immunity in all other groups collapsed. None of the groups showed significant clinical signs (Supplementary Fig. S10e, f), α-H3N2 nAbs were rapidly rebuilt within 28 days of A/WI/67/2005 (H3N2) challenge (Supplementary Fig. S10g), and only low levels of virus shedding were detectable 24 h after infection (Supplementary Fig. S10h), suggesting equivalent cross-reactive cell-mediated immunity derived from the pdmCA09 challenge in animals of all groups, which is consistent with previous reports for both the ferret model and human patients<sup>17–21</sup>. All animals furthermore mounted a robust humoral α-CDV response post-recovery and were fully protected against homotypic challenge with non-attenuated recCDV-5804p 130 days after the original CDV infection (Supplementary Fig. S11).

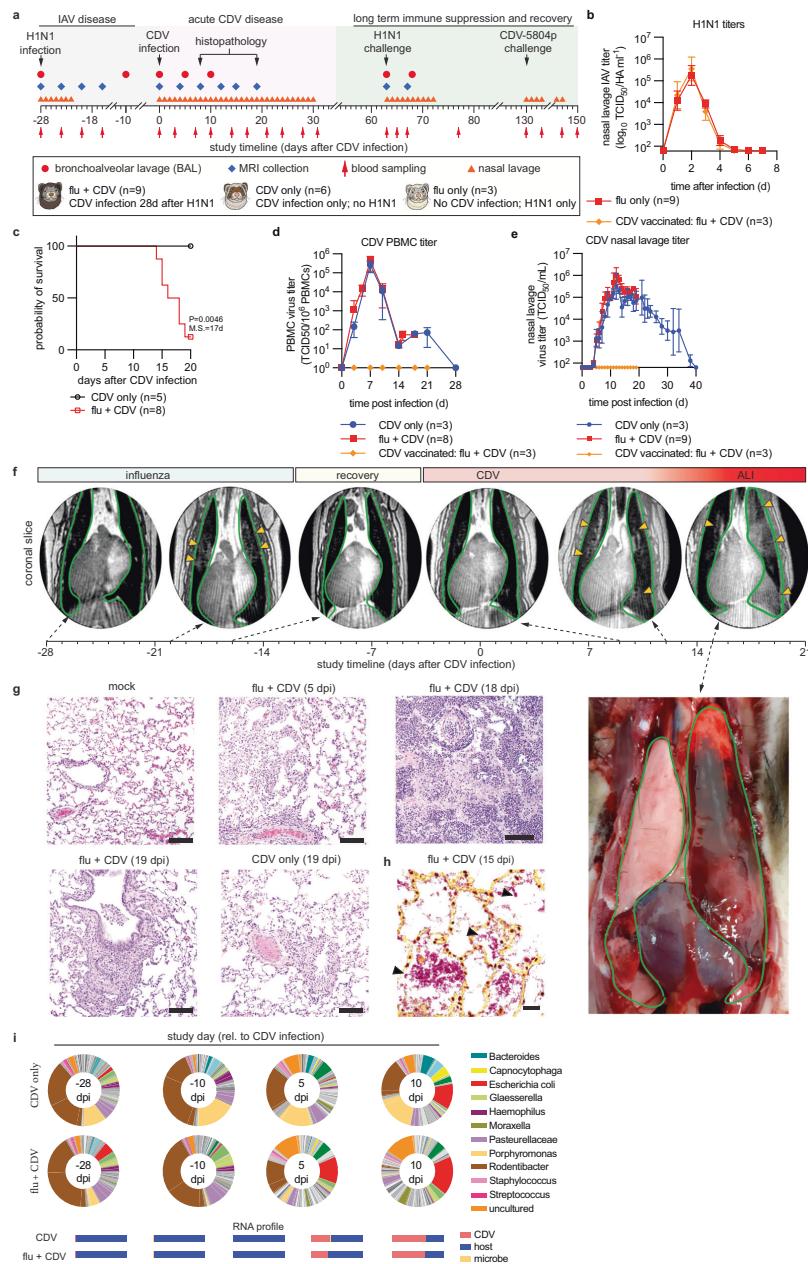
These results indicate that treatment initiated at the onset of first clinical signs of morbillivirus disease (fever; 5 dpi in the CDV ferret model) fully protects, while treatment started at the onset of rash (7 dpi) partially preserves, pre-existing immunity. Later onset of treatment improves outcome of morbillivirus disease but does not subvert immune amnesia.

#### Fatal lung disease after unrelated respiratory virus infection followed by morbillivirus invasion

Naturally acquired IAV immunity is more robust than vaccine-induced protection<sup>22</sup>. To better mimic such immunity, we developed a consecutive infection ferret model that establishes a prior disease history in the animals (Fig. 4a). Influenza virus-naïve ferrets were inoculated 28 days before CDV infection with pdmCA09, with the intent to be followed for 5 months including challenge with pdmCA09 and CDV. Animals in reference groups were CDV vaccinated, or not infected with pdmCA09, respectively. Ferrets in all influenza virus groups developed fulminant clinical signs of IAV infection (Supplementary Fig. S12) and reached peak shed viral loads of 10<sup>5</sup>–10<sup>6</sup> TCID<sub>50</sub> units/ml nasal lavage 2 dpi (Fig. 4b). pdmCA09 shedding ceased and all clinical signs resolved by 6 dpi, and ferrets had mounted robust humoral α-IAV (H1N1)







immunity (Supplementary Fig. S13) when infected with recCDV NΔ425-479 4 weeks later (study day 0).

Unexpectedly, most animals consecutively infected with this non-lethal IAV and low-lethal recCDV succumbed to acute hemorrhagic pneumonia with extensive spontaneous bleeding 14–18 dpi (Fig. 4c; Supplementary Fig. S14a–c). Fatalities did not coincide with enhanced PBMC-associated CDV viremia titers or prolonged CDV shedding

(Fig. 4d, e). Postmortems of moribund vehicle-treated animals that presented with severe respiratory distress revealed major lung tissue injury with inflammatory lesions and wide-spread edema affecting several lobes (Supplementary Fig. S14d–f).

We employed pulmonary ferret MRI for longitudinal non-invasive assessment of lung disease progression (Supplementary Movie S1, S2). Transient viral pneumonia with localized fluid accumulation was

## Article

<https://doi.org/10.1038/s41467-024-45418-5>

**Fig. 4 | Fatal lung disease in ferrets infected with respiratory viruses prior to CDV infection.** **a** Study schematic. **b** pdmCA09 (H1N1) nasal lavage virus titers after primary IAV infection, 28 days prior to recCDV-5804p NΔ425-479 as specified in (a). **c** Survival curves of ferrets from (a). log-rank (Mantel-Cox) test, median survival is stated; *n* numbers as specified. **d, e** PBMC-associated CDV viremia (**d**) and nasal lavage (**e**) titers after infection of ferrets with recCDV-5804p NΔ425-479. Symbols in (**b, d, e**) represent geometric means ± geometric SD; *n* = 3–9 as specified. **f** MRI timeline performed on ferrets during primary pdmCA09 (0, 4, 8, and 12 dpi with influenza) and subsequent recCDV-5804p NΔ425-479 infection (8, 12, and 15 dpi with CDV). Lungs are outlined in green (dark appearance in MRI images),

arrowheads denote fluid accumulation. Bottom right: necropsy of the ferret MRI-imaged on D15. **g** Histopathology of ferret lungs from (a), extracted 5, 18, or 19 dpi with CDV. **h** Gram staining of lung samples taken 15 dpi with CDV showing bacterial pneumonia. Purple-brown staining indicates Gram-positive bacteria, pink-red color marks gram-negative organisms; scale bars in (**g, h**) represent 100 μm. **i** Metagenomics analysis of bacterial transcripts in BAL fluids collected from consecutively infected or CDV-only ferrets. Below each pie graph, RNA profiles of the relative composition of transcripts are shown. Source data are provided as a Source Data file.

present 8 days after pdmCA09, but fully resolved by 12 dpi (Fig. 4f). Infection of ferrets without prior influenza history with recCDV NΔ425-479 did not cause pulmonary edema. In contrast, pdmCA09-experienced animals developed pneumonia that was first detectable 12 days after CDV and rapidly advanced to major hemorrhage 14–19 dpi (Fig. 4f; Supplementary Movie S3, S4; Supplementary Fig. S15).

Histopathology of lung tissue extracted in repeat studies when vehicle-treated pdmCA09 and recCDV NΔ425-479-infected animals became moribund (15–19 dpi) revealed widespread edema, necrosis, and vasculitis in the small airways (Fig. 4g; Supplementary Fig. S16). Lung samples extracted 19 dpi from ferrets that were infected only with recCDV NΔ425-479 contained areas of inflammatory cellular infiltrates, bronchial epithelial hyperplasia and epithelial sloughing consistent with mild interstitial viral pneumonia, but showed no signs of edema and vasculitis, reflected by significantly lower pathology scores than those of the consecutively-infected group (Supplementary Fig. S17). Lung tissues of CDV-vaccinated consecutively infected animals were unremarkable, their pathology scores resembling those of mock-infected ferrets. Gram-staining of tissue samples from consecutively-infected animals showed fulminant bacterial superinfections that were absent from animals infected with CDV only, which clinical microbiology identified as part of the commensal microbiome (Fig. 4h; Supplementary Fig. S17a, b). Metagenomics furthermore revealed a relative expansion of the *Escherichia* population in the lung microbiome 10 dpi with CDV in both singly and consecutively infected animals (Fig. 4i; Supplementary Dataset S2).

To assess whether priming for exacerbated disease is correlated with severity of the initial viral pneumonia, is strictly dependent on the 28-day interval between infections, or is IAV-specific, we treated the initial pdmCA09-infected animals with the broad-spectrum nucleoside-analog antiviral 4'-fluorouridine (4'-FU; EIDD-2749)<sup>23</sup>, infected animals with pdmCA09 67 days before CDV, or inoculated ferrets with RSV-A2-L19F<sup>24</sup> instead of pdmCA09, respectively (Fig. 5a). Bronchoalveolar lavages (BALs) were sampled at 5 predefined time points throughout the study. Consistent with previously demonstrated α-IAV efficacy of 4'-FU<sup>25</sup>, once daily (q.d.) oral administration at 2 mg/kg bodyweight initiated 24 h after infection with pdmCA09 statistically significantly shortened viral shedding and alleviated clinical signs (Supplementary Fig. S18a, b). However, pharmacological mitigation of IAV disease did not significantly alter viremia titers or virus shedding after subsequent infection with recCDV NΔ425-479 (Fig. 5b, c) and the majority of animals succumbed to hemorrhagic pneumonia (Fig. 5d). An expanded 67-day interval between IAV and CDV infections had no major alleviating effect on CDV disease presentation and hemorrhagic pneumonia outcome (Fig. 5e–g).

Inoculation of ferrets with RSV-A2-L19F resulted in productive infection, characterized by efficient RSV shedding into nasal lavages (Supplementary Fig. S19a), but animals did not display overt clinical signs (Supplementary Fig. S19b). No cross-protective immunity with paramyxovirus infection was observed when we inoculated ferrets 28 days after RSV with recCDV NΔ425-479 (Supplementary Fig. S19c–e), and the majority of animals again succumbed to hemorrhagic pneumonia (Supplementary Fig. S19f).

### Differential expression of TFF peptides after CDV infection as a consequence of prior disease history

RNA-qPCR analysis of BAL samples taken during and after IAV infection of ferrets for expression levels of selected pro-inflammatory and wound-healing cytokines relative to those prior to exposure suggested that respiratory tissues of IAV-experienced animals may be in an anti-inflammatory state at the time of CDV infection compared to immune homeostasis of IAV-naïve animals (Supplementary Fig. S20).

Comparative RNAseq screening of BAL samples extracted 5 dpi from ferrets infected with recCDV NΔ425-479, or consecutively infected with pdmCA09 followed by recCDV NΔ425-479, identified 9 genes as significantly differentially expressed between study groups (Fig. 5h). These included all three genes encoding trefoil factor (TFF) peptides (Fig. 5i), which are known to be involved in protection and repair of gastrointestinal<sup>26</sup> and, although less well studied, respiratory<sup>27</sup> epithelia. Follow-up RT-qPCR of lung tissue extracts harvested 10 days after CDV infection confirmed that TFF-encoding mRNAs were upregulated several 100-fold (TFF1 and 2) to 1000-fold (TFF3) in animals infected only with CDV compared to the consecutively infected groups (Fig. 5j). pdmCA09 infection alone resulted in only slightly increased TFF1 and 2 expression 10 dpi and TFF3 was not upregulated (Supplementary Fig. S21a–c), indicating that extreme induction of TFF1 and 3 is morbillivirus-specific rather than a general response to respiratory virus infections. In the mouse respiratory tract, TFF1 and 3 reportedly colocalize with mucins Muc5AC and Muc5B<sup>28</sup>. However, RT-qPCR did not reveal an equivalent differential upregulation of either Muc5 expression level in the different infection groups (Supplementary Fig. S21d, e).

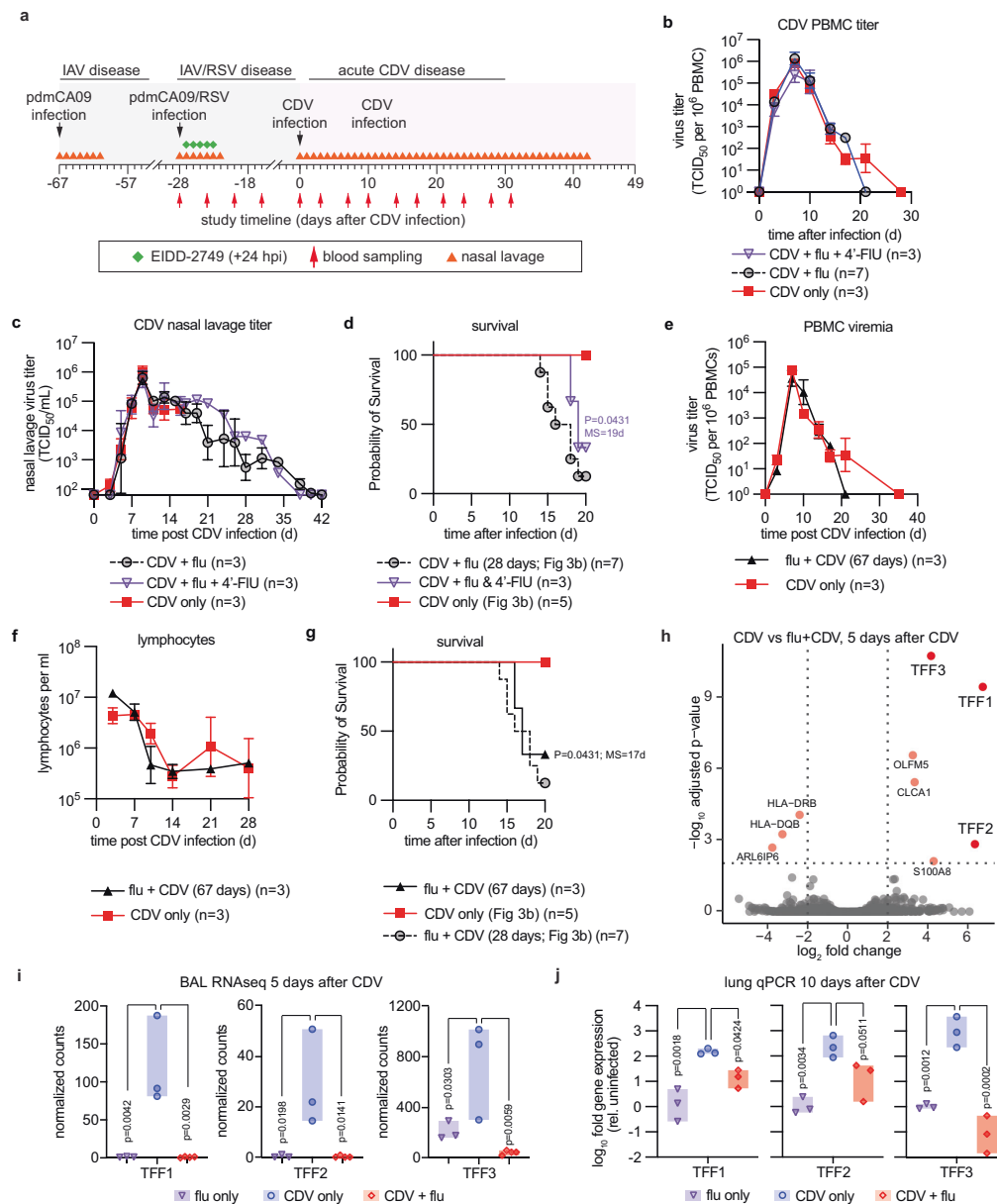
These results demonstrated that immune priming through unrelated primary viral pneumonia sets the stage for exacerbated subsequent morbillivirus disease. CDV infection during, or shortly after, the recovery phase of an inflammatory episode alters the quality of the host defense to morbillivirus disease, resulting in significantly lower expression of respiratory epithelium protective TFFs, which emerged as correlative for risk to advance to hemorrhagic pneumonia.

### Late onset treatment of CDV infection does not mitigate signs of CDV disease, but alters lethal outcome

To assess the effect of treatment of morbillivirus infection on disease outcome, we again consecutively infected animals with pdmCA09 (Supplementary Fig. S22) followed by recCDV NΔ425-479, and initiated oral treatment with GHP-88309 5, 7, 10, and 14 dpi with CDV (Fig. 6a). Consistent with results of the previous GHP-88309 treatment studies, PBMC-associated CDV viremia was mitigated only when treatment was initiated 5 dpi (Fig. 6b). All animals started on GHP-88309 5 or 7 dpi with CDV survived, whereas vehicle-treated animals succumbed to hemorrhagic pneumonia between days 14–19 after CDV infection (Fig. 6c). A majority of animals in the 10 dpi treatment group recovered, but most ferrets first treated with GHP-88309 14 dpi with CDV developed lethal pneumonia. Lymphocyte counts were fully preserved in CDV-vaccinated control animals and ferrets of the 5 dpi treatment group, and were partially preserved in animals of the 7 dpi group (Fig. 6d). Although later treatment start did not mitigate lymphocytopenia, PBMC repopulation was accelerated in the 10 dpi treatment group. Circulating granulocyte populations did not deviate from the



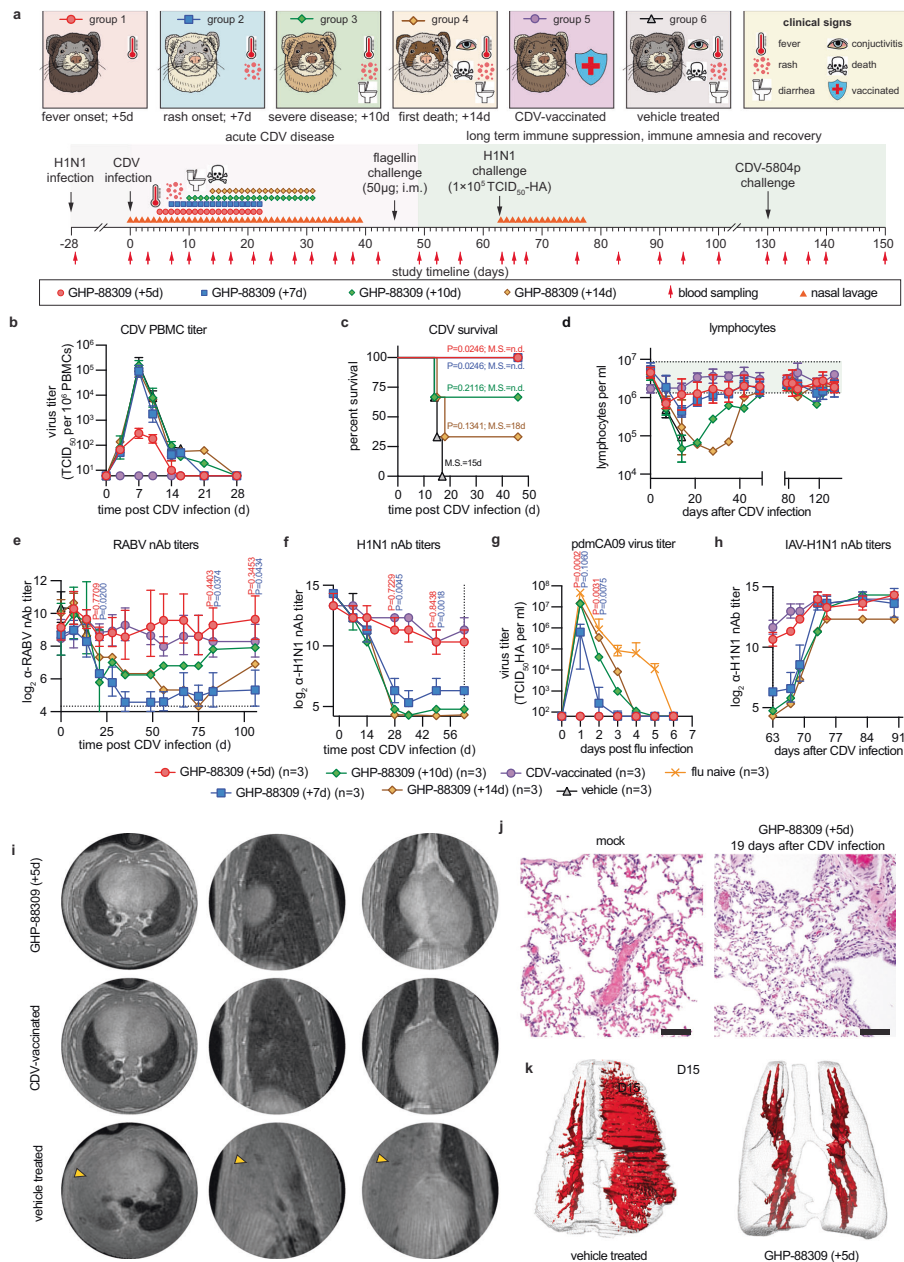
## Article

<https://doi.org/10.1038/s41467-024-45418-5>

**Fig. 5 | Disease history affects CDV-induced TFF upregulation.** **a** Schematic of study design. **b**, **c** PBMC-associated CDV viremia (**b**) and nasal lavage (**c**) titers of ferrets infected with recCDV-5804p N4425-479. **d** Survival of consecutively IAV + CDV-infected ferrets after treatment of primary IAV with 4'-Flu. **e**–**g** PBMC-associated primary viremia titers (**e**), circulating lymphocyte counts (**f**), and survival (**g**) of ferrets infected with recCDV-5804p N4425-479 67 dpi with primary pdmCA09. Symbols represent geometric means  $\pm$  geometric SD (**b**, **c**, **e**, **f**), lines intersect means; log-rank (Mantel-Cox) test, median survival is stated (**d**, **g**); *n* numbers as specified. **h** RNAseq screen of differentially expressed transcripts present in BAL fluids extracted 5 dpi with CDV from consecutively infected versus CDV-only ferrets. Differentially expressed genes were determined with the Wald

test and *P* values corrected for multiple tests using the method of Benjamini and Hochberg. Significance thresholds (adjusted *p* < 0.01, log<sub>2</sub> fold change > 2) are shown as dotted horizontal and vertical lines, respectively. **i** Trefoil factor (TFF1, TFF2, and TFF3) transcripts in BAL fluids harvested 5 dpi with CDV from consecutively infected versus CDV-only ferrets. **j** RT-qPCR quantification of relative presence of trefoil factor-encoding message in lung tissue of consecutively infected versus CDV-only ferrets, extracted 10 dpi with CDV. Symbols (**i**, **j**) represent individual animals, bars show range; 1-way ANOVA with Dunnett's post-hoc test (**i**, **j**); *n* = 3. Source data are provided as a Source Data file.

## Article

<https://doi.org/10.1038/s41467-024-45418-5>

normal range in any study group, making granulocytes transiently the predominant white blood cell population in animals experiencing lymphocytopenia (Supplementary Fig. S23). nAb titers against RABV and IAV H1N1 reflected the lymphocytopenia results; fully preserved in vaccinated and 5 dpi GHP-88309-treated animals, partially preserved in the 7 dpi treatment group, and not preserved when GHP-88309 was initiated 10 or 14 dpi with CDV (Fig. 6e, f). Accordingly, only ferrets in

the 5 and 7 dpi GHP-88309 treatment groups were fully or partially, respectively, protected against pdmCA09 challenge 62 days after CDV (Fig. 6g). However, surviving animals of all GHP-88309 treatment groups mounted a robust de novo  $\alpha$ -IAV H1N1 nAb response following challenge with pdmCA09 (Fig. 6h). At study end, all ferrets had furthermore developed robust immunity against CDV reinfection (Supplementary Fig. S24).

## Article

<https://doi.org/10.1038/s41467-024-45418-5>

**Fig. 6 | Effect of therapeutic intervention on severe disease outcomes.** **a** Study schematic. **b–f** PBMC-associated viremia titers (**b**), survival (**c**), lymphocyte counts (**d**), and RABV (**e**) and IAV H1N1 (**f**) nAb titers of consecutively infected and GHP-88309-treated ferrets from (**a**). Green shading in (**d**) denotes normal range. **g** pdmCA09 nasal lavage titers after IAV challenge of ferrets recovered from CDV disease. **h** IAV H1N1 nAb titers after challenge of ferrets recovered from CDV disease with pdmCA09 on study day 65. **i** MRI slices of consecutively infected and GHP-88309-treated (top row), CDV-vaccinated (middle row), or vehicle-treated (bottom row) ferrets, taken 15 dpi with CDV. Axial, coronal, and sagittal slices of the same lung are shown. Arrow heads denote hemorrhagic infiltrates. **j** 3D MRI

reconstructions and segmentations of lungs from consecutively IAV CDV-infected and GHP-88309 or vehicle-treated ferrets. Images were collected 15 dpi with CDV; fluids shown in red. **k** Lung histopathology of consecutively infected and GHP-88309-treated or uninfected (mock) ferrets, assessed 19 dpi with CDV; scale bars represent 100  $\mu$ m. Symbols (**b**, **d–h**) represent geometric means  $\pm$  geometric SD, lines intersect means; error was not calculated for later timepoints of the GHP-88309 (+10d) and GHP-88309 (+14d) conditions, when individual animals had reached endpoints and subgroup sizes were below 3. Log-rank (Mantel-Cox) test (**c**), median survival is stated; 2-way ANOVA with Dunnett's post-hoc test (**e–g**); *n* numbers as specified. Source data are provided as a Source Data file.

Longitudinal MRI analysis 15 dpi with CDV of consecutively IAV and CDV-infected animals treated with GHP-88309 demonstrated suppression of pulmonary edema and hemorrhage (Fig. 6i, j; Supplementary Movies S5, S6), which was confirmed by histopathology of treated animals (Fig. 6k). Again, whole genome sequencing of CDV recovered from GHP-88309-treated ferrets 9–19 dpi revealed no known<sup>12</sup> resistance mutations (Supplementary Dataset S3).

Outcome reversal of lethal hemorrhagic pneumonia through late-onset GHP-88309 established precedent for therapeutic benefit of direct-acting antiviral therapy initiated after the time window for mitigation of primary clinical signs of morbillivirus disease has closed. The results demonstrate that GHP-88309 treatment paradigms for mitigation of morbillivirus-induced immune amnesia are independent of whether immunity was naturally acquired or vaccine-induced.

## Discussion

Reflecting a paucity of effective antiviral therapeutics, their benefit is poorly defined for most pathogenic paramyxoviruses and unknown for members of the Morbillivirus genus, specifically. Recent work testing remdesivir therapy in a non-human primate model of MeV infection reported transient reduction of viral RNA through post-exposure prophylactic treatment, but lymphocytopenia and clinical disease parameters were not improved and virus replication rebounded<sup>29</sup>. Since remdesivir was designed to yield high liver exposure<sup>30</sup>, sustained inhibitory concentrations may not be reached in MeV-relevant target cells and tissues. Having identified orally efficacious morbillivirus<sup>11,31</sup> and broadened-spectrum paramyxovirus<sup>12</sup> inhibitors, we established in this study treatment paradigms for morbillivirus disease. Results support five major conclusions: i) efficacious antivirals such as GHP-88309 expand the therapeutic time window to eight days compared to therapeutic vaccination; ii) infections with engineered attenuated recCDV confirm the morbillivirus immune amnesia hypothesis in the ferret model; iii) therapeutic mitigation of primary clinical signs of morbillivirus disease and immune amnesia is beneficial when treatment is initiated before, or at peak, of primary viremia; iv) prior disease history of the host defines the risk for exacerbated, fatal morbillivirus infection; and v) late-onset anti-morbillivirus treatment prevents lethal bacterial superinfection.

The impact of prior infection on the outcome of morbillivirus infection was most unexpected. Although heightened long-term susceptibility to secondary infections after severe primary viral or bacterial pneumonia was described in mice<sup>32</sup>, this sepsis-induced transient immunosuppression was attributed to poor antigen-presentation capacity of DCs and AMs in the TGF- $\beta$ -driven anti-inflammatory microenvironment established during the tissue healing phase after resolution of the primary infection<sup>33</sup>. However, immune priming for catastrophic morbillivirus disease did not require severe primary pneumonia, since highly efficacious treatment of pdmCA09 infection with 4'-FIU<sup>25</sup> did not prevent hemorrhagic pneumonia after subsequent CDV infection. Unlike therapeutic intervention with the primary IAV infection, late-onset treatment of the morbillivirus infection with GHP-88309 initiated shortly before uncontrolled amplification of commensal bacteria changed outcome, indicating that CDV replication in

the respiratory epithelium after basolateral re-invasion of lungs is instrumental for progression to lethal secondary complications. Our study revealed that morbillivirus triggers massive upregulation of TFF1, TFF3 and, to a lesser degree, TFF2 expression, provided infection occurred during lung immune homeostasis. In the respiratory tract, TFFs are predominantly produced by glandular and mucus-secreting epithelial and hematopoietic cells<sup>27,34–36</sup>, and TFF1 and 3 specifically enhance mucociliary bacterial clearance through increasing mucus viscosity<sup>27,37,38</sup>.

Based on these observations, we propose an immune-priming-based mechanism leading to exacerbated disease. IAV infection reportedly results in transient population of the respiratory tract with functionally altered DCs and AMs to restore immune homeostasis after the pro-inflammatory response, which are unable to clear bacterial pathogens efficiently<sup>33</sup>. CDV infection during the recovery phase, followed by basolateral invasion of the respiratory epithelium after primary viremia, further depletes DCs and AMs<sup>6</sup> and fails to upregulate TFF expression, setting the stage for catastrophic bacterial pneumonia through impaired clearance of commensal bacteria. How does prior IAV infection affect TFF1 and 3 upregulation? Type 2 cytokines IL-4 and IL-13 stimulate TFF3 synthesis in the GI tract in a STAT6-dependent process<sup>27</sup>. Upregulation of immunosuppressive cytokines such as TGF $\beta$  and downregulation of pro-inflammatory IL-1 $\beta$  at the time of CDV infection after influenza may create an environment incompatible with TFF induction after CDV, but regulation of TFF3 expression in the airway epithelium is overall poorly understood. In mice, IAV stimulates lung-resident lineage-negative epithelial progenitor (LNEP) cells that are the major responders in distal lung after tissue damage<sup>39</sup> and express high levels of TFF2<sup>27</sup> potentially creating a negative feedback loop that prevents TFF1 and 3 upregulation. Future work must focus on the regulation of TFF3 levels in the homeostatic respiratory tract to better understand the molecular basis for long-lasting impaired expression after influenza virus priming.

It is currently unknown whether MeV equally induces TFF1 and 3 expression in the human respiratory tract and what impact disease history of measles patients may have on severity of secondary complications. Anecdotal cases of hemorrhagic pneumonia associated with measles have been reported<sup>40,41</sup>, but prior disease history of the patients was not documented. However, bacterial superinfection after measles such as laryngitis, bronchitis, and otitis media are common<sup>5</sup>. Typically attributed to impaired adaptive immunity due to lymphocytopenia, our ferret data support that respiratory disease history of measles patients should be considered as risk factor for advance to severe bacterial superinfections. Limitations affecting the predictive power of the CDV ferret model for human measles include different disease dynamics<sup>42</sup>, higher mortality rates of the attenuated recCDV N $\Delta$ 425-479, higher inherent neurotropism of CDV than MeV<sup>42</sup>, and untested cross-species consistency of pharmacokinetic and efficacy performance of GHP-88309.

This study establishes treatment paradigms for efficacious pharmacological intervention in morbillivirus disease, defines respiratory disease history as a correlate for the risk of severe bacterial superinfection, and provides precedent for therapeutic benefit of treatment

## Article

<https://doi.org/10.1038/s41467-024-45418-5>

of an acute RNA virus infection with direct-acting antivirals initiated after the window for mitigation of primary clinical signs has closed.

## Methods

### Study design

The objectives of this study were to determine the efficacy of GHP-88309 against morbillivirus disease in the CDV-ferret animal model and identify therapeutic windows for the successful treatment of a lethal morbillivirus infection. The CDV-ferret model was chosen because it provides a surrogate animal model of severe morbillivirus disease, including many of the hallmark symptoms and clinical signs of measles virus in humans. Female ferrets (*Mustela putorius furo*), family mustelids, genus *Mustela*, 6–10 months of age, were used for all experiments. Group sizes were three individual animals per conditions unless otherwise stated. The effect of treatment on virus replication and clinical signs in ferrets was determined using multiple therapeutic treatment regimens. Treatment was considered efficacious when statistically significant reductions in viremia and shed virus titers in PBMCs and nasal lavages, respectively, were observed and the duration and severity of clinical signs and immune suppression were decreased. Study endpoints were predefined prior to initiating experiments. At least two ferrets were used in all PK and tolerability studies. Groups of at least three ferrets were used in all in vivo efficacy studies. Before initiating experiments, animals were randomly assigned into groups. Exact numbers of independent biological repeats (individual animals) for each experiment are specified in the figures or figure legends. All quantitative source data are provided in the Source Data file.

### Cell lines and transfections

MDCK cells (American Type Culture Collection, CCL-34), Human carcinoma (HEp-2, American Type Culture Collection, CCL-23), and African green monkey kidney epithelial cells (American Type Culture Collection CCK-81) stably expressing canine signaling lymphocytic activation molecule (Vero-cSLAM<sup>43</sup>) were maintained at 37 °C and 5% CO<sub>2</sub> in Dulbecco's modified Eagle's medium (DMEM) supplemented with 7.5% fetal bovine serum (FBS). All immortalized cell lines used in this study were regularly tested for microbial contamination (6-month intervals).

### Viruses

recCDV-5804p, recCDV-5804p-Nectin-4-blind-eGFP, and recCDV-5804p-NA425-479 stocks were propagated on Vero-cSLAM and titrated by TCID<sub>50</sub> assay. recRSV-A2-L19 stocks were propagated on HEp-2 cells and titrated by TCID<sub>50</sub> assay. A/California/7/2009 (H1N1) and A/Wisconsin/67/2005 (H3N2) were propagated on MDCK cells for 2 to 3 days at 37 °C. Influenza viruses were titrated by TCID<sub>50</sub>-hemagglutination (TCID<sub>50</sub>-HA) assay on MDCK cells<sup>44</sup>.

### Viral Whole Genome Sequencing

For whole genome sequencing of recCDV-5804p-NA425-479 stocks and ferret nasal lavages or BALF following established methods<sup>42</sup>, genomic DNA was first depleted from the RNA extracts with Turbo DNase (Thermo #AMI907). First-strand cDNA synthesis was performed using SuperScript IV (Thermo) and random hexamers (Thermo) followed by second strand synthesis with Sequenase 2.0 kit (Thermo). Double-stranded cDNA was simultaneously fragmented and barcoded using Nextera chemistry (Nextera XT and Nextera Flex). The resulting libraries were pooled at equal concentrations, and average library size was determined using Agilent DNA D1000 Tape Station kit (Agilent). Pooled libraries were sequenced on a Nextseq 500 or Novaseq 6000. Reads were quality and adapter-trimmed with fastp<sup>45</sup>. The 3 leading bases, 3 trailing bases, and bases with mean phred < 20 in a 4-bp sliding window were cut from each read. Reads shorter than 45 bp and reads in which > 40% bases had phred < 15 were removed.

Consensus genomes for the recCDV-5804p-NA425-479 stocks were generated from the trimmed reads using REVICA (<https://github.com/greninger-lab/revica>) with the Canine distemper virus strain 5804 P (GenBank #AY386316.1) as the initial reference. The LAVA pipeline, available at [https://github.com/greninger-lab/lava/tree/Rava\\_Slippage-Patch](https://github.com/greninger-lab/lava/tree/Rava_Slippage-Patch), was used to interrogate allele frequency changes from the 425 input consensus genome<sup>42</sup>. Samples with < 10,000 mapped reads or < 95% coverage breadth were excluded from variant analysis. Interactive HTML plots highlighting viral allele frequencies relative to inoculum are included as (Supplementary Datasets 1 and 3). Sequence reads have been uploaded to the sequence read archive under a.

### Virus yield reduction

For virus yield-based dose–response assays, cells were infected (M.O.I. = 0.01 TCID<sub>50</sub> units per cell) in a 24-well plate format with recCDV-5804, recCDV-5804p-NA425-479, or drug resistant recombinants, in the presence of serial compound dilutions. Cell-associated progeny virus was harvested 48 h after infection. Viral titers were determined through TCID<sub>50</sub> titration. Four-parameter variable slope regression modeling was used to determine EC<sub>50</sub> and EC<sub>90</sub> concentrations.

### Pharmacokinetics studies in ferrets

Female ferrets (6 to 10 months of age) received from Triple F Farms were rested for 1 week, randomly assigned to study groups, and dosed orally with GHP-88309 dissolved in 1% methylcellulose. Blood was collected from the anterior vena cava and tissue sampling at the specified time points. Two to three animals per group were sampled for PK analyses. Plasma was separated from blood in microvette CB300 EDTA tubes (2000 × g; 5 min; 4 °C) (Sarstedt Inc) and tissue samples were snap frozen and stored at –80 °C prior to analysis by LC-MS/MS. The calibration curve range was 10–100,000 ng ml<sup>-1</sup> in blank plasma for single-dose PK and 10 ng/ml to 50,000 ng/ml for all other studies. Quality control samples of 30, 300, 7500, and 50,000 ng/ml of blank plasma were run before and after the single-dose PK samples and quality control samples of 30, 750, and 5000 ng/ml were run before and after all other plasma samples. The calibration curve range was 1.00–2000 ng/ml of tissue lysate for blank tissues. Quality control samples of 3, 30, and 600 ng/ml of tissue lysate in blank tissues were analyzed at the beginning of each sample set. Calibration in each matrix showed linearity with R<sup>2</sup> values of > 0.99.

### RSV and IAV infections of ferrets

Female ferrets were purchased from Triple F Farms and housed in an ABSL-2 facility. Prior to study start, ferrets were rested for 1 week, then randomly assigned to study groups. Animals infected with RSV-A2-L19 were in a separate ABSL2 room from influenza infected ferrets. For influenza virus and RSV infections, ferrets were anesthetized using dexmedetomidine/ketamine. Anesthetized ferrets were inoculated intranasally with 1 × 10<sup>5</sup> TCID<sub>50</sub> units of IAV-A/CA/07/2009 (H1N1) or 1 × 10<sup>6</sup> TCID<sub>50</sub> units of RSV-A2-L19 in a volume of 300 μl per nare. Clinical signs (bodyweight and temperature) were monitored once daily. Nasal lavages were performed once daily using 1 ml of PBS containing 2× antibiotics-antimycotics (Gibco). Treatment with 4'-FIU through oral gavage was administered using a once daily (q.d.) regimen.

### CDV infections of ferrets

Female ferrets were received from Triple F Farms and housed in an ABSL-2 facility. Ferrets were rested for one week prior to the start of each study and randomly assigned into groups. Influenza vaccinations (quadrivalent, Flucelvax; Seqirus, Inc.) were administered at specified time points prior to CDV infection. Prior to infection, ferrets were anesthetized with dexmedetomidine/ketamine, and infected intranasally with 2 × 10<sup>5</sup> TCID<sub>50</sub> of recCDV-5804p, recCDV-5804p-Nectin-4-



## Article

<https://doi.org/10.1038/s41467-024-45418-5>

blind-eGFP or recCDV-5804p-NA425-479 in 200  $\mu$ l (100  $\mu$ l per nare). Twice daily treatment with GHP-88309 was initiated at specified times after infection (3, 5, 7, 10, or 24 days after infection). GHP-88309 was administered by oral gavage in 3.5 ml 1% methylcellulose and flushed with 3.5 ml high-calorie liquid dietary supplement. Control groups were administered equivalent volumes of 1% methylcellulose. Body weight and temperature were monitored daily. Additional monitoring for clinical signs and any potential adverse effects was performed daily. Blood was harvested at specified time points. To assess viremia, PBMCs were isolated from blood by Ficoll gradient centrifugation. Viremia titers were determined by coculturing serial dilutions of purified PBMCs with Vero-cSLAM cells and expressed as TCID<sub>50</sub> per 10<sup>6</sup> PBMCs. Complete blood count (CBC) analyses were performed using a VetScan HM5 (Abaxis) in accordance with the manufacturer's protocol. Shed viral loads were determined from nasal lavages and titrated by TCID<sub>50</sub>. For studies involving influenza challenges, surviving CDV-infected ferrets were anesthetized with dexmedetomidine/ketamine, and infected intranasally with  $1 \times 10^5$  [recIAV-A/California/07/2009 (H1N1)] or  $2 \times 10^5$  TCID<sub>50</sub>HA [A/Wisconsin/67/2005 (H3N2)] in 200  $\mu$ l (100  $\mu$ l per nare). Animals were monitored once daily for clinical signs, including loss of bodyweight and fever. Upper respiratory virus load was measured from nasal lavages performed once daily for up to 7 days post influenza infection. Rash was scored using a scale of 0-2 (0, no rash; 1, mild and localized rash; 2, severe and widespread rash). Diarrhea was scored using a scale of 0-2 (0, normal stool; 1, soft stool; 2, runny stool and/or rectal inflammation). Conjunctivitis was scored using a scale of 0-2 (0, clear eyes; 1, puffiness or mild swelling in at least one eye; 2, presence of puss in both eyes or unable to open eyes without cleaning).

**Systemic interferon and cytokine profiling**

The relative expression of interferon, cytokines, and interferon-stimulated genes (ISGs) was determined by real-time PCR analysis. RNA was isolated from purified PBMCs that were harvested at different time points after infection. Complementary DNA was synthesized by reverse transcription using SuperScript III (Invitrogen) using oligo-dT primers in accordance with the manufacturer's protocol. Real-time PCR was performed using Fast SYBR Green Master Mix (Applied Biosystems) on a QuantStudio 3 real-time PCR system (Applied Biosystems). Values were normalized to glyceraldehyde-3-phosphate dehydrogenase mRNA, analyzed by the comparative threshold cycle ( $\Delta\Delta C_T$ ) method and expressed relative to mock-infected animals. Sequences of primers are shown in Supplementary Table S3.

**Determination of neutralizing antibody titers**

Plasma was heat inactivated and serially diluted (twofold steps) in serum-free DMEM, mixed with 100 TCID<sub>50</sub> units of recCDV-5804p, recIAV-A/California/07/2009 (H1N1), or VSV-RABV-G and incubated for 1 h at 37 °C. Mixtures were transferred to cell monolayers and virus neutralization was measured after 3 d by visualization of syncytia, hemagglutination assay, or GFP-positive infected cells for recCDV-5804p, recIAV-A/California/07/2009 (H1N1), and VSV-RABV-G, respectively. Equal amounts of virus in FBS, DMEM containing 7.5% FBS, and serum-free DMEM served as controls. Each blood sample was tested in two technical repeats.

**Quantitation of CDV N protein-encoding RNA in PBMCs**

CDV N protein-encoding RNA was detected using the a primer-probe set *cdv\_n\_taq\_fw*, *cdv\_n\_taq\_rev*, and *cdv\_n\_probe*. RT-qPCR reactions were performed using a QuantStudio 3 real-time PCR system and the QuantStudio Design and Analysis package (version 1.5.2). The CDV N primer-probe set was used with Taqman Fast Virus 1-step master mix (Thermo Fisher Scientific) to detect viral RNA. To calculate RNA copy numbers, a standard curve was created using a linearized pTMI-CDV N

plasmid of known concentration as template. Samples were normalized to the numbers of input PBMCs.

**Ferret MRI**

All ferrets were imaged on a high-resolution 7 T Bruker (70/20) Biospec MRI scanner at Georgia State University using the ParaVision software package (Bruker, Billerica, MA, version 360.3.4). Animals were anesthetized using a combination of dexmethasone and isoflurane. Respiration rates and body temperature were continuously monitored and maintained using a small-animal physiological monitoring system (SA Instruments Inc, Stony Brook, NY and Kent Scientific, Somnosit Systems, Torrington, CT). Anesthesia was adjusted to maintain a respiration rate of 40-60 breaths per minute. A 112/86 mm circularly polarized transmitter/receiver coil was employed for in-vivo imaging. Following the localizer scan to position the animal in the center of the magnet, two types of MR protocols were used to capture the lungs in coronal and axial orientations. To overcome the limitations imposed by short T<sub>2</sub>\* of lungs and to reduce motion, a 3D Ultra short echo time (3D UTE) was used to acquire high-quality images with the following parameters: MR acquisition parameters include: 4.3  $\mu$ s RF block pulse; flip angle ( $\alpha$ ) = 3.9°; 51,360 radial projections; 128 points on free induction decay (FID); field-of-view (FOV) = 58 × 54 × 67 (mm<sup>3</sup>); image matrix size = 128 × 128 × 128 (voxels<sup>3</sup>); receiver bandwidth (BW) = 200 kHz; TE = 0.06 (ms); repetition time (TR) = 4.206 (ms) and 2 signal averages. The total acquisition time for an individual ferret UTE scan was ~7 minutes. An additional 2D T1 IG FLASH (intra-gate fast low angle shot) self-gated MRI was used to collect images along coronal direction with the following parameters: TR/TE = 400/3 msec, flip angle = 30°, oversampling = 10, 30 slices, matrix size 140 × 128, FOV = 70 mm × 64 mm. The total acquisition time was 8 min. The images were converted into DICOM/Nifti formats using Bruker PV-360 software and reconstructed and processed using ImageJ (version 2.9.0) and ITK-SNAP (version 3.6.2-alpha).

**Histopathology**

Pathology scoring was performed according to the following scale: for alveoli, bronchiolitis, and pleuritis scores, scoring was based upon distribution: 0 = no lesions, 1 = focal, 2 = multifocal, 3 = multifocal to coalescing, 4 = diffuse; for perivascular cuffing (PVC) score: 1 = 1 layer of leukocytes surrounding most affected vessel, 2 = 2-5 layers, 3 = 6-10 layers, 4 = more than 10 layers; for vasculitis score: 1 = infiltration of vessel wall by leukocytes, 2 = infiltration and separation of smooth muscle cells by edema, 3 = same changes as 2 with fibrinoid change, 4 = effacement of the vessel wall; for interstitial pneumonia score: 1 = infiltration of alveolar septa by 1 leukocyte layer thickness, 2 = expansion by 2 leukocyte thickness, 3 = 3 leukocytes thick, 4 = 4 leukocytes thick or more. The sum of individual scores represents a total histopathology score, generated for each animal.

**RNAseq**

Total RNA was treated with Turbo DNase (ThermoFisher) and used as input for the Illumina Stranded Total RNA (Ribo-Zero Plus Microbiome) library preparation kit using the manufacturer's specifications, then sequenced on an Illumina NovaSeq 6000 to obtain approximately 25 million paired end 150 bp reads. Raw reads were quality- and adapter-trimmed with Trimmomatic v0.39<sup>46</sup>. Metagenomic analysis of trimmed read pairs was performed using the CZID pipeline<sup>47-49</sup> and host and CDV-specific proportions determined. Trimmed read pairs were pseudoaligned to the draft ferret transcriptome MusPutFur1.0, INSDC Assembly GCA.000215625.1<sup>50</sup> using Kallisto v0.46<sup>51</sup> and transcripts aggregated by gene. Genes with an average raw expression level less than 1 raw count per sample were filtered prior to analysis. Differential expression between groups of CDV-infected and flu-pretreated CDV-infected ferret samples collected during survival BAL procedures was calculated with the Wald test in DESeq<sup>52</sup>, with an

## Article

<https://doi.org/10.1038/s41467-024-45418-5>

adjusted p value significance threshold of 0.01. All analyses were performed using R v4.2.1. Raw sequence reads used for RNAseq analysis have been uploaded to the sequence read archive, BioProject PRJNA1004336.

**Inclusion and ethics statement**

All animal work was performed in compliance with the Guide for the Care and Use of Laboratory Animals of the National Institutes of Health and the Animal Welfare Act Code of Federal Regulations. Experiments involving ferrets were approved by the Georgia State University IACUC under protocols A22035 and A18035. All ferret studies were carried out with female animals only and no sex-based analyses have been performed for the following reason: per IACUC protocol, co-housing studies may not be carried out with male ferrets, since males are territorial and combative when co-housed, resulting in severe injury or death from fight wounds that would require termination of the study. Vivarium capacity for long-term housing of large animals in ABSL-2 containment does not permit the use of singly-housed male ferrets. All experiments using infectious CDV, RSV IAV, and VSV-deltaG were approved by the Georgia State Institutional Biosafety Committee under protocol B21029 and performed in BSL-2/ABSL-2 facilities at Georgia State University.

**Statistics and reproducibility**

One-way or two-way analysis of variance (ANOVA) with Dunnett's or Sidak's multiple comparison post-hoc tests, was used to assess statistical differences. All statistical analyses were carried out in GraphPad Prism software (Version 9.3.1). Specific statistical tests applied to individual data sets are specified in the corresponding figure legends. The number of individual biological replicates for all graphical representations are shown in the figures. Representations of mean  $\pm$  SD or median  $\pm$  95% CI of experimental uncertainty are shown and specified in the figure legends. Fourteen-day tolerability studies were based on two ferrets. All statistical analyses and exact P-values are shown in the Supplementary Dataset S4. Alpha levels were set to 0.05 for all significance analyses.

**Reporting summary**

Further information on research design is available in the Nature Portfolio Reporting Summary linked to this article.

**Data availability**

The amplicon tiling sequencing reads generated in this study have been deposited in the NCBI BioProject database under accession code PRJNA1004336. All other data generated in this study are provided in the Supplementary Information, Supplementary Datasets S1–S4, and the Source Data file. Quantitative source data have been deposited in Figshare (<https://doi.org/10.6084/m9.figshare.24076626>). Source data are provided with this paper.

**Code availability**

Sequencing reads were analyzed using the TAYLOR pipeline, available at [https://github.com/greninger-lab/covid\\_swift\\_pipeline](https://github.com/greninger-lab/covid_swift_pipeline) (<https://doi.org/10.5281/zenodo.6142073>). All commercial computer codes and algorithms used are specified in Methods.

**References**

1. Guha-Sapir, D., Moitinho de Almeida, M., Keita, M., Greenough, G. & Bendavid, E. COVID-19 policies: Remember measles. *Science* **369**, 261 (2020).
2. Laurie, K. L. & Rockman, S. Which influenza viruses will emerge following the SARS-CoV-2 pandemic? *Influenza Other Respir. Viruses* **15**, 573–576 (2021).
3. Petrova, V. N. et al. Incomplete genetic reconstitution of B cell pools contributes to prolonged immunosuppression after measles. *Sci. Immunol.* **4**, eaay6125 (2019).
4. Mina, M. J. et al. Measles virus infection diminishes preexisting antibodies that offer protection from other pathogens. *Science* **366**, 599–606 (2019).
5. Plemper, R. K. & Lamb, R. A. in *Fields Virology* Vol. 1 (eds D. M. Knipe, P. M. Howley, & S. Whelan) Ch. 33, 504–558 (Wolters Kluwer/Lippincott Williams & Wilkins, 2020).
6. Laksono, B. M., de Vries, R. D., McQuaid, S., Duprex, W. P. & de Swart, R. L. Measles Virus-Host Invasion and Pathogenesis. *Viruses* **8**, 210 (2016).
7. Mina, M. J., Metcalf, C. J., de Swart, R. L., Osterhaus, A. D. & Grenfell, B. T. Long-term measles-induced immunomodulation increases overall childhood infectious disease mortality. *Science* **348**, 694–699 (2015).
8. Plemper, R. K. Measles resurgence and drug development. *Curr. Opin. Virol.* **41**, 8–17 (2020).
9. Moss, W. J. & Griffin, D. E. Measles. *Lancet* **379**, 153–164 (2012).
10. Centers for Disease Control and Prevention. Global Measles Outbreaks. <https://www.cdc.gov/globalhealth/measles/data/global-measles-outbreaks.html> (last accessed 07/10/2023). (2023).
11. Krumm, S. A. et al. An orally available, small-molecule polymerase inhibitor shows efficacy against a lethal morbillivirus infection in a large animal model. *Sci. Transl. Med.* **6**, 232ra252 (2014).
12. Cox, R. M. et al. Orally efficacious broad-spectrum allosteric inhibitor of paramyxovirus polymerase. *Nat. Microbiol.* **5**, 1232–1246 (2020).
13. von Messling, V., Milosevic, D. & Cattaneo, R. Tropism illuminated: lymphocyte-based pathways blazed by lethal morbillivirus through the host immune system. *Proc. Natl. Acad. Sci. USA.* **101**, 14216–14221 (2004).
14. Thakkar, V. D. et al. The Unstructured Paramyxovirus Nucleocapsid Protein Tail Domain Modulates Viral Pathogenesis through Regulation of Transcriptase Activity. *J. Virol.* **92**, e02064–17 (2018).
15. Nelson, A. N. et al. Association of persistent wild-type measles virus RNA with long-term humoral immunity in rhesus macaques. *JCI Insight* **5**, e134992 (2020).
16. Schulman, J. L. & Kilbourne, E. D. Induction of Partial Specific Heterotypic Immunity in Mice by a Single Infection with Influenza A Virus. *J. Bacteriol.* **89**, 170–174 (1965).
17. Gooch, K. E. et al. Heterosubtypic cross-protection correlates with cross-reactive interferon-gamma-secreting lymphocytes in the ferret model of influenza. *Sci Rep* **9**, 2617 (2019).
18. Bodewes, R. et al. Infection of the upper respiratory tract with seasonal influenza A(H3N2) virus induces protective immunity in ferrets against infection with A(H1N1)pdm09 virus after intranasal, but not intratracheal, inoculation. *J. Virol.* **87**, 4293–4301 (2013).
19. Sridhar, S. et al. Cellular immune correlates of protection against symptomatic pandemic influenza. *Nat. Med.* **19**, 1305–1312 (2013).
20. Wilkinson, T. M. et al. Preexisting influenza-specific CD4+ T cells correlate with disease protection against influenza challenge in humans. *Nat. Med.* **18**, 274–280 (2012).
21. Hayward, A. C. et al. Natural T Cell-mediated Protection against Seasonal and Pandemic Influenza. Results of the Flu Watch Cohort Study. *Am. J. Respir. Crit. Care Med.* **191**, 1422–1431 (2015).
22. Krammer, F. The human antibody response to influenza A virus infection and vaccination. *Nat. Rev. Immunol.* **19**, 383–397 (2019).
23. Sourimant, J. et al. 4'-Fluorouridine is an oral antiviral that blocks respiratory syncytial virus and SARS-CoV-2 replication. *Science* **375**, 161–167 (2022).
24. Yan, D. et al. Cross-resistance mechanism of respiratory syncytial virus against structurally diverse entry inhibitors. *Proc. Natl. Acad. Sci. USA.* **111**, E3441–E3449 (2014).
25. Lieber, C. M. et al. 4'-Fluorouridine mitigates lethal infection with pandemic human and highly pathogenic avian influenza viruses. *PLoS Pathog* **19**, e1011342 (2023).

## Article

<https://doi.org/10.1038/s41467-024-45418-5>

26. Aihara, E., Engevik, K. A. & Montrose, M. H. Trefoil Factor Peptides and Gastrointestinal Function. *Annu. Rev. Physiol.* **79**, 357–380 (2017).
27. Rossi, H. L. et al. Trefoil Factor Family: A Troika for Lung Repair and Regeneration. *Am. J. Respir. Cell Mol. Biol.* **66**, 252–259 (2022).
28. Miyahara, N. et al. Expression of Trefoil factor family peptides in the nasal allergic mucosa. *Rhinology* **50**, 408–416 (2012).
29. Peart Akindele, N. A. et al. Effect of remdesivir post-exposure prophylaxis and treatment on pathogenesis of measles in rhesus macaques. *Sci. Rep.* **13**, 6463 (2023).
30. Eastman, R. T. et al. Remdesivir: A Review of Its Discovery and Development Leading to Emergency Use Authorization for Treatment of COVID-19. *ACS Cent. Sci.* **6**, 672–683 (2020).
31. Wittwer, K. et al. Small-molecule polymerase inhibitor protects non-human primates from measles and reduces shedding. *Nat. Commun.* **12**, 5233 (2021).
32. Roquilly, A. et al. Local Modulation of Antigen-Presenting Cell Development after Resolution of Pneumonia Induces Long-Term Susceptibility to Secondary Infections. *Immunity* **47**, 135–147.e135 (2017).
33. Kumar, V. Pulmonary Innate Immune Response Determines the Outcome of Inflammation During Pneumonia and Sepsis-Associated Acute Lung Injury. *Front. Immunol.* **11**, 1722 (2020).
34. Madsen, J., Nielsen, O., Tornøe, I., Thim, L. & Holmskov, U. Tissue localization of human trefoil factors 1, 2, and 3. *J. Histochem. Cytochem.* **55**, 505–513 (2007).
35. Lee, S. H. et al. Expression of mRNA of trefoil factor peptides in human nasal mucosa. *Acta. Otolaryngol.* **121**, 849–853 (2001).
36. dos Santos Silva, E., Ulrich, M., Doring, G., Botzenhart, K. & Gott, P. Trefoil factor family domain peptides in the human respiratory tract. *J. Pathol.* **190**, 133–142 (2000).
37. Jarva, M. A. et al. Trefoil factors share a lectin activity that defines their role in mucus. *Nat. Commun.* **11**, 2265 (2020).
38. Roy, M. G. et al. Muc5b is required for airway defence. *Nature* **505**, 412–416 (2014).
39. Vaughan, A. E. et al. Lineage-negative progenitors mobilize to regenerate lung epithelium after major injury. *Nature* **517**, 621–625 (2015).
40. Roett, R. O. A Case of Hemorrhagic Measles. *J. Natl. Med. Assoc.* **10**, 71–73 (1918).
41. Children’s Hospital of Philadelphia. News and Views: Measles — the Virus, the Disease, the Vaccine. <https://www.chop.edu/news/news-and-views-measles-virus-disease-vaccine> (last accessed 07/10/2023). (2019).
42. Laksono, B. M., de Vries, R. D., Duprex, W. P. & de Swart, R. L. Measles pathogenesis, immune suppression and animal models. *Curr. Opin. Virol.* **41**, 31–37 (2020).
43. Seki, F., Ono, N., Yamaguchi, R. & Yanagi, Y. Efficient isolation of wild strains of canine distemper virus in Vero cells expressing canine SLAM (CD150) and their adaptability to marmoset B95a cells. *J. Virol.* **77**, 9943–9950 (2003).
44. Toots, M. et al. Characterization of orally efficacious influenza drug with high resistance barrier in ferrets and human airway epithelia. *Sci. Transl. Med.* **11**, eaax5866 (2019).
45. Chen, S., Zhou, Y., Chen, Y. & Gu, J. fastp: an ultra-fast all-in-one FASTQ preprocessor. *Bioinformatics* **34**, i884–i890 (2018).
46. Bolger, A. M., Lohse, M. & Usadel, B. Trimmomatic: a flexible trimmer for Illumina sequence data. *Bioinformatics* **30**, 2114–2120 (2014).
47. Kalantar, K. L. et al. IDseq-An open source cloud-based pipeline and analysis service for metagenomic pathogen detection and monitoring. *Gigascience* **9**, giaa111 (2020).
48. Saha, S. et al. Unbiased Metagenomic Sequencing for Pediatric Meningitis in Bangladesh Reveals Neuroinvasive Chikungunya Virus Outbreak and Other Unrealized Pathogens. *mBio* **10**, e02877–19 (2019).
49. Ramesh, A. et al. Metagenomic next-generation sequencing of samples from pediatric febrile illness in Tororo, Uganda. *PLoS One* **14**, e0218318 (2019).
50. Peng, X. et al. The draft genome sequence of the ferret (*Mustela putorius furo*) facilitates study of human respiratory disease. *Nat. Biotechnol.* **32**, 1250–1255 (2014).
51. Bray, N. L., Pimentel, H., Melsted, P. & Pachter, L. Near-optimal probabilistic RNA-seq quantification. *Nat. Biotechnol.* **34**, 525–527 (2016).
52. Love, M. I., Huber, W. & Anders, S. Moderated estimation of fold change and dispersion for RNA-seq data with DESeq2. *Genome Biol.* **15**, 550 (2014).

**Acknowledgements**

We thank the Georgia State University Department of Animal Resources, the Georgia State University Advanced Translational Imaging Facility (ATIF), and the University of Georgia Pathogenesis Core for expert assistance. The VSV-ΔG and recCDV-5804p genomic plasmids and Vero-canine SLAM cells were kind gifts of M.J. Schnell, V. von Messling, and Y. Yanagi, respectively. This study was supported, in part, by public health service grants AI071002 (to R.K.P.) and AI171403 project 3 (to R.K.P.) and AI171403 Scientific Core D (to A.L.G.) from the NIH/NIHAIID.

**Author contributions**

R.K.P. and R.M.C. conceived and designed the experiments. R.M.C., J.D.W., C.M.L., H.-J.K., J.-J.Y., and R.K.P. conducted most of the experiments. R.M.C. created all figure schematics. A.L.G., N.A.L., and E.B.S. performed next-generation sequencing. Z.M.S., M.K.A., R.E.K., and A.A.K. performed mass spectrometry analysis. K.H. performed MRI imaging. K.S. performed a histopathology analysis. M.G., M.G.N., A.T.G., and R.L.d.S. provided critical materials. R.M.C., J.D.W., C.M.L., N.A.L., A.L.G., and R.K.P. analyzed the data. R.K.P. and R.M.C. wrote the manuscript.

**Competing interests**

R.K.P. and R.M.C. are co-inventors on a patent filing covering method of use of GHP-88309 for antiviral therapy. This study could affect their personal financial status. R.K.P. reports contract testing from Enanta Pharmaceuticals and Atea Pharmaceuticals, and research support from Gilead Sciences, outside of the described work. R.M.C. reports consulting for Merck & Co., outside of the described work. A.L.G. reports contract testing from Abbott, Cepheid, Novavax, Pfizer, Janssen and Hologic and research support from Gilead Sciences, outside of the described work. R.L.d.S. reports research support from Gilead Sciences and Themis Biosciences, outside of the described work. All other authors declare that they have no competing interests to report.

**Additional information**

**Supplementary information** The online version contains supplementary material available at <https://doi.org/10.1038/s41467-024-45418-5>.

**Correspondence** and requests for materials should be addressed to Richard K. Plemper.

**Peer review information** *Nature Communications* thanks the anonymous reviewers for their contribution to the peer review of this work. A peer review file is available.

**Reprints and permissions information** is available at <http://www.nature.com/reprints>

**Publisher’s note** Springer Nature remains neutral with regard to jurisdictional claims in published maps and institutional affiliations.



**Article**<https://doi.org/10.1038/s41467-024-45418-5>

**Open Access** This article is licensed under a Creative Commons Attribution 4.0 International License, which permits use, sharing, adaptation, distribution and reproduction in any medium or format, as long as you give appropriate credit to the original author(s) and the source, provide a link to the Creative Commons license, and indicate if changes were made. The images or other third party material in this article are included in the article's Creative Commons license, unless indicated otherwise in a credit line to the material. If material is not included in the article's Creative Commons license and your intended use is not permitted by statutory regulation or exceeds the permitted use, you will need to obtain permission directly from the copyright holder. To view a copy of this license, visit <http://creativecommons.org/licenses/by/4.0/>.

© The Author(s) 2024

---

<sup>1</sup>Center for Translational Antiviral Research, Georgia State University Institute for Biomedical Sciences, Atlanta, GA 30303, USA. <sup>2</sup>Virology Division, Department of Laboratory Medicine, University of Washington, Seattle, WA 98195, USA. <sup>3</sup>Emory Institute for Drug Development, Emory University, Atlanta, GA 30322, USA. <sup>4</sup>Department of Viroscience, Erasmus MC, Rotterdam, Netherlands. <sup>5</sup>Advanced Translational Imaging Facility, Georgia State University, Atlanta, GA 30303, USA. <sup>6</sup>Department of Pathology, College of Veterinary Medicine, University of Georgia, Athens, GA 30602, USA.  
✉ e-mail: [rplemper@gsu.edu](mailto:rplemper@gsu.edu)

## 2.2.2 Small-molecule Polymerase Inhibitor Protects Non-Human Primates from Measles and Reduces Shedding



ARTICLE

<https://doi.org/10.1038/s41467-021-25497-4>

OPEN

# Small-molecule polymerase inhibitor protects non-human primates from measles and reduces shedding

Kevin Wittwer<sup>1</sup>, Danielle E. Anderson<sup>2</sup>, Kristin Pfeiffermann<sup>1</sup>, Robert M. Cox<sup>1b</sup><sup>3</sup>, Josef D. Wolf<sup>3</sup>, Sabine Santibanez<sup>4</sup>, Annette Mankertz<sup>4</sup>, Roland Plesker<sup>1</sup>, Zachary M. Sticher<sup>1b</sup><sup>5</sup>, Alexander A. Kolkykhalov<sup>5</sup>, Michael G. Natchus<sup>5</sup>, Christian K. Pfaller<sup>1b</sup><sup>✉</sup>, Richard K. Plemper<sup>1b</sup><sup>3✉</sup> & Veronika von Messling<sup>1,6</sup>

Measles virus (MeV) is a highly contagious pathogen that enters the human host via the respiratory route. Besides acute pathologies including fever, cough and the characteristic measles rash, the infection of lymphocytes leads to substantial immunosuppression that can exacerbate the outcome of infections with additional pathogens. Despite the availability of effective vaccine prophylaxis, measles outbreaks continue to occur worldwide. We demonstrate that prophylactic and post-exposure therapeutic treatment with an orally bioavailable small-molecule polymerase inhibitor, ERDRP-0519, prevents measles disease in squirrel monkeys (*Saimiri sciureus*). Treatment initiation at the onset of clinical signs reduced virus shedding, which may support outbreak control. Results show that this clinical candidate has the potential to alleviate clinical measles and augment measles virus eradication.

<sup>1</sup>Veterinary Medicine Division, Paul-Ehrlich-Institute, Langen, Germany. <sup>2</sup>Programme in Emerging Infectious Diseases, Duke-NUS Medical School, Singapore, Singapore. <sup>3</sup>Institute for Biomedical Sciences, Georgia State University, Atlanta, GA, USA. <sup>4</sup>WHO European Regional Reference Laboratory for Measles and Rubella, Robert Koch-Institute, Berlin, Germany. <sup>5</sup>Emory Institute for Drug Development, Emory University, Atlanta, GA, USA. <sup>6</sup>Life Sciences Unit, Federal Ministry of Education and Research, Berlin, Germany. ✉email: [Christian.Pfaller@pei.de](mailto:Christian.Pfaller@pei.de); [rplemper@gsu.edu](mailto:rplemper@gsu.edu)

## ARTICLE

NATURE COMMUNICATIONS | <https://doi.org/10.1038/s41467-021-25497-4>

**M**easles virus (MeV) invades the body via the respiratory route and infects immune cells in the upper respiratory tract through the signaling lymphocytic activation molecule receptor SLAMF7/CD150. During an incubation period of ~10–14 days, infected cells home to mediastinal lymph nodes, where the virus infects resident SLAMF7<sup>+</sup>T- and B-cells<sup>1,2</sup>. This event results in peripheral blood mononuclear cell (PBMC)-associated viremia and is followed by viral spread to epithelial cells, which coincides with the onset of clinical signs including fever, conjunctivitis, and the measles-typical rash<sup>2</sup>. While many patients fully recover, mortality increases substantially in the presence of pre-existing conditions or malnutrition<sup>3</sup>, which led to over 200,000 measles virus-related deaths in 2019<sup>4</sup>. Prolonged immunosuppression in the aftermath of measles impairs memory responses to non-related infectious diseases<sup>5</sup>, compromising the health prospect of recoverees. Humans are the sole MeV reservoir and infection or vaccination usually result in long-lasting immunity, making the virus a candidate for eradication<sup>6</sup>. Despite major concerted efforts for two decades, a recent evaluation of global measles eradication concluded that the anticipated progress has not been made and previous gains on vaccine coverage were lost<sup>4,7</sup>. Past achievements are further challenged by the SARS-CoV-2 pandemic, which led to suspension of vaccination programs in developing countries, leaving 78 million children susceptible to measles<sup>8</sup>. Due to the exceptionally high contagiousness of MeV ( $R_0 = 13.7\text{--}18$ )<sup>9</sup>, measles is typically among the first diseases to reemerge when vaccination coverage drops in an area<sup>10</sup>. Since 2017, and thus before COVID-19, lapsed vaccination coverage has resulted in measles reappearing in geographic regions that had previously been declared measles-free. These challenges create an urgent need for the development of effective pharmacological countermeasures that can consolidate progress towards global measles control and support vaccination-based eradication efforts<sup>11</sup>.

Previous studies have established high in vitro efficacy of the small-molecule viral polymerase inhibitor ERDRP-0519 (Fig. 1a) against MeV and related pathogens of the *Morbillivirus* genus, such as canine distemper virus (CDV)<sup>12–14</sup>. In vivo proof-of-concept efficacy was established in a lethal CDV-ferret surrogate model of human measles, demonstrating unprecedented complete survival of all treated animals and nearly complete suppression of clinical signs after post-exposure therapeutic dosing<sup>15</sup>. To assess the clinical potential of the compound, we evaluated in this study the oral efficacy against a clinical MeV isolate in non-human primates, which develop human measles-like disease.

## Results

**Efficacy of ERDRP-0519 against MeV at concentrations achieved in vivo.** A single-dose pharmacokinetic (PK) study was performed in squirrel monkeys by oral (intra-gastric) delivery of 50 mg ERDRP-0519/kg bodyweight and blood sampling at seven predefined time points after dosing (Fig. 1b). Serum concentrations peaked ~2 h post-administration ( $C_{max} = 3.27 \mu\text{M}$ ), which exceeded the in vitro  $EC_{50}$  values (0.07–0.3  $\mu\text{M}$ , depending on the MeV-strain<sup>13</sup>) by 10- to more than 40-fold. Based on this PK profile, we recapitulated a once daily (*q.d.*) and twice daily (*b.i.d.*) treatment regimen ex vivo in human PBMCs infected with reference MeV strain MV/New Jersey,USA/94/1 (genotype D6) over a 48-h period, initially assuming no significant drug accumulation (Fig. 1c, d, Supplementary methods section, and Supplementary Table 3). Resulting progeny MeV titers were significantly ( $p < 0.0001$ ) lower than in untreated controls (Fig. 1e). The *b.i.d.* dosing regimen furthermore showed significantly ( $p = 0.0002$ ) higher potency than *q.d.* administration. Continuous exposure of MeV-infected hPBMCs to a

conservatively estimated 1.5  $\mu\text{M}$  ERDRP-0519 was nearly sterilizing, resulting in a greater than three orders of magnitude reduction in progeny virus titer (Fig. 1e). Informed by the ex vivo recapitulation of the antiviral effect of drug levels achievable after 50 mg/kg oral ERDRP-0519, we selected this dose level, given in a *b.i.d.* regimen, for the efficacy study.

**Clinical signs of measles virus infection in non-human primates are reduced under ERDRP-0519 treatment.** To assess antiviral efficacy in vivo, squirrel monkeys were infected intranasally with  $10^6$  TCID<sub>50</sub> of the MeV field isolate MV/FrankfurtMain.DEU/17.11 (genotype D8), which has recently been highly prevalent in Europe<sup>15</sup> and responsible for major measles outbreaks. A total of six animals per group were either left untreated, treated with ERDRP-0519 12 h prior to infection (prophylactic group), or treated 3 or 7 days after virus challenge (therapeutic groups), representing the onset of viremia and the appearance of first clinical signs, respectively (Fig. 2a). In all cases, treatment was continued for 14 days *b.i.d.* Untreated animals developed characteristic measles rash with inflammation around the mouth, nose and ears, and half of the monkeys in this control group presented a generalized rash (Fig. 2b, c, right panel). Prophylactically treated animals remained free of measles-typical clinical signs throughout the study (Fig. 2b, c, left panel). Four of six animals in the day 3 therapeutic group and all animals of the day 7 therapeutic group developed spots or mild rash in the face or inguinal region (Fig. 2b). However, none of the treated animals experienced severe or generalized rash, indicating a treatment benefit even when drug is administered late, at the time of onset of clinical signs.

**ERDRP-0519 treatment results in reduced viral replication and immunosuppression but efficient humoral response.** Assessment of trough serum concentration during multi-dose *b.i.d.* administration of ERDRP-0519 in 15 animals confirmed that repeat-dosing does not result in ERDRP-0519 accumulation (Fig. 3a). Mean drug plasma concentration of all animals over the full study period was ~1.6  $\mu\text{M}$ , and mean trough concentrations at individual time points exceeded the conservatively estimated 1.5  $\mu\text{M}$  in a 12-day window after treatment start used for ex vivo hPBMC recapitulation experiments (Fig. 1e). Rash coincided with increases in body temperature in some of the animals but mean temperatures in the distinct groups remained within the pre-infection range of less than 40 °C (Fig. 3b). Body weight changes remained negligible in all animals throughout the study. One animal in the day 3 therapeutic group developed mild diarrhea and deceased on day 15 post-infection (illustrated in parenthesis). Viremia titers and throat swab titers in this monkey were in the lower range of animals in the group and leukocyte numbers were in the normal range. Drug serum concentrations of this animal were in the peak group of all treated animals (Fig. 1a), but none of the other monkeys with similar drug serum concentrations showed adverse effects. Nevertheless, to rule out toxic effects of the administered compound, we performed histological analysis of the liver of the deceased animal and found no pathological alternations when compared to an untreated control animal (Supplementary Fig. 1a–d). Furthermore, we examined the gut histologically since a potential, underlying parasitic infections may have worsened under stress of the study procedure. No multicellular parasites were found in the lumen of the deceased animal and no infiltration of eosinophilic granulocytes was detected, indicating absence of a parasitic infection (Supplementary Fig. 1e–h). We concluded that the isolated death was due to causes unrelated to ERDRP-0519 administration and/or MeV infection and continued the study unchanged.

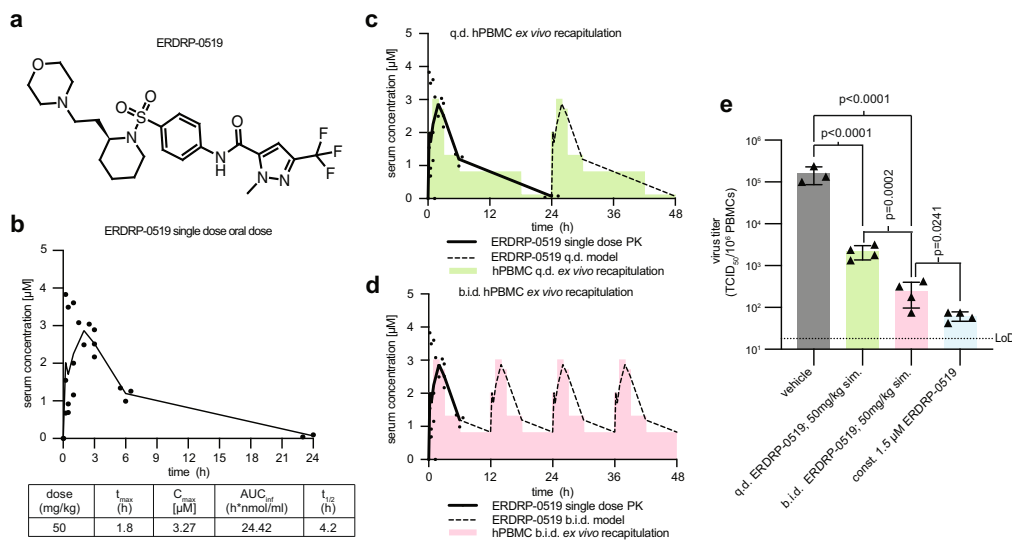


**Fig. 1** Single-dose oral pharmacokinetic study of ERDRP-0519 in squirrel monkeys. **a, b** ERDRP-0519 (**a**) was administered intragastrically at 50 mg/kg bodyweight in a poly(ethylene glycol)-200 formulation at a concentration of 10 mg/ml. ERDRP-0519 serum concentrations from blood samples were measured by liquid chromatography with tandem mass spectrometry (LC/MS/MS) (**b**); mean plasma concentrations are shown ( $n = 3$ ). Pharmacokinetic parameters were calculated using the WinNonlin PK software package.  $C_{max}$  maximum calculated concentration,  $AUC_{0-\infty}$  area under the curve extrapolated to infinity,  $t_{1/2}$  terminal elimination half-life. **c, d** PK-informed ex vivo assessment of anti-MeV efficacy in human peripheral mononuclear cells (hPBMCs) recapitulating once (*quaque die*; q.d.) or twice (*bis in die*; b.i.d.) daily ERDRP-0519 dosing. Solid lines show the experimentally measured single-dose PK profile of the compound in squirrel monkeys; dashed lines represent the projected PK profiles, assuming no drug build-up after multi-dose administration; green and magenta blocks illustrate the experimentally applied concentrations in the 48-h ex vivo recapitulation of physiologically-achievable drug levels. **e** Progeny MeV titers observed in the ex vivo recapitulations shown in **c, d**. Statistical analysis through one-way ANOVA with Tukey's multiple comparison post-hoc test. Symbols show individual biological repeats and bars illustrate the mean.  $N = 3$  (vehicle) or  $n = 4$  (all other groups), exact  $p$  values are stated, and error bars represent standard deviations; LoD limit of detection.

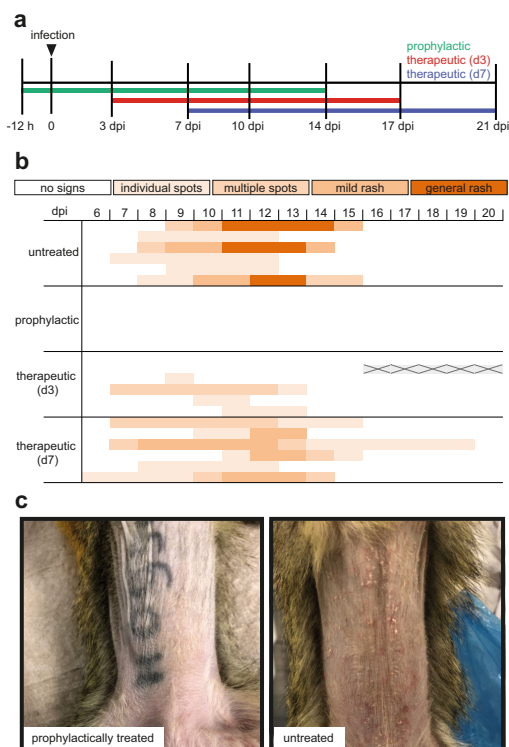
Blood samples and throat swabs were collected twice weekly throughout the study (Fig. 2a) and viral load was determined. In untreated animals, PBMC-associated viremia titers peaked around day 7 before gradual resolution. Virus burden on day 7 post-infection was significantly higher in the untreated group than in the prophylactic treatment group ( $p < 0.0001$ ) and the day 3 ( $p = 0.0023$ ) and day 7 ( $p = 0.0324$ ) therapeutic treatment groups, respectively. Prophylactic treatment with ERDRP-0519 decreased viremia titers on average by up to 250-fold compared to untreated animals, and day 3 therapeutic administration likewise effectively suppressed virus replication (Fig. 3c). However, initiation of treatment at day 7 post-infection had no significant effect on the height of maximum virus load, which was reached on day 10 post-infection in this group. These results illustrate that pre- or early post-exposure treatment prevents or strongly alleviates, respectively, PBMC infection. Direct comparison of serum ERDRP-0519 concentrations (Fig. 3a) and PBMC-associated virus titers (Fig. 3c) in the individual animals at day 7 post-infection revealed that the drug was similarly efficacious over a wide range of concentrations and that onset of treatment was indeed the essential parameter influencing viremia (Supplementary Fig. 2). Viral titers in PBMCs correlated with MeV *N* RNA, further underlining the inhibitory effect of ERDRP-0519 on viral replication (Supplementary Fig. 3a). Virus was cleared in general within 21 days. Throat swab titers of animals in all study groups resembled the PBMC-mediated viremia profile, except for the day 7 therapeutic group. Shed virus was first detectable 7 days after infection (Fig. 3d).

Compared to untreated animals, shed virus titers in the day 7 therapeutic group dropped significantly ( $p = 0.0199$ ) by two orders of magnitude within 72 h of treatment initiation (Fig. 3d), indicating that the duration and/or efficiency of virus transmission from an index case to social contacts may be reduced by the drug, even when treatment is first initiated after the onset of the measles rash.

Total white blood cell counts revealed typical MeV-induced leukopenia in untreated animals, which peaked on day 10 after infection and was followed by slow recovery (Fig. 3e). In contrast, no leukopenia was observed in the prophylactic and day 3 treatment groups. In the day 7 treatment group, we observed a trend for lower total white blood cell counts, but this was not significant, and cell counts increased more rapidly at later time points compared to the untreated group, making alleviated immunosuppression in all animals that had received ERDRP-0519 conceivable (Fig. 3e). Furthermore, animals of all groups including those prophylactically treated developed on average protective neutralizing antibody titers of  $\geq 120$  (Fig. 3f).

To assess clearance of MeV from the lymphatic system, MeV *N*-gene RNA levels were evaluated in lymph nodes of all animals 21 days post-infection and for the deceased animal at the day of its death. Whereas some of the untreated monkeys still showed high MeV *N*-gene RNA prevalence in lymph nodes, RNA levels were significantly decreased in the prophylactic ( $p = 0.0295$ ) and therapeutic day 3 ( $p = 0.0346$ ) dose groups, indicating accelerated virus clearance in these groups compared to the untreated group (Supplementary Fig. 3b).

## ARTICLE

NATURE COMMUNICATIONS | <https://doi.org/10.1038/s41467-021-25497-4>

**Fig. 2** Effect of ERDRP-0519 on manifestation of clinical signs in MeV-infected squirrel monkeys. **a** Schematic illustration of the experimental design. Each group was treated twice daily (*b.i.d.*) over a 14-day period, illustrated by colored lines. Prophylactic treatment started 12 h prior to infection (green); therapeutic treatment started on day 3 post-infection (therapeutic (d3), red), or on day 7 post-infection (therapeutic (d7), blue). Dpi, days post-infection. **b** Clinical scores of infected animals. Each row represents one animal of the respective group and color intensity indicates severity of clinical signs categorized as no signs (white) or individual spots, multiple spots, mild rash, and general rash (light to dark graduation). Gray, crossed areas represent deceased animal. **c** Representative photographs of the abdomen of a prophylactically treated animal (left) and an untreated animal (right), taken 13 days post-infection.

**Safety of ERDRP-0519 treatment.** All monkeys were sacrificed on day 21, followed by gross- and histopathological analyses. No histological signs of pharmacotoxicity were detected, but we noted mild histopathological changes such as lymphatic lesions in the lung (Fig. 4a, b), enlarged germinal centers in lymph nodes (Fig. 4c, d), hematopoiesis in spleen (Fig. 4e, f), and mesangial proliferation in glomeruli of the kidney (Fig. 4g, h), which are consistent with a recent virus infection. These and other manifestations emerged in a subset of animals of all treatment groups and thus cannot be linked to distinct treatment regimens (Supplementary Table 1).

Viral RNA was recovered from five animals per group at the last time point of viremia or positive swab titers for Sanger sequencing of the polymerase *L*-gene. No mutations causing amino acid changes were identified in the known clusters of the MeV polymerase protein associated with viral resistance to ERDRP-0519 *in vitro*<sup>13,16</sup>.

## Discussion

This study demonstrates the potential of ERDRP-0519 to improve management of severe measles and augment MeV eradication in primates. Our results show that mean attained compound serum titers in non-human primates after oral *b.i.d.* dosing were sufficient to significantly reduce MeV replication in an *ex vivo* recultivation, anticipating that this dosing regimen inhibits viral replication *in vivo*. Indeed, we demonstrate a strong beneficial effect of ERDRP-0519 in MeV-infected squirrel monkeys leading to reduced clinical signs. Treatment started as late as 7 days post-infection prevented appearance of general rash. Earlier onsets of the treatment regimen further reduced disease severity.

ERDRP-0519 treatment reduced viral titers in PBMCs and throat swabs. Notably, prophylactic treatment nearly completely prevented MeV viremia, and treatment started 3 days post-infection reduced viremia markedly. In agreement with the intra-host life cycle of MeV<sup>17,18</sup>, treatment starting 7 days post-infection was unable to prevent PBMC-associated viremia, but still led to reduced viral titers in the throat of these animals, indicating decreased viral spread into and replication in epithelial tissues. The reduced viral load in airways may affect host-to-host transmission and thus have additional benefits in breaking outbreak chains.

Lymphocytopenia is a hallmark of MeV infection in humans, leading to immunosuppression during and after acute infection<sup>5</sup>. In our hands, animals treated with ERDRP-0519 trended to exhibit reduced immunosuppression compared to untreated animals, but this was not statistically significant. However, previous experiments of MeV-infected macaques had shown that elevated numbers of monocytes and eosinophils can compensate for MeV-induced lymphocytopenia<sup>19</sup>, indicating that a modest reduction in total white blood cells may be associated with an even more profound lymphocytopenia.

An important aspect of MeV infections in humans is the generation of life-long humoral immune responses that protect efficiently against re-infection. We demonstrate here that ERDRP-0519 treatment does not prevent the generation of humoral immune responses. All animals from the therapeutically treated groups developed high levels of neutralizing antibodies. In the prophylactically treated group, two animals did not develop neutralizing antibodies until the end of the study. It is possible that ERDRP-0519 treatment was so efficient in these individual animals that it prevented the minimal amount of viral replication required to mount efficient immune responses. However, PBMC-associated viral titers were similarly low in all animals of this group.

Absence of pathological alternations during necropsy and abnormalities that could be linked to a distinct group in histological examination suggests that ERDRP-0519 does not evoke toxic side effects at the administered dose, which is in line with previous *in vivo* experiments of ERDRP-0519 treatment in ferrets<sup>13</sup>.

The evolution of drug-resistant mutant viruses is a potential problem for the safety of any antiviral drug. Escape mutant hotspots occurring in the morbillivirus polymerase after ERDRP-0519 treatment have been characterized in cell culture and *in vivo*<sup>13,16</sup>. The relative fitness of these ERDRP-0519-resistant viruses was reduced compared to that of the drug-sensitive parent virus in all cases<sup>13</sup>, indicating that escape from the compound is associated with a selection disadvantage. Viruses re-isolated from ERDRP-0519-treated animals did not evolve resistance mutations, adding an additional positive aspect to the safety profile of the drug. Although it is challenging to predict the impact of emerging resistance on circulating MeV populations, the available datasets suggest that sustained circulation of ERDRP-0519-resistant MeV variants is unlikely.

Consistent with the devastating measles burden found in pediatric patients in many low- and middle-income countries, we believe that a viable therapeutic option must be amenable to cost-effective

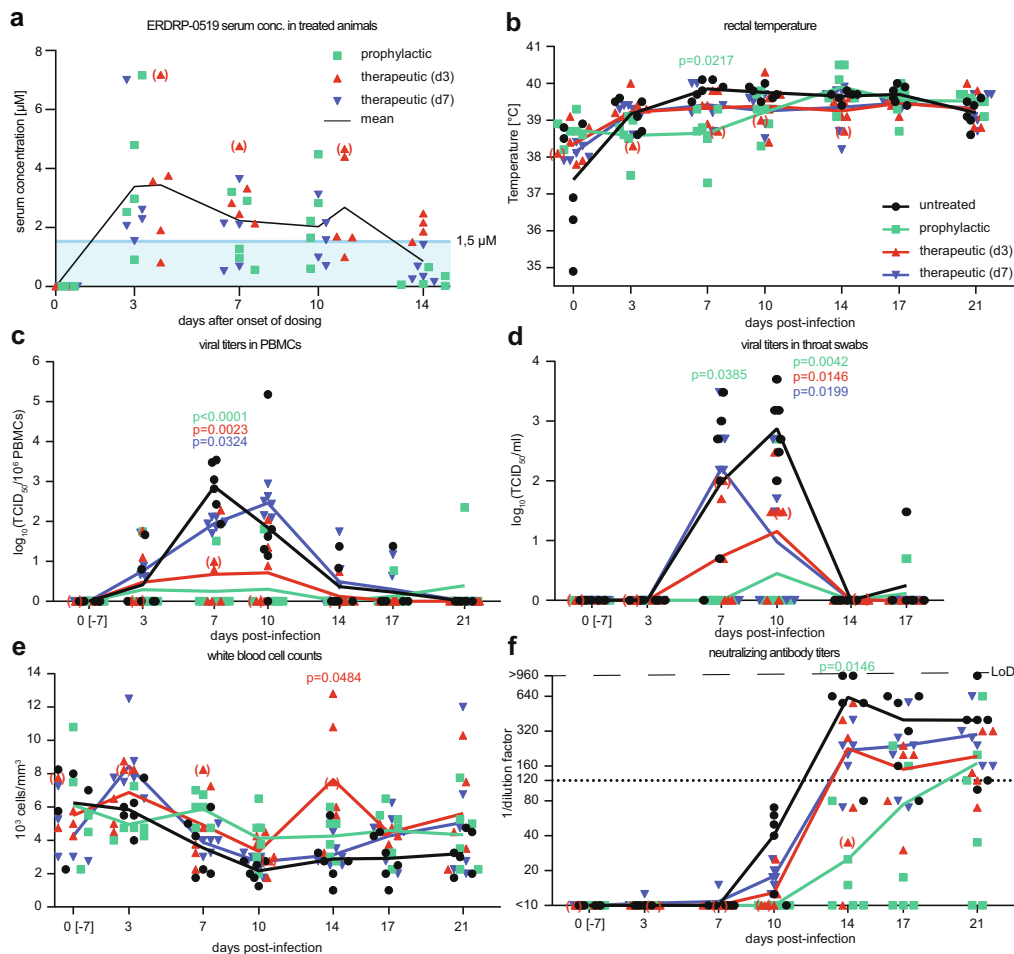


**Fig. 3** Clinical parameters of MeV infection in squirrel monkeys. **a** Trough serum concentrations of ERDRP-0519 in infected squirrel monkeys ( $n = 15$ ) participating in this study followed over a 14-day *b.i.d.* oral treatment period. Solid black line shows mean values; blue line and square show the constant drug concentration ( $1.5 \mu\text{M}$ ) applied in the *ex vivo* steady-state recapitulation to assess anti-MeV activity in hPBMCs shown in Fig. 1e. **b** Rectal temperature measured in the morning. **c**, **d** PBMC and throat swab titers, determined by end point dilution assay and expressed as  $\log_{10}(\text{TCID}_{50}/10^6 \text{ PBMCs})$  or  $\log_{10}(\text{TCID}_{50}/\text{ml})$  throat swab suspension, respectively. **e** White blood cell counts from whole blood, expressed as  $10^3 \text{ cells}/\text{mm}^3$ . **f** Neutralizing antibody titers, expressed as reciprocals of the highest serum dilution showing no signs of infection. Dotted line represents the expected protective antibody titer. LoD limit of detection. The day 0 blood samples and swabs were collected 7 days before the start of the experiment (0[-7] days post-infection). Statistical analysis with two-way ANOVA with Dunnett's multiple comparisons post-hoc test was applied in **b-f**, using the untreated group as reference. Significant  $p$  values ( $p < 0.05$ ) are shown, color-coded by group. For **a-f**  $n = 6$  for all groups, except  $n = 5$  for the 17 and 21 dpi time points in the therapeutic d3 group and  $n = 5$  for the 0 dpi time points for Fig. 3e. Deceased animal is illustrated in parenthesis in all sub-panels; therapeutic (d3) and therapeutic (d7), therapeutically treated groups where treatment started on day 3 or day 7 post-infection, respectively.

production, shelf-stable at ambient temperature, and orally bioavailable to allow administration independent of trained health care professionals<sup>11</sup>. The clinical candidate ERDRP-0519 meets these requirements, and is a therapeutic option for newborns and pregnant women not eligible to vaccination. In light of the current surge in MeV outbreaks in geographical regions with generally intermediate to high measles vaccine coverage<sup>20</sup>, an effective antiviral with the product profile of ERDRP-0519 could represent the critical

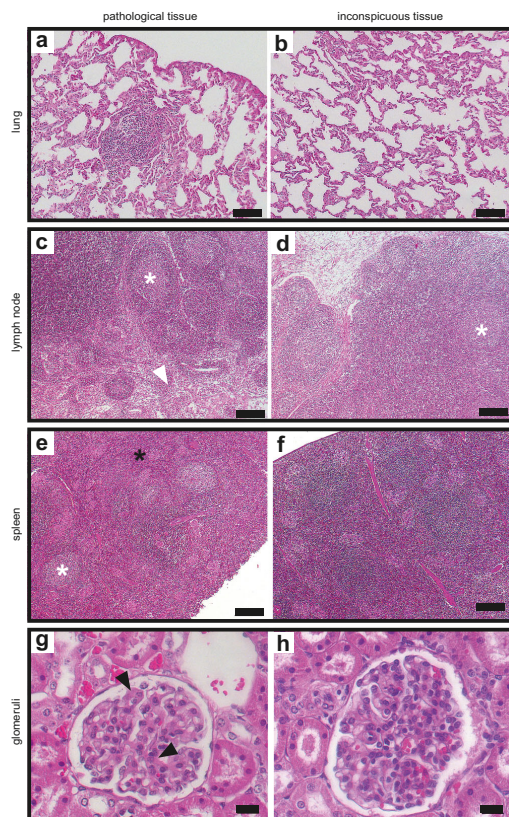
missing link to ultimate global measles elimination, synergizing with vaccination by establishing a double-pronged prophylactic and post-exposure therapeutic anti-measles platform<sup>21</sup>.

## Methods

**Study design.** All animal experiments were carried out in compliance with the regulations of German animal protection laws and authorized by the Regierungsspräsidium Darmstadt, Germany (Dezernat V54 – Veterinärwesen und Verbraucherschutz, Hilpertstrasse 31, 64295 Darmstadt). Adult male and female



## ARTICLE

NATURE COMMUNICATIONS | <https://doi.org/10.1038/s41467-021-25497-4>

**Fig. 4** Histological examination on day 21 post-infection. H&E-stained tissues from all animals of the study ( $n = 24$ ) were examined and representative pictures from individual animals are shown. **a** Perivascular lesion due to lymphocytic infiltration in the lung. **b** Normal lung tissue. **c** Lymph nodes with germinal centers (white asterisk) and histiocytosis (white arrow). **d** Normal lymph node. **e** Spleen with germinal centers (white asterisk) and hematopoiesis (black asterisk). **f** Normal spleen tissue. **g** Mesangial proliferation (black arrow) in glomeruli of the kidney. **h** Normal glomerulus. Black bar represents 100  $\mu\text{m}$  (**a**, **b**), 200  $\mu\text{m}$  (**c**–**f**), 20  $\mu\text{m}$  (**g**, **h**). Representative pictures are shown from untreated group (**c**, **g**, **h**), therapeutic day 3 (**a**, **b**, **f**), or therapeutic day 7 (**d**, **e**) group.

squirrel monkeys (*Saimiri sciureus*) were obtained from BioPRIM, 31450 Baziege, or CNRS 0846 Primatologie, 13790 Rousset, France. Each experimental group was housed in a separate room, and animals of the same sex were caged together within the respective groups. For the single-dose pharmacokinetic experiment, animals were anesthetized, and the drug was given through a stomach tube at a concentration of 50 mg/kg bodyweight. Blood samples were collected after 15, 30, and 60 min, and 2, 3, 6, and 24 h. For efficacy assessment, groups of 6 animals were left untreated or treated with 50 mg/kg of ERDRP-0519 twice daily for two weeks, starting either 12 h before or 3 or 7 days after intranasal infection with  $10^6$  TCID<sub>50</sub> of MV/FrankfurtMain.DEU/17.11. Clinical signs, rectal temperature, and weight were recorded daily, and throat swabs and blood samples were collected before infection and twice weekly thereafter. On day 21 post-infection, the animals were euthanized, necropsied, and samples were collected for histological analysis.

**Cell culture and viruses.** Vero cells stably expressing human SLAM (Vero/hSLAM) were maintained in Dulbecco's modified Eagle's medium (DMEM) with 5% fetal bovine serum and 1% L-Glutamine. For infection experiments, DMEM

supplemented with 2% FBS and 1% L-Glutamine was used. Human peripheral blood mononuclear cells (iQ Biosciences; Donor 4327; Lot# P19L1400) were cultured in RPMI-1640 and stimulated with 0.2  $\mu\text{g}/\text{ml}$  phytohemagglutinin (PHA; Sigma–Aldrich) for 24 h prior to use. The isolate MV/FrankfurtMain.DEU/17.11 was used for infections of animals, and the isolate MeV/NewJersey.USA/94/1 was used for hPBMC infections. Each will be provided upon request.

**Compound synthesis and formulation.** In total, 100 mg of ERDRP-0519<sup>22</sup> was dissolved in 1 ml of poly(ethylene glycol)-200 (Sigma–Aldrich). On the days of treatment, the drug stock was diluted 1:10 in 0.5% methylcellulose under vigorous agitation to avoid precipitation. During all procedures, the drug was protected from light to avoid degradation.

**Pharmacokinetics.** Drug concentrations were determined using an internal standard and a reversed phase isocratic HPLC method with positive ion electrospray ionization (ESI) mass spectrometry detection (LC/MS/MS) on an AB-SCIEX API 5500 MS/MS instrument (5  $\mu\text{l}$  injection volume). Pharmacokinetic parameters were estimated using WinNonlin 5.3 (Pharsight).

**PK and PD recapitulation in human blood mononuclear cells.** Human peripheral blood mononuclear cells (hPBMCs) were infected (MOI = 0.1 TCID<sub>50</sub> units per cell) in a 24-well plate format with MeV/NewJersey.USA/94/1 (genotype D6) in the presence of ERDRP-0519 or DMSO (0.1%). The concentration of ERDRP-0519 was maintained at a constant 1.5  $\mu\text{M}$  (recapitulation of trough steady-state drug levels achieved during *b.i.d.* dosing regimen in squirrel monkeys) or adjusted at various times post-infection to recapitulate *ex vivo* dynamic plasma drug concentrations for once (*q.d.*) or twice (*b.i.d.*) daily dosing regimens, based on single-dose pharmacokinetics in squirrel monkeys. Cells were collected 48 h after infection and virus was subsequently harvested after two freeze thaw cycles. Released virus titers were then determined by limited dilution method (TCID<sub>50</sub>) on Vero/hSLAM cells. Four biological repeats were used for each *ex vivo* PK recapitulation and three biological repeats were used for DMSO-treated hPBMCs.

**Virological and immunological sample analyses.** White blood cell counts, viral load quantification in PBMCs, and quantification of neutralizing antibody titers were performed as follows: for white blood cell counts, blood was diluted 1:100 in 3% acetic acid and cells were counted using a Neubauer chamber. For viral load quantification in PBMCs, blood was centrifuged at 3000 rpm for 15 min and serum was frozen at  $-20^\circ\text{C}$  until further use. Red blood cell lysis was performed and the remaining PBMCs were counted using a Neubauer chamber. Viral titers in PBMCs were quantified in quadruplicates using limited dilution method and calculated as TCID<sub>50</sub>/10<sup>6</sup> PBMCs. Neutralizing antibody titers were quantified by incubating MeV with 2-fold serial dilutions of the respective serum for 20 min at room temperature in quadruplicates. Vero/hSLAM cells were added and incubated for 3 days at  $37^\circ\text{C}$ . Neutralizing antibody titers are expressed as the reciprocal of the highest serum dilution showing no signs of infection. For virus titration from throat swabs, swabs were placed in 150  $\mu\text{l}$  DMEM with 3% penicillin/streptomycin and the titer was quantified by limited dilution method.

#### Quantitative RT-PCR analysis of viral RNA in lymph nodes and PBMCs.

Organs (21 days post-infection) and PBMCs (twice a week) were frozen in RNAlater (Qiagen) at  $-80^\circ\text{C}$  until further processing. For the deceased animal, organs were frozen in RNAlater at the day of death. Lymph nodes were thawed on ice, transferred to TRIzol (ambion life technologies) and homogenized using a tissue homogenizer. Total RNA of lymph nodes and PBMCs was extracted following the TRIzol manufacturer's protocol. RNA (1000 ng for lymph nodes; 110 ng for PBMCs) was then subjected to reverse transcription using random hexamer primers and Superscript III reverse transcriptase in accordance with the manufacturer's protocols. Subsequent quantitative PCR (qPCR) was carried out using primer pairs specific for a fragment in the MeV *N* gene<sup>23</sup> or *GAPDH* gene (Supplementary Table 2) and the PowerUp SYBR Green Master Mix (Thermo Fisher Scientific) in an Applied Biosystems 7500 Real-Time PCR system. Samples were normalized for GAPDH. The comparative ( $\Delta\Delta\text{Ct}$ ) Ct method was applied to determine relative amounts of N-encoding RNA present in samples from treated animals compared to those obtained from untreated control animals (lymph nodes) or compared to those obtained from untreated control animals on day 7 post-infection (peak PBMC virus titer).

**Genetic analysis.** Viruses isolated from PBMCs and throat swabs were grown on Vero/hSLAM cells for one passage and RNA was isolated using the Direct-zol RNA MiniPrep Kit (Zymo Research) according to the manufacturer's instructions. RNA was reverse transcribed using random hexamer primers and Superscript III reverse transcriptase and cDNA sequence was assessed by Sanger sequencing for presence of resistance mutations in clusters in the MeV *L* gene known to accumulate resistance-conferring mutations in tissue culture in the presence of ERDRP-0519<sup>10</sup>. Sanger sequencing was carried out using MeV *L* gene specific primers (Supplementary Table 2) and obtained sequences were analyzed using Sequencher software (Gene Codes Corporation; Version 5.4.6).



**Necropsy and histology.** After euthanasia, each animal was examined for gross pathological changes, and samples were collected for histopathological examination. After fixation, all tissue samples were embedded in paraffin. Histology slices were mounted and stained using standard H&E staining techniques.

**Statistical analysis.** Statistical analysis was performed using GraphPad Prism 8. One-way analysis of variance (ANOVA) with Tukey's multiple comparison post-hoc test or two-way ANOVA, followed by Dunnett's multiple comparisons post-hoc test were applied for statistical comparisons using the untreated group as reference if not stated otherwise. Different time points for each individual animal were paired. Biological repeat refers to measurements taken from distinct samples, and results obtained for each individual biological repeat are shown in the figures along with the exact size ( $n$  number) of biologically independent samples, animals, or independent experiments. Measure of center (connecting lines and columns) are means throughout. Error bars represent standard deviations (SD) throughout. For all experiments, the statistical significance level  $\alpha$  was set to  $<0.05$ , exact  $p$  values (color-coded by experimental group) are shown in individual graphs wherever possible and significant.

**Reporting summary.** Further information on research design is available in the Nature Research Reporting Summary linked to this article.

#### Data availability

All data that support the findings of this study are contained within the manuscript and the associated source data documents are provided in the supplement. Source data are provided with this paper.

Received: 19 February 2021; Accepted: 12 August 2021;

Published online: 02 September 2021

#### References

- Mühlbach, M. D. et al. Adherens junction protein nectin-4 is the epithelial receptor for measles virus. *Nature* **480**, 530–533 (2011).
- Laksono, B. M., Vries, R. D. de, McQuaid, S., Duprex, W. P. & Swart, R. L. de. Measles virus host invasion and pathogenesis. *Viruses* **8**, 210 (2016).
- Mahmud, A. S., Alam, N. & Metcalfe, C. J. E. Drivers of measles mortality: the historic fatality burden of famine in Bangladesh. *Epidemiol. Infect.* **145**, 3361–3369 (2017).
- Patel, M. K. et al. Progress toward regional measles elimination - worldwide, 2000–2019. *MMWR Morbidity Mortal. Wkly Rep.* **69**, 1700–1705 (2020).
- Petrova, V. N. et al. Incomplete genetic reconstitution of B cell pools contributes to prolonged immunosuppression after measles. *Sci. Immunol.* **4**, eaay6125 (2019).
- Holzmann, H., Hengel, H., Tenbusch, M. & Doerr, H. W. Eradication of measles: remaining challenges. *Med. Microbiol. Immunol.* **205**, 201–208 (2016).
- Orenstein, W. A. et al. Measles and Rubella Global Strategic Plan 2012–2020 midterm review report: background and summary. *Vaccine* **36**, A35–A42 (2018).
- Roberts, L. Pandemic brings mass vaccinations to a halt. *Science* **368**, 116–117 (2020).
- Anderson, R. M. & May, R. M. Directly transmitted infectious diseases: control by vaccination. *Science* **215**, 1053–1060 (1982).
- Plempner, R. K. & Snyder, J. P. Measles control—can measles virus inhibitors make a difference? *Curr. Opin. Investig. Drugs* **10**, 811–820 (2009).
- Plempner, R. K. Measles resurgence and drug development. *Curr. Opin. Virol.* **41**, 8–17 (2020).
- White, L. K. et al. Nonnucleoside inhibitor of measles virus RNA-dependent RNA polymerase complex activity. *Antimicrob. Agents Chemother.* **51**, 2293–2303 (2007).
- Krumm, S. A. et al. An orally available, small-molecule polymerase inhibitor shows efficacy against a lethal morbillivirus infection in a large animal model. *Sci. Transl. Med.* **6**, 232ra52 (2014).
- Cox, R. M., Sourimant, J., Govindarajan, M., Natchus, M. G. & Plempner, R. K. Therapeutic targeting of measles virus polymerase with ERDRP-0519 suppresses all RNA synthesis activity. *PLoS Pathog.* **17**, e1009371 (2021).
- Santibanez, S. et al. Molecular surveillance of measles and rubella in the WHO European Region: new challenges in the elimination phase. *Clin. Microbiol. Infect.* **23**, 516–523 (2017).
- Yoon, J.-J. et al. Target analysis of the experimental measles therapeutic AS-136A. *Antimicrob. Agents Chemother.* **53**, 3860–3870 (2009).
- Navaratnarajah, C. K., Generous, A. R., Yousaf, I. & Cattaneo, R. Receptor-mediated cell entry of paramyxoviruses: Mechanisms, and consequences for tropism and pathogenesis. *J. Biol. Chem.* **295**, 2771–2786 (2020).

- Ayasoufi, K. & Pfaller, C. K. Seek and hide: the manipulating interplay of measles virus with the innate immune system. *Curr. Opin. Virol.* **41**, 18–30 (2020).
- Auwaerter, P. G. et al. Measles virus infection in rhesus macaques: altered immune responses and comparison of the virulence of six different virus strains. *J. Infect. Dis.* **180**, 950–958 (1999).
- Phadke, V. K., Bednarczyk, R. A., Salmon, D. A. & Omer, S. B. Association between vaccine refusal and vaccine-preventable diseases in the United States: a review of measles and pertussis. *JAMA* **315**, 1149–1158 (2016).
- Plempner, R. K. & Hammond, A. L. Synergizing vaccinations with therapeutics for measles eradication. *Expert Opin. Drug Discov.* **9**, 201–214 (2014).
- Ndungu, J. M. et al. Non-nucleoside inhibitors of the measles virus RNA-dependent RNA polymerase: synthesis, structure-activity relationships, and pharmacokinetics. *J. Med. Chem.* **55**, 4220–4230 (2012).
- Hummel, K. B., Lowe, L., Bellini, W. J. & Rota, P. A. Development of quantitative gene-specific real-time RT-PCR assays for the detection of measles virus in clinical specimens. *J. Virol. Methods* **132**, 166–173 (2006).

#### Acknowledgements

We thank M. T. Saindaine and M. A. Lockwood for chemical synthesis. This work was supported in part by Public Health Service grant A1071002 (to R.K.P.) from the NIH/ NIAID and by Collaborative Research Center 1021 (project number 197785619/B09) of the German Research Foundation (to V.v.M.).

#### Author contributions

K.W.: study design, investigation, analysis, visualization, and writing; D.E.A.: investigation, review and editing; K.P.: investigation; R.M.C.: investigation, analysis, and visualization; J.D.W.: investigation and analysis; S.S.: resources; A.M.: resources; R.P.: investigation and analysis; Z.B.S.: analysis; A.A.K.: analysis; M.G.N.: analysis; C.K.P.: analysis, resources, supervision, writing, review, and editing; R.K.P.: study design, resources, investigation, analysis, writing, review, and editing; V.v.M.: study design, resources, investigation, supervision, writing, review and editing.

#### Funding

Open Access funding enabled and organized by Projekt DEAL.

#### Competing interests

R.K.P. is a co-inventor on US patent US9499489B2, “Myxovirus therapeutics, compounds, and uses related thereto”, which covers composition of matter and the method of use of ERDRP-0519 for measles therapy. This study could affect his personal financial status. All other authors declare no competing interests.

#### Additional information

**Supplementary information** The online version contains supplementary material available at <https://doi.org/10.1038/s41467-021-25497-4>.

**Correspondence** and requests for materials should be addressed to C.K.P. or R.K.P.

**Peer review information** *Nature Communications* thanks Lijun Rong and the other, anonymous, reviewer(s) for their contribution to the peer review of this work.

**Reprints and permission information** is available at <http://www.nature.com/reprints>

**Publisher's note** Springer Nature remains neutral with regard to jurisdictional claims in published maps and institutional affiliations.



**Open Access** This article is licensed under a Creative Commons Attribution 4.0 International License, which permits use, sharing, adaptation, distribution and reproduction in any medium or format, as long as you give appropriate credit to the original author(s) and the source, provide a link to the Creative Commons license, and indicate if changes were made. The images or other third party material in this article are included in the article's Creative Commons license, unless indicated otherwise in a credit line to the material. If material is not included in the article's Creative Commons license and your intended use is not permitted by statutory regulation or exceeds the permitted use, you will need to obtain permission directly from the copyright holder. To view a copy of this license, visit <http://creativecommons.org/licenses/by/4.0/>.

© The Author(s) 2021

## 2.2.3 Structural Basis of Paramyxo- and Pneumovirus Polymerase Inhibitors with Non-Nucleoside Small-Molecule Antivirals



Antimicrobial Agents  
and Chemotherapy



Virology | Minireview

### Structural basis of paramyxo- and pneumovirus polymerase inhibition by non-nucleoside small-molecule antivirals

Josef D. Wolf,<sup>1</sup> Michael R. Serrine,<sup>1</sup> Robert M. Cox,<sup>1</sup> Richard K. Plemper<sup>1</sup>

**AUTHOR AFFILIATION** See affiliation list on p. 19.

**ABSTRACT** Small-molecule antivirals can be used as chemical probes to stabilize transitory conformational stages of viral target proteins, facilitating structural analyses. Here, we evaluate allosteric pneumo- and paramyxovirus polymerase inhibitors that have the potential to serve as chemical probes and aid the structural characterization of short-lived intermediate conformations of the polymerase complex. Of multiple inhibitor classes evaluated, we discuss in-depth distinct scaffolds that were selected based on well-understood structure-activity relationships, insight into resistance profiles, biochemical characterization of the mechanism of action, and photoaffinity-based target mapping. Each class is thought to block structural rearrangements of polymerase domains albeit target sites and docking poses are distinct. This review highlights validated druggable targets in the paramyxo- and pneumovirus polymerase proteins and discusses discrete structural stages of the polymerase complexes required for bioactivity.

**KEYWORDS** chemical probe, polymerase structure, paramyxovirus, pneumovirus, mononegavirales, measles virus, respiratory syncytial virus, parainfluenza virus, viral polymerase, polymerase inhibitor

The paramyxoviruses and pneumoviruses families include highly contagious human and animal pathogens such as mumps virus, measles virus (MeV), respiratory syncytial virus (RSV), human parainfluenza viruses (HPIVs), and the highly pathogenic zoonotic Nipah (NiV) and Hendra (HeV) viruses (1). In 2019, for instance, more than 200,000 MeV deaths were reported worldwide despite global access to a safe and efficacious vaccine, which was the highest number of reported cases in 23 years (2–6). RSV remains one of the leading causes of acute respiratory tract infections (ARIs) in both adults and children. In 2016, it was estimated that RSV was responsible for more than 24 million ARIs and 76,000 deaths globally each year (7, 8). As of 2024, three vaccines, Abrysvo, Arexvy, and mRESVIA, have been approved by the US Food and Drug Administration (FDA) to prevent RSV in adults ages 60 and over (9–11). The Abrysvo vaccine has also been approved in pregnant women between 32 and 36 weeks gestational age to safeguard infants from RSV infection through transplacentally acquired maternal antibodies (9) although concerns were raised about increased risk of preterm birth after maternal vaccination (12). Annually, HPIV infections contribute to more than 700,000 hospitalizations and 34,000 deaths worldwide (13). NiV, causing nearly annual outbreaks since 1998, has a case fatality rate of approximately 75% and has been recognized as a global public health problem with epidemic or pandemic potential (14, 15). Because each of these viruses is associated with major global health and economic burdens, novel effective therapeutics that can augment vaccine prophylaxis, when available, are urgently required.

Paramyxo- and Pneumoviruses belong to the order *Mononegavirales*, which contains RNA viruses with protein-encapsidated non-segmented single-stranded genomes of negative polarity (1). The mononegavirus RNA-dependent RNA polymerase (RdRP)

**Editor** Miguel Angel Martinez, IrsiCaixa Institut de Recerca de la Sida, Barcelona, Spain

Address correspondence to Richard K. Plemper, rplemper@gsu.edu.

R.M.C. and R.K.P. are co-inventors on patent filings covering composition and method of use of GHP-88309 and its analogs for antiviral therapy. R.K.P. is a co-inventor on patent filings covering composition and method of use of AVG-233 and ERDRP-0519 and their analogs for antiviral therapy. This paper could affect their personal financial status. R.K.P. reports contract testing from Enanta Pharmaceuticals, Atea Pharmaceuticals, and Icosagen Biosciences and research support from Gilead Sciences, outside of the described work.

See the funding table on p. 19.

**Published** 20 August 2024

Copyright © 2024 American Society for Microbiology. All Rights Reserved.

complexes constitute attractive druggable targets since they are essential for viral genome replication and protein expression but lack host cell homologs with equivalent enzymatic activity (16). Conserved across all mononegaviruses, the core RdRP complexes consist of two viral proteins: the large (L) protein, which harbors all enzymatic activity, and an obligatory chaperone, the phospho- (P) protein (16–20). These L-P complexes are subjected to specific structural rearrangements as the polymerase transitions between pre-initiation, initiation, and various elongation conformations (18, 19, 21–26). Through intra-protein domain reorganization, channels for RNA template and product strands are generated that extend from the central cavity of the polymerase, and enzymatic domains are relocated within proximity of their cognate substrate. Each of these rearrangements should, in principle, be druggable with conformation-specific small-molecular inhibitors that stabilize a distinct conformation of L-P, thus inhibiting polymerase activity by blocking cycling of the complex between its different conformational stages (16, 18, 27, 28).

Several apo structures of mononegavirus polymerase complexes have been reported (26, 29–36), and recently, RSV L-P (37) and EBOV VP35-L (38) bound to RNA have been solved. However, the resolution of individual domains that are subject to, or enable, conformational rearrangements such as the MTase and connector domain remains limited due to their inherent structural pliability, undermining therapeutic exploitation through structure-guided drug design (16, 18, 33, 34). In addition, native reconstructions of the polymerase structures of some clinically significant paramyxoviruses such as NIV have yet to be released. Here, we review the current mechanism of action of a diverse set of small-molecule inhibitors that may be suitable to serve as molecular probes for the structural analysis of distinct conformational stages of the RdRP complex.

### L PROTEIN DOMAIN ORGANIZATION AND ENZYMATIc FUNCTIONS

The multidomain L protein mediates phosphodiester bond formation, messenger RNA (mRNA) capping and cap methylation, and mRNA polyadenylation (18, 19, 23, 25). Throughout the *Mononegavirales* order, L proteins feature five conserved domains (Fig. 1A): the RdRP, polyribonucleotidyltransferase (PRNTase), connector (CD), methyltransferase (MTase), and C-terminal (CTD) domains (Fig. 1B), which are separated by short linker regions that allow for some domain rearrangements relative to each other (22, 25, 26, 39, 40). Positioned at an intersection between the RdRP, PRNTase, and CT domains is a central cavity that is the site of active polymerization, containing the highly conserved GDN motif that constitutes the active site for phosphodiester bond formation (23, 24, 26, 41). Sequence alignments of paramyxo- and -pneumoviruses revealed six conserved regions (CRs I-VI) located in the RdRP domain (CRs I-III) (Fig. 1C), PRNTase domain (CRs IV-V) (Fig. 1D), and MTase domain (CR VI) (Fig. 1E), respectively (17–19, 22, 23, 41).

CR I, which is located adjacent to the RNA template entry channel and is part of a central cavity mediating phosphodiester bond formation, is thought to directly engage in interaction with the P protein (20). CRs II and III are directly involved in mediating RNA synthesis and contain a set of conserved motifs (A–F) that are present in all mononegavirus polymerases. Specifically, CR II is involved in RNA binding, whereas CR III harbors a highly conserved GDN motif that constitutes the active site for phosphodiester bond formation (17, 18, 23, 25). CR IV contributes to mRNA cap methylation, CR V has PRNTase catalytic activity, and CR VI contributes to MTase activity (19, 23–25, 40). CR V is considered to contain priming and, at least for some family members, intrusion loops that are located within the central polymerase cavity near the GDN active site (Fig. 1F). These flexible loops are instrumental for the initiation of *de novo* RNA synthesis through proper positioning of the initial nucleoside triphosphate (NTP) by means of base-stacking interactions with an aromatic side chain and preventing the formation of viral RNA hairpins (26, 28, 42, 43).

Minireview

Antimicrobial Agents and Chemotherapy

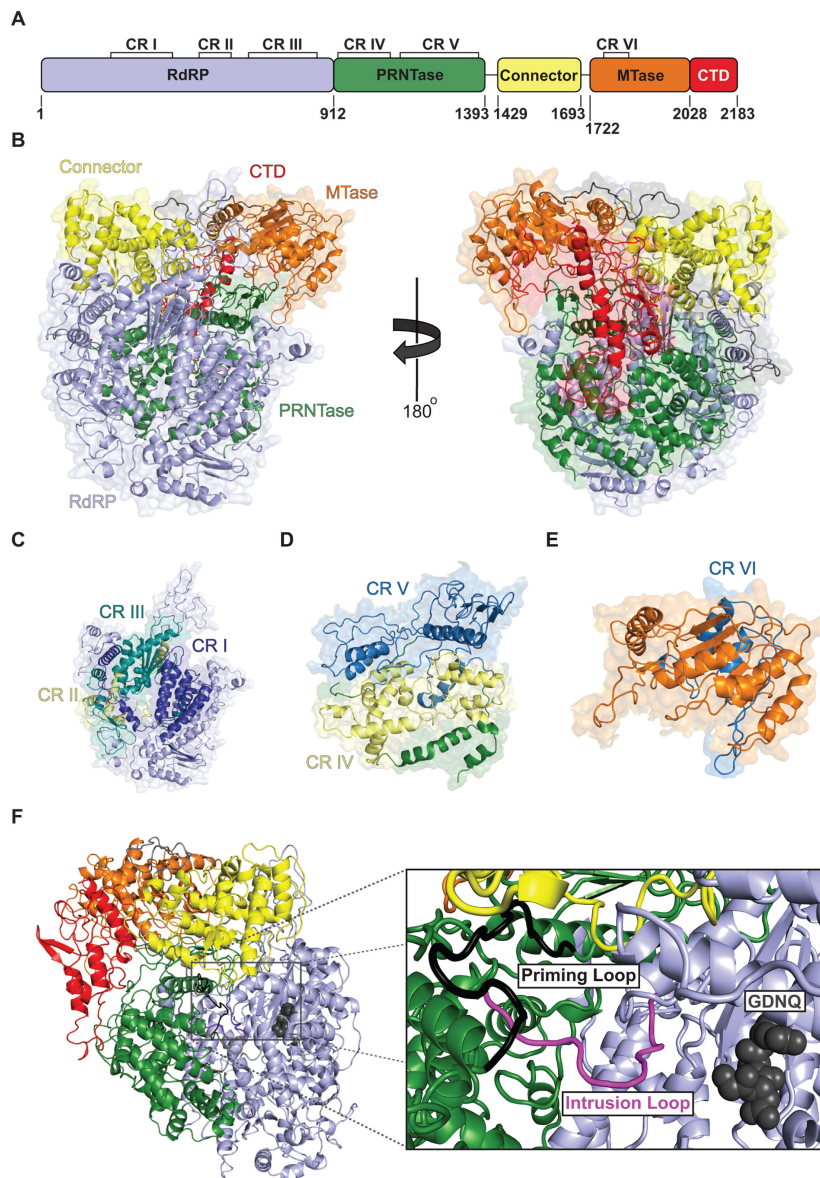


**FIG 1** Architecture of the MeV L protein. (A) 2D schematic of the organization of the five conserved MeV L protein domains. RNA-dependent RNA polymerase (RdRP) domain in light blue (residues 1–912), polyribonucleotidyltransferase (PRNTase) domain in forest green (residues 913–1393), connector domain in yellow (residues 1429–1693), methyltransferase (MTase) domain in orange (residues 1722–2028), and the C-terminal domain (CTD) in red (residues 2029–2183). (B) Homology model of MeV L protein (Edmonston strain, GenBank: QOT47606.1) in its elongation-3 stage that is based on the cryoEM structure of parainfluenza virus 5 (PDB: 6v86), generated using the Swiss model server. Domains are colored as in the 2D schematic. (C) Conserved regions of the RdRP domain: CR I in deep blue (residues 217–409), CR II in pale yellow (residues 495–596), and CR III in deep teal (residues 653–869) with the GDN shown as spheres. (D) Conserved regions of the PRNTase domain: CR IV in (Continued on next page)

FIG 1 (Continued)

pale yellow (residues 928–1093) and CR V in sky blue (residues 1129–1376). (E) Conserved region of the MTase domain: VI in marine blue (residues 1753–1832). Spatial orientation of CRs in C–E is conserved from the homology model on the left in B. (F) MeV L central cavity showing the GDN (residues 772–775) in gray as spheres, the putative priming loop in black (residues 1200–1233), and the putative intrusion loop in magenta (residues 1279–1302).

### REARRANGEMENTS OF MONONEGAVIRUS L PROTEIN DOMAINS AND LOOPS ARE REQUIRED FOR TRANSCRIPTION AND REPLICATION

Transcription and replication of paramyxo- and pneumovirus genomes are initiated by recognition and binding of a promoter sequence, monopartite for pneumoviruses, bipartite for paramyxoviruses, at the 3' end of the genome by the L-P complex (24, 41, 43, 44). Once the polymerase complex is engaged, nucleocapsid (N) protein must be displaced to unveil the RNA ahead of the RdRP, allowing the RNA strand to enter the template channel as the N protomers are routed over the outer surface of the polymerase. Depending on whether an approximately 55-nucleotide leader sequence that is synthesized first is N-encapsidated, the RdRP proceeds either as a replicase or as a transcriptase. In replication mode, the nascent RNA is concomitantly encapsidated by N protein units as the polymerase advances along the template, and all intergenic termination signals are bypassed to generate full-length antigenomes. If the leader sequence is not encapsidated, it is released from the polymerase, which then scans in transcriptase mode the RNA template for the first gene start (GS) signal, at which transcription reinitiates until a gene stop signal is reached (45–51). Nascent viral mRNAs are capped and methylated by the RdRP as they leave the product exit channel and appear on the surface of the complex (21, 22, 40). Each subsequent GS signal triggers re-initiation of transcription. However, the frequency of re-initiation is less than 100%, leading to a gradient of mRNAs that decreases with increasing distance from the 3' end of the genome (46, 49, 52).

Both transcription and replication require orderly structural rearrangements of the RdRP complex (19, 20, 24–26, 32–34, 41, 53), which properly position catalytic regions of the polymerase within proximity of the template and nascent RNA product and mediate the formation of product exit channels that extend from the central cavity to the exterior of the polymerase (Fig. 2A) (25). Loop and domain rearrangements can be used to posit the different transitional stages of the polymerase and have been well supported by cryo-electron microscopy (cryo-EM) reconstructions of different mononegavirus polymerase complexes including those of PIV3 (35), PIV5 (34), mumps virus (MuV) (36), RSV (33), human metapneumovirus (hMPV) (30), rabies virus (RABV) (32), vesicular stomatitis virus (VSV) (31), Ebola virus (EBOV) (42), and NDV (26) polymerase complexes. Owing to the recently published Newcastle disease virus (NDV) L-P complex (PDB: [7you](#)), an intriguing new model has been proposed that includes three distinct stages of elongation based on the varying distances of the VSV, hMPV, NDV, and PIV5 priming and intrusion loops in relation to the GDN site and domain arrangements (26).

Based on currently published L protein structures, we propose that the polymerase transitions through five distinct stages: (i) pre-initiation, (ii) initiation, (iii) elongation-1, (iv) elongation-2, and (v) elongation-3. In the pre-initiation state, as demonstrated by the RSV L-P-RNA complex (Fig. 2B), the priming and intrusion loops of the polymerase are extended away from the GDN site which allows space for incoming promoter RNA (Fig. 2C) (37). Within the central cavity, a supporting loop, located within the RdRP domain, stabilizes the first nucleotides of the incoming RNA promoter, resulting in a slight inward shift (~1.8 Å) of the PRNTase domain, generating a more compact and stable catalytic pocket (37). Subsequently, the polymerase transitions into an initiation state, as seen in the RABV and VSV polymerase structures; the priming loop moves within proximity of the GDN to properly position the initial NTP and the intrusion loop is extended into a cavity within the PRNTase domain (Fig. 2D) (31, 32). Upon the synthesis of the initial dinucleotide and the first few nucleotides, the polymerase transitions from an initiation



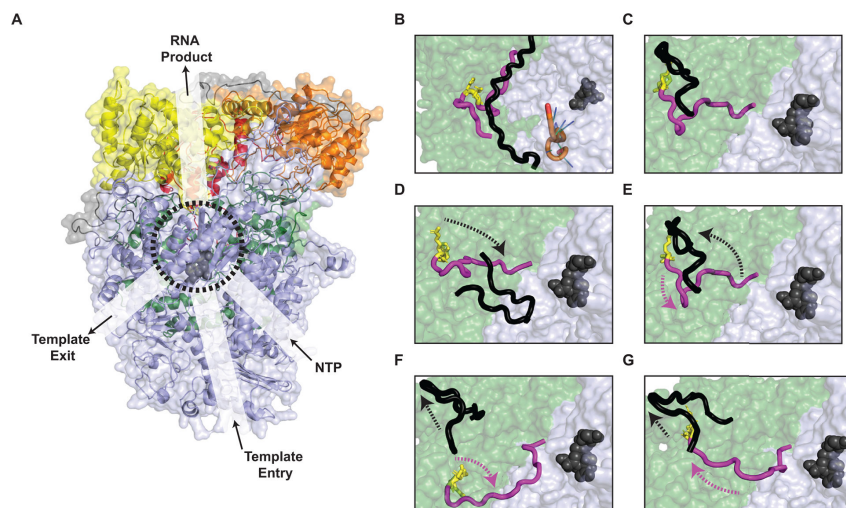


**FIG 2** Channels and loop re-arrangements of the mononegavirus polymerase. (A) NTP entry, template entry, template exit, and RNA product exit channels extending from the central cavity (black dashed circle) of a MeV L homology model (PDB: 6v86). (B) RSV L with promoter bound (PDB: 8snx) representing a pre-initiation state for *de novo* RNA synthesis. RNA (orange). (C) In a pre-initiation state, the priming and intrusion loops are extended away from the active site allowing space for the incoming RNA template. (D) Upon transitioning into an initiation state, the priming loop is positioned within proximity of the GDN and the intrusion loop is extended into the PRNTase domain. (E) Entering an elongation-1 stage, the priming loop moves away from the active site and into the PRNTase domain while the intrusion loop moves slightly closer to the GDN. (F) As the polymerase enters an elongation-2 stage, the priming loop extends deeper into the PRNTase domain and the intrusion loop continues to move closer to the GDN. (G) In the elongation-3 stage, the priming loop is retracted even further into the PRNTase domain, and the intrusion loop begins to move away from the GDN toward the PRNTase domain. (C–G) Different MeV L homology models that were generated based on the coordinates of RSV (C; PDB: 8snx), VSV (D; PDB: 5a22), HMPV (E; PDB: 6u5o), NDV (F; PDB: 7you), and PIV5 (G; PDB: 6v86), respectively, and aligned to show loop arrangements within the central cavity in relation to the GDN. To improve clarity, only residues 1217–1233 of the priming loop are shown. RdRP (light blue), PRNTase (forest green), connector (yellow), MTase (orange), CTD (red), GDN (gray spheres), priming loop (black), intrusion loop (magenta), HR motif (yellow sticks). Arrows show loop movement.

to an elongation-1 stage, as observed in the HMPV, RSV, and EBOV polymerases (30, 33, 42). In this stage, the PRNTase domain swings away from the RdRP domain to open an RNA product exit channel, the priming loop begins to extend back in the PRNTase domain and away from the active site, and the intrusion loop moves slightly toward the GDN (Fig. 2E) (26).

The committed polymerase then transitions into elongation-2 stage where, during transcription, the MTase-CTD domains reposition directly above the PRNTase domain, allowing for capping by extending the nascent RNA exit channel from the PRNTase into the MTase (26). While in the elongation-2 stage, the priming loop extends further into the PRNTase domain, and the intrusion loop continues to move closer to the GDN as was reported in the NDV polymerase structure (Fig. 2F) (26). Finally, in elongation-3 stage, the priming loop reaches maximum retraction into the PRNTase domain and the intrusion loop relocates away from the GDN site (Fig. 2G), as has been observed in the PIV5 polymerase structure (34).

The relocation of the intrusion loop during elongation-1 and -2 within proximity of the 5' end of the nascent RNA appears necessary for the highly conserved HR motif to facilitate the production of capped, methylated, m<sup>7</sup>GpppNm-RNAs (catalyzed by the MTase) through the formation of an intermediate covalent interaction between a conserved histidine and the 5'  $\alpha$ -phosphate of mono-phosphorylated RNA (pRNA) (Fig. 3A through D) (22, 40, 54). When the polymerase is in replicase mode, however, in which the nascent RNA strand remains uncapped and non-methylated, the MTase-CTD module

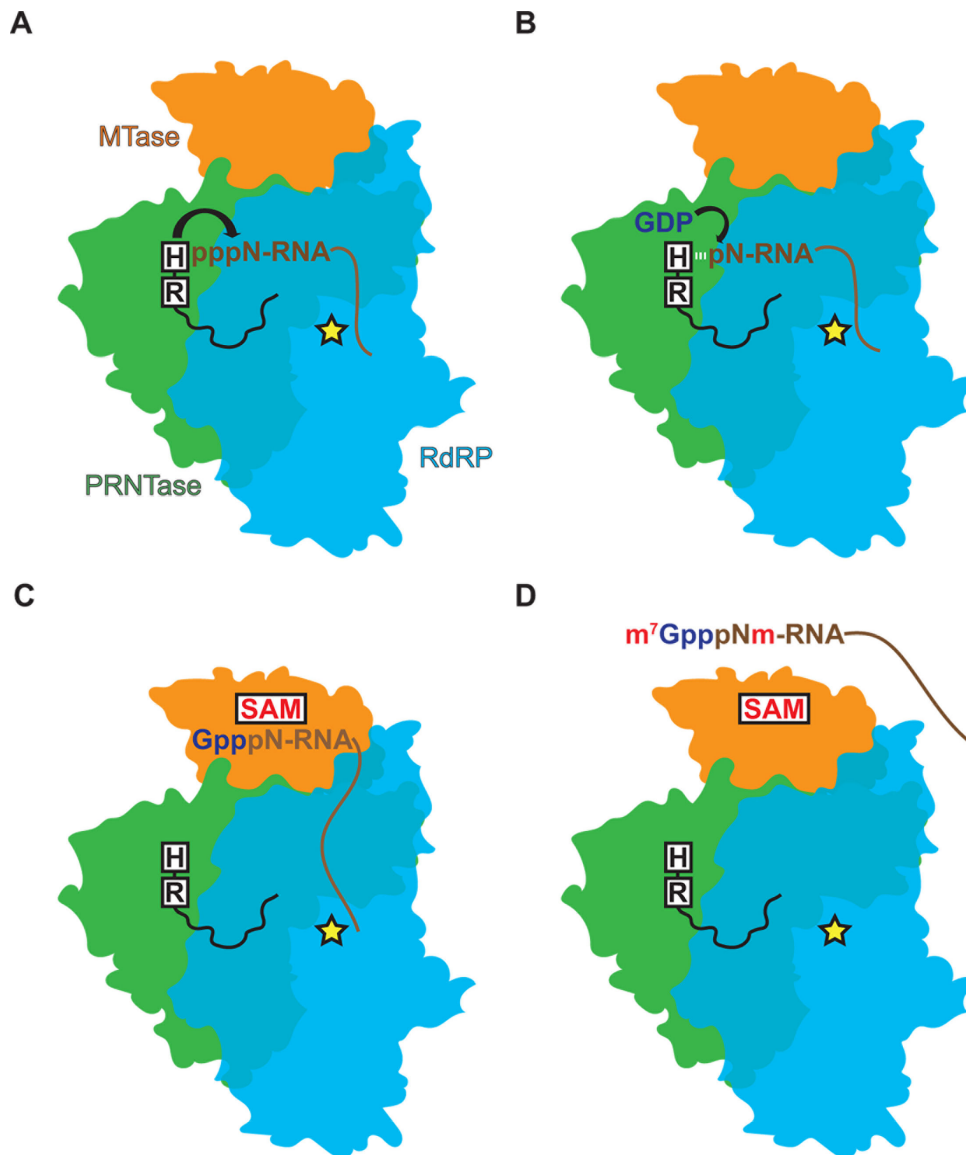


**FIG 3** Overview of viral mRNA capping and methylation. (A) The N<sup>2</sup> of the highly conserved histidine of the HR motif nucleophilically attacks the  $\alpha$ -phosphate of 5'-pppN-RNA and forms a covalent interaction. (B) Within the PRNTase active site GDP, generated from GTP through the guanosine, 5'-triphosphatase activity of L protein is transferred to pN-RNA when the  $\beta$ -phosphate of GDP nucleophilically attacks the  $\alpha$ -phosphate of the pN-RNA that is covalently linked to histidine. (C) With GpppN-RNA now in the S-adenosyl-L-methionine (SAM)-dependent MTase core, the 5'-cap is methylated at the adenosine-2'-O and guanine-N<sup>7</sup> positions, (D) yielding a bioactive mRNA product, m<sup>7</sup>GppNm-RNA. RdRP (light blue), PRNTase (forest green), MTase (orange), GDN (yellow star), intrusion loop (black), nascent RNA (brown), GDP (dark blue), SAM and methyl groups (red).

relocates even further away from the PRNTase domain into a conformation distinct from that observed during transcription (34).



In the elongation-3 stage and transcriptase mode, further elongation of the nascent pppA-RNA covalently linked to a histidine of the HR motif may pull the flexible intrusion loop up toward the PRNTase domain and active site of capping (26). The intrusion loop may then continue to extend away from the GDN active site toward the MTase-CTD catalytic domain, possibly due to some non-covalent interaction between the HR motif and the now capped GpppA-RNA.

### MECHANISTIC OVERVIEW OF SOME NON-NUCLEOSIDE INHIBITORS OF PARAMYXO- AND PNEUMOVIRUS POLYMERASES

All major domains of the PIV3, PIV5, MuV, RABV, VSV, and NDV L protein have been resolved, but the structural organization of multiple flexible regions remains unidentified (26, 31–35). Of the other polymerase complex reconstructions (i.e., RSV, HMPV, and EBOV), only the RdRP and PRNTase domains have been visualized due to inherent structural flexibility of the connector, MTase, and CT domains (30, 33, 42).

Although resolution of these domains has yet to be achieved for RSV RdRP, two substrate-bound, stabilized RSV polymerase structures provide proof of concept that structural resolution can be improved when the protein is complexed with its substrate or a chemical probe, respectively. In one structure, binding of the RNA promoter to RSV L improved the density of a flexible supporting helix that has not been previously visible in any cryo-EM maps of the apo polymerase complex (37). In the second structure, binding of the well-characterized, non-nucleoside inhibitor JNJ-8003 to RSV L stabilized the L-P complex, as evidenced by an increased melting temperature in a thermal shift assay, which allowed for the visualization of a novel-binding pocket within the PRNTase domain that surrounds the HR motif and may play a role in mRNA capping (55).

In search of candidate chemotypes that may aid further structural analyses of paramyxo- and pneumovirus RdRP complexes, we will focus in the following predominantly on advanced experimental polymerase inhibitor drugs that have met the following criteria: well-understood structure-activity relationships (SARs), insight into viral resistance profiles, biochemical characterization of the MOA, and photoaffinity crosslinking or docking pose reconstruction-based target site mapping (Table 1). Four distinct chemical classes meet these requests with a comprehensive set of medicinal chemistry, viromics, and biochemical data: the broadened-spectrum paramyxovirus inhibitor GHP-88309 (Fig. 4A), the RSV inhibitors JNJ-8003 (Fig. 4B) and AVG-233 (Fig. 4C), and the morbillivirus blocker ERDRP-0519 (Fig. 4D) (27, 28, 35, 56–59). Based on

TABLE 1 Fully characterized compound classes

Compound	Virus	Hypothesized MOA	Resistance mutation(s)	RdRP assay	Target identification	Refs
AVG-233	RSV	Blocks <i>de novo</i> polymerase initiation at the promoter by preventing RdRP, PRNTase, and MTase reorganization	L1502Q H1632Q	Yes	Yes	(27)
ERDRP-0519	MeV	Prevents phosphodiester bond formation by inhibiting priming and intrusion loop rearrangements	H589Y S768A T776A L1170F R1233Q V1239A	Yes	Yes	(28, 29)
GHP-88309	MeV <sup>a</sup> CDV HPIV1/3	Blocks <i>de novo</i> polymerase initiation at the promoter by preventing RdRP and PRNTase reorganization	S869P Y942H I1009F Y1106S	Yes	Yes	(56)
JNJ-8003	RSV <sup>b</sup> HMPV	Blocks <i>de novo</i> polymerase initiation at the promoter by preventing intrusion loop and domain rearrangements	R526W R999G D1026N Y1361F I1381S/T C1388G K1464N	Yes	Yes	(55)

<sup>a</sup>Target identification through photoaffinity labeling.

<sup>b</sup>Target identification through cryo-EM.

Minireview

Antimicrobial Agents and Chemotherapy

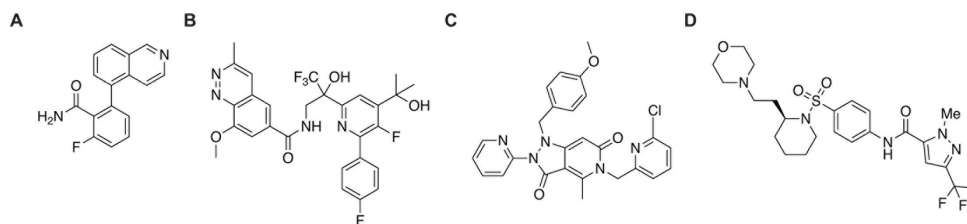


FIG 4 GHP-88309, ERDRP-0519, JNJ-8003, and AVG-233 compound structures. Structures of (A) GHP-88309, (B) JNJ-8003, (C) AVG-233, and (D) ERDRP-0519.

the available experimental data, each of these compounds is thought to block RdRP activity by stabilizing distinct polymerase conformations. Multiple other compounds have been identified that target the RSV polymerase, such as AZ-27 (43, 60, 61), BI-compound D (62, 63), BRD3969 (64), Compound 1 (65), PC786 (66, 67), Triazole-1 (68), and the parent compound of AZ-27, YM-53403 (60, 69). However, the characterization of these inhibitors is less complete (Table 2), limiting their contribution to advancing the structural understanding of different polymerase conformations through their use as chemical probes.

GHP-88309 emerged from a high-throughput screening (HTS) campaign against human parainfluenza virus type-3 (HPIV3) and has originally demonstrated oral efficacy in respirovirus mouse. The compound showed an unusual expanded anti-paramyxovirus indication spectrum, however, that includes, in addition to pathogens of the respirovirus genus, morbilliviruses such as MeV and CDV, and some members of the henipavirus genus (56, 70). The potent oral efficacy of GHP-88309 against morbilliviruses has been demonstrated subsequently in the canine distemper virus (CDV) ferret model, which serves as a surrogate system for human measles (71). AVG-233 and JNJ-8003 likewise emerged from HTS campaigns (55, 72). The lead analog of this first-in-class anti-RSV chemotype, AVG-388, efficiently reduced viral replication in human airway epithelium organoids and the RSV mouse model, in which treatment dose-dependently lowered viral load, alleviated lung histopathology, and prevented viral pneumonia (27). JNJ-8003 demonstrated subnanomolar efficacy against RSV A and B clinical isolates, and nanomolar efficacy against HMPV in a reporter assay (55). ERDRP-0519 is the lead compound of a pan-morbillivirus series (28, 57, 59) with demonstrated oral efficacy against a clinical MeV isolate in a non-human primate model in addition to activity in the CDV ferret model (28, 57, 73).

TABLE 2 Compound classes with incomplete biochemical characterization<sup>a</sup>

Compound	Virus	Hypothesized MOA	Resistance mutation(s)	RdRP assay	Target identification	Refs
AZ-27	RSV	Blocks <i>de novo</i> polymerase initiation at the promoter by an unknown mechanism	Y1631H	Yes	No	(43, 60, 61)
BI-Compound D	RSV	Prevents 5' capping of transcripts	E1269D I1381S L1421F	Yes	No	(62, 63)
BRD3969	RSV	May prevent capping, methylation, or polyadenylation	ND	Yes	No	(64)
Compound 1	RSV	ND	I1413T Y1631C	No	No	(65)
PC786	RSV	ND	Y1631H	No	No	(66, 67)
Triazole-1	RSV	ND	T1684A	No	No	(68)
YM-53403	RSV	Blocks <i>de novo</i> polymerase initiation at the promoter by an unknown mechanism	Y1631H	Yes	No	(60, 69)

<sup>a</sup>ND, not determined.

### MOA CHARACTERIZATION THROUGH BIOCHEMICAL RDRP ASSAYS

The first evidence that inhibition by GHP-88309, JNJ-8003, AVG-233, and ERDRP-0519 is mechanistically distinct came from biochemical RdRP activity assays, which demonstrated that GHP-88309, JNJ-8003, and AVG-233 block *de novo* polymerase initiation at the promoter after the synthesis of the first few nucleotides, but not RNA elongation by an already committed polymerase complex (27, 55, 56, 72). Chemically distinct experimental leads AZ-27 and YM-53403, that were both likewise subjected to *in vitro* biochemical assays for MOA characterization, mechanistically resembled this activity pattern of GHP-88309, JNJ-8003, and AVG-233; *de novo* polymerase initiation at the promoter was inhibited, halting RNA synthesis after the addition of the first few nucleotides, suggesting that also these compounds block an early stage of RNA synthesis (43, 60, 69). Inhibition of RNA synthesis, but not phosphodiester bond formation, by these structurally distinct inhibitors suggests that these compounds may interfere with conformational rearrangements of the polymerase complex as it transitions between initiation and elongation states.

In contrast, ERDRP-0519 blocked RNA amplification in a primer extension assay, which is considered to represent elongation by a committed polymerase complex, prevented the synthesis of the very first phosphodiester bond upon *de novo* polymerase initiation at the promoter, and, as the only compound subjected to *in vitro* paramyxovirus and pneumovirus RdRP assays, suppressed 3' extension from a back-primed template (28). Although likely an artifact of the non-encapsidated synthetic RNA templates used in the assay, back-priming is thought to mechanistically resemble RNA elongation by a committed polymerase (74, 75). The unique MOA pattern of ERDRP-0519 strongly suggested direct suppression of phosphodiester bond formation by this compound.

In contrast, the mechanisms that have been demonstrated for BI-compound D and BRD3969 do not involve the prevention of RNA synthesis. In the presence of BI-compound D, short transcripts are synthesized that lack a 5' cap, suggesting this compound may target the PRNTase domain and prevent capping, potentially through targeting the site of guanylation (62). Also, BRD3969 does not inhibit RNA synthesis but may block viral replication through the prevention of capping, methylation, or polyadenylation (64).

These biochemical data provided general mechanistic insight for AZ-27, AVG-233, BI-compound D, BRD3969, ERDRP-0519, GHP-88309, JNJ-8003, and YM-53403 but did not provide direct insight into the nature of their physical target sites. Physical target sites for AZ-27, BI-compound D, Compound 1, PC786, Triazole-1, and YM-53403 have been hypothesized based on resistance profiling. In the case of GHP-88309, JNJ-8003, AVG-233, and ERDRP-0519, additional insight into the docking poses came from both resistance profiling and photoaffinity labeling-based target mapping (GHP-88309, AVG-233, and ERDRP-0519) or structural data (JNJ-8003).

### RESISTANCE PROFILING

To place this mechanistic information into a structural context, all four compound classes were resistance profiled. The unique resistance profiles of GHP-88309 and ERDRP-0519, as well as the absence of cross-resistance, support that these compounds have distinct pharmacophores and target different regions within the central cavity of the MeV polymerase (28, 56). Resistance mutations to GHP-88309 and ERDRP-0519 emerged exclusively in the core region of the polymerase complex formed by the RdRP and PRNTase domains, suggesting that these compounds dock into the central cavity of the polymerase. Specifically, GHP-88309 resistance sites mapped to L residues S869P (in the RdRP domain) and Y942H, I1009F, and Y1106S (in the PRNTase domain) (Fig. 5A) (56). In contrast to recently emerged members of the henipavirus genus such as Ghanian henipavirus (70, preprint), NiV L naturally contains a histidine residue (H1156) at the position homologous to Y1106, which was associated with natural low susceptibility of NiV, to GHP-88309 (56). Viral escape from ERDRP-0519 was achieved by substitutions H589Y, S768A, or T776A in the RdRP domain and L1170F, R1233Q, or V1239A in the PRNTase domain of the morbillivirus L proteins (Fig. 5B) (28).

Minireview

Antimicrobial Agents and Chemotherapy

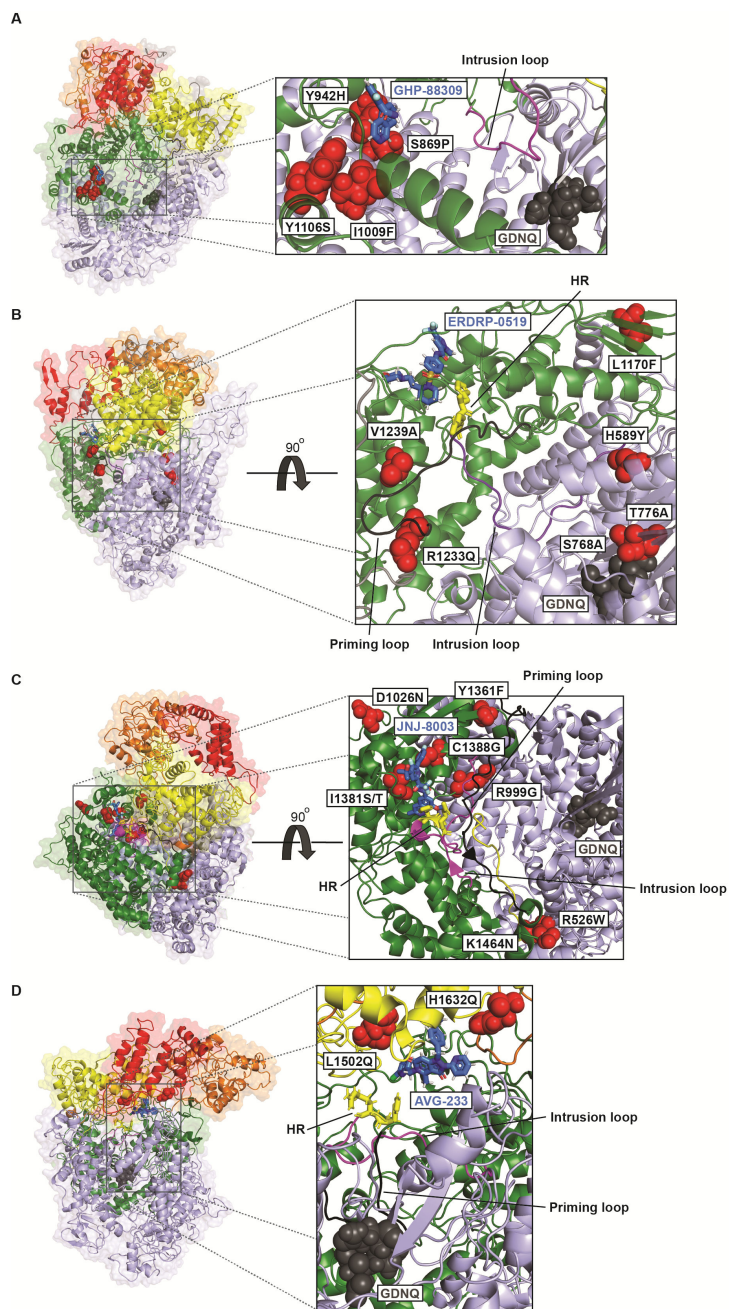


**FIG 5** Spatial arrangement of resistance mutations. (A) Resistance sites are tightly clustered around GHP-88309. (B) Location of ERDRP-0519 resistance sites. (C) The majority of JNJ-8003 resistance mutations cluster around the binding site. (D) AVG-233 resistance mutations are observed within proximity of the compound. For GHP-88309, ERDRP-0519, and AVG-233, the original (Continued on next page)

## FIG 5 (Continued)

docking pose of each compound is shown. The cryo-EM structure (PDB: 8fu3) is shown for JNJ-8003 and RSV L-P (residues 1–1461), residues 1462–2165 have been modeled. Resistance mutation (red sphere), compound (marine blue), RdRP (light blue), PRNTase (forest green), connector (yellow), MTase (orange), CTD (red), GDN (gray spheres), priming loop (black), intrusion loop (magenta), HR motif (yellow sticks).

In contrast to these resistance hot-spots located in the central RdRP cavity, resistance mutations to JNJ-8003 emerged in the RdRP domain (R526W), the PRNTase domain (R999G, D1026N, Y1361F, I1381S/T, and C1388G), and the CD (K1464N) (Fig. 5C) (55). Resistance mutations to AVG-233 mapped to residues L1502Q and H1632Q, which are positioned in the flexible connector domain of the RSV polymerase complex (Fig. 5D) (27). Resistance has also been observed at an adjacent residue in the RSV polymerase, Y1631H, in the chemically unrelated RSV inhibitors AZ-27 (60, 61), Compound 1 (65), PC786 (66), and YM-53403 (69). Strikingly, little cross-resistance was noted between AVG-233 and AZ-27 since the Y1631H substitution only slightly reduced the sensitivity of the polymerase to AVG-233 and neither L1502Q nor H1632Q mediates escape from AZ-27 (60, 61). These adjacent, but distinct, resistance sites suggest that although AVG-233 and the structurally unrelated RSV inhibitors AZ-27, Compound 1, PC786, and YM-53403 may bind to the same target domain, their specific docking poses remain distinct.

RSV L resistance to BI-compound D was observed in the PRNTase domain (I1381S, E1269D, and L1421F) (62), to Compound 1 in the PRNTase (I1431T) (65), and Triazole-1 in the CD (T1684A) (68). The locations of resistance to BI-compound D are not surprising given its RdRP assay phenotype and hypothesized MOA. It is plausible that the mechanism of inhibition of Compound 1 and PC786 may resemble that of AZ-27.

#### TARGETING PRNTASE DOMAIN REARRANGEMENTS

GHP-88309 cross-linked to MeV L residues 992–994, which line the inner wall of the central polymerase cavity and are adjacent to a cluster of GHP-88309 resistance mutations. A top-scoring docking pose derived from these data positioned GHP-88309 at an intersection between the RdRP and PRNTase domains, binding near the RNA template channel (56). In this pose, the ligand is predicted to simultaneously interact with residue R865 and a resistant site residue, Y942, in the RdRP domain (Fig. 6A) (56), suggesting that GHP-88309 may lock the polymerase into an initiation stage by preventing PRNTase domain rearrangement relative to the RdRP domain. This original docking pose of GHP-88309 was extracted from a MeV L homology model based on the coordinates reported for PIV 5 L (34). Since recent data (26) suggest that the PIV 5 L structure may alternatively represent an elongation-3 stage, we re-evaluated the *in silico* docking pose of GHP-88309 using a MeV L model based on the pre-initiation VSV L-P structure (PDB: 5a22). In this conformation, a top-scoring pose predicted three different ligand-residue interactions but, importantly, still positioned GHP-88309 within the same binding pocket as previously described (56). In our model, interactions of GHP-88309 with L were predicted to engage residues A935, M940, R1011 in the RdRP domain (Fig. 6B and C).

Because GHP-88309 impairs *de novo* polymerase initiation at the promoter after the synthesis of the first phosphodiester bonds, when template RNA must be present in the template entry channel and the active site, this compound likely does not prevent template entry or polymerase transition between a pre-initiation and initiation stage. Furthermore, since GHP-88309 cannot inhibit an already engaged polymerase, inhibition of the transition between any of the hypothesized elongation stages is not likely. Accordingly, plausible mechanisms of GHP-88309 include the prevention of (i) PRNTase domain movement away from the RdRP domain to generate an RNA exit channel, (ii) retraction of the priming loop from the active site, or (iii) intrusion loop rearrangement allowing contact with nascent RNA. Blocking rearrangement of the PRNTase domain relative to the RdRP domain could also indirectly lock the priming loop in place and



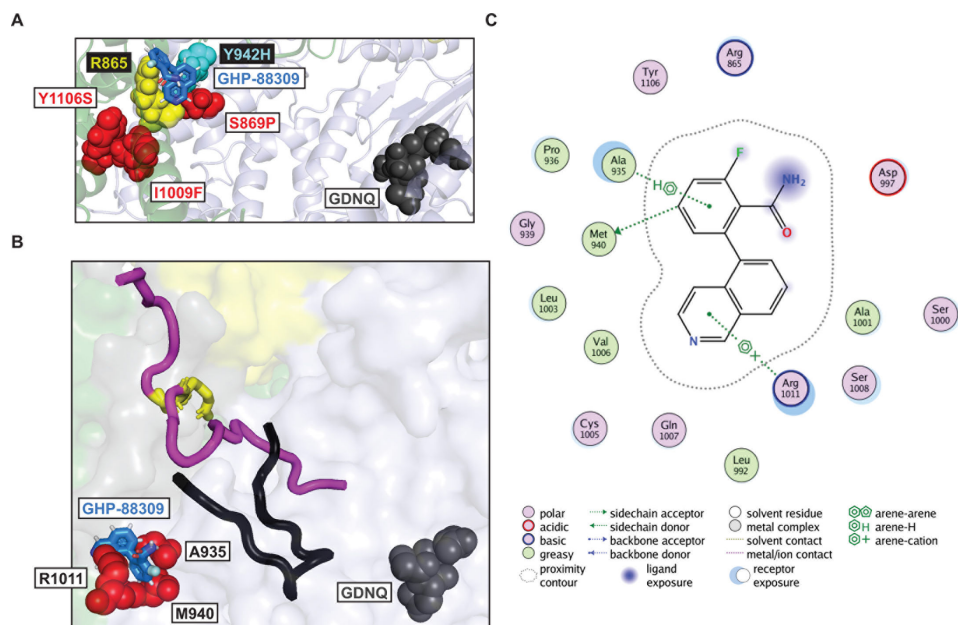


**FIG 6** *In silico* docking of GHP-88309 in MeV L. (A) Original top-scoring docking pose of GHP-88309 in a MeV L homology model based on PIV5 P-L (PDB: 6v86). Resistance mutation (red spheres), predicted interaction residue (yellow spheres), resistance residue that is predicted to interact (cyan). (B) Top-scoring docking pose of GHP-88309 in a MeV L homology model based on VSV P-L (PDB: 5a22), representing the polymerase in an initiation stage which is the predicted, targeted conformation. Predicted interaction residue (red spheres), priming loop (black), intrusion loop (magenta), HR motif (yellow sticks). (C) 2-D ligand map of new predicted interactions. (A and B) Compound (marine blue), GDN (gray spheres), RdRP (light blue), PRNTase (forest green), connector (yellow). Docking poses and ligand maps were generated using the molecular operating environment (MOE) software package.

prevent rearrangement of the intrusion loop. If the priming loop cannot retract from the active site and/or the intrusion loop cannot relocate to within proximity of the 5'-end of the nascent RNA, polymerization should stop after the first few nucleotides since the polymerase cannot transition into an elongation-1 stage, which is consistent with the performance of GHP-88309 in the biochemical polymerase assays. Consequently, GHP-88309 used as a chemical probe should stabilize morbillivirus and respirovirus polymerase complexes in an initiation confirmation.

#### TARGETING REARRANGEMENTS OF THE PRIMING AND INTRUSION LOOP

ERDRP-0519 affinity-mapped to two peptides of interest within the PRNTase domain, residues 952–966 and 1151–1176, which are both located near the intersection of the PRNTase, connector, and MTase domains. The identified peptides are in 3-way proximity to the HR motif, priming, and intrusion loops (28, 59). Docking pose extraction positioned ERDRP-0519 between the RdRP and PRNTase domains, bringing the ligand in direct contact with PRNTase residues Y1155, N1285, and H1288 (Fig. 7A), which may prevent reorganization of the priming and intrusion loops. Notably, ERDRP-0519 resistance residues are not predicted to be in direct contact with the ligand in this docking pose but are located in highly conserved regions surrounding the photoaffinity-mapping-derived physical target site. Accordingly, these substitutions may mediate viral escape through secondary resistance, possibly through altered orientation of the priming loop when the polymerase is transitioning to an initiation conformation that reduces compound affinity for the target. The docking pose of ERDRP-0519 suggests that primary resistance may not be feasible since residues predicted to be in direct

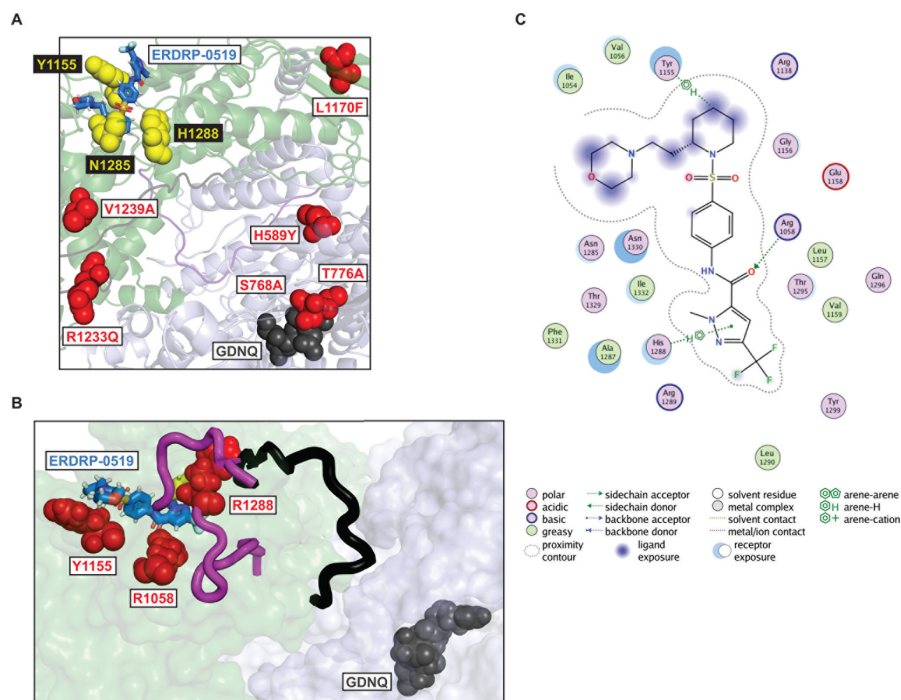


**FIG 7** Docking of ERDRP-0519 into MeV L. (A) Original top-scoring docking pose of ERDRP-0519 in a MeV L homology model based on PIV5 P-L (PDB: 6v86). Resistance mutation (red spheres), predicted interaction residue (yellow spheres). (B) ERDRP-0519 in a top-scoring pose in a MeV L homology model based on the RSV P-L-RNA structure (PDB: 8snx) to represent the hypothesized targeted pre-initiation conformation. Predicted interaction residue (red spheres), priming loop (black), intrusion loop (magenta), HR motif (yellow sticks). (C) New predicted interactions are shown in a 2-D ligand map. (A and B) Compound (marine blue), GDN (gray spheres), RdRP (light blue), PRNTase (forest green). Docking poses and ligand maps were generated using the molecular operating environment (MOE) software package.

contact with the ligand are highly conserved and may not be changeable without loss of polymerase bioactivity (28).

ERDRP-0519 is the only small-molecule paramyxo- or pneumovirus inhibitor known to be capable of blocking all phosphodiester bond synthesis at the promoter and arresting an already engaged polymerase. Considering this unique phenotype, the compound could inhibit the polymerase through distinct MOAs, which could include (i) prevention of template RNA entry, (ii) prevention of NTP base-stacking, (iii) disruption of loop reorganization, (iv) distortion of loops, (v) affecting processivity, and/or (vi) interference with the catalytic active site. Concluding from a recently reported RSV L-RNA structure (PDB: 8snx), binding of ERDRP-0519 could also (vii) affect compaction of the catalytic pocket or interactions critical for stabilizing the RNA template (28, 37). Of these candidate MOAs, (i), (ii), and (vii) appear unlikely because they should affect only initiation but not elongation. Similarly, an effect on processivity (v) should only affect elongation and not initiation. Because resistance mutations were observed near the GDN active site (S768A and T776A), direct interference with catalytic activity (vi) has to be considered. However, with both template and product loaded, ERDRP-0519 could sterically not fit, arguing against this mode of action.

Based on a predicted interaction between ERDRP-0519 and H1288 in the HR motif of the intrusion loop, it appears most likely that the compound prevents the rearrangement of both the priming and intrusion loop. By docking into an intersection of three domains



## Minireview

## Antimicrobial Agents and Chemotherapy

critical to polymerase rearrangement, ERDRP-0519 may block all loop reorganization, preventing transitions both from initiation to elongation and between elongation stages of the complex. However, formal experimental proof outside the artificial biochemical RdRP assay that ERDRP-0519 can, indeed, halt an engaged polymerase is still lacking.

Noteworthy, a preliminary *in silico* docking prediction suggested that the binding pocket of ERDRP-0519 is not present when MeV L is in an initiation conformation (28). However, re-docking of ERDRP-0519 into the MeV L model in pre-initiation conformation based on the RSV P-L-RNA structure (PDB: [8snx](#)) further supported the above mechanistic hypothesis. In a top-scoring pose, the predicted binding pocket was present and the ligand posited to interact with residues Y1155 and H1288 (HR motif) through interactions with its piperidine and pyrazole rings, respectively (Fig. 7B and C). Additional contacts were established in this pose between the ligand and residue R1058 in the PRNTase domain.

### TARGETING TRANSITIONS BETWEEN THE ELONGATION STAGES

High-resolution cryo-EM structural data of RSV L-P complexed with JNJ-8003 revealed that the ligand established substantial interactions with four residues in the intrusion loop, L1337, H1338 (HR motif), R1345, and F1349, a single residue in the priming loop (S1266), and three residues that line a hydrophobic pocket, L1372, I1381, and F1385 (Fig. 8A) (55).

This JNJ-8003 docking pose with RSV L-P shows both the priming and intrusion loop extended away from the GDN active site and located in the PRNTase domain (55), suggesting that the polymerase may be in a pre-initiation, or elongation-1/3 stage (26). However, a comparison of the RSV L-P complex with JNJ-8003 with the RSV L-P-RNA structure favored a pre-initiation state of the complex based on the similar position of the PRNTase domain relative to the RdRP domain and how well the priming and intrusion loops align.

We, therefore, propose that binding of JNJ-8003 to RSV L inhibits the transition of the polymerase into an elongation-2 stage through either extensive interactions with the intrusion loop and/or by preventing domain rearrangements. This mechanism allows for initial phosphodiester bond formation but prevents the interaction between the HR motif and the tri-phosphorylated RNA (pppN-RNA) that is required for methylation of capped nascent RNAs.

### TARGETING PRNTASE AND MTASE DOMAIN REORGANIZATION

AVG-233 photoaffinity mapping cross-linked the compound with four peptides of the RSV L protein: one in the PRNTase domain (RSV L residues 1376–1409), two in the connecting domain (RSV L residues 1554–1576 and 1675–1678), and one in the MTase domain (RSV L residues 1880–1892) (27). Only the peptide located in the PRNTase could be observed on a native RSV L reconstruction (PDB: [6pzk](#)) since the high structural flexibility of the RSV polymerase connector and MTase domains has so far precluded the structural appreciation of the RSV L-P holoenzyme. Docking predicted AVG-233 to bind to the interface of the PRNTase, connecting, and MTase domains, suggesting an interaction between the ligand and RSV L residue W1262 of the priming loop (Fig. 8B) and placing the compound within ~4 Å proximity of residue H1388 in the HR motif (27). The aromatic priming residue(s) of RSV L have yet to be identified, but RSV L residues P1261 and W1262 are reportedly required for RNA synthesis and could, thus, play a cooperative role in forming base-stacking interactions with incoming NTPs (76).

Although the compound was predicted to engage priming loop residue W1262, it does not prevent initial phosphodiester bond formation. Therefore, this contact may be incorrect or, alternatively, an alternate residue such as Y1276 may act as the priming residue when W1262 is unavailable (76).

Based on all available evidence, AVG-233 most likely stabilizes the orientation of RSV L RdRP, PRNTase, and MTase domains relative to each other in an initiation conformation (27), presumably by preventing the polymerase from transitioning into an elongation-1

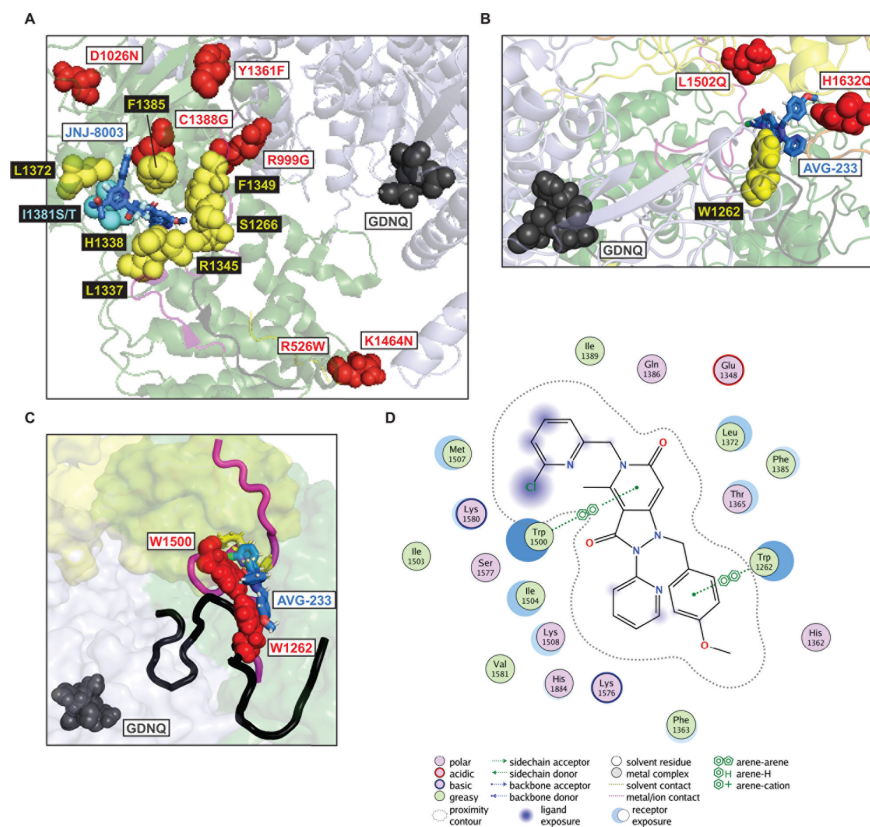


**FIG 8** JNJ-8003 bound to RSV L and AVG-233 docked into RSV L. (A) The cryo-EM structure of RSV L-P with JNJ-8003 (PDB: 8fu3). Resistance mutation (red spheres), predicted interaction residue (yellow spheres), resistance residue that is predicted to interact (cyan). (B) Original top-scoring docking pose of AVG-233 in RSV L. The RdRP and PRNTase domains are from the apo structure of RSV L-P (PDB: 6pzk), and the connector, MTase, and CTD were modeled based on VSV L-P (PDB: 5a22) and RABV L-P (PDB: 6ueb). Resistance mutation (red spheres) predicted interaction residue (yellow spheres). (C) The top-scoring docking pose of AVG-233 in an RSV L homology model based on the VSV P-L coordinates (PDB: 5a22), representing the hypothesized targeted initiation confirmation. Predicted interaction residue (red spheres), priming loop (black), intrusion loop (magenta), HR motif (yellow sticks). (D) 2-D ligand interaction map of new predicted interactions. (A–C) Compound (marine blue), GDN (gray spheres), RdRP (light blue), PRNTase (forest green), connector (yellow). Docking poses and ligand maps were generated using the molecular operating environment (MOE) software package.

stage. If this hypothesized MOA is correct, pharmacological stabilization of the flexible connector domain through AVG-233 may open a path toward reconstruction of the complete L assembly including the connector and MTase domains.

We assessed this hypothesis by re-analyzing the *in silico* docking pose of AVG-233 in an RSV L homology model based on pre-initiation VSV L-P (PDB: 5a22). AVG-233 was predicted to populate the same binding pocket as described previously and engage residue W1262, as observed in the original docking pose. In addition, a new interaction was predicted to involve residue W1500 in the MTase domain (Fig. 8C and D) (27).

### CONSERVATION OF RESISTANCE AND INTERACTING RESIDUES ACROSS VIRAL FAMILIES

How structurally conserved are validated druggable sites across different polymerases of the mononegavirus order? We analyzed the sequence conservation of (i) resistance

hot spots and (ii) residues that are predicted to interact with GHP-88309, ERDRP-0519, JNJ-8003, and AVG-233 across signature mononegaviruses, including paramyxoviruses (MeV, HPIV3/5, NiV, HeV), pneumoviruses (RSV and HMPV), rhabdoviruses (RABV and VSV), and filoviruses (EBOV and Marburg virus). GHP-88309 resistance sites were moderately conserved in polymerases representing the different families (Fig. 9A). However, multiple ERDRP-0519 (Fig. 9B), JNJ-8003 (Fig. 9C), and AVG-233 (Fig. 9D) resistance residues showed very little to no conservation across all families with the exception of the fully conserved JNJ-8003 resistance site, R999. We observed moderate conservation of MeV L residues predicted to interact with GHP-88309 (R865, A935, and Y954) (Fig. 10A and B) and ERDRP-0519 (Y1155) (Fig. 10C and D), and the RSV L residues predicted to interact with JNJ-8003 (R1266 and L1377) (Fig. 10E) and AVG-233 (W1262) (Fig. 10F and G). However, three residues of MeV L thought to interact with ERDRP-0519 (R1058, N1285, and H1288) (Fig. 10C and D) are highly conserved across families. Additionally, two residues of RSV L shown to interact with JNJ-8003 (F1349 and F1385) are highly conserved across viral families and one residue, H1338 of the HR motif, is fully conserved (Fig. 10E). Based on the original and new *in silico* docking poses discussed above, the conservation of the predicted interacting residues of these

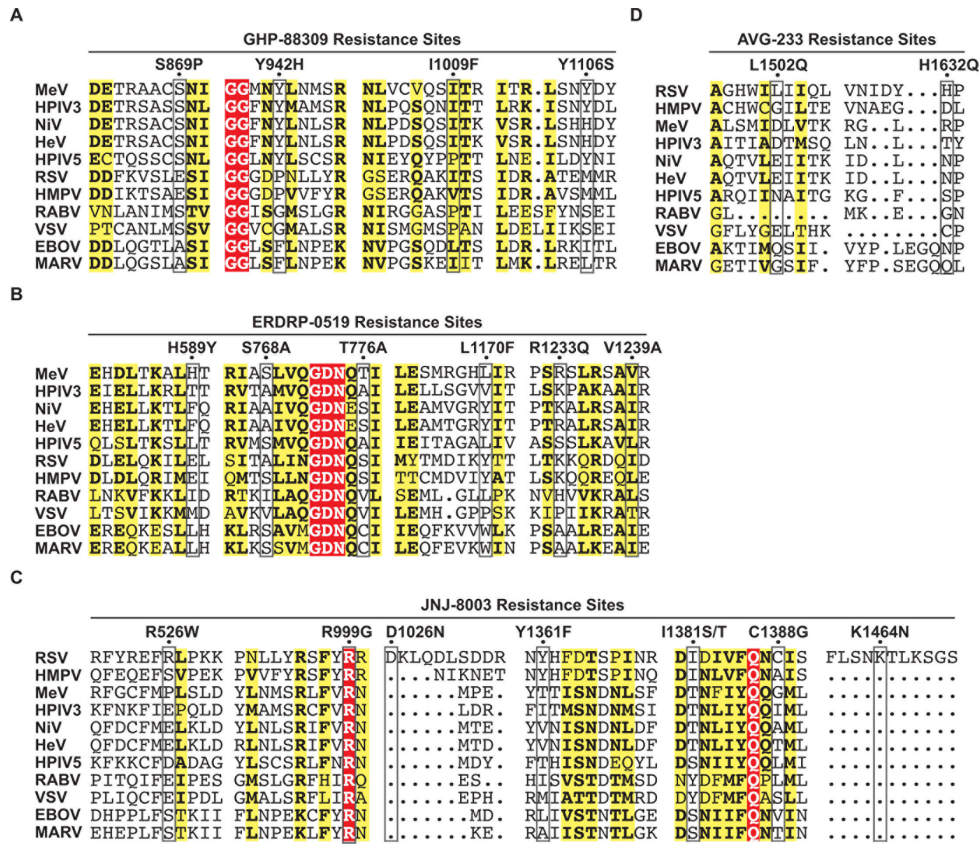
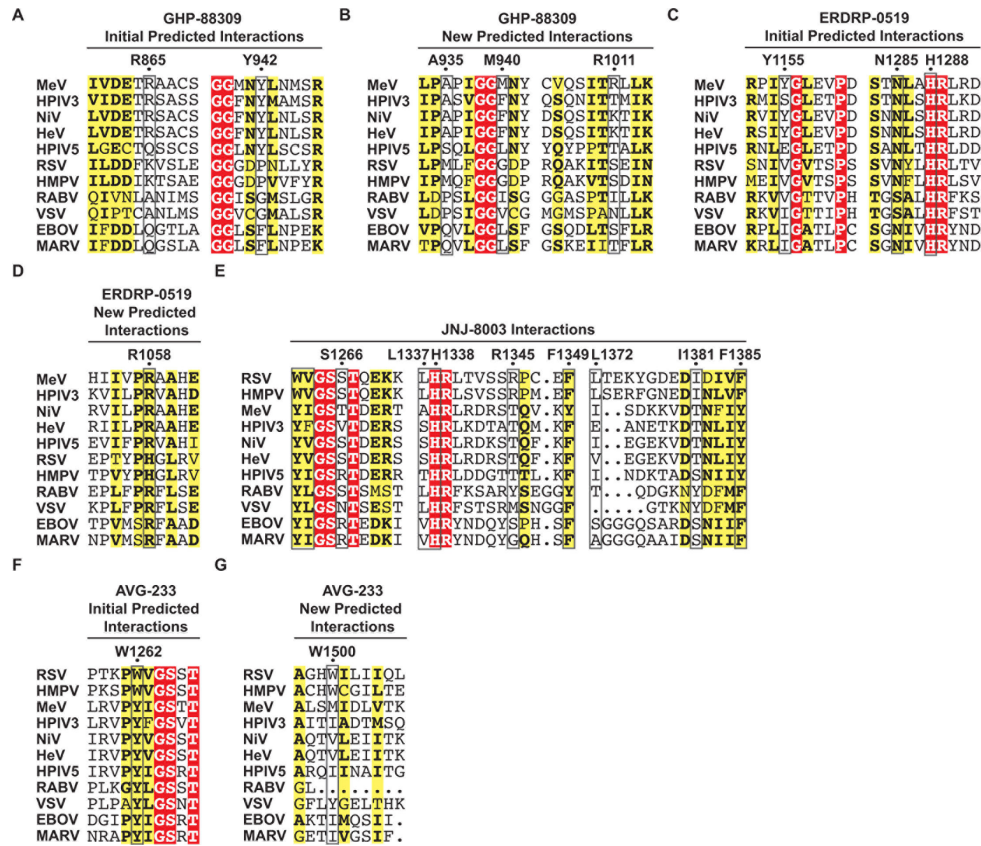


FIG 9 GHP-88309, ERDRP-0519, JNJ-8003, and AVG-233 sequence identity analysis of resistance sites. Resistance profile alignments of (A) GHP-88309, (B) ERDRP-0519, (C) JNJ-8003, and (D) AVG-233. High sequence identity (highlighted red and bold). Partial sequence identity (highlighted yellow and bold). Sequences alignments: MeV (NP\_056924), HPIV3 (AXU38775), NiV (ACT32616), HeV (APT69531), HPIV5 (YP138518), RSV (YP\_009518860), HMPV (AAQ67700), RABV (ABN11300), VSV (UTK57347), EBOV (AHX24663), Marburg virus; MARV (ABA87130).



**FIG 10** GHP-88309, ERDRP-0519, JNJ-8003, and AVG-233 sequence identity analysis of predicted interacting residues. (A) MeV L residues originally predicted to interact with GHP-88309 and (B) new predicted interactions based on docking into MeV L in an initiation conformation. (C) Residues of MeV L originally predicted to interact with ERDRP-0519 and (D) new predicted interactions based on docking into MeV L in a pre-initiation conformation. (E) RSV L residues that were identified to interact with JNJ-8003 in the cryo-EM structure. (F) Original predicted RSV L residue interactions with AVG-233 and (G) new predicted interactions based on docking into RSV L in an initiation conformation. Residues that are both a site of resistance and prediction interaction or are both an original and new predicted site of interaction for a given compound are not shown twice. High sequence identity (highlighted red and bold). Partial sequence identity (highlighted yellow and bold). Sequence alignments: MeV (NP\_056924), HPIV3 (AXU38775), NiV (ACT32616), HeV (APT69531), HPIV5 (YP138518), RSV (YP\_009518860), HMPV (AAQ67700), RABV (ABN11300), VSV (UTK57347), EBOV (AHX24663), Marburg virus; MARV (ABA87130).

compounds suggests that some druggable sites may be conserved across polymerases of the mononegavirus families.

## CONCLUSIONS

Groundbreaking progress has been made in the last decade toward the structural understanding of mononegavirus polymerase complexes. However, a paucity of fully resolved L protein structures in different conformational stages still hampers the complete molecular understanding of polymerase function and regulation. Ample precedent supports the use of chemical and biological probes to advance structural knowledge through the stabilization of flexible protein domains and physiologically short-lived conformational intermediates. For instance, antibodies and nanobodies (77) have been used successfully as structural stabilizers that allowed for the analysis of



## Minireview

## Antimicrobial Agents and Chemotherapy

proteins such as a beta2-adrenergic receptor (78), interphotoreceptor retinoid-binding protein (79), the antitoxin MazE (80), the SecY protein-translocation channel (81), the solute carrier 11 transporter (82), and the human M2 muscarinic acetylcholine receptor (83).

The high-resolution cryo-EM structure of the RSV L-P complex with JNJ-8003 bound provides proof-of-concept that a small-molecule inhibitor can be used to stabilize the conformation of a mononegavirus polymerase. JNJ-8003 stabilized the RSV polymerase and allowed for the first-time visualization of a novel pocket surrounding the HR motif, which is hypothesized to play an essential role in capping, that has not been observed in the apo RSV, HMPV, or VSV polymerase structures (55). Although full resolution of the RSV L-P complex could not be achieved with JNJ-8003, it is tantalizing to speculate that complete resolution may be achievable when a second probe with a distinct target site, such as AVG-233, is used.

Well-validated and -behaved small-molecule viral polymerase inhibitors with high binding affinity and distinct target sites (Fig. 11A through C) have great potential to improve the resolution of flexible domains in the paramyxovirus and pneumovirus L proteins and reveal transient conformational stages. The resulting deepened knowledge into the organization and regulation of the RdRP complex may pave the path toward future synthetic optimization of drug-binding affinity and, potentially,

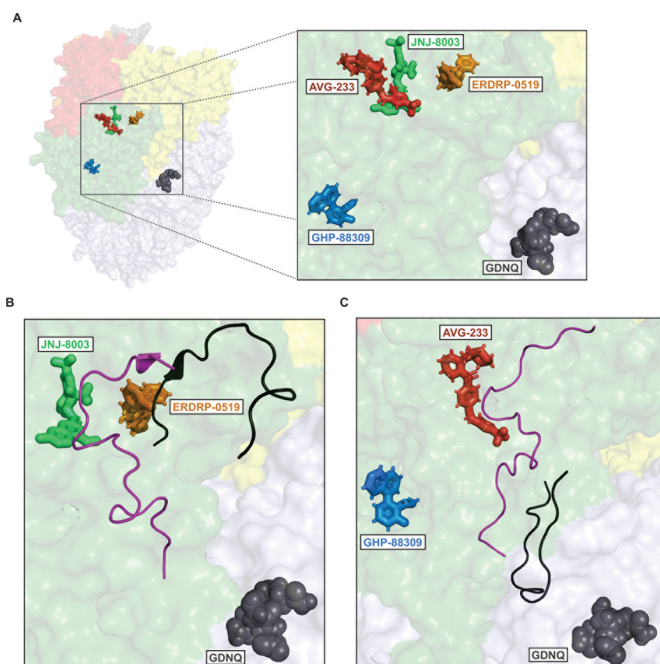


**FIG 11** Distinct binding sites of GHP-88309, ERDRP-0519, AVG-233, and JNJ-8003 in the mononegavirus polymerase. (A) *In silico* predicted binding sites of GHP-88309, ERDRP-0519, and AVG-233 and the structure-informed target site of JNJ-8003 in a polymerase model generated using MeV L-based PIV5 coordinates (PDB: 6v86). Close-up view of compounds predicted to target the polymerase when the priming and intrusion loops are extended away from the active site, either in a pre-initiation or elongation-1/3 stage (B), and in an initiation (C) conformation, modeled based on RSV P-L-RNA (PDB: 8snx) and VSV P-L (PDB: 5a22), respectively. GHP-88309 (blue), ERDRP-0519 (orange), AVG-233 (red), JNJ-8003 (green), RdRP (light blue), PRNTase (forest green), connector (yellow), MTase (orange), CTD (red), GDN (gray spheres), priming loop (black), intrusion loop (magenta).

## Minireview

## Antimicrobial Agents and Chemotherapy

support structure-guided target hopping toward related members of the paramyxo- or pneumovirus families, or other pathogens in the mononegavirus order, currently not inhibited by advanced experimental therapeutics and clinical candidates. This notion is supported by the tight clustering of the binding sites of these compounds in areas of overall high sequence conservation, suggesting docking to conserved microdomains that may be druggable in different virus families within the mononegavirus order. As more chemically diverse inhibitor classes are identified and mechanistically characterized for different mononegaviruses, a comprehensive map of druggable targets in the mononegavirus L protein may come into view that has the potential to serve as a blueprint for accelerated drug development against newly emerging mononegaviruses of pandemic threat. Although *in silico* drug discovery has yet to deliver proof-of-concept, recent advances in artificial intelligence (AI) assisted *in silico* drug design (84, 85) may accelerate future hit identification and lead development.

## ACKNOWLEDGMENTS

This work was supported, in part, by public health service grants AI171403 (to R.K.P.), AI153400 (to R.K.P.), AI141222 (to R.K.P.), and AI071002 (to R.K.P.).

## AUTHOR AFFILIATION

<sup>1</sup>Center for Translational Antiviral Research, Georgia State University Institute for Biomedical Sciences, Atlanta, Georgia, USA

## AUTHOR ORCIDS

Richard K. Plemper  <http://orcid.org/0000-0003-2034-2107>

## FUNDING

Funder	Grant(s)	Author(s)
HHS   NIH   National Institute of Allergy and Infectious Diseases (NIAID)	AI171403, AI153400, AI141222, AI071002	Richard K. Plemper

## AUTHOR CONTRIBUTIONS

Josef D. Wolf, Conceptualization, Writing – original draft | Michael R. Serrine, Visualization, Writing – original draft | Robert M. Cox, Visualization, Writing – review and editing | Richard K. Plemper, Conceptualization, Project administration, Supervision, Writing – original draft, Writing – review and editing

## REFERENCES

- Kuhn JH, Abe J, Adkins S, Alkhovsky SV, Avšič-Županc T, Ayllón MA, Bahl J, Balkema-Buschmann A, Ballinger MJ, Kumar Baranwal V, et al. 2023. Annual (2023) taxonomic update of RNA-directed RNA polymerase-encoding negative-sense RNA viruses (realm *Riboviria*: kingdom *Orthornavirae*: phylum *Negarnaviricota*). *J Gen Virol* 104:001864. <https://doi.org/10.1099/jgv.0.001864>
- Plemper RK, Hammond AL. 2014. Synergizing vaccinations with therapeutics for measles eradication. *Expert Opin Drug Discov* 9:201–214. <https://doi.org/10.1517/17460441.2014.867324>
- Plemper RK. 2020. Measles resurgence and drug development. *Curr Opin Virol* 41:8–17. <https://doi.org/10.1016/j.coviro.2020.02.007>
- WHO. 2020. Worldwide measles deaths climb 50% from 2016 to 2019 claiming over 207 500 lives in 2019. World Health Organization. Available from: <https://www.who.int/news/item/12-11-2020-worldwide-measles-deaths-climb-50-from-2016-to-2019-claiming-over-207-500-lives-in-2019>. Retrieved 21 Feb 2022.
- Olsen LF, Truty GL, Schaffer WM. 1988. Oscillations and chaos in epidemics: a nonlinear dynamic study of six childhood diseases in Copenhagen, Denmark. *Theor Popul Biol* 33:344–370. [https://doi.org/10.1016/0040-5809\(88\)90019-6](https://doi.org/10.1016/0040-5809(88)90019-6)
- WHO. 2019. Measles. World Health Organization. Available from: <https://www.who.int/news-room/fact-sheets/detail/measles>. Retrieved 21 Feb 2022.
- Vakrilova L, Nikolova SH, Slavov S, Radulova P, Slancheva B. 2021. An outbreak of RSV infections in a neonatology clinic during the RSV-season. *BMC Pediatr* 21:567. <https://doi.org/10.1186/s12887-021-03053-9>
- Li Y, Wang X, Blau DM, Caballero MT, Feikin DR, Gill CJ, Madhi SA, Omer SB, Simões EAF, Campbell H, et al. 2022. Global, regional, and national disease burden estimates of acute lower respiratory infections due to respiratory syncytial virus in children younger than 5 years in 2019: a systematic analysis. *Lancet* 399:2047–2064. [https://doi.org/10.1016/S0140-6736\(22\)00478-0](https://doi.org/10.1016/S0140-6736(22)00478-0)

9. FDA. 2023. Respiratory Syncytial Virus (RSV). Available from: <https://www.fda.gov/consumers/covid-19-flu-and-rsv/respiratory-syncytial-virus-rsv>. Retrieved 28 May 2024.
10. FDA. 2024. MRESVIA. Available from: <https://www.fda.gov/vaccines-blood-biologics/vaccines/mresvia>. Retrieved 26 Jul 2024.
11. FDA. 2024. AREXVY. Available from: <https://www.fda.gov/vaccines-blood-biologics/arexvy>. Retrieved 26 Jul 2024.
12. Boytchev H. 2023. FDA advisers back Pfizer's maternal RSV vaccine after voicing safety concerns. *BMJ* 381:1187. <https://doi.org/10.1136/bmj.p1187>
13. Wang X, Li Y, Deloria-Knoll M, Madhi SA, Cohen C, Arguelles VL, Basnet S, Bassat Q, Brooks WA, Echavarría M, et al. 2021. Global burden of acute lower respiratory infection associated with human parainfluenza virus in children younger than 5 years for 2018: a systematic review and meta-analysis. *Lancet Glob Health* 9:e1077–e1087. [https://doi.org/10.1016/S2214-109X\(21\)00218-7](https://doi.org/10.1016/S2214-109X(21)00218-7)
14. WHO. 2018. WHO research and development blueprint: 2018 annual review of diseases prioritized under the research and development blueprint. World Health Organization. Available from: <https://www.who.int/news-room/events/detail/2018/02/06/default-calendar/2018-annual-review-of-diseases-prioritized-under-the-research-and-development-blueprint>. Retrieved 24 Jul 2024.
15. Skowron K, Bauza-Kaszewska J, Grudlewska-Buda K, Wiktorczyk-Kapischke N, Zacharski M, Bernaciak Z, Gospodarek-Komkowska E. 2021. Nipah virus—another threat from the world of zoonotic viruses. *Front Microbiol* 12:811157. <https://doi.org/10.3389/fmicb.2021.811157>
16. Picarazzi F, Vicenti I, Saladini F, Zazzi M, Mori M. 2020. Targeting the RdRp of emerging RNA viruses: the structure-based drug design challenge. *Molecules* 25:5695. <https://doi.org/10.3390/molecules25235695>
17. Te Velthuis AJW, Grimes JM, Fodor E. 2021. Structural insights into RNA polymerases of negative-sense RNA viruses. *Nat Rev Microbiol* 19:303–318. <https://doi.org/10.1038/s41579-020-00501-8>
18. Sourimant J, Plemper RK. 2016. Organization, function, and therapeutic targeting of the Morbillivirus RNA-dependent RNA polymerase complex. *Viruses* 8:251. <https://doi.org/10.3390/v8090251>
19. Fearn R, Plemper RK. 2017. Polymerases of paramyxoviruses and pneumoviruses. *Virus Res* 234:87–102. <https://doi.org/10.1016/j.virusres.2017.01.008>
20. Du Pont V, Jiang Y, Plemper RK. 2019. Bipartite interface of the measles virus phosphoprotein X domain with the large polymerase protein regulates viral polymerase dynamics. *PLoS Pathog* 15:e1007995. <https://doi.org/10.1371/journal.ppat.1007995>
21. Sutto-Ortiz P, Tcherniuk S, Ysebaert N, Abeywickrema P, Noël M, Decombe A, Debart F, Vasseur JJ, Canard B, Roymans D, Rigaux P, Eléouët JF, Decroly E. 2021. The methyltransferase domain of the respiratory syncytial virus L protein catalyzes cap N7 and 2'-O-methylation. *PLoS Pathog* 17:e1009562. <https://doi.org/10.1371/journal.ppat.1009562>
22. Ogino T, Green TJ. 2019. RNA synthesis and capping by non-segmented negative strand RNA viral polymerases: lessons from a prototypic virus. *Front Microbiol* 10:1490. <https://doi.org/10.3389/fmicb.2019.01490>
23. O'Reilly EK, Kao CC. 1998. Analysis of RNA-dependent RNA polymerase structure and function as guided by known polymerase structures and computer predictions of secondary structure. *Virology (Auckl)* 252:287–303. <https://doi.org/10.1006/viro.1998.9463>
24. Jordan PC, Liu C, Raynaud P, Lo MK, Spiropoulou CF, Symons JA, Beigelman L, Deval J. 2018. Initiation, extension, and termination of RNA synthesis by a paramyxovirus polymerase. *PLoS Pathog* 14:e1006889. <https://doi.org/10.1371/journal.ppat.1006889>
25. Dochow M, Krumm SA, Crowe JE, Moore ML, Plemper RK. 2012. Independent structural domains in paramyxovirus polymerase protein. *J Biol Chem* 287:6878–6891. <https://doi.org/10.1074/jbc.M111.325258>
26. Cong J, Feng X, Kang H, Fu W, Wang L, Wang C, Li X, Chen Y, Rao Z. 2023. Structure of the Newcastle disease virus L protein in complex with tetrameric phosphoprotein. *Nat Commun* 14:1324. <https://doi.org/10.1038/s41467-023-37012-y>
27. Sourimant J, Lieber CM, Yoon J-J, Toots M, Govindarajan M, Udumula V, Sakamoto K, Natchus MG, Patti J, Vernachio J, Plemper RK. 2022. Orally efficacious lead of the AVG inhibitor series targeting a dynamic interface in the respiratory syncytial virus polymerase. *Sci Adv* 8:eabo2236. <https://doi.org/10.1126/sciadv.abo2236>
28. Cox RM, Sourimant J, Govindarajan M, Natchus MG, Plemper RK. 2021. Therapeutic targeting of measles virus polymerase with ERDRP-0519 suppresses all RNA synthesis activity. *PLoS Pathog* 17:e1009371. <https://doi.org/10.1371/journal.ppat.1009371>
29. White LK, Yoon JJ, Lee JK, Sun A, Du Y, Fu H, Snyder JP, Plemper RK. 2007. Nonnucleoside inhibitor of measles virus RNA-dependent RNA polymerase complex activity. *Antimicrob Agents Chemother* 51:2293–2303. <https://doi.org/10.1128/AAC.00289-07>
30. Pan J, Qian X, Lattmann S, El Sahili A, Yeo TH, Jia H, Cressey T, Ludeke B, Noton S, Kalocsay M, Fearn R, Lescar J. 2020. Structure of the human metapneumovirus polymerase phosphoprotein complex. *Nat New Biol* 577:275–279. <https://doi.org/10.1038/s41586-019-1759-1>
31. Liang B, Li Z, Jenni S, Rahmeh AA, Morin BM, Grant T, Grigorieff N, Harrison SC, Whelan SPJ. 2015. Structure of the L protein of vesicular stomatitis virus from electron cryomicroscopy. *Cell* 162:314–327. <https://doi.org/10.1016/j.cell.2015.06.018>
32. Horwitz JA, Jenni S, Harrison SC, Whelan SPJ. 2020. Structure of a rabies virus polymerase complex from electron cryo-microscopy. *Proc Natl Acad Sci U S A* 117:2099–2107. <https://doi.org/10.1073/pnas.1918809117>
33. Gilman MSA, Liu C, Fung A, Behera I, Jordan P, Rigaux P, Ysebaert N, Tcherniuk S, Sourimant J, Eléouët JF, Sutto-Ortiz P, Decroly E, Roymans D, Jin Z, McLellan JS. 2019. Structure of the respiratory syncytial virus polymerase complex. *Cell* 179:193–204. <https://doi.org/10.1016/j.cell.2019.08.014>
34. Abdella R, Aggarwal M, Okura T, Lamb RA, He Y. 2020. Structure of a paramyxovirus polymerase complex reveals a unique methyltransferase-CTD conformation. *Proc Natl Acad Sci U S A* 117:4931–4941. <https://doi.org/10.1073/pnas.1919837117>
35. Xie J, Ouizougou-Oubari M, Wang L, Zhai G, Wu D, Lin Z, Wang M, Ludeke B, Yan X, Nilsson T, Gao L, Huang X, Fearn R, Chen S. 2024. Structural basis for dimerization of a paramyxovirus polymerase complex. *Nat Commun* 15:3163. <https://doi.org/10.1038/s41467-024-47470-7>
36. Li T, Liu M, Gu Z, Su X, Liu Y, Lin J, Zhang Y, Shen QT. 2024. Structures of the mumps virus polymerase complex via cryo-electron microscopy. *Nat Commun* 15:4189. <https://doi.org/10.1038/s41467-024-48389-9>
37. Cao D, Gao Y, Chen Z, Gooneratne I, Roesler C, Mera C, D' Cunha P, Antonova A, Katta D, Romanelli S, Wang Q, Rice S, Lemons W, Ramanathan A, Liang B. 2024. Structures of the promoter-bound respiratory syncytial virus polymerase. *Nature New Biol* 625:611–617. <https://doi.org/10.1038/s41586-023-06867-y>
38. Peng Q, Yuan B, Cheng J, Wang M, Gao S, Bai S, Zhao X, Qi J, Gao GF, Shi Y. 2023. Molecular mechanism of *de novo* replication by the Ebola virus polymerase. *Nature New Biol* 622:603–610. <https://doi.org/10.1038/s41586-023-06608-1>
39. Valle C, Martin B, Debart F, Vasseur JJ, Imbert I, Canard B, Coutard B, Decroly E. 2020. The C-terminal domain of the Sudan ebolavirus L protein is essential for RNA binding and methylation. *J Virol* 94:e00520-20. <https://doi.org/10.1128/JVI.00520-20>
40. Neubauer J, Ogino M, Green TJ, Ogino T. 2016. Signature motifs of GDP polyribonucleotidyltransferase, a non-segmented negative strand RNA viral mRNA capping enzyme, domain in the L protein are required for covalent enzyme-pRNA intermediate formation. *Nucleic Acids Res* 44:330–341. <https://doi.org/10.1093/nar/gkv1286>
41. Noton SL, Fearn R. 2015. Initiation and regulation of paramyxovirus transcription and replication. *Virology (Auckl)* 479–480:545–554. <https://doi.org/10.1016/j.virol.2015.01.014>
42. Yuan B, Peng Q, Cheng J, Wang M, Zhong J, Qi J, Gao GF, Shi Y. 2022. Structure of the Ebola virus polymerase complex. *Nature New Biol* 610:394–401. <https://doi.org/10.1038/s41586-022-05271-2>
43. Noton SL, Nagendra K, Dunn EF, Mawhorter ME, Yu Q, Fearn R. 2015. Respiratory syncytial virus inhibitor AZ-27 differentially inhibits different polymerase activities at the promoter. *J Virol* 89:7786–7798. <https://doi.org/10.1128/JVI.00530-15>
44. Noton SL, Tremaglio CZ, Fearn R. 2019. Killing two birds with one stone: how the respiratory syncytial virus polymerase initiates transcription and replication. *PLoS Pathog* 15:e1007548. <https://doi.org/10.1371/journal.ppat.1007548>



45. Tremaglio CZ, Noton SL, Deflubé LR, Fearn R. 2013. Respiratory syncytial virus polymerase can initiate transcription from position 3 of the leader promoter. *J Virol* 87:3196–3207. <https://doi.org/10.1128/JVI.02862-12>
46. Leppert M, Rittenhouse L, Perrault J, Summers DF, Kolakofsky D. 1979. Plus and minus strand leader RNAs in negative strand virus-infected cells. *Cell* 18:735–747. [https://doi.org/10.1016/0092-8674\(79\)90127-2](https://doi.org/10.1016/0092-8674(79)90127-2)
47. Kurilla MG, Stone HO, Keene JD. 1985. RNA sequence and transcriptional properties of the 3' end of the Newcastle disease virus genome. *Virology* (Auckl) 145:203–212. [https://doi.org/10.1016/0042-6822\(85\)90154-0](https://doi.org/10.1016/0042-6822(85)90154-0)
48. Horikami SM, Moyer SA. 1991. Synthesis of leader RNA and editing of the P mRNA during transcription by purified measles virus. *J Virol* 65:5342–5347. <https://doi.org/10.1128/JVI.65.10.5342-5347.1991>
49. Hoffman MA, Banerjee AK. 2000. Precise mapping of the replication and transcription promoters of human parainfluenza virus type 3. *Virology* (Auckl) 269:201–211. <https://doi.org/10.1006/viro.2000.0223>
50. Ghosh A, Nayak R, Shaila MS. 1996. Synthesis of leader RNA and editing of P mRNA during transcription by rinderpest virus. *Virus Res* 41:69–76. [https://doi.org/10.1016/0168-1702\(95\)01276-1](https://doi.org/10.1016/0168-1702(95)01276-1)
51. Cowton VM, Fearn R. 2005. Evidence that the respiratory syncytial virus polymerase is recruited to nucleotides 1 to 11 at the 3' end of the nucleocapsid and can scan to access internal signals. *J Virol* 79:11311–11322. <https://doi.org/10.1128/JVI.79.17.11311-11322.2005>
52. Cattaneo R, Rebmann G, Schmid A, Baczkó K, ter Meulen V, Billette MA. 1987. Altered transcription of a defective measles virus genome derived from a diseased human brain. *EMBO J* 6:681–688. <https://doi.org/10.1002/j.1460-2075.1987.tb04808.x>
53. Blumberg BM, Leppert M, Kolakofsky D. 1981. Interaction of VSV leader RNA and nucleocapsid protein may control VSV genome replication. *Cell* 23:837–845. [https://doi.org/10.1016/0092-8674\(81\)90448-7](https://doi.org/10.1016/0092-8674(81)90448-7)
54. Ogino T, Banerjee AK. 2011. An unconventional pathway of mRNA cap formation by vesiculoviruses. *Virus Res* 162:100–109. <https://doi.org/10.1016/j.virusres.2011.09.012>
55. Yu X, Abeywickrema P, Bonneux B, Behera I, Anson B, Jacoby E, Fung A, Adhikary S, Bhaumik A, Carbajo RJ, et al. 2023. Structural and mechanistic insights into the inhibition of respiratory syncytial virus polymerase by a non-nucleoside inhibitor. *Commun Biol* 6:1074. <https://doi.org/10.1038/s42003-023-05451-4>
56. Cox RM, Sourimant J, Toots M, Yoon J-J, Ikegame S, Govindarajan M, Watkinson RE, Thibault P, Makhosou N, Lin MJ, Marengo JR, Sticher Z, Kolykhalov AA, Natchus MG, Greninger AL, Lee B, Plemper RK. 2020. Orally efficacious broad-spectrum allosteric inhibitor of paramyxovirus polymerase. *Nat Microbiol* 5:1232–1246. <https://doi.org/10.1038/s41564-020-0752-7>
57. Wittwer K, Anderson DE, Pfeiffermann K, Cox RM, Wolf JD, Santibanez S, Mankertz A, Plesker R, Sticher ZM, Kolykhalov AA, Natchus MG, Pfaller CK, Plemper RK, von Messling V. 2021. Small-molecule polymerase inhibitor protects non-human primates from measles and reduces shedding. *Nat Commun* 12:5233. <https://doi.org/10.1038/s41467-021-25497-4>
58. Ndungu JM, Krumm SA, Yan D, Arrendale RF, Reddy GP, Evers T, Howard R, Natchus MG, Saindane MT, Liotta DC, Plemper RK, Snyder JP, Sun A. 2012. Non-nucleoside inhibitors of the measles virus RNA-dependent RNA polymerase: synthesis, structure-activity relationships, and pharmacokinetics. *J Med Chem* 55:4220–4230. <https://doi.org/10.1021/jm201699w>
59. Yoon JJ, Krumm SA, Ndungu JM, Hoffman V, Bankamp B, Rota PA, Sun A, Snyder JP, Plemper RK. 2009. Target analysis of the experimental measles therapeutic AS-136A. *Antimicrob Agents Chemother* 53:3860–3870. <https://doi.org/10.1128/AAC.00503-09>
60. Tiong-Yip CL, Aschenbrenner L, Johnson KD, McLaughlin RE, Fan J, Challa S, Xiong H, Yu Q. 2014. Characterization of a respiratory syncytial virus L protein inhibitor. *Antimicrob Agents Chemother* 58:3867–3873. <https://doi.org/10.1128/AAC.02540-14>
61. Deval J, Fung A, Stevens SK, Jordan PC, Gromova T, Taylor JS, Hong J, Meng J, Wang G, Dyatkina N, Prhacv M, Symons JA, Beigelman L. 2016. Biochemical effect of resistance mutations against synergistic inhibitors of RSV RNA polymerase. *PLoS One* 11:e0154097. <https://doi.org/10.1371/journal.pone.0154097>
62. Liuzzi M, Mason SW, Cartier M, Lawetz C, McCollum RS, Dansereau N, Bolger G, Lapeyre N, Gaudette Y, Lagacé L, Massariol M-J, Dô F, Whitehead P, Lamarre L, Scouten E, Bordeleau J, Landry S, Rancourt J, Fazal G, Simoneau B. 2005. Inhibitors of respiratory syncytial virus replication target cotranscriptional mRNA guanylation by viral RNA-dependent RNA polymerase. *J Virol* 79:13105–13115. <https://doi.org/10.1128/JVI.79.20.13105-13115.2005>
63. McCutcheon KM, Jordan R, Mawhorter ME, Noton SL, Powers JG, Fearn R, Cihlar T, Perron M. 2016. The interferon type I/III response to respiratory syncytial virus infection in airway epithelial cells can be attenuated or amplified by antiviral treatment. *J Virol* 90:1705–1717. <https://doi.org/10.1128/JVI.02417-15>
64. Duvall JR, VerPlank L, Ludeke B, McLeod SM, Lee MD IV, Vishwanathan K, Mulrooney CA, Le Quement S, Yu Q, Palmer MA, Fleming P, Fearn R, Foley MA, Scherer CA. 2016. Novel diversity-oriented synthesis-derived respiratory syncytial virus inhibitors identified via a high throughput replicon-based screen. *Antiviral Res* 131:19–25. <https://doi.org/10.1016/j.antiviral.2016.03.015>
65. Laganas VA, Dunn EF, McLaughlin RE, Tiong-Yip CL, Yuzhakov O, Isabella VM, Hill P, Yu Q. 2015. Characterization of novel respiratory syncytial virus inhibitors identified by high throughput screen. *Antiviral Res* 115:71–74. <https://doi.org/10.1016/j.antiviral.2014.12.012>
66. Coates M, Brookes D, Kim YI, Allen H, Fordyce EAF, Meals EA, Colley T, Ciana CL, Parra GF, Sherbukhin V, Stockwell JA, Thomas JC, Hunt SF, Anderson-Dring L, Onions ST, Cass L, Murray PJ, Ito K, Strong P, DeVincenzo JP, Rapeport G. 2017. Preclinical characterization of PC786, an inhaled small-molecule respiratory syncytial virus L protein polymerase inhibitor. *Antimicrob Agents Chemother* 61:e00737-17. <https://doi.org/10.1128/AAC.00737-17>
67. Brookes DW, Coates M, Allen H, Daly L, Constant S, Huang S, Hows M, Davis A, Cass L, Ayrton J, Knowles I, Strong P, Rapeport G, Ito K. 2018. Late therapeutic intervention with a respiratory syncytial virus L-protein polymerase inhibitor, PC786, on respiratory syncytial virus infection in human airway epithelium. *Br J Pharmacol* 175:2520–2534. <https://doi.org/10.1111/bph.14221>
68. Wang L, Zhu Q, Xiang K, Zhang Y, Li B, Yu X, Yang G, Liang C, Yun H, Zhang M, Qin N, Gao L. 2021. Discovery of a novel respiratory syncytial virus replication inhibitor. *Antimicrob Agents Chemother* 65:e02576-20. <https://doi.org/10.1128/AAC.02576-20>
69. Sudo K, Miyazaki Y, Kojima N, Kobayashi M, Suzuki H, Shintani M, Shimizu Y. 2005. YM-53403, a unique anti-respiratory syncytial virus agent with a novel mechanism of action. *Antiviral Res* 65:125–131. <https://doi.org/10.1016/j.antiviral.2004.12.002>
70. Haas GD, Schmitz KS, Azarm KD, Johnson KN, Klain WR, Freiberg AN, Cox RM, Plemper RK, Lee B. 2024. Tetracistronic minigenomes elucidate a functional promoter for Ghana virus and unveils cedar virus replicase promiscuity for all henipaviruses. *bioRxiv:2024.04.16.589704*. <https://doi.org/10.1101/2024.04.16.589704>
71. Cox RM, Wolf JD, Lieberman NA, Lieber CM, Kang H-J, Sticher ZM, Yoon J-J, Andrews MK, Govindarajan M, Krueger RE, Sobolik EB, Natchus MG, Gewirtz AT, deSwart RL, Kolykhalov AA, Hekmatyar K, Sakamoto K, Greninger AL, Plemper RK. 2024. Therapeutic mitigation of measles-like immune amnesia and exacerbated disease after prior respiratory virus infections in ferrets. *Nat Commun* 15:1189. <https://doi.org/10.1038/s41467-024-45418-5>
72. Cox RM, Toots M, Yoon JJ, Sourimant J, Ludeke B, Fearn R, Bourque E, Patti J, Lee E, Vernachio J, Plemper RK. 2018. Development of an allosteric inhibitor class blocking RNA elongation by the respiratory syncytial virus polymerase complex. *J Biol Chem* 293:16761–16777. <https://doi.org/10.1074/jbc.RA118.004862>
73. Krumm SA, Yan D, Hovingh ES, Evers TJ, Enkirch T, Reddy GP, Sun A, Saindane MT, Arrendale RF, Painter G, Liotta DC, Natchus MG, von Messling V, Plemper RK. 2014. An orally available, small-molecule polymerase inhibitor shows efficacy against a lethal morbillivirus infection in a large animal model. *Sci Transl Med* 6:232ra52. <https://doi.org/10.1126/scitranslmed.3008517>
74. Noton SL, Aljabr W, Hiscox JA, Matthews DA, Fearn R. 2014. Factors affecting *de novo* RNA synthesis and back-priming by the respiratory syncytial virus polymerase. *Virology* (Auckl) 462–463:318–327. <https://doi.org/10.1016/j.virol.2014.05.032>
75. Cao D, Gooneratne I, Mera C, Vy J, Royal M, Huang B, Park Y, Manjunath A, Liang B. 2022. Analysis of template variations on RNA synthesis by respiratory syncytial virus polymerase. *Viruses* 15:47. <https://doi.org/10.3390/v15010047>

76. Cressey TN, Shareef AM, Kleiner VA, Noton SL, Byrne PO, McLellan JS, Mühlberger E, Fearn R. 2022. Distinctive features of the respiratory syncytial virus priming loop compared to other non-segmented negative strand RNA viruses. *PLoS Pathog* 18:e1010451. <https://doi.org/10.1371/journal.ppat.1010451>
77. Manglik A, Kobilka BK, Steyaert J. 2017. Nanobodies to study G protein-coupled receptor structure and function. *Annu Rev Pharmacol Toxicol* 57:19–37. <https://doi.org/10.1146/annurev-pharmtox-010716-104710>
78. Steyaert J, Kobilka BK. 2011. Nanobody stabilization of G protein-coupled receptor conformational states. *Curr Opin Struct Biol* 21:567–572. <https://doi.org/10.1016/j.sbi.2011.06.011>
79. Sears AE, Albiez S, Gulati S, Wang B, Kiser P, Kovacic L, Engel A, Stahlberg H, Palczewski K. 2020. Single particle cryo-EM of the complex between interphotoreceptor retinoid-binding protein and a monoclonal antibody. *FASEB J* 34:13918–13934. <https://doi.org/10.1096/fj.202000796RR>
80. Loris R, Marianovsky I, Lah J, Laeremans T, Engelberg-Kulka H, Glaser G, Muyldermans S, Wyns L. 2003. Crystal structure of the intrinsically flexible addiction antidote MazE. *J Biol Chem* 278:28252–28257. <https://doi.org/10.1074/jbc.M302336200>
81. Li L, Park E, Ling J, Ingram J, Ploegh H, Rapoport TA. 2016. Crystal structure of a substrate-engaged SecY protein-translocation channel. *Nature New Biol* 531:395–399. <https://doi.org/10.1038/nature17163>
82. Ehrnstorfer IA, Geertsma ER, Pardon E, Steyaert J, Dutzler R. 2014. Crystal structure of a SLC11 (NRAMP) transporter reveals the basis for transition-metal ion transport. *Nat Struct Mol Biol* 21:990–996. <https://doi.org/10.1038/nsmb.2904>
83. Kruse AC, Ring AM, Manglik A, Hu J, Hu K, Eitel K, Hübner H, Pardon E, Valant C, Sexton PM, Christopoulos A, Felder CC, Gmeiner P, Steyaert J, Weis WI, Garcia KC, Wess J, Kobilka BK. 2013. Activation and allosteric modulation of a muscarinic acetylcholine receptor. *Nature New Biol* 504:101–106. <https://doi.org/10.1038/nature12735>
84. Hekkelman ML, de Vries I, Joosten RP, Perrakis A. 2023. AlphaFill: enriching AlphaFold models with ligands and cofactors. *Nat Methods* 20:205–213. <https://doi.org/10.1038/s41592-022-01685-y>
85. Abramson J, Adler J, Dunger J, Evans R, Green T, Pritzel A, Ronneberger O, Willmore L, Ballard AJ, Bambrick J, et al. 2024. Accurate structure prediction of biomolecular interactions with AlphaFold 3. *Nature New Biol* 630:493–500. <https://doi.org/10.1038/s41586-024-07487-w>

## 2.3 Research Topic: NiV

### 2.3.1 Characterization of the Three-way Interplay Between Nipah Virus Phosphoprotein X-domain, the Polymerase, N-tail, and the N-core



Journal of  
Virology



Virology | Full-Length Text

## A three-way interface of the Nipah virus phosphoprotein X-domain coordinates polymerase movement along the viral genome

Josef D. Wolf,<sup>1</sup> Richard K. Plemper<sup>1</sup>

**AUTHOR AFFILIATION** See affiliation list on p. 15.

**ABSTRACT** Nipah virus (NiV) is a highly pathogenic paramyxovirus causing frequently lethal encephalitis in humans. The NiV genome is encapsidated by the nucleocapsid (N) protein. RNA synthesis is mediated by the viral RNA-dependent RNA polymerase (RdRP), consisting of the polymerase (L) protein complexed with the homo-tetrameric phosphoprotein (P). The advance of the polymerase along its template requires iterative dissolution and reformation of transient interactions between P and N protomers in a highly regulated process that remains poorly understood. This study applied functional and biochemical NiV polymerase assays to the problem. We mapped three distinct protein interfaces on the C-terminal P-X domain (P-XD), which form a triangular prism and engage L, the C-terminal N tail, and the globular N core, respectively. Transcomplementation assays using NiV L and N-tail binding-deficient mutants revealed that only one XD of a P tetramer binds to L, whereas three must be available for N-binding for efficient polymerase activity. The dissolution of the N-tail complex with P-XD was coordinated by a transient interaction between N-core and the  $\alpha$ -1/2 face of this XD but not unoccupied XDs of the P tetramer, creating a timer for coordinated polymerase advance.

**IMPORTANCE** Mononegaviruses comprise major human pathogens such as the Ebola virus, rabies virus, respiratory syncytial virus, measles virus, and Nipah virus (NiV). For replication and transcription, their polymerase complexes must negotiate a protein-encapsidated RNA genome, which requires the highly coordinated continuous formation and resolution of protein-protein interfaces as the polymerase advances along the template. The viral P protein assumes a central role in this process, but the molecular mechanism of ensuring polymerase mobility is poorly understood. Studying NiV polymerase complexes, we applied functional and biochemical assays to map three distinct interfaces in the NiV P XD and identified transient interactions between XD and the nucleocapsid core as instrumental in coordinating polymerase advance. These results define a conserved molecular principle regulating paramyxovirus polymerase dynamics and illuminate a promising druggable target for the structure-guided development of broad-spectrum polymerase inhibitors.

**KEYWORDS** paramyxovirus, Nipah virus, phosphoprotein, nucleocapsid, polymerase

Nipah virus (NiV) is an emerging zoonotic paramyxovirus in the henipavirus genus that is found primarily in Southeast Asia (1, 2). NiV was first identified in a 1998–1999 outbreak involving farmed pigs and hog farm workers in Malaysia and has since reemerged in nearly yearly outbreaks in other geographical areas, predominantly Bangladesh and India (3–6). Classified as a biosafety level 4 pathogen, NiV causes encephalitis in humans with case fatality rates ranging between 40% and 90% (1, 3, 7, 8).

**Editor** Martin Schwemmler, University Medical Center Freiburg, Freiburg, Germany

Address correspondence to Richard K. Plemper, rplemper@gsu.edu.

The authors declare no conflict of interest.

See the funding table on p. 15.

**Received** 4 June 2024

**Accepted** 7 August 2024

**Published** 4 September 2024

Copyright © 2024 American Society for Microbiology. All Rights Reserved.

Full-Length Text

Journal of Virology

No approved vaccines or antivirals for NiV prophylaxis or disease management currently exist (9, 10), highlighting an urgent unmet medical need that makes the identification of novel druggable target sites a priority.

NiV contains a non-segmented, negative-sense single-stranded RNA genome that consists of approximately 18 kilobases (11, 12). The N protein is composed of two domains, a mostly globular N-core that encapsidates the viral RNA and interacts with neighboring N protomers in the helical ribonucleoprotein (RNP) assembly, and an intrinsically disordered N-tail domain that protrudes from the RNP (13–17). Only encapsidated genomic and antigenomic RNA is recognized by the P-L RNA-dependent RNA polymerase (RdRP) complex as a template for RNA synthesis (13, 18–20). All enzymatic activities reside in the L protein, whereas the P homo-tetramer functions as an obligatory molecular chaperone that ensures proper folding of L and tethers the polymerase to its template through protein-protein interactions with both L and N (20–22).

All paramyxovirus P proteins feature a three-domain architecture, consisting of a structurally largely disordered N-terminal domain (NTD, NiV residues 1–469), an  $\alpha$ -helical oligomerization domain (OD, NiV residues 470–578) (23), and the C-terminal XD (NiV residues 660–709; Fig. 1A). The OD and XD are separated by a disordered flexible linker region (23). The N-terminus of all P proteins can interact with newly synthesized free N proteins, forming N<sup>o</sup>-P complexes that prevent premature N polymerization and/or unproductive random encapsidation of host cell RNAs (24–26). Each XD consists of three short  $\alpha$ -helices that form an antiparallel three-helix bundle, arranged as a triangular prism (27, 28), which serves as a three-way protein-protein interaction interface (Fig. 1B) (22, 29). The face between  $\alpha$ -helices 1 and 3 engages with L through electrostatic, hydrophobic, and hydrogen bond interactions (30). In measles virus (MeV), L binding by XD has been biochemically mapped (22), and L-P structures were solved for parainfluenza virus 5 (PIV5), Newcastle disease virus, parainfluenzavirus type 3, and recently, a partial NiV structure that confirmed contacts between the  $\alpha$ -1/3 face and L near the nucleoside triphosphate (NTP) entry site (30–33). The  $\alpha$ -2/3 face interacts with a molecular recognition element (MoRE) in N-tail, triggering the folding of MoRE into an  $\alpha$ -helix that binds to XD mainly through hydrophobic interactions (28, 34–39). This P-XD N-MoRE interaction must be transient to allow polymerase mobility along the RNP template, requiring continuous dissolution and reengagement with downstream N-MoREs. However, little is known about the molecular regulator that synchronizes resolve of the XD-MoRE interface with polymerase activity.

In contrast to the well-studied  $\alpha$ -1/3 and  $\alpha$ -2/3 faces, the biological role of the third XD side,  $\alpha$ -1/2, is poorly defined. Applying a viral evolution approach to identify candidate binding partners for morbillivirus P-XD  $\alpha$ -1/2, we recently demonstrated an interaction of this face with an acidic loop exposed on the surface of N-core, prompting us to hypothesize that this transient contact triggers the release of MoRE from the XD  $\alpha$ -2/3 face, possibly functioning as the timer for dissolution of the P-XD N-MoRE interaction (29). The resulting iterative binding and release of N-tail by P-XD is thought to ensure polymerase mobility and stabilize the interaction between RdRP and the template, reducing the risk of premature chain termination (40).

In the present study, we have experimentally tested this hypothesis through functional and biochemical mapping of the three distinct interfaces of NiV P-XD. Having identified and mechanistically validated key residues essential to polymerase bioactivity and, P-XD interaction with L, N-MoRE, and N-core, we employed functional transcomplementation assays that revealed that paramyxovirus N-MoRE release from P-XD is triggered by reorganization of the unstructured N-tail and transient contact of the P-XD  $\alpha$ -1/2 face with N-core. These data provide mechanistic insight into the NiV replication machinery, demonstrate that the P-XD faces are functionally conserved across the paramyxovirus family, and highlight a promising druggable target site.

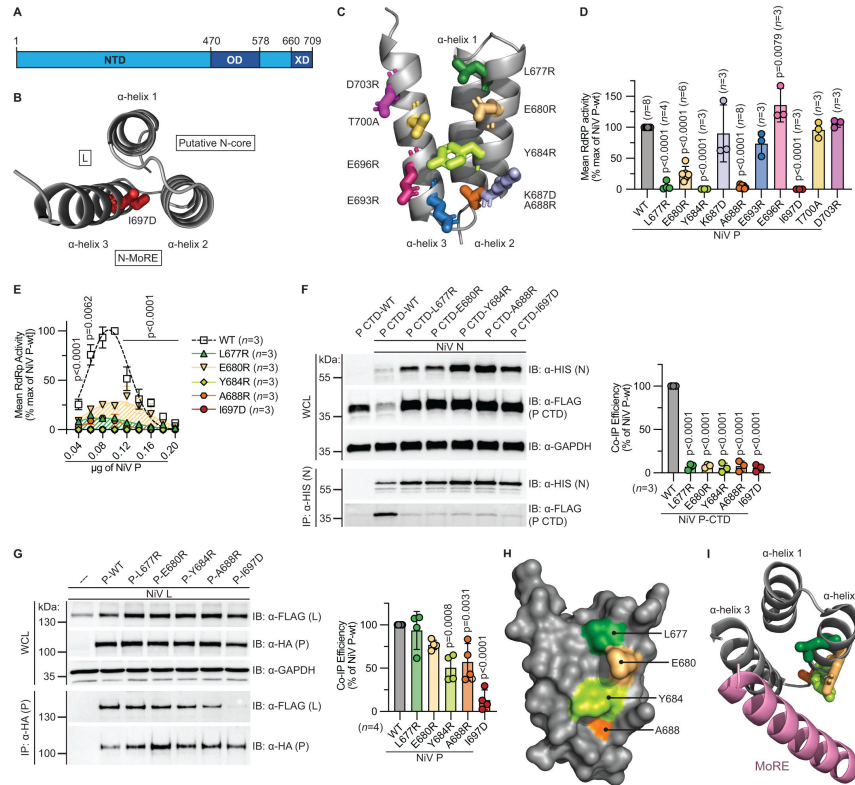


**FIG 1** Probing the N-MoRE binding interface of Niv P-XD. (A) 2D-schematic of Niv P NTD (residues 1–469), OD (residues 470–578); and X domain (XD); residues 660–709). (B) XD forms a triangular prism with two distinct faces that interact with L ( $\alpha$ -1/3 helix) and N-MoRE ( $\alpha$ -2/3 helix), and a third face that is predicted to interact with N-core ( $\alpha$ -1/2 helix). A negative charge was introduced at position 697 (I697D) in the hydrophobic core of XD to disrupt the overall conformation of XD. (C) Localization of all residues subjected to mutagenesis in a homology model of Niv P-XD (PDB: 4heo). Substituted side chains are shown as sticks and color-coded to match minigenome (MG) assay graphs. (D) MG assays of N-MoRE binding-defective candidates. (E) MG activity profiles of Niv P-WT and candidate N-MoRE binding-deficient mutants. Symbols represent means of independent biological repeats ( $n = 3$ ), error bars denoting SD. (F and G) Immunoblots of whole-cell lysates (WCL) and immunoprecipitates (IP) of P-CTD and full-length P mutants predicted to be deficient in N-MoRE binding to Niv N (F) and L (G), respectively. Niv P-CTD, Niv P, and Niv N were detected with specific antibodies directed against the FLAG, HA, and HIS<sub>6</sub> epitopes, respectively. Niv L was FLAG epitope-tagged; glyceraldehyde-3-phosphate dehydrogenase (GAPDH) was used as a loading control. Co-immunoprecipitation (coIP) efficiency was determined by densitometry. (H) Surface homology model of Niv P-XD (PDB: 4heo) showing the location of  $\alpha$ -2 residues that, when mutated, impact polymerase bioactivity and the P:N interaction. (I) Niv P-XD structure showing the spatial orientation of L677, E680, Y684, and A688 in complex with Niv N-MoRE (PDB: 7pno). Niv P-XD (gray) and N-MoRE (pink). Bars represent means of biological repeats  $\pm$  SD, and symbols show individual experiments.  $N$  numbers are shown. Analysis with one-way analysis of variance (ANOVA) with Dunnett's multiple comparisons post-hoc test, comparing mean P mutant bioactivity to that of wild-type P.

## RESULTS

To probe the individual faces of the Niv XD prism biochemically, we identified residues for directed mutagenesis that were predicted to engage in the distinct protein-protein interfaces based on the structure of the Niv P-XD N-MoRE complex (PDB: 7pno) and Niv P-XD L interaction homology models build with the coordinates released for PIV5 (PDB: 6v86) and HeV P-XD (PDB: 4heo). The effect of each candidate mutant on Nipah polymerase bioactivity and P binding efficiency to L or N was evaluated using minigenome (MG) and co-immunoprecipitation (coIP) assays, respectively.

Full-Length Text

Journal of Virology

### Residues in P-XD $\alpha$ -helix 2 are critical for the interaction with N-MoRE

We first generated a series of charge-introducing or reversing mutants in P-XD  $\alpha$ -2 and  $\alpha$ -3 residues that are predicted to affect interaction with N-MoRE (Fig. 1C). MG assays identified three substitutions in P  $\alpha$ -2, L677R, E680R, and Y684R, and one in a loop connecting P  $\alpha$ -2 and  $\alpha$ -3, A688R (38), that completely abolished or greatly reduced bioactivity, respectively (Fig. 1D). Previously, we have demonstrated that introducing a charge within the hydrophobic core of related MeV P-XD alters the global conformation of this domain, eliminating all bioactivity (22). To generate a reference construct with bio-inactive P-XD, we introduced an analogous I697D substitution into the hydrophobic core (Fig. 1B) of NiV XD.

Standard conditions for MG assay were a relative P:N:L plasmid ratio of 1:1:1. To test whether differences in activity are due to different optimal ratios of the mutant plasmids compared to the parental constructs, we generated MG activity profiles testing different relative ratios, ranging from 0.4:1:1 to 2:1:1, of the plasmid encoding wild-type P or the candidate N-MoRE binding-deficient mutants relative to the N- and L-encoding plasmids. Reduction of the relative amount of NiV P plasmid below parity with the N and L plasmids resulted in a steep decline in bioactivity (Fig. 1E), but none of the mutant P plasmids showed a relative activity maximum distinct from that of wild-type P. These results demonstrate that the NiV MG system is highly sensitive to changes in the relative ratios of the helper plasmids. However, reduced bioactivity of the mutant P plasmids tested did not reflect an altered relative ratio activity peak but indicated a true loss of function.

To compare the relative affinity of the different P-XD mutant candidates for N-MoRE, we generated N-terminally truncated P-CTD constructs that were unable to engage N in N<sup>o</sup>P complexes through the interaction of the P N-terminal domain with monomeric N. Each candidate mutant, including the P-I697D control, significantly reduced P:N-MoRE colP efficiency (Fig. 1F; Fig. S1 in Supplementary File 1). Lower signal intensities of unchanged P-CTD and N in whole-cell lysate samples are likely a consequence of the more efficient interaction between these P-CTD and N proteins, which may enhance the probability of N-P-CTD aggregate formation. This phenotype appears to be a feature of the truncated P-CTD construct. To validate that the candidate mutations specifically disturbed the P-XD N-MoRE interface rather than globally disrupting XD conformation, we examined in parallel the colP efficiency of full-length Ps with NiV L. For all of these experiments, a truncated NiV L<sub>1763</sub> construct was used (41) that lacks the methyltransferase (MTase) and C-terminal domains and is less prone to spontaneous formation of aggregates. P-L colP efficiency of the P-I697D reference construct was reduced by over 80%, indicating the impact of overall P-XD misfolding (Fig. 1G; Fig. S2). Compared to wild-type, P-L677R and -E680R fully maintained the ability to interact with L, whereas the efficiency of L interaction with P-Y684R and -A688R was reduced by nearly 50% (Fig. 1G; Fig. S2). By comparison, all candidate mutations predicted to specifically affect the MoRE-binding face of NiV P-XD maintained relative L binding-competence of at least 50% that of standard P, confirming basic folding competence of the mutated XD domains. When we located these residues in a model derived from the coordinates released for the NiV P-XD:N-MoRE complex (PDB: 7pno), they formed one continuous interface on XD (Fig. 1H) in an orientation expected to physically contact N-MoRE (Fig. 1I).

### The $\alpha$ -1/3 face of P-XD mediates interaction with NiV L

Having identified residues responsible for the interaction of P-XD with N-MoRE, we next probed the NiV P-XD  $\alpha$ -1/3 face (Fig. 2A) in search of residues that engage L. In MG assays, we shortlisted six residues of 11 candidates that, when mutated, decreased polymerase activity below 40% that of wild-type P (Fig. 2B). Substitutions P-S660R, -V663R, and -L667 in  $\alpha$ -helix 1 abolished, and P-T670R significantly reduced, polymerase activity. Two additional mutants, P-N702A and -D706R, located in  $\alpha$ -helix 3 highly reduced P-L bioactivity. MG activity profiles generated for six candidates confirmed that



Full-Length Text

Journal of Virology

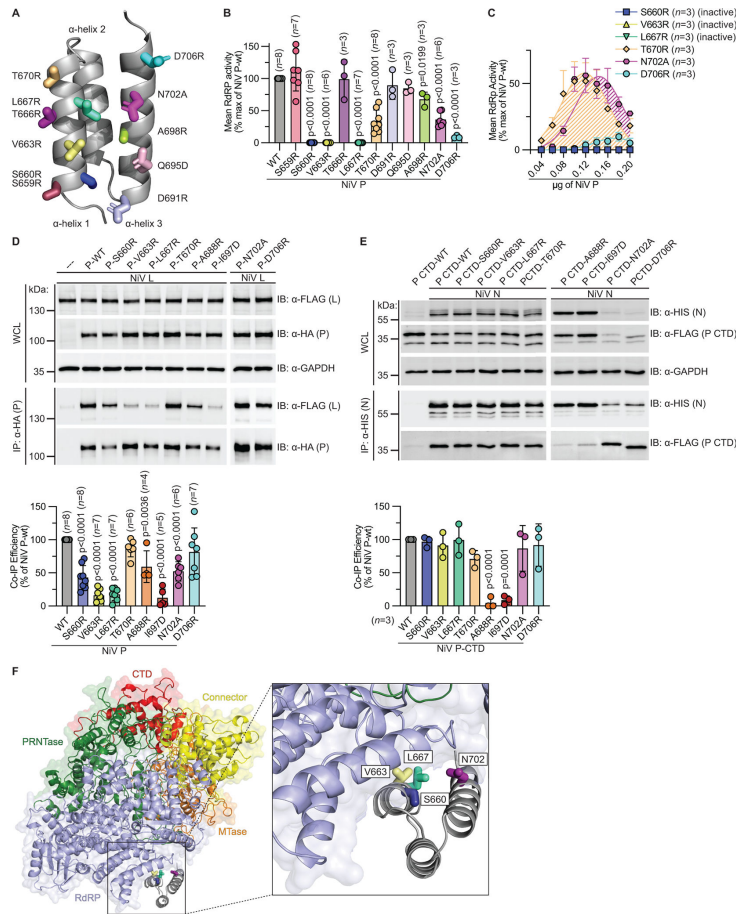


**FIG 2** Identification of an L binding microdomain in Niv P-XD. (A) Surface model of the  $\alpha$ -1/3 face of Niv P-XD with candidate L binding residues subjected to mutagenesis labeled (PDB: 4heo). Substituted side chains are shown as sticks and color-coded to matching graphs. (B) Mean RdRP bioactivity of potential L binding mutants. (C) Candidate L binding mutant MG activity profiles. Symbols represent means of three independent experiments  $\pm$  SD. (D and E) Biochemical assessment of the interaction of candidate L binding mutants with Niv N. WCL and colP immunoblots of candidate full-length P mutants and Niv L<sub>1763</sub> (D), and P-CTD mutants and Niv N (E). Antibody detection and densitometry as described in Fig. 1. (F) Homology model of Niv P-XD interacting with Niv L based on the PIV5 structure (PDB: 6v86), showing the spatial orientation of Niv P S660, V663, L667, and N702 in relation to L. XD (gray), RdRP domain (light blue), PRNTase domain (green), connector domain (yellow), MTase domain (orange), and CT domain (red). Bars represent means  $\pm$  SD, and symbols show individual experiments; N numbers are shown. Analysis with one-way ANOVA with Dunnett's multiple comparisons post-hoc test, comparing mean P mutant bioactivity to that of wild-type P.

reduced polymerase performance again was not due to altered optimal plasmid ratios but reflected an absolute loss of bioactivity (Fig. 2C).

Four of these six candidates, P-S660R, -V663R, -L667R, and -N702A, showed decreased binding to Niv L in colP (Fig. 2D; Fig. S3 to S5). However, each retained their ability to bind N-MoRE at a relative level equivalent to that of wild-type P (Fig. 2E; Fig. S6), suggesting that these four residues define a microdomain on the P-XD  $\alpha$ -1/3 face

Full-Length Text

Journal of Virology

that engages NiV L. These experimental results are fully consistent with the position of P-S660R, -V663R, -L677R, and -N702A predicted by the NiV P-XD:L homology model that we generated based on the PIV5 L-P (PDB: 6v86) complex (Fig. 2F).

### Substitutions to residues in P-XD $\alpha$ -1 helix impair polymerase bioactivity

In previous work, we proposed that morbillivirus P-XD, when bound to N-MoRE, forms a transient interface with an acidic loop in N-core (29), which triggers resolution of the N-MoRE interaction with P-XD, allowing the polymerase to advance along the RNP template. To explore whether this putative interface is conserved across different paramyxovirus genera, we mutated multiple residues along the  $\alpha$ -1/2 face of NiV P-XD (Fig. 3A) and characterized consequences for polymerase bioactivity. Three substitutions, P-D662I, -K665D, and -R669S, which form a cluster on  $\alpha$  helix 1 of XD (Fig. 3A), reduced polymerase bioactivity profiles below 50% in minigenome assays (Fig. 3B and C).

The morbillivirus model suggests that mutations disrupting the P-XD  $\alpha$ -1/2 face should not affect P interaction with L and N-MoRE in colP. All three candidate N-core binders indeed interacted efficiently with NiV L and N-MoRE (Fig. 3D; Fig. S7A through C). Whereas the colP efficiency of P-D662I and N-MoRE was statistically indistinguishable from that of wild-type P, P-K665D and P-R669S even showed a statistically significant increase in colP efficiency (Fig. 3E; Fig. S7D through F). This increase may reflect an impaired P-XD N-core-driven release mechanism of the P-XD N-MoRE interaction.

### Transcomplementation minigenome assays demonstrate that L binding and N-core binding functionalities of NiV P-XD are attributed to distinct XDs in the P tetramer

To evaluate whether the distinct P-XD functionalities are provided by different XD moieties in a P tetramer or functionally coupled, we tested combinations of the different loss-of-function mutants in transcomplementation minigenome assays. When plasmids encoding distinct P mutants,  $M_1$  and  $M_2$ , were co-transfected at a 4:1 ratio, cells were expected, based on mathematical modeling developed in our previous work (22), to produce tetramer species consisting of approximately 40%  $4 M_1/0 M_2$ , 40%  $3 M_1/1 M_2$ , slightly less than 20% of  $2 M_1/2 M_2$ , and very low amounts of  $1 M_1/3 M_2$  and  $0 M_1/4 M_2$ . These species distributions assume free homo- and heterotypic mixing of  $M_1$  and  $M_2$ . Using P-A688R as a representative N-MoRE binding-deficient and L binding-competent mutant, we explored transcomplementation of all L binding-deficient mutants with P-A688R at a 4:1 and 1:4 ratio (Fig. 4A; Table 1). The bioactivity of each L binding-deficient mutant increased significantly when transcomplemented with P-A688R at a 4:1 ratio. In the reverse experiment, a plasmid ratio of 1:4 resulted in a significant reduction in bioactivity compared to the 4:1 ratio (Fig. 4A) and to wild-type P (Table 1).

These data suggest that wild-type-like bioactivity requires P tetramers with multiple XDs capable of binding to N-MoRE and at least one XD able to engage L. Transcomplementation of L-binding deficient P-S660R with the three other N-MoRE binding-deficient mutants, P-L677R, -E680R, and -Y684R at a 4:1 significantly restored bioactivity (Fig. 4B). When we enriched the relative subpopulations of  $3 M_1/1 M_2$  or  $1 M_1/3 M_2$  tetramers by increasing the ratios of the different mutant populations to an extreme 10:1 and 1:10, bioactivities of all trans-complemented mutants decreased significantly below that of wild-type P but the P-V663R:A688R (10:1) transcomplementation pair (Fig. 4C). This reduction in bioactivity was greatest when subpopulations were enriched for L-binding competent P-XD, suggesting that more P-XD in a P tetramer must be N-binding than L-binding competent for optimal bioactivity.

Having established the transcomplementation of NiV P L binding and N-MoRE binding functionalities, we next expanded the approach to N-core binding-deficient mutants. L binding-deficient P-S660R efficiently transcomplemented with N-core defective P-D662I and R669S at a 4:1 ratio (Fig. 4D). Bioactivity of either combination was significantly greater than that of the respective N-core binding-deficient mutant alone, and the combination of P-S660R with P-R669S specifically returned polymerase function

Full-Length Text

Journal of Virology

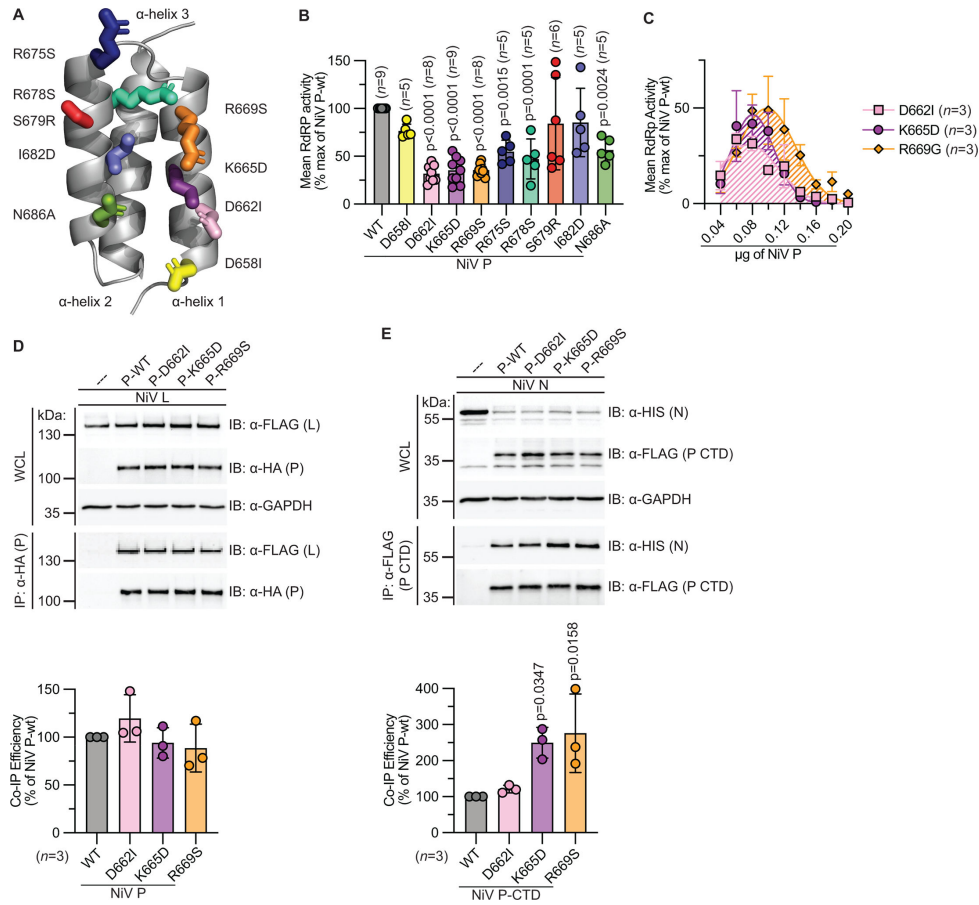


**FIG 3** Evidence for an N-core interacting face in P-XD. (A) All residue substitutions were evaluated along the outer  $\alpha$ -1/2 face of Niv P-XD model (PDB: 4heo). Substituted side chains are shown as sticks and color coded to match graphs. (B) Assessment of prospective N-core interacting mutants by MG assays. (C) Bioactivity profiles of candidate N-core binding mutants. Symbols represent means of three independent biological repeats  $\pm$  SD. (D and E) Relative coIP efficiency showing immunoblots (WCL and IP) and densitometry quantification. Interaction between candidate full-length P mutants and Niv L<sub>1763</sub> (D), and P-CTD mutants and Niv N (E). Antibody detection and densitometry as described in Fig. 1. Bars represent means  $\pm$  SD, and symbols show individual experiments; *N* numbers are shown. Analysis with one-way ANOVA with Dunnett's multiple comparisons post-hoc test, comparing mean P mutant bioactivity to that of wild-type P.

to near wild-type level. In contrast, P-K665D was unable to transcomplement with P-S660R despite efficient physical binding to L and N-MoRE. The P-K665D substitution may prevent productive interaction with either one or both binding partners through secondary structural effects that impede bioactivity but not physical contact. Efficient transcomplementation of P-S660R with P-D662I and R669S established proof-of-concept that L- and N-core-binding capacities of P-XD can be provided *trans*, indicating that the interaction of P-XD with N-core is not required to dissolve XD complexes with L.

### The P-XD engaging N-MoRE must be N-core binding competent

No appreciable transcomplementation occurred, however, when we explored uncoupling P-XD N-MoRE binding and N-core binding functionalities, combining N-core

Full-Length Text

Journal of Virology

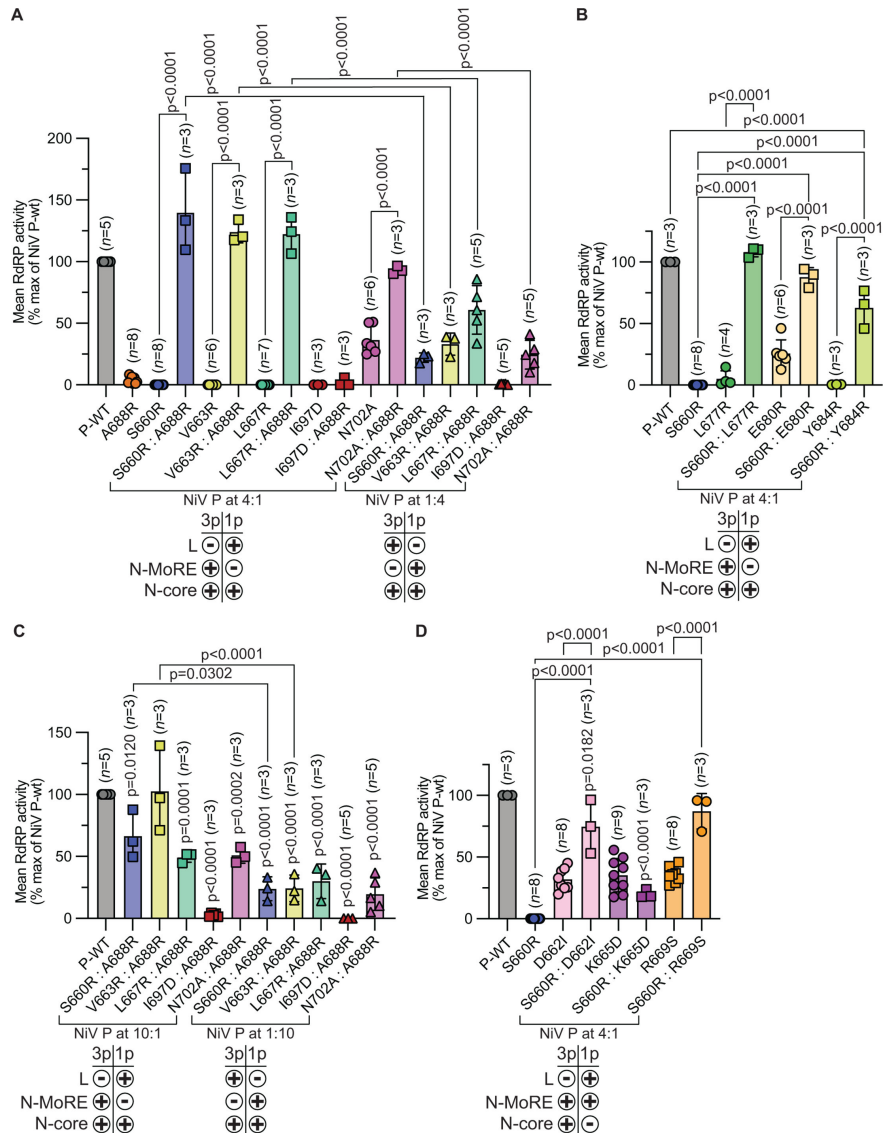


**FIG 4** Transcomplementation of L, N-MoRE, and N-core binding-deficient mutants. (A) Bioactivity of L binding-deficient mutants and P-A688R, a representative N-MoRE binding-deficient mutant, when transcomplemented at a 4:1 and 1:4 relative plasmid ratio. (B) Bioactivity of a representative L binding-deficient mutant, P-S660R, and additional N-MoRE binding-deficient constructs at a 4:1 ratio. (C) L binding-deficient mutants with N-MoRE binding-deficient P-A688R at a 10:1 and 1:10 ratio. (D) L binding-deficient P-S660R transcomplemented with N-core binding-deficient mutants at a 4:1 ratio. P-I697D was included in (A and C) as a reference for unspecific global XD disruption. In all panels, relevant homotypic mutant P bioactivities were included for statistical analysis. Schematic below graphs represent the dominant mixed P tetramer population that is competent (+) or incompetent (–) to bind L, N-MoRE, or N-core, respectively. Bars represent means  $\pm$  SD, and symbols show individual experiments; *N* numbers are shown. Analysis with one-way ANOVA with Dunnett's (when comparing to P-WT) or Tukey's (when comparing to homotypic mutants) multiple comparisons post-hoc test, comparing mean mutant P bioactivity to that of wild-type P.

Full-Length Text

Journal of Virology

TABLE 1 Statistical analysis of L-binding-deficient mutant transcomplementations with A688R<sup>a</sup>

Ratio	P <sub>1</sub> :P <sub>2</sub>	NiV P	
		P-WT	A688R
4:1	S660R:A688R	<0.0001	<0.0001
	V663R:A688R	0.0163	<0.0001
	L667R:A688R	0.0314	<0.0001
	I697D:A688R	<0.0001	>0.9999
	N702A:A688R	0.9854	<0.0001
1:4	S660R:A688R	<0.0001	0.3827
	V663R:A688R	<0.0001	0.0064
	L667R:A688R	<0.0001	<0.0001
	I697D:A688R	<0.0001	>0.9999
	N702A:A688R	<0.0001	0.0469

<sup>a</sup>Analysis of data from Fig. 4A comparing the homotypic bioactivity of (i) P-WT and (ii) A688R to transcomplemented mutants at a 4:1 and 1:4 ratio. Analysis with one-way ANOVA with Dunnett's (when comparing to P-WT) or Tukey's (when comparing to homotypic mutant(s)) multiple comparisons post-hoc tests. Table shows *P*-values; gray shading indicates *P*-values < 0.05.

binding-deficient mutants P-D662I, -K665D, and -R669S with N-MoRE-defective P-A688R at both 4:1 and 1:4 ratios (Fig. 5A). The placement of P-XD N-core and N-MoRE binding capabilities in *cis* complementation groups indicates that an individual P-XD must be capable to simultaneously interact with N-MoRE and N-core for polymerase bioactivity.

To further probe for direct mechanistic links between the three faces of the NiV P-XD moiety, we introduced double substitutions in XD to generate a family of NiV P proteins that are competent only for one of the three interactions, binding to L (N-MoRE and -core null; P-D662I A688R), N-MoRE (L and N-core null; P-S660R D662I), or N-core (L and N-MoRE null; P-S660R A688R). CoIP analyses confirmed that the resulting N-MoRE and -core null and L and N-core null double mutations were mostly unchanged in their ability to interact with L and N-MoRE, respectively, compared to the corresponding single mutants (Fig. 5B and C; Fig. S8 and S9). We did notice, however, an additional decrease in the L binding efficiency of the P-S660R + A688R mutant compared to P-S660R alone (Fig. 5B; Fig. S9). When tested in MG assays, none of the combinations in which N-MoRE and N-core binding competence were provided in *trans* showed any significant increase in bioactivity over the individual plasmids transfected alone, confirming that these functionalities must be present on the same XD moiety (Fig. 5D). Underscoring the importance of the transient interaction of XD with N-core, a P tetramer is not bioactive when all of its XDs can interact with N-MoRE, but none can engage N-core (Fig. 5E). However, we detected efficient transcomplementation of XDs lacking both N-MoRE and N-core binding competence with an L binding-deficient XD, represented by P-S660R (Fig. 5F). These results demonstrate that the P-XD to L interface is not regulated by N-core binding, but polymerase activity depends on N-core binding competence of the XD moieties physically engaging N-MoRE.

## DISCUSSION

To access their template, mononegavirus polymerases must temporarily induce local release of the encapsidated RNA from the RNP, which requires coordinated protein-protein interactions between the RdRP complex and the N protein assembly (28, 34, 35, 38, 39). Continuous release and reformation of these interactions are required to ensure polymerase mobility along the template. Induced interactions between P-XD and N-MoRE located in the exposed N-tails were identified in different paramyxoviruses (22, 28, 29, 34, 35, 38, 39, 42), and a cartwheeling model of iterative P-XD to N-MoRE binding and release was proposed early that assumes that the different XD moieties of a P tetramer are at distinct stages of interaction with, and separation from, N-MoRE at any point in time (37, 43). Subsequently, we demonstrated that a distinct P-XD face docks to L in the P-L polymerase complexes (22), which was confirmed by structural studies (30–32). Using recombinant viruses with engineered shortened N tails, we discovered

Full-Length Text

Journal of Virology

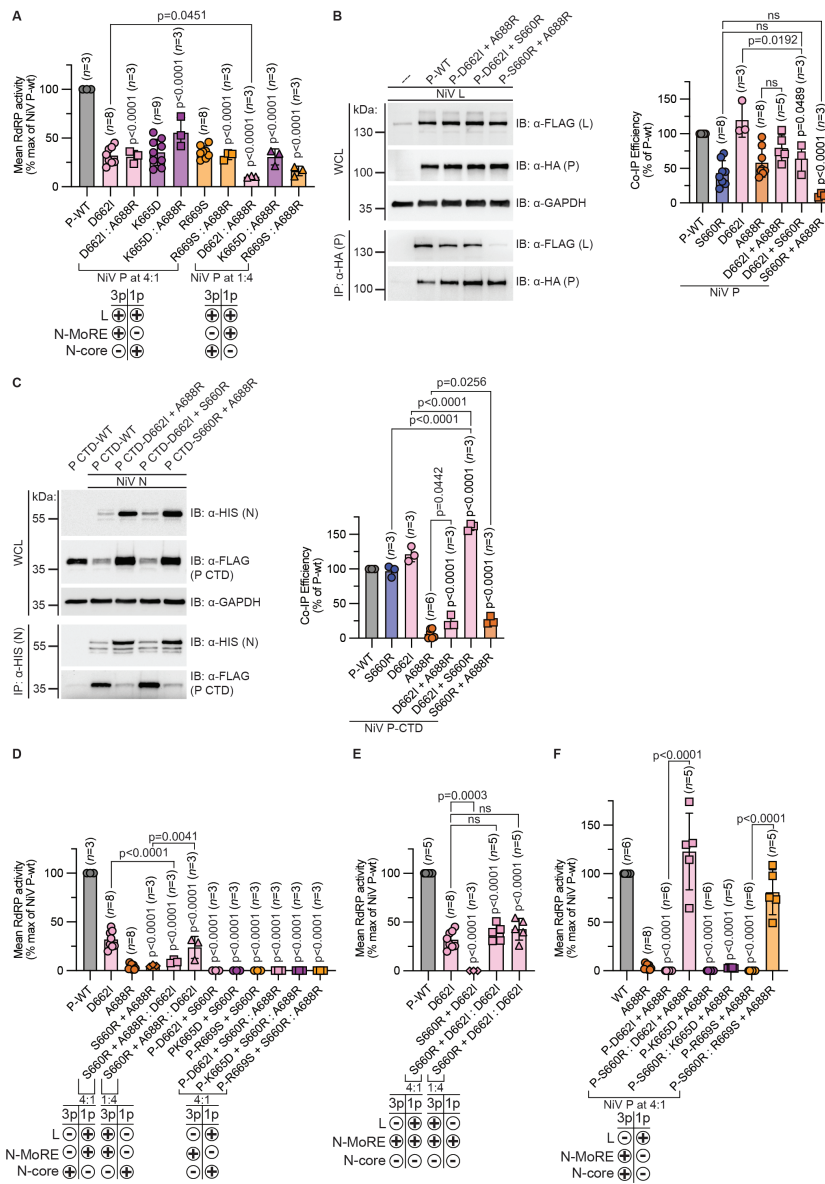


**FIG 5** Double mutant transcomplementation. (A) N-core binding-deficient mutants and N-MoRE binding-deficient P-A688R at a 4:1 and 1:4 ratio. (B and C) CoIP efficiency of double binding-deficient mutants. WCL and IP immunoblots are shown for full-length P double mutants and NIP L<sub>1763</sub> (B), and P-CTD double mutants and NIP N (C). Antibody detection and densitometry as described in Fig. 1. (D) Transcomplementation of (i) an L/N-MoRE binding-deficient double mutant and N-core binding-deficient P-D662I (4:1 and 1:4 ratio) and (ii) N-core/L binding-deficient double mutants and N-MoRE binding-deficient P-A688R at a 4:1 ratio. (E) Transcomplementation of L/N-core binding-deficient double mutant with N-core binding-deficient P-D662I at a 4:1 and 1:4 ratio. (F) Transcomplementation of L binding-deficient P-S660R and N-core/MoRE binding-deficient double mutants at a 4:1 ratio. In A–C, relative bioactivities and coIP efficiencies of selected single P mutants determined in (Continued on next page)



## FIG 5 (Continued)

Fig. 1 to 3 were included to facilitate direct comparison. Schematics below graphs as described in Fig. 4. Bars represent means  $\pm$  SD, and symbols show individual experiments; *N* numbers are shown. Analysis with one-way ANOVA with Dunnett's (when comparing to P-WT) or Tukey's (when comparing to homotypic mutants) multiple comparisons post-hoc test, comparing mean P mutant bioactivity to that of wild-type P.

that the third P-XD face transiently engages N-core in the RNP assembly (29), but the relevance of this interaction beyond members of the morbillivirus genus and its role relative to the other P-XD functionalities was unknown. Advancing our insight into the regulation of the paramyxovirus polymerase complex, the present study supports three major conclusions:

1. Three-way interactions of P-XD with L, N-MoRE, and N-core are not unique to the morbilliviruses but a conserved feature of several, and presumably all, paramyxovirus genera. We demonstrated through an array of colP and functional assays that henipavirus P-XD moieties have three distinct functionalities that are attributed to the three different faces of the triangular prism fold (35) of paramyxovirus XD. Applying structure-guided mutagenesis to the NiV P-XD problem, we identified for each XD face a set of residues that, when mutated, affect a specific protein-protein interaction while leaving the other functionalities intact, indicating that the overall folding geometry of XD was uncompromised. However, the bioactivity of the corresponding mutant polymerase complex was affected by any of these changes, confirming that each XD functionality is essential for polymerase activity. Specifically, we noted a complete lack of MG activity in the presence of mutations located in the N-MoRE and L binding face of P-XD, whereas changes in the face interacting with N-core resulted in residual bioactivity of approximately 30% that of unchanged P-L. This difference in effect size likely reflects low-frequency spontaneous release of P-XD from N-MoRE without the trigger provided by the N-core binding face under minireplicon conditions. We expect that spontaneous release is insufficient to sustain virus replication since all three XD faces are highly conserved in the family (22, 28, 38).
2. P-XD interaction with N-MoRE/N-core and L is essential but must involve distinct P-XD moieties in the P tetramer. Mutations affecting P-XD L binding competence and either interaction with N-MoRE or N-core can be complemented in *trans* in minigenome assays, indicating that they can reside on distinct XD moieties of the NiV P tetramer. This finding is consistent with our previous observation that the interaction of morbillivirus P-XD with N-MoRE or L is mutually exclusive (22). Although the experimental set-up of the NiV MG system did not allow engineering of the P tetramer composition equivalent to what we applied to the morbillivirus system, we propose based on the conservation of all XD faces that also NiV P-XD moieties can engage with either N-MoRE or L but not with both simultaneously. Likely, this feature of P interaction with L or N is conserved throughout the paramyxovirus family.
3. P-XD N-MoRE and N-core binding capabilities must be located on the same physical XD moieties and cannot be complemented in *trans*. Our NiV MG complementation studies provide compelling support that, in contrast to the alternative interactions with N-MoRE or L, XD N-core and N-MoRE binding functionalities are mechanistically linked and must be present on the same XD unit for polymerase bioactivity. This finding is consistent with a model of controlled paramyxovirus polymerase movement along the encapsidated template that involves periodic contraction of the unstructured N-tails (39), bringing the P-XD bound to N-MoRE into close proximity to N-core (Fig. 6). In the morbillivirus genus, this reorganization of the N-tail positions a basic patch on the  $\alpha$ -1/2 face of the XD:N-MoRE four-helix bundle in contact with an acidic

Full-Length Text

Journal of Virology

loop located in the N-core (29). Analogous crosstalk between the free  $\alpha$ -1/2 XD face of the NiV P-XD/N-MoRE complex and N-core may function as a trigger to dissolve the complex, creating a timer for the RdRP to regain mobility and advance along the template that is conserved across polymerases of the paramyxovirus family. For the effective release of a bound N-MoRE, the P-XD:N-MoRE complex must contact N-core since these functionalities cannot be complemented in *trans*. Likely, cross-talk between P-XD and N-core temporarily lowers the XD binding affinity for N-MoRE, possibly by inducing a transient structural reorganization in XD. Once N-MoRE has been released, the XD is free to return to its original configuration and reengage with the MoRE of a downstream N protomer.

In MeV, only a single XD moiety of a P tetramer must be L binding-competent, and engineered P complexes with such a single L-competent XD configuration in fact enhanced overall polymerase activity in MG assays. This finding was interpreted to suggest periodic release of the morbillivirus P-XD:L interaction, which requires reordering of the tetramer when more than a single XD competes for binding to L (22). Our study reveals that an analogous principle applies to the NiV polymerase complex since P tetramers enriched for single L-competent XDs supported high polymerase activity, whereas reversal of the relative P mutant ratios resulted in a steep decline in activity. Previously, it was unclear, however, whether the cross-talk between P-XD and N-core is required to induce XD release from L or N-MoRE. Using the N-core-deficient NiV P-D662I and P-R669S mutants in transcomplementation assays, we now demonstrate that XD interaction and release of L occur spontaneously and independent of XD cross-talk with N-core, whereas N-MoRE release is directly linked to XD engaging N-core. These findings advance the mechanistic understanding of molecular determinants controlling paramyxovirus polymerase processivity and identify novel druggable target sites for the structure-guided identification of non-competitive next-generation paramyxovirus polymerase inhibitors.

## MATERIALS AND METHODS

### Study design

Cells were used as an *in vitro* model to identify and characterize interactions between Nipah phosphoprotein XD and Nipah N-MoRE, Nipah L, and Nipah N-core. Minigenome assays were performed to assess how mutations of different residues within the P-XD affect polymerase bioactivity. Co-immunoprecipitations and western blots were conducted to assess the biochemistry of these distinct mutations, specifically the impact each mutation has on protein-protein interactions between P and L protein or P and N protein.

### Cells

Baby hamster kidney (BHK) cells, BHK-21 (C-13, ATCC), and stably expressing T7 (BHK7) polymerase were cultured in Dulbecco's Modified Eagle Medium (DMEM) supplemented with 7.5% heat-inactivated fetal bovine serum (FBS) and maintained in 37°C in 5% CO<sub>2</sub>. Cells were tested frequently for mycoplasma contamination. GeneJuice (MilliporeSigma) was used to transiently transfect cells according to the manufacturer's protocol.

### Molecular biology

All plasmids used were under the control of a T7 promoter. To improve the NiV nanoluciferase reporter signal to background ratio, a nanoluciferase-PEST (proline-glutamic acid-serine-threonine) reporter was used in all minigenome assays. Point mutations within the XD of NiV P (NCBI reference sequence: NP\_112022) were introduced by site-directed PCR mutagenesis. For biochemical assays, an N-terminus 2× hemagglutinin (HA)-tag was

Full-Length Text

Journal of Virology

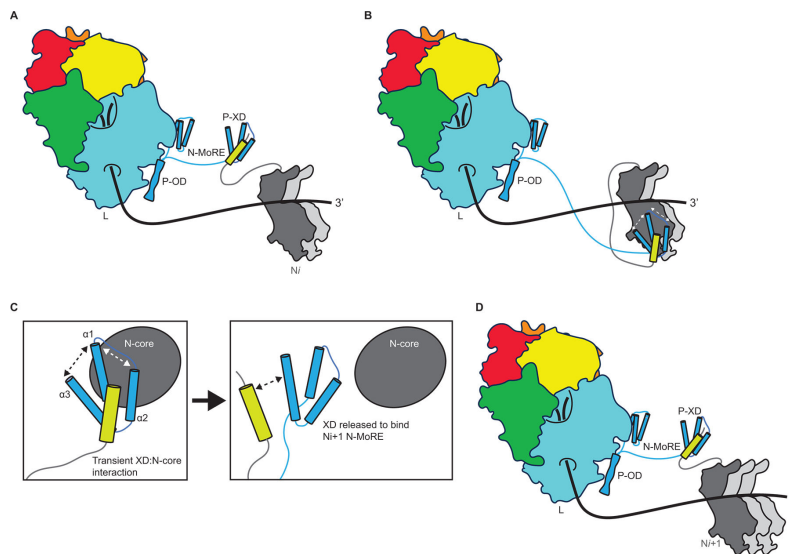


**FIG 6** Mechanistic hypothesis of P-XD:N-MoRE interaction with N-core. (A) NiV P functions as a cofactor tethering NiV L to the RNP template. A single XD of the P tetramer interacts with NiV L near the NTP entry site, and the remaining XDs are in different stages of N-MoRE binding on adjacent N-tails. NiV P (blue) with XD labeled. NiV N (gray) with MoRE (lime green). L protein RdRP domain (blue), polyribonucleotidyltransferase (PRNTase) domain (green), connector domain (yellow), methyltransferase (MTase) domain (orange), and C-terminal domain (CTD; red). For clarity, only two of the four XDs of the P tetramer are shown. (B) N-tail refolding brings the  $\alpha$ -1/2 face of the P-XD:N-MoRE complex into proximity of N-core. (C) Interaction between XD:N-MoRE and N-core transiently interrupts the conformation of XD, releasing N-MoRE. (D) The released P-XD subsequently binds to the MoRE of an N-tail of a downstream N protomers, allowing movement of the polymerase complex along the RNP template.

added to NiV P by PCR and re-ligated at a MluI site introduced through non-coding mutations within the HA sequence. A truncated NiV P $\Delta$ 1-469 (NiV P-CTD) construct containing an N-terminal 3 $\times$  FLAG-tag was generated by PCR and re-ligated at an EcoRV site. NiV N was constructed to contain a C-terminal 6 $\times$  HIS-tag that was directly added by PCR. A previously described (41) truncated NiV L protein with a C-terminal 3 $\times$  FLAG tag, which remains folding competent but is absent of the methyltransferase (MTase) and C-terminal domain, was generated by PCR and re-ligation at an added EcoRV restriction site. All constructs generated were validated by Sanger sequencing.

### Minigenome reporter assays

Cells were seeded in 96-well plates (7,500 cells/well) in 50  $\mu$ L of DMEM (7.5% FBS). To assess the bioactivity of each mutant, multiple technical repeats were performed for each biological repeat, and cells were transfected with either NiV P wild-type or mutant (0.1  $\mu$ g), NiV N (0.1  $\mu$ g), NiV L (0.1  $\mu$ g), and NiV nanoluciferase reporter (0.2  $\mu$ g). All negative controls had NiV L replaced by an empty vector, pUC-19 (0.1  $\mu$ g). In all *trans* complementation experiments, the total amount of NiV P was maintained at 0.1  $\mu$ g. Nanoluciferase activity was quantified 40 hours post-transfection by adding Nano-Glo Luciferase Assay Substrate (Promega) to each well and measuring luciferase activity using a Synergy H1 microplate reader (BioTek). Relative RdRP activities were expressed as a percentage of activity in the presence of wild-type NiV P determined by the percentage of relative activity =  $[(\text{Signal}_{\text{Sample}} - \text{Signal}_{\text{Minimum}}) / (\text{Signal}_{\text{Maximum}} - \text{Signal}_{\text{Minimum}})] \times 100$ .  $\text{Signal}_{\text{Maximum}}$  was determined by cells that had been transfected with wild-type

Full-Length Text

Journal of Virology

NiV P, and Signal<sub>Minimum</sub> was determined by cells that had been transfected with an equal concentration of the negative control.

#### SDS-PAGE, immunoblotting, and densitometry

Cells were seeded in six-well plates (30,000 cells/well) in 2 mL of DMEM (7.5% FBS), and each well was transfected with equal concentrations of plasmid DNA to a total of 1 µg. Mock wells were transfected with an empty vector, pUC19. Twenty-four hours post transfection cells were washed once in Dulbecco's phosphate buffered saline followed by chemical lysis [50 mM HEPES (pH 7.2), 300 mM NaCl, 1 mM EDTA, 1% Triton X-100, and protease inhibitor (Sigma)]. Lysates were clarified for 30 minutes at 14,000 rpm (4°C), mixed 1:1 with Laemmli buffer and then incubated for 30 minutes at 45°C. Samples were separated on 10% SDS-PAGE gels and semi-dry transferred to polyvinylidene difluoride membranes (Thermo Scientific) using the Trans-Blot Turbo Transfer System (Bio-Rad). Immunodetection of NiV P mutants was performed using anti-HA at a 1:4,000 dilution (Invitrogen; HA.C5), NiV P-CTD using anti-FLAG at a 1:10,000 dilution (Sigma; M2), NiV N using anti-HIS at a 1:4,000 dilution (ThermoFisher Scientific; HIS.H8), NiV L<sub>1763</sub> using anti-FLAG at a 1:10,000 dilution (Sigma; M2), and cellular glyceraldehyde three-phosphate dehydrogenase at a 1:10,000 dilution (GAPDH; Sigma; G8795). Immunoblots were incubated in an anti-species IgG light chain-specific secondary antibody conjugated with horseradish peroxidase at a 1:10,000 dilution (Jackson ImmunoResearch) and then developed using a ChemiDoc digital imaging system (Bio-Rad). Densitometry was performed using Image Lab (Bio-Rad; version 6.1.0 build 7) to analyze non-saturated images with global background correction. Positive controls (wild-type NiV P or NiV N) and negative controls (an equal concentration of an empty-vector, pUC-19) were present on every immunoblot. There were no across-blot normalizations performed.

#### Co-immunoprecipitation

Clarified lysates were incubated with 1 µL of antibody specific to HA, FLAG, or HIS epitopes, rotated at 4°C overnight and then clarified for 30 minutes. Pierce Protein G Agarose beads (50 µL) were washed three times in 0.5 mL of cold lysis buffer. Immune complexes were precipitated at 4°C, rotated for 1 hour, washed 2 times in 0.5 mL of cold lysis buffer, and then resuspended in 100 µL of Laemmli buffer. Relative co-immunoprecipitation efficiencies were calculated by densitometric quantification of co-precipitated NiV P, N, or L, normalized to the amount of protein co-precipitated by wild-type NiV P or wild-type NiV P-CTD, determined by the percentage of wild-type P =  $[(\text{Volume}_{\text{Sample}} - \text{Volume}_{\text{Minimum}}) / (\text{Volume}_{\text{Maximum}} - \text{Volume}_{\text{Minimum}})] \times 100$ . Volume<sub>Maximum</sub> was determined by cells that had been transfected with wild-type NiV P or wild-type NiV P-CTD, and Volume<sub>Minimum</sub> was determined by the background volume for a particular sample.

#### Statistical analysis

All experiments performed consist of a minimum of three biological repeats. Graphical representations of experimental data show the mean of biological repeats ± SDs shown as error bars. One-way analysis of variance with either a Dunnett's or Tukey's post-hoc test was used to evaluate statistical significance between samples. A statistical significance level of  $\alpha = 0.05$  was used for all experiments, and we report multiplicity-adjusted *P* values for each comparison. To analyze mutant P to wild-type P bioactivity or colP efficiency, we compared the mean of each mutant with the mean of a control column (wild-type P at 100%) with Dunnett's multiple comparisons post-hoc test. When analyzing mutant-to-mutant bioactivity in transcomplementation experiments, we compare the mean of each mutant(s) with the mean of every other mutant(s) with Tukey's multiple comparisons post-hoc test. Statistical analyses were performed using GraphPad Prism (version 10) software.

Full-Length Text

Journal of Virology

**ACKNOWLEDGMENTS**

This work was supported, in part, by public health service grants AI071002 (to R.K.P.) and AI171403 (to R.K.P.).

**AUTHOR AFFILIATION**

<sup>1</sup>Center for Translational Antiviral Research, Institute for Biomedical Sciences, Georgia State University, Atlanta, Georgia, USA

**AUTHOR ORCIDS**

Richard K. Plemper  <http://orcid.org/0000-0003-2034-2107>

**FUNDING**

Funder	Grant(s)	Author(s)
HHS   NIH   National Institute of Allergy and Infectious Diseases (NIAID)	AI071002, AI171403	Richard K. Plemper

**AUTHOR CONTRIBUTIONS**

Josef D. Wolf, Data curation, Investigation, Visualization, Writing – original draft, Writing – review and editing | Richard K. Plemper, Conceptualization, Formal analysis, Funding acquisition, Methodology, Project administration, Supervision, Writing – original draft, Writing – review and editing

**DATA AVAILABILITY**

All numerical raw data and statistical analyses are available in supplemental files Data S1 and Data S2, respectively.

**ADDITIONAL FILES**

The following material is available [online](#).

**Supplemental Material**

**Data S1 (JV100986-24-s0001.xlsx)**. All numerical source data.

**Data S2 (JV100986-24-s0002.xlsx)**. All statistical analyses.

**Supplemental figures (JV100986-24-s0003.pdf)**. Fig. S1 to S9.

**REFERENCES**

- Hauser N, Gushiken AC, Narayanan S, Kottlilil S, Chua JV. 2021. Evolution of Nipah virus infection: past, present, and future considerations. *Trop Med Infect Dis* 6:24. <https://doi.org/10.3390/tropicalmed6010024>
- Alam AM. 2022. Nipah virus, an emerging zoonotic disease causing fatal encephalitis. *Clin Med (Northfield)* 22:348–352. <https://doi.org/10.7861/clinmed.2022-0166>
- Arunkumar G, Chandni R, Mourya DT, Singh SK, Sadanandan R, Sudan P, Bhargava B, Nipah Investigators People and Health Study Group. 2019. Outbreak investigation of Nipah virus disease in Kerala, India, 2018. *J Infect Dis* 219:1867–1878. <https://doi.org/10.1093/infdis/jiy612>
- Banerjee S, Gupta N, Kodan P, Mittal A, Ray Y, Nischal N, Soneja M, Biswas A, Wig N. 2019. Nipah virus disease: a rare and intractable disease. *Intractable Rare Dis Res* 8:1–8. <https://doi.org/10.5582/irdr.2018.01130>
- Chua KB, Bellini WJ, Rota PA, Harcourt BH, Tamin A, Lam SK, Ksiazek TG, Rollin PE, Zaki SR, Shieh W-J, Goldsmith CS, Gubler DJ, Roehrig JT, Eaton B, Gould AR, Olson J, Field H, Daniels P, Ling AE, Peters CJ, Anderson LJ, Mahy BWJ. 2000. Nipah virus: a recently emergent deadly paramyxovirus. *Science* 288:1432–1435. <https://doi.org/10.1126/science.288.5470.1432>
- Soman Pillai V, Krishna G, Valiya Veettil M. 2020. Nipah virus: past outbreaks and future containment. *Viruses* 12:465. <https://doi.org/10.3390/v12040465>
- Cui Z, Li J, Meng L, Zhang Z. 2024. Nipah virus: a re-emerging public health concern. *Lancet Microbe* 5:e212. [https://doi.org/10.1016/S2666-5247\(23\)00361-0](https://doi.org/10.1016/S2666-5247(23)00361-0)
- Watanabe S, Yoshikawa T, Kaku Y, Kurosu T, Fukushi S, Sugimoto S, Nishisaka Y, Fuji H, Marsh G, Maeda K, Ebihara H, Morikawa S, Shimojima M, Saijo M. 2023. Construction of a recombinant vaccine expressing Nipah virus glycoprotein using the replicative and highly attenuated vaccinia virus strain LC16m8. *PLoS Negl Trop Dis* 17:e0011851. <https://doi.org/10.1371/journal.pntd.0011851>
- Satterfield BA, Dawes BE, Milligan GN. 2016. Status of vaccine research and development of vaccines for Nipah virus. *Vaccine (Auckl)* 34:2971–2975. <https://doi.org/10.1016/j.vaccine.2015.12.075>
- van Doremalen N, Avanzato VA, Goldin K, Feldmann F, Schulz JE, Haddock E, Okumura A, Lovaglio J, Hanley PW, Cordova K, Saturday G, de Wit E, Lambe T, Gilbert SC, Munster VJ. 2022. ChAdOx1 NIV vaccination protects against lethal Nipah Bangladesh virus infection in

- African green monkeys. *NPJ Vaccines* 7:171. <https://doi.org/10.1038/s41541-022-00592-9>
11. Harcourt BH, Tamin A, Ksiazek TG, Rollin PE, Anderson LJ, Bellini WJ, Rota PA. 2000. Molecular characterization of Nipah virus, a newly emergent paramyxovirus. *Virology (Auckl)* 271:334–349. <https://doi.org/10.1006/viro.2000.0340>
  12. Wang L, Harcourt BH, Yu M, Tamin A, Rota PA, Bellini WJ, Eaton BT. 2001. Molecular biology of Hendra and Nipah viruses. *Microbes Infect* 3:279–287. [https://doi.org/10.1016/s1286-4579\(01\)01381-8](https://doi.org/10.1016/s1286-4579(01)01381-8)
  13. Cox RM, Plemper RK. 2017. Structure and organization of paramyxovirus particles. *Curr Opin Virol* 24:105–114. <https://doi.org/10.1016/j.coviro.2017.05.004>
  14. Sourimant J, Plemper RK. 2016. Organization, function, and therapeutic targeting of the morbillivirus RNA-dependent RNA polymerase complex. *Viruses* 8:251. <https://doi.org/10.3390/v8090251>
  15. Karlin D, Ferron F, Canard B, Longhi S. 2003. Structural disorder and modular organization in *Paramyxovirinae* N and P. *J Gen Virol* 84:3239–3252. <https://doi.org/10.1099/vir.0.19451-0>
  16. Longhi S. 2009. Nucleocapsid structure and function. *Curr Top Microbiol Immunol* 329:103–128. [https://doi.org/10.1007/978-3-540-70523-9\\_6](https://doi.org/10.1007/978-3-540-70523-9_6)
  17. Cox RM, Krumm SA, Thakkar VD, Sohn M, Plemper RK. 2017. The structurally disordered paramyxovirus nucleocapsid protein tail domain is a regulator of the mRNA transcription gradient. *Sci Adv* 3:e1602350. <https://doi.org/10.1126/sciadv.1602350>
  18. Ker DS, Jenkins HT, Greive SJ, Antson AA. 2021. CryoEM structure of the Nipah virus nucleocapsid assembly. *PLoS Pathog* 17:e1009740. <https://doi.org/10.1371/journal.ppat.1009740>
  19. Noton SL, Fearn R. 2015. Initiation and regulation of paramyxovirus transcription and replication. *Virology (Auckl)* 479–480:545–554. <https://doi.org/10.1016/j.virol.2015.01.014>
  20. Ogino T, Green TJ. 2019. RNA synthesis and capping by non-segmented negative strand RNA viral polymerases: lessons from a prototypic virus. *Front Microbiol* 10:1490. <https://doi.org/10.3389/fmicb.2019.01490>
  21. Bloyet L-M, Welsch J, Enchery F, Mathieu C, de Breyne S, Horvat B, Grigorov B, Gerlier D. 2016. HSP90 chaperoning in addition to phosphoprotein required for folding but not for supporting enzymatic activities of measles and Nipah virus L polymerases. *J Virol* 90:6642–6656. <https://doi.org/10.1128/JVI.00602-16>
  22. Du Pont V, Jiang Y, Plemper RK. 2019. Bipartite interface of the measles virus phosphoprotein X domain with the large polymerase protein regulates viral polymerase dynamics. *PLoS Pathog* 15:e1007995. <https://doi.org/10.1371/journal.ppat.1007995>
  23. Bruhn JF, Barnett KC, Bibby J, Thomas JMH, Keegan RM, Rigden DJ, Bornholdt ZA, Saphire EO. 2014. Crystal structure of the Nipah virus phosphoprotein tetramerization domain. *J Virol* 88:758–762. <https://doi.org/10.1128/JVI.02294-13>
  24. Yabukarski F, Lawrence P, Tarbouriech N, Bourhis J-M, Delaforge E, Jensen MR, Ruigrok RWH, Blackledge M, Volchkov V, Jamin M. 2014. Structure of Nipah virus unassembled nucleoprotein in complex with its viral chaperone. *Nat Struct Mol Biol* 21:754–759. <https://doi.org/10.1038/nsmb.2868>
  25. Aggarwal M, Leser GP, Kors CA, Lamb RA. 2018. Structure of the paramyxovirus parainfluenza virus 5 nucleoprotein in complex with an amino-terminal peptide of the phosphoprotein. *J Virol* 92:e01304-17. <https://doi.org/10.1128/JVI.01304-17>
  26. Curran J, Marq JB, Kolakofsky D. 1995. An N-terminal domain of the Sendai paramyxovirus P protein acts as a chaperone for the NP protein during the nascent chain assembly step of genome replication. *J Virol* 69:849–855. <https://doi.org/10.1128/JVI.69.2.849-855.1995>
  27. Habchi J, Blangy S, Mamelli L, Jensen MR, Blackledge M, Darbon H, Oglesbee M, Shu Y, Longhi S. 2011. Characterization of the interactions between the nucleoprotein and the phosphoprotein of henipavirus. *J Biol Chem* 286:13583–13602. <https://doi.org/10.1074/jbc.M111.219857>
  28. Bourhis JM, Yabukarski F, Communie G, Schneider R, Volchkova VA, Frénaat M, Gérard FC, Ducournau C, Mas C, Tarbouriech N, Ringkjøbing Jensen M, Volchkov VE, Blackledge M, Jamin M. 2022. Structural dynamics of the C-terminal X domain of Nipah and Hendra viruses controls the attachment to the C-terminal tail of the nucleocapsid protein. *J Mol Biol* 434:167551. <https://doi.org/10.1016/j.jmb.2022.167551>
  29. Sourimant J, Thakkar VD, Cox RM, Plemper RK. 2020. Viral evolution identifies a regulatory interface between paramyxovirus polymerase complex and nucleocapsid that controls replication dynamics. *Sci Adv* 6:eaa1590. <https://doi.org/10.1126/sciadv.aaz1590>
  30. Cong J, Feng X, Kang H, Fu W, Wang L, Wang C, Li X, Chen Y, Rao Z. 2023. Structure of the Newcastle disease virus L protein in complex with tetrameric phosphoprotein. *Nat Commun* 14:1324. <https://doi.org/10.1038/s41467-023-37012-y>
  31. Abdella R, Aggarwal M, Okura T, Lamb RA, He Y. 2020. Structure of a paramyxovirus polymerase complex reveals a unique methyltransferase-CTD conformation. *Proc Natl Acad Sci U S A* 117:4931–4941. <https://doi.org/10.1073/pnas.1919837117>
  32. Xie J, Ouizougoun-Oubari M, Wang L, Zhai G, Wu D, Lin Z, Wang M, Ludeke B, Yan X, Nilsson T, Gao L, Huang X, Fearn R, Chen S. 2024. Structural basis for dimerization of a paramyxovirus polymerase complex. *Nat Commun* 15:3163. <https://doi.org/10.1038/s41467-024-47470-7>
  33. Hu S, Kim H, Yang P, Yu Z, Ludeke B, Mobilia S, Pan J, Stratton M, Bian Y, Fearn R, Abraham J. 2024. Structural and functional analysis of the Nipah virus polymerase complex. *bioRxiv*. <https://doi.org/10.1101/2024.05.29.596445>
  34. Guseva S, Milles S, Blackledge M, Ruigrok RWH. 2019. The nucleoprotein and phosphoprotein of measles virus. *Front Microbiol* 10:1832. <https://doi.org/10.3389/fmicb.2019.01832>
  35. Johansson K, Bourhis JM, Campanacci V, Cambillau C, Canard B, Longhi S. 2003. Crystal structure of the measles virus phosphoprotein domain responsible for the induced folding of the C-terminal domain of the nucleoprotein. *J Biol Chem* 278:44567–44573. <https://doi.org/10.1074/jbc.M308745200>
  36. Kingston RL, Gay LS, Baase WS, Matthews BW. 2008. Structure of the nucleocapsid-binding domain from the mumps virus polymerase; an example of protein folding induced by crystallization. *J Mol Biol* 379:719–731. <https://doi.org/10.1016/j.jmb.2007.12.080>
  37. Kingston RL, Hamel DJ, Gay LS, Dahlquist FW, Matthews BW. 2004. Structural basis for the attachment of a paramyxoviral polymerase to its template. *Proc Natl Acad Sci U S A* 101:8301–8306. <https://doi.org/10.1073/pnas.0402690101>
  38. Communie G, Habchi J, Yabukarski F, Blocquel D, Schneider R, Tarbouriech N, Papageorgiou N, Ruigrok RWH, Jamin M, Jensen MR, Longhi S, Blackledge M. 2013. Atomic resolution description of the interaction between the nucleoprotein and phosphoprotein of Hendra virus. *PLoS Pathog* 9:e1003631. <https://doi.org/10.1371/journal.ppat.1003631>
  39. Longhi S, Receveur-Bréchet V, Karlin D, Johansson K, Darbon H, Bhella D, Yeo R, Finet S, Canard B. 2003. The C-terminal domain of the measles virus nucleoprotein is intrinsically disordered and folds upon binding to the C-terminal moiety of the phosphoprotein. *J Biol Chem* 278:18638–18648. <https://doi.org/10.1074/jbc.M300518200>
  40. Krumm SA, Takeda M, Plemper RK. 2013. The measles virus nucleocapsid protein tail domain is dispensable for viral polymerase recruitment and activity. *J Biol Chem* 288:29943–29953. <https://doi.org/10.1074/jbc.M113.503862>
  41. Dochow M, Krumm SA, Crowe JE, Moore ML, Plemper RK. 2012. Independent structural domains in paramyxovirus polymerase protein. *J Biol Chem* 287:6878–6891. <https://doi.org/10.1074/jbc.M111.325258>
  42. Baronti L, Erales J, Habchi J, Felli IC, Pierattelli R, Longhi S. 2015. Dynamics of the intrinsically disordered C-terminal domain of the Nipah virus nucleoprotein and interaction with the x domain of the phosphoprotein as unveiled by NMR spectroscopy. *Chembiochem* 16:268–276. <https://doi.org/10.1002/cbic.201402534>
  43. Curran J. 1998. A role for the Sendai virus P protein trimer in RNA synthesis. *J Virol* 72:4274–4280. <https://doi.org/10.1128/JVI.72.5.4274-4280.1998>



### 3. CONCLUSIONS

The key findings for each research topic in this dissertation are summarized in three separate sections. In addition, each section includes a discussion that delves into the three specific, related topics:

i) Evaluating therapeutic options for treating SARS-CoV-2 (Cox et al., 2023; Cox, Wolf, Lieber, et al., 2021; Cox, Wolf, & Plemper, 2021; Gildemann et al., 2024; Lieber et al., 2022; Rhodin et al., 2024; Sourimant et al., 2022).

ii) Secondary bacterial superinfections and the necessity for enhanced treatment strategies for viral infections (Cox et al., 2024).

iii) Limitations of using high-throughput screening to identify novel antiviral NiV targets (Wolf & Plemper, 2024).

#### 3.1 Research Topic: SARS-CoV-2

##### 3.1.1 Summary of Key SARS-CoV-2 Findings

This dissertation thoroughly evaluated six different therapeutic options for treating/preventing SARS-CoV-2 infection: i) molnupiravir, ii) Paxlovid-like nirmatrelvir/ritonavir, iii) GS-621763, iv) 4'-fluorouridine (4'-Flu), v) EDP-235, and vi) BioBlock. Each therapy varies in its potential treatment indications, benefits, drawbacks, and the ability of each compound to select for resistance mutations.

i) In studies using the ferret model for asymptomatic SARS-CoV-2 infection, both prophylactic and therapeutic twice daily administration of molnupiravir (5mg/kg), initiated 12 hours after infection, effectively prevented the transmission of SARS-CoV-2 between cohabitating ferrets (Cox et al., 2023; Cox, Wolf, Lieber, et al., 2021; Cox, Wolf, & Plemper,

2021; Lieber et al., 2022). Similarly, in the Roborovski dwarf hamster model, which mimics severe COVID-19-like lung disease, 5mg/kg of molnupiravir treatment initiated 12 hours after infection led to complete survival, reduced viral lung levels, and lessened lung damage associated with the delta, gamma, and omicron variants (Lieber et al., 2022).

ii) In ferrets, twice daily treatment with a Paxlovid-like combination of nirmatrelvir and ritonavir 12 hours after infection reduced viral shedding of SARS-CoV-2 Wuhan lineage A. However, when administered at a dose equivalent to that used in humans (human effect size equivalent dose, HESED) 12 hours after infection, there was a decrease in lung viral titers, but transmission was not fully prevented. Increasing the dose to five times the HESED only partially prevented transmission, but prophylactic treatment at this higher dose successfully prevented transmission. In dwarf hamsters, treatment administered 12 hours post infection reduced viral lung titers and ensured complete survival against VOCs delta and omicron (Cox et al., 2023).

iii) GS-621763 (10mg/kg) given twice daily, 12 hours after infection, showed therapeutic oral efficacy against both the Wuhan lineage A and the VOC gamma in the ferret model. Additionally, GS-621763 effectively prevented direct-contact transmission of VOC gamma (Cox, Wolf, Lieber, et al., 2021).

iv) Once daily treatment of ferrets with 4'-FIU (20mg/kg) when initiated 12 hours after infection effectively reduced viral lung titers of Wuhan lineage A as well as VOCs alpha, gamma, and delta to undetectable levels. Although this study did not include a transmission assessment, the rapid reduction in viral shedding achieved with 4'-FIU suggests it is likely to prevent transmission as well (Cox et al., 2023; Cox, Wolf, Lieber, et al., 2021; Cox, Wolf, & Plemper, 2021; Carolin M. Lieber & Richard K. Plemper, 2022; Rhodin et al., 2024).

v) In ferrets infected with SARS-CoV-2 Wuhan lineage A, treatment with EDP-235 (200mg/kg) 12 hours after infection and administered twice daily successfully reduced viral lung titers and prevented transmission (Rhodin et al., 2024).

vi) After ferrets were infected with the SARS-CoV-2 Wuhan lineage A, they received an intranasal spray formulation of the SARS-CoV-2 neutralizing antibody, known as BioBlock. This treatment began 4 hours before placing infected and uninfected ferrets together. When the spray was applied every 4 hours during a 12-hour co-housing period, it effectively stopped the virus from spreading among the ferrets (Gildemann et al., 2024).

### ***3.1.2 Evaluating Therapeutic Options for Treating SARS-CoV-2***

Early in the pandemic, it was highly encouraging to find that administering a twice-daily HESED of molnupiravir could effectively block SARS-CoV-2 transmission in infected ferrets, a result supported by several of our studies (Cox et al., 2023; Cox, Wolf, & Plemper, 2021; Lieber et al., 2022). In contrast, the Paxlovid-like combination of nirmatrelvir and ritonavir, when given twice daily, could only partially prevent transmission if the HESED dose was increased by fivefold (Cox et al., 2023). Therapeutic treatments with GS-621763 (10mg/kg) and EDP-235 (200mg/kg) also demonstrated potent SARS-CoV-2 transmission inhibition (Cox, Wolf, Lieber, et al., 2021; Rhodin et al., 2024). A direct comparison of the SARS-CoV-2 protease inhibitors Paxlovid-like nirmatrelvir/ritonavir and EDP-235 shows that EDP-235 offers a notable advantage: it requires only once-daily dosing and does not require coadministration of ritonavir, which avoids the interactions and contraindications associated with Paxlovid (Hoertel et al., 2022). Based on these data, molnupiravir, GS-621763, and EDP-235 are recommended for preventing the transmission of SARS-CoV-2 from an infected individual to an uninfected one.

During the COVID-19 pandemic, household transmission significantly contributed to SARS-CoV-2 spread (Madewell et al., 2021). In a direct comparison of prophylactically administered HESEDs of molnupiravir and Paxlovid-like nirmatrelvir/ritonavir, neither drug effectively prevented direct-contact transmission (Cox et al., 2023). Effective prophylactic blockage of transmission required doses of molnupiravir and Paxlovid-like nirmatrelvir/ritonavir that were 4x and 5x higher than the currently recommended HESED, respectively. These findings align with conclusions from the EPIP-PEP (Paxlovid) and MOVE-ahead (molnupiravir) trials, which indicated that post-exposure prophylactic (PEP) treatment with either drug did not significantly reduce household SARS-CoV-2 transmission events (Alpizar et al., 2023; Mullard, 2022).

However, these trials relied on viral RNA copy numbers as their primary endpoint, and molnupiravir, which acts as a viral mutagen, reduces viral infectivity titers without a proportional decrease in RNA copy numbers (Cox et al., 2023; Kabinger et al., 2021; Strizki et al., 2023). In contrast, Paxlovid reduces both viral titers and RNA copy numbers proportionally. Consequently, the MOVE-ahead trial may have underestimated the PEP potential of molnupiravir due to this design limitation. This issue is also reflected in clinical trials that use SARS-CoV-2 RNA levels as a quantitative measure and claim greater efficacy for Paxlovid over molnupiravir, potentially missing the impact of molnupiravir-induced reductions in viral titers (Schilling et al., 2024). This underscores the importance of considering drug mechanisms of action when designing clinical trials and selecting primary endpoints.

An alternative post-exposure prophylactic option is BioBlock, which requires only intranasal administration. However, BioBlock efficacy was only evaluated with administration

every 4 hours, so a more practical treatment regimen that requires less frequent administration would need further testing and may in fact require such frequent dosing in high-risk exposure situations (Gildemann et al., 2024). The PEP efficacy of GS-621763 and EDP-235 was not assessed in these studies (Cox, Wolf, Lieber, et al., 2021; Rhodin et al., 2024).

Antiviral drug resistance poses a significant public health threat and, if not effectively managed, can lead to the spread of drug resistant virus (Irwin et al., 2016) similar to what was observed after use of adamantanes to treat influenza virus infections, which resulted in the global emergence of adamantane-resistant influenza A variants (Dong et al., 2015). The potential for viral resistance to develop against a specific compound can be evaluated *in vitro* by applying selective pressure through serial passaging of the virus in cell culture with progressively increasing, sub-sterilizing concentrations of the compound. It is crucial to thoroughly assess the genetic barrier to resistance for all SARS-CoV-2 treatments and consider this factor when physicians prescribe these medications. For example, Paxlovid treatment has selected for moderate *in vitro* resistance and naturally occurring SARS-CoV-2 resistance to Paxlovid has been detected in the population, as reported in several studies (Hu et al., 2023; Jochmans et al., 2023; Science, 2022a, 2022b; Zhou et al., 2022). While resistance profiling for 4'FIU against SARS-CoV-2 has not been conducted, the moderate resistance that has been selected for and observed with influenza A virus *in vitro* (Lieber et al., 2024) suggests that SARS-CoV-2 resistance could potentially develop, although this is not certain.

In contrast, both molnupiravir and Remdesivir have demonstrated a high genetic barrier to SARS-CoV-2 infection (Hedskog et al., 2023; Strizki et al., 2024). This indicates that these drugs, along with GS-621763, an oral prodrug of the Remdesivir nucleoside, offer a significant

advantage over other SARS-CoV-2 therapies. Notably, no *in vivo* virus resistant mutants were detected in GS-621763 treated SARS-CoV-2-infected ferrets (Cox, Wolf, Lieber, et al., 2021). Combined treatment with Paxlovid and molnupiravir (Jeong et al., 2022) or GS-621763 may increase the genetic barrier to resistance mutation amplification and enhance treatment efficacy. Although EDP-235 and BioBlock have not been resistance profiled against SARS-CoV-2, EDP-235 has demonstrated activity against known SARS-CoV-2 nirmatrelvir-resistant variants and showed no *in vivo* virus resistance in EDP-235 treated ferrets (Rhodin et al., 2024).

### **3.2 Research Topic: MeV and CDV**

#### **3.2.1 Summary of Key MeV and CDV Findings**

In this study, we employed a CDV-ferret model as a surrogate for MeV infection (Cox et al., 2024). In ferrets, infection with wild-type CDV is always lethal, typically leading to death within 12 days. However, our findings show that administering the orally effective paramyxovirus polymerase inhibitor GHP-88309 (50 mg/kg) twice daily, starting up to 5 days post-infection, at the onset of viremia and rash, ensures complete survival and significantly reduces viral load. Given the 100% lethality of wild-type CDV within two weeks, we used an attenuated recombinant CDV to demonstrate that infection results in severe lymphocytopenia and completely disrupts preexisting immunity to influenza and rabies viruses, supporting the morbillivirus immune amnesia hypothesis.

When ferrets were infected with attenuated CDV, treatment with GHP-88309 (50 mg/kg) twice daily fully prevented lymphocytopenia when started 5 days post-infection and reduced its duration when initiated 7 days after infection. To enhance physiological relevance, ferrets were subsequently infected with influenza virus (H1N1; pandemic CA09) to assess how



CDV infection impacts neutralizing antibody titers in a more robust immune response.

Unexpectedly, nearly all ferrets infected with influenza 28 days before CDV infection developed acute, fatal hemorrhagic bacterial pneumonia. We attribute this severe pneumonia to an overgrowth of commensal bacteria driven by an influenza-induced immune priming mechanism, which ultimately suppresses a family of trefoil factor (TFF) peptides necessary for effective mucociliary bacterial clearance. Therapeutic administration of GHP-88309 twice daily, even when started 7 days after CDV infection, prevented hemorrhagic pneumonia in all influenza-primed ferrets.

### ***3.2.2 Secondary Bacterial Superinfections and the Necessity for Enhanced Treatment***

#### ***Strategies for Viral Infections***

The human microbiota consists of a diverse array of microorganisms residing in areas such as the skin, oronasopharynx, respiratory tract, and intestinal tract, which interact symbiotically with the host (Hou et al., 2022; Ursell et al., 2014). These symbiotic relationships are crucial for maintaining homeostasis and play a significant role in regulating the immune system (Ogunrinola et al., 2020). Disruption of this dynamic balance, known as dysbiosis, can lead to a range of chronic conditions, including cancer, heart disease, diabetes, and inflammatory bowel disease (Hou et al., 2022; Lau et al., 2017), as well as increase susceptibility to acute illnesses such as bacterial superinfections (Hament et al., 1999).

Many viral infections, including SARS-CoV-2, influenza (IAV), parainfluenza virus, human rhinovirus, RSV, and MeV, have been linked to disruptions in microbiota composition, which in some cases may directly contribute to secondary bacterial infections (Cox et al., 2024; Groves et al., 2018; Gu et al., 2020; Hament et al., 1999; Hofstra et al., 2015; Manna et al., 2020; Morse &

Horwitz, 2021; Sencio et al., 2021; Zhang et al., 2020; Zuo et al., 2021; Zuo et al., 2020). Early evidence suggesting a connection between secondary bacterial infections and preceding viral respiratory infections dates back to the 1920s and 1930s (Hament et al., 1999; Noble et al., 1928; Webster & Clow, 1932). For instance, during the influenza pandemics of 1918, 1957, and 1968, there was a notable increase in cases of bacterial pneumonia caused by *Staphylococcus aureus*, a bacterium that typically colonizes the human nose (Barker & Mullooly, 1982; Cate, 1998; Krismer et al., 2017; Luria et al., 1959; Schwarzmann et al., 1971). Bacterial superinfections following RSV infection have also been documented (Jeannoël et al., 2019), and human rhinovirus, a common cold virus, has been shown to cause dysbiosis, leading to bacterial infections like pneumonia and otitis media (Hofstra et al., 2015). Proposed mechanisms for microbiota imbalance include enhanced bacterial adherence to host cells due to viral infections, suppressed host immune responses to bacterial pathogens, physical damage to cells, reduced bacterial clearance, and virus-induced interactions with bacteria (Bartelt & Duncan, 1978; Cox et al., 2024; Hament et al., 1999; Harrison, 1954; Paget & Trottein, 2019; Ramphal et al., 1980; Sanford et al., 1978).

Unlike bacterial infections associated with a single viral infection, a recent study presented in this thesis (Cox et al., 2024) identified as a significant risk factor for bacterial superinfection consecutive infections by different viruses. This finding may help explain why some patients experience post-measles complications such as bacterial pneumonia, bronchitis, and otitis media (Blutinger et al., 2023; Moss & Griffin, 2012; Perry & Halsey, 2004; Thakur et al., 2022). Post-measles complications can occur in up to 40% of cases. The study found that ferrets infected with measles-like CDV after recovering from IAV or RSV infection developed

fatal hemorrhagic bacterial pneumonia due to unregulated overgrowth of microbiota in the lungs. In this model, a prior respiratory infection altered the immune system in a way that inhibited CDV from upregulating trefoil-factor peptides (TFFs) in the respiratory tract. This suppression of TFF activity likely led to localized dysbiosis by impairing the TFF-induced mucociliary clearance of certain bacterial populations in the lungs (Cox et al., 2024). This observation in the ferret model, that a previous respiratory infection exacerbates CDV disease might be an extreme example of why some human patients develop bacterial infections following MeV infection.

Bacterial infections pose a significant public health threat, greatly contributing to the morbidity and mortality associated with viral respiratory infections (Morens et al., 2008; Morris et al., 2017; Shafran et al., 2021). While prophylactic use of broad-spectrum antibiotics might seem like a potential strategy to prevent these infections, this approach has notable drawbacks. For instance, broad-spectrum antibiotic use can increase bacterial resistance (Zegers et al., 2017) and, in some cases, may worsen outcomes of viral-induced bacterial infections (Yokomichi et al., 2023). If the IAV-CDV-ferret model accurately reflects potential post-measles bacterial complications in humans, it is crucial to enhance measles prevention and treatment strategies through global vaccine coverage and, as a backup to ensure the availability of highly effective antiviral therapies. Furthermore, the fact that treatment with the broad-spectrum preclinical antiviral 4'-fluorouridine did not prevent fatal respiratory bacterial superinfections in IAV-infected ferrets (Cox et al., 2024) underscores the critical importance of vaccination against viruses like influenza when available.

We demonstrated that treatment with GHP-88309 after the peak of viremia and after the peak of fever, when the therapeutic window has closed for treating primary clinical signs, can still prevent a severe disease outcome (Cox et al., 2024). These findings could potentially transform treatment approaches. Traditionally, if an antiviral were available for MeV, it might not be given to a child already diagnosed with measles and exhibiting the classic MeV rash, under the assumption that the patient is in the recovery phase. However, our data indicate that late treatment, even after the rash has appeared, can still be beneficial. If our model reflects human outcomes, administering antiviral treatment during this phase could help prevent secondary complications such as otitis media or other bacterial superinfections.

Given that this phenomenon is likely not exclusive to an IAV/RSV primed immune response to CDV, these findings highlight the urgent need for further research into how sequential infections by other common viral pathogens might influence the likelihood of subsequent bacterial superinfections. By gaining a broader understanding of these interactions, we may be able to prevent or mitigate bacterial infections in high-risk populations through proactive and intensive treatment of viral infections before secondary bacterial infections can take hold. It is crucial, therefore, to continue identifying and developing novel antiviral therapeutics for viruses that currently lack treatment options, ensuring we are prepared with a comprehensive range of antiviral treatments.

### **3.3 Research Topic: NiV**

#### ***3.3.1 Summary of Key NiV Findings***

In this study we had two main objectives: i) to identify and mechanistically validate key residues that are crucial for the bioactivity of the NiV polymerase, as well as P-XD interaction

with L, N-MoRE, and N-core; and ii) gain insight into the tightly regulated process that advances the polymerase along its template, which is driven by transient interactions between P and N proteins (Wolf & Plemper, 2024). To achieve these goals, we employed minigenome assays and co-immunoprecipitation to functionally and biochemically map the three distinct interfaces of the NiV P-XD. We also aimed to elucidate how the Nipah P protein facilitates the release of N-tails, allowing the polymerase to regain mobility along the ribonucleoprotein (RNP) assembly.

Our results identified clusters of key residues on each of the three P-XD interfaces, defining distinct microdomains that independently mediate interactions with L, N-MoRE, or N-core: i) residues L677, E680, Y684, and A688 on the N-MoRE binding face of P-XD (alpha 2/3) are essential for polymerase bioactivity and efficient interaction with N-MoRE; ii) residues S660, V663, L667, and N702 on the L binding face of P-XD (alpha 1/3) are crucial for polymerase activity and its interaction with NiV L; and iii) residues D662, K665, and R669 on the N-core binding face of P-XD (alpha 1/2) are necessary for polymerase bioactivity, although mutations to these residues do not affect P-XD's ability to bind L or N-MoRE.

After identifying the residues on each face of the XD that drive these crucial protein-protein interactions, we employed transcomplementation minigenome assays to restore the bioactivity of two functionally distinct, bioinactive mutants. Our data indicate that wild-type-like bioactivity necessitates that most P-XDs within a tetramer can bind to N-MoRE, provided at least one XD can interact with L. Notably, an interaction between P-XD and N-core is not required to disrupt XD complexes with L. However, an individual P-XD must be capable of simultaneously interacting with both N-MoRE and N-core to effectively release the N-tail. Based on these findings, we propose that changes in the microenvironment of the P-XD:N-MoRE

interface disrupt the interaction between P-XD and the N-tail, enabling the polymerase to regain mobility along the template.

### ***3.3.2 Limitations of Using High-throughput Screening to Identify Novel Antivirals NiV Targets***

Nipah virus poses a significant health risk due to its high pathogenicity and the absence of existing vaccines or antiviral treatments. This underscores an urgent medical need that makes identification of novel druggable target sites a priority. High-throughput screening (HTS) of libraries containing hundreds of thousands of compounds (Follmann et al., 2019) can significantly accelerate the discovery of new therapeutics for emerging infectious diseases. Successful HTS campaigns have previously been conducted in BSL-4 labs, screening approximately 10,000 compounds against NiV and 200,000 compounds against Ebola virus (Luthra et al., 2018; Tigabu et al., 2014). However, conducting HTS in a biosafety level 4 (BSL-4) laboratory is both expensive and complex, and simplified assay designs are needed to reduce the biocontainment challenges.

To avoid the need for HTS in a BSL-4 environment, researchers often conduct screenings in BSL-2 labs using pseudotyped viruses, virus-like particles (VLPs), surrogate viruses, or replicon and minigenome assays (Basu et al., 2010; Jasenosky et al., 2010; Porotto et al., 2009). For example, HTS for NiV inhibitors can be performed in BSL-2 using Cedar virus (CedV), a non-pathogenic, closely related surrogate. However, these strategies, which do not involve fully replication-competent viruses, have limitations as they do not encompass all stages of viral replication and therefore hits for all potential viral targets may not be identified. A notable limitation is the risk of identifying inhibitors that are specific to the surrogate virus rather than the intended pathogen. For instance, the paramyxovirus inhibitor GHP-83309 shows low

micromolar potency against CedV (Haas et al., 2024) and would be identified as a hit in a NiV HTS using CedV as a surrogate. However, despite its activity against CedV, GHP-83309 is ineffective against NiV due to a histidine at amino acid residue 1156 in the NiV RdRP, which makes NiV inherently resistant to this compound (Cox et al., 2020).

#### 4. FUTURE DIRECTIONS

An alternative strategy for identifying NiV polymerase-specific inhibitors through HTS involves creating a replication-competent chimeric virus. This hypothetical chimeric virus would feature the native NiV polymerase within a non-pathogenic CedV genetic background, that includes at least the M, F, and G proteins from Cedar virus. If successfully developed, such a chimeric virus might be suitable for evaluation to potentially be downgraded to a BSL-3 or BSL-2 agent.

##### 4.1 Essential Criteria of a Theoretical Chimeric Virus that Replicates using a NiV Polymerase in a CedV Genetic Background

NiV's pathogenicity is linked to its ability to infect the central nervous system (CNS) and its capacity to antagonize the innate immune response (Al-Obaidi et al., 2024; Satterfield et al., 2019; Satterfield et al., 2016; Wagner et al., 2022). Thus, there are two key reasons for integrating a CedV genetic background into the chimeric virus to prevent or greatly diminish its pathogenicity:

i) Unlike NiV, which interacts with the host cell receptor ephrin-B3 that is abundant in the central nervous system (Laing et al., 2019; Maisner et al., 2009; Marsh et al., 2012; Pernet et al., 2012; Vigant & Lee, 2011), the CedV receptor-binding protein (G protein) does not bind to ephrin-B3. This lack of neurotropism should mitigate or prevent the neuropathogenesis



typically associated with NiV infections (Al-Obaidi et al., 2024; Dawes & Freiberg, 2019; Xu et al., 2012).

ii) The CedV P protein does not antagonize the interferon (IFN) pathway and lacks an mRNA editing function needed to produce immune-modulatory accessory proteins (Laing et al., 2018; Lieu et al., 2015). In contrast, the NiV P gene encodes four proteins: P, C, V, and W. During transcription, the viral polymerase occasionally slips at a sequence-specific mRNA editing site (AAAAAGGGC), adding one or two non-templated G nucleotides, which produces the V (+1G) or W (+2G) proteins with unique C-termini (Figure 5). The C protein is generated when the polymerase recognizes an alternative start codon within the P gene open reading frame (Satterfield et al., 2019; Satterfield et al., 2016). Each of these four proteins contains a signal transducer and activator of transcription-1 (STAT-1) binding domain, enabling interaction with host cell STAT-1 to antagonize the type I IFN response (Satterfield et al., 2019). Additionally, the W protein can inhibit toll-like receptor 3 (TLR3) (Satterfield et al., 2016), and the V protein, which features a zinc-finger motif that can suppress melanoma differentiation-associated protein 5 (MDA5) and retinoic acid-inducible gene I (RIG-I)-dependent IFN signaling (Uchida et al., 2018; Wagner et al., 2022).

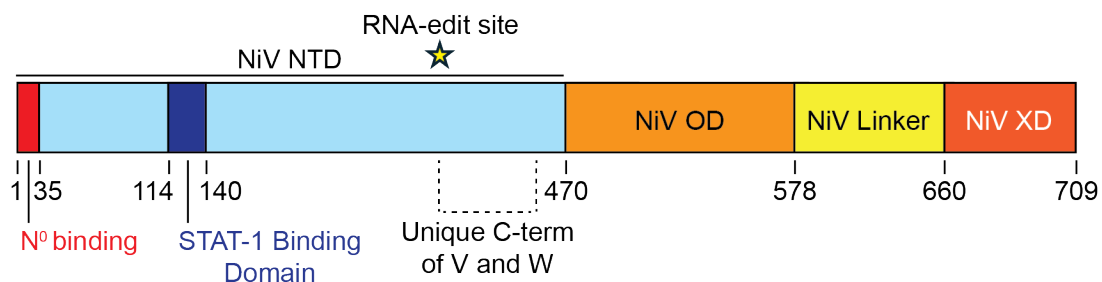


**Figure 1. 2D Schematic of Nipah Virus Phosphoprotein**  
 The NiV P protein consists of an N-terminal domain (NTD), oligomerization domain (OD), and a C-terminal domain known as the X-domain (XD). The first 35 residues of the NTD interact with N-core forming N<sup>o</sup>P complexes (Yabukarski et al., 2014).

Given our current understanding of NiV pathogenicity, a theoretical non-pathogenic chimeric virus must fulfill two key criteria: i) it should lack immune-modulatory NiV P elements (specifically NiV P NTD residues 114-470), and ii) it must incorporate CedV surface proteins (F and G) to avoid ephrin-B3-mediated CNS infection. For the chimeric virus to replicate using a genuine NiV polymerase, CedV untranslated regions (UTRs) must be replaced with NiV UTRs, as the NiV polymerase does not efficiently recognize CedV promoters (Haas et al., 2024). However, it is still unclear whether the NiV polymerase can accurately recognize gene start and gene signals within the CedV intragenic regions (IGRs) (Ghosh et al., 1996; Laing et al., 2018; Leppert et al., 1979; Tremaglio et al., 2013). Therefore, the appropriate IGR origins for the chimeric virus cannot be determined without further experimental investigation.

Building on the current understanding of NiV protein-protein interactions as detailed in this dissertation (Wolf & Plemper, 2024), three strategies are proposed that utilize different configurations of chimeric N and/or P protein elements which could be used to generate a chimeric virus (Figure 2A-C). These strategies are designed to facilitate critical protein-protein interactions, between P-NTD:N, P-XD:L, P-XD:N-MoRE, and P-XD:N-MoRE:N-core. Each proposed chimeric construct will feature four shared genes, with open reading frames encoding the full-length Cedar M, F, G, and NiV L proteins.

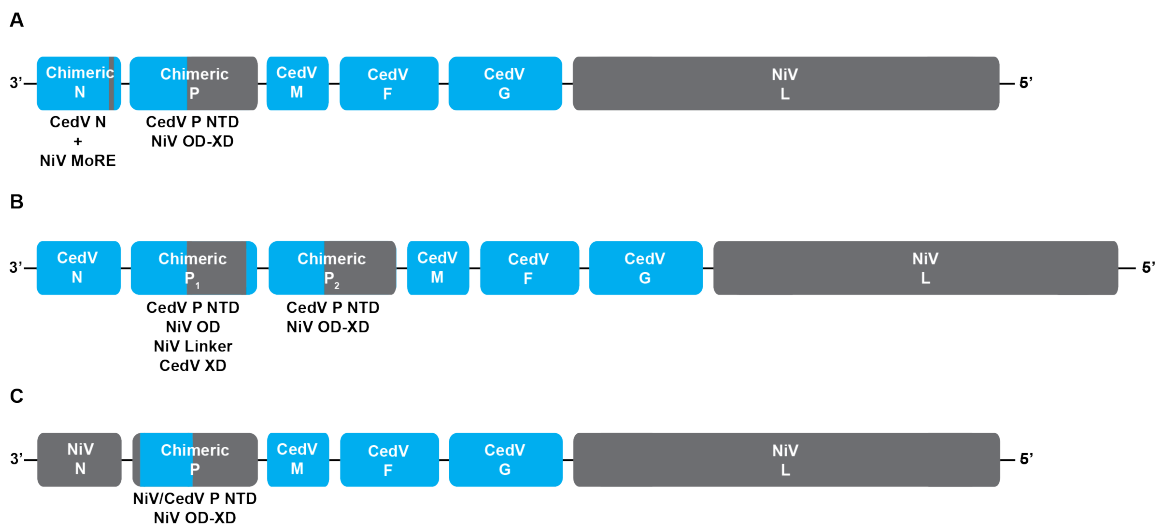


*Figure 2. Genome Organization of Proposed Recombinant Chimeric Virus Constructs. All constructs should commonly consist of NiV derived 3' and 5' UTRs, Cedar M, Cedar F, Cedar G, and NiV L and different arrangements of N and/or P protein elements. (A) Cedar N containing a NiV N MoRE and a P protein consisting of a CedV P-NTD + a NiV P OD-Linker-XD (OD-XD), (B) Tandem Ps composed of a CedV P-NTD + NiV OD-Linker + CedV P-XD [ $P_1$ ] and a CedV P-NTD + NiV OD-XD [ $P_2$ ], (C) NiV/CedV P-NTD + NiV OD-XD.*

## 4.2 Strategies for Development of a Replication-competent Virus Utilizing a Native NiV

### Polymerase, with Potential for Evaluation of Suitability for BSL3 Downgrading

#### 4.2.1 Generation of a Chimeric Virus - Approach One

By substituting the box 2 (molecular recognition element, MoRE) at the C-terminus of Cedar N with Nipah N-MoRE, and replacing the oligomerization domain (OD), linker, and X-domain (XD) of Cedar P with those from Nipah P (Figure 2A), these chimeric protein configurations are expected to support crucial interactions between the N, P, and L proteins. The CedV P-NTD combined with NiV OD-Linker-XD (OD-XD) should facilitate the formation of N<sup>0</sup>P complexes, keeping the N protein in a monomeric, soluble state until it is needed for genome encapsidation (Bourhis et al., 2022; Chen et al., 2007; Curran et al., 1995; Guryanov et

al., 2015; Mavrakis et al., 2006; Yabukarski et al., 2014). Since some residues within the OD, linker, and XD of P are known to interact with L (Du Pont et al., 2019), the OD-XD from NiV P should provide all necessary interactions for effective P-L protein interactions and polymerase activity (Abdella et al., 2020; Cong et al., 2023; Du Pont et al., 2019; Hu et al., 2024; Wolf & Plemper, 2024; Xie et al., 2024). Moreover, incorporating the NiV MoRE into the CedV N-tail should enable productive interactions with the NiV P-XD (Bourhis et al., 2022; Communie et al., 2013; Guseva et al., 2019; Johansson et al., 2003; Kingston et al., 2008; Kingston et al., 2004; Longhi et al., 2003). However, a potential limitation is that the NiV XD bound to CedV N-MoRE might not interact properly with CedV N-core, potentially affecting the release process (Sourimant et al., 2020; Wolf & Plemper, 2024). Despite this, because the interaction between P-XD:N-MoRE and N-core does not fully inhibit polymerase activity in mini-genome assays (Wolf & Plemper, 2024), a chimeric virus lacking this interaction might still be viable and could potentially optimize its interface through a viral evolution approach (Sourimant et al., 2020).

#### ***4.2.2 Generation of a Chimeric Virus - Approach Two***

Two P constructs are proposed where the CedV P OD-Linker (P1) and CedV P OD-XD (P2) are exchanged with their NiV counterparts (Figure 2B). In these chimeric P constructs, the CedV P-NTD will enable efficient formation of N<sup>0</sup>P complexes. The CedV P1, containing an XD of CedV origin, should interact effectively with CedV N-MoRE. Importantly, CedV P-XD:N-MoRE could interact naturally with the CedV N-core, facilitating the release of N-MoRE (Sourimant et al., 2020; Wolf & Plemper, 2024). Meanwhile, the NiV P OD-XD in P2 will mediate interactions with NiV L. To minimize potential undesired interactions between CedV P-XD and NiV L, or NiV P-XD and CedV N, it is advisable to include mutations in CedV P-XD that reduce L binding, analogous

to NiV P-S660R, and in NiV P-XD that impair N-MoRE binding, such as A688R (Wolf & Plemper, 2024). The tandem P constructs (P1 and P2) can leverage the intrinsic paramyxovirus transcription gradient (Du Pont et al., 2019; Iverson & Rose, 1981) to generate a dominant tetramer population. This would ensure that more Ps within a tetramer interact with CedV N-MoRE rather than NiV L (Du Pont et al., 2019; Wolf & Plemper, 2024).

#### ***4.2.3 Generation of a Chimeric Virus - Approach Three***

It is proposed to construct a single chimeric P protein that includes a full-length N-terminal domain (NTD) partially derived from NiV and a NiV OD-XD that can interact with NiV N exchanged for CedV N (Figure 2C). This approach uses only the N-terminal NiV P-NTD residues necessary for N<sup>0</sup>P complex formation, while substituting the immune-suppressive NiV P-NTD residues with those from CedV P-NTD. This configuration should support interactions between NiV P-XD and both NiV N-MoRE and NiV N-core, as well as between NiV P-XD and NiV L. To potentially enhance the packaging of progeny virions, the NiV N box 3 should be replaced with CedV N box 3, which may facilitate interactions between NiV N and CedV M (Iwasaki et al., 2009; Ray et al., 2016; Thakkar et al., 2018).

## REFERENCES

- Abdella, R., Aggarwal, M., Okura, T., Lamb, R. A., & He, Y. (2020). Structure of a paramyxovirus polymerase complex reveals a unique methyltransferase-CTD conformation. *Proc Natl Acad Sci U S A*, *117*(9), 4931-4941. <https://doi.org/10.1073/pnas.1919837117>
- Acosta, P. L., Caballero, M. T., & Polack, F. P. (2015). Brief History and Characterization of Enhanced Respiratory Syncytial Virus Disease. *Clin Vaccine Immunol*, *23*(3), 189-195. <https://doi.org/10.1128/cvi.00609-15>
- Aggarwal, M., & Plemper, R. K. (2020). Structural Insight into Paramyxovirus and Pneumovirus Entry Inhibition. *Viruses*, *12*(3). <https://doi.org/10.3390/v12030342>
- Al-Obaidi, M. M. J., Muthanna, A., & Desa, M. N. M. (2024). Nipah Virus Neurotropism: Insights into Blood-Brain Barrier Disruption. *J Integr Neurosci*, *23*(5), 90. <https://doi.org/10.31083/j.jin2305090>
- Alam, A. M. (2022). Nipah virus, an emerging zoonotic disease causing fatal encephalitis. *Clin Med (Lond)*, *22*(4), 348-352. <https://doi.org/10.7861/clinmed.2022-0166>
- Alpizar, S. A., Accini, J., Anderson, D. C., Eysa, B., Medina-Piñón, I., Ohmagari, N., Ostrovskyy, M. M., Aggrey-Amable, A., Beck, K., Byrne, D., Grayson, S., Hwang, P. M. T., Lonchar, J. D., Strizki, J., Xu, Y., Paschke, A., De Anda, C. S., & Sears, P. S. (2023). Molnupiravir for intra-household prevention of COVID-19: The MOVE-AHEAD randomized, placebo-controlled trial. *J Infect*, *87*(5), 392-402. <https://doi.org/10.1016/j.jinf.2023.08.016>
- Amr, S. S., & Tbakhi, A. (2007). Abu Bakr Muhammad Ibn Zakariya Al Razi (Rhazes): philosopher, physician and alchemist. *Ann Saudi Med*, *27*(4), 305-307. <https://doi.org/10.5144/0256-4947.2007.305>
- Antivirals Agents, Including Antibody Products Summary Recommendations*. (2024). NIH. Retrieved May 1, 2024 from <https://www.covid19treatmentguidelines.nih.gov/therapies/antivirals-including-antibody-products/molnupiravir/>
- Barker, W. H., & Mullooly, J. P. (1982). Pneumonia and influenza deaths during epidemics: implications for prevention. *Arch Intern Med*, *142*(1), 85-89.
- Bartelt, M. A., & Duncan, J. L. (1978). Adherence of group A streptococci to human epithelial cells. *Infect Immun*, *20*(1), 200-208. <https://doi.org/10.1128/iai.20.1.200-208.1978>
- Basu, A., Mills, D. M., & Bowlin, T. L. (2010). High-throughput screening of viral entry inhibitors using pseudotyped virus. *Curr Protoc Pharmacol*, Chapter 13, Unit 13B.13. <https://doi.org/10.1002/0471141755.ph13b03s51>
- Berche, P. (2022). History of measles. *Presse Med*, *51*(3), 104149. <https://doi.org/10.1016/j.lpm.2022.104149>
- Bieringer, M., Han, J. W., Kendl, S., Khosravi, M., Plattet, P., & Schneider-Schaulies, J. (2013). Experimental adaptation of wild-type canine distemper virus (CDV) to the human entry receptor CD150. *PLoS One*, *8*(3), e57488. <https://doi.org/10.1371/journal.pone.0057488>
- Blount, R. E., Jr., Morris, J. A., & Savage, R. E. (1956). Recovery of cytopathogenic agent from chimpanzees with coryza. *Proc Soc Exp Biol Med*, *92*(3), 544-549. <https://doi.org/10.3181/00379727-92-22538>

- Bloyet, L. M., Welsch, J., Enchery, F., Mathieu, C., de Breyne, S., Horvat, B., Grigorov, B., & Gerlier, D. (2016). HSP90 Chaperoning in Addition to Phosphoprotein Required for Folding but Not for Supporting Enzymatic Activities of Measles and Nipah Virus L Polymerases. *J Virol*, *90*(15), 6642-6656. <https://doi.org/10.1128/jvi.00602-16>
- Blutinger, E., Schmitz, G., Kang, C., Comp, G., Wagner, E., Finnell, J. T., Cozzi, N., & Haddock, A. (2023). Measles: Contemporary considerations for the emergency physician. *J Am Coll Emerg Physicians Open*, *4*(5), e13032. <https://doi.org/10.1002/emp2.13032>
- Bourhis, J. M., Yabukarski, F., Communie, G., Schneider, R., Volchkova, V. A., Frén at, M., G erard, F. C., Ducournau, C., Mas, C., Tarbouriech, N., Ringkj bing Jensen, M., Volchkov, V. E., Blackledge, M., & Jamin, M. (2022). Structural Dynamics of the C-terminal X Domain of Nipah and Hendra Viruses Controls the Attachment to the C-terminal Tail of the Nucleocapsid Protein. *J Mol Biol*, *434*(10), 167551. <https://doi.org/10.1016/j.jmb.2022.167551>
- Campagnola, G., Gong, P., & Peersen, O. B. (2011). High-throughput screening identification of poliovirus RNA-dependent RNA polymerase inhibitors. *Antiviral Res*, *91*(3), 241-251. <https://doi.org/10.1016/j.antiviral.2011.06.006>
- Cate, T. R. (1998). Impact of influenza and other community-acquired viruses. *Semin Respir Infect*, *13*(1), 17-23.
- Causes of severe pneumonia requiring hospital admission in children without HIV infection from Africa and Asia: the PERCH multi-country case-control study. (2019). *Lancet*, *394*(10200), 757-779. [https://doi.org/10.1016/s0140-6736\(19\)30721-4](https://doi.org/10.1016/s0140-6736(19)30721-4)
- CDC. (2023, July 17, 2023). *RSV Surveillance & Research*. Retrieved May 2, 2024 from <https://www.cdc.gov/rsv/research/index.html>
- CDC. (2024a, April 24, 2024). *Global Measles Outbreaks*. Retrieved May 3, 2024 from <https://www.cdc.gov/globalhealth/measles/data/global-measles-outbreaks.html>
- CDC. (2024b, May 9, 2024). *History of Measles*. Retrieved June 17, 2024 from <https://www.cdc.gov/measles/about/history.html>
- CDC. (2024c, June 14, 2024). *Measles Cases and Outbreaks*. Retrieved June 17, 2024 from <https://www.cdc.gov/measles/data-research/index.html>
- CDC. (2024d, April 18, 2024). *Measles Clinical Diagnosis Fact Sheet*. Retrieved June 18, 2024 from <https://www.cdc.gov/measles/resources/clinical-diagnosis-fact-sheet.html>
- CDC. (2024e, June 5, 2024). *Symptoms of RSV*. Retrieved July 2, 2024 from <https://www.cdc.gov/rsv/symptoms/index.html>
- CDC. (March 15, 2023). *CDC Museum COVID-19 Timeline*. Retrieved July 11, 2024 from <https://www.cdc.gov/museum/timeline/covid19.html>
- Chen, M., Ogino, T., & Banerjee, A. K. (2007). Interaction of vesicular stomatitis virus P and N proteins: identification of two overlapping domains at the N terminus of P that are involved in N0-P complex formation and encapsidation of viral genome RNA. *J Virol*, *81*(24), 13478-13485. <https://doi.org/10.1128/jvi.01244-07>
- Chu, H., Chan, J. F., & Yuen, K. Y. (2022). Animal models in SARS-CoV-2 research. *Nat Methods*, *19*(4), 392-394. <https://doi.org/10.1038/s41592-022-01447-w>
- Clayton, B. A. (2017). Nipah virus: transmission of a zoonotic paramyxovirus. *Curr Opin Virol*, *22*, 97-104. <https://doi.org/10.1016/j.coviro.2016.12.003>



- Communie, G., Habchi, J., Yabukarski, F., Blocquel, D., Schneider, R., Tarbouriech, N., Papageorgiou, N., Ruigrok, R. W., Jamin, M., Jensen, M. R., Longhi, S., & Blackledge, M. (2013). Atomic resolution description of the interaction between the nucleoprotein and phosphoprotein of Hendra virus. *PLoS Pathog*, *9*(9), e1003631. <https://doi.org/10.1371/journal.ppat.1003631>
- Cong, J., Feng, X., Kang, H., Fu, W., Wang, L., Wang, C., Li, X., Chen, Y., & Rao, Z. (2023). Structure of the Newcastle Disease Virus L protein in complex with tetrameric phosphoprotein. *Nat Commun*, *14*(1), 1324. <https://doi.org/10.1038/s41467-023-37012-y>
- Cox, R. M., Lieber, C. M., Wolf, J. D., Karimi, A., Lieberman, N. A. P., Sticher, Z. M., Roychoudhury, P., Andrews, M. K., Krueger, R. E., Natchus, M. G., Painter, G. R., Kolykhalov, A. A., Greninger, A. L., & Plemper, R. K. (2023). Comparing molnupiravir and nirmatrelvir/ritonavir efficacy and the effects on SARS-CoV-2 transmission in animal models. *Nat Commun*, *14*(1), 4731. <https://doi.org/10.1038/s41467-023-40556-8>
- Cox, R. M., Sourimant, J., Govindarajan, M., Natchus, M. G., & Plemper, R. K. (2021). Therapeutic targeting of measles virus polymerase with ERDRP-0519 suppresses all RNA synthesis activity. *PLoS Pathog*, *17*(2), e1009371. <https://doi.org/10.1371/journal.ppat.1009371>
- Cox, R. M., Sourimant, J., Toots, M., Yoon, J. J., Ikegame, S., Govindarajan, M., Watkinson, R. E., Thibault, P., Makhsous, N., Lin, M. J., Marengo, J. R., Sticher, Z., Kolykhalov, A. A., Natchus, M. G., Greninger, A. L., Lee, B., & Plemper, R. K. (2020). Orally efficacious broad-spectrum allosteric inhibitor of paramyxovirus polymerase. *Nat Microbiol*, *5*(10), 1232-1246. <https://doi.org/10.1038/s41564-020-0752-7>
- Cox, R. M., Wolf, J. D., Lieber, C. M., Sourimant, J., Lin, M. J., Babusis, D., DuPont, V., Chan, J., Barrett, K. T., Lye, D., Kalla, R., Chun, K., Mackman, R. L., Ye, C., Cihlar, T., Martinez-Sobrido, L., Greninger, A. L., Bilello, J. P., & Plemper, R. K. (2021). Oral prodrug of remdesivir parent GS-441524 is efficacious against SARS-CoV-2 in ferrets. *Nat Commun*, *12*(1), 6415. <https://doi.org/10.1038/s41467-021-26760-4>
- Cox, R. M., Wolf, J. D., Lieberman, N. A., Lieber, C. M., Kang, H. J., Sticher, Z. M., Yoon, J. J., Andrews, M. K., Govindarajan, M., Krueger, R. E., Sobolik, E. B., Natchus, M. G., Gewirtz, A. T., deSwart, R. L., Kolykhalov, A. A., Hekmatyar, K., Sakamoto, K., Greninger, A. L., & Plemper, R. K. (2024). Therapeutic mitigation of measles-like immune amnesia and exacerbated disease after prior respiratory virus infections in ferrets. *Nat Commun*, *15*(1), 1189. <https://doi.org/10.1038/s41467-024-45418-5>
- Cox, R. M., Wolf, J. D., & Plemper, R. K. (2021). Therapeutically administered ribonucleoside analogue MK-4482/EIDD-2801 blocks SARS-CoV-2 transmission in ferrets. *Nat Microbiol*, *6*(1), 11-18. <https://doi.org/10.1038/s41564-020-00835-2>
- Crum, F. S. (1914). A STATISTICAL STUDY OF MEASLES. *Am J Public Health (N Y)*, *4*(4), 289-309. <https://doi.org/10.2105/ajph.4.4.289-a>
- Cui, Z., Li, J., Meng, L., & Zhang, Z. (2024). Nipah virus: a re-emerging public health concern. *Lancet Microbe*, *5*(3), e212. [https://doi.org/10.1016/s2666-5247\(23\)00361-0](https://doi.org/10.1016/s2666-5247(23)00361-0)
- Curran, J., Marq, J. B., & Kolakofsky, D. (1995). An N-terminal domain of the Sendai paramyxovirus P protein acts as a chaperone for the NP protein during the nascent

- chain assembly step of genome replication. *J Virol*, *69*(2), 849-855. <https://doi.org/10.1128/jvi.69.2.849-855.1995>
- Davis, B. C., Brown, J. A., & Thorpe, I. F. (2015). Allosteric inhibitors have distinct effects, but also common modes of action, in the HCV polymerase. *Biophys J*, *108*(7), 1785-1795. <https://doi.org/10.1016/j.bpj.2015.03.005>
- Dawes, B. E., & Freiberg, A. N. (2019). Henipavirus infection of the central nervous system. *Pathog Dis*, *77*(2). <https://doi.org/10.1093/femspd/ftz023>
- de Vries, R. D., Ludlow, M., Verburch, R. J., van Amerongen, G., Yüksel, S., Nguyen, D. T., McQuaid, S., Osterhaus, A. D., Duprex, W. P., & de Swart, R. L. (2014). Measles vaccination of nonhuman primates provides partial protection against infection with canine distemper virus. *J Virol*, *88*(8), 4423-4433. <https://doi.org/10.1128/jvi.03676-13>
- Deem, S. L., Spelman, L. H., Yates, R. A., & Montali, R. J. (2000). Canine distemper in terrestrial carnivores: a review. *J Zoo Wildl Med*, *31*(4), 441-451. [https://doi.org/10.1638/1042-7260\(2000\)031\[0441:Cditca\]2.0.Co;2](https://doi.org/10.1638/1042-7260(2000)031[0441:Cditca]2.0.Co;2)
- Delgado, M. F., Coviello, S., Monsalvo, A. C., Melendi, G. A., Hernandez, J. Z., Batalle, J. P., Diaz, L., Trento, A., Chang, H. Y., Mitzner, W., Ravetch, J., Melero, J. A., Irusta, P. M., & Polack, F. P. (2009). Lack of antibody affinity maturation due to poor Toll-like receptor stimulation leads to enhanced respiratory syncytial virus disease. *Nat Med*, *15*(1), 34-41. <https://doi.org/10.1038/nm.1894>
- Denel-Bobrowska, M., & Olejniczak, A. B. (2022). Non-nucleoside structured compounds with antiviral activity-past 10 years (2010-2020). *Eur J Med Chem*, *231*, 114136. <https://doi.org/10.1016/j.ejmech.2022.114136>
- Domachowske, J. B., Bonville, C. A., & Rosenberg, H. F. (2004). Animal models for studying respiratory syncytial virus infection and its long term effects on lung function. *Pediatr Infect Dis J*, *23*(11 Suppl), S228-234. <https://doi.org/10.1097/01.inf.0000144672.81955.a4>
- Dong, G., Peng, C., Luo, J., Wang, C., Han, L., Wu, B., Ji, G., & He, H. (2015). Adamantane-resistant influenza A viruses in the world (1902-2013): frequency and distribution of M2 gene mutations. *PLoS One*, *10*(3), e0119115. <https://doi.org/10.1371/journal.pone.0119115>
- Du Pont, V., Jiang, Y., & Plemper, R. K. (2019). Bipartite interface of the measles virus phosphoprotein X domain with the large polymerase protein regulates viral polymerase dynamics. *PLoS Pathog*, *15*(8), e1007995. <https://doi.org/10.1371/journal.ppat.1007995>
- Düx, A., Lequime, S., Patrono, L. V., Vrancken, B., Boral, S., Gogarten, J. F., Hilbig, A., Horst, D., Merkel, K., Prepoint, B., Santibanez, S., Schlotterbeck, J., Suchard, M. A., Ulrich, M., Widulin, N., Mankertz, A., Leendertz, F. H., Harper, K., Schnalke, T., . . . Calvignac-Spencer, S. (2020). Measles virus and rinderpest virus divergence dated to the sixth century BCE. *Science*, *368*(6497), 1367-1370. <https://doi.org/10.1126/science.aba9411>
- eClinicalMedicine. (2024). Concerning global rise in measles cases. *EClinicalMedicine*, *68*, 102502. <https://doi.org/10.1016/j.eclinm.2024.102502>
- Faus-Cotino, J., Reina, G., & Pueyo, J. (2024). Nipah Virus: A Multidimensional Update. *Viruses*, *16*(2). <https://doi.org/10.3390/v16020179>

- FDA. (2020, October 22, 2020). *FDA Approves First Treatment for COVID-19*. Retrieved July 11, 2024 from <https://www.fda.gov/news-events/press-announcements/fda-approves-first-treatment-covid-19>
- FDA. (2023a). *FDA Approves First Oral Antiviral for Treatment of COVID-19 in Adults*. Retrieved July 11, 2024 from <https://www.fda.gov/news-events/press-announcements/fda-approves-first-oral-antiviral-treatment-covid-19-adults>
- FDA. (2023b, May 4, 2023). *FDA Approves First RSV Vaccine*. <https://www.fda.gov/news-events/press-announcements/fda-approves-first-respiratory-syncytial-virus-rsv-vaccine>
- FDA. (2023c, July 17, 2023). *FDA Approves New Drug to Prevent RSV in Babies and Toddlers*. Retrieved June 20, 2024 from <https://www.fda.gov/news-events/press-announcements/fda-approves-new-drug-prevent-rsv-babies-and-toddlers>
- Fearn, R., & Plemper, R. K. (2017). Polymerases of paramyxoviruses and pneumoviruses. *Virus Res*, 234, 87-102. <https://doi.org/10.1016/j.virusres.2017.01.008>
- Felicetti, T., Sarnari, C., Gaito, R., Tabarrini, O., & Manfroni, G. (2024). Recent Progress toward the Discovery of Small Molecules as Novel Anti-Respiratory Syncytial Virus Agents. *J Med Chem*. <https://doi.org/10.1021/acs.jmedchem.4c00630>
- Field, H., Young, P., Yob, J. M., Mills, J., Hall, L., & Mackenzie, J. (2001). The natural history of Hendra and Nipah viruses. *Microbes Infect*, 3(4), 307-314. [https://doi.org/10.1016/s1286-4579\(01\)01384-3](https://doi.org/10.1016/s1286-4579(01)01384-3)
- Follmann, M., Briem, H., Steinmeyer, A., Hillisch, A., Schmitt, M. H., Haning, H., & Meier, H. (2019). An approach towards enhancement of a screening library: The Next Generation Library Initiative (NGLI) at Bayer - against all odds? *Drug Discov Today*, 24(3), 668-672. <https://doi.org/10.1016/j.drudis.2018.12.003>
- Gaudino, M., Aurine, N., Dumont, C., Fouret, J., Ferren, M., Mathieu, C., Reynard, O., Volchkov, V. E., Legras-Lachuer, C., Georges-Courbot, M. C., & Horvat, B. (2020). High Pathogenicity of Nipah Virus from Pteropus lylei Fruit Bats, Cambodia. *Emerg Infect Dis*, 26(1), 104-113. <https://doi.org/10.3201/eid2601.191284>
- Ghosh, A., Nayak, R., & Shaila, M. S. (1996). Synthesis of leader RNA and editing of P mRNA during transcription by rinderpest virus. *Virus Res*, 41(1), 69-76. [https://doi.org/10.1016/0168-1702\(95\)01276-1](https://doi.org/10.1016/0168-1702(95)01276-1)
- Gildemann, K., Tsernant, M.-L., Liivand, L., Ennomäe, R., Poikalainen, V., Lepasalu, L., Rom, S., Kavak, A., Cox, R. M., Wolf, J. D., Lieber, C. M., Plemper, R. K., Männik, A., Ustav, M., Ustav, M., & Gerhold, J. M. (2024). Anti-SARS-CoV-2 antibodies in a nasal spray efficiently block viral transmission between ferrets. *iScience*, 27(7), 110326. <https://doi.org/https://doi.org/10.1016/j.isci.2024.110326>
- Graham, B. S., Rutigliano, J. A., & Johnson, T. R. (2002). Respiratory syncytial virus immunobiology and pathogenesis. *Virology*, 297(1), 1-7. <https://doi.org/10.1006/viro.2002.1431>
- Groves, H. T., Cuthbertson, L., James, P., Moffatt, M. F., Cox, M. J., & Tregoning, J. S. (2018). Respiratory Disease following Viral Lung Infection Alters the Murine Gut Microbiota. *Front Immunol*, 9, 182. <https://doi.org/10.3389/fimmu.2018.00182>
- Gu, S., Chen, Y., Wu, Z., Chen, Y., Gao, H., Lv, L., Guo, F., Zhang, X., Luo, R., Huang, C., Lu, H., Zheng, B., Zhang, J., Yan, R., Zhang, H., Jiang, H., Xu, Q., Guo, J., Gong, Y., . . . Li, L. (2020).

- Alterations of the Gut Microbiota in Patients With Coronavirus Disease 2019 or H1N1 Influenza. *Clin Infect Dis*, 71(10), 2669-2678. <https://doi.org/10.1093/cid/ciaa709>
- Gurley, E. S., Montgomery, J. M., Hossain, M. J., Bell, M., Azad, A. K., Islam, M. R., Molla, M. A., Carroll, D. S., Ksiazek, T. G., Rota, P. A., Lowe, L., Comer, J. A., Rollin, P., Czub, M., Grolla, A., Feldmann, H., Luby, S. P., Woodward, J. L., & Breiman, R. F. (2007). Person-to-person transmission of Nipah virus in a Bangladeshi community. *Emerg Infect Dis*, 13(7), 1031-1037. <https://doi.org/10.3201/eid1307.061128>
- Gurley, E. S., Montgomery, J. M., Hossain, M. J., Islam, M. R., Molla, M. A., Shamsuzzaman, S. M., Akram, K., Zaman, K., Asgari, N., Comer, J. A., Azad, A. K., Rollin, P. E., Ksiazek, T. G., & Breiman, R. F. (2007). Risk of nosocomial transmission of Nipah virus in a Bangladesh hospital. *Infect Control Hosp Epidemiol*, 28(6), 740-742. <https://doi.org/10.1086/516665>
- Guryanov, S. G., Liljeroos, L., Kasaragod, P., Kajander, T., & Butcher, S. J. (2015). Crystal Structure of the Measles Virus Nucleoprotein Core in Complex with an N-Terminal Region of Phosphoprotein. *J Virol*, 90(6), 2849-2857. <https://doi.org/10.1128/jvi.02865-15>
- Guseva, S., Milles, S., Blackledge, M., & Ruigrok, R. W. H. (2019). The Nucleoprotein and Phosphoprotein of Measles Virus [Review]. *Frontiers in Microbiology*, 10. <https://doi.org/10.3389/fmicb.2019.01832>
- Haas, G. D., Schmitz, K. S., Azarm, K. D., Johnson, K. N., Klain, W. R., Freiberg, A. N., Cox, R. M., Plemper, R. K., & Lee, B. (2024). Tetracistronic Minigenomes Elucidate a Functional Promoter for Ghana Virus and Unveils Cedar Virus Replicase Promiscuity for all Henipaviruses. *bioRxiv*. <https://doi.org/10.1101/2024.04.16.589704>
- Hall, C. B. (2010). Respiratory syncytial virus in young children. *Lancet*, 375(9725), 1500-1502. [https://doi.org/10.1016/s0140-6736\(10\)60401-1](https://doi.org/10.1016/s0140-6736(10)60401-1)
- Hament, J. M., Kimpen, J. L., Fleer, A., & Wolfs, T. F. (1999). Respiratory viral infection predisposing for bacterial disease: a concise review. *FEMS Immunol Med Microbiol*, 26(3-4), 189-195. <https://doi.org/10.1111/j.1574-695X.1999.tb01389.x>
- Harrison, T. R. (1954). Principles of internal medicine. In *Principles of internal medicine* (pp. 1703-1703).
- Hedskog, C., Rodriguez, L., Roychoudhury, P., Huang, M. L., Jerome, K. R., Hao, L., Ireton, R. C., Li, J., Perry, J. K., Han, D., Camus, G., Greninger, A. L., Gale, M., Jr., & Porter, D. P. (2023). Viral Resistance Analyses From the Remdesivir Phase 3 Adaptive COVID-19 Treatment Trial-1 (ACTT-1). *J Infect Dis*, 228(9), 1263-1273. <https://doi.org/10.1093/infdis/jiad270>
- Hoertel, N., Boulware, D. R., Sánchez-Rico, M., Burgun, A., & Limosin, F. (2022). Prevalence of Contraindications to Nirmatrelvir-Ritonavir Among Hospitalized Patients With COVID-19 at Risk for Progression to Severe Disease. *JAMA Netw Open*, 5(11), e2242140. <https://doi.org/10.1001/jamanetworkopen.2022.42140>
- Hoffmann, M., Kleine-Weber, H., Schroeder, S., Krüger, N., Herrler, T., Erichsen, S., Schiergens, T. S., Herrler, G., Wu, N. H., Nitsche, A., Müller, M. A., Drosten, C., & Pöhlmann, S. (2020). SARS-CoV-2 Cell Entry Depends on ACE2 and TMPRSS2 and Is Blocked by a Clinically Proven Protease Inhibitor. *Cell*, 181(2), 271-280.e278. <https://doi.org/10.1016/j.cell.2020.02.052>
- Hofstra, J. J., Matamoros, S., van de Pol, M. A., de Wever, B., Tanck, M. W., Wendt-Knol, H., Deijns, M., van der Hoek, L., Wolthers, K. C., Molenkamp, R., Visser, C. E., Sterk, P. J.,

- Lutter, R., & de Jong, M. D. (2015). Changes in microbiota during experimental human Rhinovirus infection. *BMC Infect Dis*, *15*, 336. <https://doi.org/10.1186/s12879-015-1081-y>
- Hoover, J., Eades, S., & Lam, W. M. (2018). Pediatric Antiviral Stewardship: Defining the Potential Role of Ribavirin in Respiratory Syncytial Virus-Associated Lower Respiratory Illness. *J Pediatr Pharmacol Ther*, *23*(5), 372-378. <https://doi.org/10.5863/1551-6776-23.5.372>
- Hossain, M. J., Gurley, E. S., Montgomery, J. M., Bell, M., Carroll, D. S., Hsu, V. P., Formenty, P., Croisier, A., Bertherat, E., Faiz, M. A., Azad, A. K., Islam, R., Molla, M. A., Ksiazek, T. G., Rota, P. A., Comer, J. A., Rollin, P. E., Luby, S. P., & Breiman, R. F. (2008). Clinical presentation of nipah virus infection in Bangladesh. *Clin Infect Dis*, *46*(7), 977-984. <https://doi.org/10.1086/529147>
- Hou, K., Wu, Z. X., Chen, X. Y., Wang, J. Q., Zhang, D., Xiao, C., Zhu, D., Koya, J. B., Wei, L., Li, J., & Chen, Z. S. (2022). Microbiota in health and diseases. *Signal Transduct Target Ther*, *7*(1), 135. <https://doi.org/10.1038/s41392-022-00974-4>
- Hu, B., Guo, H., Zhou, P., & Shi, Z.-L. (2021). Characteristics of SARS-CoV-2 and COVID-19. *Nature Reviews Microbiology*, *19*(3), 141-154. <https://doi.org/10.1038/s41579-020-00459-7>
- Hu, S., Kim, H., Yang, P., Yu, Z., Ludeke, B., Mobilia, S., Pan, J., Stratton, M., Bian, Y., Fearn, R., & Abraham, J. (2024). Structural and functional analysis of the Nipah virus polymerase complex. *bioRxiv*, 2024.2005.2029.596445. <https://doi.org/10.1101/2024.05.29.596445>
- Hu, Y., Lewandowski, E. M., Tan, H., Zhang, X., Morgan, R. T., Zhang, X., Jacobs, L. M. C., Butler, S. G., Gongora, M. V., Choy, J., Deng, X., Chen, Y., & Wang, J. (2023). Naturally Occurring Mutations of SARS-CoV-2 Main Protease Confer Drug Resistance to Nirmatrelvir. *ACS Cent Sci*, *9*(8), 1658-1669. <https://doi.org/10.1021/acscentsci.3c00538>
- Irwin, K. K., Renzette, N., Kowalik, T. F., & Jensen, J. D. (2016). Antiviral drug resistance as an adaptive process. *Virus Evol*, *2*(1), vew014. <https://doi.org/10.1093/ve/vew014>
- Iverson, L. E., & Rose, J. K. (1981). Localized attenuation and discontinuous synthesis during vesicular stomatitis virus transcription. *Cell*, *23*(2), 477-484. [https://doi.org/10.1016/0092-8674\(81\)90143-4](https://doi.org/10.1016/0092-8674(81)90143-4)
- Iwasaki, M., Takeda, M., Shirogane, Y., Nakatsu, Y., Nakamura, T., & Yanagi, Y. (2009). The matrix protein of measles virus regulates viral RNA synthesis and assembly by interacting with the nucleocapsid protein. *J Virol*, *83*(20), 10374-10383. <https://doi.org/10.1128/jvi.01056-09>
- Jasenosky, L. D., Neumann, G., & Kawaoka, Y. (2010). Minigenome-based reporter system suitable for high-throughput screening of compounds able to inhibit Ebolavirus replication and/or transcription. *Antimicrob Agents Chemother*, *54*(7), 3007-3010. <https://doi.org/10.1128/aac.00138-10>
- Jeannoël, M., Lina, G., Rasigade, J. P., Lina, B., Morfin, F., & Casalegno, J. S. (2019). Microorganisms associated with respiratory syncytial virus pneumonia in the adult population. *Eur J Clin Microbiol Infect Dis*, *38*(1), 157-160. <https://doi.org/10.1007/s10096-018-3407-3>
- Jeong, J. H., Chokkakula, S., Min, S. C., Kim, B. K., Choi, W. S., Oh, S., Yun, Y. S., Kang, D. H., Lee, O. J., Kim, E. G., Choi, J. H., Lee, J. Y., Choi, Y. K., Baek, Y. H., & Song, M. S. (2022).

- Combination therapy with nirmatrelvir and molnupiravir improves the survival of SARS-CoV-2 infected mice. *Antiviral Res*, 208, 105430. <https://doi.org/10.1016/j.antiviral.2022.105430>
- Jiang, M. Y., Duan, Y. P., Tong, X. L., Huang, Q. R., Jia, M. M., Yang, W. Z., & Feng, L. Z. (2023). Clinical manifestations of respiratory syncytial virus infection and the risk of wheezing and recurrent wheezing illness: a systematic review and meta-analysis. *World J Pediatr*, 19(11), 1030-1040. <https://doi.org/10.1007/s12519-023-00743-5>
- Jochmans, D., Liu, C., Donckers, K., Stoycheva, A., Boland, S., Stevens, S. K., De Vita, C., Vanmechelen, B., Maes, P., Trüeb, B., Ebert, N., Thiel, V., De Jonghe, S., Vangeel, L., Bardiot, D., Jekle, A., Blatt, L. M., Beigelman, L., Symons, J. A., . . . Vandyck, K. (2023). The Substitutions L50F, E166A, and L167F in SARS-CoV-2 3CLpro Are Selected by a Protease Inhibitor In Vitro and Confer Resistance To Nirmatrelvir. *mBio*, 14(1), e0281522. <https://doi.org/10.1128/mbio.02815-22>
- Johansson, K., Bourhis, J. M., Campanacci, V., Cambillau, C., Canard, B., & Longhi, S. (2003). Crystal structure of the measles virus phosphoprotein domain responsible for the induced folding of the C-terminal domain of the nucleoprotein. *J Biol Chem*, 278(45), 44567-44573. <https://doi.org/10.1074/jbc.M308745200>
- Johnson, K. A., & Dangerfield, T. (2021). Mechanisms of inhibition of viral RNA replication by nucleotide analogs. *Enzymes*, 49, 39-62. <https://doi.org/10.1016/bs.enz.2021.07.001>
- Kabinger, F., Stiller, C., Schmitzová, J., Dienemann, C., Kokic, G., Hillen, H. S., Höbartner, C., & Cramer, P. (2021). Mechanism of molnupiravir-induced SARS-CoV-2 mutagenesis. *Nat Struct Mol Biol*, 28(9), 740-746. <https://doi.org/10.1038/s41594-021-00651-0>
- Ker, D. S., Jenkins, H. T., Greive, S. J., & Antson, A. A. (2021). CryoEM structure of the Nipah virus nucleocapsid assembly. *PLoS Pathog*, 17(7), e1009740. <https://doi.org/10.1371/journal.ppat.1009740>
- Kingston, R. L., Gay, L. S., Baase, W. S., & Matthews, B. W. (2008). Structure of the nucleocapsid-binding domain from the mumps virus polymerase; an example of protein folding induced by crystallization. *J Mol Biol*, 379(4), 719-731. <https://doi.org/10.1016/j.jmb.2007.12.080>
- Kingston, R. L., Hamel, D. J., Gay, L. S., Dahlquist, F. W., & Matthews, B. W. (2004). Structural basis for the attachment of a paramyxoviral polymerase to its template. *Proc Natl Acad Sci U S A*, 101(22), 8301-8306. <https://doi.org/10.1073/pnas.0402690101>
- Kokic, G., Hillen, H. S., Tegunov, D., Dienemann, C., Seitz, F., Schmitzova, J., Farnung, L., Siewert, A., Höbartner, C., & Cramer, P. (2021). Mechanism of SARS-CoV-2 polymerase stalling by remdesivir. *Nat Commun*, 12(1), 279. <https://doi.org/10.1038/s41467-020-20542-0>
- Krismer, B., Weidenmaier, C., Zipperer, A., & Peschel, A. (2017). The commensal lifestyle of *Staphylococcus aureus* and its interactions with the nasal microbiota. *Nat Rev Microbiol*, 15(11), 675-687. <https://doi.org/10.1038/nrmicro.2017.104>
- Krumm, S. A., Yan, D., Hovingh, E. S., Evers, T. J., Enkirch, T., Reddy, G. P., Sun, A., Saindane, M. T., Arrendale, R. F., Painter, G., Liotta, D. C., Natchus, M. G., von Messling, V., & Plemper, R. K. (2014). An orally available, small-molecule polymerase inhibitor shows efficacy against a lethal morbillivirus infection in a large animal model. *Sci Transl Med*, 6(232), 232ra252. <https://doi.org/10.1126/scitranslmed.3008517>

- Kulkarni, D. D., Tosh, C., Venkatesh, G., & Senthil Kumar, D. (2013). Nipah virus infection: current scenario. *Indian J Virol*, *24*(3), 398-408. <https://doi.org/10.1007/s13337-013-0171-y>
- Kumar, G. N., Rodrigues, A. D., Buko, A. M., & Denissen, J. F. (1996). Cytochrome P450-mediated metabolism of the HIV-1 protease inhibitor ritonavir (ABT-538) in human liver microsomes. *J Pharmacol Exp Ther*, *277*(1), 423-431.
- Laing, E. D., Amaya, M., Navaratnarajah, C. K., Feng, Y. R., Cattaneo, R., Wang, L. F., & Broder, C. C. (2018). Rescue and characterization of recombinant cedar virus, a non-pathogenic Henipavirus species. *Virology*, *15*(1), 56. <https://doi.org/10.1186/s12985-018-0964-0>
- Laing, E. D., Navaratnarajah, C. K., Cheliout Da Silva, S., Petzing, S. R., Xu, Y., Sterling, S. L., Marsh, G. A., Wang, L. F., Amaya, M., Nikolov, D. B., Cattaneo, R., Broder, C. C., & Xu, K. (2019). Structural and functional analyses reveal promiscuous and species specific use of ephrin receptors by Cedar virus. *Proc Natl Acad Sci U S A*, *116*(41), 20707-20715. <https://doi.org/10.1073/pnas.1911773116>
- Laksono, B. M., de Vries, R. D., McQuaid, S., Duprex, W. P., & de Swart, R. L. (2016). Measles Virus Host Invasion and Pathogenesis. *Viruses*, *8*(8). <https://doi.org/10.3390/v8080210>
- Laksono, B. M., de Vries, R. D., Verburch, R. J., Visser, E. G., de Jong, A., Fraaij, P. L. A., Ruijs, W. L. M., Nieuwenhuijse, D. F., van den Ham, H. J., Koopmans, M. P. G., van Zelm, M. C., Osterhaus, A., & de Swart, R. L. (2018). Studies into the mechanism of measles-associated immune suppression during a measles outbreak in the Netherlands. *Nat Commun*, *9*(1), 4944. <https://doi.org/10.1038/s41467-018-07515-0>
- Lamp, B., Dietzel, E., Kolesnikova, L., Sauerhering, L., Erbar, S., Weingartl, H., & Maisner, A. (2013). Nipah virus entry and egress from polarized epithelial cells. *J Virol*, *87*(6), 3143-3154. <https://doi.org/10.1128/jvi.02696-12>
- Lau, K., Srivatsav, V., Rizwan, A., Nashed, A., Liu, R., Shen, R., & Akhtar, M. (2017). Bridging the Gap between Gut Microbial Dysbiosis and Cardiovascular Diseases. *Nutrients*, *9*(8). <https://doi.org/10.3390/nu9080859>
- Leppert, M., Rittenhouse, L., Perrault, J., Summers, D. F., & Kolakofsky, D. (1979). Plus and minus strand leader RNAs in negative strand virus-infected cells. *Cell*, *18*(3), 735-747. [https://doi.org/10.1016/0092-8674\(79\)90127-2](https://doi.org/10.1016/0092-8674(79)90127-2)
- Li, Y., Wang, X., Blau, D. M., Caballero, M. T., Feikin, D. R., Gill, C. J., Madhi, S. A., Omer, S. B., Simões, E. A. F., Campbell, H., Pariente, A. B., Bardach, D., Bassat, Q., Casalegno, J. S., Chakhunashvili, G., Crawford, N., Danilenko, D., Do, L. A. H., Echavarria, M., . . . Nair, H. (2022). Global, regional, and national disease burden estimates of acute lower respiratory infections due to respiratory syncytial virus in children younger than 5 years in 2019: a systematic analysis. *Lancet*, *399*(10340), 2047-2064. [https://doi.org/10.1016/s0140-6736\(22\)00478-0](https://doi.org/10.1016/s0140-6736(22)00478-0)
- Lieber, C. M., Cox, R. M., Sourimant, J., Wolf, J. D., Juergens, K., Phung, Q., Saindane, M. T., Smith, M. K., Sticher, Z. M., Kalykhalov, A. A., Natchus, M. G., Painter, G. R., Sakamoto, K., Greninger, A. L., & Plemper, R. K. (2022). SARS-CoV-2 VOC type and biological sex affect molnupiravir efficacy in severe COVID-19 dwarf hamster model. *Nat Commun*, *13*(1), 4416. <https://doi.org/10.1038/s41467-022-32045-1>
- Lieber, C. M., Kang, H. J., Aggarwal, M., Lieberman, N. A., Sobolik, E. B., Yoon, J. J., Natchus, M. G., Cox, R. M., Greninger, A. L., & Plemper, R. K. (2024). Influenza A virus resistance to



- 4'-fluorouridine coincides with viral attenuation in vitro and in vivo. *PLoS Pathog*, 20(2), e1011993. <https://doi.org/10.1371/journal.ppat.1011993>
- Lieber, C. M., & Plemper, R. K. (2022). 4'-Fluorouridine Is a Broad-Spectrum Orally Available First-Line Antiviral That May Improve Pandemic Preparedness. *DNA Cell Biol*, 41(8), 699-704. <https://doi.org/10.1089/dna.2022.0312>
- Lieber, C. M., & Plemper, R. K. (2022). 4'-Fluorouridine Is a Broad-Spectrum Orally Available First-Line Antiviral That May Improve Pandemic Preparedness. *DNA and Cell Biology*, 41(8), 699-704. <https://doi.org/10.1089/dna.2022.0312>
- Lieu, K. G., Marsh, G. A., Wang, L. F., & Netter, H. J. (2015). The non-pathogenic Henipavirus Cedar paramyxovirus phosphoprotein has a compromised ability to target STAT1 and STAT2. *Antiviral Res*, 124, 69-76. <https://doi.org/10.1016/j.antiviral.2015.09.017>
- Liu, Q., Stone, J. A., Bradel-Tretheway, B., Dabundo, J., Benavides Montano, J. A., Santos-Montanez, J., Biering, S. B., Nicola, A. V., Iorio, R. M., Lu, X., & Aguilar, H. C. (2013). Unraveling a three-step spatiotemporal mechanism of triggering of receptor-induced Nipah virus fusion and cell entry. *PLoS Pathog*, 9(11), e1003770. <https://doi.org/10.1371/journal.ppat.1003770>
- Longhi, S., Receveur-Bréchet, V., Karlin, D., Johansson, K., Darbon, H., Bhella, D., Yeo, R., Finet, S., & Canard, B. (2003). The C-terminal domain of the measles virus nucleoprotein is intrinsically disordered and folds upon binding to the C-terminal moiety of the phosphoprotein. *J Biol Chem*, 278(20), 18638-18648. <https://doi.org/10.1074/jbc.M300518200>
- Looi, L. M., & Chua, K. B. (2007). Lessons from the Nipah virus outbreak in Malaysia. *Malays J Pathol*, 29(2), 63-67.
- Louria, D. B., Blumenfeld, H. L., Ellis, J. T., Kilbourne, E. D., & Rogers, D. E. (1959). Studies on influenza in the pandemic of 1957-1958. II. Pulmonary complications of influenza. *J Clin Invest*, 38(1 Part 2), 213-265. <https://doi.org/10.1172/jci103791>
- Lunardi, M., Darold, G. M., Amude, A. M., Headley, S. A., Sonne, L., Yamauchi, K. C. I., Boabaid, F. M., Alfieri, A. F., & Alfieri, A. A. (2018). Canine distemper virus active infection in order Pilosa, family Myrmecophagidae, species Tamandua tetradactyla. *Vet Microbiol*, 220, 7-11. <https://doi.org/10.1016/j.vetmic.2018.04.030>
- Luthra, P., Liang, J., Pietzsch, C. A., Khadka, S., Edwards, M. R., Wei, S., De, S., Posner, B., Bukreyev, A., Ready, J. M., & Basler, C. F. (2018). A high throughput screen identifies benzoquinoline compounds as inhibitors of Ebola virus replication. *Antiviral Res*, 150, 193-201. <https://doi.org/10.1016/j.antiviral.2017.12.019>
- Ma, J., Qi, X., Chen, H., Li, X., Zhang, Z., Wang, H., Sun, L., Zhang, L., Guo, J., Morawska, L., Grinshpun, S. A., Biswas, P., Flagan, R. C., & Yao, M. (2021). Coronavirus Disease 2019 Patients in Earlier Stages Exhaled Millions of Severe Acute Respiratory Syndrome Coronavirus 2 Per Hour. *Clin Infect Dis*, 72(10), e652-e654. <https://doi.org/10.1093/cid/ciaa1283>
- Madewell, Z. J., Yang, Y., Longini, I. M., Jr., Halloran, M. E., & Dean, N. E. (2021). Factors Associated With Household Transmission of SARS-CoV-2: An Updated Systematic Review and Meta-analysis. *JAMA Netw Open*, 4(8), e2122240. <https://doi.org/10.1001/jamanetworkopen.2021.22240>

- Maisner, A., Neufeld, J., & Weingartl, H. (2009). Organ- and endotheliotropism of Nipah virus infections in vivo and in vitro. *Thromb Haemost*, *102*(6), 1014-1023. <https://doi.org/10.1160/th09-05-0310>
- Manna, S., Baidara, P., & Mandal, S. M. (2020). Molecular pathogenesis of secondary bacterial infection associated to viral infections including SARS-CoV-2. *J Infect Public Health*, *13*(10), 1397-1404. <https://doi.org/10.1016/j.jiph.2020.07.003>
- Marsh, G. A., de Jong, C., Barr, J. A., Tachedjian, M., Smith, C., Middleton, D., Yu, M., Todd, S., Foord, A. J., Haring, V., Payne, J., Robinson, R., Broz, I., Crameri, G., Field, H. E., & Wang, L. F. (2012). Cedar virus: a novel Henipavirus isolated from Australian bats. *PLoS Pathog*, *8*(8), e1002836. <https://doi.org/10.1371/journal.ppat.1002836>
- Martinez-Gutierrez, M., & Ruiz-Saenz, J. (2016). Diversity of susceptible hosts in canine distemper virus infection: a systematic review and data synthesis. *BMC Vet Res*, *12*, 78. <https://doi.org/10.1186/s12917-016-0702-z>
- Mavrakis, M., Méhouas, S., Réal, E., Iseni, F., Blondel, D., Tordo, N., & Ruigrok, R. W. (2006). Rabies virus chaperone: identification of the phosphoprotein peptide that keeps nucleoprotein soluble and free from non-specific RNA. *Virology*, *349*(2), 422-429. <https://doi.org/10.1016/j.virol.2006.01.030>
- Meyerowitz, E. A., & Richterman, A. (2022). SARS-CoV-2 Transmission and Prevention in the Era of the Delta Variant. *Infect Dis Clin North Am*, *36*(2), 267-293. <https://doi.org/10.1016/j.idc.2022.01.007>
- Meyerowitz, E. A., Richterman, A., Gandhi, R. T., & Sax, P. E. (2021). Transmission of SARS-CoV-2: A Review of Viral, Host, and Environmental Factors. *Ann Intern Med*, *174*(1), 69-79. <https://doi.org/10.7326/m20-5008>
- Mina, M. J., Kula, T., Leng, Y., Li, M., de Vries, R. D., Knip, M., Siljander, H., Rewers, M., Choy, D. F., Wilson, M. S., Larman, H. B., Nelson, A. N., Griffin, D. E., de Swart, R. L., & Elledge, S. J. (2019). Measles virus infection diminishes preexisting antibodies that offer protection from other pathogens. *Science*, *366*(6465), 599-606. <https://doi.org/10.1126/science.aay6485>
- Morales, G. B., & Muñoz, M. A. (2021). Immune amnesia induced by measles and its effects on concurrent epidemics. *J R Soc Interface*, *18*(179), 20210153. <https://doi.org/10.1098/rsif.2021.0153>
- Morens, D. M., Taubenberger, J. K., & Fauci, A. S. (2008). Predominant role of bacterial pneumonia as a cause of death in pandemic influenza: implications for pandemic influenza preparedness. *J Infect Dis*, *198*(7), 962-970. <https://doi.org/10.1086/591708>
- Morris, D. E., Cleary, D. W., & Clarke, S. C. (2017). Secondary Bacterial Infections Associated with Influenza Pandemics. *Front Microbiol*, *8*, 1041. <https://doi.org/10.3389/fmicb.2017.01041>
- Morse, Z. J., & Horwitz, M. S. (2021). Virus Infection Is an Instigator of Intestinal Dysbiosis Leading to Type 1 Diabetes. *Front Immunol*, *12*, 751337. <https://doi.org/10.3389/fimmu.2021.751337>
- Moss, W. J., & Griffin, D. E. (2012). Measles. *Lancet*, *379*(9811), 153-164. [https://doi.org/10.1016/s0140-6736\(10\)62352-5](https://doi.org/10.1016/s0140-6736(10)62352-5)
- Mullard, A. (2008). Vaccine failure explained. *Nature*. <https://doi.org/10.1038/news.2008.1302>

- Mullard, A. (2022). Pfizer's small-molecule antiviral misses on COVID prevention. *Nat Rev Drug Discov*, 21(6), 406. <https://doi.org/10.1038/d41573-022-00089-z>
- Mullard, A. (2024). FDA approves mRNA-based RSV vaccine. *Nat Rev Drug Discov*, 23(7), 487. <https://doi.org/10.1038/d41573-024-00095-3>
- Nair, H., Nokes, D. J., Gessner, B. D., Dherani, M., Madhi, S. A., Singleton, R. J., O'Brien, K. L., Roca, A., Wright, P. F., Bruce, N., Chandran, A., Theodoratou, E., Sutanto, A., Sedyaningsih, E. R., Ngama, M., Munywoki, P. K., Kartasasmita, C., Simões, E. A., Rudan, I., . . . Campbell, H. (2010). Global burden of acute lower respiratory infections due to respiratory syncytial virus in young children: a systematic review and meta-analysis. *Lancet*, 375(9725), 1545-1555. [https://doi.org/10.1016/s0140-6736\(10\)60206-1](https://doi.org/10.1016/s0140-6736(10)60206-1)
- Narayanan, S. A., Jamison, D. A., Jr., Guarnieri, J. W., Zaksas, V., Topper, M., Koutnik, A. P., Park, J., Clark, K. B., Enguita, F. J., Leitão, A. L., Das, S., Moraes-Vieira, P. M., Galeano, D., Mason, C. E., Trovão, N. S., Schwartz, R. E., Schisler, J. C., Coelho-Dos-Reis, J. G. A., Wurtele, E. S., & Beheshti, A. (2024). A comprehensive SARS-CoV-2 and COVID-19 review, Part 2: host extracellular to systemic effects of SARS-CoV-2 infection. *Eur J Hum Genet*, 32(1), 10-20. <https://doi.org/10.1038/s41431-023-01462-1>
- Negrete, O. A., Levroney, E. L., Aguilar, H. C., Bertolotti-Ciarlet, A., Nazarian, R., Tajyar, S., & Lee, B. (2005). EphrinB2 is the entry receptor for Nipah virus, an emergent deadly paramyxovirus. *Nature*, 436(7049), 401-405. <https://doi.org/10.1038/nature03838>
- Negrete, O. A., Wolf, M. C., Aguilar, H. C., Enterlein, S., Wang, W., Mühlberger, E., Su, S. V., Bertolotti-Ciarlet, A., Flick, R., & Lee, B. (2006). Two key residues in ephrinB3 are critical for its use as an alternative receptor for Nipah virus. *PLoS Pathog*, 2(2), e7. <https://doi.org/10.1371/journal.ppat.0020007>
- NIH. (2024a, February 29, 2024). *Antivirals, Including Antibody Products: Molnupiravir*. Retrieved July 11, 2024 from <https://www.covid19treatmentguidelines.nih.gov/therapies/antivirals-including-antibody-products/molnupiravir/#:~:text=On%20December%2023%2C%202021%2C%20the,for%20whom%20alternative%20antiviral%20therapies>
- NIH. (2024b, February 29, 2024). *Clinical Spectrum of SARS-CoV-2*. Retrieved July 15, 2024 from <https://www.covid19treatmentguidelines.nih.gov/overview/clinical-spectrum/>
- Noble, W., Jr, Fisher, E., & Brainard, D. (1928). Studies of Acute Respiratory Infections. I. A Comparison of the Aerobic Flora of the Upper Respiratory Tract of Persons in Health and with Colds.
- Ogino, T., & Green, T. J. (2019). RNA Synthesis and Capping by Non-segmented Negative Strand RNA Viral Polymerases: Lessons From a Prototypic Virus. *Front Microbiol*, 10, 1490. <https://doi.org/10.3389/fmicb.2019.01490>
- Ogunrinola, G. A., Oyewale, J. O., Oshamika, O. O., & Olasehinde, G. I. (2020). The Human Microbiome and Its Impacts on Health. *Int J Microbiol*, 2020, 8045646. <https://doi.org/10.1155/2020/8045646>
- Ohno, S., Seki, F., Ono, N., & Yanagi, Y. (2003). Histidine at position 61 and its adjacent amino acid residues are critical for the ability of SLAM (CD150) to act as a cellular receptor for measles virus. *J Gen Virol*, 84(Pt 9), 2381-2388. <https://doi.org/10.1099/vir.0.19248-0>

- Paget, C., & Trottein, F. (2019). Mechanisms of Bacterial Superinfection Post-influenza: A Role for Unconventional T Cells. *Front Immunol*, *10*, 336. <https://doi.org/10.3389/fimmu.2019.00336>
- Pandey, A., & Galvani, A. P. (2023). Exacerbation of measles mortality by vaccine hesitancy worldwide. *Lancet Glob Health*, *11*(4), e478-e479. [https://doi.org/10.1016/s2214-109x\(23\)00063-3](https://doi.org/10.1016/s2214-109x(23)00063-3)
- Pavan, M., Bolcato, G., Bassani, D., Sturlese, M., & Moro, S. (2021). Supervised Molecular Dynamics (SuMD) Insights into the mechanism of action of SARS-CoV-2 main protease inhibitor PF-07321332. *J Enzyme Inhib Med Chem*, *36*(1), 1646-1650. <https://doi.org/10.1080/14756366.2021.1954919>
- Peart Akindele, N. A., Katamoni, L. D., Brockhurst, J., Ghimire, S., Suwanmanee, S., Pieterse, L., Metcalf Pate, K. A., Bunyan, E., Bannister, R., Cihlar, T., Porter, D. P., & Griffin, D. E. (2023). Effect of remdesivir post-exposure prophylaxis and treatment on pathogenesis of measles in rhesus macaques. *Sci Rep*, *13*(1), 6463. <https://doi.org/10.1038/s41598-023-33572-7>
- Pernet, O., Wang, Y. E., & Lee, B. (2012). Henipavirus receptor usage and tropism. *Curr Top Microbiol Immunol*, *359*, 59-78. [https://doi.org/10.1007/82\\_2012\\_222](https://doi.org/10.1007/82_2012_222)
- Perry, R. T., & Halsey, N. A. (2004). The clinical significance of measles: a review. *J Infect Dis*, *189* Suppl 1, S4-16. <https://doi.org/10.1086/377712>
- Petrova, V. N., Sawatsky, B., Han, A. X., Laksono, B. M., Walz, L., Parker, E., Pieper, K., Anderson, C. A., de Vries, R. D., Lanzavecchia, A., Kellam, P., von Messling, V., de Swart, R. L., & Russell, C. A. (2019). Incomplete genetic reconstitution of B cell pools contributes to prolonged immunosuppression after measles. *Sci Immunol*, *4*(41). <https://doi.org/10.1126/sciimmunol.aay6125>
- Pfizer. (August 21, 2023). *U.S. FDA Approves ABRYSVO™, Pfizer's Vaccine for the Prevention of Respiratory Syncytial Virus (RSV) in Infants Through Active Immunization of Pregnant Individuals 32-36 Weeks of Gestational Age* Retrieved June 20, 2024 from <https://www.pfizer.com/news/press-release/press-release-detail/us-fda-approves-abrysvotm-pfizers-vaccine-prevention-0>
- Porotto, M., Orefice, G., Yokoyama, C. C., Mungall, B. A., Realubit, R., Sganga, M. L., Aljofan, M., Whitt, M., Glickman, F., & Moscona, A. (2009). Simulating henipavirus multicycle replication in a screening assay leads to identification of a promising candidate for therapy. *J Virol*, *83*(10), 5148-5155. <https://doi.org/10.1128/jvi.00164-09>
- Quintero-Gil, C., Rendon-Marin, S., Martinez-Gutierrez, M., & Ruiz-Saenz, J. (2019). Origin of Canine Distemper Virus: Consolidating Evidence to Understand Potential Zoonoses. *Front Microbiol*, *10*, 1982. <https://doi.org/10.3389/fmicb.2019.01982>
- Rago, A. R. P., D'Arrigo, S. F., Osmani, M., Espinosa, C. M., & Torres, C. M. (2024). Respiratory Syncytial Virus: Epidemiology, Burden of Disease, and Clinical Update. *Adv Pediatr*, *71*(1), 107-118. <https://doi.org/10.1016/j.yapd.2024.02.003>
- Ramphal, R., Small, P. M., Shands, J. W., Jr., Fischlschweiger, W., & Small, P. A., Jr. (1980). Adherence of *Pseudomonas aeruginosa* to tracheal cells injured by influenza infection or by endotracheal intubation. *Infect Immun*, *27*(2), 614-619. <https://doi.org/10.1128/iai.27.2.614-619.1980>

- Ray, G., Schmitt, P. T., & Schmitt, A. P. (2016). C-Terminal DxD-Containing Sequences within Paramyxovirus Nucleocapsid Proteins Determine Matrix Protein Compatibility and Can Direct Foreign Proteins into Budding Particles. *J Virol*, *90*(7), 3650-3660. <https://doi.org/10.1128/jvi.02673-15>
- Rendon-Marin, S., da Fontoura Budaszewski, R., Canal, C. W., & Ruiz-Saenz, J. (2019). Tropism and molecular pathogenesis of canine distemper virus. *Virol J*, *16*(1), 30. <https://doi.org/10.1186/s12985-019-1136-6>
- Resch, B. (2017). Product review on the monoclonal antibody palivizumab for prevention of respiratory syncytial virus infection. *Hum Vaccin Immunother*, *13*(9), 2138-2149. <https://doi.org/10.1080/21645515.2017.1337614>
- Rhodin, M. H. J., Reyes, A. C., Balakrishnan, A., Bisht, N., Kelly, N. M., Gibbons, J. S., Lloyd, J., Vaine, M., Cressey, T., Crepeau, M., Shen, R., Manalo, N., Castillo, J., Levene, R. E., Leonard, D., Zang, T., Jiang, L., Daniels, K., Cox, R. M., . . . Or, Y. S. (2024). The small molecule inhibitor of SARS-CoV-2 3CLpro EDP-235 prevents viral replication and transmission in vivo. *Nat Commun*, *15*(1), 6503. <https://doi.org/10.1038/s41467-024-50931-8>
- Sakai, K., Yoshikawa, T., Seki, F., Fukushi, S., Tahara, M., Nagata, N., Ami, Y., Mizutani, T., Kurane, I., Yamaguchi, R., Hasegawa, H., Saijo, M., Komase, K., Morikawa, S., & Takeda, M. (2013). Canine distemper virus associated with a lethal outbreak in monkeys can readily adapt to use human receptors. *J Virol*, *87*(12), 7170-7175. <https://doi.org/10.1128/jvi.03479-12>
- Sanford, B. A., Shelokov, A., & Ramsay, M. A. (1978). Bacterial adherence to virus-infected cells: a cell culture model of bacterial superinfection. *J Infect Dis*, *137*(2), 176-181. <https://doi.org/10.1093/infdis/137.2.176>
- Satterfield, B. A., Borisevich, V., Foster, S. L., Rodriguez, S. E., Cross, R. W., Fenton, K. A., Agans, K. N., Basler, C. F., Geisbert, T. W., & Mire, C. E. (2019). Antagonism of STAT1 by Nipah virus P gene products modulates disease course but not lethal outcome in the ferret model. *Sci Rep*, *9*(1), 16710. <https://doi.org/10.1038/s41598-019-53037-0>
- Satterfield, B. A., Cross, R. W., Fenton, K. A., Borisevich, V., Agans, K. N., Deer, D. J., Graber, J., Basler, C. F., Geisbert, T. W., & Mire, C. E. (2016). Nipah Virus C and W Proteins Contribute to Respiratory Disease in Ferrets. *J Virol*, *90*(14), 6326-6343. <https://doi.org/10.1128/jvi.00215-16>
- Schilling, W. H. K., Jittamala, P., Watson, J. A., Boyd, S., Luvira, V., Siripoon, T., Ngamprasertchai, T., Batty, E. M., Cruz, C., Callery, J. J., Singh, S., Saroj, M., Kruabkontho, V., Ngernseng, T., Tanglakmankhong, N., Tubprasert, J., Abdad, M. Y., Madmanee, W., Kouhathong, J., . . . White, N. J. (2024). Antiviral efficacy of molnupiravir versus ritonavir-boosted nirmatrelvir in patients with early symptomatic COVID-19 (PLATCOV): an open-label, phase 2, randomised, controlled, adaptive trial. *Lancet Infect Dis*, *24*(1), 36-45. [https://doi.org/10.1016/s1473-3099\(23\)00493-0](https://doi.org/10.1016/s1473-3099(23)00493-0)
- Schwarzmann, S. W., Adler, J. L., Sullivan, R. J., & Marine, W. M. (1971). Bacterial pneumonia during the Hong Kong influenza epidemic of 1968-1969: experience in a city-county hospital. *Archives of internal medicine*, *127*(6), 1037-1041.

- Science. (2022a). *Bad news for Paxlovid? Coronavirus can find multiple ways to evade COVID-19 drug*. Retrieved August 25, 2024 from <https://www.science.org/content/article/bad-news-paxlovid-coronavirus-can-find-multiple-ways-evade-covid-19-drug>
- Science. (2022b). Paxlovid Resistance: Is It Just a Matter of Time Now? [Commentary]. *Science*. <https://www.science.org/content/blog-post/paxlovid-resistance-it-just-matter-time-now>
- Sejvar, J. J., Hossain, J., Saha, S. K., Gurley, E. S., Banu, S., Hamadani, J. D., Faiz, M. A., Siddiqui, F. M., Mohammad, Q. D., Mollah, A. H., Uddin, R., Alam, R., Rahman, R., Tan, C. T., Bellini, W., Rota, P., Breiman, R. F., & Luby, S. P. (2007). Long-term neurological and functional outcome in Nipah virus infection. *Ann Neurol*, 62(3), 235-242. <https://doi.org/10.1002/ana.21178>
- Sencio, V., Machado, M. G., & Trottein, F. (2021). The lung-gut axis during viral respiratory infections: the impact of gut dysbiosis on secondary disease outcomes. *Mucosal Immunol*, 14(2), 296-304. <https://doi.org/10.1038/s41385-020-00361-8>
- Shafran, N., Shafran, I., Ben-Zvi, H., Sofer, S., Sheena, L., Krause, I., Shlomai, A., Goldberg, E., & Sklan, E. H. (2021). Secondary bacterial infection in COVID-19 patients is a stronger predictor for death compared to influenza patients. *Sci Rep*, 11(1), 12703. <https://doi.org/10.1038/s41598-021-92220-0>
- Singh, A., Fatima, L., Shaikh, B., & Khatri, G. (2024). South Asia's Strategic Readiness Amidst Worsening Nipah Virus Threats: Current Situation and Imperatives. *Asia Pac J Public Health*, 10105395241248327. <https://doi.org/10.1177/10105395241248327>
- Sourimant, J., Lieber, C. M., Aggarwal, M., Cox, R. M., Wolf, J. D., Yoon, J. J., Toots, M., Ye, C., Sticher, Z., Kolykhalov, A. A., Martinez-Sobrido, L., Bluemling, G. R., Natchus, M. G., Painter, G. R., & Plemper, R. K. (2022). 4'-Fluorouridine is an oral antiviral that blocks respiratory syncytial virus and SARS-CoV-2 replication. *Science*, 375(6577), 161-167. <https://doi.org/10.1126/science.abj5508>
- Sourimant, J., Thakkar, V. D., Cox, R. M., & Plemper, R. K. (2020). Viral evolution identifies a regulatory interface between paramyxovirus polymerase complex and nucleocapsid that controls replication dynamics. *Sci Adv*, 6(10), eaaz1590. <https://doi.org/10.1126/sciadv.aaz1590>
- Staadegaard, L., Caini, S., Wangchuk, S., Thapa, B., de Almeida, W. A. F., de Carvalho, F. C., Njouom, R., Fasce, R. A., Bustos, P., Kyncl, J., Novakova, L., Caicedo, A. B., de Mora Coloma, D. J., Meijer, A., Hooiveld, M., Huang, S., Wood, T., Guimar, R., Rodrigues, A. P., . . . Paget, J. (2021). The Global Epidemiology of RSV in Community and Hospitalized Care: Findings From 15 Countries. *Open Forum Infect Dis*, 8(7), ofab159. <https://doi.org/10.1093/ofid/ofab159>
- Steichen, O., & Dautheville, S. (2009). Koplik spots in early measles. *Cmaj*, 180(5), 583. <https://doi.org/10.1503/cmaj.080724>
- Steiner, S., Kratzel, A., Barut, G. T., Lang, R. M., Aguiar Moreira, E., Thomann, L., Kelly, J. N., & Thiel, V. (2024). SARS-CoV-2 biology and host interactions. *Nat Rev Microbiol*, 22(4), 206-225. <https://doi.org/10.1038/s41579-023-01003-z>
- Strizki, J. M., Gaspar, J. M., Howe, J. A., Hutchins, B., Mohri, H., Nair, M. S., Kinek, K. C., McKenna, P., Goh, S. L., & Murgolo, N. (2024). Molnupiravir maintains antiviral activity against SARS-CoV-2 variants and exhibits a high barrier to the development of

- resistance. *Antimicrob Agents Chemother*, 68(1), e0095323. <https://doi.org/10.1128/aac.00953-23>
- Strizki, J. M., Grobler, J. A., Murgolo, N., Fridman, A., Johnson, M. G., Du, J., Carmelitano, P., Brown, M. L., Paschke, A., & De Anda, C. (2023). Virologic Outcomes with Molnupiravir in Non-hospitalized Adult Patients with COVID-19 from the Randomized, Placebo-Controlled MOVE-OUT Trial. *Infect Dis Ther*, 12(12), 2725-2743. <https://doi.org/10.1007/s40121-023-00891-1>
- Sun, X., Sui, H., Fisher, J. T., Yan, Z., Liu, X., Cho, H. J., Joo, N. S., Zhang, Y., Zhou, W., Yi, Y., Kinyon, J. M., Lei-Butters, D. C., Griffin, M. A., Naumann, P., Luo, M., Ascher, J., Wang, K., Frana, T., Wine, J. J., . . . Engelhardt, J. F. (2010). Disease phenotype of a ferret CFTR-knockout model of cystic fibrosis. *J Clin Invest*, 120(9), 3149-3160. <https://doi.org/10.1172/jci43052>
- Thakkar, V. D., Cox, R. M., Sawatsky, B., da Fontoura Budaszewski, R., Sourimant, J., Wabbel, K., Makhsous, N., Greninger, A. L., von Messling, V., & Plemper, R. K. (2018). The Unstructured Paramyxovirus Nucleocapsid Protein Tail Domain Modulates Viral Pathogenesis through Regulation of Transcriptase Activity. *J Virol*, 92(8). <https://doi.org/10.1128/jvi.02064-17>
- Thakur, M., Zhou, R., Mohan, M., Marathe, A., Chen, J., Hoops, S., Machi, D., Lewis, B., & Vullikanti, A. (2022). COVID's collateral damage: likelihood of measles resurgence in the United States. *BMC Infect Dis*, 22(1), 743. <https://doi.org/10.1186/s12879-022-07703-w>
- Tian, L., Qiang, T., Liang, C., Ren, X., Jia, M., Zhang, J., Li, J., Wan, M., YuWen, X., Li, H., Cao, W., & Liu, H. (2021). RNA-dependent RNA polymerase (RdRp) inhibitors: The current landscape and repurposing for the COVID-19 pandemic. *Eur J Med Chem*, 213, 113201. <https://doi.org/10.1016/j.ejmech.2021.113201>
- Tigabu, B., Rasmussen, L., White, E. L., Tower, N., Saeed, M., Bukreyev, A., Rockx, B., LeDuc, J. W., & Noah, J. W. (2014). A BSL-4 high-throughput screen identifies sulfonamide inhibitors of Nipah virus. *Assay Drug Dev Technol*, 12(3), 155-161. <https://doi.org/10.1089/adt.2013.567>
- Tremaglio, C. Z., Noton, S. L., Deflubé, L. R., & Fearn, R. (2013). Respiratory syncytial virus polymerase can initiate transcription from position 3 of the leader promoter. *J Virol*, 87(6), 3196-3207. <https://doi.org/10.1128/jvi.02862-12>
- Trimpert, J., Vladimirova, D., Dietert, K., Abdelgawad, A., Kunec, D., Dökel, S., Voss, A., Gruber, A. D., Bertzbach, L. D., & Osterrieder, N. (2020). The Roborovski Dwarf Hamster Is A Highly Susceptible Model for a Rapid and Fatal Course of SARS-CoV-2 Infection. *Cell Rep*, 33(10), 108488. <https://doi.org/10.1016/j.celrep.2020.108488>
- Uchida, S., Horie, R., Sato, H., Kai, C., & Yoneda, M. (2018). Possible role of the Nipah virus V protein in the regulation of the interferon beta induction by interacting with UBX domain-containing protein1. *Sci Rep*, 8(1), 7682. <https://doi.org/10.1038/s41598-018-25815-9>
- Update: outbreak of Nipah virus--Malaysia and Singapore, 1999. (1999). *MMWR Morb Mortal Wkly Rep*, 48(16), 335-337.
- Ursell, L. K., Haiser, H. J., Van Treuren, W., Garg, N., Reddivari, L., Vanamala, J., Dorrestein, P. C., Turnbaugh, P. J., & Knight, R. (2014). The intestinal metabolome: an intersection



- between microbiota and host. *Gastroenterology*, 146(6), 1470-1476.  
<https://doi.org/10.1053/j.gastro.2014.03.001>
- Ventre, K., & Randolph, A. G. (2007). Ribavirin for respiratory syncytial virus infection of the lower respiratory tract in infants and young children. *Cochrane Database Syst Rev*(1), Cd000181. <https://doi.org/10.1002/14651858.CD000181.pub3>
- Vicenti, I., Zazzi, M., & Saladini, F. (2021). SARS-CoV-2 RNA-dependent RNA polymerase as a therapeutic target for COVID-19. *Expert Opin Ther Pat*, 31(4), 325-337.  
<https://doi.org/10.1080/13543776.2021.1880568>
- Vigant, F., & Lee, B. (2011). Hendra and nipah infection: pathology, models and potential therapies. *Infect Disord Drug Targets*, 11(3), 315-336.  
<https://doi.org/10.2174/187152611795768097>
- von Messling, V., Svitek, N., & Cattaneo, R. (2006). Receptor (SLAM [CD150]) recognition and the V protein sustain swift lymphocyte-based invasion of mucosal tissue and lymphatic organs by a morbillivirus. *J Virol*, 80(12), 6084-6092. <https://doi.org/10.1128/jvi.00357-06>
- von Messling, V., Zimmer, G., Herrler, G., Haas, L., & Cattaneo, R. (2001). The hemagglutinin of canine distemper virus determines tropism and cytopathogenicity. *J Virol*, 75(14), 6418-6427. <https://doi.org/10.1128/jvi.75.14.6418-6427.2001>
- Wagner, N. D., Liu, H., Rohrs, H. W., Amarasinghe, G. K., Gross, M. L., & Leung, D. W. (2022). Nipah Virus V Protein Binding Alters MDA5 Helicase Folding Dynamics. *ACS Infect Dis*, 8(1), 118-128. <https://doi.org/10.1021/acsinfecdis.1c00403>
- Walls, A. C., Park, Y. J., Tortorici, M. A., Wall, A., McGuire, A. T., & Veesler, D. (2020). Structure, Function, and Antigenicity of the SARS-CoV-2 Spike Glycoprotein. *Cell*, 181(2), 281-292.e286. <https://doi.org/10.1016/j.cell.2020.02.058>
- Wang, X., Li, Y., Shi, T., Bont, L. J., Chu, H. Y., Zar, H. J., Wahi-Singh, B., Ma, Y., Cong, B., Sharland, E., Riley, R. D., Deng, J., Figueras-Aloy, J., Heikkinen, T., Jones, M. H., Liese, J. G., Markić, J., Mejias, A., Nunes, M. C., . . . Nair, H. (2024). Global disease burden of and risk factors for acute lower respiratory infections caused by respiratory syncytial virus in preterm infants and young children in 2019: a systematic review and meta-analysis of aggregated and individual participant data. *Lancet*, 403(10433), 1241-1253.  
[https://doi.org/10.1016/s0140-6736\(24\)00138-7](https://doi.org/10.1016/s0140-6736(24)00138-7)
- Watson, A. M., Cushing, A. C., Sheldon, J. D., Anis, E., Wilkes, R. P., Dubovi, E. J., & Craig, L. E. (2020). Natural Canine Distemper Virus Infection in Linnaeus's 2-Toed Sloths (*Choloepus didactylus*). *Vet Pathol*, 57(2), 311-315. <https://doi.org/10.1177/0300985819900017>
- Webster, L. T., & Clow, A. D. (1932). THE ASSOCIATION OF PNEUMOCOCCI, HEMOPHILUS INFLUENZAE, AND STREPTOCOCCUS HEMOLYTICUS WITH CORYZA, PHARYNGITIS, AND SINUSITIS IN MAN. *J Exp Med*, 55(3), 445-453. <https://doi.org/10.1084/jem.55.3.445>
- WHO. (2018). *Nipah virus*. Retrieved May 23, 2024 from <https://www.who.int/news-room/fact-sheets/detail/nipah-virus>
- WHO. (2023a). *Statement on the fifteenth meeting of the IHR (2005) Emergency Committee on the COVID-19 pandemic*. Retrieved July 11, 2024 from [https://www.who.int/news/item/05-05-2023-statement-on-the-fifteenth-meeting-of-the-international-health-regulations-\(2005\)-emergency-committee-regarding-the-coronavirus-disease-\(covid-19\)-pandemic](https://www.who.int/news/item/05-05-2023-statement-on-the-fifteenth-meeting-of-the-international-health-regulations-(2005)-emergency-committee-regarding-the-coronavirus-disease-(covid-19)-pandemic)

- WHO. (2023b). *WHO COVID-19 dashboard*. Retrieved May 2, 2024 from <https://data.who.int/dashboards/covid19/cases>
- WHO. (2024). *WHO COVID-19 dashboard*. <https://data.who.int/dashboards/covid19/deaths?n=0>
- Wilkes, R. P. (2022). Canine Distemper Virus in Endangered Species: Species Jump, Clinical Variations, and Vaccination. *Pathogens*, *12*(1). <https://doi.org/10.3390/pathogens12010057>
- Wolf, J. D., & Plemper, R. K. (2024). A three-way interface of the Nipah virus phosphoprotein X-domain coordinates polymerase movement along the viral genome. *J Virol*, e0098624. <https://doi.org/10.1128/jvi.00986-24>
- Wolf, J. D., Serrine, M. R., Cox, R. M., & Plemper, R. K. (2024). Structural basis of paramyxo- and pneumovirus polymerase inhibition by non-nucleoside small-molecule antivirals. *Antimicrob Agents Chemother*, e0080024. <https://doi.org/10.1128/aac.00800-24>
- Wölfel, R., Corman, V. M., Guggemos, W., Seilmaier, M., Zange, S., Müller, M. A., Niemeyer, D., Jones, T. C., Vollmar, P., Rothe, C., Hoelscher, M., Bleicker, T., Brünink, S., Schneider, J., Ehmman, R., Zwirgmaier, K., Drosten, C., & Wendtner, C. (2020). Virological assessment of hospitalized patients with COVID-2019. *Nature*, *581*(7809), 465-469. <https://doi.org/10.1038/s41586-020-2196-x>
- Wrotek, A., Wrotek, O., & Jackowska, T. (2023). The Impact of RSV Hospitalization on Children's Quality of Life. *Diseases*, *11*(3). <https://doi.org/10.3390/diseases11030111>
- Xie, J., Ouizougoun-Oubari, M., Wang, L., Zhai, G., Wu, D., Lin, Z., Wang, M., Ludeke, B., Yan, X., Nilsson, T., Gao, L., Huang, X., Fearn, R., & Chen, S. (2024). Structural basis for dimerization of a paramyxovirus polymerase complex. *Nat Commun*, *15*(1), 3163. <https://doi.org/10.1038/s41467-024-47470-7>
- Xu, K., Broder, C. C., & Nikolov, D. B. (2012). Ephrin-B2 and ephrin-B3 as functional henipavirus receptors. *Semin Cell Dev Biol*, *23*(1), 116-123. <https://doi.org/10.1016/j.semcdb.2011.12.005>
- Yabukarski, F., Lawrence, P., Tarbouriech, N., Bourhis, J. M., Delaforge, E., Jensen, M. R., Ruigrok, R. W., Blackledge, M., Volchkov, V., & Jamin, M. (2014). Structure of Nipah virus unassembled nucleoprotein in complex with its viral chaperone. *Nat Struct Mol Biol*, *21*(9), 754-759. <https://doi.org/10.1038/nsmb.2868>
- Yanagi, Y., Takeda, M., & Ohno, S. (2006). Measles virus: cellular receptors, tropism and pathogenesis. *J Gen Virol*, *87*(Pt 10), 2767-2779. <https://doi.org/10.1099/vir.0.82221-0>
- Yokomichi, H., Mochizuki, M., Lee, J. J., Kojima, R., Horiuchi, S., Ooka, T., & Yamagata, Z. (2023). Antibiotic prescription for outpatients with influenza and subsequent hospitalisation: A cohort study using insurance data. *Influenza Other Respir Viruses*, *17*(11), e13221. <https://doi.org/10.1111/irv.13221>
- Yoon, J. J., Krumm, S. A., Ndungu, J. M., Hoffman, V., Bankamp, B., Rota, P. A., Sun, A., Snyder, J. P., & Plemper, R. K. (2009). Target analysis of the experimental measles therapeutic AS-136A. *Antimicrob Agents Chemother*, *53*(9), 3860-3870. <https://doi.org/10.1128/aac.00503-09>
- Yu, X., Abeywickrema, P., Bonneux, B., Behera, I., Anson, B., Jacoby, E., Fung, A., Adhikary, S., Bhaumik, A., Carbajo, R. J., De Bruyn, S., Miller, R., Patrick, A., Pham, Q., Piassek, M., Verheyen, N., Shareef, A., Sutto-Ortiz, P., Ysebaert, N., . . . Jin, Z. (2023). Structural and

- mechanistic insights into the inhibition of respiratory syncytial virus polymerase by a non-nucleoside inhibitor. *Commun Biol*, 6(1), 1074. <https://doi.org/10.1038/s42003-023-05451-4>
- Zegers, S. H., Dieleman, J., van der Bruggen, T., Kimpfen, J., & de Jong-de Vos van Steenwijk, C. (2017). The influence of antibiotic prophylaxis on bacterial resistance in urinary tract infections in children with spina bifida. *BMC Infect Dis*, 17(1), 63. <https://doi.org/10.1186/s12879-016-2166-y>
- Zhang, Q., Hu, J., Feng, J. W., Hu, X. T., Wang, T., Gong, W. X., Huang, K., Guo, Y. X., Zou, Z., Lin, X., Zhou, R., Yuan, Y. Q., Zhang, A. D., Wei, H., Cao, G., Liu, C., Chen, L. L., & Jin, M. L. (2020). Influenza infection elicits an expansion of gut population of endogenous *Bifidobacterium animalis* which protects mice against infection. *Genome Biol*, 21(1), 99. <https://doi.org/10.1186/s13059-020-02007-1>
- Zhou, Y., Gammeltoft, K. A., Ryberg, L. A., Pham, L. V., Tjørnelund, H. D., Binderup, A., Duarte Hernandez, C. R., Fernandez-Antunez, C., Offersgaard, A., Fahnøe, U., Peters, G. H. J., Ramirez, S., Bukh, J., & Gottwein, J. M. (2022). Nirmatrelvir-resistant SARS-CoV-2 variants with high fitness in an infectious cell culture system. *Sci Adv*, 8(51), eadd7197. <https://doi.org/10.1126/sciadv.add7197>
- Zuo, T., Liu, Q., Zhang, F., Lui, G. C., Tso, E. Y., Yeoh, Y. K., Chen, Z., Boon, S. S., Chan, F. K., Chan, P. K., & Ng, S. C. (2021). Depicting SARS-CoV-2 faecal viral activity in association with gut microbiota composition in patients with COVID-19. *Gut*, 70(2), 276-284. <https://doi.org/10.1136/gutjnl-2020-322294>
- Zuo, T., Zhang, F., Lui, G. C. Y., Yeoh, Y. K., Li, A. Y. L., Zhan, H., Wan, Y., Chung, A. C. K., Cheung, C. P., Chen, N., Lai, C. K. C., Chen, Z., Tso, E. Y. K., Fung, K. S. C., Chan, V., Ling, L., Joynt, G., Hui, D. S. C., Chan, F. K. L., . . . Ng, S. C. (2020). Alterations in Gut Microbiota of Patients With COVID-19 During Time of Hospitalization. *Gastroenterology*, 159(3), 944-955.e948. <https://doi.org/10.1053/j.gastro.2020.05.048>

## VITAE

### Education

- Doctor of Philosophy (December 2024): Translational Biomedical Sciences; Georgia State University, Atlanta, GA
- Bachelor of Science (May 2017): Biology/Biological Sciences; Georgia State University, Atlanta, GA

### Research and Teaching Experience

- Graduate Research Assistant: Institute for Biomedical Sciences; June 2019 – present; Georgia State University, Atlanta, GA
- Graduate Research Assistant: Department of Biology; Sept. 2017 – June 2019; Georgia State University, Atlanta, GA
- Lead Graduate Teaching Assistant: Department of Biology; Aug. 2018 – June 2019; Georgia State University, Atlanta, GA
- Graduate Teaching Assistant: Department of Biology; Aug. 2017 – Aug. 2018; Georgia State University, Atlanta, GA
- Undergraduate Research Assistant: National B Virus Research Laboratory and Viral Immunology Center; Nov. 2016 – Aug. 2017; Georgia State University, Atlanta, GA

### Presentations

- American Society for Virology Conference: June 2024; Columbus, OH
- Southeast Regional Virology Conference: April 2024; Emory Conference Center, Atlanta, GA
- Translational Biomedical Sciences Association Research Day: March 2024; Georgia State University, Atlanta, GA
- Atlanta Magnetic Resonance Symposium: Dec. 2023; Georgia State University, Atlanta, GA
- Antiviral Countermeasures Development Center Retreat: Oct. 2023; Emory Conference Center, Atlanta, GA
- American Society for Virology Conference: July 2023; University of Georgia, Athens, GA
- Southeast Regional Virology Conference: Sept. 2022; Emory Conference Center, Atlanta, GA
- American Society for Virology Conference: July 2022; University of Wisconsin, Madison, WI
- Measles Virus Mini Symposium: July 2022; Mayo Clinic, Rochester, MN
- Gordon Research Conference: June 2019; Bates College, Lewiston, ME

- International Herpes Workshop: July 2018; University of British Columbia, Vancouver, BC Canada
- Georgia State Undergraduate Research Conference: April 2016; Georgia State University, Atlanta, GA

**Awards**

- Best Oral Presentation Award (2023); Antiviral Countermeasures Development Center Retreat
- American Society for Virology Student Travel Award (2024)
- American Society for Virology Student Travel Award (2023)
- American Society for Virology Student Travel Award (2022)
- American Society for Virology Student Travel Award (2021); meeting cancelled due to COVID-19 pandemic